Ministry of Education
Department of Higher Education
East Yangon University

East Yangon University
Research Journal

Vol.12, No.2 June, 2026

Ministry of Education
Department of Higher Education
East Yangon University

East Yangon University Research Journal

Vol.12, No.1 June, 2026

Ministry of Education
Department of Higher Education
East Yangon University
Research Journal
2026 Vol.12, No.1

Editorial Board

Contents

Preparation and Characterization of Handmade Paper from Agro-Waste Materials

Ommar Thet Kyaw[1], Khin Saw Oo[2], Nu Nu Khine[3]

Abstract

This project deals with on finding environmentally friendly economical process for handmade paper sheets. Agro-waste materials are one of the most important materials that uses for pulp and paper production due to its abundance and cost-effectiveness. The physicochemical properties such as pH, moisture content, ash content, specific gravity and bulk density of agro materials were measured by conventional methods. In the present work, different concentrations of sodium hydroxide were varied as (4, 6, 8 %) w/v NaOH liquor the ratio of agro-waste materials (rice straw/grass) to liquor NaOH ratio of (10:1) weight by volume, temperature at 170 ℃ and cooking time 2h. Kraft pulping process is chosen because process control is relatively easy and cooking chemicals are not expensive and then spent chemicals can be recovered. The characterization of prepared papers were measured by the physicomechanical properties such as thickness, tensile strength, elongation at break, tear strength, water absorption and oil absorption. The prepared papers were carried out by FTIR and SEM analysis. This study will provide that agro-waste materials can reduce the reliance on trees and other non-renewable sources for the production of paper and it can also reduce environmental pollution.

Keywords: paper sheet, sodium hydroxide, agro-waste, kraft pulping, liquor

Introduction

Rice straw is an abundant and easily available raw material in Asian countries as it is produced in almost equal quantities during grain production and can be procured by paper mills at a lower cost. Bleached straw pulp can be applied into a common culture paper making, also can be used with wood pulp to make high-quality printing paper and writing paper (Joseph *et al.*, 1994).The main components of paper are cellulose and hemicellulose. The plant fibers for papermaking include wood fiber and non-wood fiber. The main compositions of plant fibers are cellulose, hemicellulose, and lignin.

Paper pulping is a process of removing lignin as much as possible and retaining cellulose and hemicellulose. Wood fiber is a high-quality papermaking material and it has a great advantage in the paper industry. With the rapid development of industry, the contradiction between supply and demand of wood, the search for non-wood fiber paper raw material is a realistic and urgent problem to be solved (Joseph, *et al.*, 1994).

Kraft pulping is able to remove much of the lignin, which can discolor the pulp and weaken its fibers. As a result, kraft pulping often produces bright, strong, and high-quality pulp. The high pH of the sodium hydroxide solution also helps to remove any impurities in the wood such as resin and fat. NaOH is a highly effective lignin solvent, which makes it possible to achieve high yields of pulp with a relatively short cooking time. Secondly, sodium hydroxide is relatively cheap and readily available, making it a cost-effective choice for kraft pulping (Krishna, *et al.*, 2012).

At present, the recycling of waste paper in developed countries in the world has been quite horizontal in terms of scale and production technology. The recycling of forest paper has gradually become the two developing trends of modern paper pulping and paper making industry. About 40% of the fiber raw materials in paper pulping industry comes from waste paper of which the amount and proportion will continue to grow (Krishna, *et al.*, 2012).

[1]Dr, Associate Professor, Department of Chemistry, East Yangon University University
[2]Dr. Professor and Head, Department of Chemistry, East Yangon University University
[3]Dr. Professor, Department of Chemistry, East Yangon University University

Figure 1 grass

Figure 2 rice straw

Materials and Methods

Collection of Samples

The samples were collected from Nyaung Ni Village, Thongwa Townships, Yangon Division.

Determination of Physicochemical Properties of Agro-Waste Materials

The physicochemical properties such as pH, moisture content, ash content, specific gravity and bulk density of agro-waste materials were measured with their respective methods.

Sodium hydroxide in Kraft Pulping

Sodium hydroxide is used in the production of pulp by the kraft pulping process. Kraft pulping is typically used to produce pulp for packaging, corrugated cardboard, and other types of paper products. One of the main advantages of kraft pulping is that it produces high-quality pulp that is well-suited for use in a variety of paper products. Kraft pulping is able to remove much of the lignin, which can discolor the pulp and weaken its fibers. As a result, kraft pulping often produces bright, strong, and high-quality pulp.

Preparation of Pulp Solution from Waste Materials

150g of agro-waste material was cut into 0.5 cm length and washed with tap water to remove impurities. Waste material was treated with 6g of sodium hydroxide with 1000 mL of distilled water at 1 hr. In pulping process, waste material was treated with 4,6,8 % w/v NaOH respectively. The best result from caustic percentage was (6%NaOH) because the resulting pulp showed the less amount of lignin as shown in Table 2. After boiling for 1h, the liquid was run off and waste paper was washed with water carefully and then the mixture was added 2 g sodium carbonate, Na_2CO_3 and 5 mL of acetic acid with 1000 mL of distilled water. The solution was boiled at 1 h and then 5g of Bees wax was added into the solution during the heating. The bleaching agent 30 mL sodium hypochlorite was poured. Then the pulp solution was obtained.

Handmade paper processing from Agro -Waste materials

Rice straw was cut into small pieces with knife. Rice straw was cleaning with tap water to remove other impurities. Rice straw was soaked for 30 min in a 15 % solution of sodium carbonate, Na_2CO_3 at 100 °C. After removing of impurities from rice straw, the mass ratio of NaOH solution to straw 10:1 was cooked with ((4,6,8 %) w/v NaOH) reaction time 2 hrs and reaction temperature at 170 °C. For quick digesting and consistent pulp, two knives containing beater were used. The beating was carried out until the pulp consistency. To

smooth out of the pulp, cylinder mold press with rollers was used. Traces of water in pulp were removed with tetron cloth sheet by pressing. The wet sheet was dried at 110 ℃ by sheet former machine. Finally, the smooth product of paper was obtained (Krishna, *et al.*, 2012).

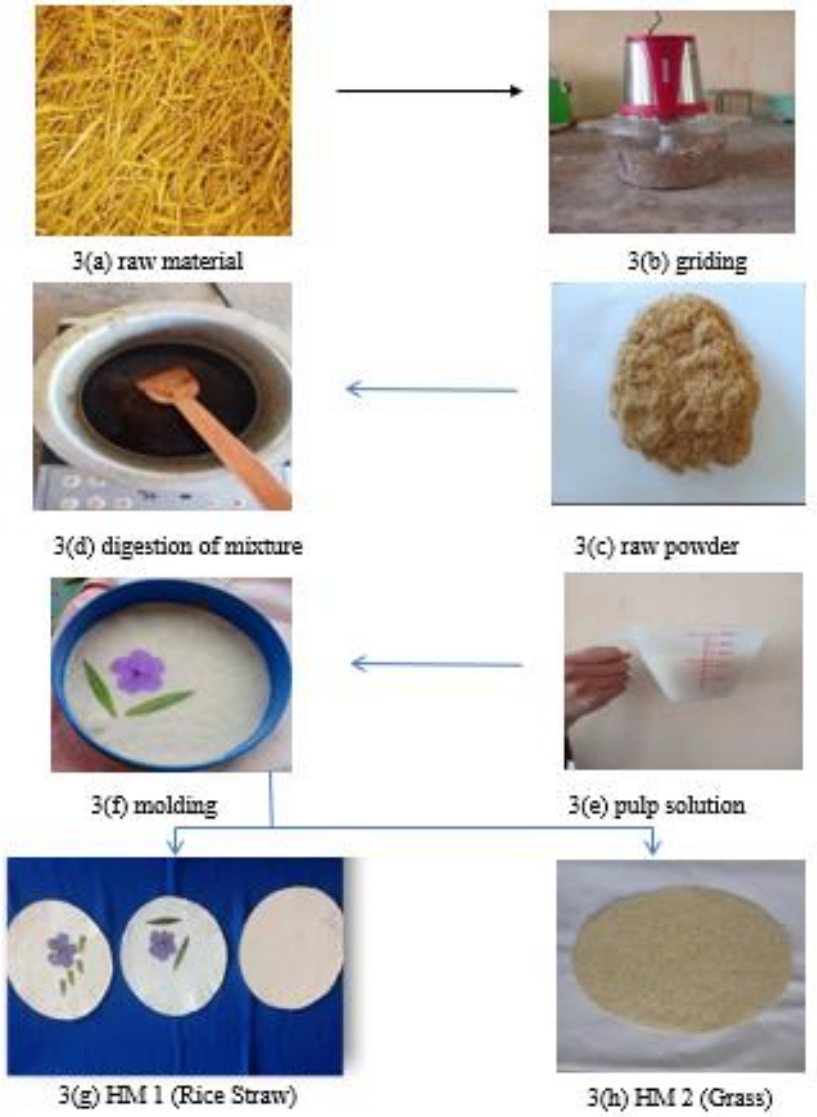

Characterization of Physicomechanical Properties of Agro-Waste Material Paper

On the physicomechanical properties, the prepared handmade paper with colloidal mixtures with the additive materials such as NaOH, Na_2CO_3, acetic acid, NaClO and beeswax. All of the cellulose base paper mixtures were determined based physicomechanical parameters of weight, thickness, tensile strength, tear endurance strength, water absorption and oil absorption shown in table 3.

Results and Discussion

Physicochemical Properties of Raw Agro-Waste Materials

In the present work, physicochemical properties such as pH, moisture, ash, specific gravity and bulk density of agro materials were studied as shown in table 1.

Table 1 Physicochemical Properties of Raw Agro-Waste Materials

Properties	Rice Straw	Grass
Moisture content(%)	10.06	11.2
Ash content(%)	40	30
pH value	9.2	8.9
Specific gravity(kgm^{-3})	2.05	2.39
Bulk density(gcm^{-3})	65	70

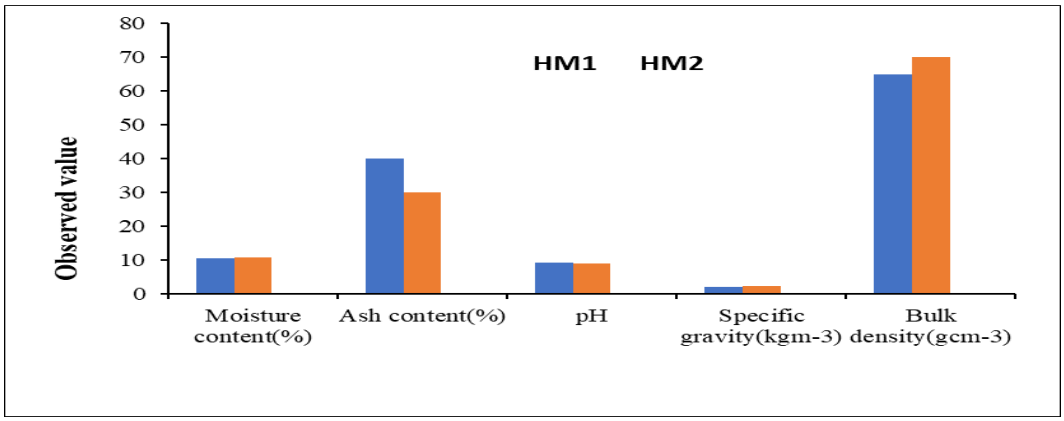

Figure 4 Physicochemical properties of agro-waste materials

Pulp Properties of Agro-Waste Materials

The properties such as yield%, Kappa Number of agro-waste materials were investigated by Tappi method.

Table 2 Produced Pulp Properties

% w/v NaOH	Yield %	Kappa Number
4	42	24
6	46	18
8	34	13

Characterization of Prepared Handmade Papers

FTIR Analysis

FTIR spectrum of selected prepared handmade paper figure showed the strong band 3343 cm^{-1} to stretching vibration for –OH group. The band at 1651 cm^{-1} can be attributed due to the stretching of carbonyl group.

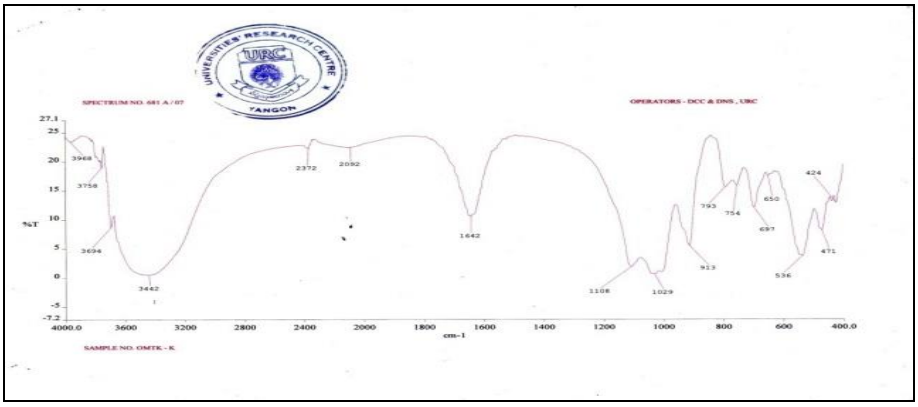

Figure 5 FTIR spectrum of agro- waste materials for HM1

Table 3 FTIR band assignment for Prepared Paper for Rice Straw, HM1

Observed Frequency (cm^{-1})	Literature Frequency* (cm^{-1})	Band Assignment
3442	3200 – 3600	υ_{O-H}, stretching
1108	1000 – 1110	υ_{Si-O} stretching
1029	1000-1080	$\upsilon_{Si-O-Si}$ stretching
424-793	450-1000	δ_{Si-H}, δ_{Si-H} bending

*** (Silverstein, *et.al.*, 1998)**

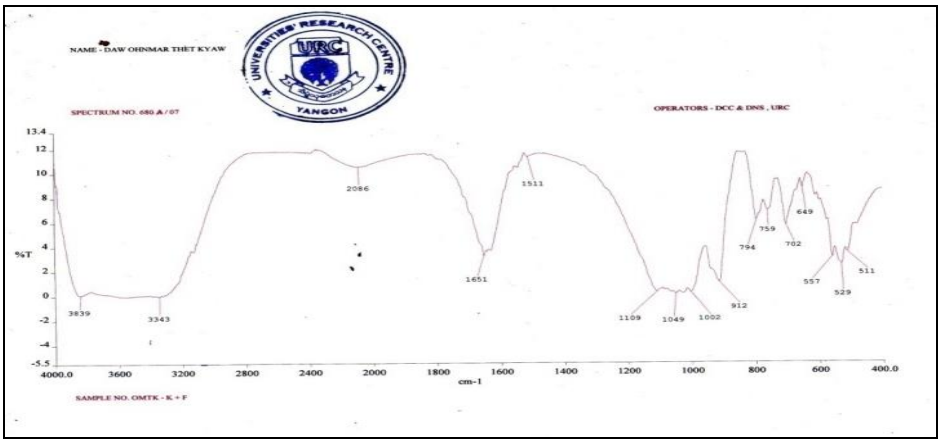

Figure 5 FTIR spectrum of agro- waste material for HM2

Table 4 FTIR band assignment for Prepared Paper for Grass, HM2

Observed Frequency (cm^{-1})	Literature Frequency* (cm^{-1})	Band Assignment
3343	3200 – 3600	υ_{O-H}, stretching
1109	1000 – 1110	υ_{Si-O} stretching
1049	1000-1080	$\upsilon_{Si-O-Si}$ stretching
511-912	450-1000	δ_{Si-H}, δ_{Si-H} bending

*** (Silverstein, *et.al.*, 1998)**

SEM analysis

Figure (a) and (b) show the surface morphology of prepared handmade papers from agro-waste materials. The SEM image in figure (a) has the thread matrix and porous mixture. The SEM image in figure (a) has amorphous sponge like shape.

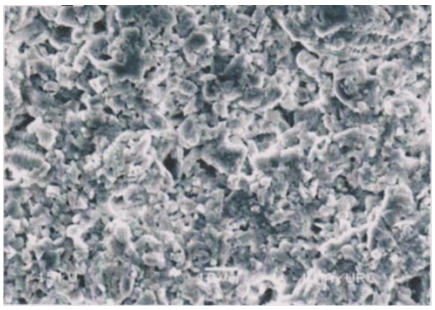

(a) HM 1 (Rice Straw)

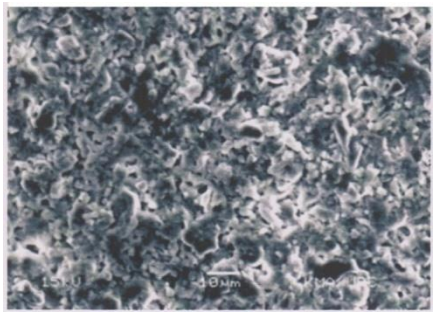

(a) HM 2 (Grass)

Figure 6 SEM micrograph of prepared handmade papers (a) HM1 and (b) HM2

Table 5 Physicomechanical Properties of Prepared Handmade Paper from Agro-Waste Materials

Physicomechanical Properties	HM1	HM2
Thickness (Mm)	0.02	0.03
Tensile strength (MPa)	0.1	0.2
Elongation at break(%)	2	2
Tear strength (kN/m)	4.5	3.6
Water absorption(%)	0.33	0.53
Oil absorption (%)	0.64	0.43

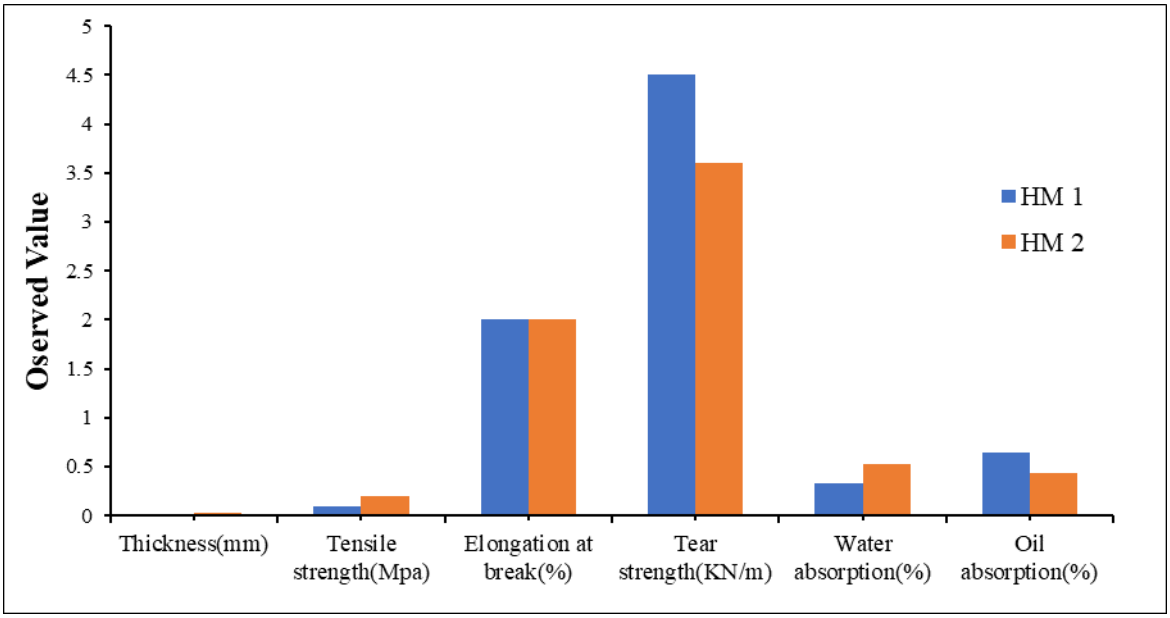

Figure 7 Physicomechanical properties of prepared handmade paper from agro-waste materials

Conclusion

The prepared handmade paper derived from agro-waste materials such as rice straw and grass. The physicochemical properties such as moisture content, ash content, pH, specific gravity and bulk density of agro waste materials were done. The pulp of rice straw and grass obtained by kraft pulping process. The handmade papers were carried out cooking time 2 h at 170℃, 6% w/v NaOH used in pulping process. The optimum amount of the preparation of paper was obtained by using 150g of pulp solution and 2000 mL of water and additive materials Na_2CO_3, NaOH, NaClO and acetic acid. The prepared handmade papers from waste materials were measured by physicomechanical properties. By comparison between the rice straw paper (HM1) and grass (HM2) such as thickness 0.02mm and 0.03mm, tensile strength 0.1 MPa and 0.2 MPa , elongation at break 2 %, tear strength 4.5 KN/m and 3.6 KN/m, water absorption 0.33 % and 0.53 % and oil absorption 0.64% and 0.43. From the data, HM1 paper was high quality than HM2 paper. This research is great economic and environmental benefits in reducing pollution, improving the environment, saving energy and protecting forest resources.

Acknowledgements

We would like to express special thanks to Dr. Myo Min Tun, Pro-rector of East Yangon University for his encouragement, motivation and provision of the research facility to do this work. We are also greatly indebted to Dr. Aye Aye Ko and Dr. Thida Aung , Pro-rectors of East Yangon University for their invaluable suggestion throughout the course of the research . We would like to express deep sense of gratitude to Dr. Khin Saw Oo, Professor and Head, Dr. Nu Nu Khaing , Professor, Department of Chemistry, East Yangon University for their close numerous invaluable suggestion and guidance. Special thank are extended to the colleage in the department of Chemistry, East Yangon University for their help and for working together throughout the research work.

References

Atuheire,G.K. (2012).“Handmade Paper”, A Guide to its Production and Uses, Handbook,**124**

Beckmann, R.A. (1956). “Anleitungzur Technologie”, Karl Keim, Das Papier, 2nd edition. Otto Blersch Verlag, Stuttgart Fisher International, 67,Bioplous Sized Paper (Cobb Test TAPPI T432) **54**: 674-685

Guess, J. M. (1949). “*The Strong Bond/ Weak Bond Theory of Sizing*”. Tappi Journal, Research Laboratory. Physical and Chemical Properties of Book Paper, (Permanence/ Durability of the Book-VII) Richmond, Virginia: Barrow Research Laboratory, 115

Hari, Muraleedhan. K.P. (2010). “Eco-Friendly Handmade Paper”, Shri AMM Murugappachettiar Research Centre, Taramani Chennai, 113

Jha, P. A.S.K. Sinha. (2011). “Application of Rice Straw as Raw Material for Production of Handmade Paper”.Department of Chemical Tech, Sliet, Longowall, Sangroor, IPPTA, **23**, (2), 68

Joseph A. (1994). “Present Status and Future Prospects for Use of Non-wood Plant Fibers for Paper Grade Pulps”, Presentation at American Forest & Paper Association Pulp and Fiber full Seminar, Arizona, November, 14-16

Krishna, M.K. (2012). “Innovation in Papermaking: An LCA of Printing and Writing Paper from Conventional and High Yield Pulp”, Science of the Total Environment, **43**, 307-320

Muraleedhan, K.P. (2010). “Eco-Friendly Handmade paper” Shri AMM Murugappachettiar Research Centre, Taramani Chennai, 600 113

Panshin, A.H. (1964). “Textbook of Wood Technology”, Mac Graw Hill Book Company New York, **13,** 268

Poland, H.K. (2013).“International Presence in A Locally Focused T&TMarket”, Country report, Tissue World Magazine, **12**, 175

Soren, H., (2011). “Manufacture of Straw MDF Fiberboards.” Department of Natural Sciences, Engineering and Mathematics, Mid Sweden University, 224

Tappi. (1969). “A Theory for the Tensile Strength of Paper”, **34**, 235

Wikha, A.S. (2010) “Chemical Pulp Production from Rice Straw by Alkaline Soaking and Cooking with added Alkaline and Alkali.” Department of Forest Products Faculty of Forestry, Kasetsart University, Bangkok 10900, Thailand 3, **124-138**.

Synthesis and Characterization of Basic Soap as a Value-Added Product from Waste Frying Oil

Ko Ko Lwin[1], Ye Yint Naing[2], Yu Nandar Soe[3], Nan Wa Thone Oo[4]

Abstract

Waste frying oil (WFO) is a suitable material for making basic soap. It was purified by using a loofah, corn starch, and activated charcoal. Different percentages of sodium hydroxide were used in basic soap preparation, with glycerine added as a plasticizer. The physicochemical properties of the basic soap, including acid value, pH value, moisture content, foaming activity, free caustic alkali and cleansing activity were evaluated. The antimicrobial activity of the optimum basic soap was also determined. Among the different percentages of 20 % NaOH gave the best results, with an acid values 1.404 ± 0.02 (mg/g), pH 9.896 ± 0.03, moisture content 13.426 ± 0.12 %, foam height of 1.8 ± 0.05 cm and free caustic alkali content of 1.414 ± 0.01 %. These results were within the standard range. The basic soap has been tested against common bacteria (*Bacillus pumilus, Bacillus subtilis, Candida albicans, Escherichia coli, Pseudomonas aeruginosa and Salmonella typhi*). Interpreting the results correctly will help determine the soap's effectiveness against microbes. This research presents a sustainable, cost-effective and environmentally friendly innovation that promotes waste recycling while providing an affordable hygiene product.

Keywords: Waste frying oil, physicochemical property, caustic soda, glycerine

Introduction

Waste frying oil is produced in large amounts from households, restaurants, and food industries. Waste cooking oil use negatively affects both human and animal health, while improper disposal worsens environmental degradation, clogs drains, and contaminates land and aquatic environments. Reusing cooking oil when preparing meals can also increase the body's levels of free radicals, which can lead to inflammation, the main factor in the development of most illnesses like diabetes, and obesity. Excessive bodily inflammation might lower immunity and make you more susceptible to diseases (Gomez and Machado, 2015). WFOs have also been reported to cause serious human health hazards such as heart diseases, stroke, Parkinson's disease, Alzheimer's disease, liver disease, gastrointestinal disorders and even mutagenesis in human body (Potgieter *et al.*, 2004). Therefore, finding effective ways to recycle and reuse waste frying oil is essential for reducing and protecting the environment. It is mainly applied in preparation of biodiesel, chemical raw materials, feed and demeshing agent of concrete product. WFO is one of the low-cost raw materials for making soap. Waste frying oil is rich in triglycerides, which can be converted into soap through a saponification reaction. Transforming waste frying oil into basic soap not only provides a practical solution for waste management but also offers a sustainable and cost-effective alternative to commercial soap (Gomez and Machado, 2015).

Materials and Methods

Collection of Waste Frying Oil Samples

Waste frying oil (WFO) samples were collected from local households and university canteens from East Yangon University in the month of June 2025.

[1] Assistant Lecturer, Department of Chemistry, East Yangon University
[2,3,4] Demonstrators, Department of Chemistry, East Yangon University

Pre-treatment of WFO

Waste frying oil samples were initially filtered using a loofah to remove suspended impurities and solid residues. After filtration, corn starch was added to the oil, and the mixture was heated at approximately 60 ℃ for 15 minutes with gentle stirring. The heated mixture was then filtered again to separate the impurities absorbed by the corn starch. Subsequently, activated charcoal was added to the filtrate and the mixture was shaken thoroughly to enhance adsorption of remaining impurities. Finally, the oil was filtered to obtained purified waste frying oil for further soap production.

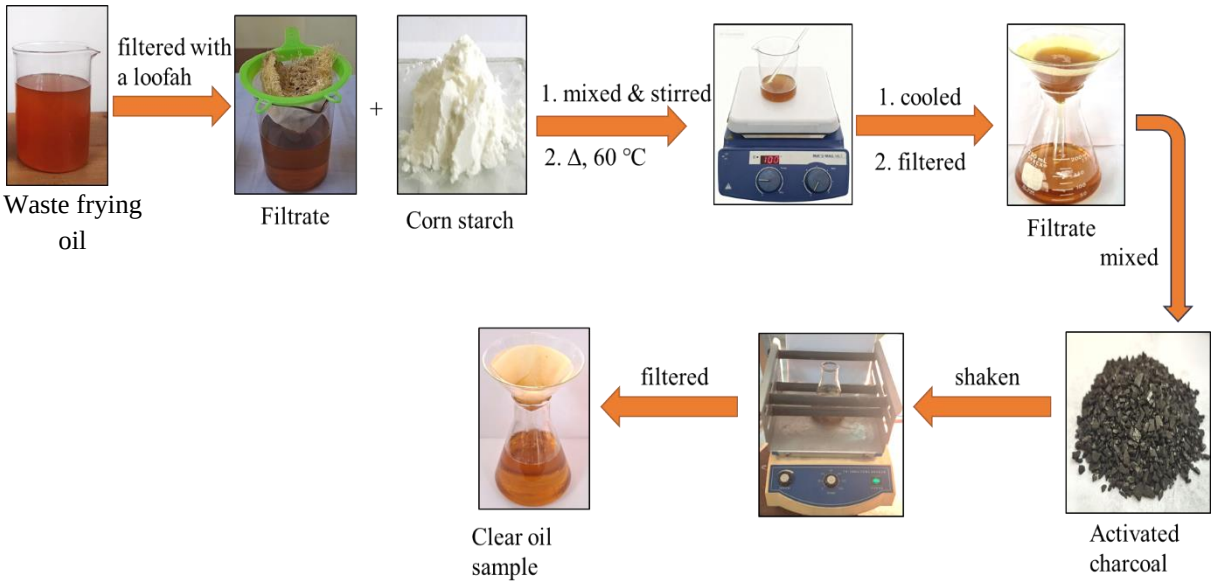

Preparation of Soap

150 g of waste frying oil was placed in 1000 mL beaker and heated at 60 ℃ for 10 minutes. It was filtered and added sodium hydroxide solution (10 %, 20 %, 30 % ,40 % and 50 %). Stirred with a glass rod till the solution turns into paste. It was poured into the mold. After, the paste was left overnight. Soap is obtained.

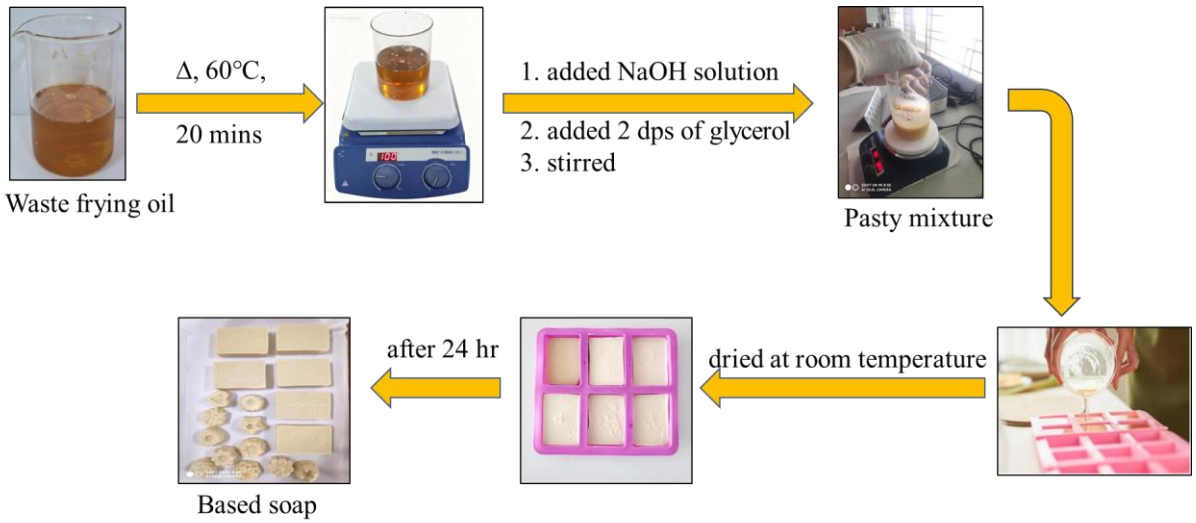

Determination of Physicochemical Properties

Determination of Acid Value

The acid value represents the number of milligrams of sodium hydroxide (NaOH) required to neutralize the free organic acids in one gram of fat and oil. It serves as an indicator of the free fatty acid content in fats and oils. To prepare the titration solution, 25 cm^3 of diethyl ether was mixed with 25 cm^3 of ethanol. Then, 1.0 cm^3 of 1 % phenolphthalein solution was added, and the mixture was titrated with 0.1 M NaOH to neutralize the ethanol. Separately, 10 g of the oil sample was placed in a conical flask and titrated to complete neutralization. The mixture was titrated against 0.1 M sodium hydroxide and a few drops of phenolphthalein indicator was added (Obanla, *et al*., 2018; AOAC, 2006). These results were shown in Table 1.

Determination of pH

The pH value indicates the acidity or alkalinity of a solution. Prior to measuring the pH of the soap solutions, the pH meter was calibrated using buffer solutions at pH 7 and pH 10. A HORIBA (F-71) pH meter was used for all measurements. For each soap sample, 2 grams were dissolved in 20 mL of distilled water and allowed to fully dissolve before the pH was recorded using the calibrated meter. This results as shown in Table 2.

Determination of Moisture Content

Two grams of soap sample was weighed and then put into a pan of moisture analyzer. The value of moisture percent was determined by aczet MB-120.These results were shown in Table 3.

Determination of Foaming Activity

One gram of soap was placed into a 100 mL measuring cylinder containing 50 mL of distilled water. The mixture was shaken vigorously to produce foam. After shaking for 10 seconds, the cylinder was left undisturbed for 10 minutes, then the height of the foam was measured and recorded. These results were shown in Table 4.

Determination of Free Caustic Alkali (FCA)

Five grams portion of the chosen soap sample was accurately weighed and dissolved in 30 mL of ethanol. Then, a few drops of phenolphthalein indicator and 10 mL of 20 % barium chloride ($BaCl_2$) solution were added to the mixture. This solution was titrated with 0.05 M sulfuric acid (H_2SO_4) until the color changed to colorless. For the caustic alkali the volume of the acid contain was calculated using Equation (Carlos *et al.*, 2011). These results were shown in Table 5.

Testing of Cleansing Power and Lather Formation of the Prepared Soap

One gram of soap was weighed and dissolved in 20 mL of distilled water and tap water. Cotton cloth was cut about 2 inches and one drop of ink was put to the center of cotton cloth. It was dried at room temperature, and then the cotton cloth was dipped into the above soap Da cotton cloth from beaker and rub the cotton cloth. Note that, the ink spot on the cotton cloth was disappeared or not.

Determination of Antimicrobial Activity of the Soap

The soap sample were tested with eight microorganisms to investigate the nature of antimicrobial activity. After preparing the bacteriological medias, the soap sample were placed on the agar with flamed forceps and gently passed down to ensure proper contact. The plates were incubated immediately or within 30 min after incubation. After overnight incubation at 37 ℃. These results are as shown in Table 6 and Figure 1.

Results and Discussion

This research deals with the production of baisc soap and elevation of their physiochemical properties for safety use.

Determination of Acid Value

Acid value was taken as an important indicator of oxidation of oil. The acid value is the number of mg of sodium hydroxide required to neutralize the free acid in 1g of the substance. The acid value is measure of the breakdown of the triacyclglycerols into free fatty acids, which has and adverse effect (Sharma and Jain, 2015). The acid value is an important parameter in assessing the quality and usability of oils, particularly in the food and skin related products. Oils with high acid values may have a shorter shelf life and impact their usability in soap formulation.

Table 1 Acid Value of Waste Frying Oil

Sr. No	Type of Oil	Acid Value (mg NaOH/g)	Std*
1	Waste frying oil	1.404 ± 0.02	0.1- 2.5

* E.G. Thomssen, 1992

Analysis of Soap

Determination of pH

For handmade basic soap, pH testing is important to know whether the soap is ready to use on skin. Handmade paper soap is always alkaline (cleansing ability) with a safe range pH between 8 to 10 to use on skin and it can vary depending on the ingredients and the manufacturing process. Anything above pH 11 is too harsh for skin and will cause irritations (EAS, 2013).

It can be seen that the pH values of soap samples were observed, 7.432 (10 % NaOH), 9.896 (20 % NaOH), 12.307 (30 % NaOH), 12.519 (40 % NaOH) and 12.519 (50 % NaOH).

Table 2 pH Value of Basic Soap Samples

Sr. No	Ratio of NaOH (%)	pH value**	Std*
1	10 %	7.432 ± 0.05	9.01 – 10.00
2	20 %	9.896 ± 0.03	
3	30 %	12.307 ± 0.04	
4	40 %	12.519 ± 0.06	
5	50 %	13.231 ± 0.02	

*Tarun, 2014

** Mean Value ± Standard deviation

Determination of Moisture Content

Moisture content refers to the amount of water present in the final soap product and is an important factor in determining its shelf life. Though typically the moisture level of plodded soap bars is maintained in the range of about 10 % to about 14 % (EAS, 2013), 20 % NaOH soap has the optimum moisture percent (13.426 %).

Table 3 Moisture Content of Basic Soap Samples

Sr. No	Ratio of NaOH (%)	Moisture Content (%)	Std*
1	10 %	33.366 ± 0.81	
2	20 %	13.426 ± 0.12	
3	30 %	35.258 ± 0.25	5.40 – 15.12 %
4	40 %	36.530 ± 0.40	
5	50 %	36.685 ± 0.35	

*Mahesar, *et al*., 2019

Determination of Foaming Activity

Foaming activity test is an important parameter for acceptability of soap standard requirement grade. In the study, foam height of prepared soap samples 10 %, 20 %, 30 %, 40 % and 50 % were found to be within satisfiable foaming height (foamability) 0.5 cm, 1.8 cm, 0.7 cm, 0.8 cm and 0.4 cm respectively. 50 % gave the lowest foamability value and 20 % gave the highest foamability value of 1.8 cm. The soap with the maximum foaming capacity is thus, said to be having the best cleaning capacity.

Table 4 Foaming Activity of Basic Soap Samples

Sr. No	Ratio of NaOH (%)	Foam High (cm)
1	10 %	0.5 ± 0.002
2	20 %	1.8 ± 0.050
3	30 %	0.7 ± 0.025
4	40 %	0.8 ± 0.030
5	50 %	0. ± 0.012

Determination Free Caustic Alkali (FCA)

The free caustic alkali is the amount of alkali free to counter and avert the soap from becoming oily. Excess free caustic alkali causes skin itching. According to Bureau of Indian Standards (BIS), good quality soaps must have less than 5 % of alkali content whereas according to ISO specification, soaps should have only below 2 % of alkali content (Onyekwere, 1996).

Table 5 Caustic Alkali (FCA) Content of Optimum Soap and Some Commercial Soaps

Sr. No	Type of Soaps	FCA (%)	Std*
1	Optimum Soap (20 %)	1.414 ± 0.01	< 2 %

* Onyekwere C., 1996

Testing of Cleansing Power and Lather Formation of the Prepared Soap

The key attributes typically used to asses soap quality include cleansing ability, foam production, hardness, conditioning effect, creaminess and leather formation. These features are largely influenced by the fatty acid profile of the oils utilized in the soap-making process. For instance, the presence of saturated fatty acids such as lauric acid and myristic acids is known to produce soap with fluffy lather and high cleansing power (Phansteil *et al*., 1998).

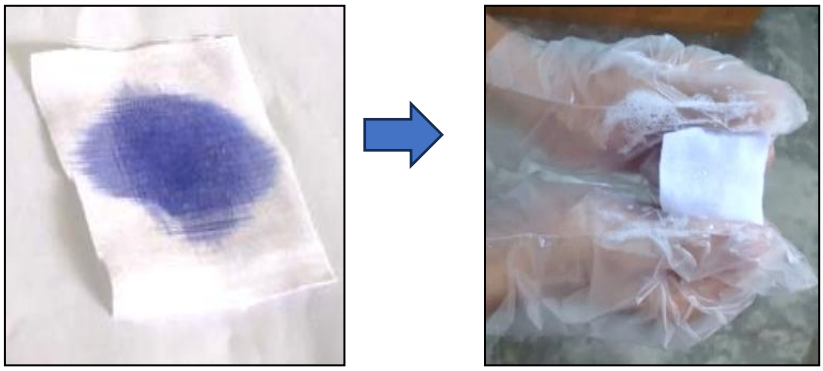

Determination of Antimicrobial Activity

Testing the antimicrobial activity of basic soap is important to determine the effectiveness against bacteria and fungi. Below are different methods for conducting an antimicrobial test. Antimicrobial activity of soap was shown in Table 6 and Figure 3.5. The test organisms were *Bacillus pumilus, Bacillus subtilis, Candida albicans, Escherichia coli, Pseudomonas aeruginosa, Salmonella typhi*. A zone of inhibition is a area around the point in the media where the test sample is introduced and where no test organisms (pathogenic bacterial strains) are found to be growing (Thambi *et al*., 2016). A diameter of zone inhibition of 14 or less indicates the test product being low activity to the test organisms (pathogens), diameter zone of inhibition of 15 to 20 indicates the test product having a medium resistance to test organisms. A diameter with a zone inhibition of 21 or above indicates the test product is highly resistance to test organisms. The result revealed that 20 % NaOH soap showed highest inhibiting activity against pathogens by showing a zone of inhibition of 21.00 mm for B. *pumilis*, 24.00 mm for B. *subtilis*. The study observed that the naturally produced soap samples have more effect and pronounce on the strains of all microorganisms.

Table 6 Antimicrobial Activity of Optimum Soap

Microorganisms / Sample	Inhibition zone diameter (mm)					
	B. pumilus	*B. subtilis*	*C. albicans*	*E. coli*	*P. aeruginosa*	*S. typhi*
20 % NaOH Soap	21.00 (+++)	24.00 (+++)	18.00 (++)	-	-	-

Agar well = 8 mm

(-) = No Activity

(+), Low activity = 9- 14 mm

(++), Medium activity = 15-20 mm

(+++), High activity = 21 mm and above

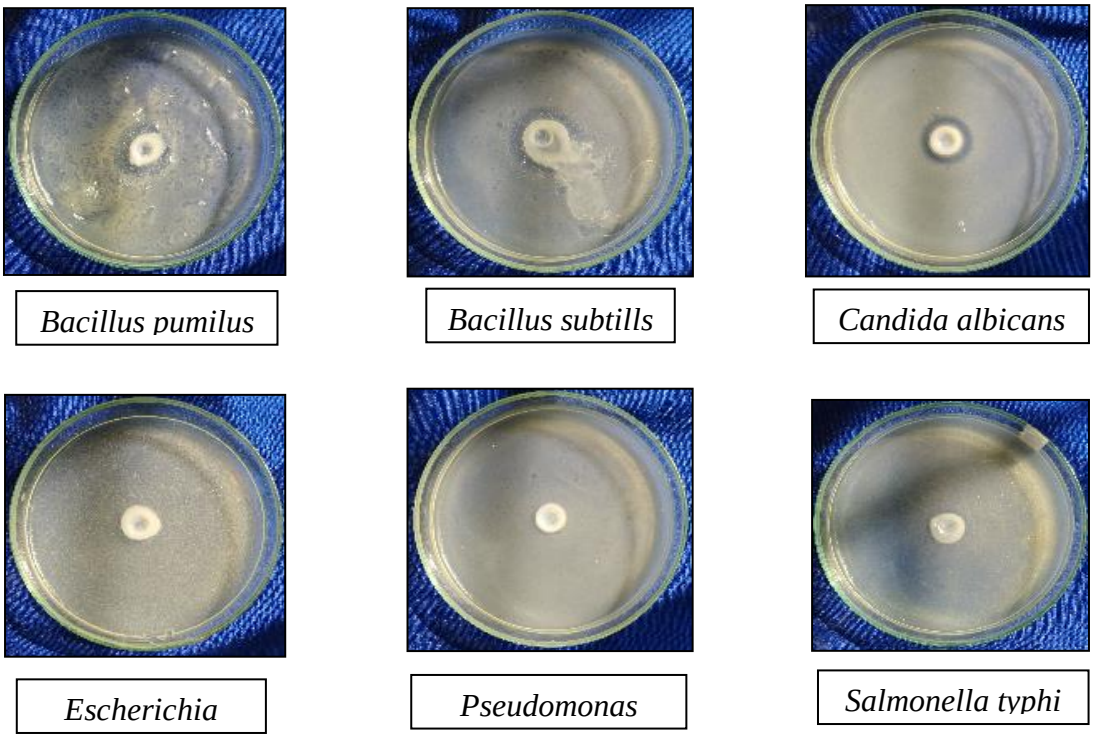

Figure 1 Antimicrobial activities of water extracts of soap

Conclusion

Soap is used for cleaning and washing the body and it ensures that the microbes in the external parts would be removed. So, basic soaps were prepared using WFOs obtained from local households and university canteens from East Yangon University in the month of June 2025. Physicochemical properties of selected soap, it was found that pH value (9.896), moisture content of (13.426 %), (1.404 mg NaOH/g) of acid value and (1.414 %) of FCA. Comparability of the physicochemical properties (data) obtained for the prepared basic soaps and 20 % NaOH soap indicated that WFOs can be used to prepare basic soap of acceptable quality. One of the advantages is its use to minimize environmental pollution caused by WFOs. Replacing palm oil and animal fats in soap making which are going to be scarce in the near future because of their utilization as raw materials for biodiesel. WFO can be successfully used in basic soap production, but it requires proper purification to ensure good quality. The antimicrobial activity of soap extract (water) was tested against six pathogenic microorganisms by using agar well diffusion method. The extract of soap could inhibit three pathogenic microorganisms. The largest antimicrobial activity was observed in *Bacillus subtilis* (24 mm) of soap extract. So, these basic soap include the ability to reduce dirt on the body and no harm to the skin. This research confirms that WFO can be effectively used for soap production, offering a sustainable and economical alternative to fresh oils. With proper purification, formulation, and antimicrobial activitiy, WFO soap can be a high- quality, eco-friendly product with good cleansing and antibacterial properties.

Acknowledgements

The authors would like to thank to the Department of Higher Education (Lower Myanmar), Ministry of Education, Yangon, Myanmar. We would like to express our sincere thanks to Dr Myo Min Tun (Acting-Reactor), Dr Aye Aye Ko and Dr Thidar Aung (Pro-Reactors), East Yangon University. Our warmest thanks are also extended to Dr Khin Saw Oo (Professor and Head), Dr Nu Nu Khine (Professor), Department of Chemistry, East Yangon University, for their kind encouragement, permission to submit this paper and gave many helpful suggestions.

References

AOAC. (2002). "Official Method of Analysis. *Internal Food Research Journal,* vol.**17**, pp. 426- 432Carlos A., F. Guerrero, G. R. Andres and E. S. Fabio. (2011). "Biodiesel Production from Waste Cooking Oil" DOI: 10.5772/25313.

East American Standard (EAS) (2013). Laundry soap-Specification East African community; Arusha; Tanzania.

Gomez C.P, APC. Machada (2015). "From using cooking oil to soap: the role of the stakeholders to implement a reverse logistic program". *Brazilian Journal of Operations and Production Management,* vol. 12, pp. 66-72

Mahesar S. A., R. Chohan and A. T. H. Sherazi. (2019). "Evaluation of Physico-Chemical Properties in Selected Branded Soaps". *Pakistan Journal of Analytical & Environmental Chemistry*, vol. **20(**2), pp. 1- 30

Obanla, O. R., Ajani O. O., Omadara O.J., and Omolewa D. A. (2016). "Extraction, Comparative Study and Property Evaluation of Synthesized Bar Soap from ocally Sources Rubber Seed II and Plam Kernal Oil*". International Journal of Mechanical Enginnering and Technology*, vol. 9, pp. 308-319

Onyekwere C (1996). Cassava peels ash: An alternative source of alkali in soap production. BEng Thesis, Department of Chemical Engineering, University of Port-Harcourt, pp. 1-33.

Phansteil O.N, E. Dueno, W.Q Xianghong (1998). "Synthesis of exotic soaps in the Chemistry laboratory". *Journal of Chemical Education*, vol. 75, pp. 612-614

Potgieter H, S. S, Potgier, D. D, Tona, L. Anelich, M. P, Roux, W. Delport (2004). "A proposed of alternative suggestion for the disposal of used cooking oil". *Journal of Applied Science*, vol. 4, pp. 313-316

Sharma S., and V. K. Jain. (2015). "Acid Value of Various Domestic Uses Oil", Research J. Science and Tech., vol. 7, pp. 109-110

Tarun J., J. Susan, J. Suria, V. J. Susan and S. Criton. (2014). "Evaluation of pH of Bathing Soaps and Shampoos for Skin and Hair Care" *Indian J Dermatol.*, vol. **95(**5), pp. 442- 444

Thambi P. A., S. John, E. Lydia, P. lyer, and S. J. Monica. (2016). "Antimicrobial Efficacy of Mango Peel Powder and Formulation of Recipes Using Mango Peel Powder (Mangifera indica L.)". *International Journal of Home Science*, vol. 2, pp. 155-161

Production of Shrimp Paste by using Bromelain from Pineapple

Khin Yadanar Ko Ko[1], Ye Yint Naing[2], Kay Thi Khine[3]

Abstract

Bromelain (EC 3.4.22.33) is a proteolytic enzyme that is found in the tissue of the pineapple plant. This enzyme plays a vital role in various industrial applications, including meat and fish or shrimp tenderization, beer clarification, bread baking, and the textile and cosmetic industries. In this study, the pineapple samples were collected from Myoma market, Thanlyin Township, Yangon Region, and identified at the Department of Botany, East Yangon University. Bromelain was extracted from 180 g of the pineapple fruit using the ammonium sulphate precipitation method, yielding 1.97 g of enzyme. Bromelain breaks down proteins, and tyrosine is produced as the major product. Bromelain activity was measured by tyrosine released from casein at 275 nm. The activity and enzyme unit of bromelain were observed to be 0.0246 μmol min^{-1} mL^{-1} and 0.269 EU per gram, respectively. The protein content of the bromelain enzyme was determined by the Biuret method and found to be 0.163 mg protein mL^{-1}. The optimum pH and temperature of the bromelain-catalyzed reactions were 7.0 and 57 ºC, respectively. The K_m and V_{max} values were found to be 0.509×10^{-2} g mL^{-1} and 2.501×10^{-5} M min^{-1}, respectively. The reaction order (n) was found to be 1.04, indicating first-order kinetics. In this research, the extracted bromelain was applied as a biocatalyst in the production of shrimp paste to accelerate protein hydrolysis.

Keywords: Bromelain, tyrosine, casein, UV-visible spectroscopic method, Biuret method

Introduction

Pineapple is the third most important tropical fruit in the world. It contains considerable amounts of calcium, potassium, vitamin C, carbohydrates, protein, crude fiber, water, and different minerals (Farid and Shaheen, 2015). All the different parts of the pineapple plant-roots, leaves, stem, crown, peel, and fruit have various amounts of proteolytic enzymes, with a high level of protease enzymes in the stem and fruit and low levels in the core, leaves, and peel (Alsaady *et al*., 2016).

Bromelain (EC 3.4.22.33) is one of the proteolytic enzymes derived from pineapple with extensive application in the food industry (Robinson, 2015). Bromelain hydrolyzes casein, resulting in the production of tyrosine. Bromelain activity can be influenced by several factors, namely the source of the enzyme, pH, temperature, substrate, and inhibitors. Its strong proteolytic activity has created a wide interest in numerous applications, mainly in tenderization, food processing, detergents, medicine, and the textile industry. It can be utilized in shrimp paste processing to modify texture and enhance flavor through controlled protein hydrolysis. Its proteolytic action breaks down shrimp proteins, potentially improving product consistency and accelerating fermentation. This application aligns with efforts to optimize traditional food production using enzymatic methods. Fermented products of fish and shrimp are commonly used as food condiments in Southeast Asia including Myanmar (Aung Myint, 1984). Most of the fermented products are strictly traditional and limited to local consumption. Shrimp paste using different fermentation technologies has different fermentation cycles.

[1] Demonstrator, Department of Chemistry, East Yangon University
[2] Demonstrator, Department of Chemistry, East Yangon University
[3] Demonstrator, Department of Chemistry, East Yangon University

Materials and Methods

Sample Collection

A pineapple fruit sample was collected from Myoma Market, Thanlyin Township, Yangon Region. The pineapple fruit sample was identified at the Department of Botany, East Yangon University.

Extraction of Bromelain from Pineapple

Fresh pineapple fruits were thoroughly washed with distilled water, peeled using a stainless steel knife, and cut into small pieces. A total of 180 g of pineapple flesh was mixed with 360 mL of pH 7.0 sodium phosphate buffer and homogenized using a blender. The homogenate was filtered through cheesecloth and centrifuged at 5000 rpm for 30 minutes. After centrifugation, the supernatant was decanted and collected as the crude enzyme extract. Ammonium sulphate (42.168 g) was gradually added to the filtrate to achieve 30% saturation. The mixture was stirred using a magnetic stirrer for 2 hours and centrifuged at 5000 rpm for 30 minutes. The supernatant was decanted, and the resulting filtrate was retained. Subsequently, 37.78 g of ammonium sulphate was added to the filtrate to reach 70% saturation. The solution was stirred for 2 hours and allowed to stand overnight (Chaurasiya and Hebbarn, 2013). Finally, the precipitated bromelain enzyme was collected by filtration using filter paper, yielding 1.97 g of bromelain enzyme precipitate.

Determination of Wavelength of Maximum Absorption of Tyrosine

Tyrosine (0.01 g) was dissolved in 5% trichloroacetic acid, and the final volume was adjusted to 50 mL using the same solvent (Boyd and Marr, 1980). The maximum absorbance wavelength of tyrosine was determined using a UV-Visible spectrophotometer within the 250-300 nm range.

Construction of Calibration Curve for Standard Tyrosine Solutions

A serial of standard solutions was prepared to obtain concentrations of 0.550, 0.275, 0.138, 0.069, 0.034, and 0.017 mM. The absorbance of each standard solution was measured at 275 nm to construct calibration curve of absorbance versus concentration.

Protein Assay

The protein concentration was determined according to the Biuret method using a calibration curve made with bovine serum albumin as standard.

Characterization of Bromelain from Pineapple

For the enzyme assay, bromelain activity was measured via UV-Visible spectrophotometer at 275 nm, utilizing casein as the substrate. Enzyme Unit (EU) was derived from the observed activity, while the protein concentration was quantified using the Biuret method with Bovine Serum Albumin (BSA) as the standard at 540 nm. Additionally, the effects of pH, temperature, reaction time, and substrate concentration were evaluated. Kinetic parameters, including K_m, V_{max}, and the reaction order, were also determined. Finally, the extracted bromelain was applied as a biocatalyst to enhance shrimp paste production.

Preparation of Shrimp Paste Fermented with Salt Only and a Mixture of Salt and Enzyme

Shrimp paste was prepared from semi-dry salted shrimp using salt only or salt combined with an enzyme. The enzyme-treated paste was fermented for 7 days, while the salt-only paste was fermented for 3 months. The nutritional values of both shrimp pastes were analyzed and compared using AOAC method.

Rsesults and Discussion

Extraction of Bromelain from Pineapple

The bromelain enzyme was extracted from pineapple fruit (*Ananas comosus* L.) using ammonium sulphate precipitation method. The final amount of bromelain enzyme obtained after precipitation was 1.97 g.

Wavelength of Maximum Absorption of Tyrosine Solution

In this study, bromelain breaks down proteins such as casein and produces tyrosine. The maximum absorption wavelength of tyrosine was measured in the range of 250–300 nm (Aitken and Learnmonth, 2009). The λ_{max} of tyrosine was found to be 275 nm, as shown in Table 1 and Figure 1.

Calibration Curve for Standard Tyrosine Solution using Ultraviolet Spectroscopy

In this study, the absorbance of six standard tyrosine solutions (0.550, 0.275, 0.138, 0.069, 0.034, and 0.017 mM) was measured at 275 nm. Plotting absorbance against tyrosine concentration produced a straight line through the origin, indicating that Beer's Law was followed (Table 2 and Figure 2).

Activity of Bromelain from Pineapple

The activity of bromelain was found to be 0.0246 μmol min^{-1} mL^{-1}. The enzyme unit (EU) of bromelain was found to be 0.269 EU per gram of pineapple.

Construction of Standard Calibration Curve for Protein using Visible Spectroscopy (Modified Biuret Test)

Bovine serum albumin (BSA) was used as a standard, and the protein concentration was determined using the biuret test (Table 3 and Figure 3). Absorbance was measured at 540 nm using a UV–visible spectrophotometer. A linear relationship between absorbance and standard protein concentration was observed, indicating that Beer's law was obeyed (Table 4 and Figure 4). The bromelain enzyme solution produced a purple color, confirming the presence of protein. The protein content of the pineapple extract was 0.163 mg protein mL^{-1}.

Optimum pH for Bromelain-Catalyzed Reaction

Enzyme activity is affected by pH, with maximum activity at the optimum pH. In this study, enzyme activity was measured using phosphate buffer solutions ranging from pH 5.5 to 8.5. The maximum bromelain activity (0.0519 μmol min^{-1} mL^{-1}) was observed at pH 7.0 (Table 5 and Figure 5).

Table 1 Relationship between Wavelength and Absorbance of Tyrosine Solution

Wavelength(nm)	Absorbance
250	0.521
255	0.649
260	0.855
265	1.084
270	1.293
275	**1.369**
280	1.274
285	0.859
290	0.407
295	0.218
300	0.136

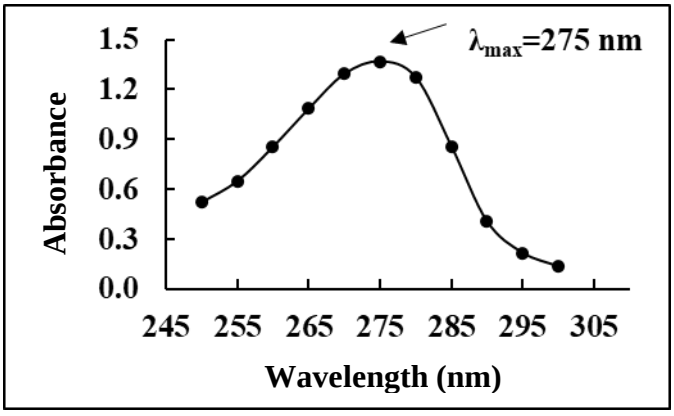

Figure 1 UV spectrum of tyrosine solution

Table 2 Relationship between Absorbance and Standard Tyrosine Concentration

No.	Concentration (mM)	Absorbance at 275 nm
1	0.017	0.024
2	0.034	0.057
3	0.069	0.105
4	0.138	0.190
5	0.275	0.357
6	0.550	0.698

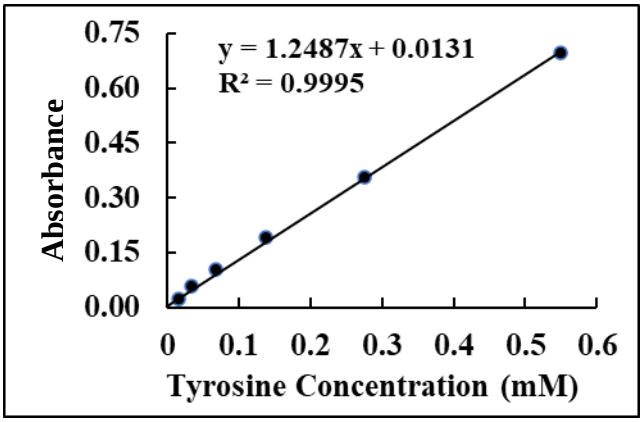

Figure 2 Calibration curve for standard tyrosine solutions

Table 3 Relationship between Wavelength and Absorbance of Standard Protein Solutions

Wavelength(nm)	Absorbance
510	0.298
520	0.321
530	0.383
540	**0.471**
550	0.358
560	0.311
570	0.294
580	0.271
590	0.243
600	0.214

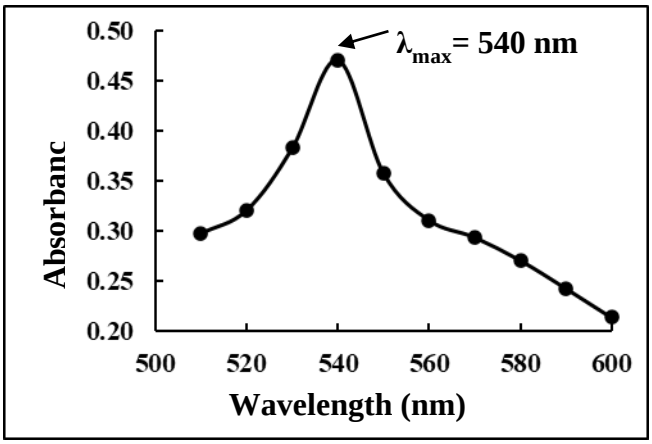

Figure 3 Wavelength of maximum absorption of copper- protein complex by Biuret method

Optimum Temperature for Bromelain-Catalyzed Reaction

The optimum temperature for bromelain was 57 °C, with an activity of 0.0493 μmol min^{-1} mL^{-1}. Activity increased from 37 °C to 57 °C and decreased at higher temperatures, likely due to enzyme denaturation (Table 6 and Figure 6).

Effect of Reaction Time on Proteolytic Activity of Bromelain-Catalyzed Reaction

Bromelain released tyrosine at pH 7.0, with activity measured at 30, 60, 90,120 and 150 min. Activity declined linearly up to 90 min; 30 min was used for kinetic analysis (Table 7 and Figure 7).

Effect of Substrate Concentration on Bromelain-Catalyzed Reaction

The rate of enzyme action is also influenced by the concentration of substrate (Bell *et al.*, 1972). The determination of K_m and V_{max} enables these two effects to be studied separately. K_m depends on the formation of the enzyme-substrate complex, whereas V_{max} is a measure of

the rate of its breakdown. Statistical methods were used for obtaining K_m and V_{max} from experimental results (Table 8). These values are shown in Table 9 in comparison with those obtained from the Michaelis-Menten plots. The values obtained from various methods are not much different from each other, implying that the methods are comparable on the basic of qualitative aspects (Figure 8 and 9).

Table 4 Relationship between Absorbance and Concentration of Standard Protein Solutions by Biuret Method

No.	Standard Protein Concentration (mg mL^{-1})	Absorbance at 540 nm
1	2	0.103
2	4	0.188
3	6	0.259
4	8	0.359
5	10	0.467

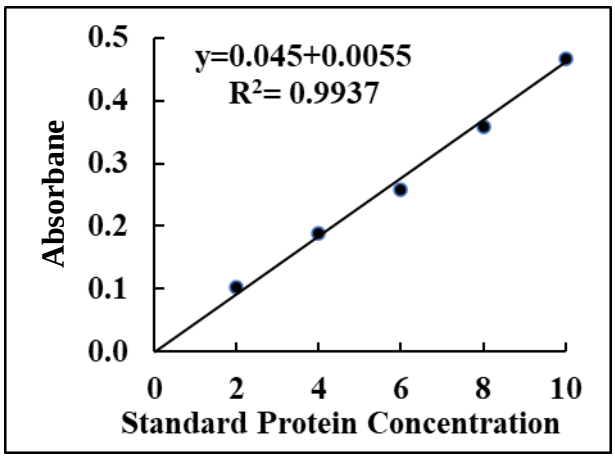

Figure 4 Calibration curve for standard protein solution

Table 5 Relationship between Bromelain Activity and pH of its Solution

No.	pH	Bromelain Activity (μ mol min^{-1} mL^{-1})
1	5.5	0.0231
2	6.0	0.0433
3	6.5	0.0491
4	**7.0**	**0.0519**
5	7.5	0.0468
6	8.0	0.0307
7	8.5	0.0242

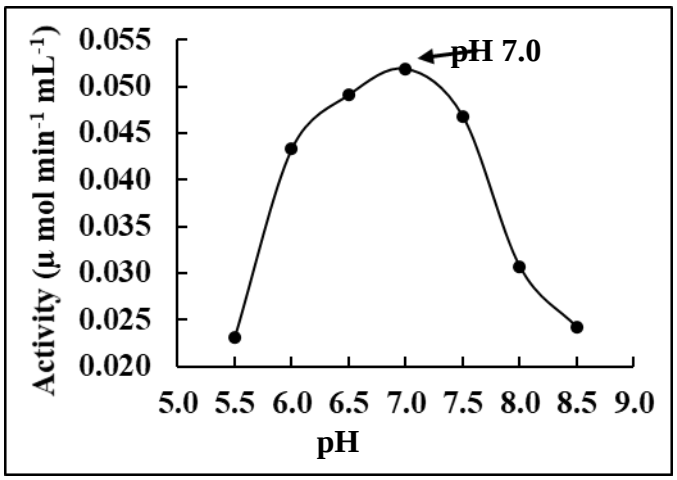

Figure 5 A plot of bromelain enzyme activity as a function of pH

Reaction Order (n) for Bromelain-Catalyzed Reaction

K_m and n values were determined from the plot of Log V/V_{max} – V *vs*. Log [S] for bromelain using the linear regression method (Table 10 and Figure 10). The reaction order (n) for bromelain was calculated to be 1.04 proving that the reaction order is first order.

Table 6 Relationship between Bromelain Activity and Temperature of its Solution

No.	Temperature (°C)	Bromelain Activity (μ mol min^{-1} mL^{-1})
1	37	0.0341
2	47	0.0453
3	**57**	**0.0493**
4	67	0.0468
5	77	0.0422
6	87	0.0398

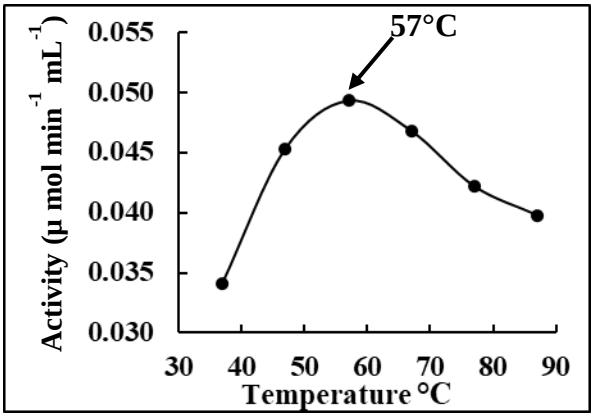

Figure 6 A plot of bromelain enzyme activity as a function of temperature

Table 7 Relationship between Reaction Time and Velocity of Bromelain-Catalyzed Reaction

Reaction Time (min)	Velocity × 10^5 ($Mmin^{-1}$)
30	1.760
60	1.158
90	0.761
120	0.507
150	0.490

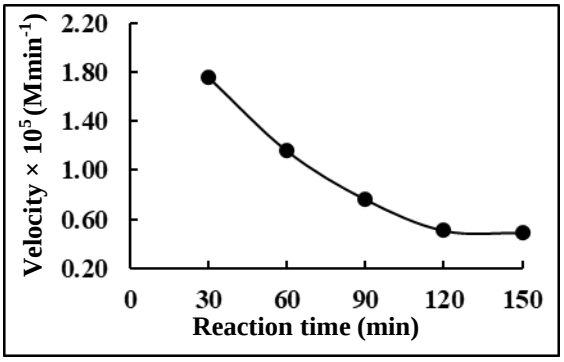

Figure 7 A plot of velocity as a function of reaction time for bromelain-catalyzed reaction

Nutritional Values of Shrimp Paste

In this study, the nutritional composition of samples prepared with salt-only and with a mixture of enzyme solution and salt is shown in Table 11 and Figure 11. The moisture content of the salt-only sample was 47.89 %, while the enzyme-treated sample showed a lower value of 40.57 %, indicating that enzyme treatment reduced moisture retention in the paste. The ash content decreased significantly from 21.72% in the salt-only sample to 11.92 % in the enzyme-treated sample.

The protein content of the salt-only sample was 22.60 % while the enzyme-treated sample showed 22.83 %, respectively, because the bromelain treatment did not lead to protein loss but may have improved protein digestibility through hydrolysis into peptides and amino acids. Fat content was low in both samples, 0.7% and 0.3%, respectively. The fibre contents were not detected in both samples.

Carbohydrate content increased from 7.09% in the salt-only sample to 24.38% in the enzyme-treated sample. Accordingly, the energy value increased from 125.1 to 191.5 kcal/100 g.

Overall, the results indicate that bromelain enzyme treatment combined with lower salt addition improves the nutritional profile of shrimp paste by reducing ash and salt contents while maintaining protein and fat levels.

Table 8 Relationship between Substrate Concentration and Velocity of Bromelain-Catalyzed Reaction

$[S]\times10^{2}$ (gmL^{-1})	$1/[S]\times10^{-2}$ ($g^{-1}mL$)	$V\times10^{5}$ ($Mmin^{-1}$)	$1/V\times10^{-5}$ ($M^{-1}min$)	$V/[S]\times10^{3}$ ($Mmin^{-1}\,g^{-1}mL$)	$[S]/V\times10^{-3}$ ($M^{-1}min\,gmL^{-1}$)
0.25	4.000	0.830	1.205	3.320	0.301
0.50	2.000	1.211	0.826	2.422	0.412
0.75	1.333	1.472	0.860	1.962	0.509
1.00	1.000	1.655	0.604	1.655	0.604
1.25	0.800	1.780	0.562	1.424	0.702
1.50	0.667	1.905	0.525	1.270	0.787
1.75	0.571	1.930	0.518	1.102	0.906
2.00	0.500	2.021	0.495	1.010	0.989

Table 9 Comparison of K_m and V_{max} Values of Bromelain Calculated from Different Methods

Method	Linear regression		Plot	
	K_m ($10^2\,gmL^{-1}$)	V_{max} ($10^5\,Mmin^{-1}$)	K_m ($10^2\,gmL^{-1}$)	V_{max} ($10^5\,Mmin^{-1}$)
Michaelis-Menten	-	-	0.38	2.03
Lineweaver-Burk	0.509	2.501	0.50	2.50
Eadie-Hofstee	0.509	2.511	0.53	2.52
Hanes-Wilkinson	0.588	2.588	0.52	2.36
Eisenthal-Cornish Bowden	-	-	0.51	2.52

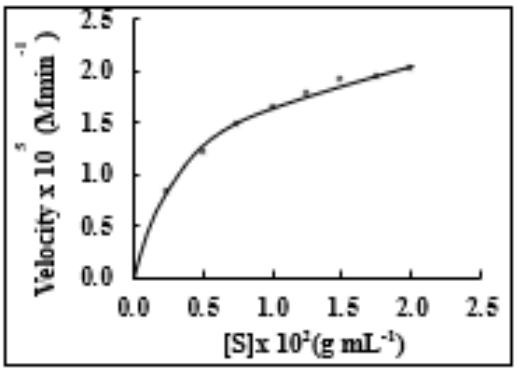

Figure 8 Michaelis-Menten plot used for graphic evaluation of V_{max} and K_m for bromelain

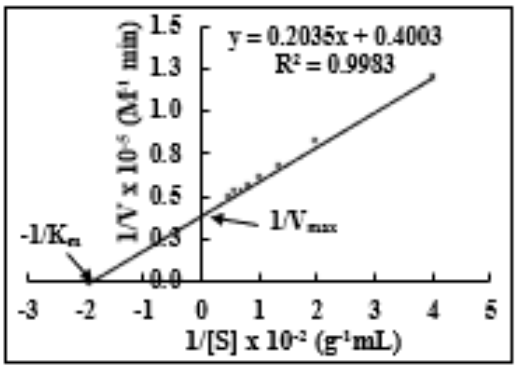

Figure 9 Lineweaver-Burk plot of 1/V *vs.* 1/[S] used for graphic evaluation of V_{max} and K_m for bromelain

Table 10 Relationship between Log $V/V_{max} - V$ as a Function of Log [S] for Bromelain-Catalyzed Reaction

[S] $\times 10^2$ (g mL^{-1})	Log [S]	V $\times 10^5$ (M min^{-1})	Log $V/V_{max} - V$
0.25	-2.602	0.830	-0.303
0.50	-2.301	1.211	-0.027
0.75	-2.142	1.472	0.156
1.00	-2.000	1.655	0.291
1.25	-1.903	1.780	0.393
1.50	-1.824	1.905	0.505
1.75	-1.756	1.930	0.529
2.00	-1.699	2.021	0.625

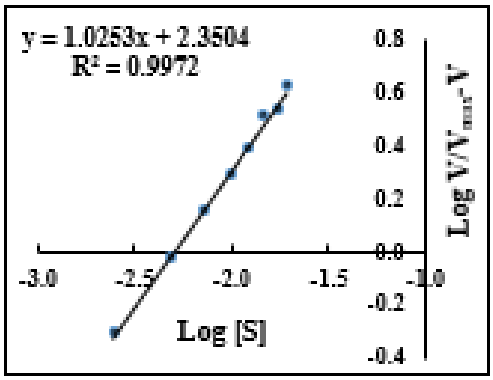

Figure 10 Plot of Log V/V_{max}-V as a function of Log [S] for bromelain-catalyzed reaction

(A) (B)

Figure 11 Comparison of Shrimp Paste Quality
(A) Fermented with a mixture of 15% salt and enzyme
(B) Fermented with 30% salt only

Table 11 Nutritional Values of Shrimp Paste

Parameters	Salt Only	Mixture of enzyme solution and salt
Moisture (%)	47.89	40.57
Ash (%)	21.72	11.92
Protein (%)	22.60	22.83
Fibre	0	0
Fat (%)	0.7	0.3
Carbohydrate (%)	7.09	24.38
Energy value (kcal/100 g)	125.06	191.54

Conclusion

In this study, bromelain enzyme was successfully extracted from 180 g of pineapple, yielding 1.97 g of crude enzyme using the ammonium sulphate precipitation method. The extracted bromelain exhibited an enzymatic activity of 0.0246 μmol min^{-1} mL^{-1} and an enzyme unit of 0.269 EU per gram, while the protein concentration of the enzyme solution was 0.163 mg mL^{-1}. The optimum conditions for bromelain-catalyzed reactions were observed at pH 7.0 and a temperature of 57 °C. Kinetic analysis revealed K_m and V_{max} values of 0.509×10^{-2} g mL^{-1} and 2.501×10^{-5} M min^{-1}, respectively, and the calculated reaction order (n) of 1.04 indicated first-order kinetics. Furthermore, fermentation using a combination of salt and bromelain enzyme resulted in a smoother and more homogeneous texture compared to the conventional salt-only method. The enzymatic treatment enhanced meat tenderness and flavor while reducing bacterial contamination, indicating its potential as a natural processing method. According to the nutritional point of view, the shrimp paste fermented with the bromelain is suitable for human consumption and health.

Acknowledgements

The authors would like to thank to the Department of Higher Education (Lower Myanmar), Ministry of Education, Yangon, Myanmar. We would like to express our sincere thanks to Dr Myo Min Tun (Acting-Reactor), Dr Aye Aye Ko and Dr Thida Aung (Pro-Reactors), East Yangon University. Our warmest thanks are also extended to Dr Khin Saw Oo (Professor and Head), Dr Nu Nu Khine (Professor), Department of Chemistry, East Yangon University, for their kind encouragement, permission to submit this paper and gave many helpful suggestions.

References

Aitken, A and P. M. Learnmonth. (2009) *Protein Protocols Handbook*. Inc: Walker JM(ed) Springer Protocols Handbooks. Chaps 1. Humana Press, News York, pp3-6

Alsaady, A. J. R., W. G. A. Alhadban and A. A. Aluzubaidy. (2016) "Optimal Conditions for Bromelain Extraction from Pineapple Fruit (*Ananas comosus*)." *Eng. & Tech. Journal*., vol. 34 (5). pp675-682.

AOAC. (2000) *Official Methods of Analysis*. Association of Official Analytical Chemists. Washington D.C: 17th Ed., pp526-530

Aung Myint. (1984) "Burma Shrimp Paste and Shrimp Sauce." *Foodstuff and General Merchandise Trade Corporation*, vol.35

Bell, G.H., Davidson, G.H., and Smith, D.E. (1972) *Text Book of Physiology and Biochemistry*, E. and S., Livingstone Ltd., London.93

Boyd, R.F. and J.J. Marr. (1980) *Medical Microbiology*. Boston: Little Brown Company: pp155-160

Chaurasiya, R. S. and H. U. Hebbar. (2013) "Extraction of Bromelain from Pineapple and Purification by RME and Precipitation Methods." *Sep. Purif. Technol*., vol. 111. pp90-97

Farid, M. H. and A. Shaheen. (2015) "Nutritional Value and Medicinal Benefits of Pineapple." *International Journal of Nutrition and Food Sciences*., vol. 4(1), pp84-88

Robinson, P. K. (2015) *Enzymes: Principles and Biotechnological Applications*. U.K, College of Science and Technology, University of Central Lancashire, vol. 59, pp1-41

Role of Activated Carbon Derived from Peanut Shells Biowaste for Electrochemical Performance in Supercapacitor Electrodes

Zin Min Tun[1], Zin Min Myat[2], Ye Hlan Win[3], Yin Maung Maung[4]

Abstract

In this research, activated carbon from peanut shell activated carbon (PSAC) were produced through a one-step chemical activation process using potassium hydroxide (KOH) and studied the electrochemical properties analysis of peanut shell activated carbon. Peanut shell biomass was heated in a muffle furnace at 300 °C, 400 °C, 500 °C and 600 °C for 1h respectively to obtain activated carbon. Bulk density, pH and electrical conductivity of activated carbon were studied. The surface morphology of peanut shell activated carbon (PSAC) from potassium hydroxide (KOH) activation was characterized by Scanning Electron Microscope (SEM). The elemental compositions of these samples were analyzed by Energy Dispersive X-ray Fluorescence (EDXRF). Fourier Transform Infrared Spectroscopy (FTIR) was applied to determine the chemical properties of the peanut shell activated carbon. The specific capacitance, energy density and power density of peanut activated carbon were calculated from the measurements of cyclic voltammetry (CV) and electrochemical impedance spectroscopy (EIS). all the peanut shell activated carbon at different temperatures exhibited improved electrochemical performances, PSAC at 600 ^{o}C sample showed prominently the highest specific capacitive value, energy density and power density of 315.51 Fg^{-1}, 24.11 $Whkg^{-1}$ and 10840.23 Wkg^{-1} at 50 mV s^{-1} scan rate which was the maximum values in the fabricated electrodes due to their increment of conducting ions. According to the data analysis, the excellent performance of activated carbon prepared from peanut shell could be considered as an electroactive material for supercapacitors.

Keywords: Peanut Shells, Activated Carbon, SEM, FTIR, CV, Supercapacitors

Introduction

Activated carbon (AC) is a kind of carbon that has undergone an activation process to make it exceptionally porous and capable of efficiently adsorbing different chemicals (Bansal & Goyal, 2005; Marsh & Reinoso, 2006; Ngu, 2022; Ray, 1940; Schanz & Parry, 1962). The mechanism of adsorption of AC is commonly due to the micropores present in the carbon or the weak Van der Waals forces that can attract the impurities. Activated carbon that is available in the market is made using carbonization and activation techniques on organic materials of plant-based origin (Gómez-García, 2018; Gundogdu et al., 2013; Ozdemir et al., 2014). Activated carbon can be made from variety of materials, notably coal, coconut shells, wood, and lignite. Due to its accessibility and affordability as compared to other resources, activated carbon made from coal has become one of the most often utilized forms. The preparation process consists of phosphoric acid impregnation followed by carbonization in nitrogen at 400–600 °C for 1–3 h. Alternatively, high-quality coal is heated to a temperature between 900 °C and 1100 °C in the absence of oxygen to produce coal-based activated carbon, which eliminates most volatile materials and leaves behind a microporous, high adsorption substance (Teng et al., 1998). Coal-based activated carbon used to be favored by industrial users compared to other sources of activated carbon because of its outstanding ability to adsorb and stability in a variety of acidic and basic conditions (Wang et al., 2022; Zheng et al., 2022). In addition to that, coal is a by-product of the coal mining process and is easily accessible in many areas. Moreover, there is flexibility in the source of materials since coal-based activated carbon may be produced from both bituminous and sub-bituminous coal tested several coal-based activated carbons in eliminating pollutants (Wang et al., 2022).

[1] Associate Professor, Department of Physics, West Yangon University
[2] Associate Professor, Department of Physics, West Yangon University
[3] Associate Professor, Department of Physics, East Yangon University
[4] Professor and Head, Department of Physics, University of Yangon

Experimental Procedure

Preparation of Peanut Shell Activated Carbon

The peanut shells were cleaned with fresh water to remove the dust and impurities. These shells were dried in sun for one day and then hand crushed to smaller pieces. Then, the smaller pieces of these shells were dried at room temperature about one week. The weight of peanut shells was measured with electronic digital balance. And then, these raw peanut shells (PS) were carbonized in the muffle furnace at 300 °C, 400 °C, 500 °C and 600 °C for 1 h. Finally, the prepared biochars were ground into powder by pestle. Biochar powders were obtained. The obtained peanut shell biochar powders were characterized by chemical properties analysis of Fourier Transform Infrared Spectroscopy (FTIR) and elemental analysis of EDXRF (Energy Dispersive X-ray Fluorescence) method. After carbonization, these PS biochars were mixed with deionized water and KOH in a stainless-steel beaker with weight ratio of KOH/PS biochar equal to 1:1. Water was evaporated at 130 °C for 6 h, and these dried mixtures were heated in the muffle furnace at 800 °C for 1 h. The products were cooled to room temperature and washed with HCl and deionized water until the pH of the washing solution reached 6-7. Finally, the activate carbon obtained from peanut shell (PS) biochars. Table 1 show the weight loss and weight loss % of peanut shell biochar at different temperatures.

Table 1 Weight loss percent of peanut shell biochar at different temperatures

Temperature	Initial weight, W_i	Final weight, W_f	Weight loss, $W = W_i - W_f$	Weight loss (%)
300 °C	50 g	33 g	17 g	34 %
400 °C	50 g	22 g	28 g	56 %
500 °C	50 g	13 g	37 g	74 %
600 °C	50 g	8 g	42 g	84 %

Results and Discussion

pH Measurement

pH is a measure of the hydrogen ion concentration in solution and is also referred to as the degree of acidity or alkalinity. The pH scale typically ranges from 0 to 14, where a pH of 7 is neutral, pH higher than 7 is alkaline, and pH lower than 7 is acidic. These results clearly showed that the physical and **chemical properties** of peanut shell biochar varied as a function of biomass collection and pyrolysis temperatures. Researchers have reported that the biomass wastes had a significant impact of the pH of the resulting biochar product. Biochars produced under high temperatures (>300°C) are likely to have greater pH values than the low temperature (< 300°C) biochars from the biomass wastes.

Bulk Density Measurement

The bulk densities of peanut shell activated carbon were determined by the weight of biochars placed in a container divided by the volume occupied. In this research, bulk density was determined for peanut shell activated at different carbonization temperatures. The activated were crushed and sieved through a mesh to obtain uniform activated carbon powder. An empty 10 ml graduated measuring cylinder was dried naturally and weighed its

mass. It was then filled up to a volume of 10 ml with the biochar. With the filling of every 2 ml, the cylinder was tapped gently a few times to achieve compaction. According to the measurement results, the bulk densities of biochar were increased with increasing temperatures as shown in Figure 4.1.

Electrical Conductivity Measurement

Electrical conductivity of peanut biochars were determined by mixing the known weight of biochar, 1 g with the deionized water, 100 ml for about 1h. Electrical conductivity is measured by HORIBA, COND METER, ES-51 Model. An understanding of the number of soluble salts in a biochar solution is important since high rates of biochar application. EC is proportional to the quantity and nature of salts dissolved in solution. It is based on the principle that solutions with a high concentration of salts have a greater ability to conduct an electrical current. Figure 4.1(a-c) and Table 4.1 showed pH, bulk density and electrical conductivity measurements for peanut shell biochar.

Table 1 pH, Electrical Conductivity and Bulk Density of Peanut Shell Activated Carbon

Sr. No.	Temperatures (°C)	Electrical Conductivity ($\mu S/cm$)	pH	Bulk Density (g/ml)
1.	300 °C	100.3	7.12	0.56
2.	400 °C	268.5	7.63	0.39
3.	500 °C	305.7	8.41	0.33
4.	600 °C	320.4	9.11	0.26

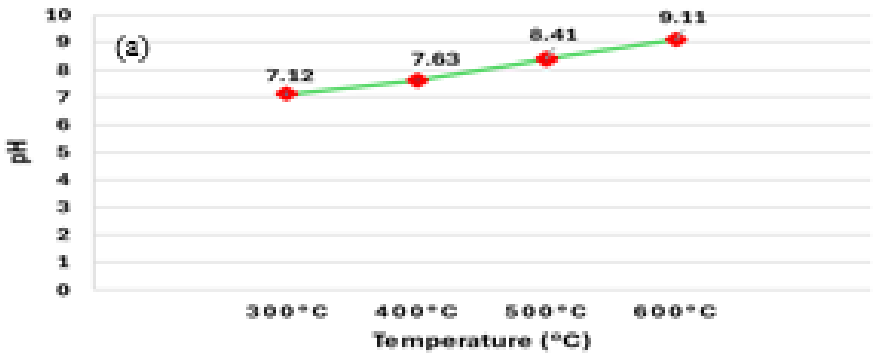

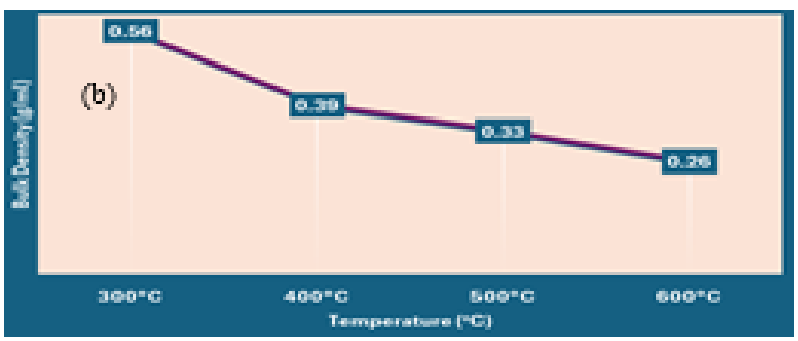

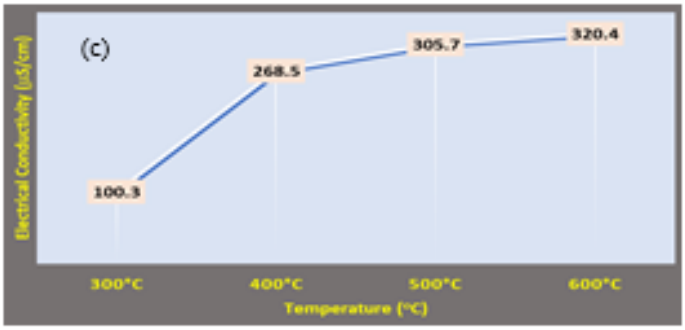

Figure 2 (a-c) pH value, Electrical Conductivity and Bulk Density of Peanut Activated Carbon

FTIR Analysis of Peanut Shell Activated Carbon

The FTIR analysis demonstrated the functional groups presented on PS activated carbon. The functional groups of samples PS have found to be O-H stretching vibration, C-H stretching vibration, C=O stretching vibration and C=C stretching vibration respectively. The spectrum of these samples showed some characteristic bands related to physical and chemical changes. As shown in figure 3 (a-d), the infrared spectra of these activated carbons are comparable but there are some changes in the functional groups. The strong hydroxyl group can display in the PS for about 3334.54 cm^{-1}, 3338.65 cm^{-1} and 3335.82 cm^{-1} at four different temperatures respectively. The absorption bands, between 3000 cm^{-1}-3300 cm^{-1} indicated the presence of strong carboxylic acid O-H stretch. Comparing with other biochar types, PS were associated with strong absorption bands at 3180.95 cm^{-1} and 3214.62 cm^{-1}, respectively. According to FTIR analysis, all of the absorption bands are found in peanut shell activated carbon due to hydroxyl group in cellulose, carbonyl groups of acetyl ester in hemicellulose, and carbonyl aldehyde in lignin.

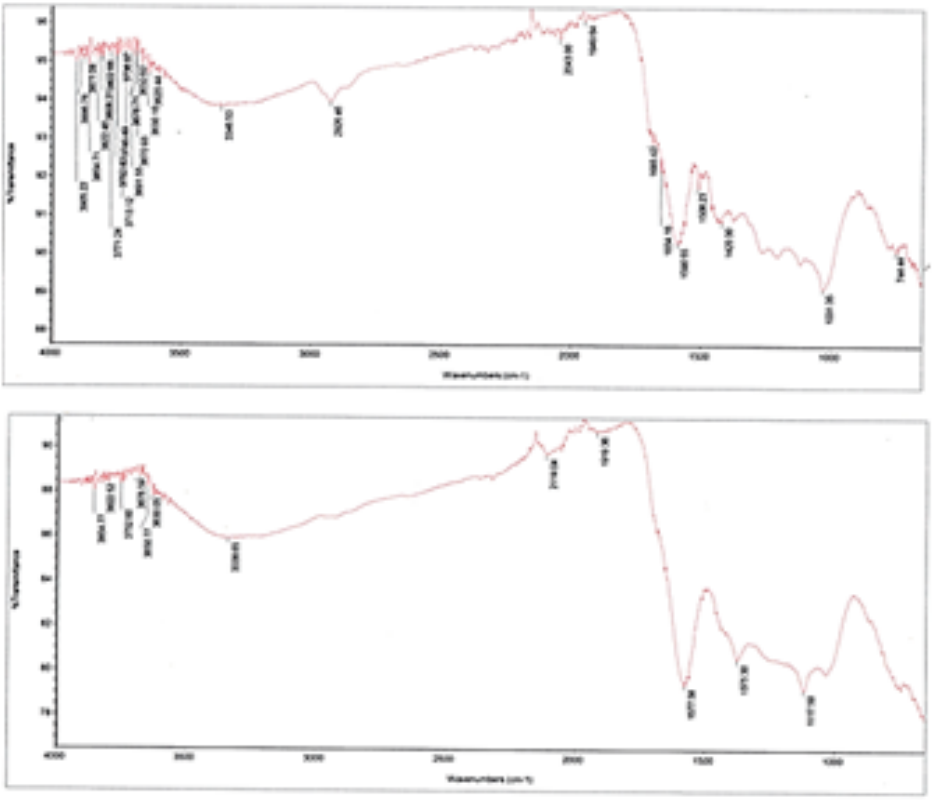

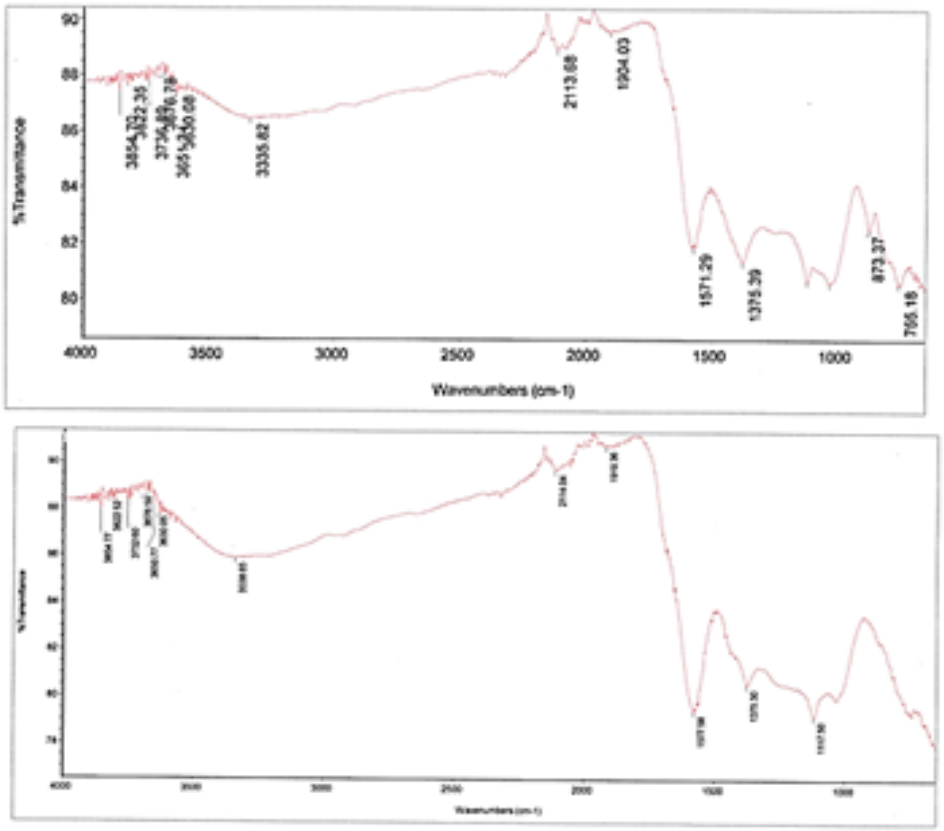

Figure 3(a-d) FTIR Spectrum of PS Activated Carbon at Different Temperatures

SEM Analysis of Peanut Shells Activated Carbon (PSAC)

SEM is one of the most versatile instruments available for the examination and analysis of the microstructure characteristics of a solid. SEM micrographs for external morphology of PSACs at different temperatures for 1 h were shown in figure 4. From SEM analysis as shown in figures, it can be observed that the microstructure of PSAC samples by varying the pore sizes with different temperatures. At 300 °C, the pores of PS biochar were non-uniform and not clear. At 400 °C, the pores looked like tube shape and the more uniformly microporous structure was found at 500 °C and 600 °C of PSACs. For PSACs, the average pore sizes of the samples were found to be about 3.42 μm at 300 °C, 3.54 μm at 400 °C and 2.52 μm at 500 °C and 2.11 μm at 600 °C respectively.

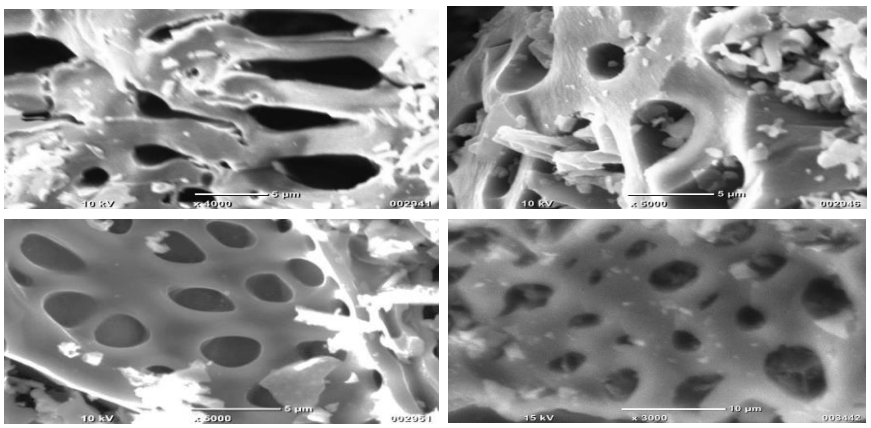

Figure 4 SEM Micrographs of PS Activated Carbon at Different Temperatures

Electrochemical Performance Analysis of PS Activated Carbons

The electrochemical performances of as fabricated AC electrodes were individually tested in electrolyte of 1 M NaOH aqueous solution, using three electrodes experimental set up, consisting of as fabricated AC electrodes separately as working electrode, Pt-plate as counter electrode and Ag/AgCl as reference electrode. The cell was connected to ‘‘CorrTest Electrochemical Workstation (potentiostat / galvanostat)” system to perform the experiment under room temperature. For the Cyclic Voltammetry measurement, the potential window of -0.4 to 0 V was chosen. The scan rate of 50 mVs^{-1} was used in this experiment. The electrochemical performance setup was shown in figure 5.

Cyclic Voltammetry (CV) Measurement of AC-Electrodes

Cyclic voltammetry (CV) measurements were used to show the supercapacitive behaviors This behavior is expected to enable easy and smooth transport of electrolyte ions. Such a mechanism is in agreement with the results of carbonized biomass reported by other research groups. For the calculation, 1 mg of the mass of active materials, 0.39 V of the potential window from CV curves and 50 mV/s of the scan rate was used. According to these calculated CV results, peanut shell activated carbons at 600 ^{o}C were the highest specific capacitance values. The comparison of all the specific capacitance values and CV for activated carbon samples was shown in figure 5and 6.

Table 4 Specific capacitances (C_{sp}) for PSAC electrodes at different temperatures

Samples	A(AV) ($\times 10^{-2}$)	K (mV/s)	V_2-V_1 (V)	m (g)	C_{sp} (F/g)
300 ^{o}C	1.71	100	0.39	0.001	219.23
400 ^{o}C	1.75	100	0.39	0.001	224.36
500 ^{o}C	1.82	100	0.39	0.001	233.33
600 ^{o}C	2.47	100	0.39	0.001	316.67

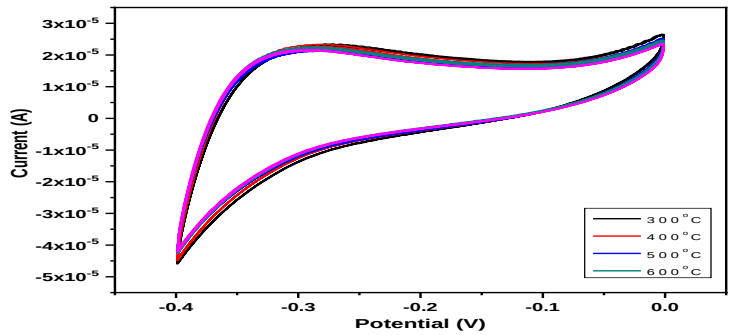

Figure 5 Cyclic Voltammograms for PSACs at Different Temperatures

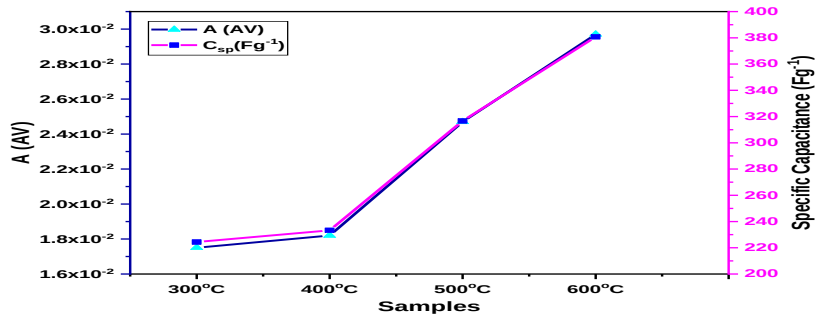

Figure 6 Comparison of all the specific capacitance values for PSACs

Energy Density and Power Density of Activated Carbon Electrodes

The Energy density and Power density plotted in figure 7 were calculated. According to the calculated results, the AC-electrodes at 600 ^{o}C had highest energy densities and power densities. However, as the results, all AC-electrodes played the major source of capacitive characteristics in storing energy. So, these activated carbon materials were suitable to use as battery, supercapacitors, etc. The overall results of energy density and power density of AC-electrodes were tabulated in Table 5.

Table 5 Energy densities and power densities of PSAC electrodes

Samples	Energy density (Wh/kg)	Power density (W/kg)
300 ^{o}C	16.67	7502.63
400 ^{o}C	17.06	7678.13
500 ^{o}C	17.75	7985.25
600 ^{o}C	24.08	10837.13

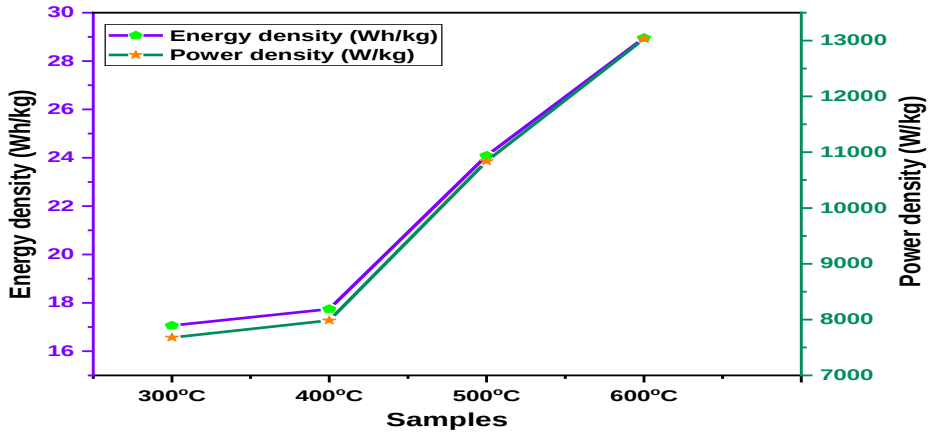

Figure 7 Plot of Energy Density and Power Density for PSACs

Conclusion

In this research work, the activated carbon prepared from agricultural wastes (peanut shell) with pyrolysis temperatures followed by KOH activation was successfully used as the electrode materials for supercapacitors. The chemical and morphological properties were determined by FTIR and SEM analyses. The electrochemical performances were examined by "CorrTest Electrochemical Workstation (potentiostat / galvanostat)". The electrochemical properties results revealed the improvement of conductivity by PSAC at 600 ^{o}C sample loading over the rest samples. Although all the peanut shell activated carbon at different temperatures exhibited improved electrochemical performances, PSAC at 600 ^{o}C sample showed prominently the highest specific capacitive value, energy density and power density of 316.67 Fg^{-1}, 24.08 $Whkg^{-1}$ and 10837.13 Wkg^{-1} at 50 mV s^{-1} scan rate which is the maximum values in the fabricated electrodes due to their increment of conducting ions. Owing to the unique characteristic, the simple preparation and the large available of material, these peanut shells activated carbons will become one kind of potential material for low cost energy conversion and storage devices such as supercapacitors.

Acknowledgements

I would like to express our sincere thanks to Professor Dr Maung Maung Shwe, Head of the Department of Physics, West Yangon University for his kind encouragement and permission to perform this research work. I would like to thank Professor Dr Aye Moe Soe, Professor Dr Thu Zar Aung and Professor Dr Yin Yin Thein, department of Physics, West Yangon University for their kind advice, encouragements and suggestions for this research.

References

Sun, Y., Sills, R. B., Hu, X., She, Z. W., Xiao, X., Xu, H., Luo, W., Jin, X., Xin, Y., & Li, T. (2015). A bamboo-inspired nanostructure design for flexible, foldable, and twistable energy storage devices. *Nano Letters*, *15*(6), 3899–3906.

Ndiaye, N. M., Ngom, B. D., Sylla, N. F., Masikhwa, T. M., Madito, M. J., Momodu, D., Ntsoane, T., & Manyala, N. (2018). Three-dimensional vanadium pentoxide/graphene foam composite as positive electrode for high performance asymmetric electrochemical super capacitor. *Journal of Colloid and Interface Science*, *532*, 395–406.

Yu, J., Gao, X., Cui, Z., Jiao, Y., Zhang, Q., Dong, H., Yu, L., & Dong, L. (2019). Facile synthesis of binary transition metal sulfide tubes derived from NiCo-MOF-74 for high-performance supercapacitors. *Energy Technology*, *7*(10), 1900018.

Lee, Y. J., Park, H. W., Park, S., & Song, I. K. (2012). Electrochemical properties of Mn-doped activated carbon aerogel as electrode material for supercapacitor. *Current Applied Physics*, *12*(1), 233–237.

Yang, G., & Park, S. J. (2018). Facile hydrothermal synthesis of $NiCo_{2}O_{4}$ decorated filter carbon as electrodes for high performance asymmetric supercapacitors. *Electrochimica Acta*, *285*, 405–414.

Yaglikci, S., Gokce, Y., Yagmur, E., & Aktas, Z. (2020). The performance of sulphur doped activated carbon supercapacitors prepared from waste tea. *Environmental Technology*, *41*(1), 36–48.

Zhang, Z., Wang, L., Li, Y., Wang, Y., Zhang, J., Guan, G., Huang, Z., Lin, G., Wei, Z., & Peng, H. (2017). Nitrogen-doped core-sheath carbon nanotube array for highly stretchable supercapacitor. *Advanced Energy Materials*, *7*(13), 1601814.

Chang, W. M., Wang, C. C., & Chen, C. Y. (2019). Fabrication of ultrathin carbon nanofibers by centrifuged-electrospinning for application in high-rate supercapacitors. *Electrochimica Acta*, *296*, 268–275.

Ke, Q., & Wang, J. (2016). Graphene-based materials for supercapacitor electrodes—A review. *Journal of Materiomics*, *2*(1), 37–54.

Zhu, J., Yang, X., Fu, Z., He, J., Wang, C., Wu, W., & Zhang, L. (2016). Three-dimensional macroassembly of sandwich-like, hierarchical, porous carbon/graphene nanosheets towards ultralight, superhigh surface area multifunctional aerogels. *Chemistry – A European Journal*, *22*(7), 2515–2524.

Li, X., Xing, W., Zhuo, S., Zhuo, J., Li, F., Qiao, S. Z., & Lu, D. Q. (2011). Preparation of capacitor's electrode from sunflower seed shell. *Bioresource Technology*, *102*(2), 1118–1123.

Xie, Y., Wang, L., Guo, Q., Yin, J., Liu, J., Fan, L., & Wu, J. (2018). Preparation of MnO_{2}/porous carbon material with core-shell structure and its application in supercapacitor. *Journal of Materials Science: Materials in Electronics*, *29*(10), 7957–7964.

Zhao, H. B., Cheng, J. B., Zhu, J. Y., & Wang, Y. Z. (2019). Ultralight CoNi/rGO aerogels toward excellent microwave absorption at ultrathin thickness. *Journal of Materials Chemistry C*, *7*(2), 441–448.

El-Barbary, M. H., & Philip, H. S. (2009). Characterization of fast pyrolysis bio-oils produced from pretreated pine wood. *Applied Biochemistry and Biotechnology*, *153*(1-3), 3–13.

Experimental Research on Direct Electricity Generated in Plant-Microbial Fuel Cells (P-MFC) Using Aloe vera Plants for Renewable Energy Sources

Zin Min Myat[1], Zin Min Tun[2], Thaung Thandar Soe[3], Yin Maung Maung[4]

Abstract

A plant microbial fuel cell (PMFC) is an advanced form of microbial fuel cell, which uses living plants to generate bioelectricity. In this research work, a new concept for a device that can directly generate continuous bioelectricity from the plant associated with microbial fuel cells (MFCs), in which *Aloe vera* plants were proven to have a potential for renewable energy source by embedding parts of electrodes into it to allow flow of ions and hence generate electricity. For the experimental process, firstly, plant microbial fuel cells (P-MFC) were built at five containers using the Cu-Zn electrodes. Next, the physicochemical properties of the prepared soil were investigated. In order to understand the optical and chemical nature of the *Aloe vera* plants were carried out using UV-Vis and FTIR analysis. Then, this study tested the potential of generating electricity from different containers of *Aloe vera* plants in a P-MFC set up. After that, open circuit voltage and short circuit current were continuously monitored to determine the power output of the P-MFC. Analytical tests using different containers in P-MFC were suggested that voltages are produced to greater or smaller extends with different containers using electrodes and the maximum power output were calculated from resulting experimental data. According to data analysis, the current and voltage were measured separately in the morning and evening hours, and it was observed that pot-4 produced the maximum power [15.92 μW (am)and 12.20 μW (pm)] in both time. The obtained results were confirmed the direct generation of electricity is responsible for the mechanism of the energy production from living plants and soil bacteria. This research can be supported an age of renewable energy for electricity scarce regions in Myanmar in the days to come.

Keywords: *Aloe vera* Plants, P-MFC, I-V Measurement, UV-Vis and FTIR

Introduction

Environmental safety and welfare are some of the most important effects for human beings as well as the survival of future generations (Marsh & Reinoso, 2006). One of the negative influences of the environment is the huge usage of electrical energy which grows day by day. For our daily lives, we requisite energy, and the crucial sources of energy are provided via the combustion of fossil fuels, which leads to high levels of air pollution and the emanation of greenhouse gasses (Bansal & Goyal, 2005; Ngu, 2022). The bioenergy contained in plant biomass has a solar origin and may include considerable shares in future sustainable renewable energy production (Ray, 1940). P-MFCs have increased much attention in recent years as a type of transforming organic waste containing wastewaters into electricity. P-MFCs are the chief type of bioelectrochemical systems that alter biomass spontaneously into electricity through the metabolic activity of the symbiotic microorganisms. P-MFC is deliberated to be an auspicious sustainable technology to meet growing energy needs, exclusively consuming wastewaters as substrates, which can produce electricity (González-García, 2018). The purpose of the P-MFC is to convert solar energy into electrical energy through the oxidation of rhizodeposits by electrochemically active bacteria. Photosynthesis in plants happens in its leaves whereby solar energy is used to fix carbon dioxide in the form of carbohydrates (Ozdemir et al., 2014). Depending on plant species, age, and environmental situations up to 60% of the net fixed carbon can be moved from its leaves to the roots (Danish & Ahmad, 2018). The plant root system yields and releases different types of organic

[1] Associate Professor, Department of Physics, West Yangon University
[2] Associate Professor, Department of Physics, West Yangon University
[3] Lecturer, Department of Physics, East Yangon University
[4] Professor and Head, Department of Physics, University of Yangon

compounds into the soil, which contains exudates of sugars, organic acids, polymeric carbohydrates, enzymes, lysates of dead cell materials, and gases like ethylene and CO_2 (Köseoğlu & Akmil-Başar, 2015). In this work, we propose a plant microbial fuel cell (plant-MFC) perception, which deficiencies these disadvantages and promises high yields. The plant-MFC purposes to alter solar radiation into green electricity in a clean and efficient manner by integrating the roots of a living plant in the anode compartment of a microbial fuel cell. Organic matters were manufactured by plants during photosynthesis. Some part of this organic matter is applied for plant-growth (Dias et al., 2007). Plant-based energy generation is a method that harvests electrical energy from living plants.

Materials and Methods

Aloe Vera Plant

Aloe vera plant has been known and used for its health, beauty, medicinal and skin care properties. *Aloe vera* gel play an important role in the treatment of tumors, diabetes, ulcer and cancer. *Aloe vera* is a photosynthetic plant of great interest for several biomedical and pharmaceutical preparations due to its therapeutic properties. Aloe vera exhibits significant bioelectrical properties, acting as a natural, sustainable, and eco-friendly solid polymer electrolyte with high ionic conductivity. Its gel contains organic acids and moisture (over 96%), allowing it to function as a green electrolytic solution in batteries. Aloe vera is an herb with succulent leaves that are arranged in a rosette. The leaves are grey to green and sometimes have white spots on their surfaces. They have sharp, pinkish spines along their edges and are the source of the colourless gel found in many commercial and medicinal products. In plant-microbial fuel cells (P-MFC) and displaying memristor-like behavior in its electrical network. The electrical properties of Aloe vera are primarily due to the presence of water, salts, and organic acids, providing a natural alternative to harmful chemical electrolytes.

Copper (Cu) Electrode

A copper electrode is a piece of copper used as an electrical conductor in an electrochemical cell. It plays a crucial role in various applications due to copper's excellent properties. It has good resistance to corrosion although it can react with certain chemicals and oxidizing environments. It can act as either an anode or cathode depending on the specific reaction taking place. Copper is a highly conductive metal making it ideal for transferring electrons in an electrochemical system. Copper improves initial conductivity and the anticorrosive properties of the electrode, thermal conductivity and melting point of copper is higher as compared to that of other metals. Copper is undergoing oxidation, therefore, it is an anode. Electrons flow from the anode to the cathode.

Zinc (Zn) Electrode

Zinc electrode is a component used in electrochemical cells, such as batteries and galvanic cells. The nature of zinc electrode is characterized by its strong tendency to oxidize, making it an excellent electron donor for power generation and a protective agent against corrosion and it refers to its inherent characteristic how it behaves in electrochemical systems. Zinc electrode designed to improve initial conductivity and the anti-corrosive properties of the electrodes. Zinc electrodes (cathode) are negatively charged electrodes. The carries of current in the cell are free electrons which move from anode to cathode and thus produce the current in the external circuit from cathode to anode.

Experimental Procedure of Plant Microbial Fuel Cells (P-MFC)

The research work selected the Aloe vera plants which were due to the vast variety of plants available locally with good potential. Five pots (compost: rice husk ash: dung: biochar = 1:1:1:1, 2:1:1:1, 3:1:1:1, 4:1:1:1 5:1:1:1) were taken for this research. Selected potted plants of Aloe vera plants, copper electrode, zinc electrodes, soil tester, conducting wires and digital multi meter as the biological specimen are the constituents of the living plant Microbial Fuel Cell (P-MFC). This research is intended to model the direct electricity generation based on the electrochemistry mechanisms. In the experiment presented a pair of clean Cu-Zn electrodes were embedded into Aloe vera plants to make the living plant microbial fuel cells (P-MFC) system. Copper is used as the anode and Zinc is used as cathode. Length of the electrodes used is 20 cm and the diameter is 6 mm. The Electrodes are placed for the flow of electron to produce electricity. With the utilization of electrodes in PMFC, electrons are attracted to the anode electrode. The anode is connected to an external load and to a cathode electrode to enable flow of electron across the load and toward the cathode. In a plant cell, the flow of energy in a plant cell begins with photosynthesis, which converts sunlight into chemical energy in the form of glucose. The equation for photosynthesis is

$$6CO_2 + 6H_2O + \text{sunlight} \longrightarrow C_6H_{12}O_6 + 6O_2 \xrightarrow[\text{Breakdown}]{\text{Microbacteria}} \text{Electrons} \longrightarrow \text{Electricity}$$

Table 1 Physical Parameters of Experiments

Materials	Bulk Density (cm^{-3})	pH	Moisture	Height of Plant (cm)
Pot-1	0.40	8	10	33
Pot-2	0.60	8	10	31
Pot-3	0.62	8	10	35
Pot-4	0.64	8	10	29
Pot-5	0.66	9	8	30

Figure 1 Soil Preparation for Plants Microbial Fuel Cells (P-MFC)

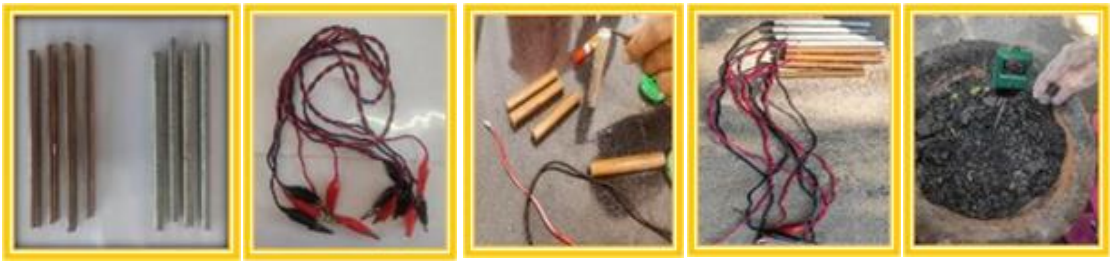

Figure 2 Electrodes Preparation for Plants Microbial Fuel Cells (P-MFC)

Figure 3 Fabrication and Measurement System of Plant-Microbial Fuel Cells

Results and Discussion

FITR Analysis of Aloe Vera Plants

The Fourier Transform Infrared Spectroscopy (FTIR) was used to characterize the Aloe Vera plant because functional groups and chemical properties can be detected that may modify the sequestration capability. FTIR spectroscopy was applied to measure the chemical properties and transmission of energy from the range of 4000 cm^{-1} - 500 cm^{-1} by studied the sample. The functional groups and their relative compound classes of these three plants were listed in Table 1 According to FTIR analysis, all of the transmittance for Aloe Vera was presented in Figure 4.

Table 1 FTIR analysis of Aloe Vera plant

Wave number (cm^{-1})	Range (cm^{-1})	Functional group	Compound class
877.96	850-895	C=C bending	Alkene
1043.87	1020-1250	C-N stretching	Amine
1086.08	1085-1150	C-O stretching	Aliphatic ether
1326.97	1266-1342	C-N stretching	Aromatic amine
1383.22	1310-1390	O-H bending	Phenol
1647.21	1638-1648	C-C stretching	Alkene
2977.17	2840-3000	C-H stretching	Alkane
3346.33	3200-3550	O-H stretching	Alcohol

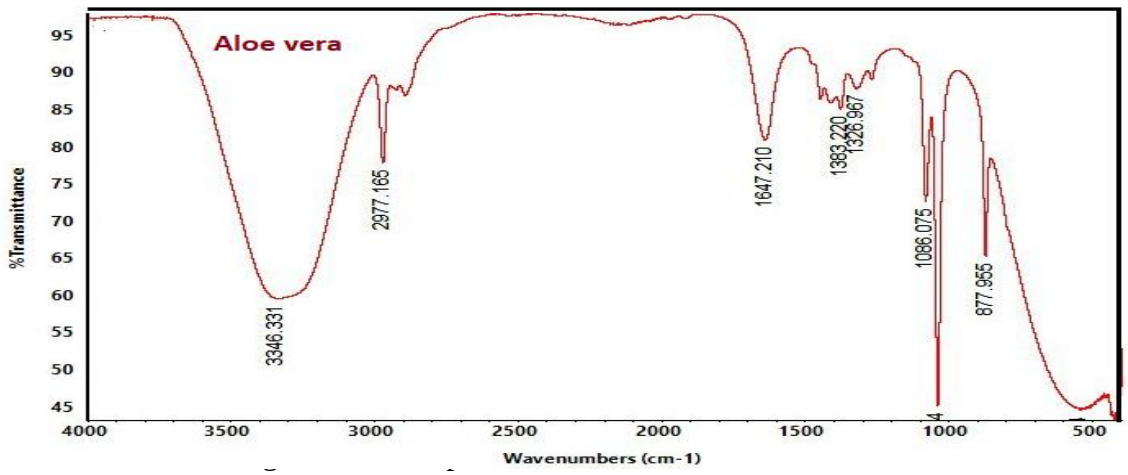

pH Testing

Soil pH testing is very important for plant microbial fuel cells (P-MFC). Soil pH measurement is very essential it is a predictor of various activities in the soil. The simplest method is to measure pH value with a portable pH meter using HORIBA, pH METER, F-51 Model. Soil pH can be considered to the acidity or alkalinity of the concentration of free hydrogen ions that are in the soil. Soil pH values can be considered five reasons that are strong acidity (pH < 5), moderate acidity (5.0 < pH <6.0), natural value (6.5 < pH < 7.5), moderate alkalinity (7.5 < pH < 8.5) and strong alkalinity (pH > 8.5- 14). According to the results, the values of soil pH were found to be 7.4 for the pot of Aloe Vera. These data available confirms that the best performance of soil pH should be in the range of 5.5 -7.5. The electrical conductivity of Aloe Vera were found to be 1761μS/cm and 7.4 at room temperature. This natural range can affect the activities of both beneficial and pathogenic microorganisms and it can support the direct generation of electricity in living pants microbial fuel cells (P-MFC).

Electrical Conductivity (EC) Testing

The electrical conductivity (EC) of the solution in the soil is a measure of the ability of the solution to conduct electricity. Living plants' microbial fuel cells and the water management system of soil are the main factor of EC on plants. Electrical conductivity is measured by HORIBA, COND METER, and ES-51 Model. An understanding of the number of soluble salts in a soil solution is important since high rates of L-MFC application. It was found that EC is proportional to the quantity and nature of salts dissolved in the solution. It is based on the principle that solutions with a high concentration of salts have a greater ability to conduct an electrical current. It was found that when ions are present, the EC of the solution increases and there were no salts indicted that the EC of the solution in soil was low which pointed out that the soil solution did not conduct electricity well.

Generate Electricity with Time and Voltage from Aloe Vera Plants

The living plant microbial fuel cell (P-MFC) was set up as in the figure 1,2, 3 & 4 and Table 2 & 3 list the investigation of the current-voltage characterization was conducted using a digital multi-meter for a period of different time especially morning section and evening section. Similar procedure was repeated for the other two potential plants. It can be seen that the charts and graph of variation voltage with respect to time and different containers as described in figure 5 and figure 6 & 7 for plant microbial fuel cell (P-MFC) of Aloe vera plants.

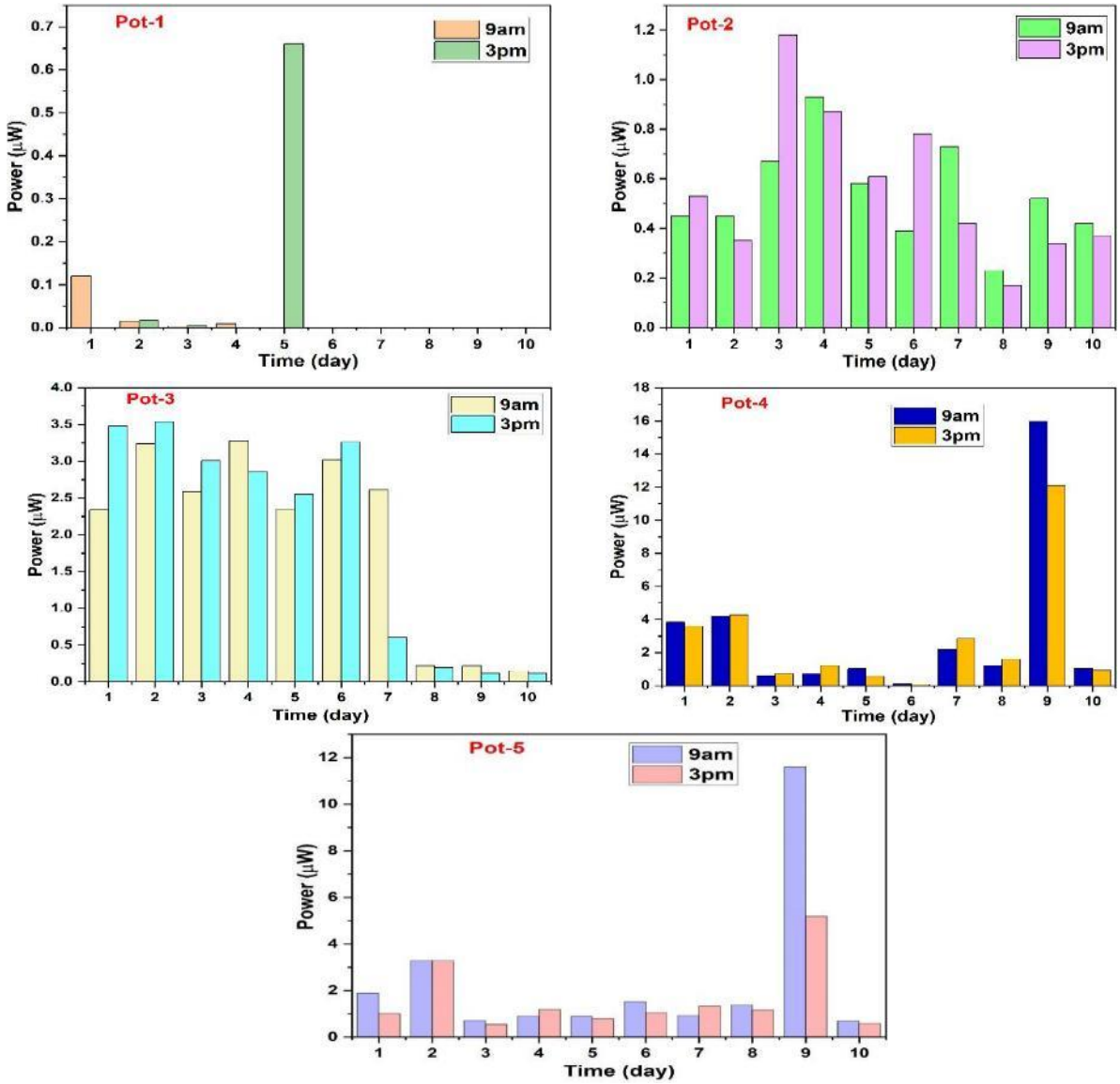

Figure 5 Chats of Power Generated from Lucky Bamboo Plant (Pot-1,2,3,4 and 5)

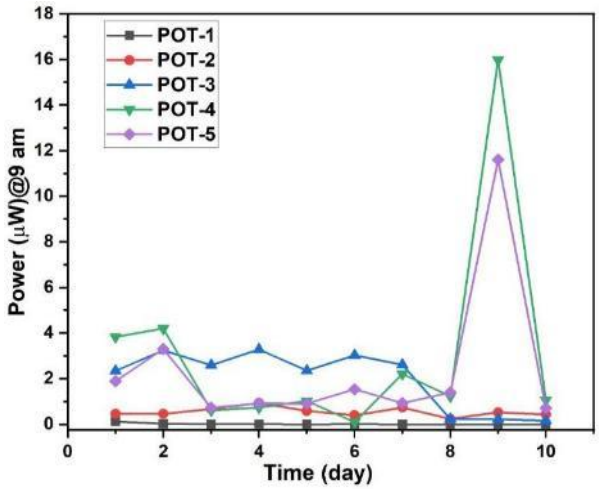

Figure 6 Graph of Time-Power generated from Five Different Pot at Morning Time

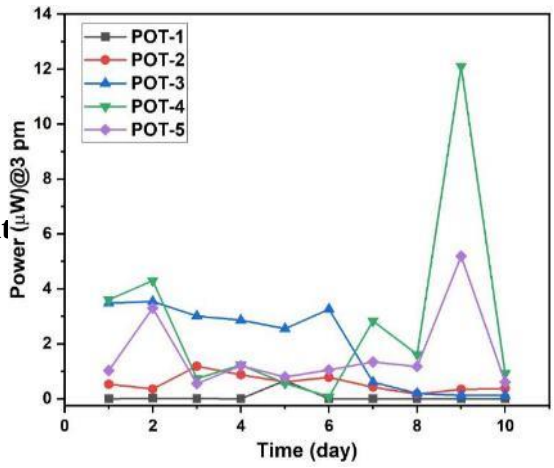

Figure 7 Graph of Time-Power generated from Five Different Pot at Evening Time

Table 3 Electrical Performances of P-MFCs at Days 1-10 (Pots 1-4)

Days	Hour of monitoring	Pot -1			Pot -2			Pot -3		
		mV	mA	μW	mV	mA	μW	mV	mA	μW
1	9am	0.12	1	0.12	0.3	1.5	0.45	0.6	3.9	2.34
	3pm	0.03	0.02	0.0006	0.22	2.4	0.53	0.59	5.9	3.48
2	9am	0.50	0.03	0.015	0.31	1.45	0.45	0.57	5.68	3.24
	3pm	0.11	0.15	0.016	0.28	1.25	0.35	0.55	6.44	3.54
3	9am	0.07	0.04	0.003	0.52	1.32	0.67	0.47	5.52	2.59
	3pm	0.09	0.05	0.005	0.79	1.50	1.18	0.52	5.79	3.01
4	9am	0.15	0.06	0.009	0.60	1.55	0.93	0.53	6.20	3.28
	3pm	0.01	0.02	0.0002	0.40	2.17	0.87	0.49	5.83	2.86
5	9am	0.01	0.03	0.0003	0.30	1.92	0.58	0.49	4.80	2.35
	3pm	0.50	1.31	0.66	0.32	1.88	0.61	0.47	5.43	2.55
6	9am	0.03	0.03	0.0009	1.69	0.23	0.39	6.3	0.48	3.02
	3pm	0.03	0.03	0.0009	2.12	0.37	0.78	6.51	0.50	3.26
7	9am	0.03	0.01	0.0003	2.36	0.31	0.73	5.11	0.51	2.61
	3pm	0.01	0.01	0.0001	1.41	0.30	0.42	1.57	0.38	0.60
8	9am	0.01	0.01	0.0001	0.74	0.31	0.23	0.70	0.31	0.22
	3pm	0.01	0.01	0.0001	0.67	0.26	0.17	0.64	0.29	0.19
9	9am	0.01	0.01	0.0001	1.94	0.27	0.52	0.71	0.31	0.22
	3pm	0.01	0.01	0.0001	1.32	0.26	0.34	0.46	0.25	0.12
10	9am	0.01	0.01	0.0001	1.36	0.31	0.42	0.56	0.27	0.15
	3pm	0.01	0.01	0.0001	1.27	0.29	0.37	0.49	0.25	0.12

Table 3 Electrical Performances of P-MFCs at Days 1-10 (Pots 4 & 5)

Days	Hour of monitoring	Pot -4			Pot -5		
		(mV)	(mA)	(μW)	(mV)	(mA)	(μW)
1	9am	0.44	8.7	3.83	0.54	3.5	1.89
	3pm	0.48	7.50	3.60	0.22	4.60	1.02
2	9am	0.49	8.50	4.20	0.54	6.10	3.30
	3pm	0.50	8.60	4.30	0.57	5.70	3.30
3	9am	0.40	1.50	0.60	0.27	2.67	0.72
	3pm	0.43	1.69	0.73	0.32	1.71	0.55
4	9am	0.36	2.02	0.73	0.40	2.28	0.91
	3pm	0.45	2.70	1.22	0.48	2.42	1.20
5	9am	0.43	2.37	1.02	0.39	2.56	0.90
	3pm	0.43	1.30	0.56	0.35	2.27	0.79
1	9am	0.44	8.7	3.83	0.54	3.5	1.89
	3pm	0.48	7.50	3.60	0.22	4.60	1.02
6	9am	0.33	0.26	0.09	3.65	0.42	1.53
	3pm	0.36	0.20	0.07	2.50	0.42	1.05
7	9am	4.81	0.46	2.21	2.13	0.44	0.93
	3pm	5.45	0.20	2.83	3.20	0.42	1.34
8	9am	3.04	0.40	1.22	3.56	0.39	1.39
	3pm	3.28	0.49	1.61	2.85	0.41	1.17
9	9am	3.01	5.31	15.92	2.37	4.90	11.60
	3pm	2.42	4.98	12.20	1.05	4.95	5.19
10	9am	2.70	0.39	1.05	1.82	0.39	0.71
	3pm	2.62	0.35	0.92	1.72	0.35	0.60

Conclusion

In this research work, the mechanism of energy production of P-MFC is modelled based on the principle of electrochemistry process. The direct electricity from living plants is a power generation into electricity without the combustion associated with conventional heat engines. This project is the combination of electrodes pairs with energy sources of the electrical energy harvested by embedding electrodes into the Aloe vera plants. According to data analysis, it was found that Aloe vera plant produces more open circuit voltage, current and power in Pot-4 and Pot-5 than other pots. This research is the combination of electrodes pairs with energy sources of the electrical energy harvested by embedding electrodes into the Aloe vera plants. According to data analysis, it was found that Aloe vera plant produces more open circuit voltage at afternoon than that of morning. Therefore, these results show that

combination of pair electrodes and the two types of pair electrodes are very important role in determining the harvested voltage output to direct generating of electricity in living plants as P-MFCs. By giving an electrode for the micro-organisms to contribute their electrons, the electrons can be garnered as electricity. This study is easy, simple, low cost and ecofriendly for assessing the direct generation of electricity from living plants with environmental friendliness. PMFCs can generate electricity from the organic matter produced by plants, offering a renewable energy source. Plant microbial fuel cells (PMFCs) offer the potential for sustainable energy generation, environmental remediation, production of renewable electricity, environmental monitoring and pollutant removal.

Acknowledgements

I would like to express our sincere thanks to Professor Dr Maung Maung Shwe, Head of the Department of Physics, West Yangon University for his kind encouragement and permission to perform this research work. I would like to thank Professor Dr Aye Moe Soe, Professor Dr Thu Zar Aung and Professor Dr Yin Yin Thein, department of Physics, West Yangon University for their kind advice, encouragements and suggestions for this research.

References

Bais, H. P., Weir, T. L., Perry, J. G., Gilroy, S., & Vivanco, J. M. (2006). The role of root exudates in rhizosphere interactions with plants and other organisms. *Annual Review of Plant Biology, 57*, 233–266.

Barua, P. K., & Deka, D. (2010). Electricity generation from biowaste based microbial fuel cells. *International Journal of Energy, Information and Communications*.

Chaudhuri, S. K., & Lovley, D. R. (2003). Electricity generation by direct oxidation of glucose in mediatorless microbial fuel cells. *Nature Biotechnology, 21*(10), 1229–1232.

Cheng, S., & Logan, B. E. (2011). Increasing power generation for scaling up single-chamber air cathode microbial fuel cells. *Bioresource Technology, 102*(6), 4468–4473.

Dayou, J., & Chow, M. S. (2011). Performance study of piezoelectric energy harvesting to flash a LED. *International Journal of Renewable Energy Research, 1*(4), 323–332.

Gowtham, R., & Sundar, K. U. S. (2015). Generating current from plants Plant-e technology. *International Journal of Recent Advances in Engineering & Technology, 3*, 2347–2812.

Helder, M., Strik, D. P., Hamelers, H. V. M., & Buisman, C. J. N. (2012). The flat-plate plant-microbial fuel cell: The effect of a new design on internal resistances. *Biotechnology for Biofuels, 5*, Article 70.

Lynch, J. M., & Whipps, J. M. (1990). Substrate flow in the rhizosphere. *Plant and Soil, 129*(1), 1–10.

Manohar, K., Shinde, A. A., & Supriya, S. (2017). Green electricity production from living plant and microbial fuel cell. *International Journal of Advance Research in Science and Engineering, 6*(9), 564–571.

Moqsud, M. A., Yoshitake, J. Q. S., Hyodo, M., Omine, K., & Strik, D. P. (2014). Compost in plant microbial fuel cell for bioelectricity generation. *Waste Management, 33*(11), 2465–2469.

Strik, D. P., Hamelers, H. V. M., Snel, F. H. J., & Buisman, C. J. N. (2008). Green electricity production with living plants and bacteria in a fuel cell. *International Journal of Energy Research, 32*(9), 870–876.

Timmers, R. A., Strik, D. P., Hamelers, H. V. M., & Buisman, C. J. N. (2010). Long-term performance of a plant microbial fuel cell with Spartina anglica. *Applied Microbiology and Biotechnology, 86*(3), 973–981.

Ueoka, N., Sese, N., Sue, M., Kouzuma, A., & Watanabe, K. (2016). Sizes of anode and cathode affect electricity generation in rice paddy-field microbial fuel cells. *Journal of Sustainable Bioenergy Systems, 6*(1), 10–15.

Comparative Study Of Zinc Oxide (Zno) Nanoparticles Synthesized Via Green And Co-Precipitation Methods

Khin Thuzar Cho[1], Ni Ni Win[2], Tin Hla Yin[3]

Abstract

Zinc Oxide (ZnO) nanoparticles were successfully synthesized using green synthesis and co-precipitation method in order to compare their structural and morphological properties. In green synthesis, Natural plant-based extracts are used as reducing agent and stabilizing agent, while conventional chemical reagents are used in the co-precipitation. In synthesize the pure ZnO nanoparticles (NPs), Zinc nitrate hexahydrate is used as precursor material. The prepared ZnO nanoparticles (NPs) were characterized using X-Ray Diffraction (XRD) to determine their crystallinity, Scanning Electron Microscopy (SEM) is used to study the morphology of the sample and Fourier Transform Infrared Spectroscopy (FTIR) is identified the functional groups. XRD analysis confirmed the formation of single-phase hexagonal wurtzite ZnO with good crystallinity. Zinc is the one of the most important elements in living organisms and similarly zinc derived compounds have attracted much attention because of their applications in various fields like agricultural, medicinal, industrial, electronics, etc. The comparative results demonstrate that green synthesis provides an eco-friendly and cost-effective alternative to the co-precipitation method while producing ZnO nanoparticles (NPs).

Keywords: Zinc oxide, nanoparticles, green synthesis, co-precipitation.

Introduction

Nanotechnology is a unique branch of science that deals with materials in a very small size between (1 – 100 nm) with different crystal shapes such as spherical nanoparticles, flower like, nanorods, nanoribbons, and nanoplatelets. (Saja Mohsen J, 2016)

Various methods have been used to produce metal oxide nanoparticles. A variety of conventional methods have been employed for the synthesis of metal oxide nanoparticles loke sol-gel method, anodization, co-precipitation, ultrasound, chemical vapor deposition (CVD), green synthesis and mechanochemical-thermal synthesis. (Balogun SW et al, 2020)

Zinc Oxide is a chemical compound found naturally in the mineral called zincite and has attracted much attention in recent times due to its low cost and because it can be obtained by simple techniques. (Koudelka L et al, 2004)

ZnO crystallizes in the typical wurtzite hexagonal structure where oxygen and zinc atoms are spatially arranged in a way that O atoms are arranged in a closed centre of the distorted tetrahedron structure. (Bruna Martinello S et al, 2015)

Moreover, it is a semiconductor material of the II – VI group with a large energy gap around Eg = 3.2 eV, a large range of excitation energy and controlled electrical conductivity, and when doped with transition metals exhibits the ferromagnetic phenomenon at room temperature, and because of that it has attracted much interest due to their potential applications in ‘spintronics’. (Prellier W et al, 2003)

The ZnO is insoluble in water and ethanol but is soluble in dilute mineral acids and is a fine powder, white or slightly yellow. It is an intrinsic n-type semiconductor material that crystallizes in the hexagonal crystal system; it is relatively inexpensive, presents low toxicity, and is very effective in protecting against UV rays. (Ramalto, 2004)

[1] Dr., Associate Professor, Department of Physics, West Yangon University
[2] Dr., Lecturer, Department of Physics, West Yangon University
[3] Dr., Associate Professor, Department of Physics, West Yangon University

In this study ZnO NPs were synthesized by green synthesis and co-precipitation method. ZnO NPs prepared by two methods were compared using XRD, SEM, and FTIR spectroscopy.

Materials and Methods

Materials

Zinc Nitrate hexahydrate ($Zn(NO_3)_2 \cdot 6H_2O$) was purchased from Chemical Store. Distilled-water was used as solvent. Sodium hydroxide (NaOH) was also used to monitoring the pH. Orange Fruits were bought from local market to prepare orange fruit peel extract.

Preparation of Orange Fruit Peel Extract

The orange fruit peel extract can be seen in figure 1(a). Orange fruits were bought from local market. The fruit peels were collected and cut in pieces. The peels were dried at room temperature for a week. The dried peels were grinded with blander to form a powder. 10 g of powder was mixed with 100 mL of distilled-water. The solution was heated at 70 °C for 45 minutes. After filtering, the orange fruit peel extract was obtained.

Synthesis of ZnO NPs by Green Method

Figure 1(b) shows the synthesis of ZnO NPs using orange fruit peel extract solution. The orange fruit peel extract was used as a reducing or capping agent. 30 g of $Zn(NO_3)_2 \cdot 6H_2O$ was dissolved in 100 mL of distilled-water to initiate the green synthesis process for ZnO NPs. After, 40 mL of orange fruit peel extract solution was slowly added to 100 mL of 1 M $Zn(NO_3)_2 \cdot 6H_2O$ solution, the pH was kept at 7.0 with NaOH. The solution then underwent to a reflux at a magnetic stirrer. The colour of the solution changed from light-orange to yellowish-white when the solution was stirring with a magnetic stirrer at 70 °C for 3 hr. After filtering the solution, the solid precipitate was washed three times with distilled-water, followed by 99% ethanol wash for ZnO NPs separation. The precipitates were dried at 100 °C until dry. And then as -prepared ZnO nanoparticles were calcined at 600 °C for 1 hr with Muffle furnace. The mixture of organic solution was then decomposed directly when calcination at 600 °C resulting in the release of ZnO nanoparticles.

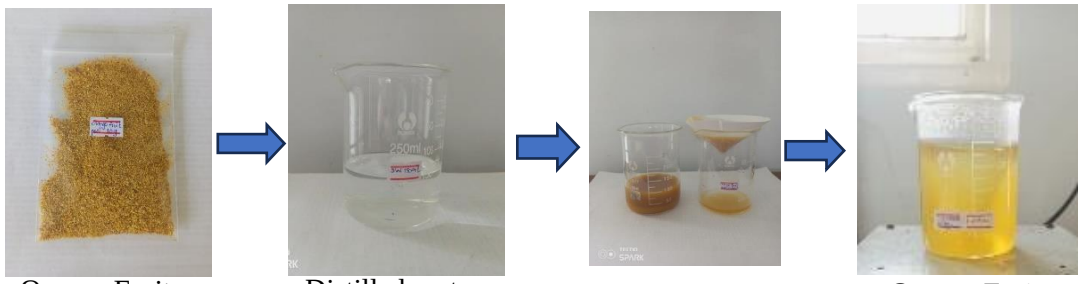

(a)

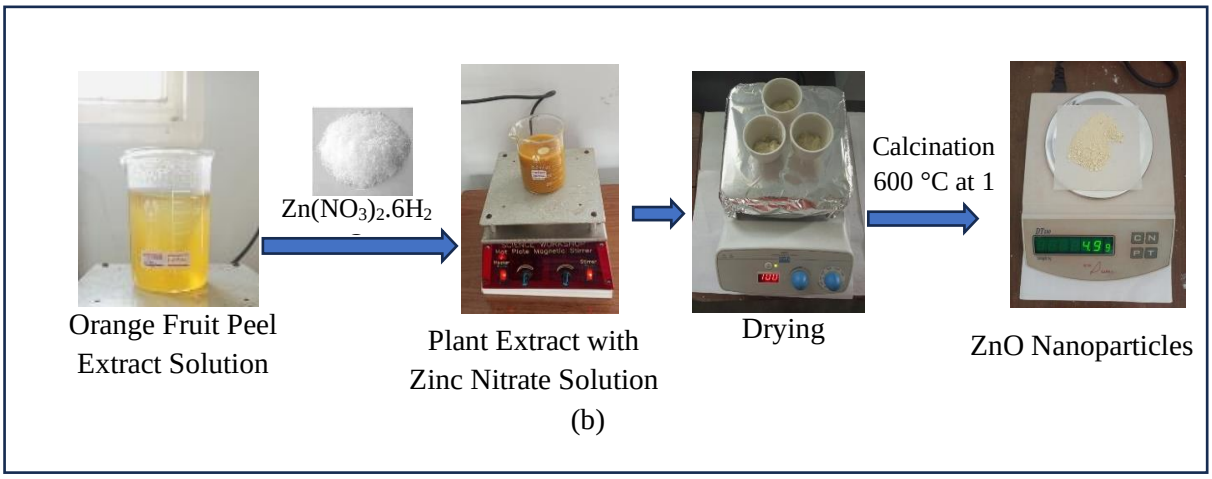

Figure 1 (a) Schematic representation of orange fruit peel extract (b) Schematic diagram of green synthesis of zinc oxide nanoparticles

Synthesis of ZnO NPs by Co-precipitation Method

Initially, a 1 M zinc nitrate solution was prepared via the addition of zinc nitrate hexahydrate to distilled-water under constant magnetic stirring (700 rpm). Then, sodium hydroxide (1 M) was poured dropwise into the solution until a pH value equal to 7 was obtained. After 60 min at 70 °C, the milky white solution was obtained. The precipitates were filtered and dried at 100 °C until dry. The dried precipitate was then calcinated at 600 °C for 1 hr, finally leading to the production of a gray powder of ZnO nanoparticles.

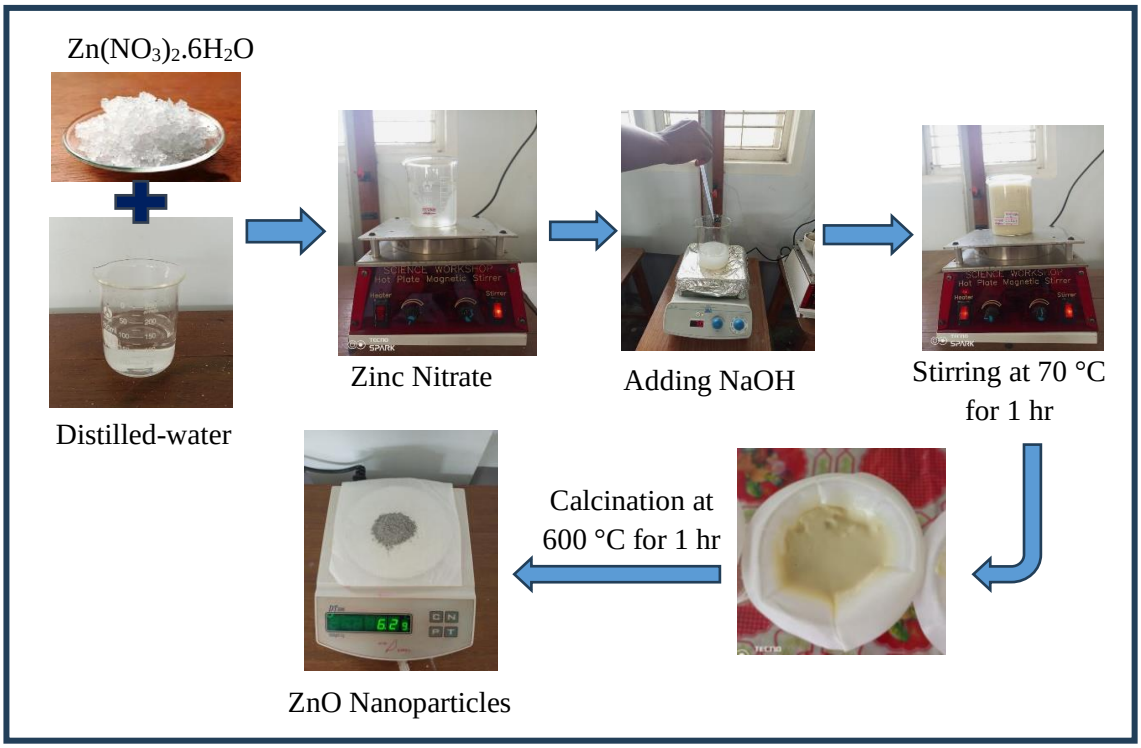

Figure 2 Schematic representation of Zinc Oxide Nanoparticles by Co-precipitation

Results

XRD analysis

The pure ZnO nanoparticles were prepared using green synthesis and co-precipitation method. The powdered sample obtained were characterized using X-ray diffraction method to analyze the crystallinity of the sample. The Debye-Scherrer equation is used for determining the crystallite size: $D = \frac{K\lambda}{\beta . \cos\theta}$.

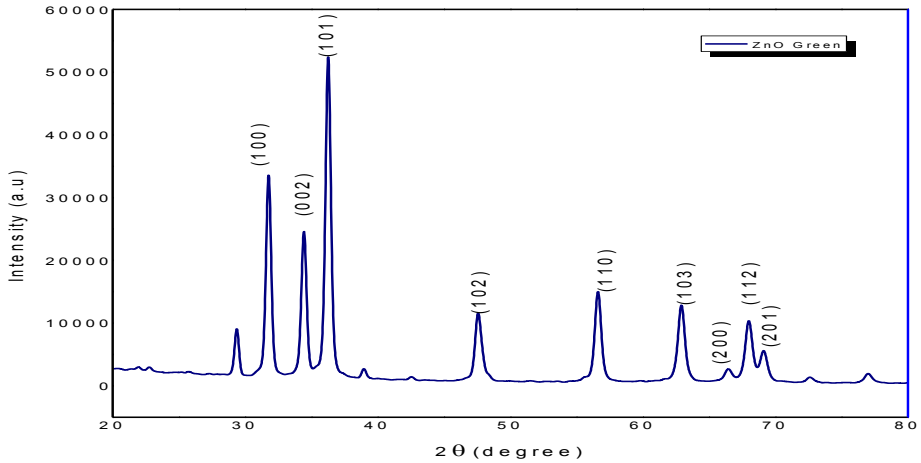

Figure 3 XRD pattern of pure ZnO nanoparticles by green synthesis

The XRD spectrum of the synthesized zinc oxide nanoparticles using green method is presented in figure 3. The sample with annealing temperature 600 °C exhibited preferred diffraction peaks at 2θ angles of 31.76°, 34.42°, 36.26°, 47.88°, 56.6°, 62.82°, 68°, and 69.12°, corresponding to lattice planes of (100), (002), (101), (102), (110), (103), (112) and (201) respectively. These observations confirmed that the ZnO NPs exhibited a hexagonal wurtzite structure. The plane alignments of the synthesized ZnO NPs were in excellent accordance with the standard ZnO nanoparticles obtained for the International Centre of Diffraction Data Card (JCPDS No 01-089-0510). XRD Results of ZnO NPs by Green Synthesis is shown in Table 1. The average crystallite size was 33.4 nm.

Table 1 XRD Results of ZnO NPs by Green Synthesis

hkl	2θ	Interplanar spacing (Å)	FWHM	Crystallite Size (nm)
(100)	31.76°	2.818	0.220	39.20
(002)	34.42°	2.606	0.218	39.90
(101)	36.26°	2.477	0.209	41.70
(102)	47.88°	1.899	0.265	34.20
(110)	56.60°	1.626	0.311	30.30
(103)	62.82°	1.479	0.304	32.00
(112)	68.00°	1.378	0.384	26.00
(201)	69.12°	1.359	0.427	23.60
Average Crystallite Size				33.40

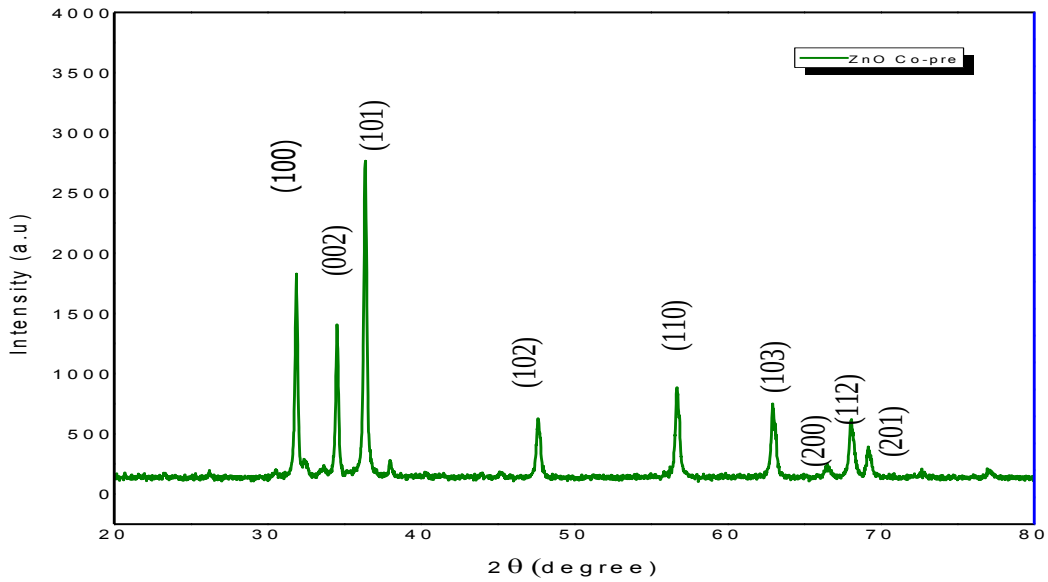

Figure 4 XRD pattern of pure ZnO nanoparticles by co-precipitation method

The XRD spectrum of the synthesized zinc oxide nanoparticles using co-precipitation method is presented in figure 4. The ZnO NPs exhibited crystalline XRD peaks at 2θ values of 31.89°, 34.55°, 36.39°, 47.72°, 56.82°, 63.11°, 68.23° and 69.37° which correspond to the planes of crystals of (100), (002), (101), (102), (110), (103) , (112) and (201), respectively. The plane alignments of the synthesized ZnO NPs were in excellent accordance with the standard ZnO nanoparticles obtained for the International Centre of Diffraction Data Card (JCPDS No 00-065-0725). XRD Results of ZnO NPs by Co-precipitation Method is shown in Table 2. The average crystallite size was 31.3 nm. The lattice constants of ZnO NPs is shown in Table 3.

Table 2 XRD Results of ZnO NPs by Co-precipitation Method

hkl	2θ	interplanar spacing (Å)	FWHM	Crystallite Size (nm)
(100)	31.88°	2.804	0.204	37.404
(002)	34.54°	2.593	0.192	39.494
(101)	36.39°	2.467	0.210	35.916
(102)	47.72°	1.904	0.258	28.159
(110)	56.82°	1.619	0.244	28.620
(103)	63.11°	1.472	0.231	29.285
(112)	68.23°	1.373	0.251	26.193
(201)	69.37°	1.354	0.258	25.297
Average Crystallite Size				31.296

Table 3 Lattice Constants of ZnO NPs

Lattice parameters	a (Å)	b (Å)	c (Å)	α, β, γ	Average crystallite size
Green Synthesis	3.24880	3.24880	5.20540	α = 90°, β = 90°, γ = 120°	33.4 nm
Co-precipitation Method	3.23794	3.23794	5.18798	α = 90°, β = 90°, γ = 120°	31.3 nm

SEM analysis

The surface morphology of ZnO NPs was investigated using scanning electron microscope (SEM). The SEM image of ZnO NPs derived from green synthesis shows highly agglomerates quasi-spherical nanoparticles forming dense clusters with a relatively uniform and fine-grained texture. The SEM micrograph of ZnO NPs by green synthesis is shown in figure 5. Average grain size was 0.26 μm.

The co-precipitated ZnO NPs exhibit larger and more distinct structures, including rod-like and plate-like morphologies along with irregular aggregates. The particles appear more strongly fused, forming denser and larger compared to the green synthesized sample. Average grain size was 0.68 μm.

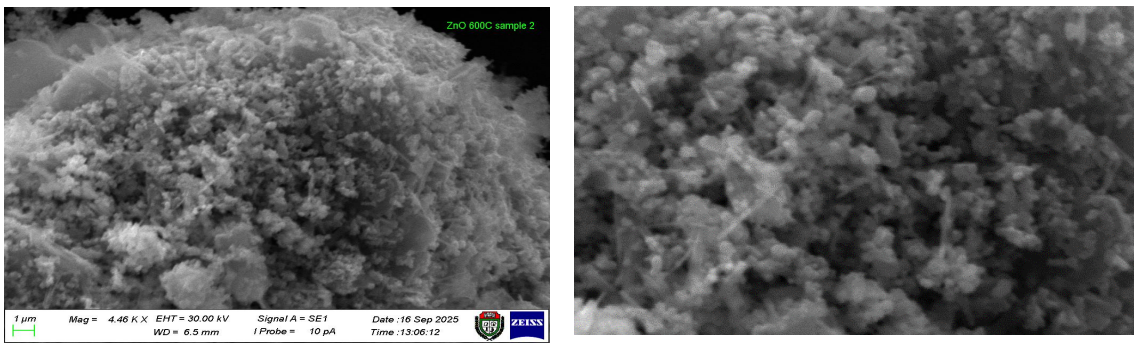

Figure 5 SEM image of ZnO nanoparticles by green synthesis at 4.46kx magnification

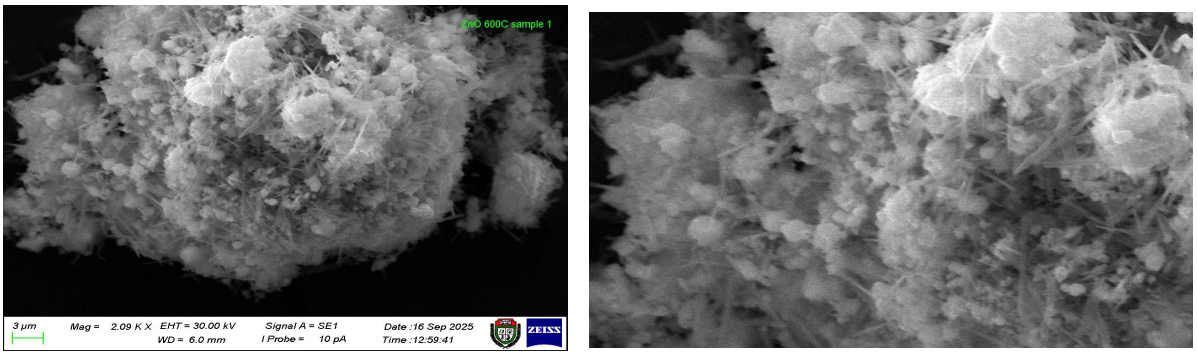

Figure 6 SEM image of ZnO nanoparticles by co-precipitation at 2.09kx magnification

FTIR spectral analysis

The spectra were collected between 4000 and 400 cm^{-1}. A type of vibrations in the ZnO materials have been determined and assigned to identify the existence of different functional groups that aid with the chemical reduction.

Broad band of O-H stretching was found at 3429 cm^{-1} due to hydroxyl groups from alcohols, phenols and absorbed water. The peak at 1661 cm^{-1} was C = O stretching vibration corresponds to amide band. It was conjugated carbonyl group. The sharp peak at 1343 cm^{-1} was C – N stretching/ O – H bending from plant metabolites. The peak was observed at 1142 cm^{-1}which was C – O stretching. This indicated residual organic substituents from plant extract on ZnO surface. The aromatic C – H bending peak was found at 823 cm^{-1}. The strong peak at 464 cm^{-1} was Zn – O stretching vibration in fingerprint region. This peak confirmed formation of ZnO nanoparticles. FTIR spectrum of ZnO NPs by green method is seen in figure 7.

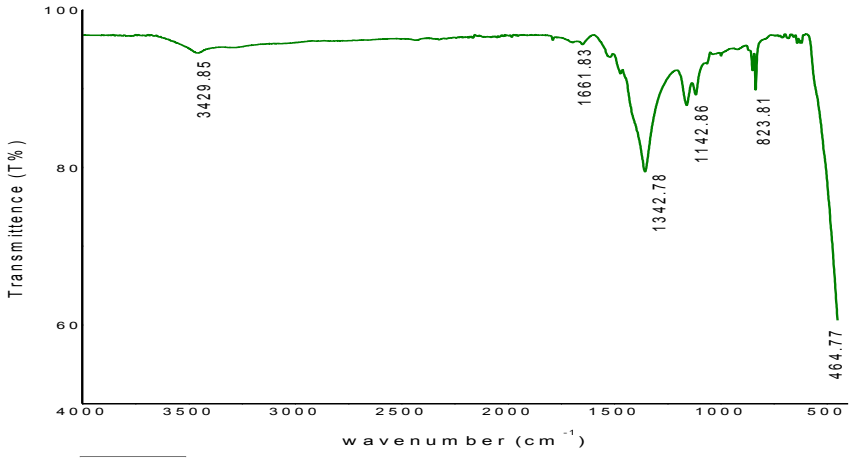

Figure 7 FTIR spectrum of ZnO nanoparticles by green synthesis

For co-precipitated ZnO NPs, FTIR spectrum is shown in figure 8. The band of O – H stretching was found at 3482 cm^{-1}. This was from absorbed water or surface hydroxyl groups. C – H stretching peak was found at 2962 cm^{-1} which is possible from residual precursor. The weak C = O stretching was observed at 1524 cm^{-1}. The peak 1419 cm^{-1} was C – O / NO_3^- related vibrations which may come from residual nitrate ions. The peaks 913 cm^{-1} and 844 cm^{-1} were Zn – OH vibrations due to surface hydroxyl groups. Zn – O stretching vibration was observed at 421 cm^{-1}. This confirmed ZnO nanoparticles formation.

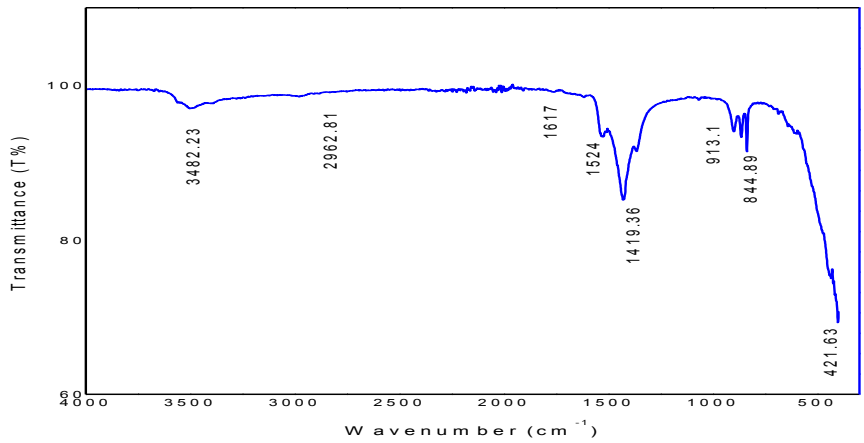

Figure 8 FTIR spectrum of ZnO nanoparticles by co-precipitation

Discussion

According to XRD results, both green synthesis and co-precipitation methods have revealed that the prepared ZnO NPs has a hexagonal wutzite structure. Average crystallite size of co-precipitation method was a little smaller than green method. The slightly larger crystallite size in green synthesis method may be attributed to the presence of phytochemicals that act as capping and stabilizing agents, promoting controlled crystal growth.

SEM confirmed the size and structure of the nanoparticles that were synthesized. The images from SEM suggest that the green synthesized ZnO NPs have a major distribution and spherical shapes, and have an average size of 25 - 35 nm. The co-precipitated ZnO NPs have larger grains, rod and plate-like structures, and have an average size of 30 – 45 nm range.

From FTIR results, Zn-O stretching band was found below 500 cm^{-1}. The green synthesized ZnO shows additional peaks corresponding to O-H, C=O, C-N, C-O functional groups. These groups indicated the presence of phytochemicals from the plant extract that act as reducing and stabilizing agents. The co-precipitated ZnO spectrum shows fewer organic functional groups. The Zn-O stretching vibration peak slightly shifts compared to green method due to different particle size or bonding environment.

Conclusions

The zinc oxide nanoparticles were synthesized with an eco-friendly methodology obtained from plant extracts such as orange fruit peel and conventional method (co-precipitation). The size, shape, and structure of the synthesized ZnO NPs were characterized by XRD, SEM and FTIR. XRD patterns suggest that the crystallites of the ZnO NPs that developed have a hexagonal wurtzite structure. The average crystallite sizes calculated from XRD patterns using the Debye-Scherrer equation were found to be 33.4 nm for green synthesized ZnO NPs and 31.3 nm for co-precipitated ZnO NPs. The slightly larger crystallite size in the green synthesis method may be attributed to the presence of phytochemicals that act as capping and stabilizing agents. The SEM image of the synthesized ZnO NPs suggests that these particles exhibit a spherical structure with an average size of the NPs was about 30 nm in green method. SEM micrograph of co-precipitated ZnO NPs suggests that the particles reveal rod-like and plate-like structure with an average size was also about 30 nm. The FTIR spectra confirm the successful formation of ZnO NPs in both green synthesis and co-precipitation methods through the characteristic Zn – O stretching bands below 500 cm^{-1}. In contrast, both two methods were suitable to synthesize of metal oxide nanoparticles. According to the comparative results, ZnO produced by green synthesis method can be eco-friendly, no toxin, cost-effective, and if it is to be mass-produced as a commercial product, co-precipitation method should be used. Since ZnO nanoparticles produced by green synthesis method are spherical in shape and nano size scale, they have broad potential for applications such as medicine and drug delivery, food industry, cosmetics, environmental remediation and water treatments. On the other hand, ZnO nanoparticles synthesized by co-precipitation have plate-like and rod-like shapes, which makes them suitable for use in electronics and optoelectronics, especially as sensors, LEDs and solar cells. In summary, whether ZnO is produced by green-synthesized method or by co-precipitation method, it can be used in a wide range of fields, including agriculture, medicine, cosmetics, food, electronics, and optoelectronics.

Acknowledgements

Special words of thanks to go everyone who gave suggestion and help to make this research reality. Especially we would like to thank Universities Research Center, at Yangon and Mgway for helping with this research paper.

References

Balogun SW, James OO and Sanisi YK (2020). "Green Synthesis and Characterization of Zinc Oxide nanoparticles using bashful (Mimosa pudica), Leaf Extract a precursor for organic electronics applications", SN Appl Sci, vol.2, pp. 504.

Bruna Martinello Savi et al, (2017). "Synthesis of ZnO Nanoparticles by Sol-gel Processing," Castellon.

Koudelka L, Horak J and Jariabka P (2004). "Morphology of polycrystalline ZnO and its physical properties", Journal of Materials Science, vol.29, no.6, pp. 1497-1500.

Prellier W et al, (2003). "Oxide-diluted magnetic Semiconductor: A review of the experimental status", Journal of Physics Condensed Matter, vol.15.

Ramalho, (2004). "ZnO preparation method by Pechini", International Journal of Engineering Material.

Saji Mohsen J, (2016). "Synthesis of CuO Nanostructure via Sol-Gel and Precipitation Chemical Methods", Ai-Khwarizmi Engineering Journal, vol.12, no.4, pp.126-131.

Assessment of Water Quality Index and Contents of Nutrient and Heavy Metal Elements in Well Water Samples from Konetalin Village in Yesagyo Township, Pakokku District

Khet Khet Tun[1], Khin Htwe[2], Sandar Min[3]

Abstract

Water is one of the essential biological components of the environment. The water quality guidelines provide a limit value for drinking water. It is necessary that the quality of drinking water should be checked due to the use of contaminated drinking water, human population suffers from varied of water borne diseases. The objective of this work is to assess the current status of physicochemical parameters and the concentrations of nutrient and heavy metal elements in five well water samples from middle, east, west, south and north from Konetalin village in Yesagyo township, Pakokku district. MW150 & MW151 Max Meter was employed to determine the physicochemical parameters. Then, the contents of nutrient elements like calcium (Ca), potassium (K), magnesium (Mg), iron (Fe) and that of heavy metal elements such as cadmium (Cd), chromium (Cr), lead (Pb), copper (Cu) and zinc (Zn) were detected by using Atomic Absorption Spectrometer (AAS) method. The obtained results in chosen well water samples were compared with drinking water quality guideline provided by World Health Organization (WHO). From the comparison, the values of pH, conductivity, turbidity, salinity, the contents of Ca, Mg, Fe and K elements were indicated within the standard values of WHO. The values of total dissolved solids in W (3), W (4) and W (5) samples were observed greater than the limiting value of WHO and the dissolved oxygen in all samples were found larger than permissible value of WHO. And then, the concentrations of heavy metal elements were observed below the detective limits. But, the status of water quality index was represented good in W (1) and W (2) samples and moderate in W (3), W (4) and W (5) samples. Therefore, the local people in this village are not harmful to drink and cook these well water samples and the information in this report is focused on the public health.

Keywords: well water samples, physicochemical parameters, nutrient and heavy metal elements, AAS, WHO

Introduction

Water is necessity for survival of existence on earth. About 70 % of Earth (often known as Blue Planet) is included with water. Developmental activities which consist of construction, transportation and manufacturing not most effective dissipate the natural sources but additionally produce massive quantity of wastes. They result in pollution of air, water, soil and oceans; global warming and acid rains.

Environmental pollutions are taking location in many components of the world, in particular within the form of air and water pollution. Human life without water is just impossible. Water is needed not only for biological systems in the human body but also for other activities related to life.

Water brings nutrients to the cells and maintains for energy production. It removes toxic wastes from the body. Many of heavy metals are among the most abundant of pollution in the ecosystem due to the fact of their resistance to decomposition in natural conditions. Water is a natural resource, essential for agriculture, industry and even human beings.

Although water is an absolute requirement for life, it can cause many diseases. Water quality is the cause of any chemical, physical or biological change due to water pollution. It

[1] Associate Professor, Department of Physics, Pakokku University
[2] Head and Professor, Department of Physics, Pakokku University
[3] Professor, Department of Physics, Pakokku University

affects the drinking and its uses or any living organisms in the water pollution. When humans drink contaminated water, it can have a negative impact on their health.

Heavy metals are a group of metal element that have a density of greater than g/cm^3 and a high relative density. Heavy metals have toxic properties down to ppb levels. Heavy metals cannot be lost naturally because they continue to accumulate so that they can cause harm to human health if exposed continuously for a long time. Contaminated well water may cause a variety of public health problems.

Many researchers have suggested that pollution entering the human body through drinking water will cause negative health impacts on the consumers. Some health problems that may additionally occur consisting of microorganism infections, reduction of the blood's ability to carry oxygen, heavy metal risks such as acute and persistent toxicity on some organs including the liver, kidneys, and intestines, and medical conditions like anemia, cancer, and hormonal disorders.

The analysis of physical parameters like potential of Hydrogen (pH), electrical conductivity (EC), turbidity, and total dissolved solid (TDS) values and chemical parameters include dissolved oxygen (DO) and salinity values were measured with MW150 & MW151 Max Meter. And then, the contents of nutrient elements such as calcium (Ca), magnesium (Mg), potassium (K) and iron (Fe) and heavy metal elements namely cadmium (Cd), chromium (Cr), copper (Cu), zinc (Zn) and lead (Pb) in five well water samples from Konetalin village in Yesagyo township, Pakokku district were detected by using Atomic Absorption Spectrometer (AAS) method.

Materials and Method

Study Area, Sampling Sites and Sample Preparation

Yesagyo township is situated on the western bank of the confluence of Ayeyarwaddy and Chindwin Rivers and northeastern part of Pakokku district, Magway Region in Central Dry Zone of Myanmar. It lies between 21º and 21º 50´ North Latitudes and 95º and 95º 20´ East Longitudes and is situated about 29.2 miles away from Pakokku city. Konetalin village includes in the Southern part of Yesagyo township and it is about 12.2 miles (19.52 kilometers) away from Yesagyo township.

In this research, the samples that were used for this work were taken from five selected well water in the following aeras of Konetalin village from Yesagyo township in Pakokku district:

(1) middle (2) east (3) west (4) south and (5) north during the period in March, 2025. The well water sample W (1) was obtained from the middle of the village. The depth of well is 17 ft which was built in 1996. The depth of well water sample W (2) from the east of the village is 30 ft which was in 2004. Well water sample W (3) was taken from the west of the village. The depth of this well is 20 ft which was drilled in 1967. The depth of W (4) well water sample from the south of the village is 23 ft which was built in 1954 and well water sample W (5) was collected from the north of the village which was in 2013. The photographs of collected well water samples in middle, east, west, south and north of Konetalin village were described in figure 1.

After collecting water, bottles were screwed with caps immediately and tightly. And then, they were put in a paper box, closed, and labeled with sample information. After that, they were measured by MW 150 & MW 151 Max Meter and AAnalyst 800 spectrometer in Universities' Research Centre, University of Yangon situated at Kamayut township. The total

time for sampling and transportation was within 2 days to obtain correct and definite values for water parameters.

Figure 1. The photographs of collected well water samples in middle, east, west, south and north of Konetalin village in Yesagyo township

Specification and Measurement Condition

Atomic Absorption Spectroscopy is a very common technique for detecting and measuring concentration of a particular metal element within a sample. It is a sensitive technique that can determine the concentration of most elements at the parts per million (ppm) level. The concentrations of nutrient and heavy metal elements in water samples were determined using AAS method.

Atomic Absorption Spectrometer is based on the absorption of virtually monochromatic light by a cloud of atoms of the detecting samples. The light is produced by emission from the same kinds of atoms as those being determined. Atomic absorption using flame atomizer was rapidly accepted as a simple technique which gave high sensitivity, accuracy and precision. Generating free atoms using an atomizer, which may be flame.

The absorption is measured at one of several wavelength characteristics of the element being determined. Absorption by free atoms at another wavelength is essentially zero. The wavelength is selected using a monochromator and is measured using a photomultiplier. The flame warms up and auto- alignment of main console unit is reached in within ~10 minutes to achieve the stated specification. Fuel adjustment, air adjustment and initial adjustment are PC's control.

The analyzing technique is the flame emission and atomic absorption. The wavelengths are iron (248.33 nm), calcium (422.67 nm), potassium (766.49 nm), magnesium (285.21 nm), cadmium (228.8 nm), chromium, (357.87 nm), copper (324.75 nm), zinc (213.86 nm) and lead (283.31 nm). The light beam slit width of all these elements is 0.7 nm. The use of flame gasses is oxygen (O_2), air acetylene (C_2H_2) (99.98%Pure), Nitrous oxide (N_2O) (99.99%Pure) and Argon (Ar) (99.99%Pure). The light sources are Hollow Cathode Lamps (HCL) and Electrode Discharge Lamps (EDL). The photograph of Perkin Elmer AAnalyst 800 Atomic Absorption Spectrometer was shown in figure 2.

Figure 2. Perkin Elmer AAnalyst 800 Spectrophotometer

Calculation of Water Quality Index (WQI)

Calculation of water quality index was carried out in this work by Weighted Arithmetic Index Method which was originally proposed by Horton and developed by Brown to find the quality of surface water for drinking purpose. Using the following equation, the weighted arithmetic water quality index (WQI) was calculated.

$$WQI = \frac{\sum_{i=1}^{n} W_i q_i}{\sum_{i=1}^{n} W_i} \quad (1)$$

In the first step, the value of quality rating or subindex (q_i) was calculated according to Brown as follow:

$$q_i = 100 \left(\frac{\text{measured values of ith parameter-ideal value of ith parameter}}{\text{standard value-ideal value}} \right) \quad (2)$$

In the second step, the calculation of relative weight (W_i) of the parameters was carried out. The unit weight (W_i) which is inversely proportional to the values of the recommended standards was obtained as:

$$W_i = \frac{K}{S_i} \quad (3)$$

$$K = \frac{1}{\sum_{i=1}^{n} \left| \frac{1}{S_i} \right|} \quad (4)$$

Results and Discussion

Analysis Physicochemical Parameters and the Contents of Nutrient Elements

Analysis of water quality in study areas using some physical and some chemical parameters to seek the states of water sources was described in figure 3 and reported in tables 1 and 2.

From the measurement of physical and chemical parameters, pH, turbidity, conductivity, salinity, iron (Fe), potassium (K), calcium (Ca) and magnesium (Mg) values except total dissolved solids (TDS) and dissolved oxygen (DO) values in some samples for all water samples were consistent within the guidelines values for drinking water standard provided by World Health Organization (WHO).

According to measurements of physical parameters, pH is very significant indicator to determine the status of water sources because water from five sampling stations had been used by local people in this area for different purpose. The pH values from all the sampling points ranged from 7.434 to 7.986. The mean value of pH was 7.64 which was observed within the standard values (6.5-8.5) by World Health Organization (WHO). The values of pH were greater than 7 indicate that they have always basic or alkaline. Therefore, the water from these well is safe to drink and cook for local people. The result from measuring pH values in all well water samples was shown in figure 4.

And then, the values of conductivity in these samples varied between 0.75 mS/cm and 2.54 mS/cm. The mean value of them was 1.78 mS/cm which was found below the limiting value (2.54 mS/cm) of WHO. The result from measuring the conductivity values in all well water samples was mentioned in figure 5.

Moreover, the values of turbidity were described from 3.19 NTU to 4.18 NTU. The mean value of them was 3.77 NTU which was observed less than the guideline value of WHO (4 NTU). The result from measuring the turbidity values in all well water samples was expressed in figure 6.

After that, the values of total dissolved solid ranged from 481.8 mg/L to 1924 mg/L. The mean value of them was 1350.72 mg/L. But, their values in samples W (3) (west of village), W (4) (south of village) and W (5) (north of village) were observed to be higher than the standard value (1000 mg/L) by World Health Organization (WHO). The high amount of total dissolved solids in water can be reduced by heating the water to its boiling point and this method is suitable for preparing high purity water. The result from measuring the total dissolved solid values in all well water samples was represented in figure 7.

From the results of chemical parameters, the values of dissolved oxygen in all these samples varied from 5.38 mg/L to 7.89 mg/L. The mean value of DO was 6.96 mg/L which was exceed indicated the limiting value of (5 mg/L) by World Health Organization (WHO). The high amount of dissolved oxygen can be removed boiling at 1 atm, boiling under reduced pressure, purging with nitrogen and sonication under reduced pressure. The result of dissolved oxygen values in all well water samples was depicted in figure 8.

Then, the salinity value in all well water samples was observed between 0.37 ppt and 3.23 ppt. The mean value of salinity was 1.79 ppt which was below the permissible value of WHO (100 ppt). The result from measuring the salinity in all well water samples was shown in figure 9.

Figure 3. The photograph of physicochemical parameters measurement

Besides, from measurable results of AAS method, the contents of iron (0.10 – 0.19) mg/L, magnesium (0.71 and 0.72) mg/L, calcium (23.28 – 36.52) mg/L and potassium (10.56 – 67.3) mg/L in all well water samples were observed within the guideline values (0.3 mg/L), (50 mg/L), (100 mg/L) and (100 mg/L) of World Health Organization (WHO). The comparison of iron, magnesium, calcium and potassium elements content in all well water samples with standard values of World Health Organization (WHO) were interpreted from figure 10 to 13.

Table 1. Analysis of physical parameters compared with WHO standard, and mean values

Parameters	Standard value (WHO)	Measured Results					Mean values
		W (1)	W (2)	W (3)	W (4)	W (5)	
pH	6.5–8.5	7.65	7.43	7.6	7.9	7.6	7.64
Conductivity (mS/cm)	2.5	1.24	0.75	2.54	2.06	2.27	1.78
Turbidity (NTU)	4	3.19	3.24	4.18	4.12	4.14	3.77
Total dissolved solid (mg/L)	1000	791.8	481.8	1924	1818	1738	1350.72

Table 2. Analysis of chemical parameters and nutrient element contents compared with WHO standard, and mean values

Parameters	Standard value (WHO)	Measured Results					Mean values
		W (1)	W (2)	W (3)	W (4)	W (5)	
Dissolved oxygen (mg/L)	5	7.89	6.586	7.256	5.382	7.702	6.963
Salinity (ppt)	100	0.62	0.37	2.43	3.23	2.27	1.79
Fe (mg/L)	0.3	0.12	0.10	0.19	0.19	0.16	0.15
Mg (mg/L)	50	0.71	0.71	0.72	0.72	0.71	0.71
Ca (mg/L)	100	36.52	23.28	34.27	34.78	26.81	31.13
K (mg/L)	100	13.6	67.3	15.45	10.56	14.24	24.23

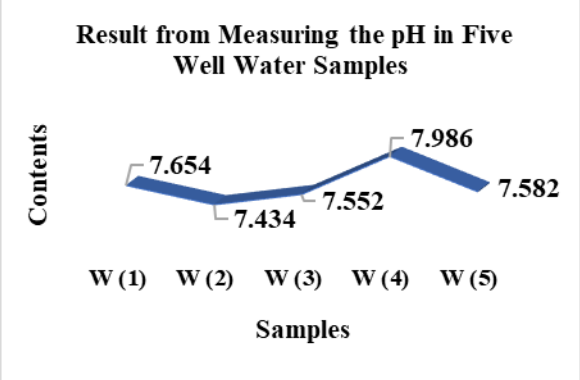

Figure 4. Result from measuring the pH

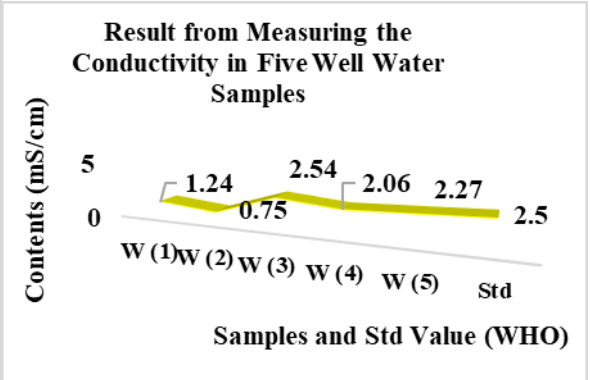

Figure 5. Results from measuring the conductivity

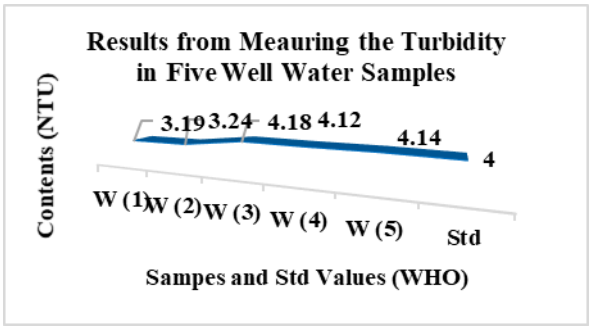

Figure 6. Result from measuring turbidity

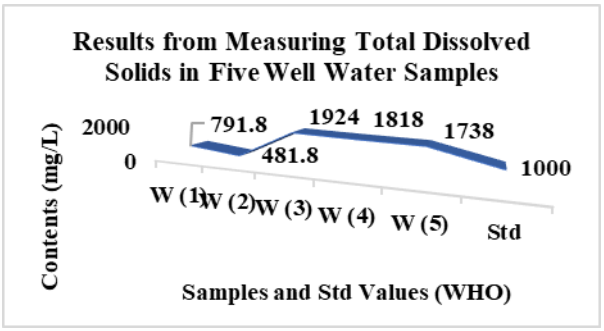

Figure 7. Results from measuring the total dissolved solids

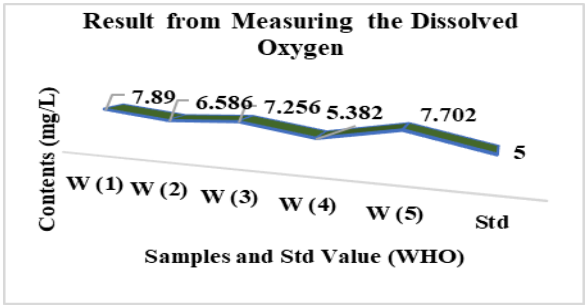

Figure 8. Result from measuring dissolved oxygen

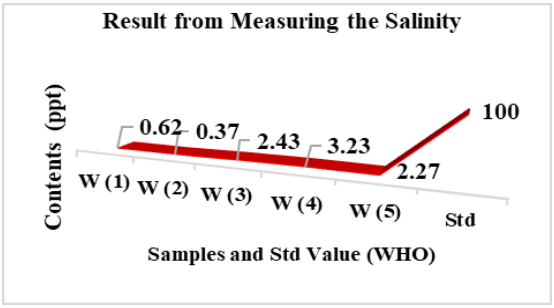

Figure 9. Results from measuring the salinity

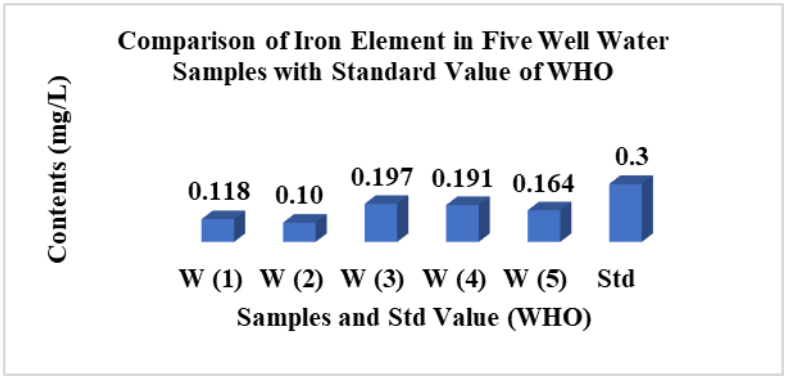

Figure 10. Comparison of Fe element in five well water samples with standard value of WHO

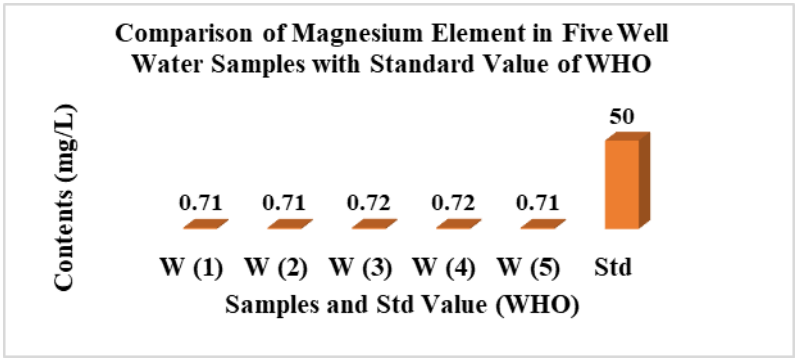

Figure 11. Comparison of Mg element in five well water samples with standard value of WHO

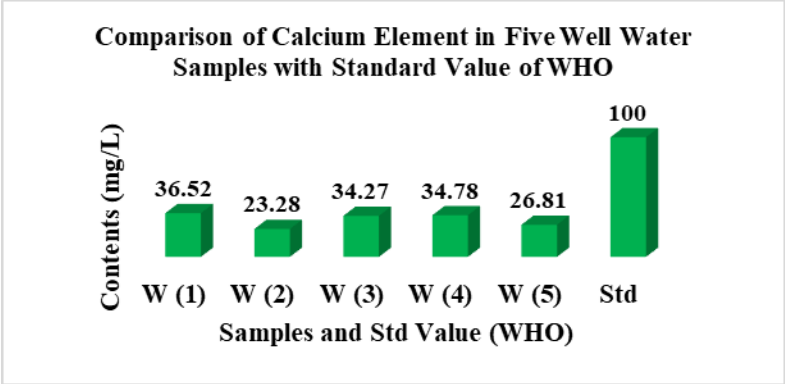

Figure 12. Comparison of Ca element in five well water samples with standard value of WHO

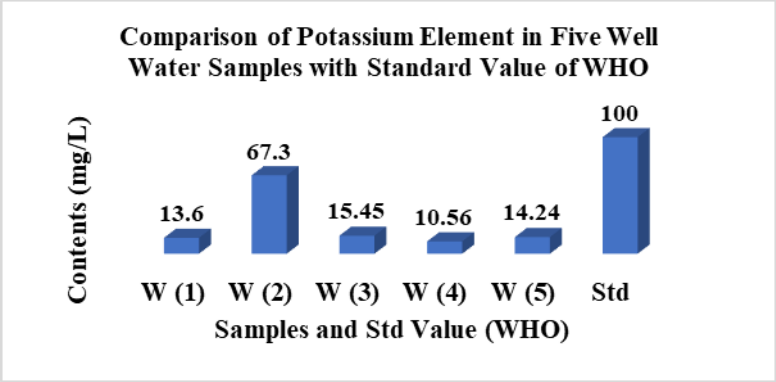

Figure 13. Comparison of K element in five well water samples with standard value of WHO

Iron is one of the earth's most plentiful resources, making up at least five percent of the earth's crust. When rainfall seeps through the soil, the iron in the earth's surface dissolves, causing it to go into almost every natural water supply, including well water.

Calcium and magnesium are essential to human health. While the concentrations of calcium and magnesium in drinking-water vary markedly from one supply to another, mineral-rich drinking waters may provide substantial contributions to total intakes of these nutrients in some populations or population subgroups.

Potassium is an essential element and is present in all animal and plant tissues. Although concentrations of potassium normally found in drinking water are generally low and do not pose health concerns, the high solubility of potassium chloride.

The Results of Calculation of Water Quality Index

The calculation of water quality index of well water samples was usually used equations 1 to 4 and the results of calculation of WQI were shown in table 3. The comparison of standard values and measured variables (the status of water quality indices (WQIs)) for all well water samples were studied with table 4.

According to table 3 and 4, the status of water quality index was predicted good in W (1) (middle of village) and W (2) (east of village) samples and moderate in W (3) (west of village), W (4) (south of village) and W (5) (north of village) samples. Figure 14 showed the status of water quality index in all well water samples.

Table 3. Calculation of water quality index of five well water samples

Samples	$\frac{1}{S_i}$	K	$\Sigma W_i = \frac{K}{S_i}$	$\Sigma W_i q_i$	WQI = $\frac{\sum_{i=1}^{n} W_i q_i}{\sum_{i=1}^{n} W_i}$	Status of WQI	Grade
W (1)	4.35198	0.22978	1	49.45766	49.45766	Good	B
W (2)	4.35198	0.22978	1	41.51217	41.51217	Good	B
W (3)	4.35198	0.22978	1	72.98097	72.98097	Moderate	C
W (4)	4.35198	0.22978	1	69.39148	69.39148	Moderate	C
W (5)	4.35198	0.22978	1	64.65128	64.65128	Moderate	C

Table 4. Water quality indices (WQIs) and corresponding water quality status (C.Chatterjee and Raziuddin)

WQIs	Rating of Water Quality	Grading
0-25	Excellent	A
26-50	Good	B
51-75	Moderate	C
76-100	Poor	D
>100	Unfit for consumption	E

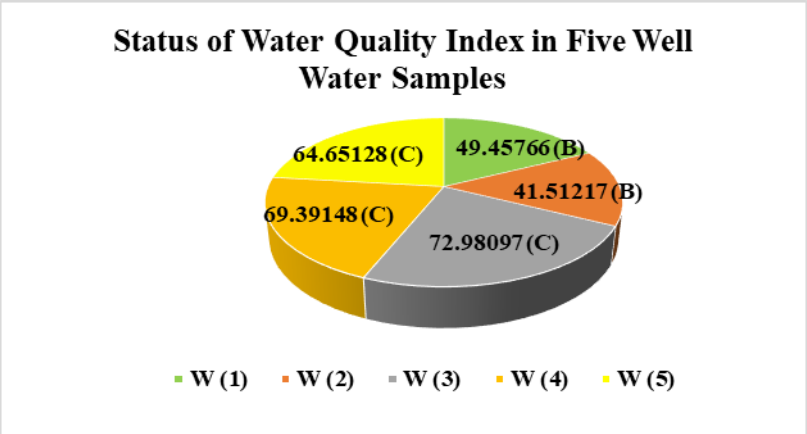

Figure 14. Status of water quality index in five well water samples

Analysis of Heavy Metal Elements

Various metals can enter surface water and diffuse into the ground water due to the different sources such as either natural process or human activities. This event can make that surface water be contaminated or concentration of metals' levels in river water can be increased and heavy metals impact on human health.

In this work, the contents of heavy metals including cadmium (Cd), chromium (Cr), copper (Cu), zinc (Zn) and lead (Pb) in five well water samples from middle, east, west, north, and south of Konetalin village were detected by using Atomic Absorption

Spectroscopy (AAS) method. The experimental result of heavy metal element contents compared with standard values by WHO and USEPA was listed in table 5.

By noticing the experiment results, the contents of non-nutritive and heavy metal elements such as cadmium (Cd), chromium (Cr), copper (Cu), zinc (Zn) and lead (Pb) in all well water samples were detected and they were observed very fewer concentrations than the detective limits.

Moreover, the comparisons of the contents of heavy metal elements such as cadmium (Cd), chromium (Cr), copper (Cu), zinc (Zn) and lead (Pb) elements with the standard values (0.003 mg/L), (0.05 mg/L), (2.00 mg/L), (0.01 mg/L) and (0.01 mg/L) of drinking water by World Health Origination (WHO) and (0.005 mg/L), (0.05 mg/L), (1.00 mg/L), (0.05 mg/L) and (0.015 mg/L) by United States of Environmental Protection Agency (USEPA) were represented in figure 15.

Table 5. Experimental results of heavy metal elements content compared with standard values by WHO and USEPA

Elements	Cadmium (Cd)	Chromium (Cr)	Copper (Cu)	Zinc (Zn)	Lead (Pb)
Samples	Contents (mg/L)				
W (1)	ND	ND	ND	ND	ND
W (2)	ND	ND	ND	ND	ND
W (3)	ND	ND	ND	ND	ND
W (4)	ND	ND	ND	ND	ND
W (5)	ND	ND	ND	ND	ND
Standard Value (WHO) (mg/L)	0.003	0.05	2.00	0.01	0.01
Standard Value (USEPA) (mg/L)	0.005	0.05	1.00	0.05	0.015

ND – not detect (may be very fewer concentration than detection limit)

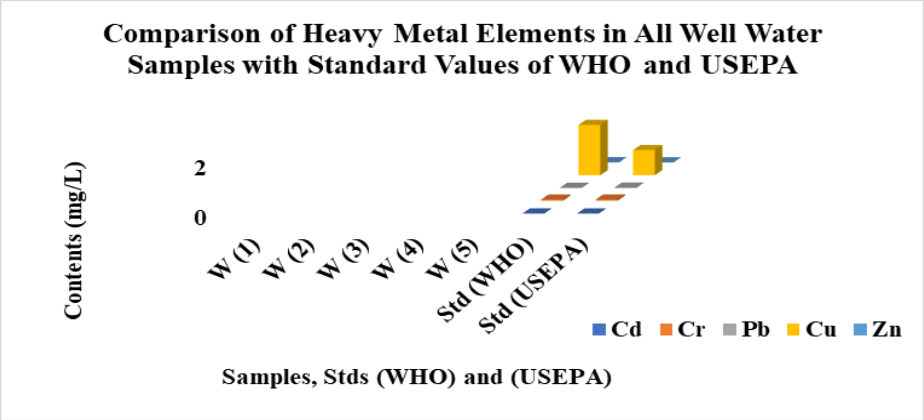

Figure 15. Comparison of heavy metal elements in five well water samples with standard values of WHO and USEPA

Cadmium is generally classified as toxic trace element. Geologic deposits of cadmium can serve as sources to groundwater and surface water, especially when in contact with soft, acidic waters. Cd appear to accumulate with age, especially in the kidney and it is considered also as a cancer and cardiovascular diseases.

Chromium is essential to animals and human. Chromium in excess amounts can be toxic especially the hexavalent form.

Copper is essential substance to human life, but chronic exposure to contaminant drinking water with copper can result in the development of anemia, liver and kidney damage. Copper in large doses is dangerous to infants and people with certain metabolic disorders.

Zinc can be found naturally in air, soil and enter the environment through anthropogenic activities like mining and metal processing. Although zinc is necessary for health, high levels can cause stomach cramps, nausea, vomiting and skin reactions.

Lead is a dangerous element; it is harmful even in small amounts. Lead enters the human body in many ways. High concentrations of lead in the body can cause death or permanent damage to the central nervous system, the brain, and kidneys.

Conclusion

The determination of five well water samples from Konetalin village in Yesagyo township, Pakokku district revealed significant insights into the water quality in times of both physicochemical parameters, nutrient and heavy metal elements contents.

From the finding of this results, most physicochemical parameters such as potential of Hydrogen (pH), electrical conductivity (EC), salinity, and turbidity were found to be within the permissible limits of set by World Health Organization (WHO) drinking water standards but the values of total dissolved solid (TDS) in samples W (3), W (4) and W (5) and the dissolved oxygen (DO) in all well water samples which were observed above the standard values of drinking water by World Health Organization (WHO). Therefore, the high amount of total dissolved solid in water can be reduced by heating the water to its boiling point and the high amount of dissolved oxygen can be removed boiling at 1 atm, boiling under reduced pressure, purging with nitrogen and sonication under reduced pressure.

Moreover, the status of water quality index in all interest of samples were found good in samples W (1) and W (2) and moderate in samples W (3), W (4) and W (5). Therefore, their qualities grading were B and C.

After that, from the measurable results with AAS method, the contents of nutrient elements such as iron, magnesium, calcium and potassium presented within the standard values of World Health Organization (WHO) and the levels of heavy metal elements including cadmium, chromium, zinc, copper and lead were observed below the detective limit.

It can be concluded that all well water samples in this area indicating general suitability for domestic use no pose potential health to the local risk population. But it is recommended to check the quality of the water sources regularly in this study area.

Acknowledgements

We would like to express our gratitude to Dr Tin Tun Aung, Acting Rector, Pakokku University and Dr Khin Khin Htoot, Pro-rector, Pakokku University for their kind permission to submit this research. We special thanks to Dr Myo Min Htun, Acting Rector, East Yangon University for allowing to read my research paper. We also thank to Universities' Research Center, Yangon University for the allowance using apparatus.

References

ATSDR. (2005) Public Health Statement Zinc. Georgia: Agency for Toxic Substances and Disease Registry.

Borah P, Gujre N, Rene ER, Rangan L, Paul RK, Karak T, et al. (2020) Assessment of mobility and environmental risks associated with copper, manganese and zinc in soils of a dumping site around a Ramsar site. Chemosphere (254:126852).

EPA: (2002) NATIONAL Primary Drinking Water Standards.

Gidlecy J A F. (2000) "Atomic Absorption Spectroscopy ", New York: Verlag Chemie.

Guideline for Drinking Water Quality: (2011) Fourth Edition, World Health Organization, Switzerland: ISBN 978-92-4-154815-1.

Guideline for Drinking Water Quality: (2022) Fourth Edition, World Health Organization, Switzerland: ISBN 978-92-4-004507-1.

Guideline for Drinking Water Quality: (2017) Fourth Edition, World Health Organization, Switzerland: ISBN 978-92-4-154995-0.

http:// www.who. int /water-sanitation- health /dwq / GDWQ 2004 web. Pdf

http://en.m.wikipedia.ord>Wiki

IARC. (2012) Monograph on The Evaluation of Carcinogenic Risks to Humans. France: International Agency for Research on Cancer.

Kubier A, Wilkin RT, Pichler T. (2019) Cadmium in soils and groundwater: A review. Appl Geochemistry.108 (August).

Minnesota river basin data center (2008), http:// mrbdc. mnsu.edul basin /wq /turbidity.html

Perkin Elmer Instrument Manual (2001) AAnalyst 800 Spectrometer.

Sazakli E, Villanueva CM, Kagevinas M, Maltezis K. (2014) Chromium in Drinking Water Association with Biomarkers of Exposure and Effect. Int J Environ Res Public Health.11:10125-45.

UNICEF (2009). Status and trends. Drinking water and sanitation in East Asia and the Pacific. A regional perspective based on the 2008 Report of the WHO/UNICEF Joint Monitoring Programmed for Water Supply and Sanitation; pp: 1-28.

UNICEF and WHO (2015). Progress on sanitation and drinking water update and MDG assessment, Geneva, Switzerland.

Investigation of Zinc Oxide Nanoparticles Extracted From *Azadirachta Indica* A. Juss. (Neem) Leaves By Green Synthesis Method

Ei Ei Phyo[1], May Thingyan Moe[2], Zin Min Tun[3], Zin Min Myat[4]

Abstract

This research aims to investigate the zinc oxide (ZnO) nanoparticles using neem *Azadirachta indica* A. Juss. (Neem) leaves extract by green synthesis method. The chemical compositions of neem leaves and zinc oxide nanoparticles were examined by Fourier Transform Infrared Spectroscopy (FTIR). The crystal structure and crystalline size of zinc oxide nanoparticles were characterized by instrumental analysis of X-ray Diffraction (XRD). The results of Scanning Electron Microscopy (SEM) studied the formation of shape and grain size of green synthesis of zinc oxide nanoparticles. The absorption wavelengths and energy band gap of zinc oxide nanoparticles were measured with the help of UV-Vis Spectroscopy. The prepared nanoparticles using green synthesis method can apply the development of nontoxic and biocompatible safe nanoparticle production at cost effective, simple and eco-friendly.

Keywords: Zinc Oxide, Neem leaves, XRD, SEM, UV-Vis and FTIR

Introduction

Nanotechnology is becoming enormous attention as a new area of research dealing with the development of nanomaterials and nanoparticles (NPs) for their utilization in diverse fields such as catalysis, electrochemistry, biomedicines, pharmaceuticals, sensors, food technology, cosmetics, ***etc*.** Nanoparticles (NPs) are nanometer-sized (<100 nm) atomic or molecular scale solid particles having some excellent physical properties compared to the bulk molecules depending on their size and morphology. Zinc oxide (ZnO) is an n-type semiconductor material with bandgap energy of 3.37eV and the energy of bonding is 60meV [Amrutha S. Ajayan and Hebsur. N. S, 2020]. The chemical synthesis followed by stabilization of toxic by-products which are harmful to the ecosystem. It has many technological applications, because of its exceptional optical and electrical, such as thin -film transistors, gas sensors, transparent conductors, biomedical and piezoelectric application [Wang ZL. J Phys Condens Matter, 2004]. Neem leaves are known for their medical value and are the plants which are easily available. The leaves extracts of these plants are contained organic molecules of high anti-oxidant activity of bulk molecules or larger molecules of zinc oxide in to its nano sized particles [Gnanasangeetha, D. and Thambavani, S.D, 2014]. In this process, the final products are formed by performing a number of irreversible chemical reactions. The white precipitate thus formed is removed using the centrifugation method. Besides possessing many versatile resources, ZnO has also been used in its polycrystalline for hundreds of years in a huge range [Surabhi SK, Putcha V, Vanka RR, et al, 2013].

Experimental Procedure

Sample Preparation of Zinc Oxide Nanoparticles

In the first step, the fresh neem leaves were thoroughly washed several times using distilled water. These washed leaves were then dried at room temperature to remove residual

[1] Demonstrator, Department of Physics, West Yangon University
[2] Demonstrator, Department of Physics, West Yangon University
[3] Associate Professor, Department of Physics, West Yangon University
[4] Associate Professor, Department of Physics, West Yangon University

moisture. Using a gate-motor, the leaves were crushed. And then 15g of crushing dried neem leaves was dissolved in 100ml distilled water (DW) with magnetic stirrer heated to 70 ºC for 45 minutes. In a typical experiment, 30 g of $Zn(NO_3)_2.6H_2O$ was dissolved in 100 ml distilled water (DW) under magnetic stirring to form a homogeneous solution at room temperature for 30 minutes. The two solutions were together mixed and stirred with magnetic stirrer heated to 80 ºC for 5 h. 2g of sodium hydroxide (NaOH) was dissolved in 50 ml distilled water and it was stirred for around 15 minutes with the glass rod. Arter mixing the neem extract with zinc precursor, the sodium hydroxide solution was added drop by drop to adjust the pH and precipitate the nanoparticles. During the end of stirring process, the level of pH value was found to be 7 and therefore this solution was directed into the neutral solution. The homogeneous solution was filtered with Whatman No.1 filter papers and it was dehydrated in a hot air oven at the temperature of 100 °C for 2 days. After drying, the samples were taken out from the muffle furnace annealed at 500 °C and 600 °C for 1 h. Finally, the homogeneous zinc oxide nanoparticles were found and the structural, morphological, and optical characterizations of zinc oxide nanoparticles were observed by XRD, SEM and UV-Vis analysis. The presence of Zn-O stretching vibration bands was revealed in Fourier Transform Infrared Spectroscopy (FTIR). The block of zinc oxide nanoparticles was shown in Figure 1. The step by step preparation of zinc oxide nanoparticles was shown in Figure 2 (a-f).

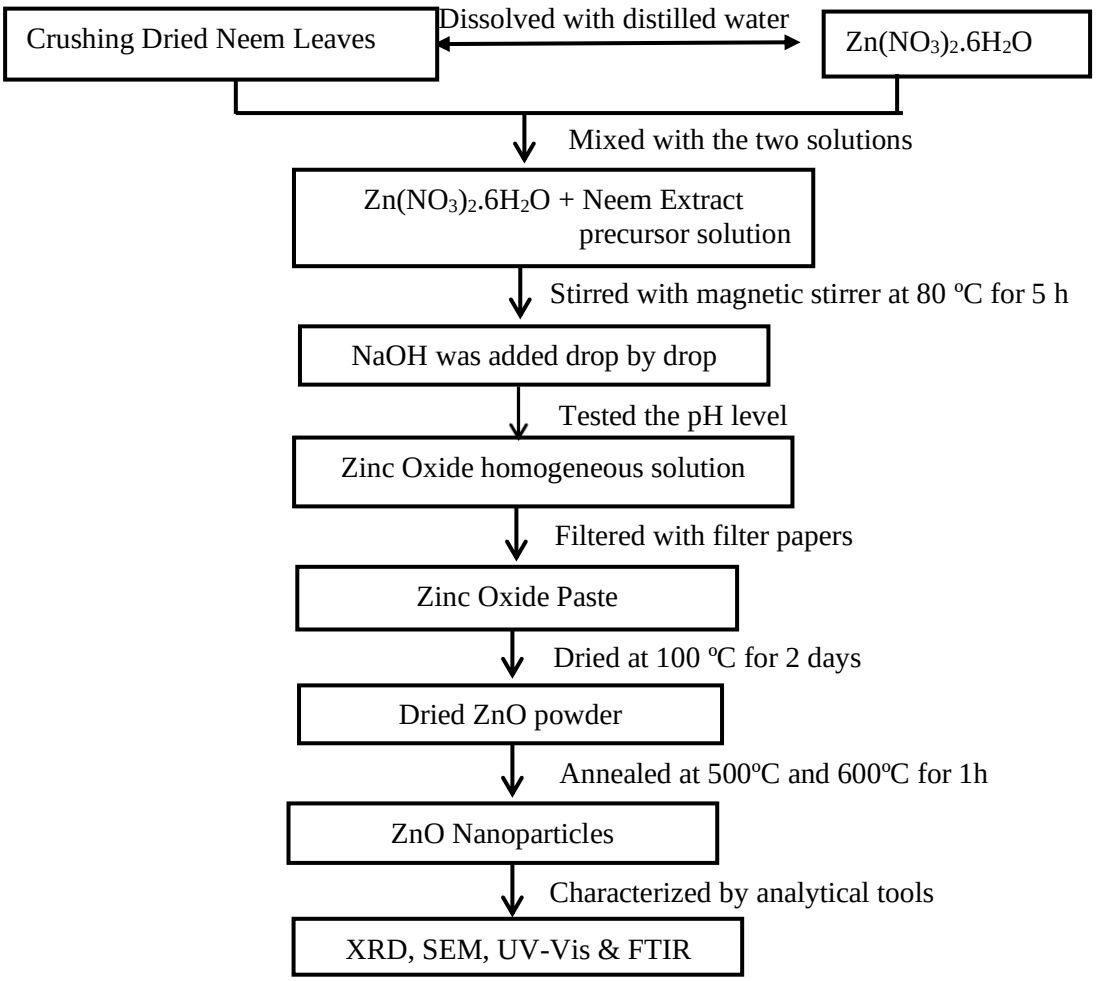

Figure 1 Block diagram of preparation of zinc oxide nanoparticles by green synthesis method

(a)Drying and Grounding

(b) Stirring and Preparing of Neem Leaves extract solution

(c) Weighting

(d) Testing pH and Filtrating

(e) Drying

(f) Annealing

Figure 2 (a-f) Photographs of preparation of zinc oxide nanoparticles by using neem leaves extract solution

Results and Discussion

XRD Analysis of Zinc Oxide (ZnO) Nanoparticles

XRD is the one of the instruments used to discover the crystalline structure and crystallite size of the prepared nanoparticles. Figures 3(a-b) showed the XRD patterns of all synthesized ZnO NPs using green synthesis method at two different temperatures (500 °C and 600 °C). The peaks with 2θ values at 31.76°, 34.42°, 36.25°, 47.54°, 56.57°, 62.84°, 66.39°, 67.93° and 69.03° were associated with the (100), (002), (101), (102), (110), (103), (200), (112) and (201) planes, respectively, indicating the formation of ZnO with hexagonal structure. This was confirmed with the JCPDS card of ZnO nanoparticles (File no: 00-036-1451). The average crystallite size was measured using Debye–Scherer's Equation and the

average crystallite size (D) was calculated to be 17.53 nm at 500 °C, and 14.14 nm at 600 °C, respectively. Debye–Scherer's Equation was shown by: $D = \frac{k\lambda}{\beta \cos\theta}$

where D is the crystallite size, k is the shape factor (0.899), λ is the wavelength (0.154056 nm), β is the full-width half maximum (FWHM) in radians and θ is the Bragg's angle. The crystallographic properties of ZnO nanoparticles were listed in Table 1 and Table 2. According to the XRD analysis, the average crystallite sizes of ZnO nanoparticles were decreased with increasing temperatures. Figure 4 showed the comparison of XRD patterns for ZnO nanoparticles at two different temperatures.

Table 1 Crystallographic properties of ZnO nanoparticles at 500 °C

(hkl)	2θ (deg)	FWHM (deg)	Crystallite size (nm)
(1 0 0)	31.76	0.4488	18.38
(0 0 2)	34.42	0.4510	18.42
(1 0 1)	36.25	0.4900	17.03
(1 0 2)	47.54	0.5780	15.00
(1 1 0)	56.57	0.6013	14.98
(1 0 3)	62.84	0.6681	13.91
(2 0 0)	66.39	0.3667	25.86
(1 1 2)	67.93	0.6257	15.29
(2 0 1)	69.03	0.5100	18.88
Average crystallite size			17.53

Table 2 Crystallographic properties of ZnO nanoparticles at 600 °C

(hkl)	2θ (deg)	FWHM (deg)	Crystallite size (nm)
(1 0 0)	31.76	0.5577	14.79
(0 0 2)	34.42	0.5701	14.57
(1 0 1)	36.25	0.5946	14.04
(1 0 2)	47.54	0.7080	12.24
(1 1 0)	56.57	0.7166	12.57
(1 0 3)	62.84	0.7950	11.69
(2 0 0)	66.39	0.4400	21.55
(1 1 2)	67.93	0.7880	12.14
(2 0 1)	69.03	0.7000	13.75
Average crystallite size			14.14

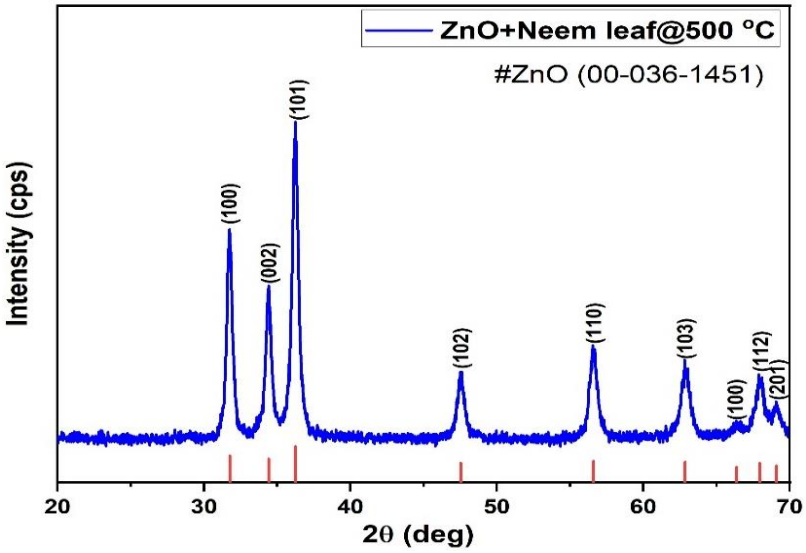

Figure 3 (a) XRD pattern of ZnO nanoparticles at 500 °C

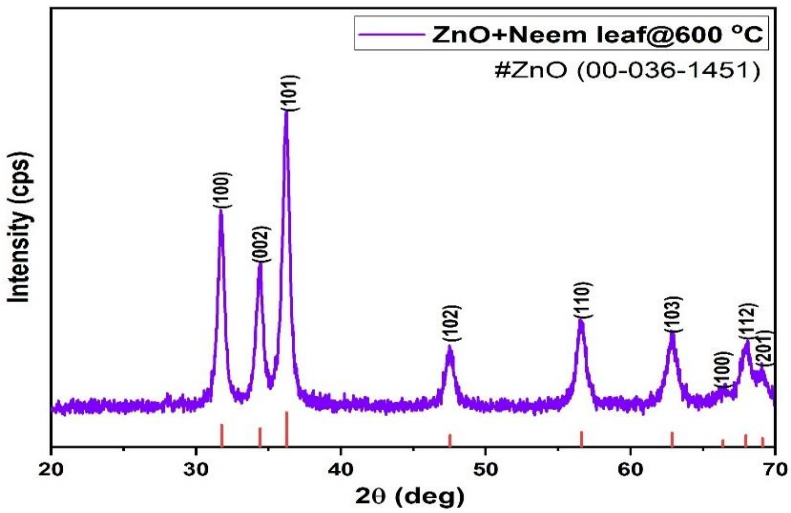

Figure 3 (b) XRD pattern of ZnO nanoparticles at 600 °C

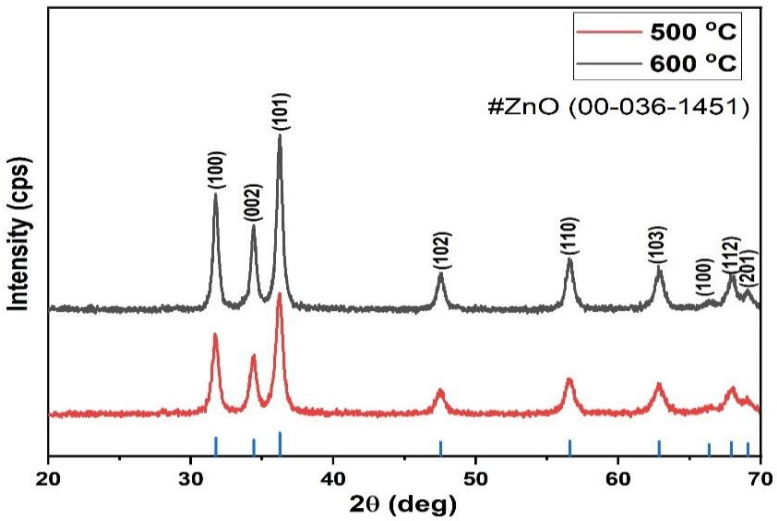

Figure 4 Comparison of XRD patterns for ZnO nanoparticles at two different temperatures

SEM Analysis of Zinc Oxide (ZnO) Nanoparticles

Scanning electron microscopy of green synthesized ZnO nanoparticles determined the morphology (size and shape) of synthesized nanoparticles. ZnO NPs synthesized from neem leaves extract were like nano-flakes or flowers and size ranged from 100-300 nm. Figure 5(a-b) showed the SEM photographs of ZnO nanoparticles with different process temperature 500 °C and 600 °C. As detail analysis of SEM micrograph, it looked rough and porous surface texture, which arises from stacking and overlapping of nanoflakes. This roughness significantly increases the effective surface area, making these structures highly suitable for applications requiring enhanced surface interactions, such as photocatalysis and antimicrobial activity. According to SEM results, these ZnO nanoparticles were composed of regular and sphere grains. ZnO nanoparticles were reported to be the average grain size of ~20-100 nm at 500 °C and ~50-200 nm at 600 °C with spherical shape by SEM images. These figures indicated that most of the grain size was regular structure and a few numbers of large grain size were found. It looks fairly dense and rough. In these results, the average grain size of the ZnO nanoparticles were depended by varying different process temperatures.

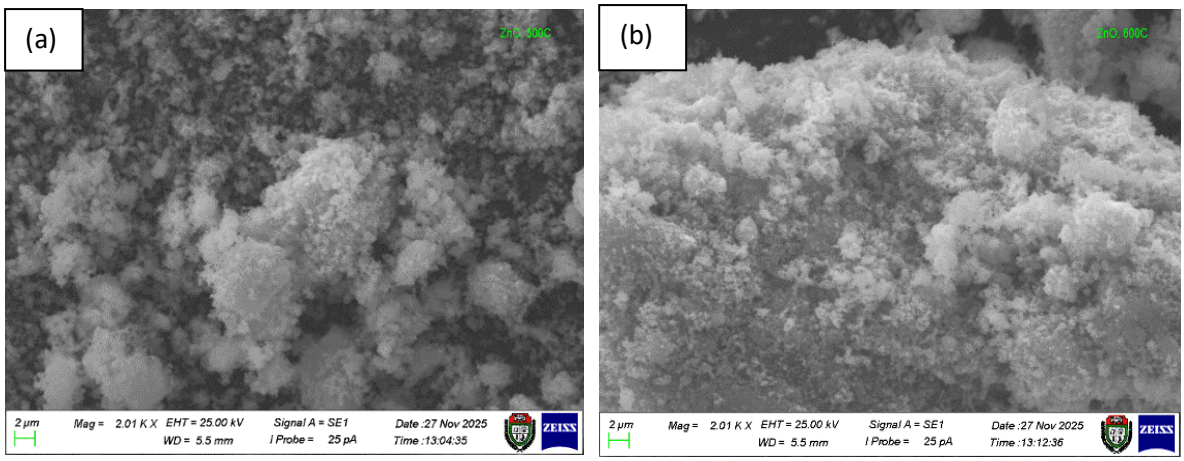

Figure 5 SEM micrographs of ZnO nanoparticles at (a) 500 °C and (b) 600 °C

UV-Vis Analysis of Zinc Oxide (ZnO) Nanoparticles

The absorbance spectra of zinc oxide nanoparticles were measured by using UV-Vis Spectrometer as shown in figure 6(a-b). The wavelength range of spectrum lied between 200 nm and 800 nm. The most observed absorption peaks of ZnO nanoparticles were (301 nm, 376 nm) at 500 °C and (301 nm, 379 nm) at 600 °C respectively. The optical bandgap is obtained by Tauc's equation, $\alpha h\upsilon = A\ (h\upsilon - E_g)^n$, where, A is constant, $h\upsilon$ is photon energy, E_g is the allowed energy band gap, n is ½ for allowed direct transition and n is 2 for indirect transition. The extrapolation of the plot of $(\alpha h\upsilon)^2$ on the Y- axis as a function of $(h\upsilon)$ on the X - axis were provided a good estimate of the band gap of the material under investigation. The alternative method to observe the band gap is Beer-Lambert law. The $(\alpha h\upsilon)^2$ and $h\upsilon$ characteristics curve of ZnO nanoparticles at 500 °C and 600 °C were shown in figure 7(a-b). On the characteristics curve, the extrapolating the straight line onto horizontal axis ($(\alpha h\upsilon)^2 = 0$), give the value of energy band gap and the obtained ZnO nanoparticles had a direct band gap 3.86 eV at 500 °C and 3.79 eV at 600 °C for the absorbance spectra.

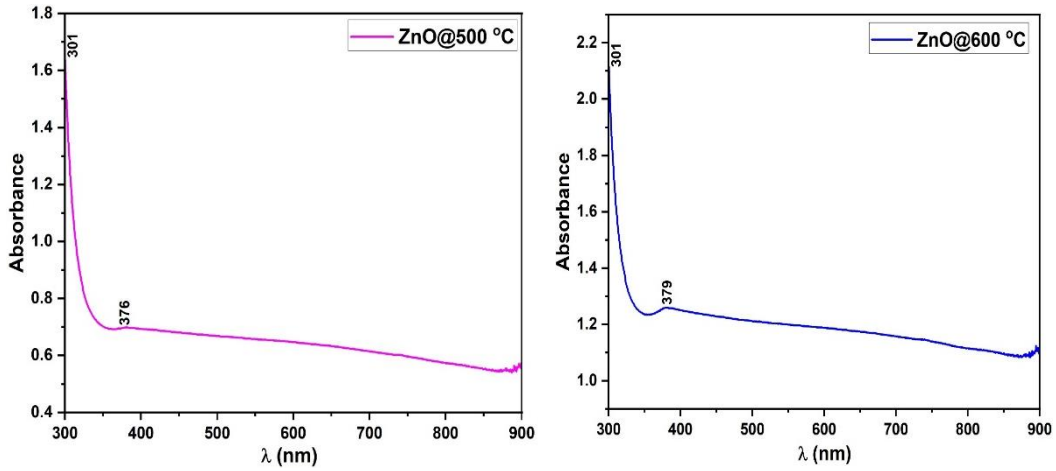

Figure 6 Absorbance spectra of ZnO nanoparticles at (a) 500 °C and (b) 600 °C

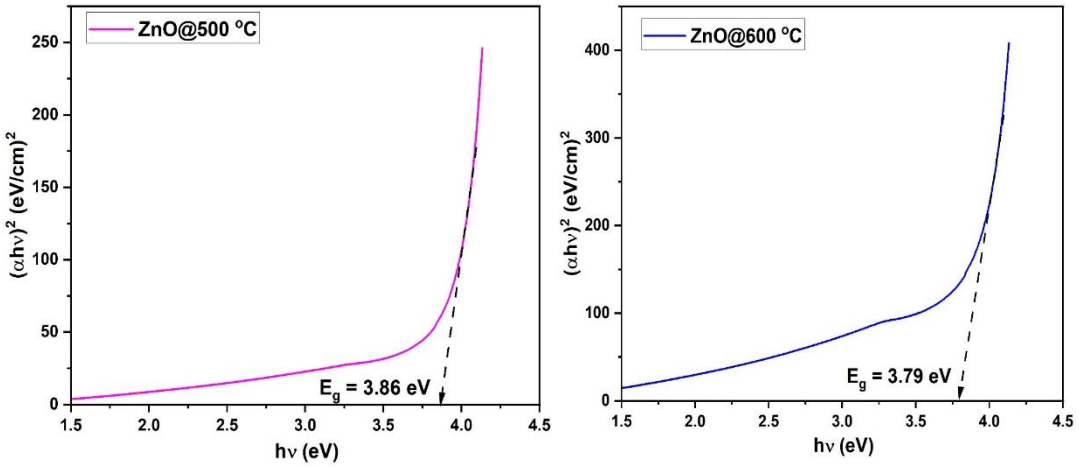

Figure 7 Energy band gaps of ZnO nanoparticles at (a) 500 °C and (b) 600 °C

FTIR Analysis of Zinc Oxide (ZnO) Nanoparticles

FTIR was carried out to determine the potential functional groups of biomolecules that are responsible for the formation of Zinc Oxide (ZnO). The prepared photocatalysts reveal the presence of some absorption bands in the ranges of 400-4000 cm^{-1}. The peak observed in all nanoparticles from 1200 to 1100 cm^{-1} was associated with C-C stretching of the methyl groups. Also, the peaks that existed between 1000 and 660 cm^{-1} in all nanoparticles showed the C-C stretching of alcohols, ethers, and carboxylic acids, which are used as the capping and reducing agents for the synthesis of nano-materials. An absorption band observed in the region between 400 and 600 cm^{-1} confirmed the presence of metal-oxygen [M-O] bond stretching vibration. The FTIR spectra (Figure 8(a-b)) of *Azadirachta indica* A. Juss. (Neem) leaves extract showed a distinct peak in the range that ZnO nanoparticles were (1120.19 cm^{-1}, 423.56 cm^{-1} and 410.86 cm^{-1}) at 500 °C and (1117.03 cm^{-1} and 409.82 cm^{-1}) at 600 °C respectively. The existence of N-H and O-H bonds in the FTIR spectrum indicated that proteins, phenolics, and flavonoid compounds in *Azadirachta indica* A. Juss. (Neem) leaves extracts are responsible for the bio reduction of Zn^{2+} ions and stabilizing process of ZnO NPs.

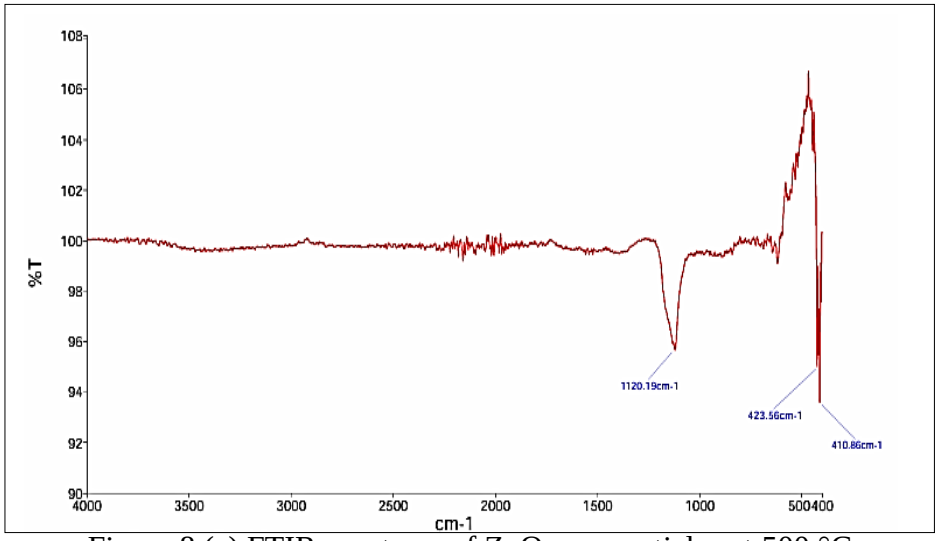

Figure 8 (a) FTIR spectrum of ZnO nanoparticles at 500 °C

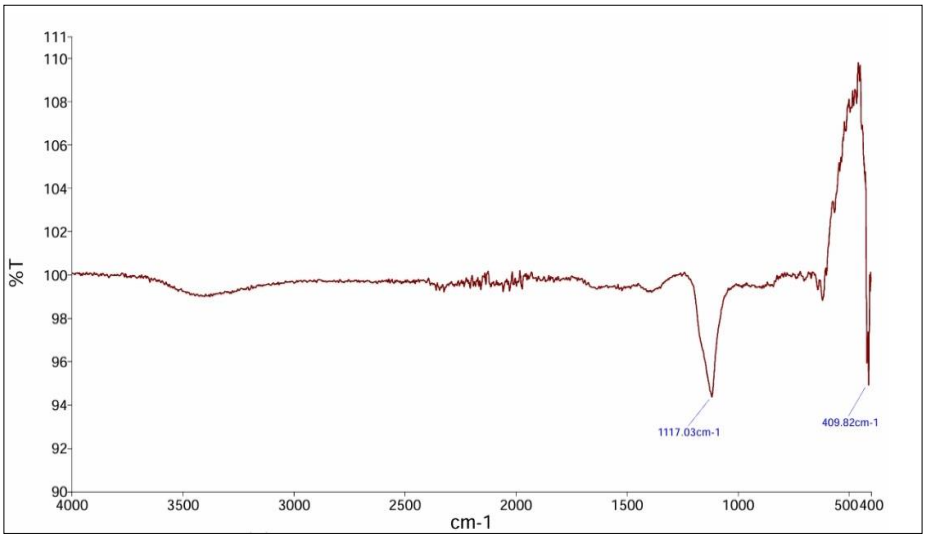

Figure 8 (b) FTIR spectrum of ZnO nanoparticles at 600 °C

Conclusion

In this research, zinc oxide nanoparticles were successfully synthesized by using green synthesis method. XRD patterns of zinc oxide nanoparticles were well matched with corresponding standard library files. The crystal structure of zinc oxide nanoparticles was found to be hexagonal structure. According the XRD results, the crystallite sizes were decreased with increasing temperature. According to SEM results, the surface morphologies of pure were composed of regular and sphere grains. SEM images of the ZnO nanoparticles at 500 °C showing that agglomeration has been taken place where as in ZnO nanoparticles at 600 °C, it is not agglomerate. In these results, the average grain size of the ZnO nanoparticles were depended by varying different process temperatures. As the UV-Vis analysis results, the widest energy bandgap of ZnO nanoparticles were 3.86 eV at 500 °C and the smallest energy bandgap was 3.79 eV at 600 °C. The intensity of absorption peak and energy band gaps decreases with increasing temperatures. From the FTIR results, the absorption bands observed in the region between 400 and 600 cm^{-1} confirmed the presence of metal-oxygen [M-O] bond stretching vibration. In conclusion, ZnO powder has been widely used as the products including ceramics, glass, cement, photovoltaic applications and energy storage devices.

Acknowledgements

We would like to express our sincere thanks to Professor Dr Maung Maung Shwe, Head of the Department of Physics, West Yangon University for his kind encouragement and permission to perform this research work. We would like to thank Professor Dr Aye Moe Soe, Professor Dr Thu Zar Aung and Professor Dr Yin Yin Thein, department of Physics, West Yangon University for their kind advice, encouragements and suggestions for this research.

References

Ajayan, A. S., & Hebsur, N. S. (2020). Green synthesis of zinc oxide nanoparticles using neem (*Azadirachta indica*) leaves extract and their characterization. *International Journal of Current Microbiology and Applied Sciences, 9*(2), 277–285.

Bhuyan, T., Mishra, K., Khanuja, M., Prasad, R., & Varma, A. (2019). Biosynthesis of zinc oxide nanoparticles from *Azadirachta indica* for antibacterial and photocatalytic applications. *Materials Science in Semiconductor Processing, 32*, 55–61.

Biron, D. S., Santos, V., & Bergmann, C. P. (2020). Synthesis and characterization of zinc oxide obtained by combining zinc nitrate with sodium hydroxide in polyol medium. *Materials Research, 23*(2), e20200080.

D. S., & J. B. (1988). Determination of crystallite and strain by X-ray diffraction. In *X-ray diffraction: A practical approach* (ch. 6, pp. 167–173). Plenum Press.

Gnanasangeetha, D., & Thambavani, S. D. (2014). Facile and eco-friendly method for the synthesis of zinc oxide nanoparticles using *Azadirachta* and *Emblica*. *International Journal of Pharmaceutical Sciences Research, 5*(7), 2866–2873.

Hessien, M., Dana, E., & Taha, A. (2021). Phytoextract assisted hydrothermal synthesis of ZnO–NiO nanocomposites using neem leaves extract. *Ceramics International, 47*(1), 811–816.

Butler, J. N. (1998). *Ionic equilibrium: Solubility and pH calculations*. Wiley.

L. C. J., et al. (2018). Characterization of zinc oxide (ZnO) nanoparticles by FTIR and UV-Vis spectroscopy. *Journal of Physics: Conference Series, 1082*(1), 012077.

Lalithambika, K. C., Thayumanavan, A., Ravichandran, K., & Sriram, S. (2017). Photocatalytic and antibacterial activities of eco-friendly green synthesized ZnO and NiO nanoparticles. *Journal of Materials Science: Materials in Electronics, 28*, 2062–2068.

Oudhia, A., Kulkarni, P., & Sharma, S. (2015). Green synthesis of zinc oxide (ZnO) nanotubes for bioapplications. *International Journal of Advanced Engineering Research and Studies, 4*(2), 280–281.

R. Y., et al. (2019). Plant extract mediated synthesis of zinc oxide (ZnO) nanoparticles: A review. *Nano-Structures & Nano-Objects, 19*, 100368.

S. A. K., et al. (2021). Green synthesis of zinc oxide nanoparticles using *Azadirachta indica* leaves extract and its antibacterial and photocatalytic activities. *Materials Today: Proceedings, 45*, 2549–2555.

Iravani, S. (2011). Green synthesis of metal nanoparticles using plants. *Green Chemistry, 13*(10), 2638–2650.

S. S., et al. (2022). Role of plant phytochemicals in green synthesis of zinc oxide nanoparticles. *Biocatalysis and Agricultural Biotechnology, 42*, 102332.

Simon, E. W., & Beevers, H. (1951). The quantitative relationship between pH and the activity of weak acids and bases in biological experiments. *Science, 114*(2953), 124–126.

Surabhi, S. K., Putcha, V., Vanka, R. R., et al. (2013). Synthesis, characterization and optical properties of zinc oxide nanoparticles. *International Nano Letters, 3*, 30.

Wang, Z. L. (2004). Zinc oxide nanostructures: Growth, properties and applications. *Journal of Physics: Condensed Matter, 16*, 829–858.

Wang, M., Li, A. D., Kong, J. Z., Gong, Y. P., Zhao, C., Tang, Y. F., & Wu, D. (2018). Fabrication and characterization of ZnO nano-clips by the polyol-mediated process. *Nanoscale Research Letters, 13*, 47–54.

Green Synthesis and Characterization of Tin Oxide (SnO_2) Nanoparticles Using Extract Solution of *Mentha spicata* L. (Spearmint) Leaves

Thuzar Hnin[1], Myat Thet Mon[2], Zin Min Myat[3], Zin Min Tun[4]

Abstract

Nanoparticles have unique properties as a consequence of size, distribution and morphology and are a very important component in the rapidly developing fields of nanotechnology. This research aimed to prepare the tin oxide (SnO_2) nanoparticles using *Mentha spicata* L. (Spearmint) leaves extract by green synthesis method. Tin oxide nanoparticles were synthesized by varying the leaves extract solution of 50 ml, 75 ml and 100 ml as the reducing agents and they were calcined at 600 ^oC for 2 h. The crystal structure and crystalline size of tin oxide nanoparticles were characterized by X-ray Diffraction (XRD). The XRD measurement showed that all peaks of tin oxide were consisted with that tin oxide standard (JCPDS) file having tetragonal structure. The functional groups identification of spearmint leaves and tin oxide nanoparticles were analyzed by Fourier Transform Infrared Spectroscopy (FTIR). The results of Scanning Electron Microscopy (SEM) were studied the formation of shape and grain size of tin oxide nanoparticles. It can be observed that the synthesized nanoparticles exhibited smooth, porous, agglomerated, and sphere-like morphology. According to the SEM analysis, the average grain sizes of SnO_2 nanoparticles were 0.12 μm, (50 ml leaf extract), 0.14 μm (75 ml leaf extract) and 0.23 μm (100 ml leaf extract) respectively. The absorption wavelengths and energy band gap were measured with the help of UV-Vis Spectroscopy. The prepared tin oxide nanoparticles can apply the development of nontoxic and biocompatible safe nanoparticle production at cost effective, simple and eco-friendly. Tin oxide (SnO_2) nanoparticles can be promoted further experimental research such as biosensor, thin films solar cells, memory devices and optoelectronic materials.

Keywords: Tin oxide, Spearmint leaves, XRD, FTIR, SEM, UV-Vis

Introduction

Tin oxide nanoparticles have garnered considerable scientific focus these days owing to their exceptional optical and electrical characteristics (Kumar et al., 2018). Tin oxide NPs are very promising nanoparticles owing to their band gap of 3.6 eV and tetragonal n-type crystal structure. It is also advantageous compared to other nanomaterials due to its high electron mobility, which enables fast photogenerated electron transport (Jia et al., 2014). The unique characteristics of SnO_2 NPs were found to be applicable in several areas, such as gas sensors (Sangami & Dharmaraj, 2012), glass coatings (Omokhua et al., 2016), electrodes (Elango & Roopan, 2015), lithium-ion batteries (Diallo et al., 2016), and photocatalysis (Ayeshamariam et al., 2014; Vidhu & Philip, 2015). To produce SnO_2 NPs, numerous procedures have been applied, inclusive of microwave heating, sol–gel, homogeneous precipitation, mechanical synthesis, chemical vapour deposition, gas-phase condensation, hydrothermal approach, co-precipitation, thermal evaporation, and laser ablation (Liu et al., 2010). Nonetheless, these chemical and physical manufacturing methods require a large amount of dangerous, poisonous substances, higher energy, and a greater cost. Today, the green synthetic method using plant extracts has attracted scientists due to its eco-friendliness and simplicity (Senthilkumar & Vickraman, 2012; Yang & Zhang, 2017; Srivastava & Mukhopadhyay, 2014; Wang et al., 2021). It is cost-effective and, consequently, can be used as an economical and feasible alternative for the sizable production of metal oxide nanoparticles. It was

[1] Demonstrator, Department of Physics, West Yangon University
[2] Demonstrator, Department of Physics, West Yangon University
[3] Associate Professor, Department of Physics, West Yangon University
[4] Associate Professor, Department of Physics, West Yangon University

discovered that the bioactive chemicals (alkaloids, carbohydrates, amino acids, flavones, and terpenes) employed as reducing and capping agents throughout the nanomaterials' synthesis determine the mechanism rate, the surface shape, and the size of the nanoproduct, as well as its stability (Sotelo-Boyás et al., 2021). X-ray diffraction (XRD), Fourier-transform infrared (FTIR), and UV–Vis analyses were used to characterize the final SnO_2 NPs.

Experimental Procedure

Preparation of Extract Solutions with Four Different Leaves

The leaves of *Mentha spicata* L. (Spearmint) leaves were collected green and fresh leaves that grow naturally at local market and then thoroughly washed in tap water and then, they were also rinsed in distilled water to remove impurities. These leaves were dried at room temperature for two days in normal atmosphere to remove the residual moisture. After which dried leaves were cut into fine pieces. 50 g of dried small leaves were mixed with 100 ml of distilled water and extracted under reflux containing at 80 ºC for 45 min. After boiling, the colour of the aqueous solution changed from watery into greenish colour and then continuous to yellowish colour the pH level was recorded. The prepared extract solution was kept into the water bath to obtain homogeneous extract solution. These solutions were filtered through Whatman No.1 filter papers to remove solid materials and heavy biomaterials. The extract solution of this leaves were done shown in figure 1. The aqueous extracts were stored at room temperature to be used for green synthesis of further experiments.

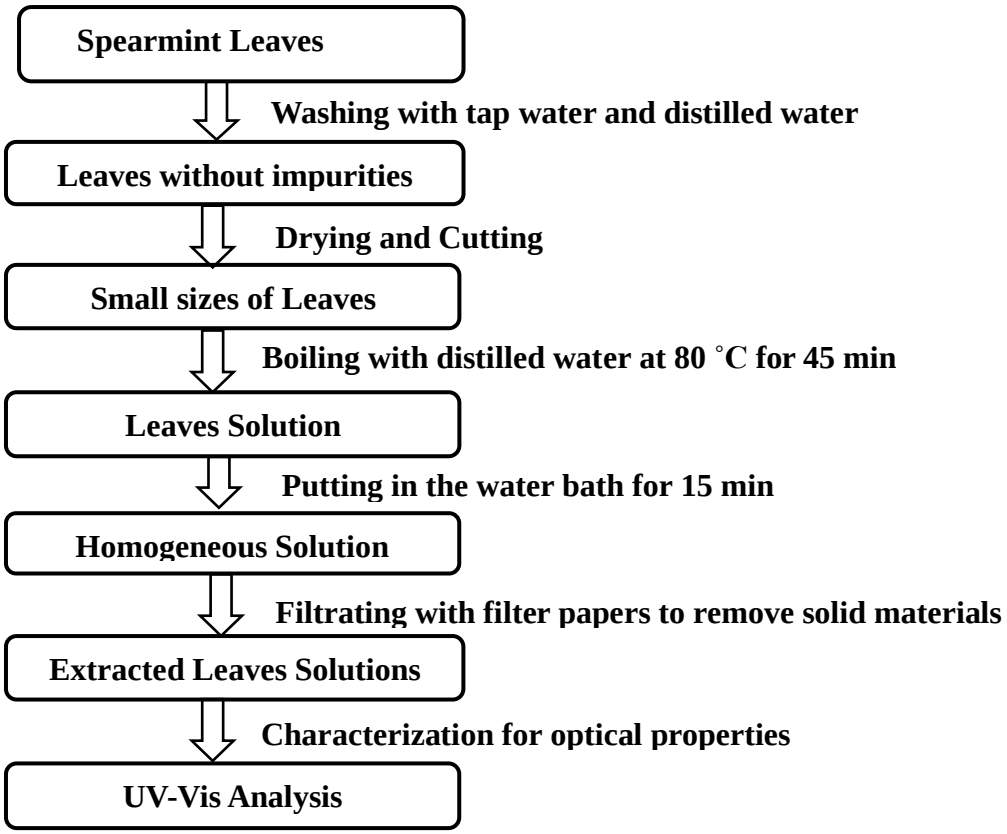

Figure 1 Experimental Procedure of Extract Solution from Spearmint Leaves

Experimental Preparation of Tin Oxide Nanoparticles

In this research, extract solution from the leaves of spearmint, tin chloride ($SnCl_2$) and distilled water were used as starting materials. Tin oxide (SnO_2) nanoparticles were prepared

according to the green synthesis method. In this research work, the preparation of tin oxide (SnO_2) nanoparticles were synthesized by green synthesis method using spearmint leaves extract solutions. For the synthesis of SnO_2 nanoparticles, the starting materials of 18 g of tin chloride $SnCl_2$ (0.5M) was dissolved to get tin chloride solution with 200 ml of distilled water. The tin chloride solution was mixed with 50 ml, 75 ml and 100 ml of leaves extract solutions and stimulated on a magnetic stirrer heated at 80 °C. The stirring was nonstop until a uniform solution was completed for 4 h and sodium hydroxide solution was poured drop by drop in this solution. During the end of stirring process, the color of solution was changed white to ivory color and the level of pH value was found to be 2 and therefore this solution was directed into the acidic solution. Next, the homogeneous solution was filtered with Whatman No.1 filter papers and it was dehydrated in a hot air oven at the temperature of 120 °C for 24 h. After drying, the samples were taken out from the furnace annealed at 600 °C for 2 h. Finally, the homogeneous tin oxide nanoparticles with spearmint extract solutions were obtained by green synthesis method. The step by step preparation of tin oxide nanoparticles from spearmint extract solution was shown in Figure 2.

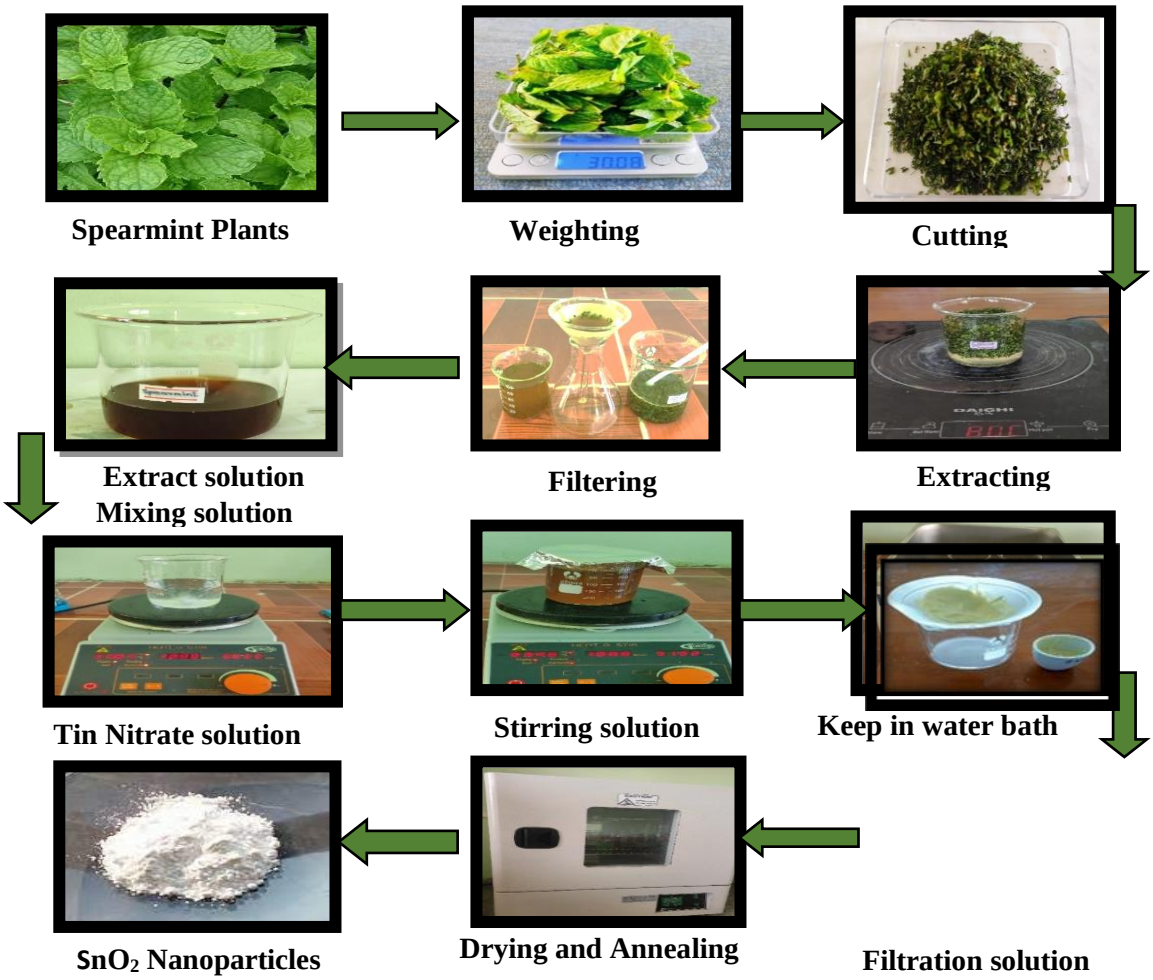

Figure 2 Step by Step Preparation of Tin Oxide Nanoparticles from Spearmint Leaves Extract Solution

FTIR Analysis of Spearmint Leaves

The Fourier Transform Infrared Spectroscopy (FTIR) was used to characterize the spearmint leaves because functional groups and chemical properties can be detected that may modify

the sequestration capability. FTIR spectroscopy was applied to measure the chemical properties and transmission of energy from the range of 4000 cm^{-1} - 450 cm^{-1} by studied the samples. The functional groups of extracted solution have found to be C-N stretching (medium) in amine at 1020-1250 cm^{-1}, O-H bending (weak) in carboxylic acid at 1395-1440 cm^{-1}, C=C stretching (strong, sharp band) in alkene at 1620-1648 cm^{-1}, O-H stretching (weak, broad band) in alcohol at 2700-3200 cm^{-1}, O-H stretching (strong, broad band) in alcohol at 3200-3550 cm^{-1} respectively. Figure 4.1 showed the FTIR spectra of spearmint leaves. The functional groups and compound classes with respect to their wave numbers of spearmint leaves were as shown in Table 1.

Table 1 Chemical Properties of FTIR Analysis for Spearmint Leaves

Wavenumber (cm^{-1})	Range (cm^{-1})	Functional group	Compound class
1049.00	1020-1250 (Medium)	C-N stretching	Amine
1256.34	1020-1250 (Medium)	C-N stretching	Amine
1406.19	1395-1440 (weak)	O-H bending	Carboxylic acid
1625.85	1620-1648 (Strong, sharp)	C=C stretching	Alkene
2904.77	2700-3200 (Weak, broad)	O-H stretching	Alcohol
3325.60	3200-3550 (Strong, broad)	O-H stretching	Alcohol

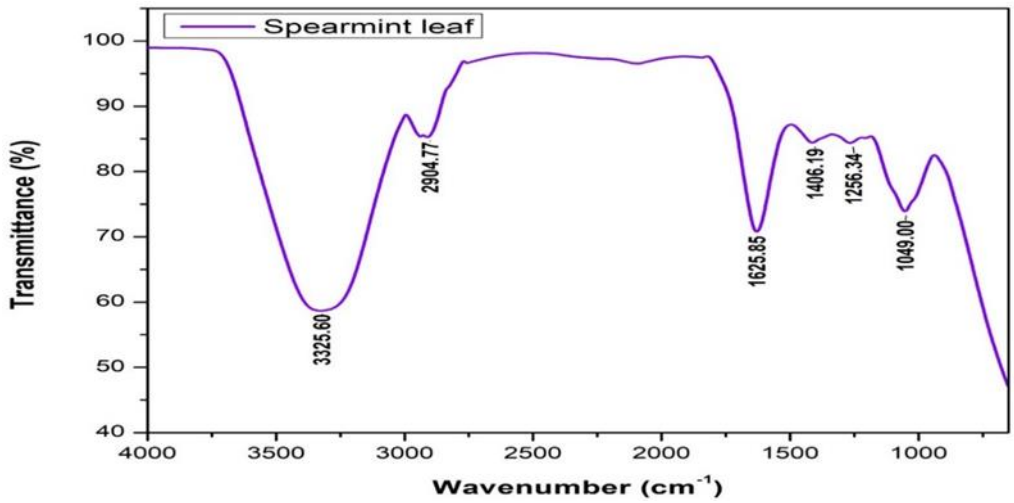

Figure 3 Fourier Transform Infrared Spectroscopy Spectra of Spearmint leaves

Results and Discussion

X-ray Diffraction (XRD) Analysis of SnO_2 Nanoparticles

XRD is the one of the instruments used to discover the crystalline structure and particle size of the prepared tin oxide (SnO_2) nanoparticles shown in figures 4 (a-c). The diffraction patterns of SnO_2 nanoparticles were identified by using JCPDS (Joint Committee of Powder Diffraction Standards) data file. The Bragg's angle of 2θ was varied between 20˚ and 70˚. In figures, all of reflection planes were well-matched with SnO_2 standard JCPDS data library. In all reflection planes, (110) and (101) peaks were the most intense peaks in all XRD spectra. XRD pattern indicates that the sample is tetragonal structures tructure According to XRD pattern from figure, the peaks were clearly observed and indicating the formation of SnO_2 with tetragonal structure. The average crystallite size was measured using Debye–Scherer's Equation and the average crystallite size (D) was calculated to be 30.34 nm for 50 ml of leaves extract, 30.92 nm for 75 ml of leaves extract and 26.62 for 100 ml of leaves extract, respectively.

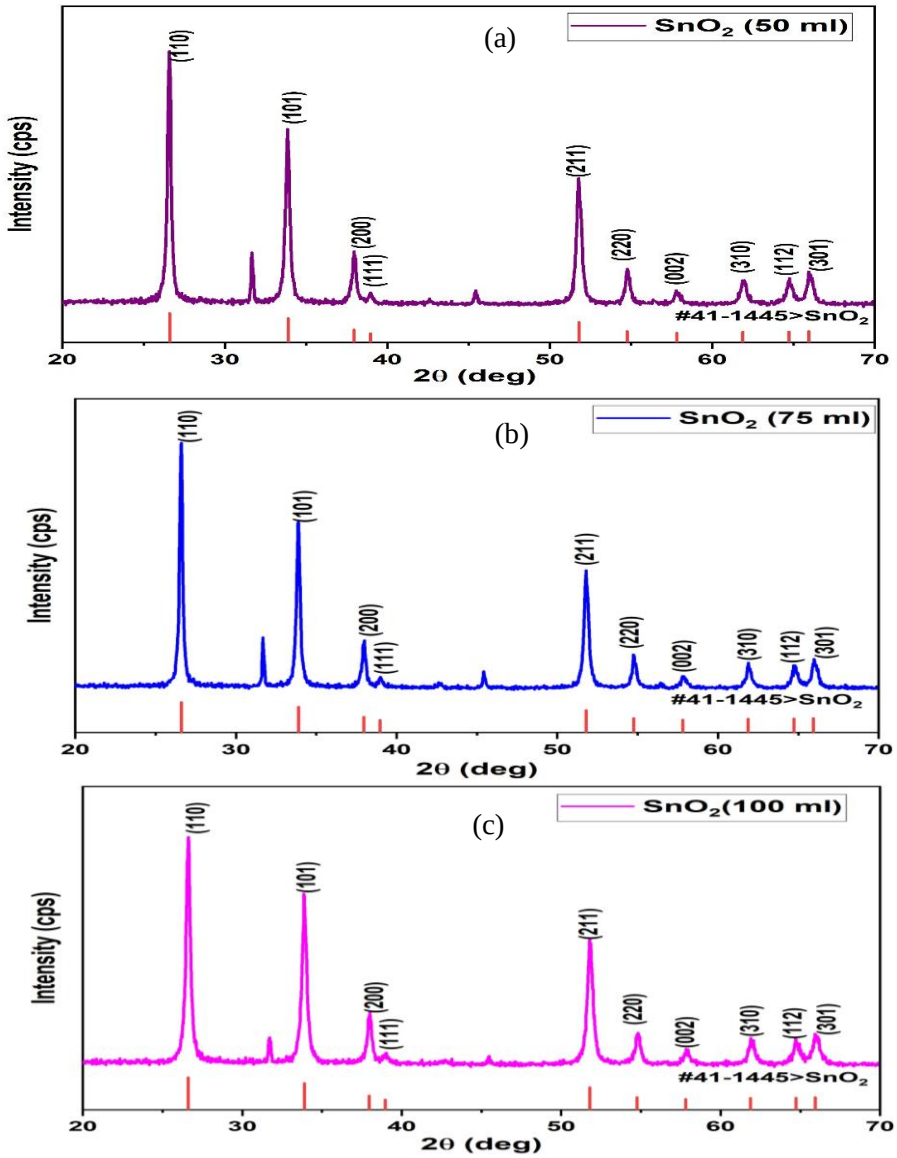

Figure 4 (a-c) XRD Image of SnO_2 Nanoparticles with Different Leaf Extract

UV-Vis Analysis of Tin Oxide Nanoparticles

The optical absorption spectrum and the energy band gap of tin oxide nanoparticles with four different extract solutions were performed using UV-Vis spectrometer. The energy band gap value E_g could be determined by analyzing the optical data with optical absorption coefficient α and the photon energy hν using Tauc's relation, $(\alpha h\nu)^2 = A(h\nu - E_g)$. Figures 5 (a-c) and 6 (a-c) show the absorption spectra, energy bandgaps by using Tauc's equation of the SnO_2 nanoparticles with three different leaves extract solutions The observed energy bandgaps for SnO_2 nanoparticles were 2.88 eV (50 ml), 3.52 eV (75 ml) and 3.61 eV (100 ml) for different leaves extract solutions respectively. Previous research papers have reported that the energy bandgap of SnO_2 nanoparticles may have the ranges from 3.0 eV to 4.5 eV.

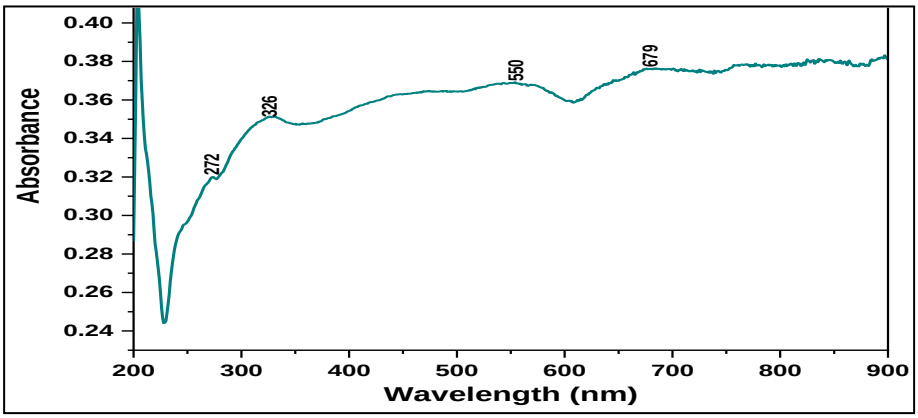

Figure 5 (a) Absorption Spectra of SnO_2 Nanoparticles (50 ml leaf extract)

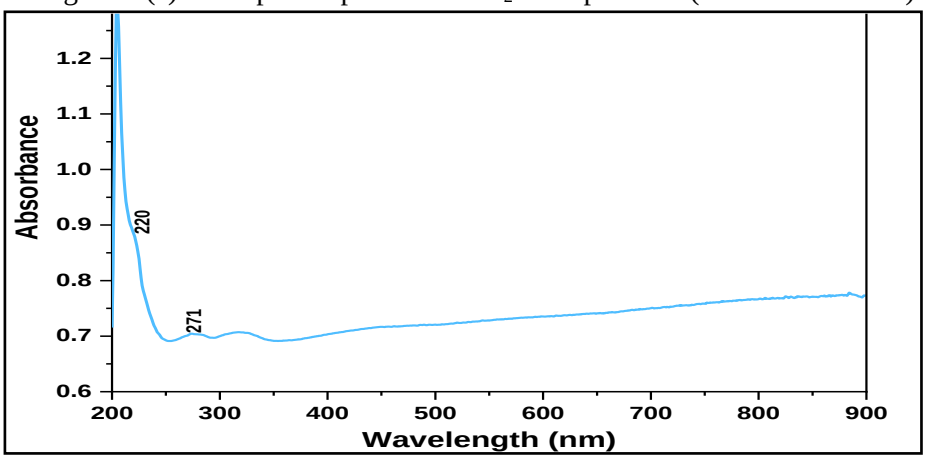

Figure 5 (b) Absorption Spectra of SnO_2 Nanoparticles (75 ml leaf extract)

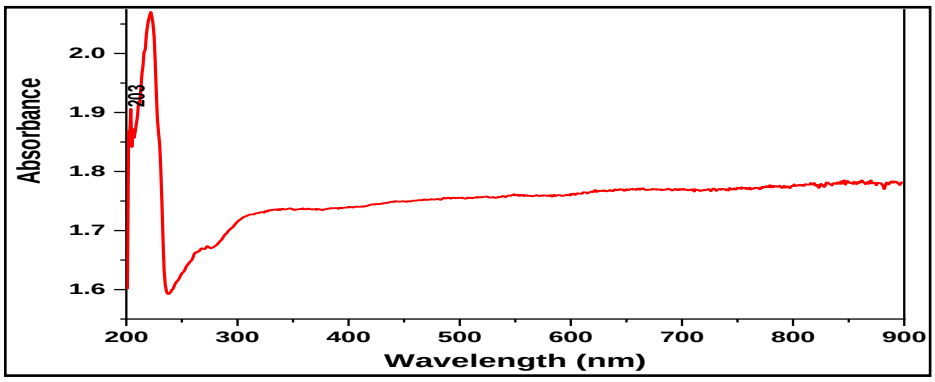

Figure 5 (c) Absorption Spectra of SnO_2 Nanoparticles (100 ml leaf extract)

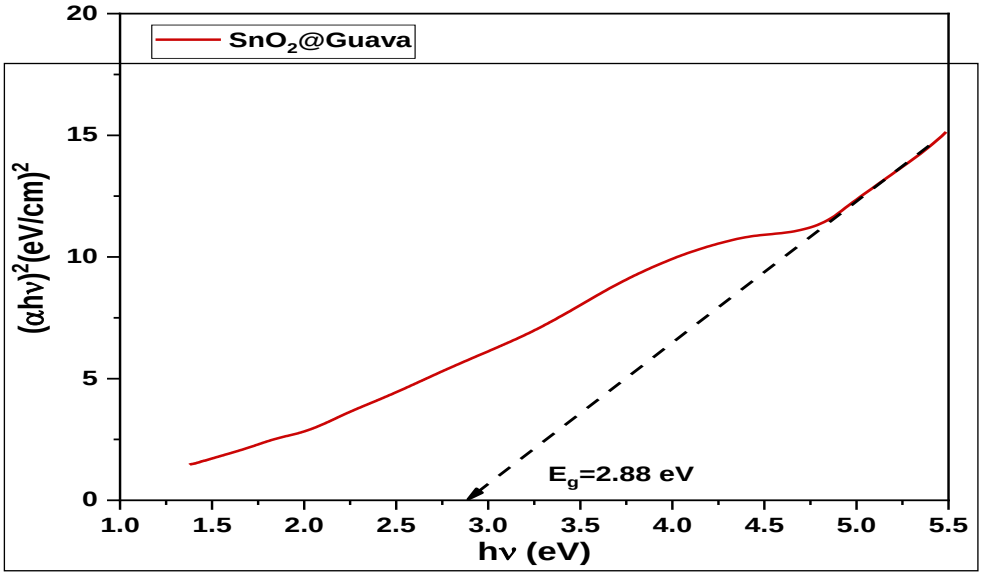

Figure 6 (a) Energy Bandgap of SnO_2 Nanoparticles (50 ml)

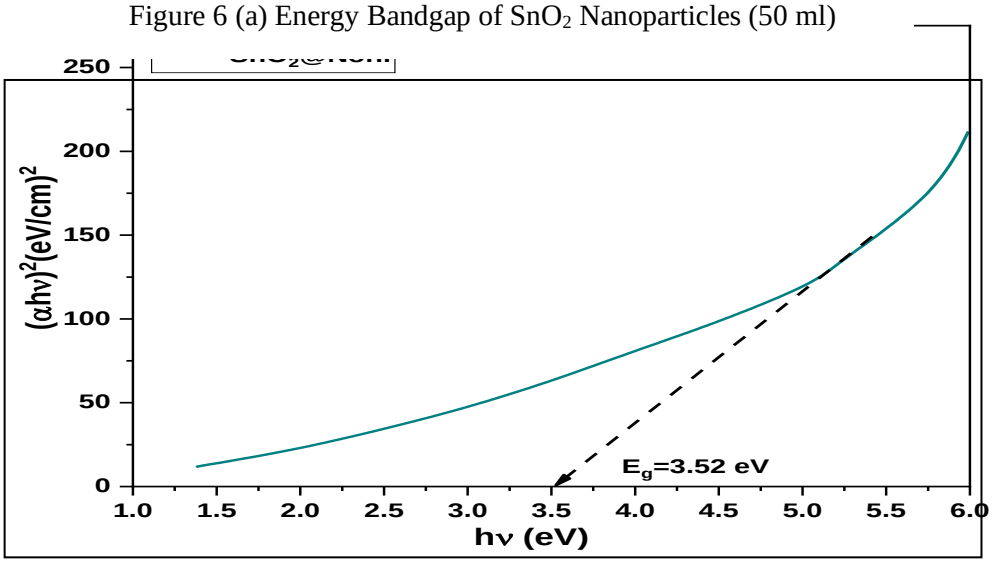

Figure 6 (b) Energy Bandgap of SnO_2 Nanoparticles (75 ml)

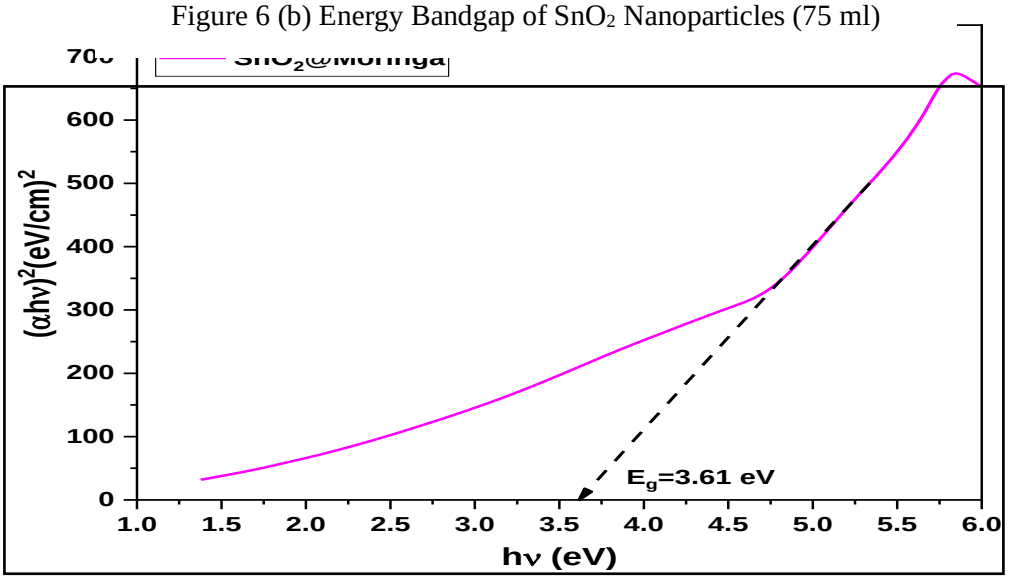

Figure 6 (c) Energy Bandgap of SnO_2 Nanoparticles (100 ml)

SEM Analysis of Tin Oxide Nanoparticles

Tin oxide nanoparticles were obtained using as the external reducing agents from spearmint leaves extract solutions were obtained by green synthesis. Figure 7 (a-c) showed the SEM analysis of tin oxide nanoparticles sintered at room temperature exhibit grained microstructure and nanostructure with small grain size. As the detail analysis of SEM images, it was found that pores, mostly smooth, and uniform particle size. The grain sizes were calculated by using well known bar code system with image J software. SEM analysis of tin oxide nanoparticles sintered at 600 °C by changing different leaves exhibit grained microstructure and nanostructure with small grain size. It was found that pores, dense, mostly smooth, and uniform particle size. Some grains are large agglomeration. The average grain size of the samples was about 0.12 µm (50 ml), 0.14 µm (75 ml) and 0.23 µm (100 ml) respectively. The grain sizes of SnO_2 nanoparticles were seemed to be sphere and uniform or non-uniform distribution. Some grains were a little large but most are uniform grain grow pattern.

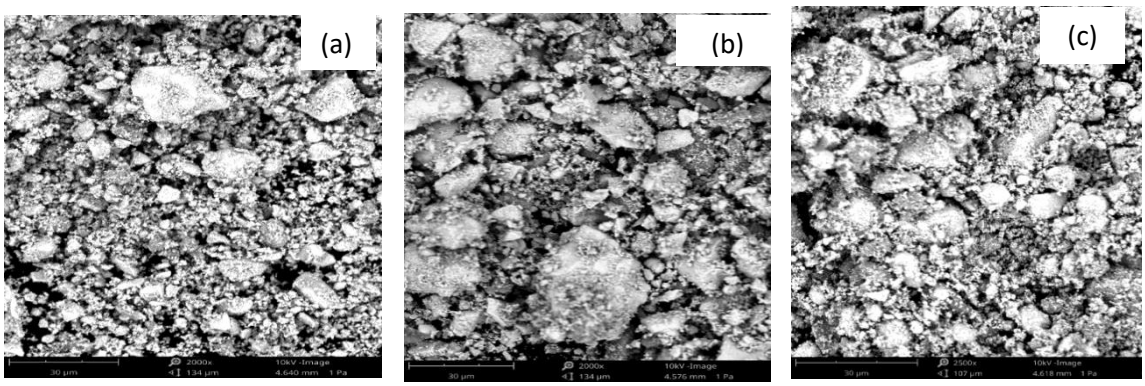

Figure 7 (a-c) SEM image of Tin Oxide Nanoparticles (50 ml, 75 ml and 100 ml)

Conclusion

In conclusion, the green synthesis of tin oxide nanoparticles has been demonstrated by different leaves extract solution of spearmint. From the FTIR spectra analysis, this spectrum confirms that the sample is some complex biological material rich in polyphenols, essential oils (specifically ketones), and structural polysaccharides. The "cleanliness" of the peaks suggests the sample was well-prepared, likely dried or extracted before testing. XRD analysis observed that, the SnO_2 nanoparticles with tetragonal structure at 600 °C and the average crystallite size of green synthesized SnO_2 nanoparticles with different leaves extract that calculated by using Debye-Scherrer's formula, the results showed that all the diffraction peaks Tin oxide nanoparticles (SnO_2 NPs) have been appropriately characterized using UV-Vis spectroscopy analysis. According to UV-Vis analysis, the absorbance wavelength of tin oxide nanoparticles was found to be between 203 nm and 300 nm and absorption peak heights and peak positions of tin oxide nanoparticles were in good agreement with standard literature value of tin oxide nanoparticles (200 nm-300 nm) and also confirmed the SnO_2 nanoparticles. In this study, the band gap energy of SnO_2 nanoparticles were found to be 2.88 eV (50 ml), 3.53 eV (75 ml) and 3.61 eV (100 ml) respectively. Therefore, the synthesized SnO_2 nanoparticles have wide band gap. of tin oxide nanoparticles can be perfectly matched with standard library file. SEM analysis showed that the SnO_2 nanoparticles had mostly spherical morphology, uniform grain distribution and clearly observed the average grain sizes of SnO_2 nanoparticles. From a technological point of view and experimental results, these green synthesized tin oxide (SnO_2) nanoparticles can be applied the potential applications such as biosensors, optoelectronic application, memory devices and some biomedical fields.

Acknowledgements

I would like to express my sincere thanks to Professor Dr Maung Maung Shwe, Head of the Department of Physics, West Yangon University for his kind encouragement and permission to perform this research work. I would like to thank Professor Dr Aye Moe Soe, Professor Dr Thu Zar Aung and Professor Dr Yin Yin Thein, department of Physics, West Yangon University for their kind advice, encouragements and suggestions for this research.

References

Ayeshamariam, A., Sankaracharyulu, M. G. V., Kashif, M., Vidhya, V. S., & Jayachandran, M. (2014). Structural, microstructural and optical properties of ZnO/SnO2 nanocomposites. *Spectrochimica Acta Part A: Molecular and Biomolecular Spectroscopy*, 125, 440–445.

Diallo, A., Ngom, B. D., Park, E., & Maaza, M. (2016). Green synthesis of ZnO nanoparticles by *Aspalathus linearis*: Structural and optical properties. *Journal of Alloys and Compounds*, 646, 425–430.

Dobrucka, R., & Dugaszewska, J. (2016). Biosynthesis and antibacterial activity of ZnO nanoparticles using *Trifolium pratense* flower extract. *Inorganic and Nano-Metal Chemistry*, 46(9), 1251–1255.

Elango, G., & Roopan, S. M. (2015). Green synthesis, characterization and antibacterial activity of ZnO nanoparticles from *Plectranthus amboinicus* leaf extract. *Spectrochimica Acta Part A: Molecular and Biomolecular Spectroscopy*, 137, 210–216.

Jia, Z. Q., Zheng, Z. Z., & Wang, J. H. (2014). Synthesis and characterization of ZnO nanoparticles by a novel solvothermal method. *Transactions of Nonferrous Metals Society of China*, 24(12), 3921–3926.

Kumar, M., Ng, M. K. L., Curran, S. A., & Ajayan, P. M. (2018). Synthesis of large-scale ZnO nanowires for solar cell applications. *Materials Letters*, 210, 268–271.

Liu, J., Huang, X., Yu, J., & Wang, G. (2010). Synthesis of ZnO nanoparticles by a simple polyol method. *Journal of Alloys and Compounds*, 491(1-2), 640–643.

Matussin, S. N., Harunsani, M. H., Tan, A. L., & Khan, M. M. (2020). Plant-extract-mediated SnO2 nanoparticles: Synthesis and applications. *ACS Sustainable Chemistry & Engineering*, 8(8), 3040–3054.

Omokhua, A. G., McGaw, L. J., Finnie, J. F., & Van Staden, J. (2016). *Chromolaena odorata* (L.) R.M. King & H. Rob. (Asteraceae) in sub-Saharan Africa: A synthesis and review of its medicinal potential. *Journal of Ethnopharmacology*, 183, 112–122.

Sangami, G., & Dharmaraj, N. (2012). Green synthesis of ZnO nanoparticles using *Cassia auriculata* leaf extract and their antibacterial activity. *Spectrochimica Acta Part A: Molecular and Biomolecular Spectroscopy*, 96, 1011–1018.

Senthilkumar, V., & Vickraman, P. (2012). Structural and optical properties of ZnO nanoparticles synthesized by micro-emulsion method. *Materials Research Bulletin*, 47(11), 3245–3250.

Sotelo-Boyás, M. E., Correa-Pacheco, Z. N., Bautista-Baños, S., & Gómez y Gómez, Y. (2021). Release of essential oils from chitosan-based nanocapsules and their use in food preservation. *Coatings*, 11(4), 445.

Srivastava, N., & Mukhopadhyay, M. (2014). Biosynthesis of ZnO nanoparticles using microbial isolates and their photocatalytic activity. *Industrial & Engineering Chemistry Research*, 53(11), 4335–4344.

Vidhu, V. K., & Philip, D. (2015). Spectroscopic, electron microscopic and catalytic studies of silver-zinc oxide nanocomposites. *Spectrochimica Acta Part A: Molecular and Biomolecular Spectroscopy*, 134, 140–147.

Wai, T. P., Lim, Y. Y., & Lee, C. K. (2021). Green synthesis of metal oxide nanoparticles: A review. *Journal of Chemistry*, 2021, 1–15.

Wang, X., & Zhang, Y. (2021). Recent advances in the green synthesis of nanomaterials. *Nano Select*, 2(10), 1845–1862.

Wang, Y., Li, X., & Zhang, Q. (2021). Progress in the application of metal-organic frameworks in sensing. *Frontiers in Chemistry*, 9, 650–662.

Yang, Y., & Zhang, L. (2017). Surface modification of ZnO nanoparticles for enhanced photocatalytic performance. *Applied Surface Science*, 405, 320–328.

Synthesis And Characterization of Activated Carbon Using Blackgram Waste Biomass

May Thingyan Moe[1],Sa Nanda Aung[2], Zin Min Tun[3], Zin Min Myat[4]

Abstract

This research aimed to prepare the activated carbon using blackgram waste biomass through a process of carbonization (pyrolysis) and chemical activation. In the present study, the blackgram stalk waste materials firstly prepared to obtain biochar by pyrolysis in a muffle furnace at 300 °C, 400 °C, 500 °C and 600 °C for 1 h. Then the activated carbon from blackgram (BGAC) were produced through a two-step chemical activation process using potassium carbonate (K_2CO_3). The prepared activated carbon was characterized by different analytical tools such as X-ray Diffraction (XRD), Fourier Transform Infrared Spectroscopy (FTIR) and Scanning Electron Microscopy (SEM) respectively. Phase formation and structural properties of samples were characterized by X-ray Diffraction (XRD). The surface morphology and different pore nature of activated carbon samples were determined by SEM. The functional groups and chemical properties of blackgram waste activated carbon were examined by FTIR. The finding results promote the development of application of biomass based activated carbon in energy storage system by analyzing the high-performance porous activated carbon from renewable and sustainable biological waste.

Keywords: Activated carbon, blackgram waste,XRD, SEM, FTIR

Introduction

Biomass

Biomass is organic material that comes from plants and animals. Biomass is probably our oldest source of energy for thousands of years, people have burned wood to beat their homes and cook their food. Biomass gets its energy from the sun. The energy from the sun is stored within all organic matter. During a process called photosynthesis, sunlight provides plants with the energy to convert water, carbon dioxide and minerals into oxygen and sugars. These sugars known as carbohydrates, supply plants (or the animals that eat plants) with energy. Foods rich in carbohydrates (like spaghetti) are a good source of energy for the human body. Biomass is a renewable because it can be replenished naturally. People will always the generation of wastes from home and industry. Usually, burning wood uses its energy for heating. Burning though is not the only way to convert biomass energy into a usable energy source. In India, cows manure is converted to methane gas to produce electricity [Anthony. B V., et el, 2000]. Most biomass used today is home grown energy. Only 3.2 % of the energy used today comes from biomass. Biomass was largely replaced by coal natural gas and petroleum. Today,79 % of biomass energy comes from burning wood and the rest of biomass come from crops waste land fill and alcohol fuel. Electric utilities also use biomass energy to generate electricity. Environmentally, biomass has some advantages over fossil fuels such as coal and petroleum [CAVIARES. P., et al. 2006]. Biomass contains little sulfur and nitrogen, so it does not produce the pollutants that cause acid rain. Growing plants for biomass fuels may also help keep global warming in check. This is because plants remove carbon dioxide (a greenhouse gas) from the atmosphere as they grow. Biomass is carbon, hydrogen and oxygen based. Biomass energy is derived from four distinct sources: garbage, wood waste, landfill gases and alcohol fuels. Wood energy is produced from lignocellulosic biomass (second generation biofuel) as fuel. Waste energy, is the second largest source of biomass energy. Biomass is an important renewable source contributing to the world's economy, sustainability and energy security. In developing countries, the use of biomass is of high interest as these

[1] Demonstrator, Department of Physics, West Yangon University
[2] Demonstrator, Department of Physics, West Yangon University
[3] Associate Professor, Department of Physics, West Yangon University
[4] Associate Professor, Department of Physics, West Yangon University

countries have economy largely based on agriculture and forestry. Use of such waste materials for production of adsorbents would be beneficial from both an economical and environmental point of view[El-barbary. M.H., 2009, Garg. V.K., 2003].

Activated carbons are carbons of highly microporous form with both high internal surface area and porosity, and commercially the most common adsorbents used for the removal of organic compounds from air and water streams. Any cheap material with high carbon content, low inorganic can be used as a raw material for the production of activated carbon. Basically, there are two different processes for the preparation of activated carbon: physical activation and chemical activation. Physical activation involves carbonization of a carbonaceous material followed by the activation of the resulting char at a temperature between 1073K and 1373K in the presence of suitable oxidizing gases such as carbon dioxide or steam. Activated carbon is an excellent adsorbent and thus is used to purify, decolorize, deodorize, de-toxicate, filter or remove the salts. They are used as catalyst or catalyst supports. The adsorbent properties of activated carbon are essentially attributed to their large surface area, a high degree of surface reactivity, universal adsorption effect and favourable pore size. These unique characteristics are dependent on the type of raw material employed and method of activation. Basically, there are two methods of activation, Physical and chemical activation. Activated carbon can be made from many substances containing high carbon content such as blackgram, walnut shells, coal, wood, bagasse etc. The raw material has a very large influence on the characteristics and performance of activated carbon and plays a major part in determining its ability to adsorb certain molecular species. In the present work blackgram were used to prepare activated carbon. Blackgram is suitable for preparing micro porous activated carbon due to its excellent natural structure and low ash content. Preparation of Activated carbon was done by carbonization followed by activation which is described below. Carbonization is the process for the conversion of an organic substance into carbon or a carbon containing residue through pyrolysis or destructive distillation. Activation is a carefully controlled oxidation process to develop a porous carbon structure. The idea behind activation is not only to increase the diameter of the pores that were formed during carbonization process but also to create some new porosity [Ashwiny, M.K.].

Pyrolysis process (carbonization process)

Pyrolysis is a thermochemical decomposition of organic material at elevated temperatures in the absence of oxygen. This process generates three main by-products: gases, oils and charcoal which can be used in various industrial applications. The process of extreme pyrolysis which leaves mostly carbon as the residue is called carbonization.

Blackgram Waste

Myanmar name is matpe. Blackgram is a important short-duration pulse crop grown in many parts of India. Blackgram grain contain 24% protein, 60% carbohydrates,1.3% fat and is the richest source of phosphoric acid among pulses (5-6% richer than others) [Anthony. B V., et al, 2000]. Blackgram is a nitrogen-fixing legume that thrives in well- drained, loamy soil and requires a pH between 6.5 and 7.8. It is resilient to adverse climates, can be grown in various soils, and specific genotypes show tolerance to drought and waterlogging.

Figure 1 Photographs of blackgram wastes

Experimental Procedures

Procedure of Biochar Preparation

The blackgram wastes were cleaned with fresh water to remove the dust and impurities. These blackgram wastes were dried in sun for one day and then hand crushed to smaller pieces. Then, the smaller pieces of these wastes were dried at room temperature about one week. The weight of blackgram wastes were measured with electronic digital balance. And then, these raw blackgram wastes were carbonized in the muffle furnace at different temperatures, which were 300 °C, 400 °C, 500 °C and 600 °C for 1 h respectively. After carbonization, these blackgram waste (BG) biochars were mixed with deionized water and K_2CO_3 in a stainless steel beaker with weight ratio of K_2CO_3/BG biochar equal to 1:1. Water was evaporated at 130 °C for 5 h, and these dried mixtures were heated in the muffle furnace at 700 °C for 1 h. The products were cooled to room temperature and washed with H_3PO_4 and deionized water until the pH of the washing solution reached 6-7. Finally, the activated carbon obtained from blackgram waste (BG) biochars. For various temperatures, the samples were remarked as BGAC-1, BGAC-2, BGAC-3 and BGAC-4 respectively. The block diagram for experimental procedure of blackgram waste (BG) biochars and blackgram activated carbon was shown in figure 2. Table 1 showed the weight loss percentage of BG biochars.

Table 1 Weight loss and shrinkage of blackgram waste biochar

Temperature	Initial weight, W_1	Final weight, W_2	Weight loss, $W = W_2 - W_1$	Weight loss (%)
300 °C	80 g	37.5g	42.5g	53.125 %
400 °C	80 g	26.5g	53.5g	66.875 %
500 °C	80 g	19.8g	60.5g	75.625%
600 °C	80 g	13.5g	66.5g	83.125%

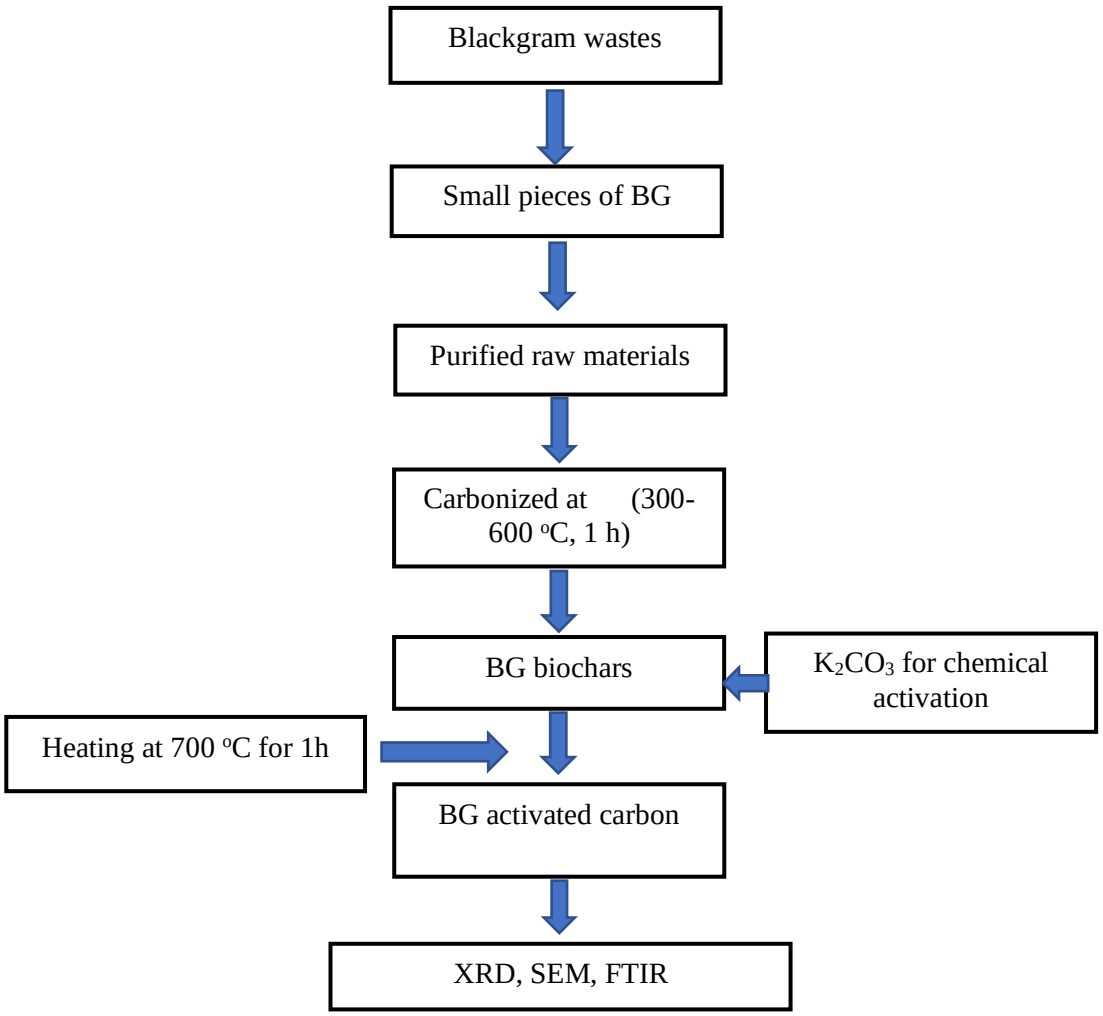

Figure 2 Block diagram of experimental procedure for biochar

Results and Discussion

X-ray Diffraction Analysis Blackgram Waste Activated Carbon

X-ray diffraction is to determine the structure properties of blackgram waste activated carbon using monochromatic CuK_{α} radiation (λ= 1.54056 A) operated at 40 kV (tube voltage) and 40 mA (tube current). Analysis of blackgram waste activated carbon at different temperature values (300 °C, 400 °C, 500°C and 600 °C) for 1 h were shown in figure 3(a-d). From XRD results, these BGACs exhibit the dominant diffraction peak located at around $2\theta = 20° - 30°$ that revealed the presence of amorphous structure which was disorderly stacked up by carbon rings. However, in the higher temperature samples (BGAC-1, BGAC-2, BGAC-3 and BGAC-4) the crystal structure changed to the crystalline calcium carbonate ($CaCO_3$) structure.

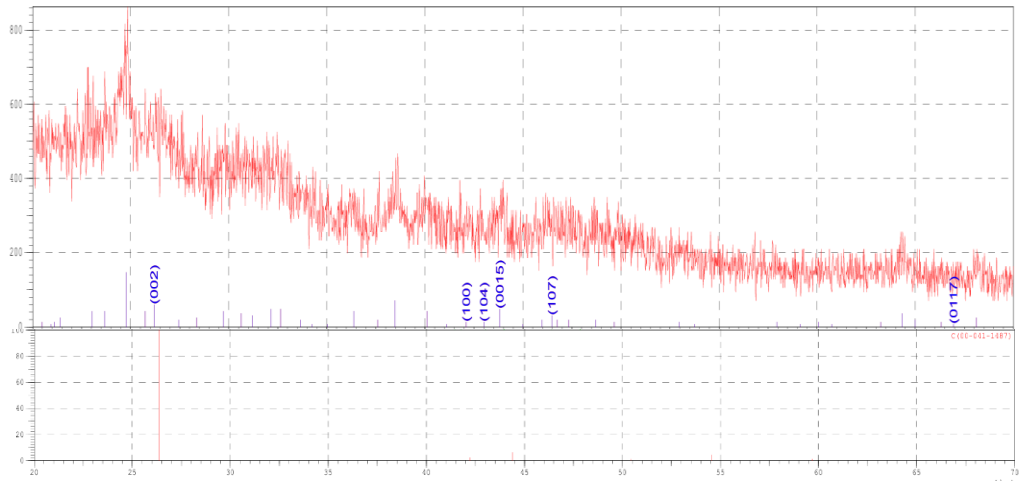

Figure 3 (a) XRD pattern of blackgram waste activated carbon at 300 °C

Figure 3 (b) XRD pattern of blackgram waste activated carbon at 400 °C

Figure 3 (c) XRD pattern of blackgram waste activated carbon at 500 °C

Figure 3 (d) XRD pattern of blackgram waste activated carbon at 600 °C

FTIR Analysis of Blackgram Waste Activated Carbon

FTIR spectroscopy was applied to measure the chemical properties and absorption of energy from the range of 4000 cm^{-1} - 500 cm^{-1} by studied samples. Spectral registration was examined with use of solid-state samples which is made of a complex organic material. The FTIR analysis demonstrated the functional groups presented on blackgram waste activated carbon. From the FTIR results, the broad band at ~3400 cm^{-1} is most prominent at BGAC-1, indicating a high concentration of hydroxyl (-OH) groups. At the BGAC-4, this band significantly flattens, confirming that higher activation temperatures lead to a more hydrophobic surface. The sharp peaks appearing in the 870-1050 cm^{-1} range at higher temperatures (especially BGAC-3 and BGAC-4) represent the formation of a more stable, aromatic carbon skeleton. This suggests that while functional groups are lost, the structural integrity of the carbon becomes more defined. Note that BGAC-1 has the most oxygen-containing groups (C-O, O-H), making it better for chemisorption of metals. In contrast, BGAC-4 has the cleanest spectrum, likely indicating a higher surface area and better performance for physical adsorption (physisorption). Figure 4 showed the FTIR spectra of blackgram waste activated carbon.

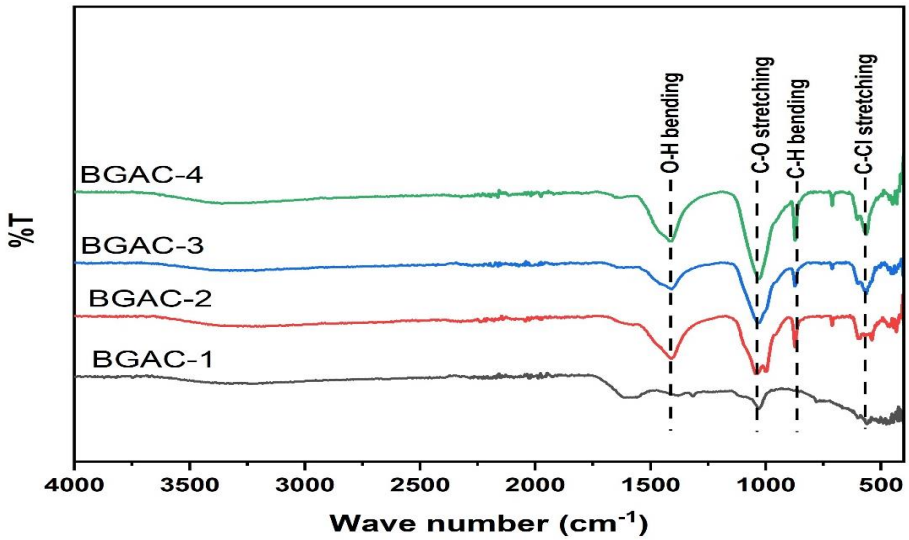

Figure 4 FTIR spectra of blackgram waste activated carbon

SEM Analysis of Blackgram Waste Activated Carbon

SEM is one of the most versatile instruments available for the examination and analysis of the microstructure characteristics of a solid. The most important reason for using SEM is high resolution that can be obtained when bulk sample are examined. SEM micrographs for external morphology of blackgram waste activated carbon were shown in figure 5(a-d). According to figure 5(a-d), the clear porous nature had observed the coconut husk biochar in BGAC-1~BGAC-4. After increasing temperature, it was found that the BGACs had clearer porous nature and uniform with microporous structure. For BGACs, the average pore sizes of the samples were found to be about 2.15 µm for BGAC-1, 2.33 µm for BGAC-2, 2.57 µm for BGAC-3 and 2.74 µm for BGAC-4 respectively.

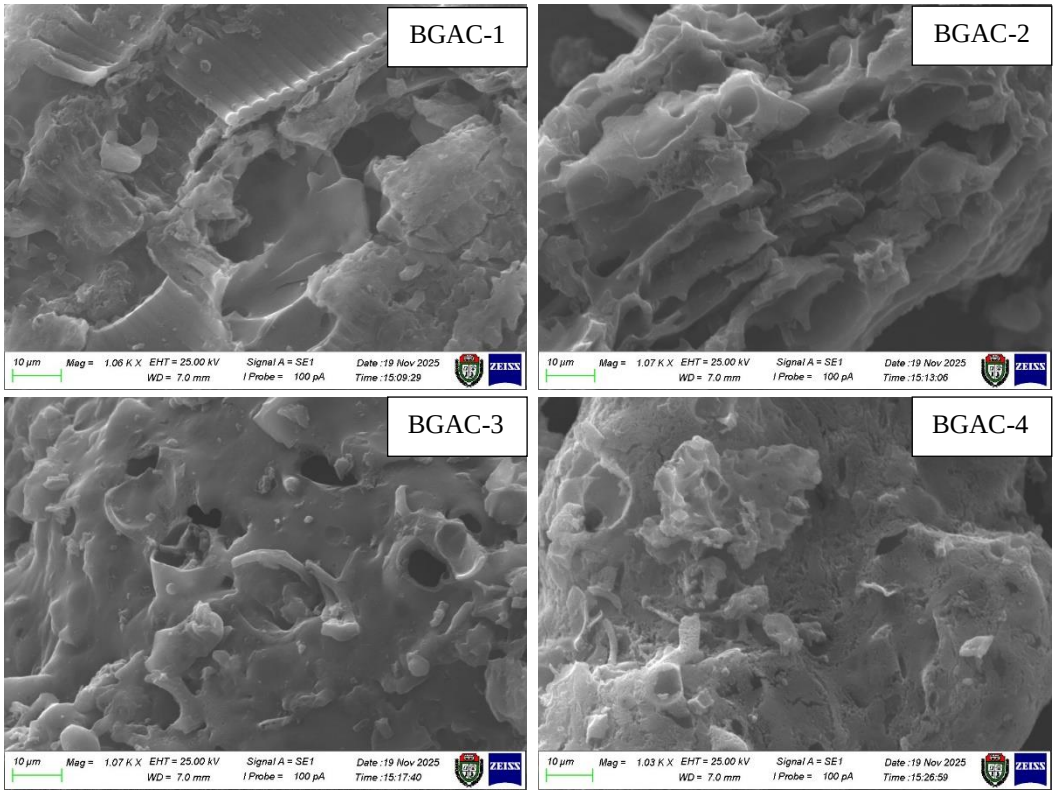

Figure 5 SEM micrographs of blackgram waste activated carbon (a) BGAC-1, (b) BGAC-2, (c) BGAC-3 and (d) BGAC-4

Conclusion

In this present work, blackgram waste were calcined at 300 °C, 400 °C 500 °C, and 600 °C for 1 h to get the biochar, which can be used in bio-fertilizer for agriculture and waste water treatment. From the results, it can be observed that the weight loss (%) of blackgram waste biochar were dependent on the carbonization temperatures. The weight loss of biochar increased with increasing temperature. From XRD results, the XRD patterns of the blackgram waste activated carbon were characteristic of graphite (carbon) structure for BGAC-1 and calcium carbonated structure for BGAC-2, BGAC-3 and BGAC-4 respectively. The functional groups of blackgram waste biochar have found to be O-H bending vibration, C-O stretching vibration, C-H bending vibration and C-Cl stretching vibration by FTIR analysis respectively. According to SEM images, the clear porous nature had observed the blackgram waste activated carbon at different temperatures. After increasing temperature, it was found that the blackgram waste activated carbon had more clearer porous nature and uniform with

microporous structure. From SEM results, these samples have microporous nature and have so many micropores. Because of microporous natures, these samples can store water and act as an absorber for other minerals. Therefore, they were used in bio-fertilizer for agriculture and it was mostly effective for plants growth. From the research findings, these BGACs were also used as electrode elements in energy storage devices because of their high porous nature.

Acknowledgements

I would like to express my sincere thanks to Professor Dr Maung Maung Shwe, Head of the Department of Physics, West Yangon University for his kind encouragement and permission to perform this research work. I would like to thank Professor Dr Aye Moe Soe, Professor Dr Thu Zar Aung and Professor Dr Yin Yin Thein, department of Physics, West Yangon University for their kind advice, encouragements and suggestions for this research**.**

References

Anthony. B V., Peacocke. G V C. (2000 Mar). Fast pyrolysis processes for biomass. *Renewable and Sustainable Energy Reviews, 4*(1), 1-73.

Ashwiny, M.K., Characterization and Applications of Activated Carbon Prepared from Corn Cobs, Dayanande Sagar College of Engineering.

CAVIARES. P., et al. (2006). Adsorption equilibrium of phenol onto chemically modified activated carbon F400. *Journal of Hazardous Materials, Amsterdam, 131*(1), 243-248.

Dural. M.U., Cavas. L., Papageorgious, S.K. (2011). Methylene blue adsorption on activated carbon prepared from *Posidonia oceanica* (L) dead leaves: Kinetics and equilibrium studies, *Chem. Eng. J, 168*, 77-85.

El-barbary. M.H., Philip. H.S. (2009). Characterization of fast pyrolysis bio-oils produced from pretreated pine wood. *Journal of Applied Biochemistry and Biotechnology, 153*(1-3), 3-13.

Garg. V.K., Gupta. R., Yaday. A.B., Kumar. R. (2003). Dye removal from aqueous solution by adsorption on treated sawdust. *Bioresour. Technol*. 89, 121-124.

Karaosmanoglu., Angin. D., Sensoz. S. (2005). Characterization of the bio-oil of rapeseed cake. *Energy Sources*. 2005; *27*(13):12217-23.

Lehmann. J and Joseph. S. (2009). Biochar for Environmental management. *Science and Technology, Earthscan, London, UK*.

DIAS. J.M., et al. 2007. Waste materials for activated carbon preparation and its use in aqueous-phase treatment: A review. *Journal of Environmental Management, London, 85*(4), 833-846.

Stecher. K., Brosowski. A., Thran. D. (2013). Biomass Potential in Africa, *International Renewable Energy Agency, Abu Dhabi, United Arab Emirates.*

Tsamba. A. (2008). Fundamental study of two selected tropical biomass for energy: Coconut and cashew nut shells. *Doctoral Thesis, Energy and Furnace Technology, Stockholm, Sweden.*

Wu. M., Guo. Q., Fu. G. 2013. Preparation and characteristics of medicinal activated carbon powders CO_2 activation of peanut shells. *Powder Technology, 247*, 188-196.

Conversion of Waste Corn Husks into Biochar for Sustainable Material Applications

Myat Thet Mon[1], Thuzar Hnin[2], Zin Min Myat[3], Zin Min Tun[4]

Abstract

Biochar is a value-added product that can be used for many purposes, particularly for environmental and agricultural purposes. In this study, pyrolysis at 300 °C, 400 °C and 500 °C for 1 h were used to upgrade agricultural wastes such as waste corn husks into biochar. The physicochemical properties of corn husk biochar such as weight loss and bulk density were evaluated. Elemental compositions were determined using Energy Dispersive X-ray Fluorescence (EDXRF), while structural and morphological characteristics were analyzed via XRD and SEM. Biochar derived from the waste corn husks (and associated corn waste like cobs and stalks) is a sustainable, high-potential method for managing agricultural waste, converting it into a valuable carbon-rich material used for soil improvement, carbon sequestration, and environmental remediation. This process mitigates environmental pollution caused by open-field burning of corn residues. According to data analysis, the prepared biochar can apply a promising functional material in energy storage devices, environmental and agricultural applications.

Keywords: Biochar, waste corn husks, EDXRF, XRD, SEM

Introduction

Biochar is produced by thermal decomposition of different biomass under oxygen-limited condition (pyrolysis), and it has received attention in soil remediation and waste disposal in recent years. Biochar can be used in many applications, ranging from heat and power production to soil amendment. Biochar is a carbon product that is generated during pyrolysis of waste biomass in the absence of oxygen or oxygen limited environment. With the interest in using biochar for promoting soil fertility, many scientific studies are being conducted to better understand how this affects the physical and chemical properties of soils and its suitability as a microbial habitat. Since soil organisms provide a myriad of ecosystem services, understanding how adding biochar to soil may affect soil ecology is critical for ensuring that soil quality and the integrity of the soil subsystem are maintained [Cao, X, et al, 2009]. Biochar is one of the major products of biomass pyrolysis in solid form. Biochar is highly resistant to microbial decomposition in soil, its storage in the soil is a promising approach to carbon sequestration. The characteristics of biochar are influenced mainly by the preparation temperature of biomass. Higher pyrolysis temperature often results in the increased surface area and carbonized fraction of biochar leading to high absorption capability for pollutants. Biochar derived from various source materials show different properties of surface area porosity and the number of functional groups which are important concerning on the effect of biochar [Chen, B, et al, 2008, Chen, B, et al, 2011, Chun, Y, 2004]. Biochar has recently been used to remediate soil with both heavy metal and organic pollutant [Glaser, B, 2001]. In addition to its potential for carbon sequestration and decrease greenhouse gas emission from agriculture, biochar is reported to have numerous benefits as a soil amendment, increased plant growth yield, improved water quality, reduced leaching of nutrients, reduced soil acidity, increased water retention and reduced irrigation and fertilizer requirements. Biochar is a stable solid, rich in carbon and can endure in soil for thousands of years [Ippolito, J. A, et al, 2012, Lentz, R. D, et al, 2012]. Biochar carbon species vary in complexity from graphite like carbon to high molecular weight aromatic rings, which are

[1] Demonstrator, Department of Physics, West Yangon University
[2] Demonstrator, Department of Physics, West Yangon University
[3] Associate Professor, Department of Physics, West Yangon University
[4] Associate Professor, Department of Physics, West Yangon University

known to persist in soil for thousands to millions of years [Al-Wabel MI, et al, 2013]. The pyrolysis of biomass to produce biochar has been proposed as a carbon sequestration mechanism to mitigate rising atmospheric carbon dioxide levels which contributes to global climate change. Biochar is a name for charcoal or carbon containing materials when it is used for purposes, especially as energy storage device or a soil amendment like all charcoal, biochar was created by pyrolysis of biomass [Bolan NS, et al, 2013].

Materials and Method

Firstly, the raw corn husks were collected. These corn husks were cut to smaller pieces and then cleaned with fresh water to remove the dust and impurities. These corn husks were dried in sun for three days. The weights of corn husks were measured with electronic digital balance. After that carbonization process using the muffle furnace at three different temperatures, which were 300 °C, 400 °C and 500 °C for 1 h respectively by pyrolysis method. After carbonization, corn husks biochar was obtained. The weights of corn husk biochar were also measured by digital balance. Finally, the prepared biochar was ground into powder by pestle. The obtained corn husk biochar powders were characterized by structural analysis of XRD (X-ray Diffraction). The morphology and microporous structures of biochar were determined by Scanning Electron Microscopy (SEM). The elemental concentrations of corn husk biochar were examined by using EDXRF. The block diagram for experimental procedure of biochar at 300 °C, 400 °C and 500 °C for 1 h were shown in figure 1. Table 1 showed the weight loss and weight loss percentage of corn husk biochar at different temperatures. The step by step preparations of corn husk biochar were showed in figure 2.

Table 1 The weight loss and weight loss percentage of corn husk biochar at different temperatures

Temperature	Initial weight, W_i	Final weight, W_f	Weight loss (%)
300 °C	50 g	14.4 g	71.2 %
400 °C	50 g	11.8 g	76.4 %
500 °C	50 g	8.9 g	82.2 %

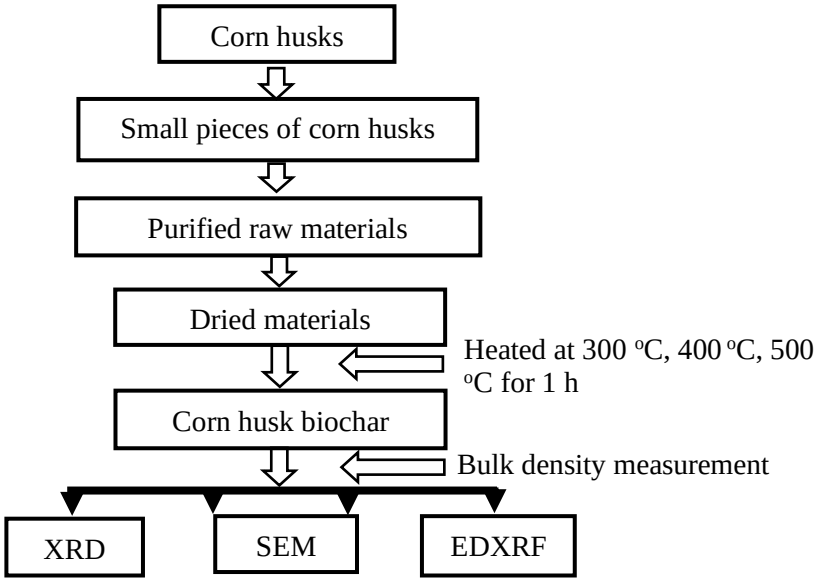

Figure 1 The block diagram for experimental procedure of corn husk biochar at different temperatures

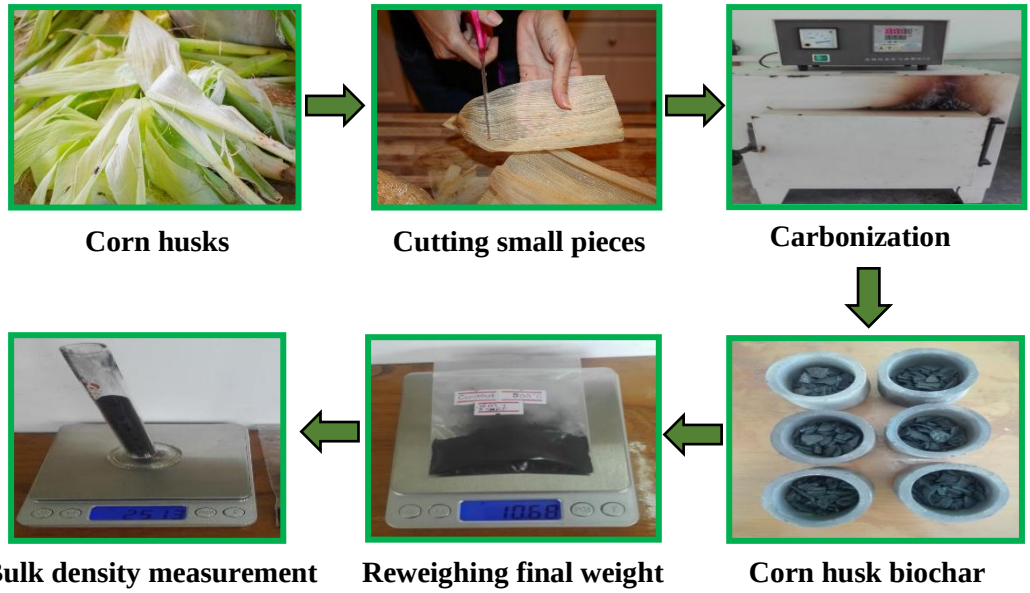

Figure 2 Step by step preparation of corn husks biochar at four different temperatures

Results and Discussion

Bulk Density Measurement

In this research, bulk density was determined for corn husks biochar at different carbonization temperatures. The biochars were crushed and sieved through a mesh to obtain uniform biochar powder. An empty 10 ml graduated measuring cylinder was dried naturally and weighed its mass. It was then filled up to a volume of 10 ml with the biochar. With the filling of every 2 ml, the cylinder was tapped gently a few times to achieve compaction. Table 2 showed the bulk density measurement of corn husks biochar at different temperatures. According to the measurement results, the bulk densities of biochar were increased with increasing temperatures as shown in figure 3.

The bulk density was calculated by $\rho = \frac{m}{V}$,

m = mass of biochar powder

V = volume of biochar powder

Table 2 Bulk density measurement of corn husk biochar at different temperatures

Temperature	Wt of cylinder	Wt of cylinder + sample	Wt of sample	Bulk Density
300 °C	20.93 g	25.14 g	4.21 g	0.421 g/cm^3
400 °C	20.93 g	27.16 g	6.23 g	0.623 g/cm^3
500 °C	20.93 g	27.90 g	6.97 g	0.697 g/cm^3

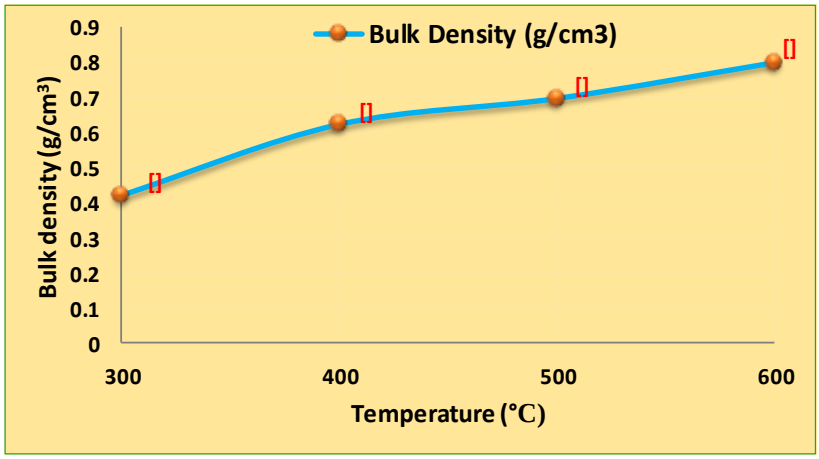

Figure 3 Chart of bulk densities for corn husk biochar at different temperatures

EDXRF Analysis of Corn Husk Biochar

In this research, the samples of corn husks biochar were analyzed by the EDXRF technique. The concentrations of elements contained in the samples were measured by using the SHIMADZU Energy Dispersive X-ray Fluorescence Spectrometer. The EDXRF analysis for all calcinated corn husk biochars was shown in figure 4. According to the result, it was found that the concentrations of elements contained in corn husks biochar at different temperatures were shown in Table 3. From the information of EDXRF measurement results, K, Ca, Si, S, P, Fe are the major elements of weight percent more than 1 percent elements. And then, Mn, Ti, Zn, Cu, Br, Sr and Rb are the minor elements of that constitute 1.0 to 0.01 weight percent.

Table 3 Concentrations of elements contained in corn husks biochar at different temperatures

Elements	Concentrations of elements (%)		
	300°C	400°C	500°C
K	51.141	57.111	52.169
Ca	29.883	23.185	22.073
Si	11.682	12.910	11.979
S	2.334	1.540	ND
P	2.070	2.408	4.688
Fe	1.437	1.719	1.484
Mn	0.856	0.577	0.748
Zn	0.428	0.209	0.221
Ti	ND	0.163	ND
Cu	0.132	0.092	0.081
Br	ND	0.041	0.030
Sr	ND	0.024	0.034
Rb	0.036	0.019	0.023

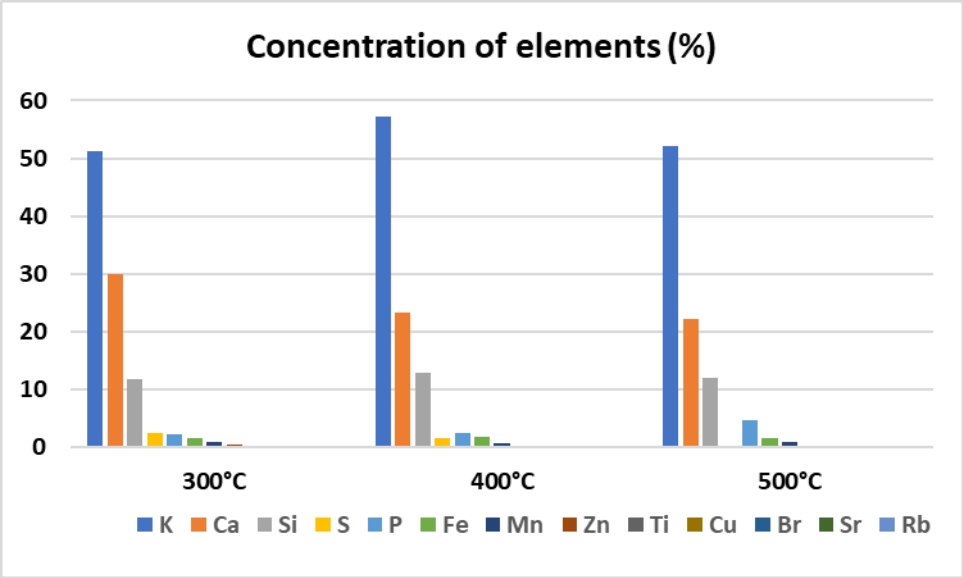

Figure 4 Comparison for elemental concentrations of corn husk biochar

X-ray Diffraction Analysis of Corn Husk Biochar

X-ray diffraction is to determine the structure properties of corn husks biochar using monochromatic Cu K_α radiation (λ = 1.54056 Å) operated at 40 kV (tube voltage) and 40 mA (tube current). Analysis of XRD patterns for corn husks biochar at different temperature values (300 °C, 400 °C and 500 °C) for 1 h were shown in figures (5-7). From XRD results, these corn husks biochar exhibit the dominant diffraction peak located at around 2θ = 20˚ - 30˚ that revealed the presence of amorphous structure which was disorderly stacked up by carbon rings. In general, diffuse and broad bands in XRD patterns characterize the existence of short range order in the carbon structure, while the sharp and narrow peaks confirm to highly crystalline phases with high degree of long-range order. The XRD patterns of the corn husks biochar were characteristic of carbon structures.

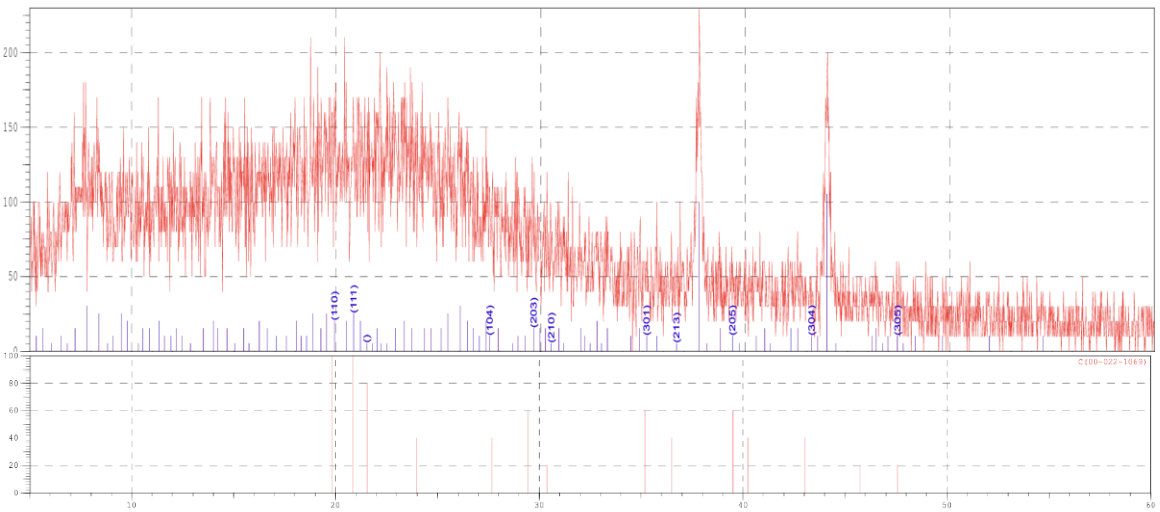

Figure 5 XRD pattern for corn husk biochar at 300 °C

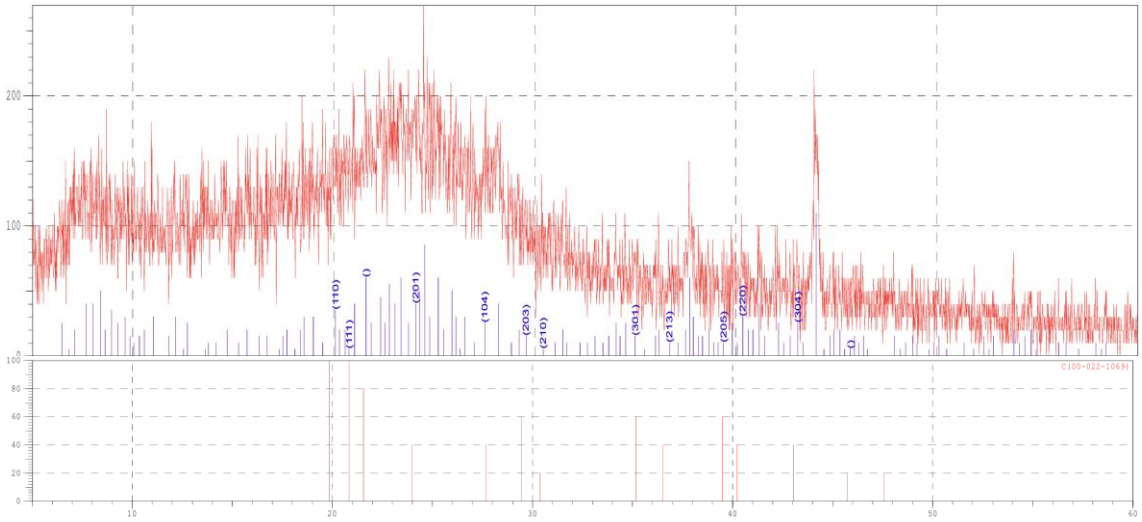

Figure 6 XRD pattern for corn husk biochar at 400 °C

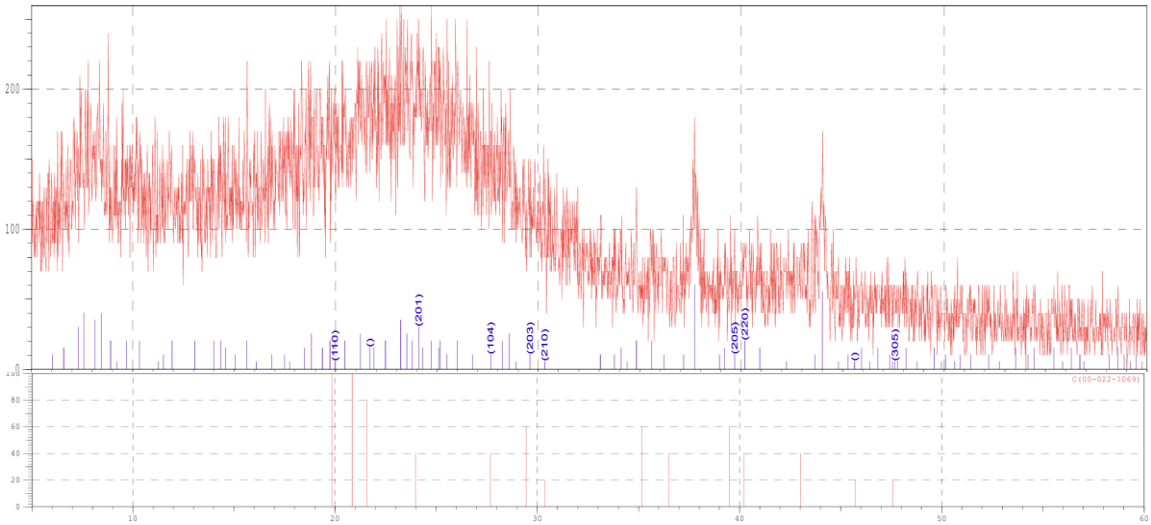

Figure 7 XRD pattern for corn husk biochar at 500 °C

Scanning Electron Microscope (SEM) Analysis of Corn husks Biochar

SEM is one of the most versatile instruments available for the examination and analysis of the microstructure characteristics of a solid. The most important reason for using SEM is high resolution that can be obtained when bulk sample are examined. SEM micrographs for external morphology of corn husks biochar at temperatures 300 °C, 400 °C and 500 °C for 1 h were shown in figure 8(a-c). From SEM analysis as shown in figures, it can be observed that the microstructure of corn husk biochar samples by varying the pore sizes with different temperatures. At 300 °C, the pores of corn husk biochar were uniform, clear and pore distances were also uniform. At 400 °C, the pores looked like tube shape, nonuniform and the natures of pores were disordered. The more uniformly microporous structure was found at 500 °C of corn husk biochar. At 500 °C, the pores distribution was good formation. According to the SEM results, the average pore sizes of corn husk biochars were found to be about 0.52 μm at 300 °C, 1.13 μm at 400 °C, 0.89 μm at 500 °C respectively.

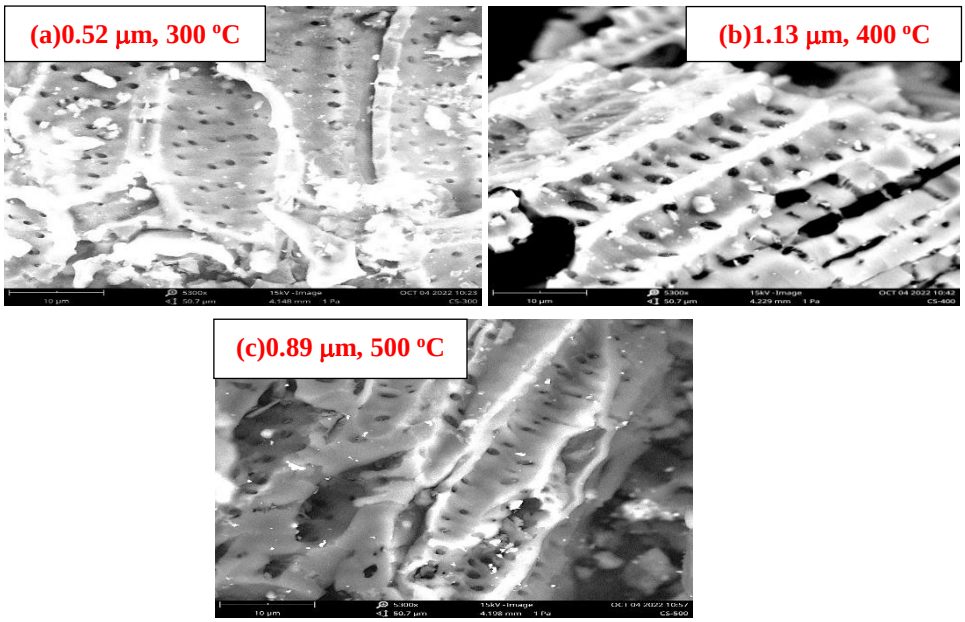

Figure 8 SEM images of corn husks biochar at (a) 300 ºC, (b) 400 ºC, and (c) 500 ºC

Conclusion

In this present work, corn husks were calcined at 300 °C, 400 °C and 500 °C to get the biochar, which can be used in bio-fertilizer for agriculture, activated carbon for supercapacitor application and adsorbent for wastewater treatment. From the physical analysis, it can be observed that the weight loss percentage of corn husk biochar and bulk density were dependent on the calcined temperature. The weight loss percentage and bulk density of biochar increased with increasing calcined temperature. From XRD results, the XRD patterns of the corn husks biochar were characteristics of carbon structures. According to SEM images, the pores of corn husk biochar were great distributions and had a distinguishable pore size which also contributed to their high surface area. From SEM results, these samples have microporous nature and have so many micropores. From the EDXRF results, potassium (K), calcium (Ca), silicon (Si), sulphur (S) and phosphorous (P) are the most concentrated elements. So, the corn husk biochar were free heavy metal pollutants. Corn husk biochar (CHB) is a carbon-rich soil amendment produced by pyrolyzing agricultural corn husk waste, typically at 300-500 °C, resulting in a porous material. It enhances soil quality by improving pH and nutrient levels (K, P, Ca) and promotes plant growth. It also shows potential for heavy metal removal from wastewater and as a promising functional material in energy storage devices.

Acknowledgements

I would like to express my sincere thanks to Professor Dr Maung Maung Shwe, Head of the Department of Physics, West Yangon University for his kind encouragement, valuable suggestions and permission to perform this research.

I also would like to acknowledge to Professor Dr Aye Moe Soe, Professor Dr Thuzar Aung and Professor Dr Yin Yin Thein, Department of Physics, West Yangon University, for their useful advice and discussion to carry out this research.

References

Al-Wabel, M. I., Al-Omran, A., El-Naggar, A. H., Nadeem, M., & Usman, A. R. A. (2013). Pyrolysis temperature induced changes in characteristics and chemical composition of biochar produced from *Conocarpus* wastes. *Bioresource Technology*, *131*, 374–379.

Bolan, N. S., Thangarajan, R., Seshadri, B., Jena, U., Das, K. C., Wang, H., & Naidu, R. (2013). Landfills as a biorefinery to produce biomass and capture biogas. *Bioresource Technology*, *135*, 578–587.

Cao, X., Ma, L., Gao, B., & Harris, W. (2009). Dairy-manure derived biochar effectively sorbs lead and atrazine. *Environmental Science & Technology*, *43*(9), 3285–3291.

Chen, B., Chen, Z., & Lv, S. (2011). A novel magnetic biochar efficiently sorbs organic pollutants and phosphate. *Bioresource Technology*, *102*(2), 716–723.

Chen, B., Zhou, D., & Zhu, L. (2008). Transitional adsorption and partition of nonpolar and polar aromatic contaminants by biochars of pine needles with different pyrolytic temperatures. *Environmental Science & Technology*, *42*(14), 5137–5143.

Chun, Y., Sheng, G., Chiou, C. T., & Xing, B. (2004). Compositions and sorptive properties of crop residue derived chars. *Environmental Science & Technology*, *38*(17), 4649–4655.

Glaser, B., Haumaier, L., Guggenberger, G., & Zech, W. (2001). The 'Terra Preta' phenomenon: A model for sustainable agriculture in the humid tropics. *Naturwissenschaften*, *88*(1), 37–41.

Ippolito, J. A., Laird, D. A., & Busscher, W. J. (2012). Environmental benefits of biochar. *Journal of Environmental Quality*, *41*(4), 967–972.

Lentz, R. D., & Ippolito, J. A. (2012). Biochar and manure affect calcareous soil and corn silage nutrient concentrations and uptake. *Journal of Environmental Quality*, *41*(4), 1033–1043.

Novak, J. M., Lima, I., Xing, B., Gaskin, J. W., Steiner, C., Das, K. C., Ahmedna, M., Rehrah, D., Watts, D. W., Busscher, W. J., Schomberg, H., & Cantrell, K. B. (2009). Characterization of designer biochar produced at different temperatures and their effects on a loamy sand. *Annals of Environmental Science*, *3*(1), 195–206.

Qiu, Y., Zheng, Z., Zhou, Z., & Sheng, G. D. (2009). Effectiveness and mechanisms of dye adsorption on a straw-based biochar. *Bioresource Technology*, *100*(21), 5348–5351.

In-Situ Polymerized Polypyrrole–Activated Carbon Composites and Their Structural Insights for Supercapacitor Potential

Khaing Cho Thet[1], Myo Sandar Lin[2], Zin Min Tun[3] and Cho Cho Thet[4]

Abstract

Activated carbon derived from broom stick (BSAC) was composited with polypyrrole (PPY) via in-situ chemical oxidative polymerization to form a PPY/BSAC composite, which was evaluated as an anode material for supercapacitor applications. The porous structure and enlarged pore size of the composite facilitate efficient ion transport and electrolyte diffusion. Structural characterization was performed using X-ray diffraction (XRD) to assess crystallinity, Fourier transform infrared spectroscopy (FT-IR) to identify functional groups, and scanning electron microscopy (SEM) to examine surface morphology. The average pore sizes of BSAC and PPY/BSAC were found to be 2.52 μm and 0.53 μm, respectively. These results confirm the successful synthesis of a structurally stable PPY/BSAC composite, highlighting its potential for future use in energy storage and adsorption technologies.

Keywords: activated carbon, polypyrrole, chemical activation, polymerization, porous structure, pore size and SEM

Introduction

Supercapacitors (CSs), also known as ultracapacitors or electrochemical capacitors, are advanced energy storage devices that bridge the gap between conventional capacitors and rechargeable batteries. As an energy storage device, supercapacitor to be of great technical potential in power systems owing to its high-power characteristics with acceptable capacity and long cycle life. It classically stores 10 to 100 times more energy per unit volume or mass than electrolytic capacitors, can accept and deliver charge much faster than batteries, and accepts many more charge and discharge cycles than rechargeable batteries. A supercapacitor is an electrochemical energy storage device, which can be used to store and transport charge by reversible adsorption and desorption of ions at the interface between the electrode material and electrolyte. The choice of anode material significantly impacts the energy density, capacitance, and cycling stability of supercapacitors. As a result, SCs are ideal choices for power buffers in applications such as electric transportation systems, automotive, energy recovery/harvesting systems, hybrid battery systems, and electric grids.

Carbon is commonly used as an anode material in supercapacitors because it is versatile and can exist in many different forms. Recently, activated carbon made from waste biomass has gained attention in energy storage research due to its large surface area and porous structure, which help store more energy. Activated carbon is a special material with a highly porous structure, it an excellent adsorbent for gases, liquids, and pollutants. Then, organic compounds are derived from the metabolism of living beings, and their basic structure consists of chains of carbon and hydrogen atoms. Today, the most widely used flexible electrode materials are paper-like carbon-based substances and electronically conducting polymers (ECPs). ECPs are valued for their metal-like conductivity, flexibility, and ease of processing. Among them, polypyrrole (PPY) stands out due to its high specific capacitance, strong electrical conductivity, simple and low-cost synthesis, and good environmental stability. However, using PPY alone has some drawbacks. It lacks mechanical

[1] Daw., Demonstrator, Department of Physics, Pakokku University
[2] Daw, Demonstrator, Department of Physics, University of Myitkyina
[3] Dr., Associate Professor, Department of Physics, West Yangon University
[4] Dr., Professor, Department of Physics, University of Myitkyina

flexibility and tends to degrade over time, which reduces its performance during repeated charging and discharging cycles.

Many types of conducting polymers have been studied for use as electrode materials in supercapacitors because they are easy to make and inexpensive. The most common ones include polypyrrole (PPY), polyaniline (PANi), and polythiophene (PTh). Compared to carbon-based materials, conducting polymers usually have higher electrical conductivity, better capacitance, and similar internal resistance. Among them, PPY is one of the most researched because it conducts electricity well, is stable in the environment, and can be easily made through a process called oxidative polymerization. PPY is made by linking pyrrole molecules (C_4H_5N) into a chain of repeating units $(C_4H_3N)_n$. It has been widely used in supercapacitors, sensors, and environmental cleanup because of its flexible structure and ability to store and release energy efficiently. When polypyrrole is combined with carbon-based materials, the resulting composites often show better electrical performance and stronger structure. This makes them useful for many different applications. However, based on what we know, there is limited research on making PPY and broom stick activated carbon (BSAC) composites using the in-situ chemical oxidative polymerization method through different preparation techniques, especially for use in capacitors. The goal of combining these materials is to create a supercapacitor electrode that is affordable, eco-friendly, and works efficiently.

Experimental Details

Synthesis of Activated Carbon Fibre by Two-Step Chemical Activation Method

In two step method, activated carbon (AC) was firstly prepared and then it was followed by activation process. 15 g of dry broom stick pieces were heated 600 °C and 700 °C for 1 h in Muffle furnace and the biochar was obtained. Then, 6 M of potassium hydroxide (KOH) solution were added to into biochar and stirred for 3 h in order to increase porosity and surface area of activated carbon. After that, AC was centrifuged with 0.4 M of HCL solution and distilled water (DW) for several times until to neutralize the KOH base residue. Finally, AC was heated at 80 ºC until to become the dried activated carbon fiber.

Figure 1 Synthesis process of activated carbon fibers by two-steps chemical activation process

Synthesis of Polypyrrole (PPY) by Chemical Oxidative Polymerization Method

In this method, a pyrrole solution was first prepared, followed by the polymerization process. A total of 100 mL of pyrrole solution was placed in an ice bath, and 230 mL of ferric chloride ($FeCl_3$) solution was slowly added drop by drop. The mixture was stirred continuously for 3 h to allow the formation of PPY as a black precipitate. The resulting product was then washed several times with distilled water using centrifugation to remove any unreacted $FeCl_3$. Afterward, the black PPY precipitate was dried at 100 °C for 2 h. This process yielded fine black polypyrrole powder.

Pyrrole solution | Dropwise $FeCl_3$ solution | Stir for 3 h | Centrifuge process | Drying | Polypyrrole powder

Figure 2 Synthesis photograph of polypyrrole (PPY) by chemical oxidative polymerization process

Synthesis of Polypyrrole (PPY) by Chemical Oxidative Polymerization Method

Firstly, 0.5 g of broom stick activated carbon (BSAC) was mixed with 50 mL of distilled water (DW) and stirred at room temperature for 2 h to create a BSAC suspension. Then, the PPY/BSAC composite was prepared by combining this suspension with PPY in a mass ratio of 0.25:0.5. The mixture was stirred continuously at room temperature for 24 h. Afterward, the product was washed several times with ethanol and DW using centrifugation to remove any impurities. The resulting black PPY/BSAC composite was then dried at 100 °C for 6 h, yielding the final black powder form of the composite.

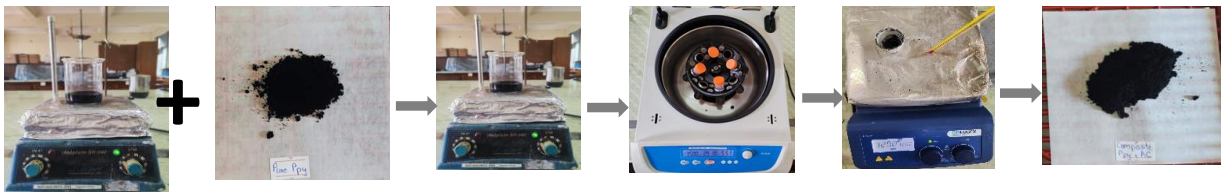

BSAC suspension | 0.25g of PPY | Stir for 24 h | Centrifuge process | Drying | PPY/BSAC composite

Figure 3 Synthesis photograph of PPY/BSAC by *In-situ* chemical oxidative polymerization process

The PPY/BSAC composite, prepared from PPY and broom stick activated carbon (BSAC), was analyzed using several characterization techniques. These included Fourier-transform infrared spectroscopy (FT-IR), X-ray diffraction (XRD), and scanning electron microscopy (SEM). FT-IR was used to identify the different functional groups present on the surface of the samples. XRD patterns were recorded using a LabX XRD-6100 (Shimadzu) to determine the semi-crystalline structure of the composite. SEM images revealed the presence of both micro- and mesopores in the PPY/BSAC composite.

Results and Discussion

Figure 4(a), (b) and (c) shows the FT-IR analysis used to identify the functional groups in BSAC, PPY, and the PPY/BSAC composite. For BSAC, peaks at 2668 and 3157.85 cm^{-1} indicate O–H stretching, showing the presence of hydroxyl groups. Other peaks at 1223.8, 1368.2, and 1554.82 cm^{-1} are related to C=O stretching, C–H bending, and C=C stretching, which help identify the organic materials in the biomass. In pure PPY, peaks at 1546 and 1471.49 cm^{-1} represent C=C stretching in the pyrrole ring and C–N bending. Additional peaks at 892.57, 1036.90, 1165.75, and 1296.75 cm^{-1} show C=C bending, C–H bending, and C–N stretching. In the PPY/BSAC composite, peaks at 3143.20 and 1562.45 cm^{-1} indicate O–H and C=C stretching. Other peaks at 787.60, 927.45, 1043.73, and 1197.08 cm^{-1} show C=H bending, C=C bending, C–H bending, and C–O stretching. The slight shift in PPY peaks in the composite suggests a π–π interaction between PPY and the carbon surface. This confirms that the PPY/BSAC composite was successfully formed with stable structure.

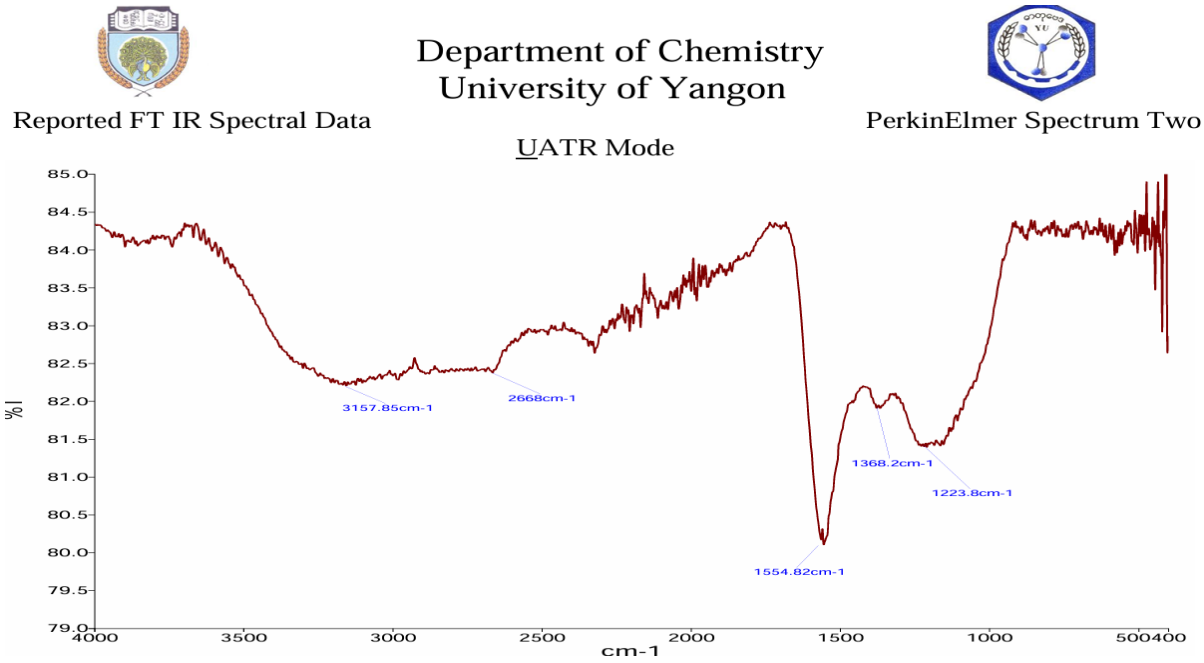

Figure 4 (a) FTIR spectrum of AC carbonized at 600 °C

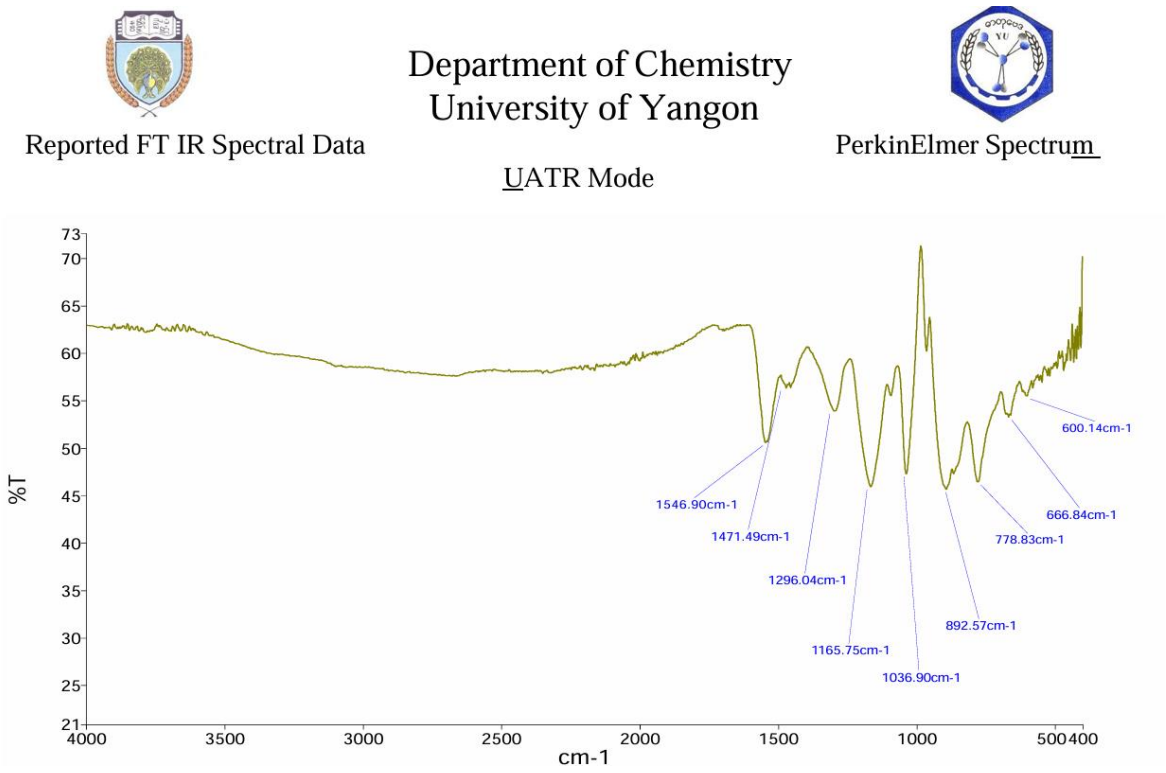

Figure 4 (b) FTIR spectrum of polypyrrole (PPY)

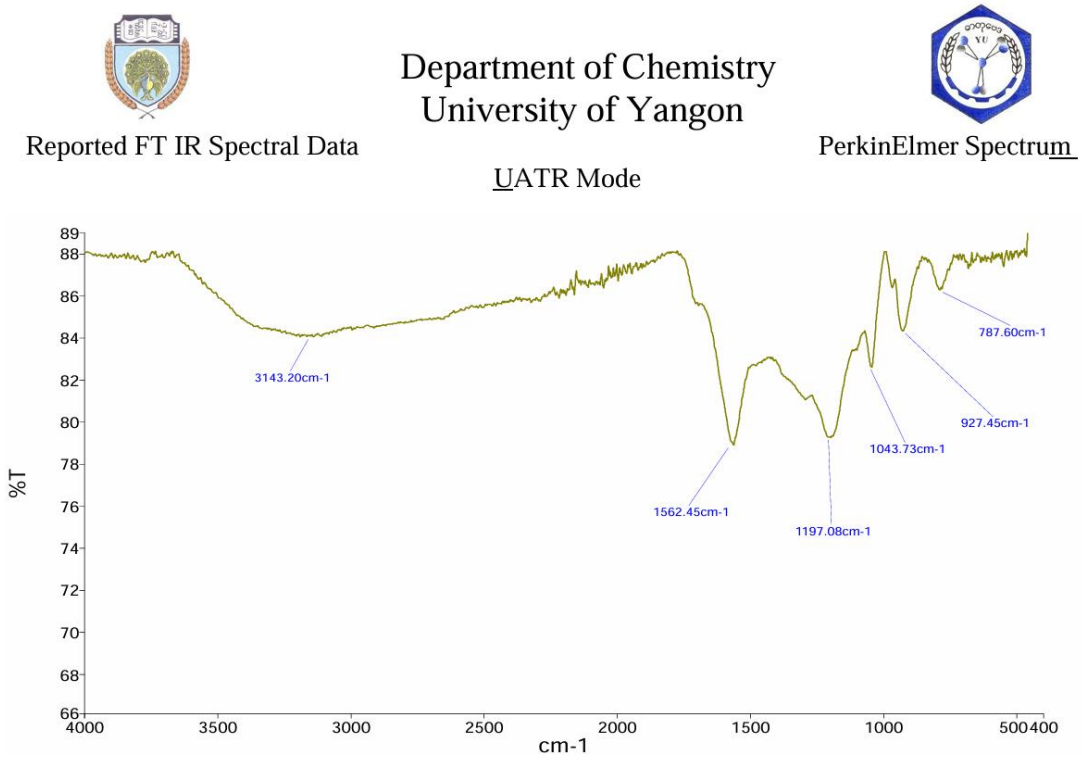

Figure 4 (c) FTIR spectrum of PPY/BSAC composite

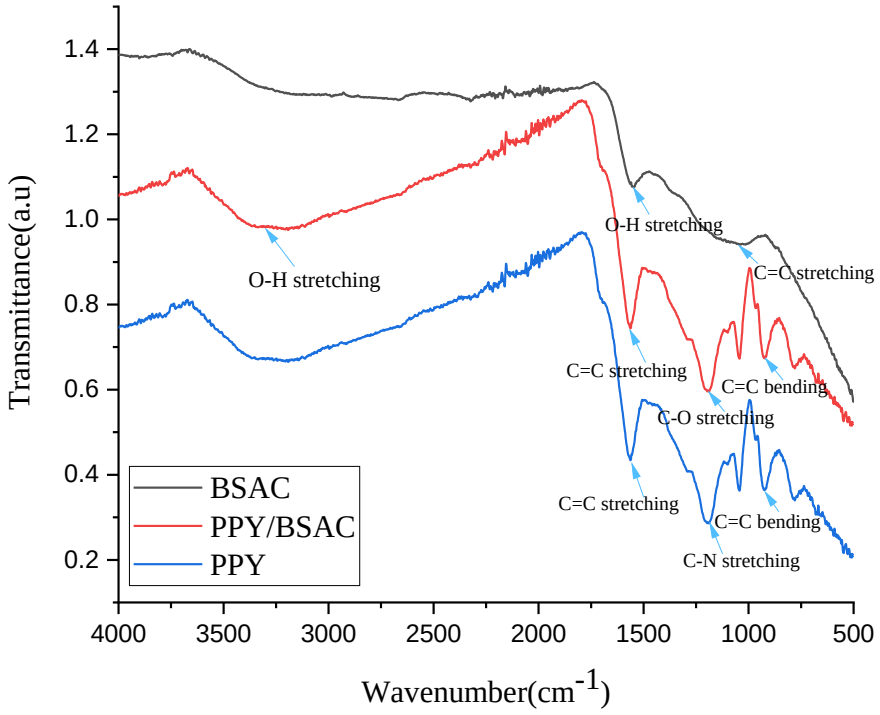

Figure 5 Compare FT-IR spectrum of BSAC, PPY and PPY/BSAC composite

Table 1: FTIR vibrational modes assigned to various functional groups in BSAC, PPY and PPY/BSAC

Functional Group Summary Table					
BSAC		Polypyrrole (PPY)		PPY/BSAC composite	
Wave number (cm^{-1})	Functional Groups	Wave number (cm^{-1})	Functional Groups	Wave number (cm^{-1})	Functional Groups
3157.85	O-H stretching	1546.90	C=C stretching	3143.20	O-H stretching
2668	O-H stretching	1471.49	C-N bending	1562.45	C=C stretching
1554.82	C=C stretching	1296.75	C-N stretching	1197.08	C-O stretching
1368.2	C-H bending	1165.75	C-N stretching	1043.73	C-H bending
1223.8	C=O stretching	1036.90	C-H bending	927.45	C=C bending
		892.57	C=C bending	787.60	C=H bending

The XRD results showed several main peaks, although some were not clearly identified. For BSAC, a broad peak between 20° and 25° indicates the presence of stacked aromatic layers, which is typical for activated carbon. In the case of pure PPY, two peaks appeared at around 25° and 44°, showing its semi-crystalline nature. A weak peak near 38°–40° might be due to changes in structure or leftover $FeCl_3$ from the synthesis process. The crystallite sizes of PPY, calculated using the Scherrer equation, were 48.6 nm, 46.3 nm, and 69.8 nm. For the PPY/BSAC composite, the XRD pattern showed both the amorphous structure of BSAC and the semi-crystalline peaks of PPY. Some peak intensities decreased slightly, while one peak became stronger compared to pure PPY. The crystallite sizes of the composite were 47.8 nm, 46.1 nm, and 85.7 nm. These results confirm that the PPY/BSAC composite was successfully formed and suggest a strong interaction between PPY and BSAC.

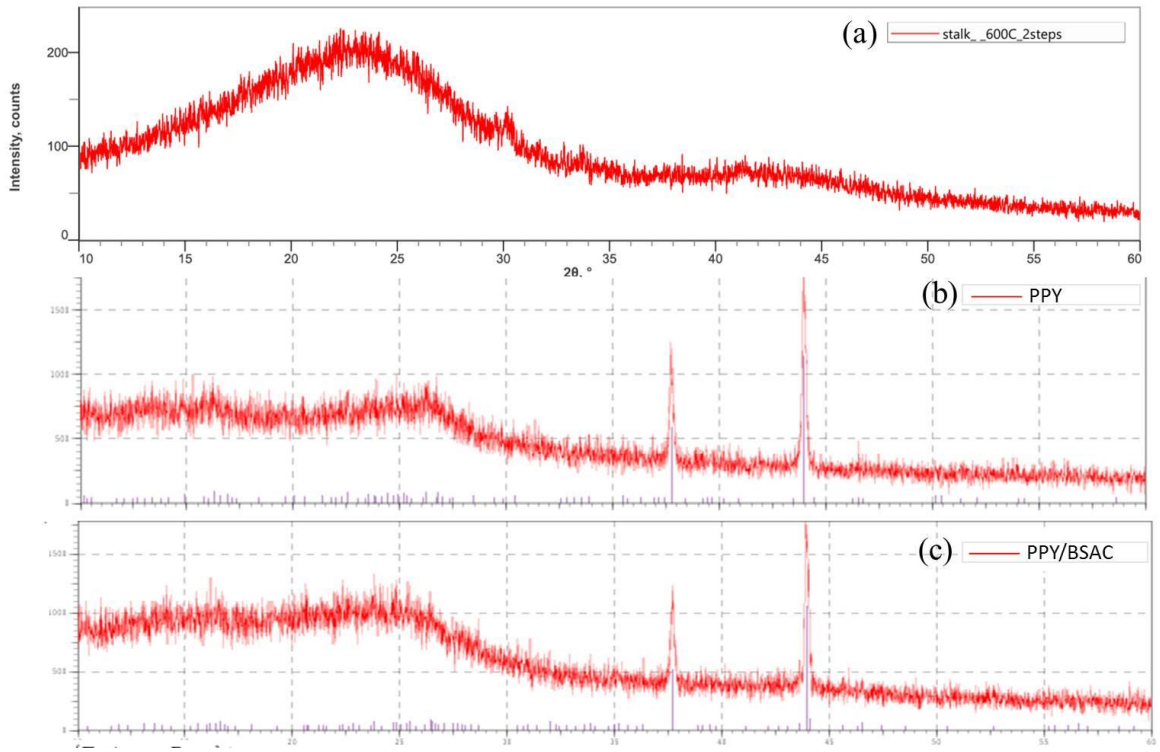

Figure 6. XRD spectrum of (a) BSAC, (b) PPY and (c) PPY/BSAC composite

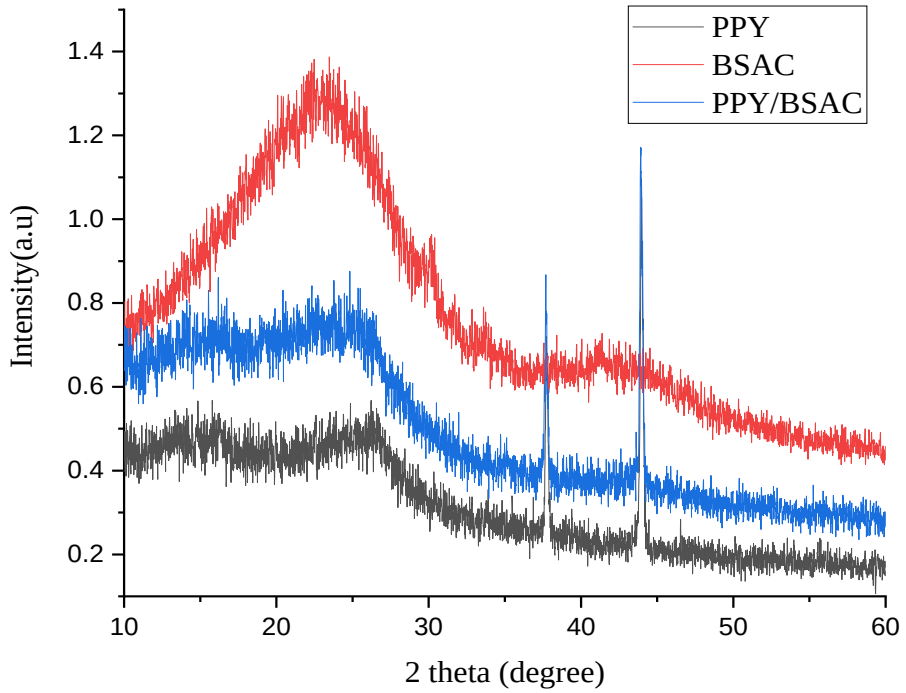

Figure 7 Compared XRD spectra of BSAC, Pure PPY and PPY/BSAC composite

The SEM image of BSAC clearly shows a porous, fibrous structure, which was developed through KOH activation that etched the surface and created numerous pores . The fibers appear well-aligned and oriented in one direction, which may help provide efficient pathways for electron transport. In contrast, the surface of pure PPY displays an irregular, sponge-like texture. This powdery structure suggests a relatively high surface area, which is beneficial for ion movement when used as an electrode material. The SEM image of the PPY/BSAC composite shows a noticeable change in surface morphology. The activated carbon appears to be coated with a thin layer of PPY, indicating that the polymer has successfully adhered to the BSAC surface. This embedded structure suggests a strong interaction between the PPY and the carbon material. Using ImageJ software, the average pore sizes were measured to be 2.52 μm for BSAC and 0.35 μm for the PPY/BSAC composite, as shown in Table 2. The reduction in pore size after composite formation confirms the successful incorporation of PPY into the porous structure of BSAC. This results in a more compact and interconnected network, which can enhance charge transfer and improve the electrical conductivity and electrochemical performance of the composite for supercapacitor applications.

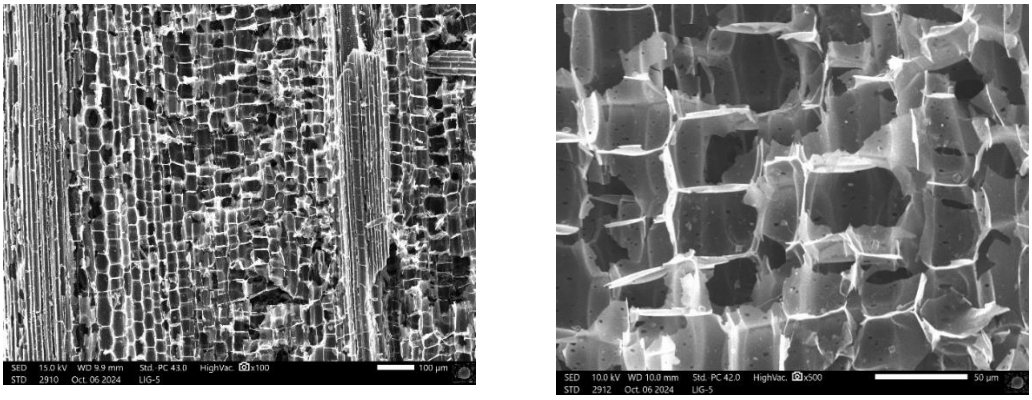

Figure 7 Different magnification of SEM image of broom stick at the carbonization temperature 600 ºC

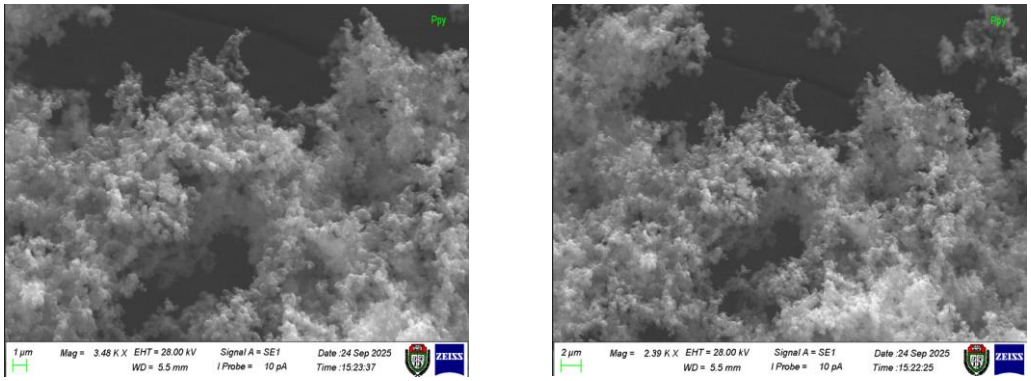

Figure 8 Different magnification of SEM images of pure PPY

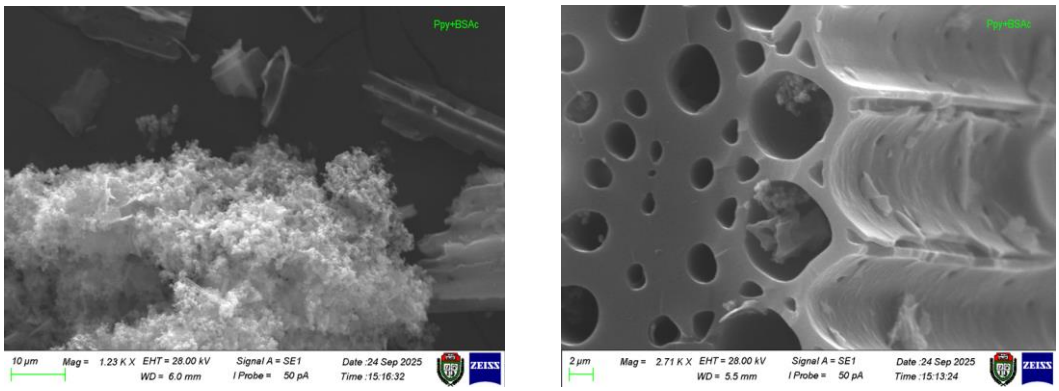

Figure 9 Different magnification of SEM images of PPY/BSAC composite

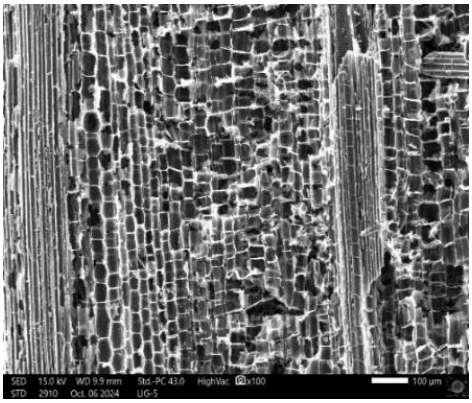

(a)

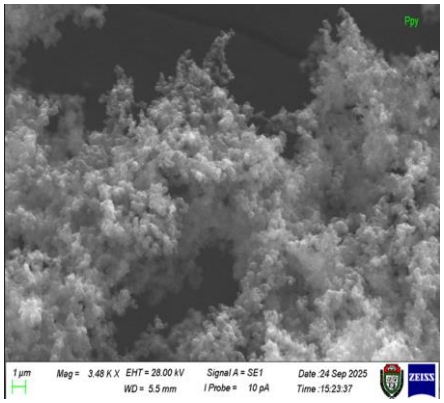

(b)

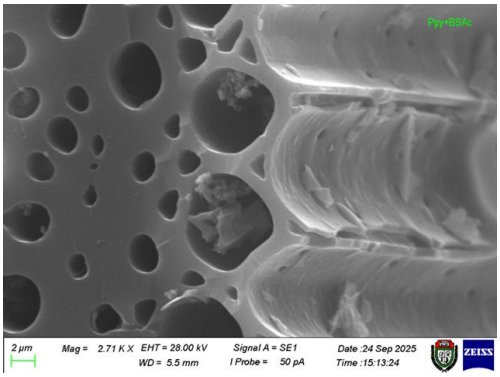

(c)

Figure 10 Compare SEM image of (a) BSAC, (b) Pure PPY and (c) PPY/BSAC composite

Table 2: Compare pore size of BSAC and PPY/BSAC

Materials	Pore Size (µm)	Remarks
BSAC	**2.52**	**Macropore**
PPY/BSAC	**0.35**	**Macropore**

Conclusion

In this study, a PPY/BSAC composite was successfully synthesized using the in-situ chemical oxidative polymerization method. Structural analysis through XRD confirmed the presence of an amorphous carbon matrix from BSAC, along with semi-crystalline features attributed to the partial alignment of PPY chains. FT-IR analysis verified the formation of the composite by identifying characteristic functional groups from both components. SEM imaging revealed a porous, fibrous morphology in BSAC, which was retained and enhanced in the composite, with PPY uniformly coating the carbon surface. The reduction in average pore size from 2.52 µm in BSAC to 0.35 µm in the PPY/BSAC composite indicates successful integration of PPY into the carbon framework, resulting in a denser and more interconnected structure. This morphological transformation is expected to facilitate

improved ion transport and charge storage, making the PPY/BSAC composite a promising candidate for high-performance supercapacitor electrode applications.

Acknowledgement

We would like to acknowledge to Prof Dr Tin Htun Aung, Rector, Pakokku University, for his encouragement and allowing us to participate in this event. Our special thanks go to Dr Khin Khin Htoot, Pro-rectors, Pakokku University, for their kind permission to contribute this work. We would like to express sincere thanks to Dr Khin Htwe, Professor, Head of Department of Physics, Pakokku University, for her kind permission to carry out this paper.

References

P. Forouzandeh, V. Kumaravel, and S. C. Pillai, "Electrode materials for supercapacitors: A review of recent advances," *Catalysts*, vol. 10, no. 9, pp. 1–73, 2020, doi: 10.3390/catal10090969.

M. E. Şahin, F. Blaabjerg, and A. Sangwongwanich, "A Comprehensive Review on Supercapacitor Applications and Developments," *Energies*, vol. 15, no. 3, pp. 1–26, 2022, doi: 10.3390/en15030674.

S. Dong *et al.*, "Dielectric-electrolyte supercapacitors," *Cell Reports Phys. Sci.*, vol. 4, no. 2, p. 101284, 2023, doi: 10.1016/j.xcrp.2023.101284.

P. Rajivgandhi, V. Thirumal, A. Sekar, and J. Kim, "Biomass-Derived Activated Porous Carbon from Foxtail Millet Husk to Utilizing High-Performance Symmetric Supercapacitor Applications," pp. 1–18, 2025.

M. Hu *et al.*, "Towards understanding the chemical reactions between KOH and oxygen-containing groups during KOH-catalyzed pyrolysis of biomass," *Energy*, vol. 245, pp. 1–28, 2022, doi: 10.1016/j.energy.2022.123286.

L. Xu, "Design and synthesis of graphene / activated carbon / polypyrrole fl exible supercapacitor," pp. 31342–31351, 2017, doi: 10.1039/c7ra04566b.

Z. S. Iro, C. Subramani, and S. S. Dash, "A Brief Review on Electrode Materials for Supercapacitor," *Int. J. Electrochem. Sci.*, vol. 11, no. 12, pp. 10628–10643, 2016, doi: 10.20964/2016.12.50.

J. Stejskal and R. G. Gilbert, "POLYANILINE . PREPARATION OF A CONDUCTING POLYMER (IUPAC Technical Report) Polyaniline . Preparation of a conducting polymer (IUPAC Technical Report)," vol. 74, no. 5, pp. 857–867, 2006.

K. Ramanathan, M. A. Bangar, M. Yun, W. Chen, N. V Myung, and A. Mulchandani, "Bioaffinity Sensing Using Biologically Functionalized Conducting-Polymer Nanowire," pp. 496–497, 2005.

P. Feng, J. Li, H. Wang, and Z. Xu, "Biomass-Based Activated Carbon and Activators : Preparation of Activated Carbon from Corncob by Chemical Activation with Biomass Pyrolysis Liquids," 2020, doi: 10.1021/acsomega.0c03494.

E. Zhang, W. Liu, X. Liu, Z. Zhao, and Y. Yang, "Pulse electrochemical synthesis of polypyrrole/graphene oxide@graphene aerogel for high-performance supercapacitor," pp. 11966–11970, 2020, doi: 10.1039/d0ra01181a.

K. Z. Setshedi, L. Kalombo, N. Nomadolo, L. Hlekelele, S. S. Ray, and A. Maity, "Polypyrrole Modified Granular Activated Carbon Nanocomposite for Treatment of Wastewater Containing Highly Toxic Hexavalent Chromium," vol. 2300392, pp. 1–14, 2024, doi: 10.1002/mame.202300392.

M. Sevilla and A. B. Fuertes, "The production of carbon materials by hydrothermal carbonization of cellulose," *Carbon N. Y.*, vol. 47, no. 9, pp. 2281–2289, 2009, doi: 10.1016/j.carbon.2009.04.026.

P. Simon, Y. Gogotsi, P. Simon, Y. Gogotsi, and N. Materials, "Materials for electrochemical capacitors To cite this version : HAL Id : hal-02417326," vol. 7, no. 11, pp. 845–854, 2019.

G. A. Snook, P. Kao, and A. S. Best, "Conducting-polymer-based supercapacitor devices and electrodes," *J. Power Sources*, vol. 196, no. 1, pp. 1–12, 2011, doi: 10.1016/j.jpowsour.2010.06.084.

H. An, Y. Wang, X. Wang, L. Zheng, and X. Wang, "Polypyrrole / carbon aerogel composite materials for supercapacitor," *J. Power Sources*, vol. 195, no. 19, pp. 6964–6969, 2010, doi: 10.1016/j.jpowsour.2010.04.074.

Wearable Obstacle Detection System Using Arduino Nano And Ultrasonic Sensor

Kay Zin Win[1], Phyu Thel Ei[2], Thazin Hlaing [3], Wint Wah Soe[4],Thet Mar Oo[5]

Abstract

This research paper presents the design, development and implementation of a cost-effective and efficient wearable obstacle detection system for enhancing personal mobility and safety, particularly for the visually impaired people. This system involves the fundamental components such as Arduino Nano, buzzer and interfaced with a HC-SR04 Ultrasonic sensor to detect obstacles within a limit range. The sensor emits ultrasonic waves and calculates the distance of the objects based on the echo. When an obstacle is detected within a limit distance range, the system activates an audible buzzer to alert the user. The device effectively identifies obstacles in the user's forward path, providing crucial reaction time to prevent collisions. The work confirms the viability of simple, open-source hardware in creating technology, offering a significant improvement in autonomous navigation. The system is a foundational step towards more advanced wearable aids, with future recommendations for integration of GPS, multiple sensors for improved field coverage and connectivity features. In Myanmar, some of the elderly persons are suffering diseases such as the blurred vision and the silent thief of sight. This project will help for their daily lives and it is easy to use for the elderly persons especially.

Keywords: Arduino Nano, HC-SR04 Ultrasonic sensor, buzzer, wearable aids

Introduction

In an increasingly dynamic and often visually demanding world, the ability to perceive and navigate around obstacle is fundamental to safety and independence. For individuals with visual impairments, the elderly or those operating in low-visibility environments, traditional mobility aids like white canes have limitations in detecting overhead or protruding obstacles beyond immediate ground contact. This paper presents the design and implementation of a compact, affordable and efficient wearable obstacle detection system. The core objective of this system is to augment spatial awareness by providing real-time, proximal feedback about nearby objects within a defined range. The system is built around the Arduino Nano and paired with a HC-SR04 ultrasonic sensor, which emits high-frequency sound waves to accurately measure distance. The wearable form factor is achieved by integrating with an audible buzzer. As the user approaches an obstacle, the system gives the beep to the user without relying on vision. Ultimately, this project underscores the potential of embedded systems to create impactful, human-centered solutions that promote greater autonomy and safety. This system can be described with the help of following block diagram in figure 1.

Figure 1. The block diagram of the whole system

[1,2,3,4,5] Demonstrators, Department of Physics, East Yangon University

Methodology of the System

To create the wearable obstacle detection project, the entire system consists of essential components, including an Arduino Nano board, HC-SR 04 Ultrasonic sensor, buzzer, glasses and a power source.

Hardware and Software Requirements of Circuit Construction

Arduino Nano

Arduino Nano is a microcontroller board based on the Atmega 328P. It has 22 digital input/output pins, 8 analog inputs, a 16 MHz (on Nano board) through IC supports 20 MHz maximum at 5 volts, a Mini-USB type B connection and a reset button. “Arduino” name came from a bar in Ivera which is located in Italy. Arduino board is easy to use and freely available in market. It also has a function that every user can develop without any problem. Figure 2 suggests the photo of Arduino board.

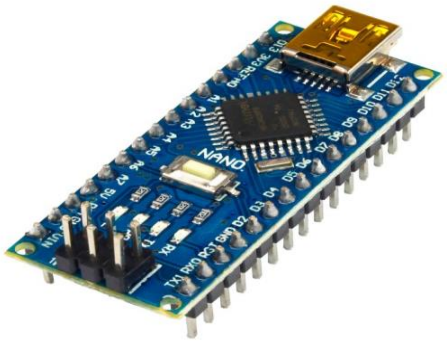

Figure 2. The photo of Arduino board

HC-SR04 Ultrasonic Sensor

The HC-SR04 is a popular, low-cost ultrasonic sensor for measuring distance using the sound waves. The HC-SR04 modules includes an ultrasonic transmitter, a receiver, and a control circuit. It emits a high-frequency sound wave and receives the echo reflected from a target object. The distance is calculated based on the time interval between sending the wave and receiving the echo. The photo of HC-SR04 module is shown in figure 3.

Figure 3. The photo of HC-SR04 module

Buzzer

A buzzer or beeper is an audio signaling device, which may be mechanical, electromechanical or piezoelectric. Typical uses of buzzers and beepers include alarm

devices, timers, train and confirmation of user input such as a mouse click or keystroke. The photograph of buzzer is shown in figure 4.

Figure 4. The photograph of buzzer

Glasses

Glasses are wearable vision aids with lenses in a frame, used to correct sight problems and sun glasses are used to protect sunlight and UV rays. In this project, sun glasses is used as a vision aids. The photograph of sun glasses is illustrated in figure 5.

Figure 5. The photograph of sun glasses

Arduino Integrated Development Environment (IDE) Software

The software exploited in this project is the Arduino Integrated Development Environment (IDE), a comprehensive platform that facilitates the programming and uploading of code to the Arduino microcontroller. The Arduino IDE software is essential for creating, editing, and managing the code that governs the behavior of the Arduino board. The photograph of uploading a program to Arduino IDE software is shown in figure 6.

Figure 6. The photograph of uploading a program to Arduino IDE software

Design and Construction of the System

Firstly, collect the necessary components. The components which are contained in the project are as given below figure 7. Then the glasses are equipped with ultrasonic sensor, typically mounted on the frame and the Arduino Nano, buzzer and the power supply respectively. The sensor continuously emits ultrasonic waves and measure the time it takes for the waves to bounce back after hitting obstacles in the user's path. This data is crucial for detecting obstacles and determining their distance from the user. The photograph of the uploading program to Arduino Nano is as shown in figure 8. For the connection of the HC-SR04's VCC and GND were connected to the Arduino's 5V and GND pins. The trigger and echo pins were connected to D8 and D9 pins. The positive terminal of the buzzer was connected to digital pin D10 and negative terminal was connected to the GND pin of the HC-SR04 ultrasonic sensor. And make the connection of power supply. The step-by-step construction of the wearable obstacle detection system is explained with the photo as shown in figure 9.

Figure 7. The photograph of the components

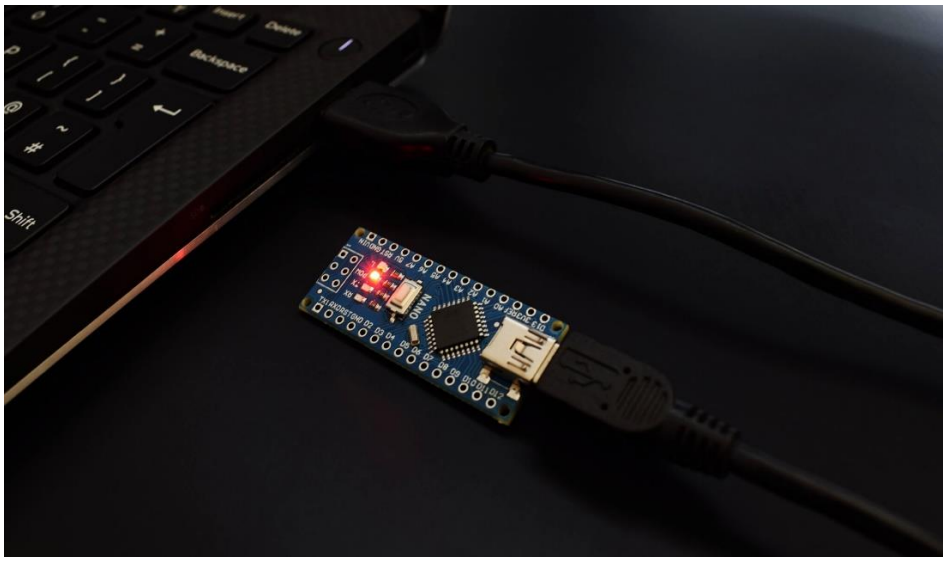

Figure 8. The photograph of uploading program to Arduino Nano

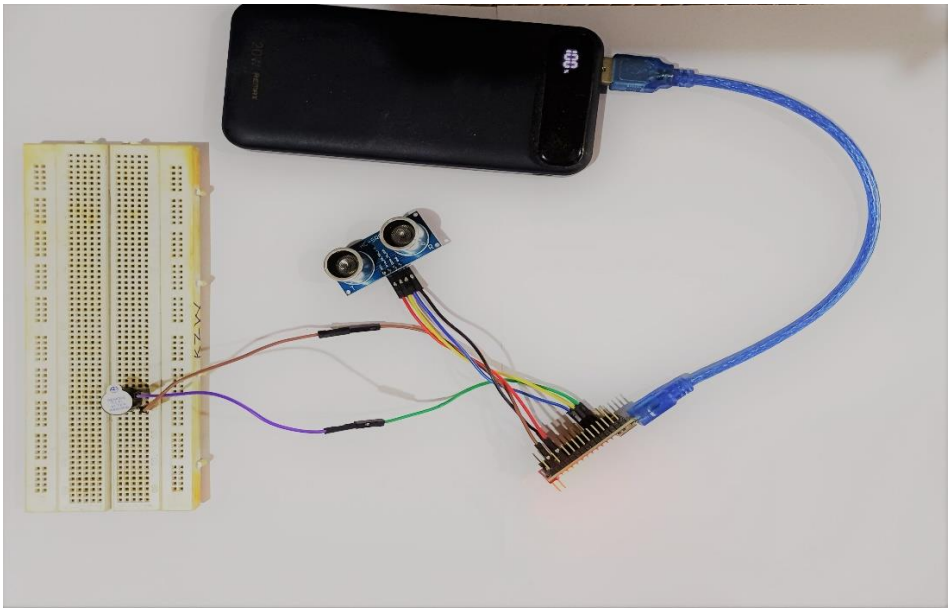

Figure 9. The photograph of step-by-step construction on breadboard

The wearable detection system is assembled correctly and the Arduino, ultrasonic sensor and buzzer are connected according to the hardware construction steps provided earlier. Then double-check all wiring to ensure that there are no loose connections or short circuits. Insulate exposed wires to prevent unintended contacts. Then upload the Arduino code to the Arduino board using the Arduino IDE and a USB cable. The whole circuit diagram is as shown in figure 10. After finishing all these steps, make a connection with the power supply and the Arduino Nano. To establish a communication link between an Arduino Nano, a HC-SR04 sensor module and buzzer, follow these wiring instructions. Connect the VCC pin of the HC-SR04 to the 5V pin on the Arduino, ensuring that the sensor module receives the required power. Next, establish a common ground by connecting the GND pin of the HC-SR04 to the GND pin on the Arduino. The photograph of the whole circuit connection system with the power bank is as shown in figure 11. The photograph of the whole system connected with 9V battery is illustrated in figure 12.

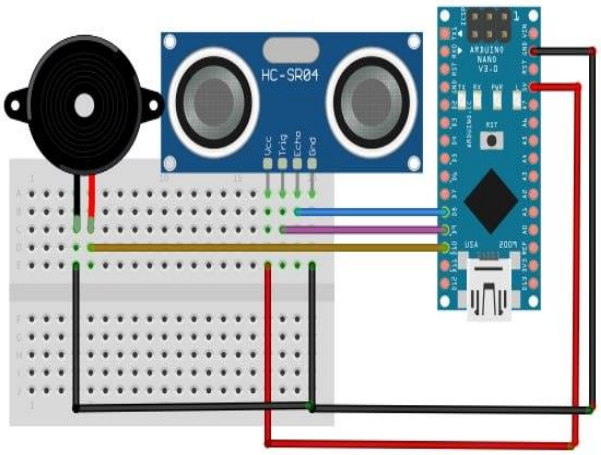

Figure 10. The circuit diagram of the whole system

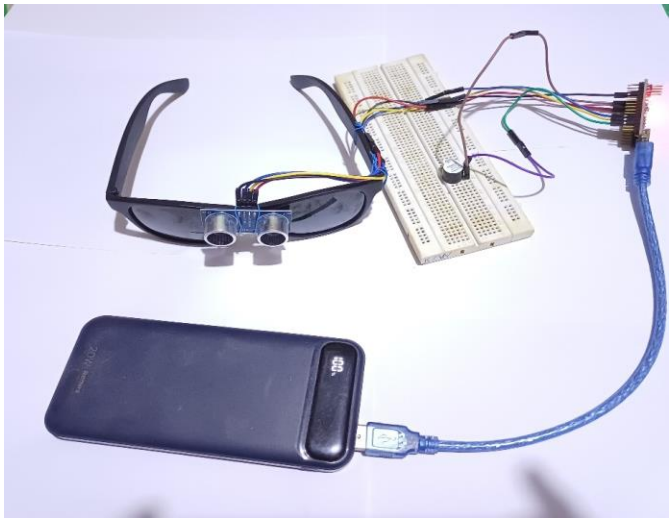

Figure 11. The photograph of the whole circuit connection system with the power bank

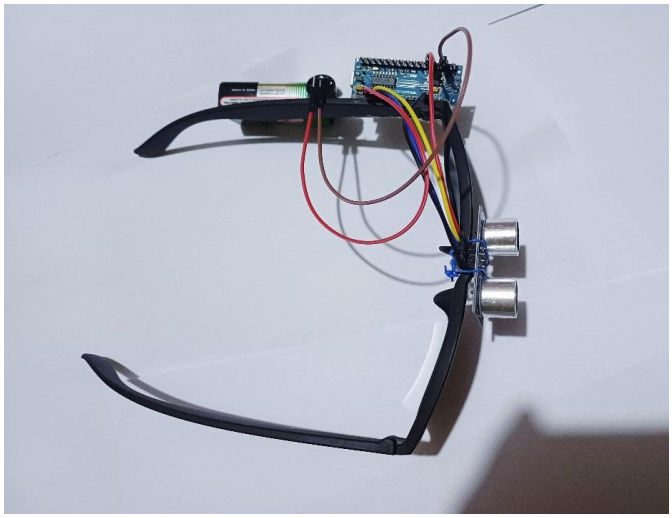

Figure 12. The photograph of the whole system connected with 9V battery

Results and Discussion

This project was successfully established, as confirmed by the result, it was also tested in common real-world scenarios (approaching walls, furniture and moving persons) to assess practical reliability and latency. In this project, the development of a wearable assistive device designed to detect obstacles for the visually impaired people. This project is a quintessential example of using basic electronics to solve a real-world problem. In this project, the distance between the ultrasonic sensor and the obstacle is about 50 cm. If the obstacle is located at within 50 cm, the buzzer is alerted. In Myanmar, some of the elderly persons are suffering diseases such as the blurred vision and the silent thief of sight. This project will help for their daily lives and it is easy to use for the elderly persons especially.

This project with the entire process from concept to a functional prototype, highlighting both the practical utility for assistive technology involved. It serves as a strong foundation for more advanced systems involving IoT, AI and multi-sensor data fusion. In the future, there is potential to further improve the device by adding new features such as directional and warning messages to prevent accidents. Additionally, the design of the device could be further developed to make it lighter and more comfortable for the user to wear.

Figure 13 is showed the photograph of the close-up position of the whole circuit. The left side and right side views of the whole circuit are as shown in figure 14 and 15.

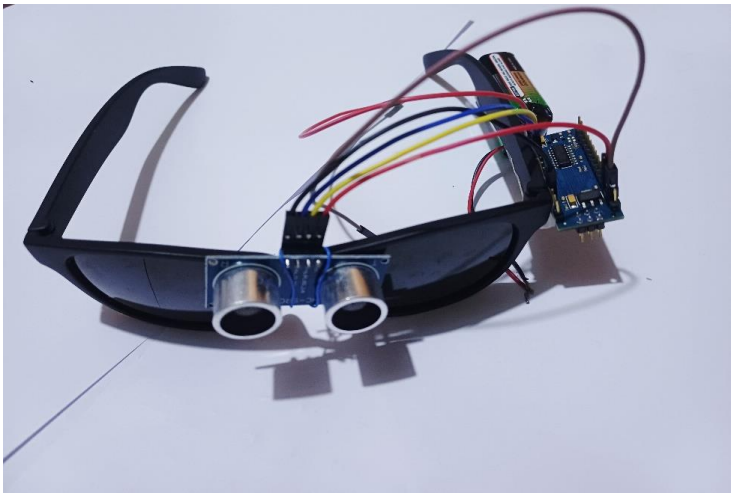

Figure 13. The photograph of the close-up position of the whole circuit

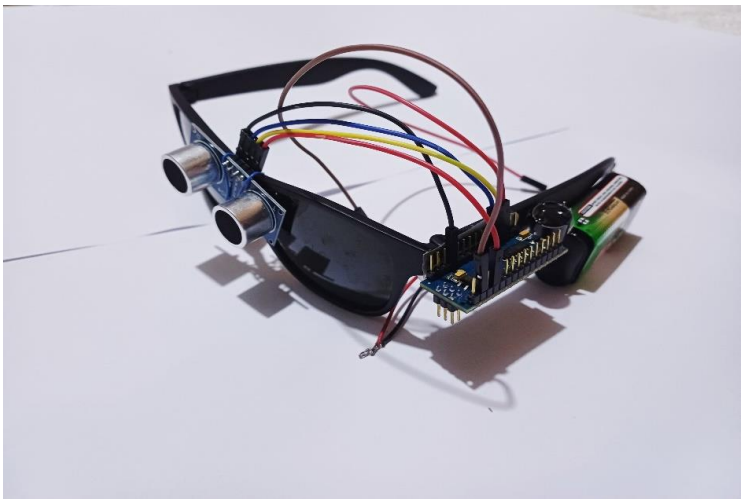

Figure 14. The left side view of the whole circuit

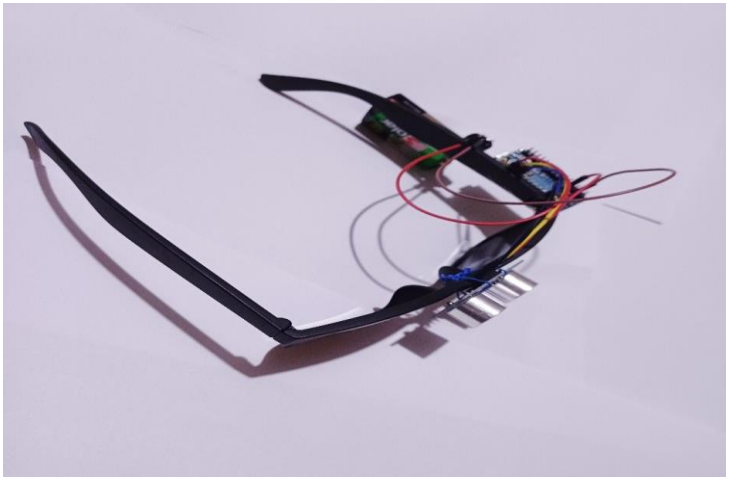

Figure 15. The right side view of the whole circuit

Conclusion

The most of the visually impaired person in the world with everyday difficulties such as navigating their work area and operating equipment without the assistance of visual aids. It could be concluded that the Arduino-powered assistive eyewear for blind persons would significantly enhance the overall navigation. The aim of the project is to create a device that is useful for visually impaired individuals, allowing them to navigate their surroundings with greater confidence and independence. The device consists of a wearable glass that uses ultrasonic waves to detect nearby obstacles and notifies the user with a buzzing sound. This allows users to move around freely and avoid obstacles. It is a very useful of embedded systems and sensor technology. The device was not difficult to use, providing effective and reliable assistance in their daily lives. The project facilitated easy verification of environmental obstacles, ensuring accuracy and efficiency.

Acknowledgements

We would like to express our gratitude to Acting Rector Dr Myo Min Tun, East Yangon University, for his permission to work this research. We would like to thank Pro-rectors Dr Aye Aye Ko and Dr Thida Aung, East Yangon University, for their permissions to work on the present research. We are greatly indebted to Professor Dr Khin Lay Nwe, Head of Department of Physics, East Yangon University, who provides with generous help and kind permission in this research paper. We would like to thank to Professor Dr Nilar Tun, Department of Physics, East Yangon University, for her help and encouragement to complete our project. We are also deeply grateful to Professor Dr Yee Yee Oo, Department of Physics, East Yangon University, for her help and guidance in this research work. We would like to express our sincere gratitude and appreciation to all those who have contributed to the completion of this project.

References

A. Kanal. and P.S. Chavan, “An Affordable Hand Glove for The Blind Using Ultrasonic Sensors,”International Journal of Innovative Research in Computer and Communication Engineering, Volume.5,2017.

Bai, J., & Lian, S., & Liu,& Wang, K., and Liu,D.(2017).”Smart Guiding Glasses for Visually Impaired People in Indoor Environment”.IEEE Transactions on Consumer Electronics, 63 (3), 258-266.

Chinese Author “An Intelligent Auxiliary System Blind Glasses”, CN 106937909A,11th July,2017.

D.E.Gbenga, A.I. Shani and A.L. Adekunle, “Smart Walking Stick for Visually Impaired People Using Ultrasonic Sensors and Arduino”,in International Journal of Engineering and Technology[IJET],Volume.9,No.5 Oct-Nov 2017

https://en.wikipedia.org/wiki/Arduino_Nano

Fabrication and Characterization of Titania Nanoparticles and Thin Films

Ngu Wah Hlaing[1], Shine Ko Ko[2]

Abstract

TTIP (Titanium tetra isopropoxide) and 2-Methoxy Ethanol ($CH_3OCH_2CH_2OH$) with the weight percent of 1:2 was used as the starting materials for Titania Nanoparticles and thin films. Titania Nanoparticles were investigated by Sol-Gel and calcinations process. The calcinations temperatures of 400 °C, 500 °C and 600 °C (about one hour) were used for the crystallization of the Titania Nanoparticles. Titania thin films were performed on the non-electrolytic glass substrates by spin coating method with the same precursor at 400 °C, 500 °C. The crystallized sizes and morphology of Titania Nanoparticles and thin films were also analyzed with X-Ray Diffraction (XRD), Fourier Transform Infrared Spectroscopy (FTIR) and Scanning Electron Microscopy (SEM).

Keywords: Titania Nanoparticles, Sol- Gel, Spin Coating, XRD, FTIR and SEM

Introduction

Today's widespread activities in nanoscience and nanotechnology are actually rooted in the ideas of some leading scientists of the last century. Among them, the foremost name was Richard P. Feynman. He delivered a legendary talk entitled "there is plenty of room at the bottom" in the Annual general body meeting of the American Physical society on December 29,1959 at California Institute of Technology. [Annika P and et.al]

Nanotechnology is the principle of manipulation atom by atom, through control of the structure of matter at the molecular level. It entails the ability to build, molecular systems with atom- by -atom precision, yielding a variety of nanomachines. Nanocrystalline semiconductors have achieved a great important in our industrial world today. They are cornerstone of nano-scale science and technology is a broad and interdisciplinary area of research and development activity that has been growing explosively worldwide in the past decade. It has the potential for revolutions the ways in which materials and products are created. The range and nature of functionalities can be accessed. It is already having a significant commercial impact, which will assuredly increase in the future.

Nanocrystalline powder due to their average particle size, below 100nm, may show different behaviors resulting from a higher surface energy due to the large surface area and the wider gap between the valence band and conduction band. These phenomena may increase the potential use of the materials, including optical, chemical, and electromagnetic, among other properties. Titania has high transmittance in the visible spectral range. It is also known as having a relatively wide band gap

3.2 eV and a high refractive index. Inorganic n-type semiconductor titanium dioxide particles have good biocompatibility, stability and environmental safety. Titania is the most attracted materials in nano science and nanotechnology because of having a lot of interesting properties from fundamental and practical point of view. Crystalline titania has three modification phases which are Rutile (tetragonal), Anatase (tetragonal) and Brookite (orthorhombic). Titania nano particles have received much interest for applications such as optical devices, sensors, and solar cell applications. There are several factors in determining important properties in the performance of Titania for

[1,2]Demonstrators, Department of Physics, East Yangon University

applications such as particle size, crystallinity and the morphology. Many methods have been established for titania synthesis such as sol-gel technique, hydrothermal method, chemical vapour deposition, direct oxidation method and others. Among them sol-gel technique is one of the most used methods due to its possibility of deriving unique metastable structure at low reaction temperatures and excellent chemical homogeneity. [Hui P and et.al]

Solar cells containing organic semiconductors have attracted considerable attention because of their electrical and optical properties can be varied widely, and generally they can be fabricated more easily than inorganic solar cells. Sol-Gel spin coated Titania thin films were prepared and the prepared thin films were analyzed in this research. The randomly porous structure of the Titania electrode gives raise to several undesirable characteristics. These include a low conductivity, which is due to the fact that the film consists of tiny crystals measuring 10-30nm in diameter. The small size of the crystals does not support the information of a space charge region. This has to enhance the recombination rate of the photo-injected electrons due to the absence of an energy barrier at the electrode/electrolyte interface. [Li D and et.al]

Sol-gel processing of titania has been extensively investigated, and modern processes have been developed to refine and control the stability, as well as the phase formation of the colloidal precursor. The hydrolysis of the titanium isopropoxide combined with acetic acid and 2- methoxyethonal with subsequent annealing has led to new materials characterized by their controlled porosity and strong adhesion to the substrate.

Titania is a very useful semiconducting transition metal oxide material and exhibits unique characteristics such as low cost, easy handling, non-toxicity and resistance to photochemical and chemical erosion. Therefore, these advantages make Titania a material in solar cells, chemical sensors, for hydrogen gas evolution, as pigments, self-cleaning surface and environmental purification applications.

Materials and Methods

The Fabrication Procedures of Titania Nanoparticles

Titanium isopropoxide (TiP) and 2-Methoxyethanol (CH3OCH2CH2OH) with the weight percent of 1:2 was used as the starting materials for Titania particles. These materials were mixed together into the covered-beaker. The magnetic stirrer was used to get the homogeneous solution about 12-hours. Meanwhile the stirring process, some drops of acetic acid was put again into the covered- beaker to make the transparent solution. A few drops of distilled water will help to increase the viscosity of the precursor solution. After making these processes, Titanium isopropoxide (TiP) and 2-Methoxyethanol (CH3OCH2CH2OH) sol-gel composite was obtained. The obtained sol-gel was calcined by the furnace with the temperature of 400˚C, 500˚C and 600˚C to perform Titania fine particles. The detail procedure of Titania Nanoparticles fabrication was shown in figure 1.

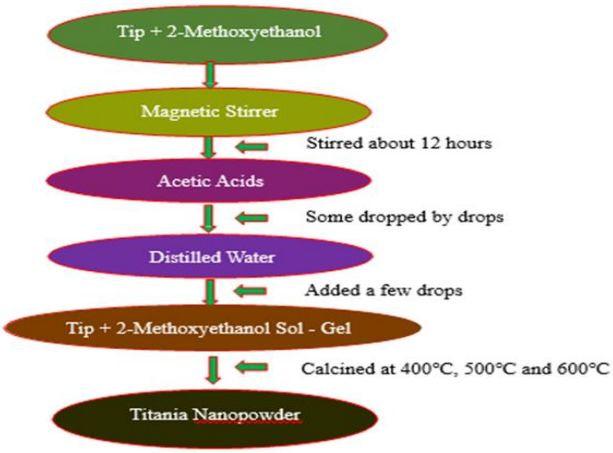

The Fabrication Procedures of Titania Thin Films

The same precursor solution (sol-gel) of Titanium isopropoxide (TiP) and 2-Methoxyethanol (CH3OCH2CH2OH) was used again to investigate Titania thin film by spin coating technique with different cycles. The non-electrolytic glass was used as a substrate. It was cleaned by acetone and distilled water to get rid out of the contaminations from the glass surface. The cleaning glass was heated on the hot plate about 70 ˚C for 15 min to diffuse easily. Titania sol-gel was coated on this glass substrate at spin rate of 1800 rpm and 2500 rpm for two circles to fabricate the homogeneous surface morphology. These Titania thin films were finally dried at 100 ˚C in vacuum oven for 15 minutes to perform the stable crystallized nature on the surface of the non-electrolytic glass substrate. The detail procedure of Titania thin film fabrication was shown in figure 2.

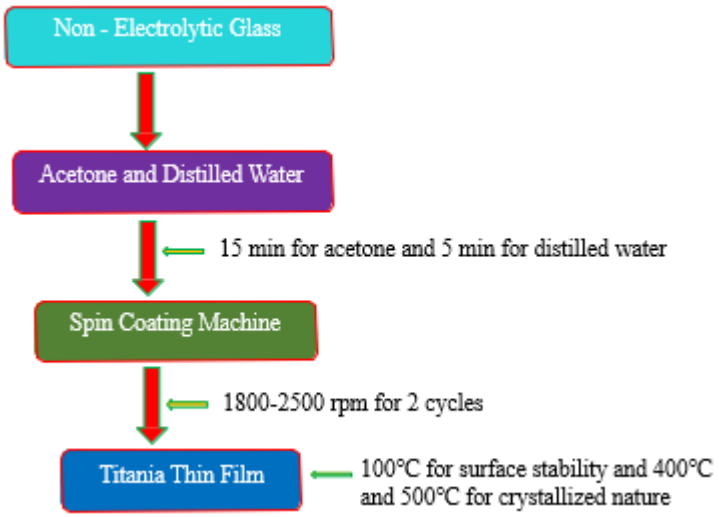

Figure 2. The detail procedure of Titania thin film fabrication

Results And Discussion

XRD Analysis of Titania Nanoparticles

Titania particles have been investigated by sol-gel technique with the weight percent 1:2 of Titanium isopropoxide (TiP) and 2-Methoxyethanol (CH3OCH2CH2OH) composite (sol-gel) at the temperature of 400 ˚C, 500 ˚C and 600 ˚C. The X-ray diffraction analysis has been performed for the crystallized nature of the Titania particles as shown in figures (3, 4, 5). The crystallized sizes were calculated by the Debye Sheerer equation. Anatase type of Titania particles was formed at the temperature of 400 ˚C and Rutile type of Titania particles were found at the temperature of 500 ˚C as shown in figures (3, 4). Almost Brookite type of Titania was also seen to be found about 600 ˚C as shown in figure 5. The average crystallized sizes of Titania were (8.42 nm) (at 400 ˚C), (26.50 nm) (at 500 ˚C) and 36.2 nm at (600 ˚C) as shown in tables 1, 2 and 3.

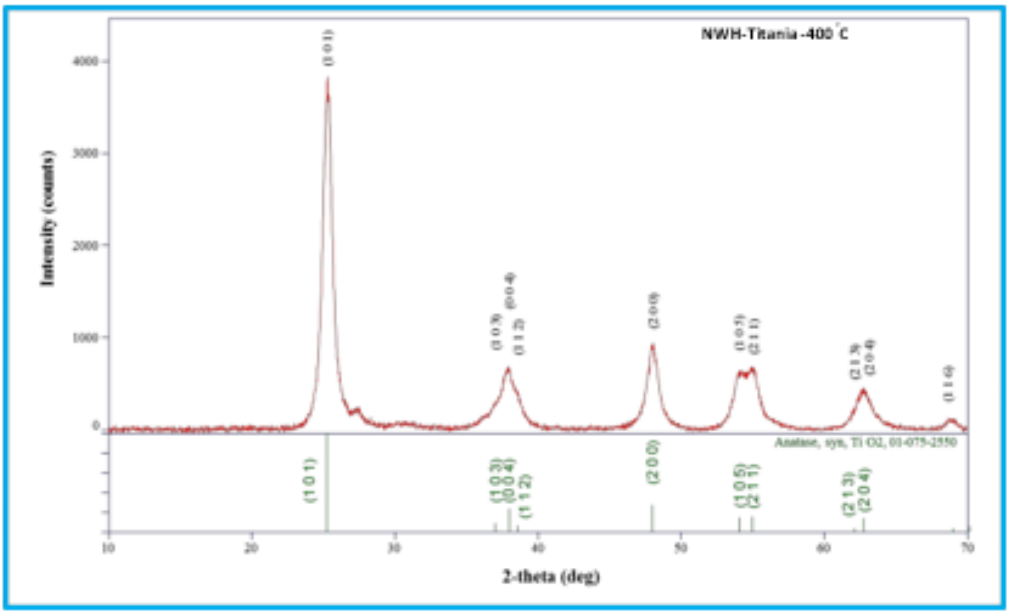

Figure 3. XRD pattern of Titania Nanoparticles at temperature of 400 ˚C

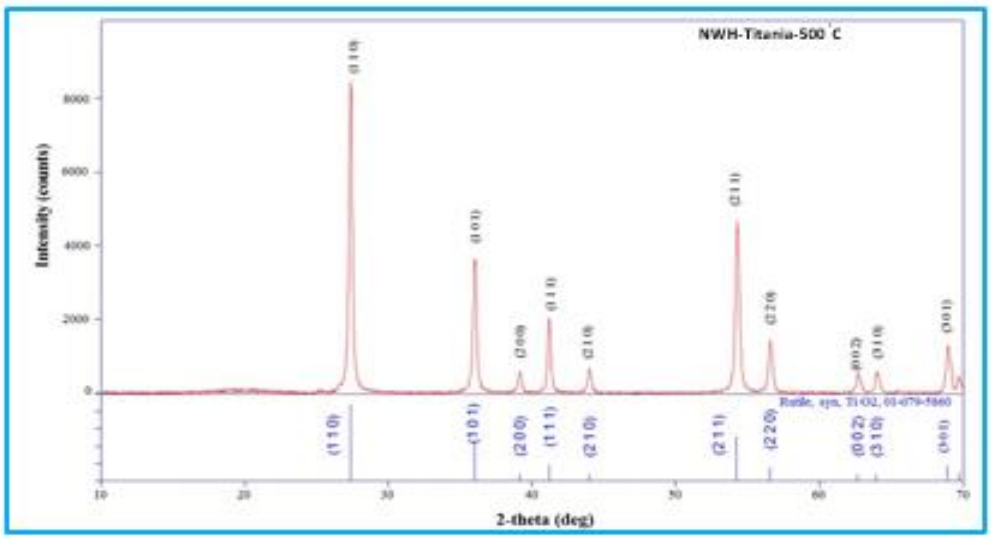

Figure 4. XRD pattern of Titania Nanoparticles at temperature of 500 ˚C

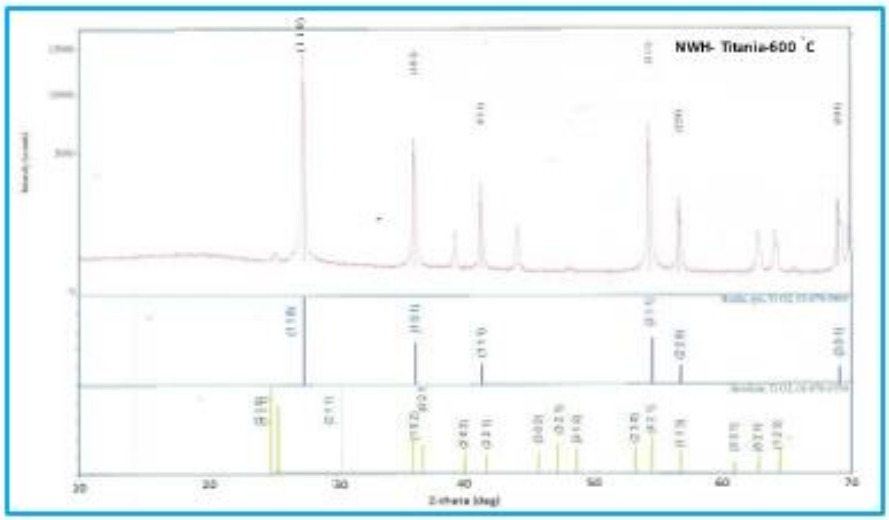

Figure 5. XRD pattern of Titania Nanoparticles at temperature of 600 °C

Table 1. The average crystallized sizes of Titania Nanoparticles at 400 °C

No	2θ Degree	FWHM (Degree)	Plane Direction	Crystallized Sizes (nm)
1	25.2869	1.022	101	7.88
2	37.9924	1.022	004	8.14
3	47.9564	1.022	200	8.42
4	62.1005	1.022	211	8.67
5	62.7555	1.022	213	8.98
Average crystallized sizes of Titania Nanoparticles				**8.42**

Table 2. The average crystallized sizes of Titania Nanoparticles at 500 °C

No	2θ Degree	FWHM (Degree)	Plane Direction	Crystallized Size (nm)
1	27.4018	0.3281	110	24.67
2	36.0267	0.3181	101	25.99
3	41.1801	0.3152	111	26.65
4	54.2432	0.3202	211	27.59
5	56.5503	0.3232	220	27.62
Average crystallized sizes of Titania Nanoparticles				**26.50**

Table 3. The average crystallized sizes of Titania Nanoparticles at 600 °C

No	2θ Degree	FWHM (Degree)	Plane Direction	Crystallized Sizes (nm)
1	27.4045	0.2440	110	33.17
2	36.0363	0.2289	101	36.12
3	41.1896	0.2249	111	37.35
4	54.2533	0.2361	211	37.42
5	56.5563	0.2416	220	36.95
Average crystallized sizes of Titania Nanoparticles				**36.20**

FTIR Analysis of Titania Nanoparticles

Fourier Transform Infrared Spectroscopy (FTIR) results also showed the identification of Titania particles as shown in figures (6, 7). FTIR spectra of synthesized Titania sample is as shown in figures (8, 9). Peaks at 3454.51 cm-1 and 3444.87 cm-1 correspond to stretching vibration of O-H bonds. Peaks observed at 2976.16 cm-1 corresponds to the C-H stretching vibrations. The sharp peak at 1589 cm-1, 1020 cm-1 corresponds to bending vibrations of water. Peak observed at 1658.78 cm-1 corresponds to the C=O vibrations. The peak at 1382.96 cm-1 and 1165 cm-1 corresponds to C-O vibrations. Peaks observed at 950.9 cm-1, and 742.9 cm-1, corresponds to Ti-O vibrations. The strong intensity of peaks was found to be (2976.16 cm-1, 1658.78 cm-1, 1382.96 cm-1 and 1165 cm-1) at 400 °C and 500 °C to confirm the vibration of Ti and O bonds for the Titania crystallization. The lowest intensity of peak was also found to be (742.59 cm-1) at 400 °C and 500°C for the crystallized nature of the Ti-O particles. [Hehm M and et.al]

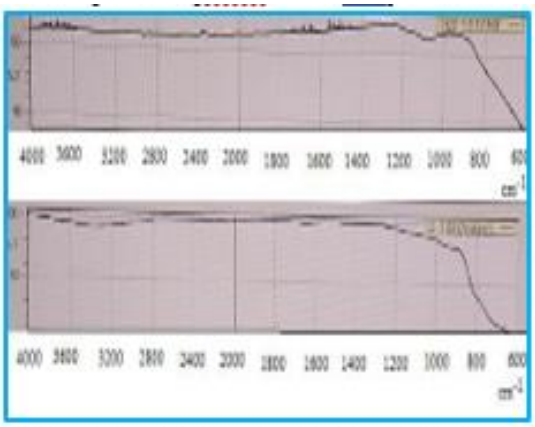

Figure 6. Comparison of FTIR spectra of library and Titania Nanoparticles at 400 °C

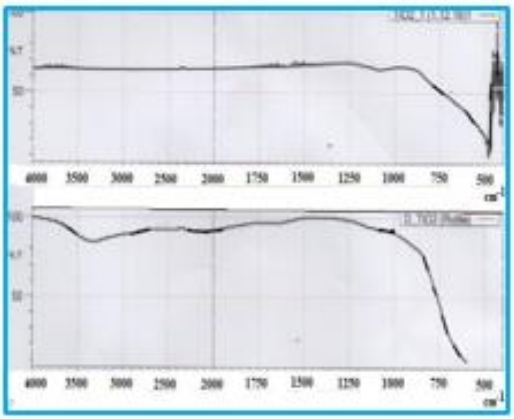

Figure 7. Comparison of FTIR spectra of library and Titania Nanoparticles at 500 °C

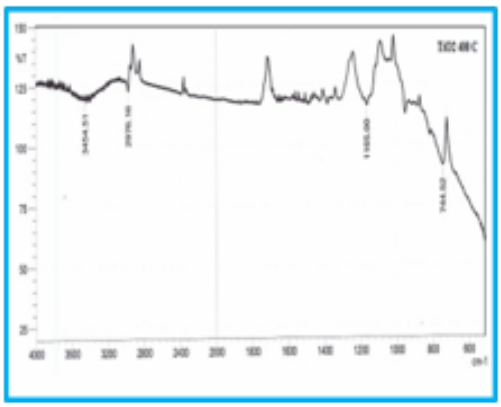

Figure 8. Expanded FTIR spectra Titania Nanoparticles at 400 °C

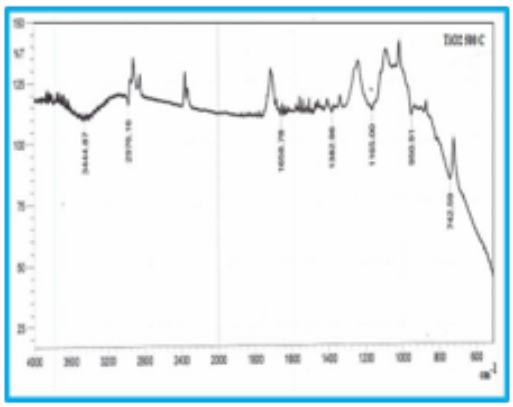

Figure 9. Expanded FTIR spectra Titania Nanoparticles at 500 °C

SEM Analysis of Titania Nanoparticles and Thin Films

The surface morphology and crystallinity of the Titania particles were determined by the Scanning Electron microscopy (SEM) technique which are shown in figures (10, 11, 12). Titania thin film was also fabricated on the non-electrolytic glass substrate by spin coating technique with different cycles for comparison of the crystal aggregation and smoothness of Titania particles at the temperature of 400 °C and 500 °C. The thickness of the thin film was measured about (594.7 nm after annealing) as shown in figure 16. The use of

the same sol-gel process in this research, led to a production of transparent Titania Thin films with reproducibility, scratch and capability of adherence on glass substrates. The film characteristics are strongly dependent on the molar ratios of alkoxide to solvent. The SEM images, presented in figures (13, 14) showed that the sol-gel films exhibit different surfaces resulting from the prepared precursor solution. The thin film surface obtained from the sol-gel preparation appeared as a thin sheet attached on the glass surface (~626.8 nm before calcination) of which the film surface was observed with visual large cracks along the glass plate as shown in figures (13, 16). In contrary, when the higher amount of solvent was applied, more smoothness of thin film was seen as shown in figure 14. And the small cracks were also found the Titania attached on the surface of glass plate. It is very clearly seemed that the role of solvent is not only the dissolubility of alkoxide but also the surface smoothness enhancement of the Titania thin film.

Figure 10. SEM image of Titania Thin Film at annealing temperature of 400°C

Figure 11. SEM image of Titania Thin Film at annealing temperature of 500°C

Figure 12. SEM image of Titania Thin Film at annealing temperature of 600°C

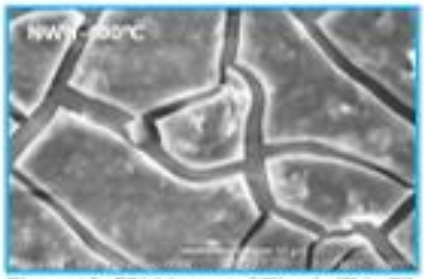

Figure 13. SEM image of Titania Thin Film at annealing temperature of 400°C

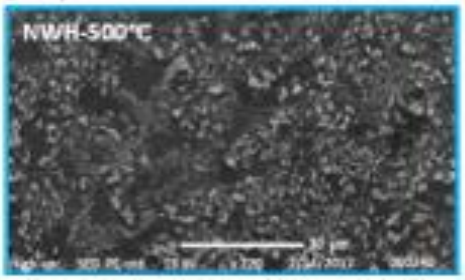

Figure 14. SEM image of Titania Thin Film at annealing temperature of 500°C

Figure 15. Thickness measurement SEM image of Titania Thin Film before annealing

Figure 16. Thickness measurement SEM image of Titania Thin Film after annealing

Conclusion

Titania nanoparticles have been fabricated by the sol-gel synthesis with the weight percent 1:2 of Titanium isopropoxide (TiP) and 2-Methoxyethanol ($CH_3OCH_2CH_2OH$) at the temperature of 400 °C, 500 °C and 600 °C about one hour. X-ray diffraction (XRD) technique was performed to analyze the crystallite nature of the Titania Nanoparticles. The average crystallized sizes about 8.42 nm at 400 °C, 26.50 nm at 500 °C and 36.2 nm at 600 °C were calculated by the Debye Scherrer equation. Anatase type of Titania particles was formed at the temperature of 400 °C and Rutile type of Titania particles were found at the temperature of 500 °C as shown in figures (3, 4). Almost Brookite type of Titania particles was also found about 600 °C as shown in figure 5.

Titania thin films were also fabricated on the non-electrolytic glass substrate by spin coating technique with different cycles for comparison of the crystal aggregation and smoothness of Titania particles at the temperature of 400 °C and 500 °C. The thickness of the thin film was measured about (594.7 nm) after annealing and (626.8 nm) before calcination. The use of the same sol-gel process in the present study provides to a production of transparent Titania Thin films with reproducibility, scratch and capability of adherence on glass substrates.

When the lower amount of precursor or sol-gel with one cycle spin coating was applied, the large number of visual cracks were observed on the glass surface compared than the higher amount of sol-gel was applied. Therefore, the investigation of the sol-gel was very important to make the homogeneity of particles on the film surface which was not only the dissolubility of alkoxide but also the surface smoothness enhancement of the Titania thin film.

Fourier Transform Infrared Spectroscopy (FTIR) results also showed the identification of Titania particles. Scanning Electron Microscopy analysis was finally confirmed the realized nature of morphology of the Titania particles and thin films. As the temperature increased, the crystallite size of titania particles increased, whereas the thickness of the titania thin films decreased. It is obviously seemed that the crystallite nature and agglomerations of Titania particles were different each other.

Acknowledgements

We would like to express our heartfelt thanks to a Rector Dr Myo Min Tun and Pro- Rectors Dr Aye Aye Ko, and Dr Thida Aung, East Yangon University, for their kindly permission to perform this research paper. Furthermore, we really special thanks to Professor Dr Khin Lay Nwe, Head of Department of Physics, East Yangon University, for her warmly advising to do our research. After that, we actually wish to thanks Professor Dr Nilar Tun, Department of Physics, East Yangon University, for her valuable instructions and supporting to carry out our research. Finally, we absolutely wish to thanks Professor Dr Yee Yee Oo, Department of Physics, East Yangon University, for her precious guidelines and helpfulness to develop our research.

References

Annika P, 2004" Sol-Gel Synthesis of CMR Maganities", PhD Dissertation, (Sweden: University of Uppasala) Egerton R F 2005 "Physical Principles of Electron Microscopy: An Introduction to TEM, SEM, and AEM" Springer 202 Hehm M, Yelil A, Tamilselvi P and Anbarasan R, 2013, Chem Sci Trans, 2 241

Hui P, Xiao Dong W and Zhi Jun Z, 2013, India J Eng and M Sci, 20 564 Kamal N C and Anil K M, 2010, "Thin Films and Their Applications in Military and Civil Sectors", 6-11, (New Delhi, India) Li D and Xia Y 2003 Chem Materials Nanoletters 3 555

Nay Myo Tun, Than Than Win and Yin Maung Maung 2011 "Formation of TiO_2 Electrospun Ultrafine Fibres", 11th MAAS conference, Yangon University (Best Paper Award)

Nay Myo Tun, Than Than Win and Yin Maung Maung 2011 "Preparation and Characterization of TiO_2 Electrospun Nano fibres", 2nd IGCSE conference, Sedona Hotel, Yangon (Best Paper Award)

Nyo Nyo, Yin Mg Mg and Ko Ko Kyaw Soe 2009 "Fabrication of Zinc Oxide Ultrafine-fibers by Electrospinning Method", 2nd Regional Conference on Materials Engineering, Thailand

Ocana M, Fornes V and Serna J V, J Solid State Chem., 1988, 75, 364 Puangrat K, Jirapat A and Siriwan P, 2005, J Sci& Teach Adv Materials 6354 Vetrivel V, Dr Rajendran K, Kalaiselvi V, 2015, Int J Chem Teach Research, 7 1095 Xu W X, Zhu S and Fu X C, J Phys Chem Solids, 1998, 59, 1647

Zin Mar Kyaw 2011 "Structural and Ferroelectric Properties of Ba TiO_3 Thin Film by Spin Coating Method" PhD Dissertation, Yangon Universi

An Air Quality Monitoring System Using Innovative IoT Technology for Public Health Protection

Phyu Thel Ei[1], Kay Zin Win[2], Thazin Hlaing[3], Thet Mar Oo[4], May Mi Tun[5]

Abstract

Air pollution has harmful effects on human health. It is essential for people to live in a clean and hygienic environment. The objective of this project is to develop a comprehensive air quality monitoring and management system using Internet of Things (IoT) technology. The system design consists of a microcontroller development board which can provide Wi-Fi internet connectivity, an OLED LCD display, real-time clock circuit, dust sensor module, gas sensor module and other components. The project recognizes the significance of maintaining optimal air quality for the well-being and safety of occupants in various environments, including homes, offices, schools, and public buildings. This project aims to develop user-friendly interfaces, such as web or mobile applications to provide real-time visualizations and notifications regarding air quality status. It can be used as an environmental support project as safer places can be created through this method.

Keywords: air pollution, dust sensor, gas sensor, IoT, OLED

Introduction

There are many developing countries and capitals suffering from the threat of air pollution from various causes, especially in those heavily populated areas. In our country, Yangon, Mandalay and other major cities face increasing risks of pollutions. The main cause of pollution is vehicle emissions, including a vast number of motorbikes, cars and buses which run on fuels. Other causes are construction sites, factory exhaust smokes from industries and smoking in public areas. The rise in pollution causes rapid aging and scarring of the lungs leading to a decrease in overall lung function as well as greater susceptibility to respiratory ailments such as pneumonia, bronchitis, emphysema and aggravated forms of asthma.

To achieve successful control of air pollution, it is important to investigate and monitor the continuous changes in the target area. According to the data results, management can be made to lower the pollution levels. It is very important for the public health of the entire nation. Therefore, an air quality monitoring system is designed and constructed to help address health issues relates to pollution. The system design consists of an Espressif microcontroller board (ESP32), a dust sensor module (DSM501A), MQ2 gas sensor module, a DHT22 digital humidity and temperature sensor module, an OLED LCD display and micro SD card module. The ESP32 was chosen because of its program memory, 32-bit dual core processor, analog input pins and Wi-Fi internet accessibility. The basic structure of the system is illustrated in the block diagram shown in figure 1. The working diagram of the system is illustrated in figure 2. The system will read sensors and display the results using two different methods, the OLED LCD display and the webserver. The display will include date, time and data. Moreover, the real-time data will be permanently stored on a micro SD card. The system will be very useful and can become an important device in monitoring and controlling air quality for public health.

[1] Demonstrator, Department of Physics, East Yangon University
[2,3,4,5]Demonstrators, Department of Physics, East Yangon University

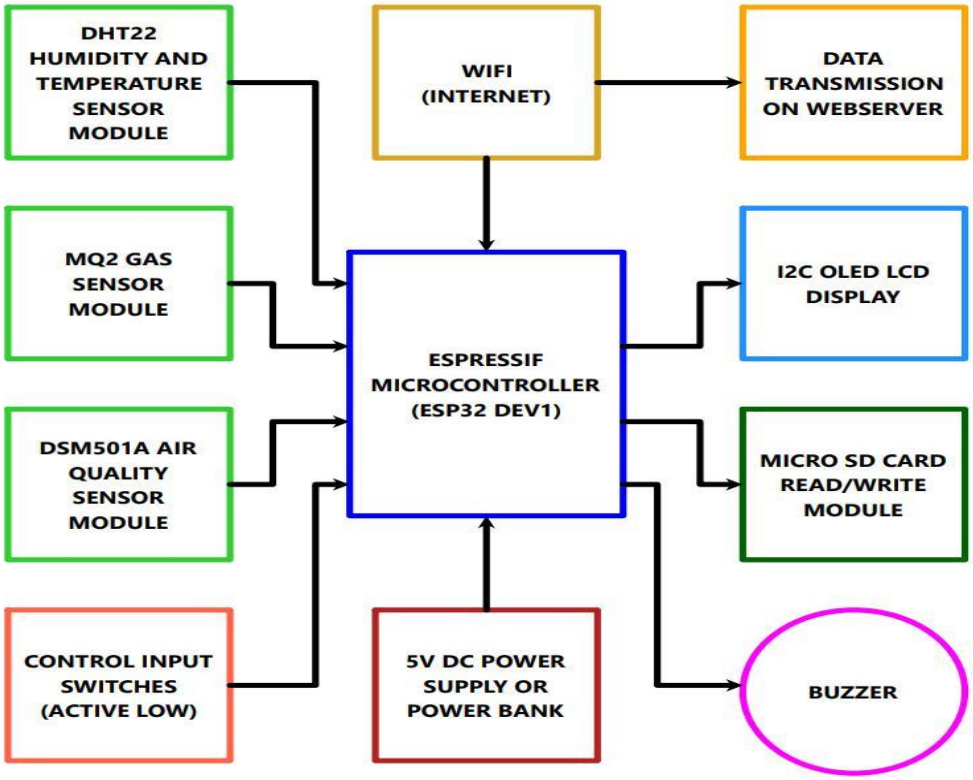

Figure 1. Block diagram of Air Quality Monitoring system

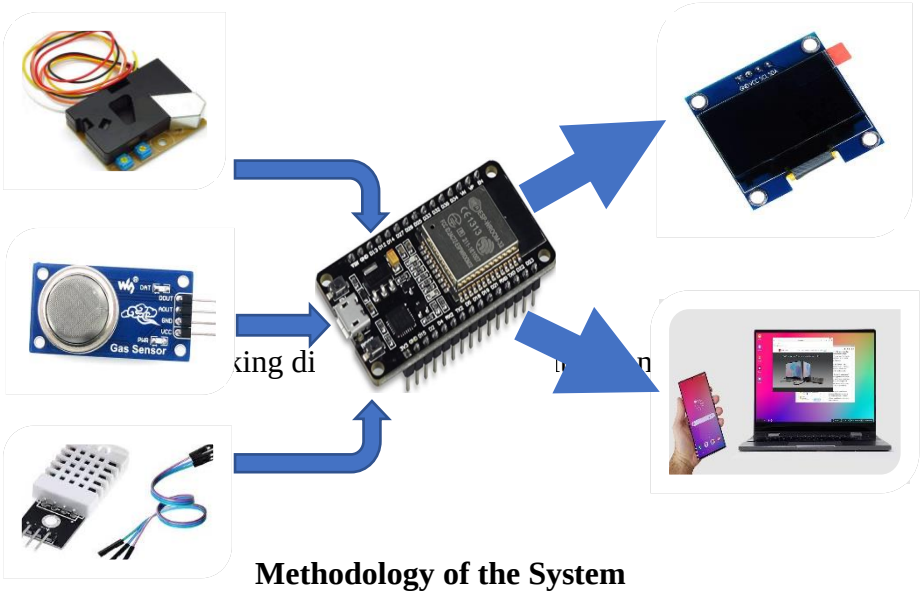

Methodology of the System

ESP32 Development board

The ESP32 development board is a flexible and affordable microcontroller platform that integrates Wi-Fi and Bluetooth connectivity, making it ideal for Internet of Things (IoT) projects. It offers a rich set of input and output pins for connecting sensors, displays and other peripherals. One of the advantages of the ESP32 is that it has many more GPIOs pins than the ESP8266. The photograph of ESP 32 Development board is shown in figure 3.

Figure 3. The photograph of ESP 32 Development Board

I2C OLED LCD Display

OLED displays are available in a range of sizes (such as 128×64 and 128×32) and colors (such as white, blue and dual-color OLEDs). Some OLED displays have an I2C interface, while others have an SPI interface. Before using the OLED display module, it is important to know the functions and nature of each pins on the display module. The photograph of OLED display is shown in figure 4.

Figure 4. The photograph of OLED display

SD Memory Card

SD Cards are the most commonly used devices in embedded applications. The terms SD card stands for "Secure Digital**"** Card, there are many types of SD cards ranging from the larger RS-MMC cards used in cameras to micro and mini SD cards that are commonly used in mobile phones, MP3 players and other portable devices. The SD cards can operate in two modes: the SD mode and the SPI mode. The pinout diagram of a micro SD card is illustrated in figure 5.

Figure 5. Pinout diagram of a micro SD card

Micro SD Card Module

The MicroSD card module is an essential add-on board that enables the ESP32 to read from and write to MicroSD memory cards. In many embedded applications, engineers will often require need to log and store large amount of data that the internal memory of a microcontroller which can handle for any logger project like data logger, temperature logger or GPS tracker. The solution to this problem is to use an SD card or micro SD card that can

store gigabytes of data while being smaller than a one-rupee coin. The pinout diagram of the Micro SD Card Module is shown in figure 6.

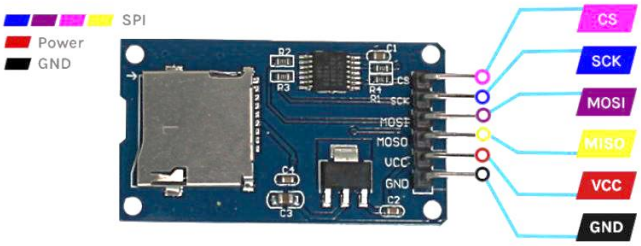

Figure 6. Pinout diagram of Micro SD card module.

Dust Sensor Module

The DSM501A dust sensor is a low cost, compact-sized dust sensor module that can be used to measure quantitative particle (>1micron). The sensor uses the particle-counting principle to measure the amount of dust in the air. PM stands for Particulate Matter and it is also called particle pollution. Particles that are 10 microns or less in diameter are called PM10 and particles that are 2.5 microns or less in diameter are called as PM2.5. Both PM2.5 and PM10 particles can be inhaled. These particles can get deep into the lungs and some may even enter the bloodstream. Exposure to these particles can affect a person's lungs and heart. The DSM501A is a compact and cost-effective dust sensor that detects airborne particles like PM2.5 and PM10 by measuring the intensity of light scattered by dust passing through its detection chamber. The photograph of DSM 501A sensor is shown in figure 7.

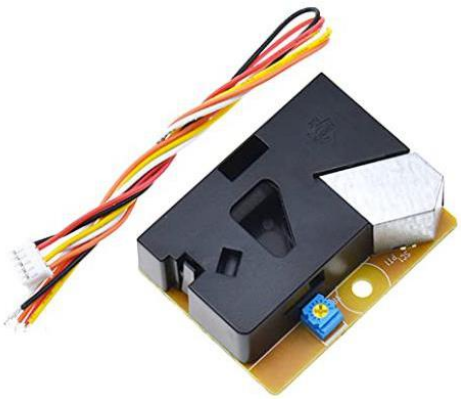

Figure 7. The photograph of DSM 501A sensor

Gas Sensor Module

The MQ-2 combustible gas and smoke sensor can not only detect gas or smoke, but also detect LPG, Alcohol, Propane, Hydrogen, Methane and Carbon Monoxide. The MQ-2 Gas detection sensor module has four pins: VCC, GND, AOUT, and DOUT that can be used to obtain the required information from the sensor. The pinout diagram of the MQ gas detection sensor is shown in figure 8.

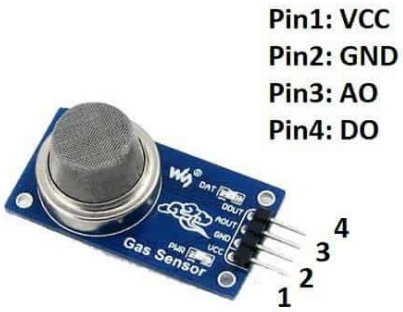

Figure 8. The pinout diagram of the MQ-2 Gas sensor

Temperature and Humidity Sensor

The DHT22 temperature and humidity sensor is a cost-effective sensor used to measure ambient temperature and humidity for a wide range of applications. It is based on a digital signal output and can provide high-accuracy measurements with a resolution of 0.1℃ for temperature and 0.1% for humidity. The sensor uses a capacitive humidity sensing element and a thermistor to measure the humidity and temperature respectively. The pin diagram of the DHT 22 sensor is shown in figure 9.

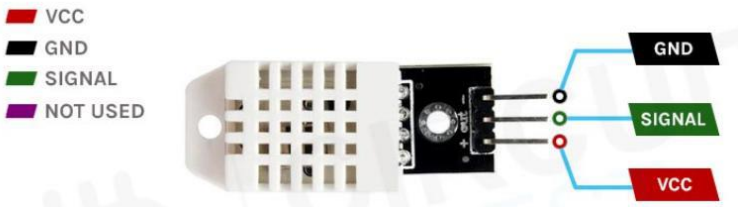

Figure 9. The pin diagram of the DHT 22 sensor

Design and Construction of the System

Circuit Construction

The schematic design of the circuit is shown in figure 10. This design includes a total of eight components: ESP32 DEV1 microcontroller, DSM501A, MQ2, DHT22, OLED display, micro DS card module, a piezo buzzer and some input switches. The system is intended to read data from three different sensors and display the results on OLED display, and sends data to webserver. It is necessary to choose a microcontroller development board with internet connectivity. Therefore, ESP32 DEV1 is selected for the circuit design. The ESP32 board has numerous I/O pins and analog pins. Moreover, the program memory is large and consists of two processors. The microcontroller board is connected to all other components in the circuit. The other components are divided into two categories; input devices and output devices. The input devices include three sensors and control switches while the output devices are OLED display, micro SD card module and piezo buzzer.

The DSM501A sensor module consists of five terminal pins (control, pm1.0, VCC, pm2.5 and GND). The VCC pin and GND pins are connected to VIN (5V) pin and GND pin of ESP32 development board. The PM1.0 and PM2.5 pins are connected with GPIO14 and GPIO13 of the ESP32 respectively. The MQ2 gas sensor module consists of four terminal pins (VCC, GND, DO and AO). The VCC and GND pins are connected to the 3.3V pin and GND pin of ESP32. The DHT22 sensor module consists of three terminal pins (VCC, OUT and GND). The VCC and GND pins are connected with 3.3V pin and GND pin of ESP32.

The data output pin OUT is connected to GPIO27 of the ESP32 to measure humidity and temperature data in the air.

The OLED display is an output device and it is used to display the operating conditions and data result from sensor modules. There are four pins on this module and they are GND, VCC, SCL and SDA. The GND and VCC pin are connected with ground line and 3.3V line of ESP32 power pins. The SCL and SDA are connected with I2C pins of ESP32 SCL and SDA. The micro SD card module is also an output device and is used to store the sensor data permanently on an external micro SD card. The module is a SPI device and consists of six terminal pins (GND, VCC, MISO, MOSI, SCK and CS). The GND pin and VCC pins are connected to ground line and VIN line of the ESP32. The four SPI pins are connected to GPIO 19, 23, 18, and 5 respectively. The last output device on the circuit is piezo buzzer. It is connected between GPIO26 and ground line of the ESP32.

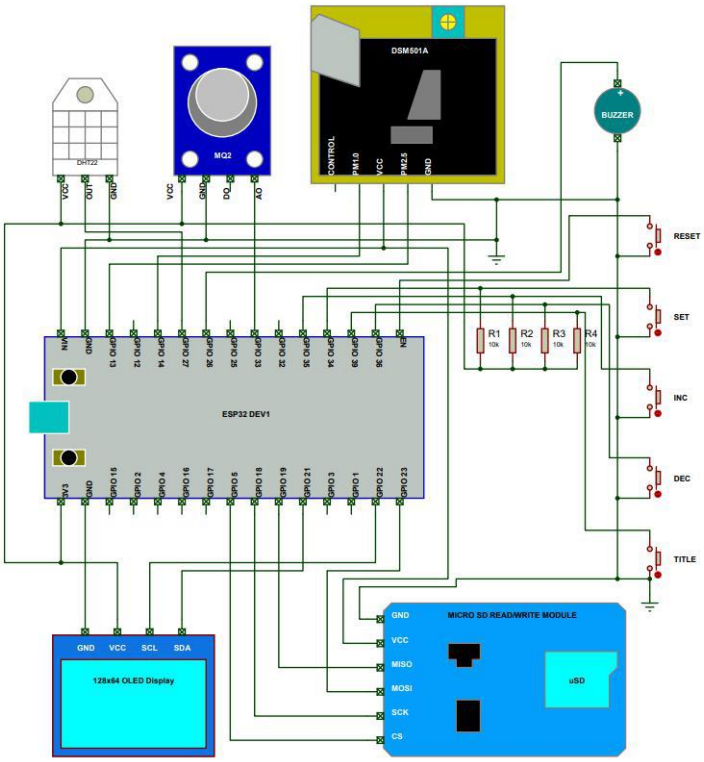

Figure 10. Schematic diagram of the whole system

Design of Printed Circuit Board

The circuit designed using a single layer printed-circuit board for the IoT Air Quality Monitoring System. The drawing layout of the circuit board is arranged and drawn with a software. It is Easily Applicable Graphical Layout Editor software which is also known as EAGLE PCB drawing software. In the design, the width of circuit tracks are 0.07inch and they are illustrated in blue. The positions of the pin holes are represented by green pads which can be circular shape, rectangle shape or octagonal shapes. The size of pads does not exceed the width of track lines and all the pads are of the same size. The completed drawing layout is shown in figure 11.

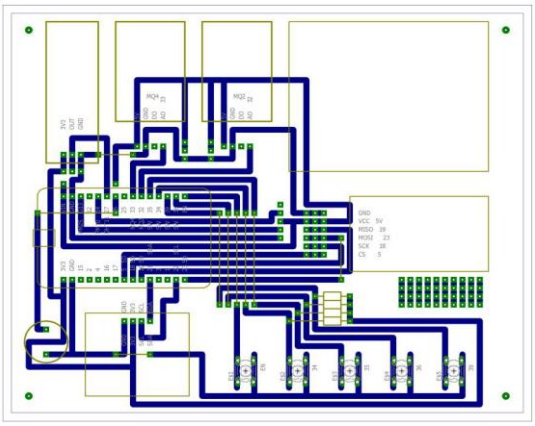

Figure 11. Complete design of PCB drawing

Construction of the whole hardware system

Circuit construction is constructed using a fabricated printed circuit board, which is specially designed for the Air Quality Monitoring System circuit. The five input switches are inserted in their positions and soldered. For the DHT22, MQ2 sensor and micro SD card modules, small printed circuit board lines are cut and soldered with female and male terminal pins to insert the components on the circuit board. The dust sensor module, micro SD card module, DHT22, MQ2 sensor and OLED display are then placed in their respective position as shown in figure 12. The ESP32 is inserted into its position as shown in figure 13. Finally, the entire circuit board is mounted on an acrylic board to prevent short circuits on the soldered side of circuit board.

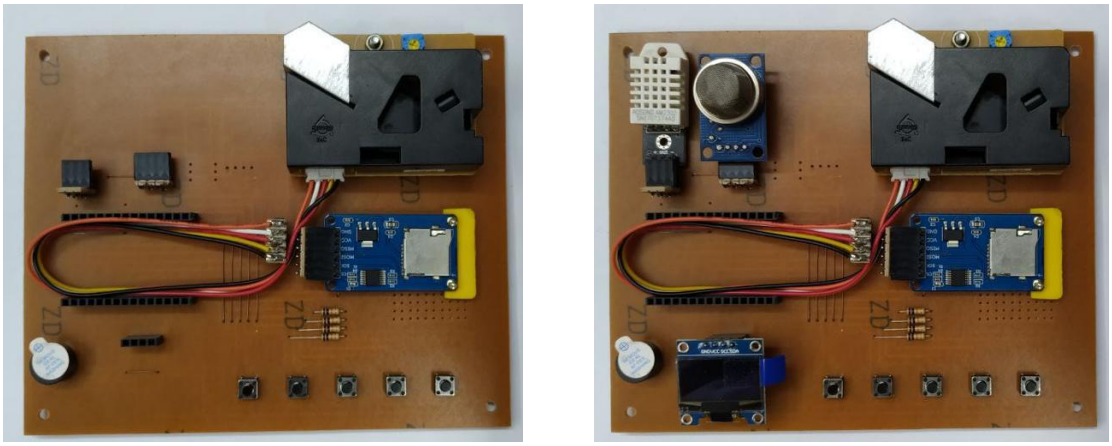

Figure 12. Installation of dust sensor module, micro SD card module, DHT22, MQ2 gas sensor and OLED display on their position.

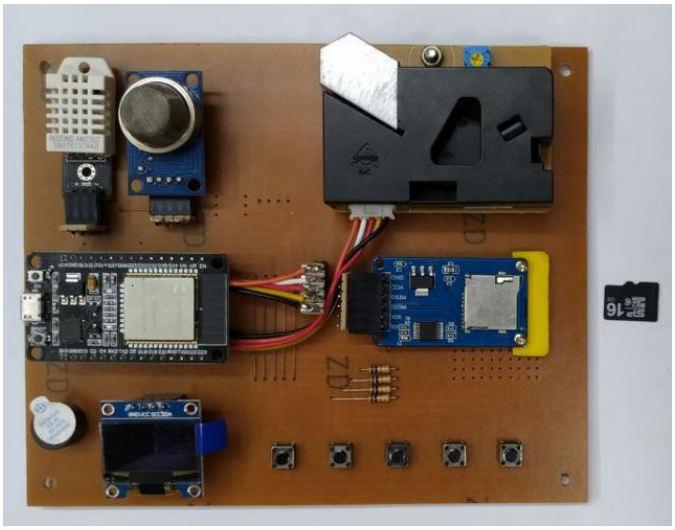

Figure 13. Installation of ESP32 board.

Results and Discussion

The developed IoT-based air quality monitoring system operated successfully and continuously measured environmental parameters including PM1.0, PM2.5, LPG, CO, smoke, temperature, and humidity. The system displayed real-time data on the mobile interface and simultaneously logged the data with date and time onto a micro SD card. The system requires a Wi-Fi SSID and password for webserver data broadcasting. The power supply for the circuit can be easily connected using a 5V DC power bank, a 5V android phone charger or any USB 5V power source. The entire circuit is illustrated from two different views in figure 14. The system was tested in three practical rooms of the Physics Department at East Yangon University, namely Room 3-301, Room 3-102 and Room 3-002. These rooms were selected to evaluate the system performance under different indoor environmental conditions. The system was placed at a fixed position in each practical room and allowed to operate for a specific duration. During the testing period, particulate matter (PM1.0 and PM2.5), gas concentrations (LPG, CO, and smoke), temperature, and humidity were measured in real time. A total of seven data parameters were recorded. The server address is typed into the search box of an internet browser on a desktop computer or an Android phone. Then the created data webpage is displayed on the browser. The recorded sensor data showed noticeable variations between three practical rooms due to differences in room size, ventilation and occupancy. All measured parameters from each practical room were successfully logged onto the micro SD card with date and time stamps. The stored data were retrieved using a card reader and verified on a computer. The screen captured results of data on the webpage is shown in figure 15. The data on micro SD card can be read on a desktop computer or laptop for later data managements. Table 1 describes the average real-time data values recorded for the three rooms. Table 2 describes a comparison between the standard values and experimental results for the three rooms.

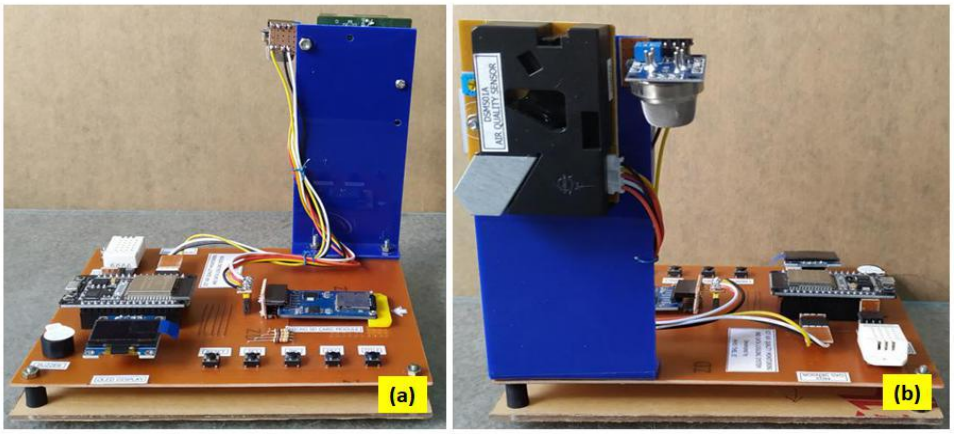

Figure 14. The photograph of the whole circuit design

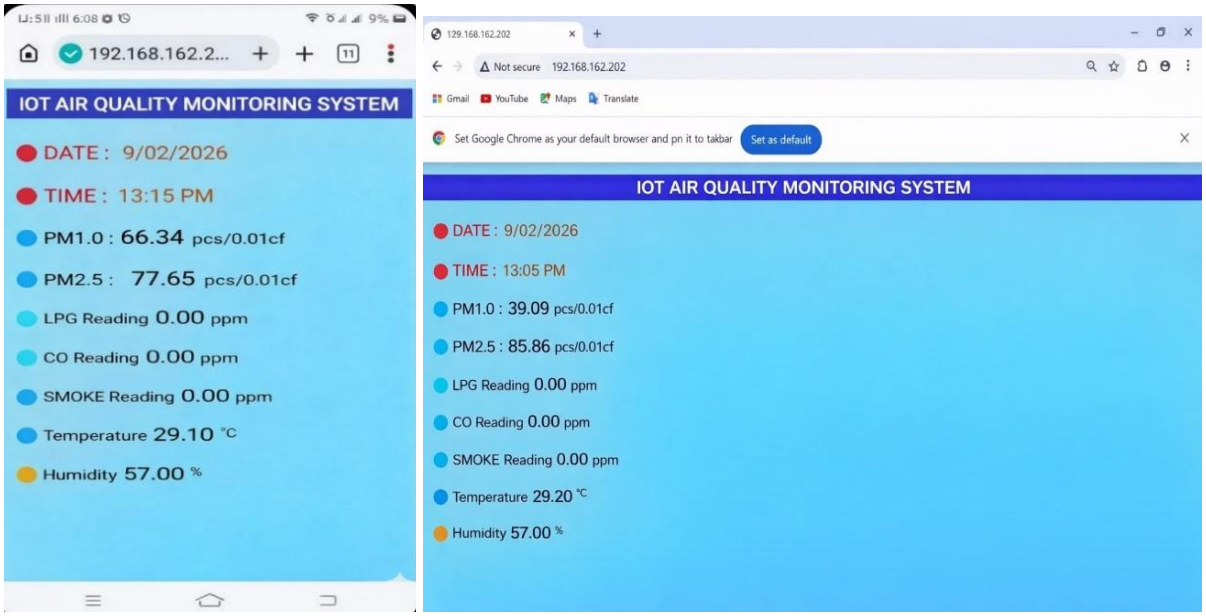

Figure 15. The screen captured results of data on webpage in android phone and computer

Table 1. Average real-time data values recorded for three rooms

Parameters	Room (3-002)	Room (3-102)	Room (3-301)
PM 1.0	75.07	73.76	72.71
PM 2.5	57.97	57.79	56.87
LPG	0.00	0.00	0.00
CO	1.00	0.57	0.42
Smoke	2.01	0.03	0.00
Temperature	30.4	28.78	28.31
Humidity	45.7	53.1	50.45

Source: Department of Physics, EYU

Table 2. Comparison of experimental results and standard values

Parameters	Standard Values	Condition	Experimental Results of three rooms
Humidity	> 70%	High	
	< 30%	Low	
	Otherwise	Normal	√
Temperature	> 30°C	High	
	< 25°C	Low	
	Otherwise	Normal	√
Dust Concentration	0 to 50	Good	√
	51 to 100	Moderate	√
	Otherwise	Danger	
Carbon monoxide	>50	Danger	
	Otherwise	Normal	√

Source: U.S. Environmental Protection Agency Air Quality Index (2024)

Conclusion

The system design is capable of detecting various air pollutants. It can detect compounds that cannot be perceived by sight, taste or smell. However, the system demonstrated reliable performance and consistent data logging capabilities across all tested practical rooms. Experimental results obtained from different practical rooms in the Department of Physics demonstrate that the system can reliably monitor variations in air quality over time. The collected data supports timely awareness and preventive actions, such as improving ventilation or reducing exposure during poor air quality conditions. The data results are presented via the OLED display, webserver screenshots and logged data files. The measured particulate matter values were interpreted by referring to the general air quality categories recommended by the United States Environmental Protection Agency (US EPA). Analysis of this data confirms that the air quality levels across the tested practical rooms in the department consistently fall within the “Good” and “Moderate” air quality categories as defined by the US EPA. Therefore, we can conclude that the air quality in these spaces is within safe limits, ensuring a secure and healthy environment for occupants. Overall, this project demonstrates that IoT-based monitoring system can serve as an effective environmental support tool for indoor air quality awareness and public health protection.

Acknowledgements

We would like to express our gratitude to Acting Rector Dr Myo Min Tun, East Yangon University, for his permission to work this research. We would like to thank Pro-rectors Dr Aye Aye Ko and Dr Thida Aung, East Yangon University, for their permissions to work on the present research. We are greatly indebted to Professor Dr Khin Lay Nwe, Head of Department of Physics, East Yangon University, who provides with generous help and kind permission in this research paper. We would like to thank Professors Dr Nilar Tun and Dr Yee Yee Oo, Department of Physics, East Yangon University, for their help and guidance in this research work. We would like to express our sincere gratitude and appreciation to all those who have contributed to the completion of this project.

References

Rafsanjani, H. N., & Ghahramani, A. (2020). *Towards utilizing internet of things (IoT) devices for understanding individual occupants' energy usage of personal and shared appliances in office buildings.* Journal of Building Engineering, 30, 101280.

Sinclair, I. R., (2001). Practical Electronics Handbook, London : B H Newnes

Floyd, T. L., (1996). Electronic Devices, New Jersey: Prentice-Hall

U.S. Environmental Protection Agency. (2012). National Ambient Air Quality Standards (NAAQS) for Particulate Matter. https://www.epa.gov/pm-pollution

Espressif Systems. ESP32 Technical Reference. https://www.espressif.com/en/products/socs

An Analysis of Airline Flight Routes Using Graph Planarity

Yuzana Min Hlaing [1]

Abstract

In this paper, the properties of graphs drawn in the plane without edge crossings are studied. Such a graph G is called a planar graph and the characterizations of the planar graphs are discussed. Some well-known necessary and sufficient conditions for a graph to be planar are presented. Finally, the concept of thickness in graph theory is explained in detail, together with its associated theorems. Based on these theorems, a thorough explanation is provided of how airline routes can be designed and represented.

Keywords: graph, planar graph, non-planar graph, planar representation, thickness

Introduction

Graph theory is an important area of mathematics that studies the relationships between objects using vertices and edges. It has many practical applications in fields such as transportation networks, communication systems, and computer science. One of the key concepts in graph theory is planarity, which refers to graphs that can be drawn on a plane without edge crossings. In airline transportation networks, airports can be represented as vertices and flight routes as edges. As the number of routes increases, the network becomes complex and many routes may intersect when represented on a map. To analyze such complex networks, the concept of graph thickness can be applied. Graph thickness is the minimum number of planar subgraphs whose union forms the original graph. This concept is closely related to the use of different flight levels in aviation. When flight routes intersect geographically, aircraft are assigned different flight levels to maintain safe separation. Similarly, by using graph thickness, airline routes can be divided into several planar layers, where each layer represents routes that do not cross each other. Therefore, this study analyzes airline flight routes using the concepts of graph planarity and graph thickness to illustrate how flight routes can be organized and represented efficiently.

Basic Concepts of Graph Theory

We use the standard graph theoretic terminology compatible with Bondy and Murty where basic definitions may be found. We use the following notations: *G* is an undirected, simple (without loops and multiple edges) and finite graph with the vertex set *V(G)* and the edge set *E(G)*. We denote $|V(G)| = p$ and $|E(G)| = q$. A **loop** is an edge whose two endpoints are the same. Two edges with the same endpoints are said to be **parallel edges** or multiple edges. A graph with neither loops nor parallel edges is called a **simple graph**. The graph K_n, called the **complete graph** on *n* vertices, has *n* vertices and every vertex is joined to every other vertex by an edge. The graph $G = (V, E)$ is a **subgraph** of the graph $G' = (V', E')$ if and only if $V \subseteq V'$ and $E \subseteq E'$. **Complete bipartite graph** on *m* and *n* vertices is the graph, denoted $K_{m,n}$, whose vertex set consists of two disjoint sets V_1 and V_2 whose cardinalities are *m* and *n* respectively, and whose edge set consists of all unordered pairs $\{v_1, v_2\}$, where $v_1 \in V_1$ and $v_2 \in V_2$. The **length** of a path is the number of edges on its path. The **n-cube** Q_n where *n* is a natural number; the graph, denote Q_n whose vertex set consists of all bit strings of length *n*, and whose edge set consists of all unordered pairs of strings that differ in exactly one position. A **walk** *W* in *G* is a sequence $\{v_0, e_1, v_1, e_2, v_2, \ldots, e_n, v_n\}$, such that each $v_k \in V$,

[1] Dr, Professor, Department of Mathematics, Taunggyi University

each $e_k \in E$, and each *k* from 1 to *n*, edge joins vertices v_{k-1} and v_k. The walk *W* is said to join v_0 and v_n, going from v_0 to v_n or a $v_0\ v_n$ walk. A $v_0\ v_n$ walk is said to be **closed** if $v_0 = v_n$. It is a **path** if all the vertices are distinct. The **cycle** (or circuit) $C_n, n \geq 3$, is a closed path, consists of *n* vertices $v_1, v_2, \ldots, v_n$ and edges $\{v_1, v_2\}, \{v_2, v_3\}, \ldots, \{v_{n-1}, v_n\}$ and $\{v_n, v_1\}$. A **connected graph** is a graph with the property that every two vertices are joined by a walk. A **component** of *G* is a maximal connected subgraph of *G*. The **degree** $\delta_G(v)$ of a vertex *v* in *G* is the number of edges of *G* incident with *v*, each loop counting as two edges. An **acyclic** graph is one that contains no cycle. A **tree** is a connected acyclic graph. A **wheel** is a graph obtained from a cycle by adding a new vertex and edges joining it to all the vertices of the cycles.

Properties of Planar Graphs

A graph is called **planar** if it can be drawn in the plane without any edges crossing. Such a drawing is called a **planar representation** of the graph.

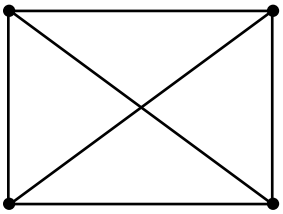

Complete graph K_4

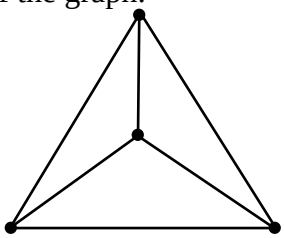

Planar representation of K_4

We first give some examples of planar graphs and nonplanar graphs. All trees, all cycles and all wheels are planar graphs and the complete graph K_5 and the complete bipartite graph $K_{3,3}$ are nonplanar graphs.

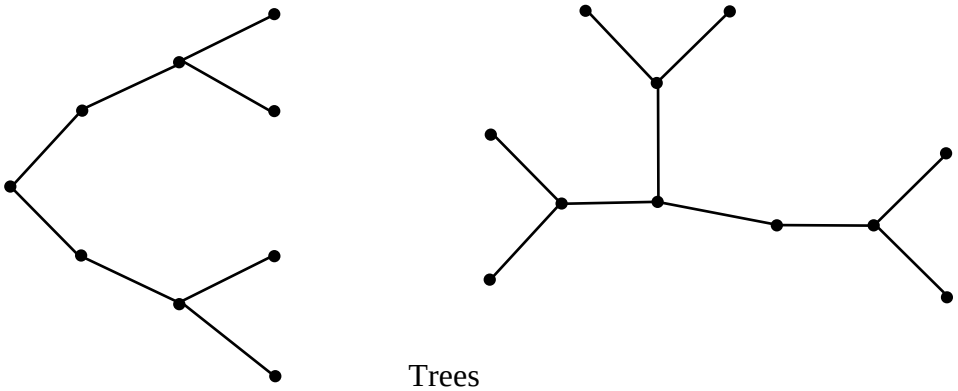

Trees

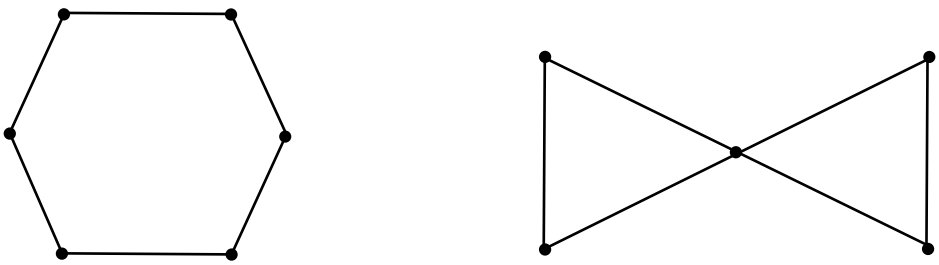

Cycles

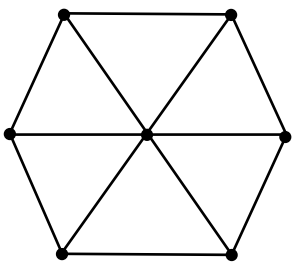

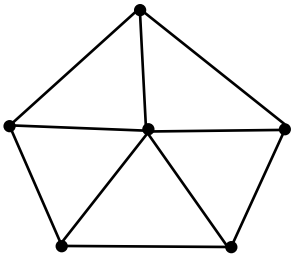

Wheels

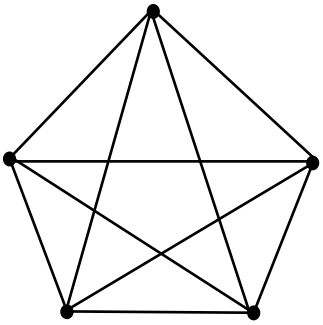

K_5

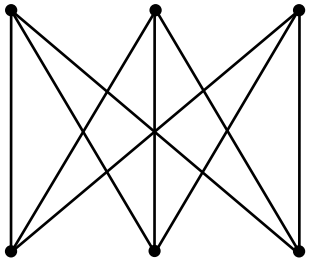

$K_{3,3}$

A **region,** or a **face**, in a planar representation is a subset of the planar bounded by a cycle without diagonal paths and the unbounded region being called the **exterior face**.

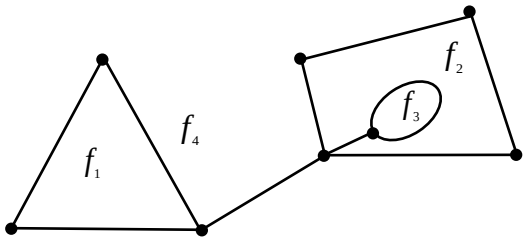

A graph with 4 faces

For any planar representation of a planar graph *G* with *p* vertices, *q* edges, *f* faces, and *c* components, $p-q+f=c+1$. This is called **Euler's Polyhedral Formula.**

For any planar representation of a connected planar graph, $p-q+f=2$.

Theorem

If *G* is a planar representation of a simple connected planar graph with *q* edges and *p* vertices, where $p \geq 3$, then $q \leq 3p-6$.

Theorem

If *G* is a planar representation of a simple connected planar graph with *q* edges and *p* vertices in which no cycle has length less than 4. Then $q \leq 2p-4$.

Theorem

If *G* is a graph with *q* edges and vertices $\{v_1, v_2, \ldots, v_n\}$, then $\sum_{i=1}^{n} \delta(v_i) = 2q$.

Example

The complete graph K_5 is nonplanar since it has $p = 5$ vertices and $q = 10$ edges and $10 > 9 = 3 \cdot 5 - 6$.

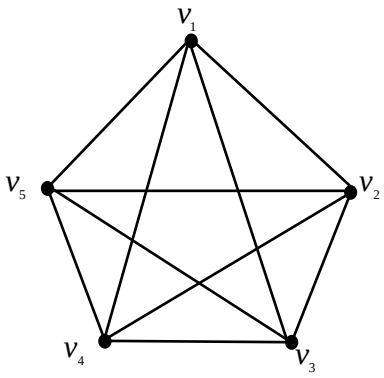

Example

The complete bipartite graph $K_{3,3}$ is nonplanar since it has $p = 6$ vertices and $q = 9$ edges and $9 > 8 = 2 \cdot 6 - 4$.

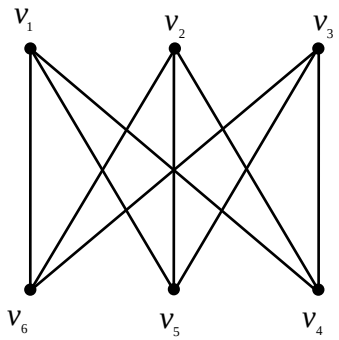

Thickness of Planar Graphs

In this section, the thickness of a graph *G* is considered. If a graph is nonplanar, it cannot be drawn in the plane. The **thickness** of a graph $G = (V, E)$ is the minimum number of planar subgraphs whose union is *G*, more precisely, it is minimum number *k* such that the edge set *E* can be partitioned as $E = E_1 \cup E_2 \cup \cdots \cup E_k$ so that each of the subgraphs $G_1 = (V, E_1), G_2 = (V, E_2), \ldots, G_k(V, E_k)$ is planar.

We will show that the complete graph K_{11} has thickness 3 and the complete bipartite graph $K_{7,7}$ has thickness 3.

In K_{11}, $p = 11$, $q = 55$. Each planar representation can contain at most $3.11 - 6 = 27$ edges. Thus two planar representation can contain at most 54 edges, one short of the 55 needed for K_{11}. Therefore, the thickness is greater than 2. The following figure shows that it is 3.

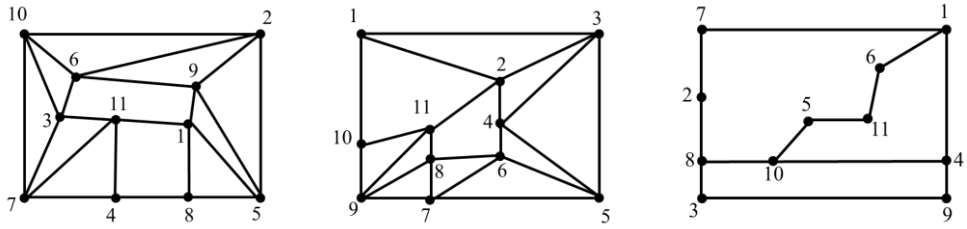

In $K_{7,7}, v = 14, q = 49$. Each planar representation can contain at most $2 \cdot 14 - 4 = 24$ edges. Thus two planar representation can contain at most 48 edges, one short of the 49 needed for $K_{7,7}$. The following figure shows that it is 3.

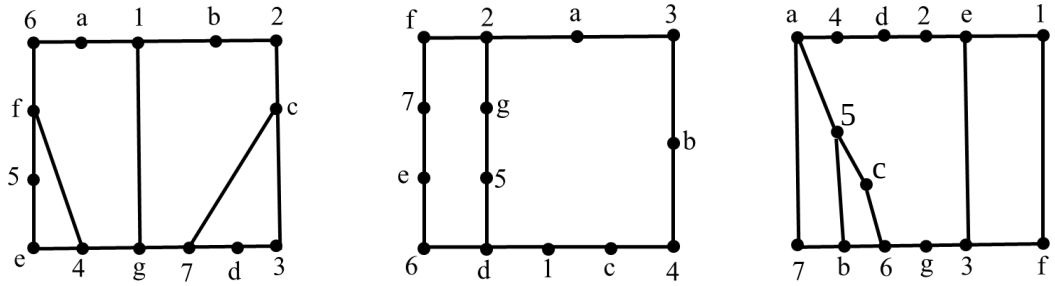

Scheduling the Trajectory of Airlines

The aviation industry is growing rapidly, and airline are facing increasing pressure to operate their flights in a safe, efficient, and cost-effective way. One of the most important aspects of airline operations is the scheduling of flight trajectories, which refers to planning the path an aircraft follows from its departure airport to its destination. Graph thickness, in the context of airlines, refers to the minimum number of planar graphs needed to represents the airline's route network. Airlines can use this concept to optimize flight schedules, resource allocation and even airport layouts. By understanding the graph thickness of their route network, airlines can minimize complexities, improve efficiency, and potentially reduce costs.

Flight level for aircraft

A flight level (FL) is a standardized way of expressing an aircraft's vertical position in the atmosphere using air pressure rather than height above sea level. It is based on a fixed reference pressure of 1013.25 hectopascals, which allows all aircraft to use the same altitude reference regardless of weather conditions. Flight levels are written as "FL" followed by a number that represents hundreds of feet; for example, FL300 means the aircraft is flying at approximately 30,000 feet. Flight levels are used above the transition altitude to maintain safe vertical separation between aircraft and to support efficient air traffic control. By using flight levels, pilots and air traffic controllers can manage air traffic more safely and consistently, especially during the cruise phase of flight.

Operational flight levels in domestic and international flight trajectories

Flight levels are selected according to the type and distance of airline operations in order to ensure safe and efficient flight performance. For domestic short-haul flights operating at relatively lower altitudes, aircraft typically cruise between FL260 and FL280. Domestic long-haul flights, which require longer cruising phases, generally operate at medium altitudes ranging from FL300 to FL340. In contrast, international airline flights usually cruise at higher altitudes, between FL350 and FL390, to achieve better fuel efficiency, reduced air traffic congestion, and improved long-range performance. These flight

level selections help air traffic controllers maintain proper vertical separation while supporting efficient trajectory scheduling.

Flight Trajectory

The following figure illustrates the flight trajectory network connecting domestic and international airports. The black vertices represent domestic airports, while the red vertices indicate international airports. The solid lines represent airline flight routes, and the arrows represent the direction of aircraft movement along each trajectory. The figure demonstrates how multiple flight paths converge and diverge at major hub airports, highlighting the complexity of airline trajectory scheduling. This network structure reflects the need for careful planning to manage air traffic flow, reduce congestion, and ensure safe and efficient flight operations across both domestic and international routes.

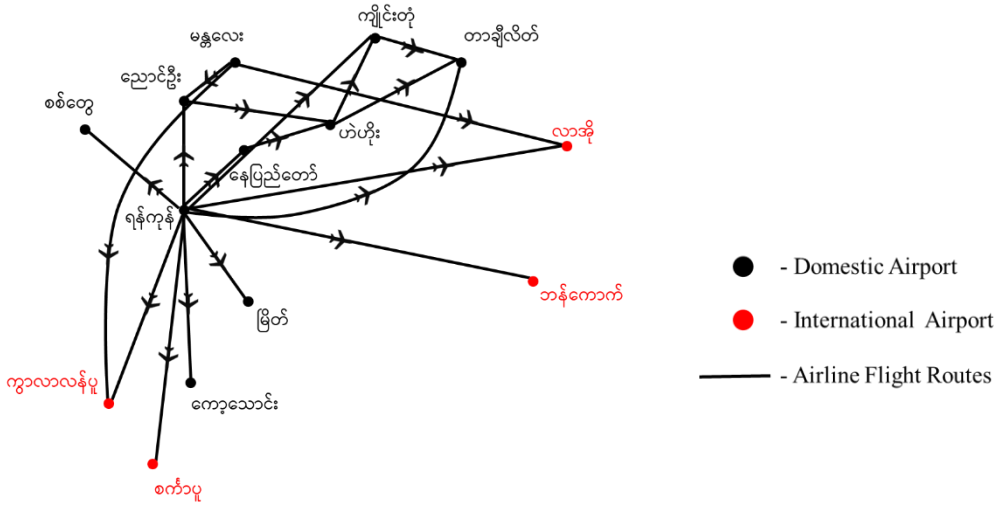

In the following, we focus on managing the complexity of intersecting and overlapping flight paths. The concept of graph thickness is used to divide the overall flight trajectory network into multiple layers. Each layer represents a planar subgraph in which route intersections are minimized, allowing flight trajectories to be scheduled at different altitude levels. By separating flight trajectories into layers using graph thickness, air traffic conflicts can be reduced, making airline operations safer and more efficient.

Flight trajectories for low altitude

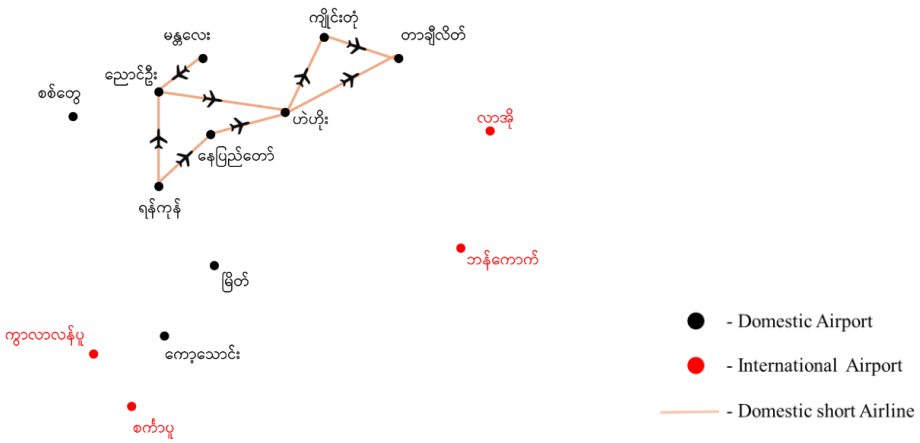

Flight trajectories for mid altitude

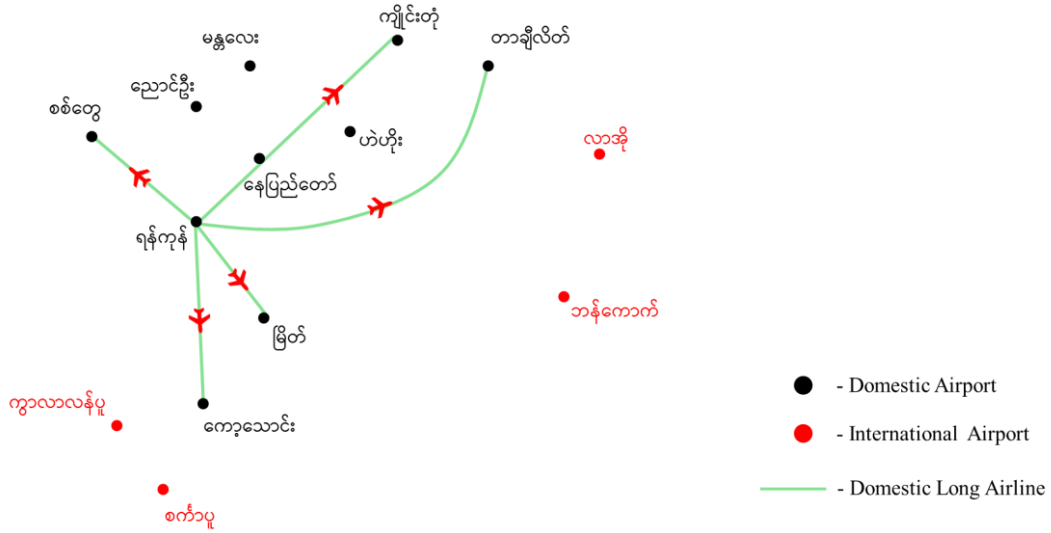

Flight trajectories for high altitude

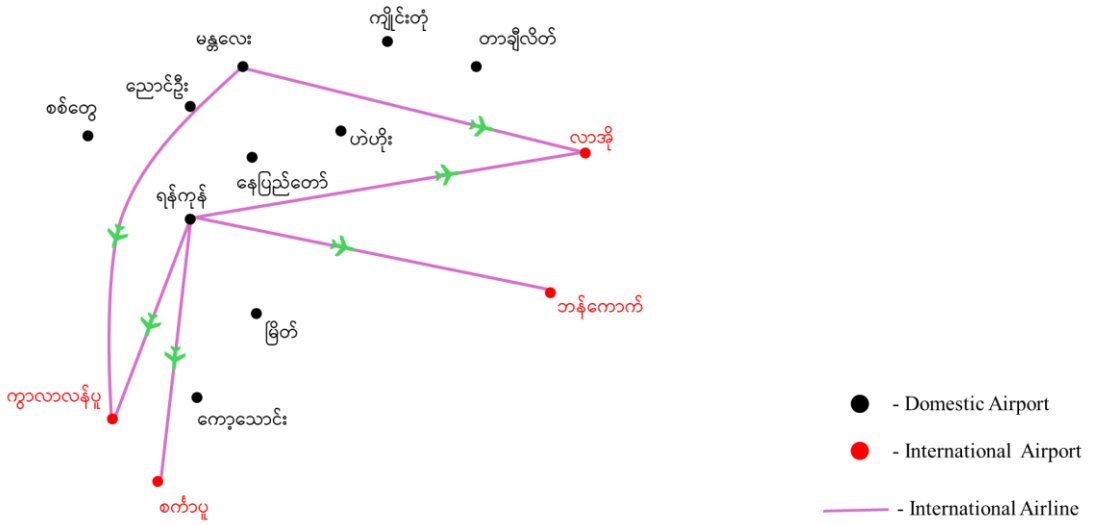

Conclusion

Graph theory is used to solve the various problems of electrical, mechanical and civil engineering. Planarity of graphs plays an important role in the design of electric circuits and in air traffic management. Flight route thickness indicates how the level of traffic on a route, with thicker routes carrying more flights between major airports or popular destinations. Busier routes require careful air traffic management to maintain safety and reduce delays, as well as improved infrastructure such as runways, radar systems and communication networks. Thick routes also result in higher fuel consumption and emissions. Therefore understanding route thickness helps airlines plan more efficient schedules, optimize traffic, and minimize environmental impact. Overall, analyzing route thickness is essential for improving operational efficiency, safety and strategic planning in aviation.

Acknowledgements

I would like to express our deepest gratitude to Dr Kay Thi Thin, Rector, Taunggyi University, for her suggestion and encouragement on my research. Then, I would like to express Dr Ko Ko Naing and Dr Aung Nay Myo, Pro-rector, Taunggyi University, for their interest on my research paper. Additionally, I would like to express my gratitude to Dr Ngwe Kyar Su Khaing, Professor, Head of Department of Mathematics, Taunggyi University, for her kind permission to present this paper.

References

Bondy, J.A and Murty, U.S.R., "Graph Theory with Applications", Macmillan Press Ltd., London, 1976.

Grossman, J.W., "Discrete Mathematics", Oakland University, New York, 1990.

Harary, F., "Graph Theory" Narosa Publishing House, New Delhi, 2000.

Johnsonbaugh, R., "Discrete Mathematics", Macmillan Publishing Company, New York, 1990.

Lipschutz, S and Lipson, M.L., "SCHAUM'S OUTLINE of Discrete Mathematics", Mc Graw-Hill, INC, New York, 2000.

Investigation of Fastest Routes From Pathein Highway Bus Station To Some Well-Known Places In Pathein

Ei Mon[1]

Abstract

We first present some definitions and notations in graph theory which are essential for this paper. Next, we discuss shortest path problem which is an important graph optimization problem and then we explore a route optimization algorithm called Dijkstra's algorithm. In this paper, using Dijkstra's algorithm, we investigate of the fastest routes from Pathein Highway Bus Station to some well-known places in Pathein, the capital of Ayeyarwady Region. The aim of this paper is to give the most efficient routes so that the visitors will be able to travel with minimal time and cost.

Keywords: path, route, shortest path, distance, weighted graph

Introduction

Graph is a mathematical structure used to model relationships between objects in real-life. In a graph model, objects are represented by dots called ***vertices*** and the relations between them are represented by lines called ***edges***. Shortest path problem is a fundamental concept in graph theory and computer science that focuses on finding the shortest path between two vertices in a graph. It is also a kind of travelling problem and finds the paths with minimum total weight (distance, time, or cost) between two distinct vertices in a connected weighted graph.

Dijkstra's algorithm is one to find the shortest path from a source vertex to any other vertices in a connected weighted graph and it was discovered by Dijkstra in 1959. In any connected graph, this algorithm can be used to find not only a shortest path from a source vertex u_0 to a specified one but also shortest paths from u_0 to all other vertices in the graph. In this paper, we use this algorithm to find the fastest routes from Pathein Highway Bus Station to some well-known places in Pathein such as Kan Thone Sint Park, Pathein University, Float Market, Ayeyarwady Region Education Office, Pathein General Hospital, Shwe Pyi Thar Zay, Shwe Moke Htaw Pagoda and Ocean Supermarket. We use symbol μ to denote the number of vertices in a graph.

Some Definitions and Notations in Graph Theory

A ***graph*** Γ consists of a set *N* of vertices and a set *M* of edges such that each edge $e \in M$ is associated with an unordered pair of vertices. If *e* is an edge associated with the vertices *v* and *w*, we can write $e = (v, w)$ or $e = (w, v)$. The vertices *v* and *w* are called the ***ends*** of *e*. A ***directed graph*** Γ consists of a set *N* of vertices (or nodes) and a set *M* of edges (or arcs) such that each edge $e \in M$ is associated with an ordered pair of vertices. If *e* is an edge associated with the ordered pair (*v*, *w*) of vertices, we write $e = (v, w)$, which denotes an edge from *v* to *w*. An edge *e* in *M* that is associated with the pair of vertices *v* and *w* is said to be ***incident*** on *v* and *w*, and *v* and *w* are said to be ***adjacent***. A ***weighted graph*** is a graph in which each edge is associated with a number called the ***weight*** of this edge (time, cost or distance).

[1] Dr., Assistant Lecturer, Department of Mathematics, Pathein University

A ***walk*** in a graph Γ is a finite sequence $S = v_0, e_1, v_1, e_2, v_2, ..., e_p, v_p$ whose terms are alternately vertices and edges, such that, for $1 \le i \le p$, the ends of e_i are v_{i-1} and v_i. The vertices v_0 and v_p are called ***origin*** and ***terminus*** of *S*. We say that *S* is a walk from v_0 to v_p, or a (v_0, v_p)- walk. The number of edges in *S* is called its ***length***. A ***path*** is a walk with no repeated vertices and edges. In a simple graph, a walk is determined by the sequence of its vertices. Two vertices *u* and *v* of Γ are said to be ***connected*** if there is a (*u, v*)-path in Γ. A ***connected graph*** is a graph in which we can get from any vertex to any other vertex on a path. If vertices *u* and *v* are connected in Γ, the ***distance*** between *u* and *v* in Γ, denoted $d(u,v)$, is the length of a shortest (*u, v*)-path in Γ. In a weighted graph, the ***length*** of a path is the total weight of this path.

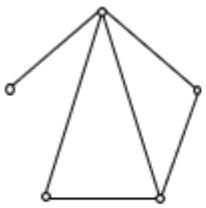

In Figure 1, walk: $v_1, e_1, v_2, e_2, v_3, e_3, v_4, e_5, v_2, e_6, v_5, e_4, v_4, e_5, v_2$.

Path: $v_1, e_1, v_2, e_2, v_3, e_3, v_4, e_4, v_5$.

Figure 1.

Shortest Path Problem

Shortest path problem is one of the optimization problems in graph theory. The aim of this problem is to find the path with minimum weight (distance, time, or cost) between two distinct vertices in a weighted graph.

Shortest Path Algorithm (Dijkstra's Algorithm)

We now present an algorithm for solving the shortest path problem. This algorithm finds the length of a shortest path from a source vertex u_0 to any other vertex *v* in a connected weighted graph Γ. In a weighted graph, the weight of each edge (a,b) is denoted by $\lambda(a,b)$ and the distance between *u* and *v*, denoted $d_\lambda(u,v)$, is the minimum total weight of (u,v)-path. We also denote the label of each vertex u_i as $l(u_i)$ for $0 \le i \le \mu - 1$ where μ is the number of vertices in Γ. If the algorithm terminates, $l(u_i)$ is the length of a shortest path from u_0 to u_i, i.e., $l(u_i) = d_\lambda(u_0, u_i)$.Now, we summarize the steps of the algorithm as follows:

Step 1. Set $l(u_0) = 0, l(v) = \infty$ for $v \ne u_0$, $\overline{P_0} = V \setminus P_0$.

Step 2. Assume that $P_i = \{u_0, u_1, \ldots u_i\}$ where $l(u) = d_\lambda(u_0, u)$ for each $u \in P_i$ and $\overline{P_i} = V \setminus P_i$.

Step 3. For each $v \in \overline{P_i}$ adjacent to u_i, replace $l(v)$ by $\min_{u_i \in P_i}\{l(v), l(u_i) + \lambda(u_i, v)\}$ where $0 \le i < \mu - 1$.

Step 4. Choose $v' \in \overline{P_i}$ such that $l(v') = \min_{v \in \overline{P_i}}\{l(v)\}$ and let $v' = u_{i+1}$.

Step 5. Set $P_{i+1} = P_i \cup \{u_{i+1}\}$.

Step 6. If $i = \mu - 1$, then $\overline{P_i} = \varnothing$ and the algorithm terminates, stop. Otherwise, go to step7.

Step 7. If $i < \mu - 1$, replace *i* by *i* +1 and go to step 3.

Application

Now we investigate of the fastest routes from Pathein Highway Bus Station to some well-known places in Pathein City applying the shortest path algorithm. The following graph represents some well-known places in Pathein City.

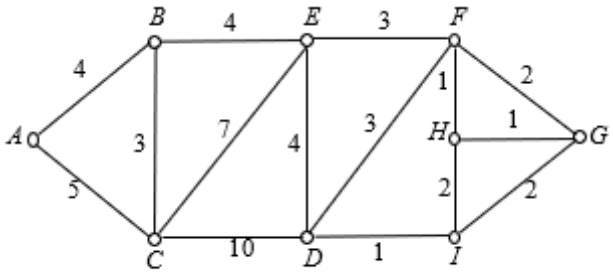

Figure 2.

In this graph model, Vertex "*A*" represents Pathein Highway Bus Station. Vertex "*B*" represents Kan Thone Sint Park. Vertex "*C*" represents Pathein University. Vertex "*D*" represents Float Market. Vertex "*E*" represents Ayeyarwady Region Education Office. Vertex "*F* " represents Pathein General Hospital. Vertex "*G*" represents Shwe Pyi Thar Zay. Vertex "*H*" represents Shwe Moke Htaw Pagoda. Vertex "*I*" represents Ocean Supermarket.

The number on each edge represents time taken from one place to another near one travelling by motorcycle at a speed of 0.2 miles per minute. Now, we wish to choose the fastest routes from Pathein Highway Bus Station to all other places mentioned in the graph so that we can save time and cost.

So, we consider the shortest paths from "*A*" to all other vertices in this graph using Dijkstra's algorithm.

According to the algorithm, set $l(A)=0$ and the labels of other vertices be ∞.

Let $P_0=\{A\}, \overline{P_0}=\{B,C,D,E,F,G,H,I\}$.

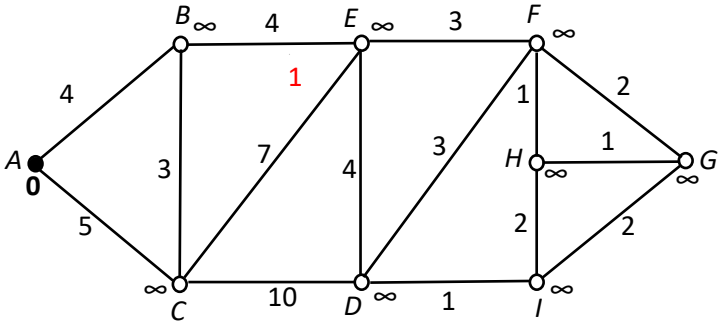

Figure 3.

The vertices adjacent to *A* are *B* and *C*. Then

$l(B)$ is replaced by $\min\{\infty, l(A)+\lambda(A,B)\}=\min\{\infty, 0+4\}=4$ and

$l(C)$ is replaced by $\min\{\infty, l(A)+\lambda(A,C)\}=\min\{\infty, 0+5\}=5.$

Since $\min\{l(B),l(C),l(D),l(E),l(F),l(G),l(H),l(I)\}=l(B)$, we choose vertex *B*.

Therefore $P_1=\{A,B\}, \overline{P_1}=\{C,D,E,F,G,H,I\}$ and hence the shortest path from *A* to *B* is "*A, B*" and d_λ (*A, B*) is 4 (see Figure 4).

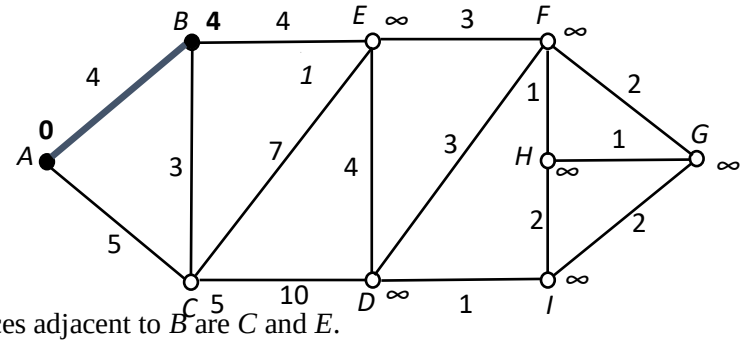

Figure 4.

The vertices adjacent to *B* are *C* and *E*.

Then $l(C)$ is replaced by $\min\{5, l(B)+\lambda(B,C)\} = \min\{5, 4+3\} = 5$ and

$l(E)$ is replaced by $\min\{\infty, l(B)+\lambda(B,E)\} = \min\{\infty, 4+4\} = 8.$

Since $\min\{l(C), l(D), l(E), l(F), l(G), l(H), l(I)\} = l(C)$, we choose vertex *C*.

Therefore $P_2 = \{A, B, C\}, \overline{P_2} = \{D, E, F, G, H, I\}$ and hence the shortest path from *A* to *C* is

"*A, C* " and d_λ (*A,C*) is 5 (see Figure 5).

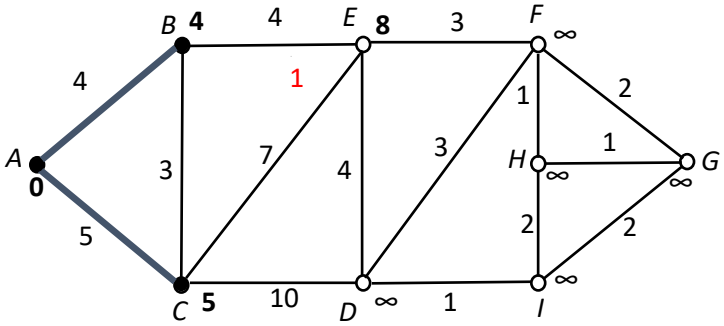

Figure 5.

The vertices adjacent to *C* are *E* and *D*.

Then $l(E)$ is replaced by $\min\{8, l(C)+\lambda(C,E)\} = \min\{8, 5+7\} = 8$ and

$l(D)$ is replaced by $\min\{\infty, l(C)+\lambda(C,D)\} = \min\{\infty, 5+10\} = 15.$

Since $\min\{l(D), l(E), l(F), l(G), l(H), l(I)\} = l(E)$,we choose vertex *E*.

Therefore $P_3 = \{A, B, C, E\}, \overline{P_3} = \{D, F, G, H, I\}$ and hence the shortest path from *A* to *E* is

"*A, B, E*" and d_λ (*A, E*) is 8 (see Figure 6).

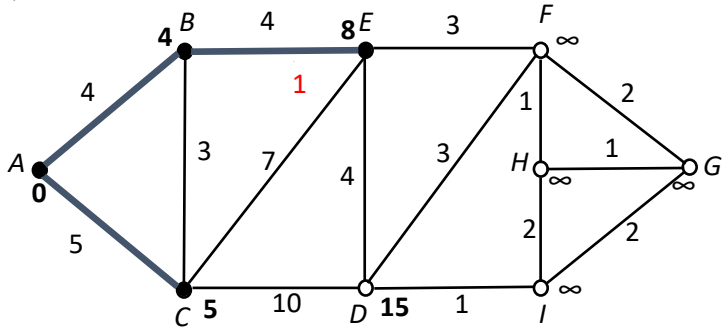

Figure 6.

The vertices adjacent to *E* are *D* and *F*.

Then $l(D)$ is replaced by $\min\{15, l(E)+\lambda(E,D)\} = \min\{15, 8+4\} = 12$ and

$l(F)$ is replaced by $\min\{\infty, l(E)+\lambda(E,F)\} = \min\{\infty, 8+3\} = 11.$

Since $\min\{l(D), l(F), l(G), l(H), l(I)\} = l(F)$, we choose vertex *F*.

Therefore $P_4 = \{A, B, C, E, F\}$, $\overline{P_4} = \{D, G, H, I\}$ and hence the shortest path from *A* to *F* is

"*A, B, E, F*" and d_λ (*A, F*) is 11 (see Figure 7).

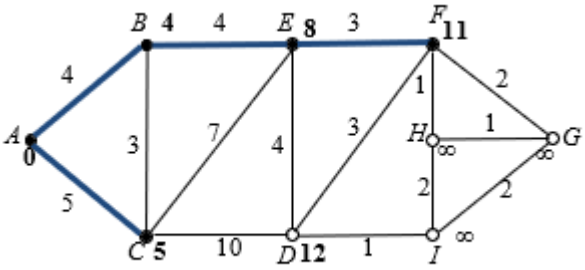

Figure 7.

The vertices adjacent to *F* are *D*, *G* and *H*. Then

$l(D)$ is replaced by $\min\{12, l(F)+\lambda(F,D)\} = \min\{12, 11+3\} = 12$,

$l(G)$ is replaced by $\min\{\infty, l(F)+\lambda(F,G)\} = \min\{\infty, 11+2\} = 13$ and

$l(H)$ is replaced by $\min\{\infty, l(F)+\lambda(F,H)\} = \min\{\infty, 11+1\} = 12$.

Since $\min\{l(D), l(G), l(H), l(I)\} = l(H)$ or $l(D)$, in this case, we can choose one of these two vertices. Now we choose vertex *H*.

Therefore $P_5 = \{A, B, C, E, F, H\}$, $\overline{P_5} = \{D, G, I\}$ and hence the shortest path from *A* to *H* is "*A, B, E, F, H*" and d_λ (*A, H*) is 12 (see Figure 8).

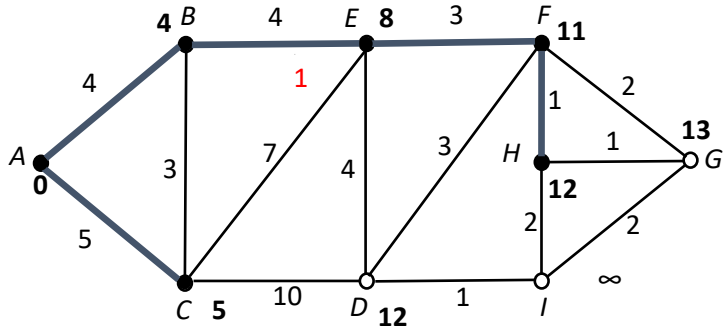

Figure 8.

The vertices adjacent to *H* are *G* and *I*. Then

$l(G)$ is replaced by $\min\{13, l(H)+\lambda(H,G)\} = \min\{13, 12+1\} = 13$ and

$l(I)$ is replaced by $\min\{\infty, l(H)+\lambda(H,I)\} = \min\{\infty, 12+2\} = 14$.

Since $\min\{l(D), l(G), l(I\} = l(D)$, we choose vertex *D*.

Therefore $P_6 = \{A, B, C, E, F, H, D\}$, $\overline{P_6} = \{G, I\}$ and hence the shortest path from *A* to *D* is "*A, B, E, D*" and d_λ (*A, D*) is 12 (see Figure 9).

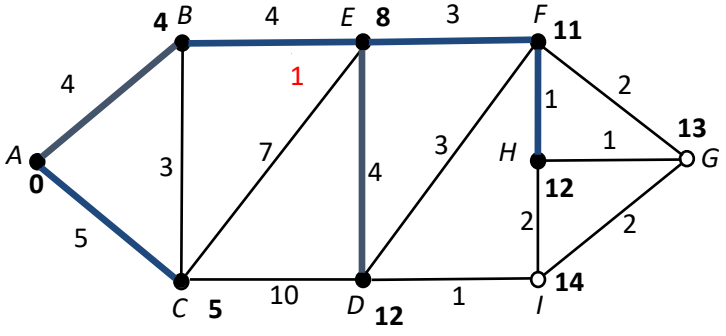

Figure 9.

The vertex adjacent to *D* is *I*.

Then $l(I)$ is replaced by $\min\{14, l(D)+\lambda(D,I)\} = \min\{14, 12+1\} = 13.$

Since $l(G) = l(I)$, we can choose any one. Now we choose *I*.

Therefore $P_7 = \{A, B, C, E, F, H, D, I\}, \overline{P_7} = \{G\}$ and hence the shortest path from *A* to *I* is "*A*, *B*, *E*, *D*, *I*" and $d_\lambda(A, I)$ is 13 (see Figure 10).

$l(G)$ is replaced by $\min\{13, l(H)+\lambda(H,G)\} = \min\{13, 12+1\} = 13$

$l(I)$ is replaced by $\min\{\infty, l(H)+\lambda(H,I)\} = \min\{\infty, 12+2\} = 14$

$P_6 = \{A, B, C, E, F, H, D\}$, $\overline{P_6} = \{G, I\}$

The shortest path from *A* to *D* is "*A*, *B*, *E*, *D*" and $d_\lambda(A, D)$ is 12 .

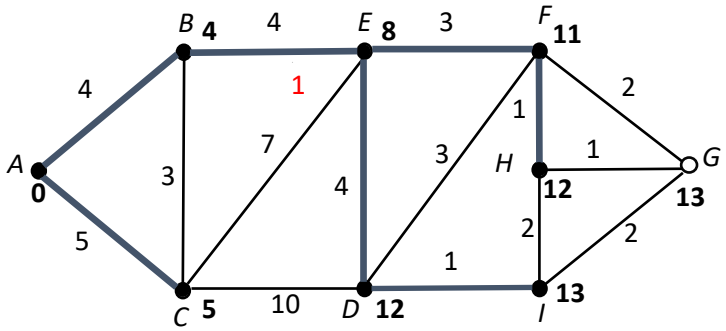

Figure 10.

The vertex adjacent to *I* is *G*. Then $l(G) = \min\{13, l(I)+\lambda(I,G)\} = \min\{13, 13+2\} = 13.$

We can only choose vertex *G*.

Therefore $P_8 = \{A, B, C, E, F, H, D, I, G\}, \overline{P_8} = \varnothing$ and hence the shortest path from *A* to *G* is "*A*, *B*, *E*, *F*, *H*, *G*" and $d_\lambda(A, G)$ is 13 (see Figure 11).

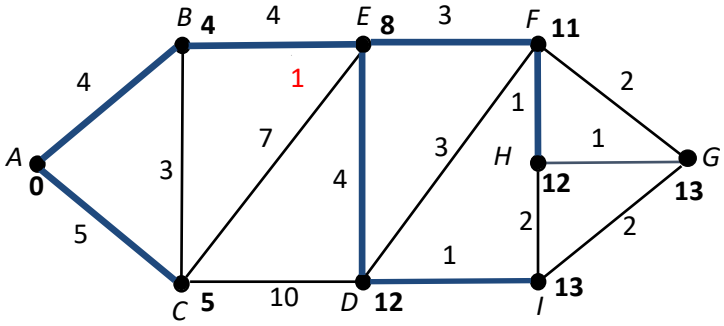

Figure 11.

At the end of this stage, we have found all fastest routes from Pathein Highway Bus Station to other well-known places in Pathein City. In each step of this investigation, the vertices to which the shortest paths have been founded are shown by black dots and the shortest paths obtained are shown by blue lines.

Result and Discussion

In this investigation, we found the efficient routes from Pathein Highway Bus Station to other eight places in Pathein and explored the time taken for these routes travelling by motorcycle at a speed of 0.2 miles per minute as the following:

Source	Destination	Route	Time taken
Pathein Highway Bus Station	Kan Thone Sint Park	*A, B*	4 mins
Pathein Highway Bus Station	Pathein University	*A, C*	5 mins
Pathein Highway Bus Station	Float Market	*A, B, E, D*	12 mins
Pathein Highway Bus Station	Ayeyarwady Region Education Office	*A, B, E*	8 mins
Pathein Highway Bus Station	Pathein General Hospital	*A, B, E, F*	11 mins
Pathein Highway Bus Station	Shwe Pyi Thar Zay	*A, B, E, F, H, G*	13 mins
Pathein Highway Bus Station	Shwe Moke Htaw Pagoda.	*A, B, E, F, H*	12 mins
Pathein Highway Bus Station	Ocean Supermarket	*A, B, E, D, I*	13 mins

Conclusion

In this paper, we successfully applied the Dijkstra's algorithm to investigate the fastest routes from Pathein Highway Bus Station to other well-known places such as Kan Thone Sint Park, Pathein University, Float Market, Ayeyarwady Region Education Office, Pathein General Hospital, Shwe Pyi Thar Zay, Shwe Moke Htaw Pagoda and Ocean Supermarket. This study indicates that a mathematical optimization method can effectively solve real-world transportation problems. Also, we will be able to find any other fastest routes from one place to other one using the explored algorithm in this paper. This research will aid the visitors in planning efficient trips within Pathein.

Acknowledgement

I would like to express my sincere gratitude to Dr Myo Min Tun, Acting Rector of East Yangon University and, Dr Aye Aye Ko and Dr Thida Aung, Pro-Rectors of East Yangon University, for their kind permission to do this research paper. I wish to express my thanks to Dr Sandar Maw, Professor and Head of Mathematics Department, East Yangon University for her kindness. Moreover, I also give my special thanks to Dr Nila Swe, Professor and Head of Mathematics Department, Pathein University for her invaluable guidance and encouragement throughout this study. Finally, I would like to thank to all my teachers including my parents for their supports and encouragement.

References

Bondy. J.A. & U.S.R. Murty, "*Graph Theory with Applications*", Fifth Printing, American Elsevier, New York, 1982.

Johnsonbaugh. R., "*Discrete Mathematics*", Sixth edition, Pearson Education, Inc., New Jersey, 2005.

Wilson. R.J., "*Introduction to Graph Theory*", Fourth Edition, Longman Group Ltd, England, 1996.

Maximum Number of Completely Independent Spanning Trees in Cycles and Complete Graphs

Aye Htet Htet Aung[1]

Abstract

In this paper, we first introduce fundamental definitions and notations in graph theory. Next, we describe some properties of trees and spanning trees, which are essential concepts in the study of network structures. We then present a characterization of completely independent spanning trees and investigate the maximum number of such trees in two significant classes of graphs: cycles and complete graphs. Finally, four locations in Pathein Township–namely City Monument, Koethein Ward, Pathein General Hospital, and Memorial Park–are modeled as the vertices of a complete graph to investigate their corresponding completely independent spanning trees. The results demonstrate how graph connectively affects network reliability and fault tolerance.

Keywords: completely independent spanning trees, cycles, complete graphs.

Introduction

Graph theory is one of the most important fields in mathematics. It is also widely used in real-life applications, including computer science, communication networks, transportation systems. Being crucial concepts in graph theory, independent spanning trees and completely independent spanning trees are also important. The paths from the rooted vertex to any vertices are openly-disjoint in independent spanning trees and the paths between any two vertices in completely independent spanning trees are also openly-disjoint. From these properties, we can see that completely independent spanning trees are more reliable and flexible. They are used in fault-tolerant communication, transportation and reliable data routing.

Some Definitions and Notations

In this section, we introduce some definitions and notations on graphs needed for our paper.

Definitions. [Bondy, 1982] A ***graph*** H consists of a set V of vertices together with a set E of edges connecting some pair of vertices. The vertices forming an edge are said to be ***incident*** with it, and the reverse is also true. Two edges which are incident with a common vertex are ***adjacent***, as are two vertices which are incident with a common edge. We use the symbols $|V(H)|$ and $|E(H)|$ to denote the numbers of vertices and edges in H. An edge is called a ***loop*** if it connects a vertex to itself. Two edges e_1 and e_2 of a graph H are said to be ***parallel*** if they have same ends. A graph with neither loops nor parallel edges is called a ***simple graph***. A ***degree*** of a vertex v denoted by $d(v)$ is the total number of edges that are incident to it. A ***path*** is a sequence of vertices and edges in which no vertex is repeated. A ***cycle*** is a path that starts and ends at the same vertex, with no repeated internal vertices. A cycle with m vertices denoted by C_m. A graph is ***connected*** when there is a path between any two vertices.

Example. We consider a graph H.

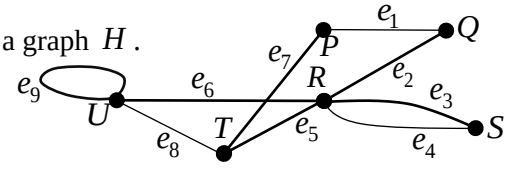

Figure 1.

[1]Assistant Lecturer, Department of Mathematics, Pathein University

In the figure, we can see that the graph H with vertex set $V(H)=\{P,Q,R,S,T,U\}$ and edge set $E(H)=\{e_1,e_2,e_3,e_4,e_5,e_6,e_7,e_8,e_9\}$. In a graph H, vertices P and Q are adjacent, and vertices P and U are not adjacent. Edges e_1 and e_2 are incident on Q. Edge e_9 is loop and edges e_3 and e_4 are parallel. Hence a graph H is not a simple graph. H is a connected graph.

Some Properties of Trees and Spanning Trees

In this section, we present some properties of trees and spanning trees with example.

Definitions. [Bondy, 1982] A ***tree*** is a connected graph in which there exists a unit path between every pair of vertices. A ***subgraph*** of a graph H is a graph whose vertex set and edge set are subsets of the $V(H)$ and *E(H).* A ***spanning tree*** of H is a subgraph which is tree and includes all the vertices of H.

Theorem. [Bondy, 1982] Let H be a graph. Then the sum of the degree of all vertices in H is twice of the number of edges in H.

Proof. See [Bondy, 1982]

Theorem. [Bondy, 1982] If H is a tree, then $|E(H)|=|V(H)|-1$.

Proof. See [Bondy, 1982]

Theorem. [Bondy, 1982] Let *T* be a spanning tree of a connected graph H and let *x* be an edge of H not in *T*. Then *T* + *x* contains a unique cycle.

Proof. See [Bondy, 1982]

Example. We consider a connected graph H, its tree I and spanning tree T.

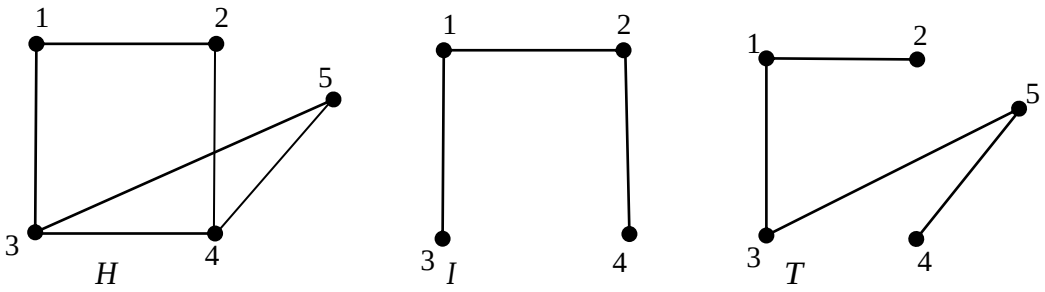

Figure 2.

The sum of the degree of all vertices in H is $2(6)=12$. Any two vertices in tree I are connected by a unique path. The number of edges in tree I is $4-1=3$ edges. *T* is a spanning tree of H and $T+(3,\ 4)$ contains a unique cycle.

A Characterization of Completely Independent Spanning Trees

In this section, we study some definitions and a characterization of completely independent spanning trees.

Definitions. [Hasunuma, 2001] Let P_1 and P_2 are paths of a graph H. We say that P_1 and P_2 are ***edge-disjoint*** if they have no edge in common. In a graph H, two paths P_1 and P_2 from a vertex x to another vertex y are called ***openly disjoint*** if P_1 and P_2 are edge-disjoint and have no common vertex except for x and y.

For example, we consider the openly disjoint paths in a graph H.

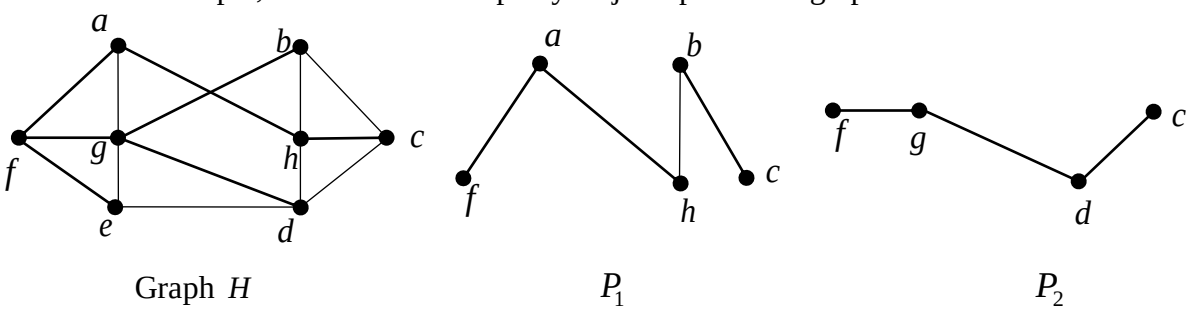

Graph H P_1 P_2

Figure 3. Two paths in graph H

In graph H, $P_1 : f\ a\ h\ b\ c$ and $P_2 : f\ g\ d\ c$. The paths from f to c in two paths are edge-disjoint and no common vertex except for f and c. Hence, P_1 and P_2 are openly disjoint.

Definition. [Hasunuma, 2001] A set of spanning trees where the paths between any two vertices in each tree are openly disjoint is called ***completely independent spanning trees.*** For a graph H, we denote the maximum number of completely independent spanning trees by $\mathrm{cist}(H)$.

The following lemma gives alternative definition of completely independent spanning trees.

Lemma. [Hasunuma, 2001] Suppose $T_1, T_2, \ldots, T_y$ are spanning trees of a graph H. Then, these spanning trees are completely independent if and only if they are edge-disjoint and, for every vertex $v \in V(H)$, there is at most one spanning tree T_j such that $d_{T_j}(v) > 1$.

Example. We consider the completely independent spanning trees in a graph H.

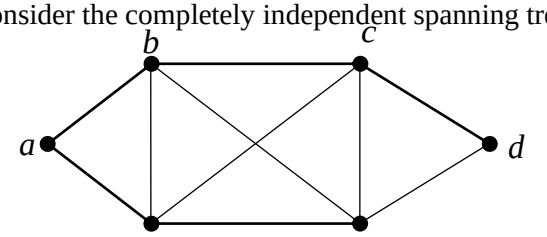

Figure 4. A graph H

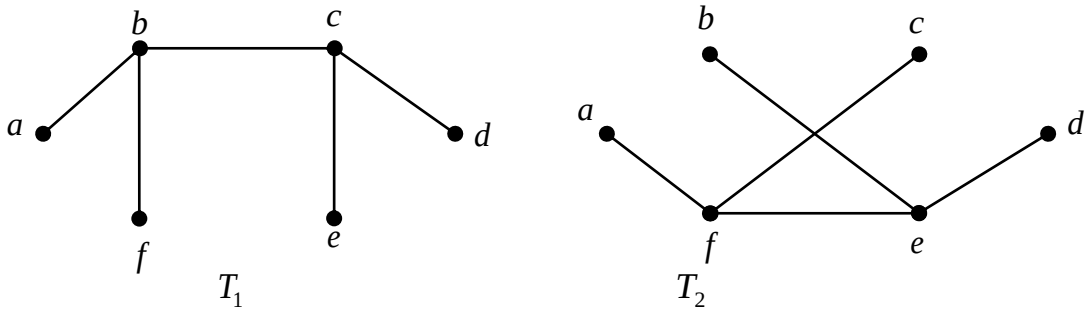

Figure 5. Completely independent spanning trees in H

In T_1 and T_2, the paths between any two vertices are openly disjoint. By Definition 3.3, T_1 and T_2 are completely independent spanning trees. Alternatively, T_1 and T_2 are edge-disjoint and for vertices b and c in H, there are at most one spanning tree T_1 such that $d_{T_1}(b) > 1$ and $d_{T_1}(c) > 1$. By Lemma 3.3, T_1 and T_2 are completely independent.

Completely Independent Spanning Trees in Cycles and Complete Graphs

In this section, we investigate the maximum number of completely independent spanning trees in some significant graphs such as cycles and complete graphs with examples.

Lemma. [Bondy, 1982] Let m be the number of vertices in cycle graph. Then the number of spanning trees in cycle graph C_m is m for $m \geq 3$.

Theorem. For $m \geq 3$, there exists a cycle C_m that does not contain two completely independent spanning trees, that is, $\text{cist}(C_m)$ is one.

Proof. We consider the cycle C_m, $m \geq 3$. A cycle C_m has only m edges. A spanning tree on m vertices require $(m-1)$ edges. We would need at least $2(m-1)$ edges to construct two completely independent spanning trees in C_m. However, since a cycle graph C_m contains only m edges, do not have enough edges to construct another spanning tree that is completely independent spanning trees. Therefore, a cycle graph C_m does not contain two completely independent spanning trees. This means that $\text{cist}(C_m) = 1$.

Example. We consider the cycle C_5. So, $V(C_5) = \{v_1, v_2, v_3, v_4, v_5\}$ and $E(C_5) = \{e_1, e_2, e_3, e_4, e_5\}$.

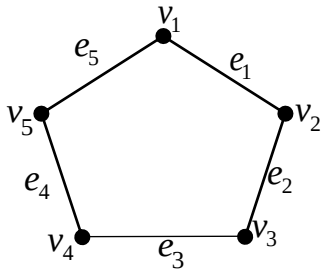

Figure 6. Cycle C_5

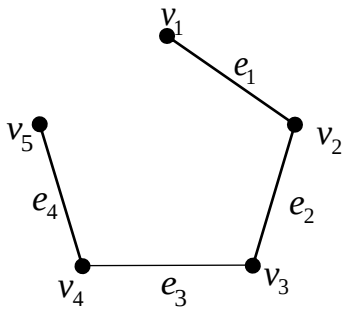

Figure 7. A spanning tree in C_5

Hence, cycle C_5 has at most one completely independent spanning trees.

Definition. [Bondy, 1982] A simple graph in which each pair of distinct vertices is joined by an edge is called a ***complete graph***. The complete graph on m vertices is denoted by K_m. The number of edges in K_m is $\frac{m(m-1)}{2}$.

Lemma. [Bondy, 1982] Let $m \geq 3$ be the number of vertices in complete graph. Then the number of spanning trees in complete graph K_m is m^{m-2}.

Theorem. [Hasunuma, 2015] For $m \geq 4$, K_m is a complete graph with m vertices. Then, $\text{cist}(K_m) = \left\lfloor \frac{m}{2} \right\rfloor$.

Proof. Since K_m has $\frac{m(m-1)}{2}$ edges and completely independent spanning trees are edge-disjoint, we obtain $\text{cist}(K_m) \leq \left\lfloor \frac{\frac{m(m-1)}{2}}{(m-1)} \right\rfloor = \left\lfloor \frac{m}{2} \right\rfloor$. Let $V(K_m) = \{u_1, u_2, u_3, u_4, ..., u_m\}$.

We first assume that $m = 2y$. For $1 \leq r \leq y$, let internal vertex set $V_r = \{u_{2r-1}, u_{2r}\}$. We define a spanning tree T_r, $1 \leq r \leq y$ as follows.

(a) Edges $u_{2r-1}u_{2r}$ is an edge of T_r.

(b) For $1 \leq s < r$, edges $u_{2r-1}u_{2s}$ and $u_{2r}u_{2s-1}$ are edges of T_r.

(c) For $r < s \leq y$, edges $u_{2r-1}u_{2s-1}$ and $u_{2r}u_{2s}$ are edges of T_r.

We can readily verify for any $r \neq s$ that two spanning trees T_r and T_s have no edge in common, and the vertices in V_r have degree 1 in T_s. Hence, by Lemma 3.3, these y spanning trees are mutually completely independent.

Next we suppose that $m = 2y+1$. For this case, we first construct y completely independent spanning trees $T_1, T_2, \ldots, T_y$ in K_{2y}. At this stage, let u_{2y+1} be the vertex of K_{2y+1} rather than in K_{2y}. By adding a vertex u_{2y+1} and an edge $u_{2y+1}u_{2r-1}$ to T_r, we construct the spanning tree T_r' of K_{2y+1}. It is evident that, $T_1', ..., T_y'$ are completely independent.

Example. We consider the complete graph K_6 with even vertices. Let $V(K_6) = \{v_1, v_2, v_3, v_4, v_5, v_6\}$. Since K_6 has 15 edges and completely independent spanning trees are edges-disjoint by Theorem 4.6, we obtain $\text{cist}(K_6) \leq \left\lfloor \frac{\frac{6(6-1)}{2}}{(6-1)} \right\rfloor = \left\lfloor \frac{6}{2} \right\rfloor = 3$.

For T_1,

when $r = 1$, edge v_1v_2 is an edge of T_1;

when $r = 1$, $s = 2$ edges v_1v_3 and v_2v_4 are edges of T_1;

when $r = 1$, $s = 3$, edges v_1v_5 and v_2v_6 are edges of T_1.

For T_2,

when $r = 2$, edge v_3v_4 is an edge of T_2;

when $r=2,\ s=1,$ edges v_3v_2 and v_4v_1 are edges of T_2;

when $r=2,\ s=3,$ edges v_3v_5 and v_4v_6 are edges of T_2.

For T_3,

when $r=3,$ edge v_5v_6 is an edge of T_3;

when $r=3,\ s=1,$ edges v_5v_2 and v_6v_1 are edges of T_3;

when $r=3,\ s=2,$ edges v_5v_4 and v_6v_3 are edges of T_3.

Therefore, the edge sets $E(T_1)=\{v_1v_2, v_1v_3, v_2v_4, v_1v_5, v_2v_6\}$, $E(T_2)=\{v_3v_4, v_3v_2, v_4v_1, v_3v_5, v_4v_6\}$ and $E(T_3)=\{v_5v_6, v_5v_2, v_6v_1, v_5v_4, v_6v_3\}$ of the three spanning trees are obtained. For clear visualization, the edges in $E(T_1), E(T_2)$, and $E(T_3)$ of K_6 are colored blue, green, and red, respectively. As a result, a colored graph K_6 is obtained, where each edge is colored uniquely and no overlapping edges are present.

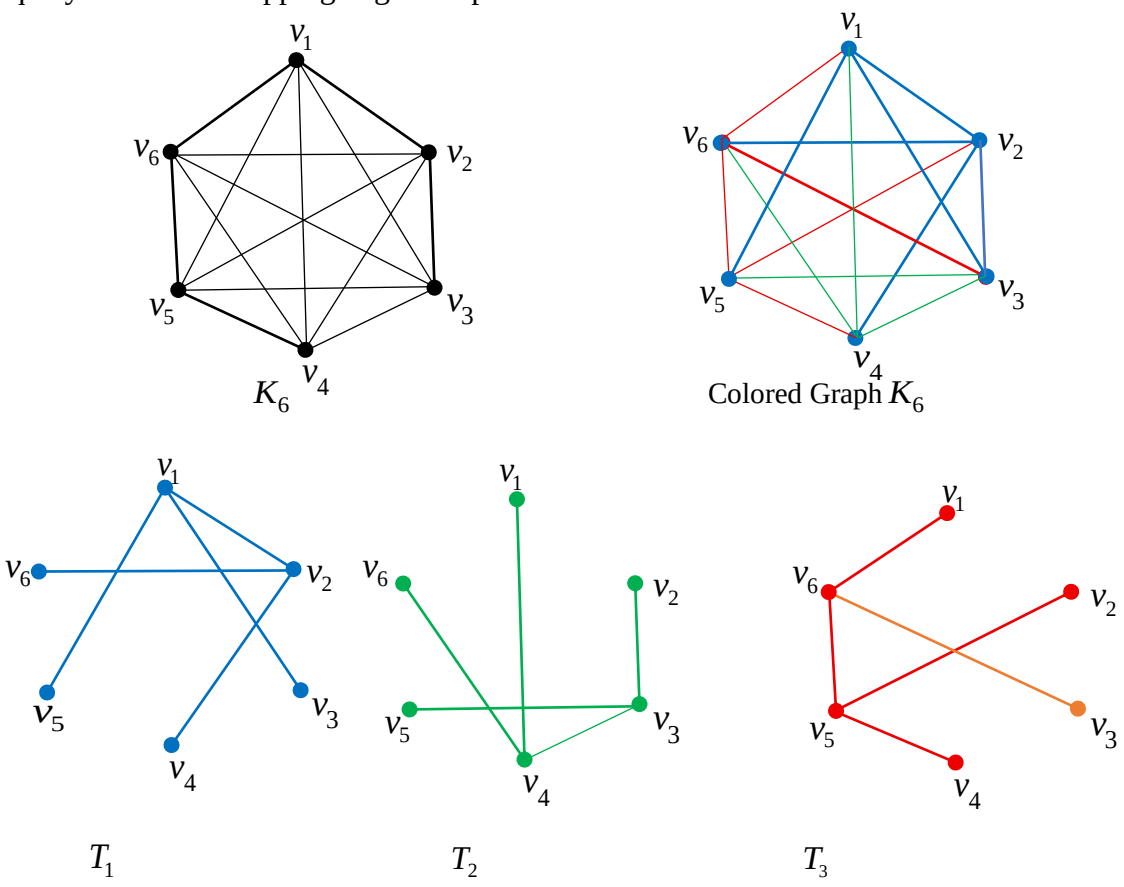

Figure 8. Completely independent spanning trees in K_6

Hence, the blue spanning tree T_1, the green spanning tree T_2 and the red spanning tree T_3 are the three completely independent spanning trees in K_6.

Completely Independent Spanning Trees in Real Life

We construct a complete graph K_4 in real life. We take four locations in Pathein Township, City Monument, Koethein Ward, Pathein General Hospital and Memoiral Park as

vertices for our graph. In the following map, each pair of distinct locations is joined by a road, represented as an edge in our graph. Thus, it is a complete.

Figure 9. A map in Pathein Township

We denote four vertices in Figure 9 as follows;

CM = City Monument,

KT = Koethein Ward,

PH = Pathein General Hospital and

MP = Memorial Park.

We describe the above map as a K_4 graph.

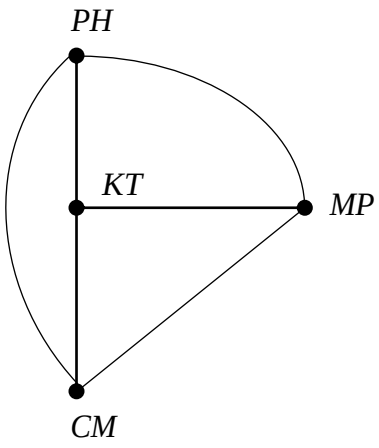

Figure 10. A K_4 graph in real life

We want to traverse all vertices in Figure 10 without sharing roads and internal locations. Therefore, applying the Theorem 4.6, we obtained

$E(T_1) = \{PH\ CM, CM\ KT, KT\ MP\}$ and $E(T_2) = \{KT\ PH, PH\ MP, MP\ CM\}$. The edges in $E(T_1)$ and $E(T_2)$ of K_4 are colored blue and green, respectively.

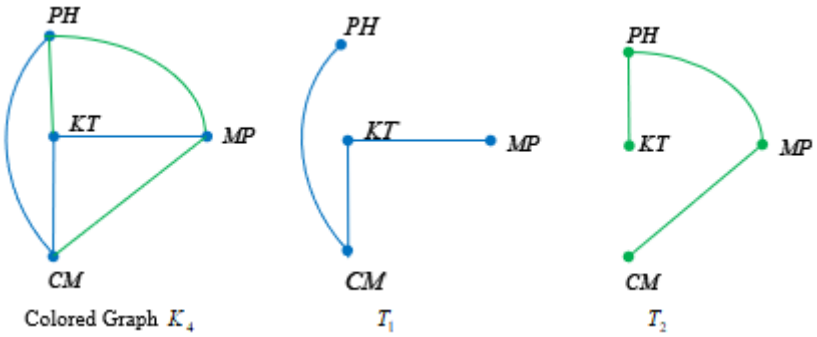

Figure.11 Completely independent spanning trees

As we can see, the above spanning trees T_1 and T_2 are completely independent with both edge-disjoint and internal vertex-disjoint. By using completely independent spanning trees, even if an edge (a road) fails in T_1, communication can still continue through the other tree T_2 without interruption.

Discussion

In this study, we explored cist(C_m) and cist(K_m). For cycles, the simple structure and limited number of edges restrict the construction to only one cist, as any additional spanning tree would inevitably share edges or internal vertices with the existing tree. In constant, complete graphs process high vertex connectively, enabling multiple cist(K_m) to exist.

Conclusion

In this paper, we have learned that although the maximum number of completely independent spanning trees in complete graph K_m is $\left\lfloor \frac{m}{2} \right\rfloor$, there cannot be two completely independent spanning trees in cycle graphs since it does not have enough edges. This paper shows that mathematical concepts are not just theoretical it also has practical uses in real life. From this paper, we have gained a deeper understanding of the usefulness of mathematics in our everyday lives.

Acknowledgements

I would like to express my deepest gratitude to Dr Myo Min Tun, Acting Rector of East Yangon University and, Dr Aye Aye Ko and Dr Thida Aung, Pro-Rectors of East Yangon University, for their permission to present the kind of research paper. I would like thank to Dr Sandar Maw, Professor and Head of Mathematics Department, East Yangon University, for her kindness me. Furthermore, I also especially thank to Dr. Nila Swe, Professor and Head of Mathematics Department, Pathein University for her advice and encouragement to do this work.

References

Bondy, J. A. & U.S.R. Murty., (1982), *Graph Theory with Applications*. Fifth Printing, American Elsevier, New York.

Hasunuma, T., (2001), “Completely independent spanning trees in the underlying graph of a line digraph”, Discrete Math, No. 234, pp 149-157.

Matsusshita, M., Y. Otachi, & T. Araki, (2015), “Completely independent spanning trees in (partial) K-trees”, Discuss. Math. Graph Theory, No. 35, pp 427-437.

A Comparative Study of Analytical Methods and Sumudu Transform Method For Solving Real-Life Differential Equation Models

San Lynn Aung[1]

Abstract

The main purpose of this paper is to conduct a comparative study of real-life differential equation models using analytical methods and Sumudu transform method. For this purpose, the basic concepts and properties of Sumudu transform are first presented. Next, the differential equation models involving first order and second order ordinary differential equations are solved by using analytical methods and Sumudu transform method. Finally, the study concludes by indicating which method, analytical or Sumudu transform, offers greater advantages in solving differential equations.

Keywords: Sumudu transform, analytical methods, linear differential equation models, real-life applications

Introduction

Ordinary differential equations play an important role in modeling many real-life phenomena arising in physics, engineering, and applied sciences. Processes such as population growth, Newton's law of cooling, mechanical vibrations, and electrical RLC circuits can be mathematically represented using first-order and second-order linear differential equations. Hence, the study of solution methods for such equations is essential for understanding real-world systems. Analytical methods, including the method of separation of variables and other classical techniques, provide direct and exact solutions for certain classes of differential equations. On the other hand, the Sumudu transform method offers a systematic and powerful approach, especially for solving linear differential equations with the given initial conditions. Each method has its own advantages and limitations depending on the nature of the problem. This study presents a comparative analysis of analytical methods and the Sumudu transform method in solving linear ordinary differential equation models.

Useful Definitions and Properties

In this section, the definitions of Sumudu transform and inverse Sumudu transform are described. Then, some properties of Sumudu transform are expressed.

Definition 1

A function h(t) is said to be of **exponential order** $\frac{1}{\mu}$, if there are positive constants $\frac{1}{\mu}$ and M such that

$$|h(t)| \le M e^{\frac{t}{\mu}}, \quad t \ge 0.$$

Definitions 2

The **Sumudu transform** defined for functions of exponential order is given over the set of functions

$$D = \{h(t) \mid \exists M, \mu_1, \mu_2 > 0 : |h(t)| < M e^{\frac{|t|}{\mu_j}}, \text{if } t \in (-1)^j \times [0, \infty)\} \tag{1}$$

by

[1] Dr., Lecturer, Department of Mathematics, Myingyan University

$$S[h(t);u]=\frac{1}{u}\int_0^{\infty}h(t)e^{-\frac{t}{u}}dt=H(u). \qquad (2)$$

The function h(t) in (2) is called the **inverse Sumudu transform** or **inverse** of H(u) and will be denoted by $S^{-1}[H(u)]$, that is, we write

$$h(t)=S^{-1}[H(u)]. \qquad (3)$$

Linear Property

If g and h are functions of t, and c is a constant, then

(i) $S[g(t)\pm h(t)]=S[g(t)]\pm S[h(t)]$,

(ii) $S[ch(t)]=cS[h(t)]$.

Change of Scale Property

If the Sumudu transform of h(t) is H(u) and c is a constant, then $S[h(ct)]=H(cu)$.

First Shifting Property

Let Sumudu transform of h(t) be H(u). Then

$$S[e^{ct}h(t)]=\frac{1}{1-cu}H\left(\frac{u}{1-cu}\right).$$

Second Shifting Property

If Sumudu transform of the function h(t) is H(u), then

$$S[h(t-a)U(t-a)]=e^{-\frac{a}{u}}H(u),$$

where U(t – a) is the unit step function defined by $U(t-a)=0$ when $t<a$ and $U(t-a)=1$ when $t>a$, $a\geq 0$.

Sumudu Transforms of Function Derivatives

If the Sumudu transform of h(t) is H(u), then

(i) $S[h'(t)]=\frac{1}{u}[H(u)-h(0)]$,

(4)

(ii) $S[h''(t)]=\frac{1}{u^2}[H(u)-h(0)-uh'(0)]$,

(5)

(iii) $S[h^{(n)}(t)]=\frac{1}{u^n}[H(u)-\sum_{k=0}^{n-1}u^k h^{(k)}(0)]$,

(6)

where $h^{(0)}(0)=h(0)$ and $h^{(k)}(0)$, $k=1,2,3,...,n-1$ is the k^{th} order derivative of the function g(t).

Sumudu Transforms of Some Elementary Functions

The Sumudu transforms of some elementary functions are presented in the following table.

Table 1

h(t)	$S[h(t)] = H(u)$
1	1
t	u
t^2	$2u^2$
$t^n,\ n \geq 0$	$n!u^n$
e^{at}	$\frac{1}{1-au}$
sin at	$\frac{au}{1+a^2u^2}$
cos at	$\frac{1}{1+a^2u^2}$

Applications to Real-Life Problems

In this section, real-life problems such as population growth, decay, Newton's law of cooling, and electrical circuit models are comparatively studied using analytical methods and Sumudu transform method.

Applications to Population Growth and Decay Problems

The population growth (growth of a plant, or a cell, or an organ, or a species) is governed by the first-order linear ordinary differential equation as

$$\frac{dR(t)}{dt} = KR(t) \tag{7}$$

with initial condition $R(t_0) = R_0$, where K is a positive real number, R is the amount of population at time t and R_0 is the initial population at time $t = t_0$.

The decay problem of the substance is defined mathematically by the following first-order linear ordinary differential equation as

$$\frac{dR(t)}{dt} = -KR(t) \tag{8}$$

with initial condition $R(t_0) = R_0$, where R is the amount of substance at time t, K is a positive real number and R_0 is the initial amount of the substance at time $t = t_0$.

Example 1

The doubling time of a population of flies is eight days. If there are initially 100 flies, then we consider the population of flies in 17 days.

This problem can be written in mathematical form as:

$$\frac{dR(t)}{dt} = KR(t), \tag{9}$$

where K is the constant of proportionality and R is the amount of flies population at time t. We consider R_0 is the initial amount of flies population at $t = 0$.

(i) *Sumudu Transform Method*

Taking Sumudu transform on both sides of (9), we get

$$\frac{1}{u}S[R(t)] - \frac{1}{u}R(0) = KS[R(t)].$$

At $t = 0$, $R = R_0 = 100$, we have

$$S[R(t)] = \frac{100}{1-Ku}.$$

Applying the inverse Sumudu transform to the above equation, we obtain

$$R(t) = 100e^{Kt}. \tag{10}$$

When $t = 8$, $R = 2R_0 = 200$, then (10) becomes

$$K = \frac{1}{8}\log_e 2 \simeq 0.0866.$$

We required R when $t = 17$, then (10) becomes

$$R(17) = 100\,e^{(0.0866)17} \simeq 435.88 \text{ flies.}$$

(ii) *Separation of Variables Method*

By using the method of separation of variables for (9), we get

$$\frac{1}{R}dR = Kdt.$$

Integrating on both sides of above equation, we have

$$R = Ae^{Kt}.$$

Using the initial condition and the boundary condition, we get

$$R(t) = 100e^{0.0866t}.$$

When $t = 17$, we get $R(17) = 100\,e^{(0.0866)17} \simeq 435.88$ flies.

Example 2

Suppose that a substance has a half-life of eight days. If there are 40 grams present now, then we consider the amount of substance left after three days.

This problem can be written in mathematical form as:

$$\frac{dR(t)}{dt} = -KR(t), \tag{11}$$

where K is the constant of proportionality and R is the amount of the substance at any time t. We consider R_0 is the initial amount of the substance at time $t = 0$.

(i) *Sumudu Transform Method*

Applying Sumudu transform on both sides of (11), we get

$$\frac{1}{u}S[R(t)] - \frac{1}{u}R(0) = -KS[R(t)].$$

At $t = 0$, $R = R_0 = 40$, we have

$$S[R(t)] = \frac{40}{1+Ku}.$$

Taking the inverse Sumudu transform to the above equation, we obtain

$$R(t) = 40e^{-Kt}. \tag{12}$$

When $t = 8$, $R = \frac{1}{2}R_0 = 20$, then (12) becomes

$$K = -\frac{1}{8}\log_e(0.5) \simeq 0.0866.$$

We required R when $t = 3$, then (12) becomes

$$R(3) = 40\,e^{-(0.0866)3} \simeq 30.85 \text{ grams.}$$

There are 30.85 grams of the substance remaining after three days.

(ii) *Separation of Variables Method*

By using the method of separation of variables for (11), we get

$$\frac{1}{R}dR = -Kdt.$$

Integrating on both sides of above equation, we have

$$R = Ae^{-Kt}.$$

Using the initial condition and the boundary condition, we get

$$R(t) = 100e^{-0.0866t}.$$

When $t = 3$, we get $R(3) = 40\,e^{-(0.0866)3} \simeq 30.85$ grams.

Application to Newton's Law of Cooling Problem

Newton's law of cooling, which has a very important position in physics, is also modeled by differential equations. This law explains how the temperature change in an object occurs depending on the difference between the temperature of the object and the temperature of the environment in which the object is located. Newton's law of cooling states that a hot body releases heat energy into its environment. While this energy transfer is taking place, as the temperature difference decreases, the energy transfer decreases and eventually the hot

body equalizes with the ambient temperature. Newton's law of cooling is generally modeled by the first-order linear ordinary differential equation:

$$\frac{dN}{dt} = -k(N - N_e) \tag{13}$$

with the initial condition $N(t_0) = N_0$, where N is the temperature of the object, N_e is the constant temperature of the environment, N_0 is the initial temperature of the object at time t_0 and k is the constant of proportionality. In (13), the negative sign in the right hand side is taken because the temperature of the body is decreasing with time and so the derivative $\frac{dN}{dt}$ must be negative.

Example 1

A hot coffee with initial temperature of 115˚F is kept in a room temperature of 35˚F. The rate of change of temperature is 20˚F per minute. We consider how long it will take coffee to cool down to a temperature of 40˚F.

According to Newton's law of cooling, this problem can be written in the mathematical form as:

$$\frac{dN}{dt} = -k(N - 35) \tag{14}$$

with initial conditions $N(0) = 115$, $N'(0) = -20$.

Using the initial condition, we get $k = 0.25$.

Then (14) becomes

$$\frac{dN}{dt} = -0.25(N - 35). \tag{15}$$

(i) *Sumudu Transform Method*

Taking the Sumudu transform to (15), we have

$$\frac{1}{u}S[N(t)] - \frac{1}{u}N(0) = -0.25S[N(t)] + 0.25(35).$$

Using the initial condition and partial fraction, we get

$$S[N(t)] = \frac{80}{1 + 0.25u} + 35.$$

Applying the inverse Sumudu transform to the above equation, we obtain

$$N(t) = 80e^{-0.25t} + 35. \tag{16}$$

We required t when $N = 40$, then (16) becomes

$$t = \frac{1}{0.25}\log_e 16 \simeq 11.09 \text{ min.}$$

The coffee will take 11.09 minutes for cooling to a temperature of 40˚F.

(ii) *Integrating Factor Method*

From (15), we get $P(t) = 0.25$ and $Q(t) = 8.75$.

The integrating factor is $e^{0.25t}$.

Multiplying (15) by the integrating factor, we get

$$e^{0.25t}\frac{dN}{dt}+0.25e^{0.25t}N=8.75e^{0.25t},$$

$$\frac{d}{dt}(Ne^{0.25t})=8.75e^{0.25t}.$$

Integrating both sides, we have

$$N(t)=35+Ce^{-0.25t}.$$

Using the initial condition, we get

$$N(t)=35+80e^{-0.25t}.$$

When $N=40$, we get $t=\frac{1}{0.25}\log_e(16)\simeq 11.09$ min.

Application to Electrical Circuit Problem

A simple electrical circuit consists of the circuit elements connected in series with a switch (K), a battery supplying an electromotive force (e.m.f) (E) (in volts), an inductor (L) (in henrys), a resistance (R) (in ohms) and a capacitor (C). When the circuit is completed, a charge Q (Coulombs) will flow to the capacitor plates. The time rate flow of charge is $\frac{dQ}{dt}=I$, where I is the current at time t.

The potential voltage drop across a circuit element are:

(i) Voltage drop across a resistance $=RI=R\frac{dQ}{dt}$.

(ii) Voltage drop across a capacitor having capacitance $=\frac{Q}{C}$.

(iii) Voltage drop across an inductor having inductance $=L\frac{dI}{dt}=L\frac{d^2Q}{dt^2}$.

(iv) Voltage drop across a generator, supplying an e.m.f = voltage rise $=-E$.

The differential equation for determination of Q is obtained by the use of Kirchhoff's law. We get

$$L\frac{d^2Q}{dt^2}+R\frac{dQ}{dt}+\frac{Q}{C}-E=0.$$

Example 1

An indicator of 2 henrys, a resistor of 16 ohms and a capacitor of 0.02 farads are connected in series with an e.m.f of 300 volts. At $t=0$, the charge on the capacitor and current in the circuit are zero. We will find the charge and current at any time t.

Let Q and I be instantaneous charge and current respectively at time t.

By using Kirchhoff's law, we have

$$L\frac{dI}{dt}+RI+\frac{Q}{C}-E=0,$$

$$2\frac{dI}{dt}+16I+\frac{Q}{0.02}=300,$$

$$\frac{d^2Q}{dt^2}+8\frac{dQ}{dt}+25Q=150$$

(17)

with initial condition $Q(0)=0,\ I(0)=Q'(0)=0$.

(i) *Sumudu Transform Method*

Taking Sumudu transform to (17), we get

$$\frac{1}{u^2}S[Q(t)]-\frac{1}{u^2}Q(0)-\frac{1}{u}Q'(0)+\frac{8}{u}S[Q(t)]-\frac{8}{u}Q(0)+25S[Q(t)]=150\ .$$

Using the initial conditions, we get

$$\left(\frac{1+8u+25u^2}{u^2}\right)S[Q(t)]=150,$$

$$S[Q(t)]=\frac{150u^2}{1+8u+25u^2}=6-\frac{6+48u}{(1+4u)^2+9u^2}$$

$$=6-6\frac{1+4u}{(1+4u)^2+(3u)^2}-8\frac{3u}{(1+4u)^2+(3u)^2}\ .$$

We take the inverse Sumudu transform of this equation, the charge is

$$Q(t)=6-6e^{-4t}\cos 3t-8e^{-4t}\sin 3t\ .$$

Then the current is

$$I=\frac{dQ}{dt}=50e^{-4t}\sin 3t\ .$$

(ii) *Method of Undetermined Coefficients*

The homogeneous equation of (17) is

$$\frac{d^2Q}{dt^2}+8\frac{dQ}{dt}+25Q=0\ . \qquad (18)$$

The characteristic equation of (18) is

$$\lambda^2+8\lambda+25=0\ ,$$

$$\lambda=-4\pm 3i\ .$$

The complementary function of (18) is

$$Q_c=e^{-4t}(A\cos 3t+B\sin 3t)\ .$$

To choice Q_p for the particular solution,

$$Q_p = K,\ \frac{dQ_p}{dt} = 0 \text{ and } \frac{d^2Q_p}{dt^2} = 0.$$

In (17), we get $K = 6$.

The particular solution is

$$Q_p = 6.$$

The general solution of (17) is

$$Q(t) = Q_c + Q_p = e^{-4t}(A\cos 3t + B\sin 3t) + 6.$$

Differentiation on both sides of above equation, we get

$$Q'(t) = e^{-4t}(-3A\sin 3t + 3B\cos 3t) - 4e^{-4t}(A\cos 3t + B\sin 3t).$$

Using the initial conditions, we get $A = -6$ and $B = -8$.

The charge Q is

$$Q(t) = e^{-4t}(-6\cos 3t - 8\sin 3t) + 6.$$

Then, the current is

$$I = \frac{dQ}{dt} = 50e^{-4t}\sin 3t.$$

Conclusion

In this paper, real-life differential equation models were solved using both classical analytical methods and the Sumudu transform method. The solutions obtained by analytical methods and the Sumudu transform method are presented and compared. For all the considered real-life models, both methods yield the same exact solutions. However, the Sumudu transform method requires fewer computational steps and provides a more systematic procedure, especially in handling initial value problems. On the other hand, analytical methods give a clearer understanding of the structure of the solutions. Therefore, the Sumudu transform method can be considered an efficient and reliable alternative for solving real-life differential equation models.

Acknowledgements

First of all, we would like to express our sincere gratitude to Acting Rector Dr Myo Min Tun and Pro-Rectors, East Yangon University, for their kind permission to submit this paper to East Yangon University Research Journal. Moreover, we deeply thank to Dr Sandar Maw, Professor and Head, Department of Mathematics, East Yangon University, for her valuable advice and guidelines to perform this paper. Finally, we want to thank Dr Nila Swe, Professor and Head, Department of Mathematics, Pathein University, for kindly granting permission to present this paper at East Yangon University.

References

Aggarwal, S., Sharma, S. D., Kumar, N. and Vyas, A., (2020), "*Solutions of Population Growth and Decay Problems Using Sumudu Transform*", International Journal of Research and Innovation in Applied Science, Vol. 5, Issue 7, pp. 21-26.

Asiru, M. A., (2002), "*Further Properties of the Sumudu Transform and its Applications*", International Journal of Mathematical Education in Science and Technology, Vol. 33, No. 3, pp. 441-449.

Edwards, C. H. and Penney, D. E., (2008), *Elementary Differential Equations*, Sixth Edition, Pearson Education, Inc., Upper Saddle River, New Jersey 07458.

Kreyszig, E., (2011), *Advanced Engineering Mathematics*, Tenth Edition, John Willey & Sons, Inc., New York.

San Lynn Aung and Khin Than Sint, (2025), "*Applications of α-Modified Sumudu Transform to Real-Life Problems*", Iconic Research and Engineering Journals, Vol. 8, Issue 12, pp. 1709-1714.

Sanap, R. S. and Patil, D. P., (2022), "*Kushare Integral Transform for Newton's Law of Cooling*", International Journal of Advances in Engineering and Management, Vol. 4, Issue 1, pp. 166-170.

Watugala, G. K., (1993), "*Sumudu Transform: A New Integral Transform to Solve Differential Equations and Control Engineering Problems*", International Journal of Mathematical Education in Science and Technology, Vol. 24, pp. 35-43.

Zill, D. G., (2024), *A First Course in Differential Equations with Modeling Applications*, Twelfth Edition, Boston, Massachusetts, Cengage Learning.

A Mathematical Model For Waste Collection on Eyu Campus

Ei Shwe Zin[1]

Abstract

The campus road network is modeled as a weighted graph, where vertices represent buildings and edges represent roads within the EYU campus. The key concepts of graph theory and fundamental theorems related to Eulerian graph, Euler tour, and Euler trail are presented. Fleury's algorithm is used to construct Euler tours in Eulerian graphs and Euler trails in semi-Eulerian graphs. For non-Eulerian graphs, the Chinese Postman Problem (CPP) algorithm is applied to obtain a route with minimal total distance, after which the graph becomes an Eulerian graph and an Euler tour is constructed using Fleury's algorithm. The results show that graph theory provides an effective solution to waste collection problems.

Keywords: Eulerian graph, Euler tour, Euler trail, Fleury's algorithm, Chinese Postman Problem (CPP) algorithm, waste collection

Introduction

Graph theory is an important branch of discrete mathematics and is widely used in real-life problems such as transportation, routing, network design, and logistics. A graph is a mathematical structure used to model relationships between objects. One of the earliest and most well-known problems in graph theory is the **Seven Bridges of Konigsberg problem**, which was solved by Leonhard Euler. This problem led to the introduction of Eulerian graphs and became the foundation of modern graph theory. Such a route can be constructed using **Fleury's algorithm,** provided that the graph satisfies Euler's conditions. However, many real-world networks do not satisfy these conditions because they contain vertices of odd degree.To address this limitation, the **Chinese Postman Problem (CPP) algorithm** was introduced. By duplicating a minimum set of edges, a non-Eulerian graph can be transformed into an Eulerian graph. This transformation allows Eulerian traversal method such as Fleury's algorithm, to be applied. In this study, the CPP is applied to a campus road network to demonstrate how graph theory can be efficiently used to solve practical routing problems.

Fundamental definitions of graphs

In this section, we introduce some basic definitions and notations of graphs.

A ***graph*** consists of a set of vertices and a set of edges. Each edge connects an unordered pair of vertices. If an edge connects vertices x and y, it is denoted by $e=(x,y)$ or $e=(y,x)$, then e is said to ***join*** x and y, the vertices are called the ***ends*** of edge e. An edge is said to be i***ncident*** with its end vertices. Two vertices are called ***adjacent*** if they are connected by a common edge. Similarly, two edges are ***adjacent*** if they share a common vertex. The number of edges incident with a vertex is called the ***degree*** of that vertex. An edge whose ends are the same vertex is called a ***loop***. A loop contributes two to the degree of the vertex. An edge with two distinct ends is called a ***link***. If a graph contains more than one edge joining the same pair of vertices, such edges are known as ***multiple edges (parallel edges)***, and the graph is called a ***multigraph***. A ***weighted graph*** is a graph in which each edge is assigned a numerical value, called its ***weight***.

A graph is said to be ***connected*** if there exists a path between every pair of vertices. Otherwise, the graph is called ***disconnected***. A ***walk*** in a graph is a finite sequence of vertices and edges in which vertices and edges appear alternately, and each edge joins the vertices that precede and follow it in the sequence. The first and last vertices of a walk are called the ***origin*** and ***terminus,*** respectively, while the remaining vertices are referred to as

[1]Dr., Lecturer, Department of Mathematics, Dawei University

internal vertices. A ***path*** is a walk in which all vertices are distinct. A ***cycle*** is a closed path in which the first and last vertices are the same, and all other vertices are distinct. A ***trail*** is a walk in which no edge is repeated. An edge is a ***bridge*** if deleting it disconnects the graph. In a weighted graph, the ***weight*** of a walk is defined as the sum of the weights of its edges. An edge is said to be ***duplicated*** if an additional edge with the same weight is added between the same pair of vertices.

Basic concepts of Eulerian graphs

In this section, we present basic concepts of Eulerian graphs and key theorems related to Eulerian graphs, Euler trails, and Euler tours.

Definitions. A trail that traverses every edge of a graph is called an ***Euler trail***. A ***tour*** of a graph is a closed walk that traverses each edge of a graph at least once. An ***Euler tour*** is a tour which traverses every edge of the graph exactly once. A graph is called an ***Eulerian graph*** if it contains an Euler tour. A graph is said to be ***semi-Eulerian graph*** if it contains an Euler trail. If a graph contains neither an Euler tour nor an Euler trail, it is called a ***non-Eulerian graph***.

Example. Figure 1 illustrates three types of graphs. Graph (i) is a non-Eulerian graph, Graph (ii) is a semi-Eulerian graph, and graph (iii) is an Eulerian graph.

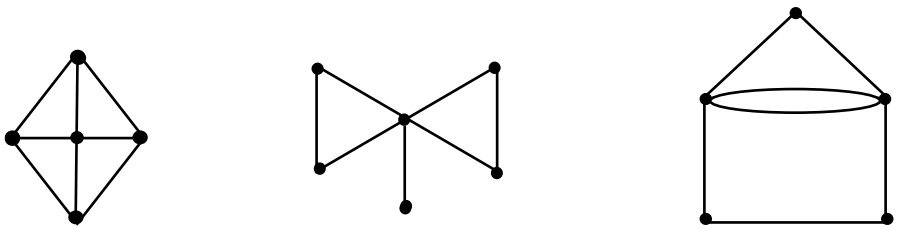

(i) (ii) (iii)

Figure 1.

Theorem. For any graph *H*, the total sum of the degrees of all vertices is equal to twice the number of edges in the graph.

Corollary. In any graph *H*, the number of vertices having odd degree is always even.

Theorem. A nonempty connected graph is an Eulerian graph if and only if it every vertex of the graph has even degree.

Theorem. A connected graph has an Euler trail if and only if it has exactly two vertices of odd degree.

Theorem. If *H* is an Eulerian graph, then any trail obtained by applying Fleury's algorithm in *H* forms an Euler tour of *H*.

Materials

For the waste collection application within the East Yangon University (EYU) campus, nine key buildings are selected and represented as vertices in the graph. The selected vertices are defined as follows:

Vertex	Represented Buildings
M	Main gate
H	Convocation hall
L	Library
P	Building (1)
Q	Building (2)
R	Building (3)
S	Building (4)
T	Teacher dormitories (3)
C	Canteen

Each edge weight denotes the vehicular travel distance between two vertices in meters (m), obtained from Google Maps. The edge weights are as follows:

Edge	Weight
(H,S)	322
(H,Q)	483
(H,M)	644
(H,P)	483
(H,R)	161
(H,L)	322
(L,R)	73
(L,C)	161
(L,T)	161
(T,R)	137
(T,C)	64
(R,C)	128
(P,C)	322
(P,M)	322
(P,Q)	322
(Q,M)	322

Based on the vertices and the weighted edges, the campus road network is represented as a connected weighted undirected graph.

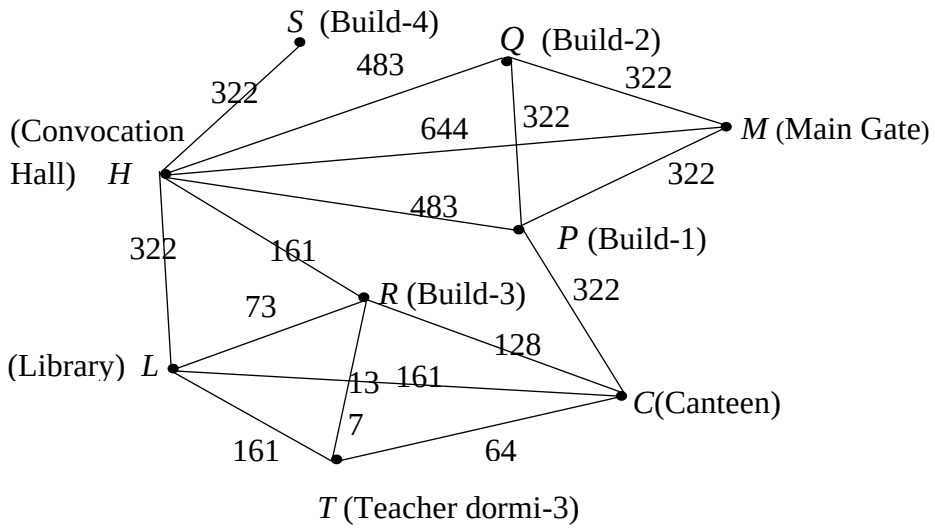

Figure 2.

Methods

The methodology of this study is based on graph degree analysis and the application of Eulerian graph algorithms to determine an optimal waste collection route.

Degree analysis of the graphs

In the given graph, the degree of each vertex is obtained by counting the number of edges connected to it. Based on the degree distribution, the graph is classified as Eulerian, semi-Eulerian, or non-Eulerian. If all vertices have even degree, the graph is Eulerian graph, and if exactly two vertices have odd degree, the graph is semi-Eulerian graph, then by using Fleury's algorithm**.** A trail can be drawn starting at one of the odd vertices and finishing at the other odd vertex. If more than two vertices have odd degree, the graph is non-Eulerian, then by using Chinese Postman Problem (CPP) algorithm.

Fleury's algorithm

An algorithm for finding an Euler tour and an Euler trail is

Step 1. If the graph has an Euler tour, start at any vertex. If the graph has only an Euler trail, start at one of the vertices with odd degree.

Step 2. From the current vertex, choose an edge that has not yet been used, provided that the chosen edge is not a bridge, unless there is no other choice.

Step 3. Traverse the chosen edge, add it to the Euler tour or Euler trail, and then delete that edge from the graph.

Step 4. Repeat Step 2 and Step 3 until all edges of the graph have been used.

Identification and pairing of odd degree vertices

If the graph is classified as non-Eulerian graph, all vertices with odd degree are identified. These vertices indicate the points at which additional traversals are required in order to obtain an Eulerian graph. In a connected weighted graph, the number of odd degree vertices is always even. In the Chinese Postman Problem (CPP) algorithm, these vertices must be paired to transform the graph into an Eulerian graph. If there are two odd degree vertices, only one is possible. For four odd degree vertices, three distinct pairing exist. As the number of odd degree vertices increases, the number of possible pairings grow rapidly. In general, for n odd degree vertices the number of possible pairing is given by $(n\text{-}1)(n\text{-}3)\ldots 1$.

Chinese Postman Problem (CPP) algorithm

An algorithm for finding an optimal Chinese Postman route is

Step 1. Find all vertices with odd numbers of edges emerging from them.

Step 2. These vertices should be listed in all the possible pairings.

Step 3. Find the shortest distance between each vertex of the pair, then add up the total for each set of pairs.

Step 4. Choose the set of all pairs with the minimum total distance. This is added on to the sum of all the edges to give the shortest distance to traverse the network and return to the original point of entry.

Example. Use Fleury's Algorithm to find an Euler tour starting with vertex *a* in the following graph.

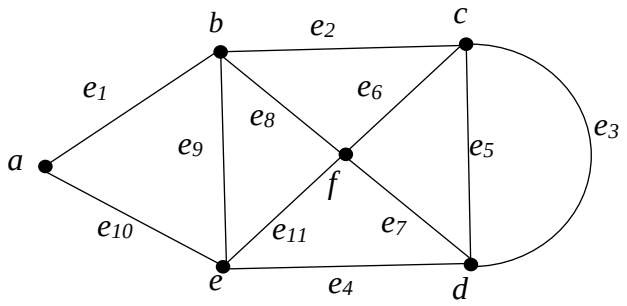

Figure 3.

Starting with the vertex *a*, we traverse the edge e_1 as e_1 is not a bridge. So, we get $C = (ae_1b)$. Then e_1 is deleted, and we obtain the following graph.

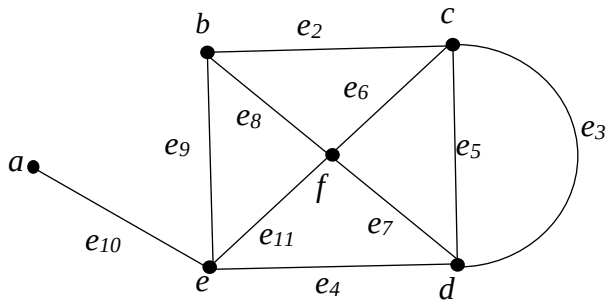

Figure 4.

Now, let us traverse the edge e_9, to get $C = (ae_1be_9e)$. Deleting the edge e_9, we get the following graph.

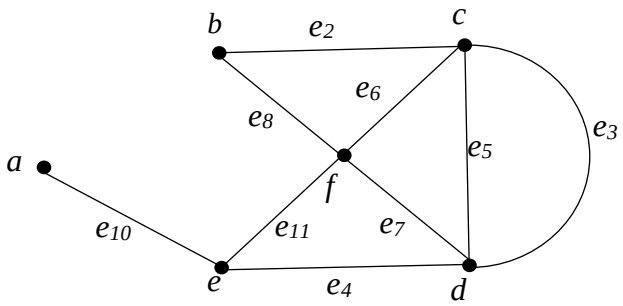

Figure 5.

We cannot traverse the edge e_{10} (which is a bridge), so we must use either e_{11} or e_4.Traversing e_{11}, we get $C = (ae_1be_9ee_{11}f)$. After deleting the edge e_{11} the graph obtain is as follows:

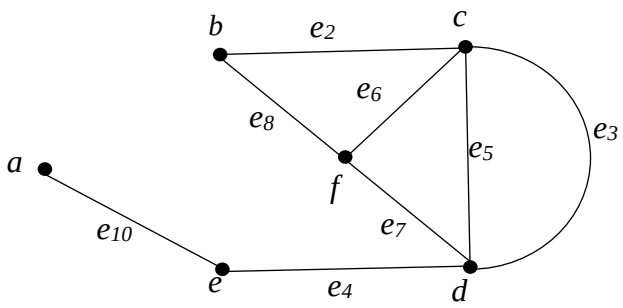

Figure 6.

Now we traverse the edge e_8 to get $C = (ae_1be_9ee_{11}fe_8b)$. The graph resulting from the removal of edge e_8 is as follows:

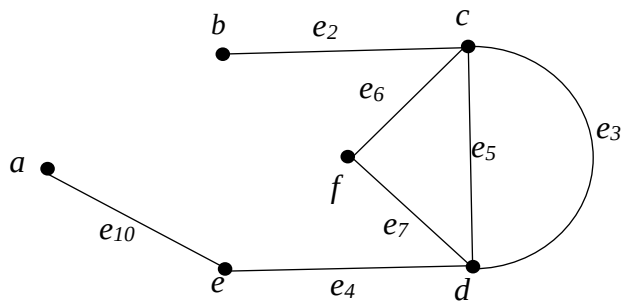

Figure 7.

Now from vertex b we have to traverse the bridge e_2 as there is no alternative. Hence $C = (ae_1be_9ee_{11}fe_8be_2c)$. Deleting the edge e_2, and also the resulting isolate vertex b , we get the as follows:

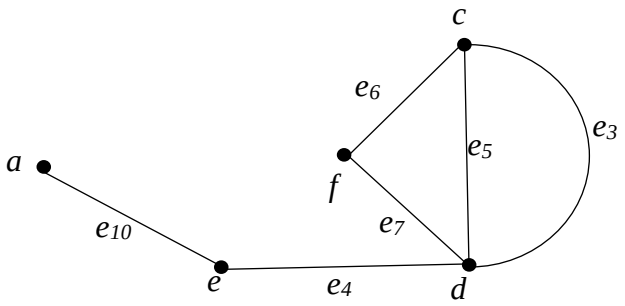

Figure 8.

Now we traverse the edge e_3 to get $C = (ae_1be_9ee_{11}fe_8be_2ce_3d)$. After deleting the edge e_3 the graph obtained is as follows

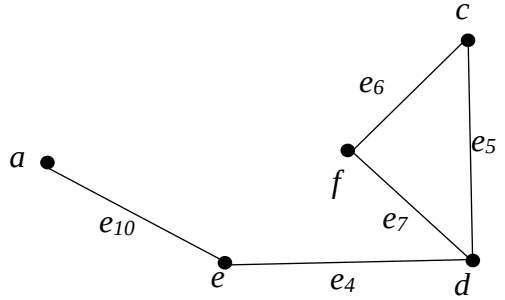

Figure 9.

From the vertex *d* we cannot traverse the bridge e_4 as there are other edges available. We traverse edge e_7 to get $C = (ae_1be_9ee_{11}fe_8be_2ce_3de_7f)$. The graph after deleting the edge e_7 is given below.

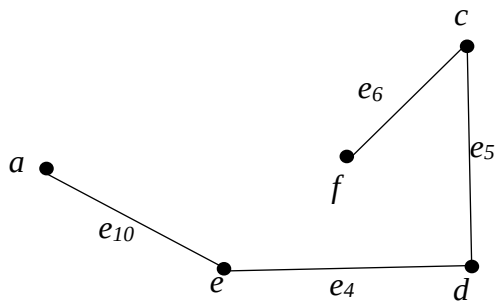

Figure 10.

Now all the edges in the graph above are bridges, and so traversing them in order we get $C = (ae_1be_9ee_{11}fe_8be_2ce_3de_7fe_6ce_5de_4ee_{10}a)$ which is the desired Euler tour.

Application of Eulerian graph

The EYU campus road network was analyzed using a weighted graph with nine vertices representing major buildings. Since the graph is not Eulerian, these vertices must be paired to apply the Chinese Postman Problem (CPP) algorithm.

Step 1. The constructed graph contains four vertices of odd degree, namely *S, Q, M,* and *T* . **Step 2 &3.** All possible pairings of the odd degree vertices were examined. Pairing *S* with *Q* gives a shortest path of length 805 *m*, while pairing *M* with *T* gives a shortest path of length 708 *m*. The total additional distance in this case is 1513 *m*. If *S* is paired with *M*, the shortest path of length 966 *m*. The remaining vertices *Q* and *T* are connected by a shortest path of length 708 *m*, giving a total additional distance of 1674 *m*. When vertices *S* and *T* are paired, the shortest path has length 620 *m*. The remaining vertices *Q* and *M* are connected by a shortest path of length 322 *m*. Hence, the total additional distance required is 942 *m*, which is the minimum among all possible pairings.

Step 4. Accordingly, the shortest paths (*S,T*) and (*Q,M*) were duplicated in the graph, resulting in an Eulerian graph.

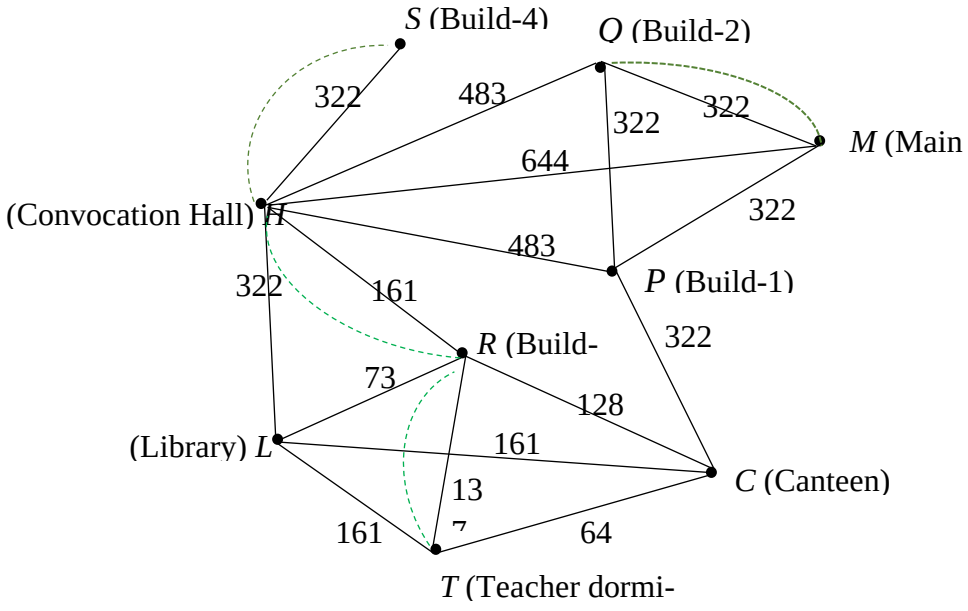

Figure 11.

After duplicating the shortest paths (*S,T*) and (*Q,M*), all vertices in the graph have even degree, and the network becomes Eulerian graph (see Figure 11). The duplicated edges are indicated in the figure 11 to distinguish them from the original edges. An Euler tour was then constructed on the modified graph using Fleury's algorithm. Starting and finishing at vertex *M* is *MQHMPCRTCLRTLHSHRHPQM*.

The total length of the original graph's edges is 4427 *m*, and the length of the duplicated edges is 942 *m*, resulting in a grand total of 5369 meters.

Results and Discussion

Based on the application, an optimal route for waste collection on the EYU campus roads was determined using the Chinese Postman Problem (CPP) algorithm. The original graph was a non-Eulerian graph because some vertices had an odd degree, so the minimum number of edges was duplicated to make it an Eulerian graph. The final route covers a total distance of 5369 meters, which is more efficient than a random traversal of the network. This route reduces repeated travel and improves overall routing efficiency.

Conclusion

In this research, the Chinese Postman Problem (CPP) algorithm was applied to optimize waste collection routes in the campus road network. By duplicating a minimum number of edges, the graph was transformed into an Eulerian graph, allowing an Euler tour to be constructed using Fleury's algorithm. According to this research work, using the CPP algorithm together with Fleury's algorithm provides an efficient route for waste collection on the EYU campus, reducing travel distance, time, and operational costs. This approach demonstrates how graph theory and algorithmic methods can be effectively used to solve practical routing problems in real-world networks.

Acknowledgements

First of all, we would like to express our sincere gratitude to Dr Myo Min Tun, Acting Rector of East Yangon University for his kind consent to the submission of this research paper. Moreover, we deeply thank to Dr Aye Aye Ko and Dr Thida Aung, Pro-Rectors, East Yangon University for their encouragement to do this research. We are also grateful to Professor Dr Sandar Maw, Head of Mathematics Department, East Yangon University, for her valuable suggestions, constructive criticisms of the manuscript and supervision. We deeply express our thanks to Dr Aye Aye Maw and Dr Wai Wai Tun, Professors of Mathematics Department, East Yangon University, for providing their advice for our research paper.

References

Bondy, J.A. & U.S.R. Murty., (1982) *Graph Theory with Application,* The Macmillan Press Ltd, New York.

Bostock, L. & Chandler, S., (2000) *Decision Mathematics*, Cheltenham, UK: Nelson Thornes.

Finding the Optimal Tourism Route Planning in Southern Shan State Using the Christofides Algorithm

Hsu Myat Htet[1]

Abstract

Tourism route planning is finding efficient travel routes between multiple destinations. This study applies the Christofides algorithm as a near-optimal mathematical method for tourism route planning in Southern Shan State. The results show that the routes created by the Christofides algorithm are very efficient and suitable for practical tourism planning. This study shows that approximation algorithms can be useful in real-world tourism networks and provides a foundation for future research on improving tourism routes.

Keywords: Christofides algorithm, Complete graph, Eulerian circuit, Hamiltonian graph, Tourism route, Travelling Salesman Problem, Weighted graph.

Introduction

Tourism is an important part of the economy, and travel planning carefully is key to improving the travel experience and saving resources. Tourists often visit many places, and finding the best route can save time, reduce costs, and make travel easier. However, as the number of destinations increases, finding the shortest route becomes computationally challenging.

The Travelling Salesman Problem (TSP) is a real-world problem that deals with finding the shortest route between multiple destinations. In mathematics, it is illustrrated using
a Hamiltonian graph, where each destination is a point (vertex) and each path between destinations is a line (edge). The goal is to find a Hamiltonian cycle that visits each point once and returns to the starting point with the shortest total distance. While it is possible to find an exact solution for a small number of places, it becomes too hard as the number of destinations grows. Therefore, approximate methods are more practical for real-world situations.

In this research, the Christofides algorithm, a well-known method for approximating the TSP, is used to plan tourism routes in Southern Shan State, Myanmar. The algorithm finds routes that are close to the shortest possible and guarantees that the total distance is the best possible route. It can create near-optimal routes that are practical and easy to use.

This method can help reduce travel time, make travel more convenient for tourists, and improve the planning of tourism routes. The results also provide a base for future research on improving tourism routes in Myanmar and similar regions. This study shows how approximation methods and Hamiltonian graphs can be used in real-world tourism route planning and why they are useful both mathematically and practically.

Aim

The aim of this study is to show how the Christofides algorithm can quickly generate near-optimal routes for short-term tourism planning and demonstrate how mathematical methods can efficiently solve real-world problems.

[1] Tutor, Department of Mathematics, Meiktila University

Methodology

Elements of graph theory

A **graph** G = (V, E) is defined as a structure consisting of a set of vertices V and a set of edges E. A graph is said to be **complete** if it is a simple graph in which every pair of distinct vertices is connected by exactly one edge; when each edge is assigned a numerical value, the graph is referred to as a **complete weighted graph**.

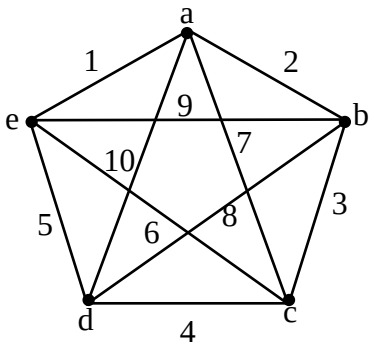

Figure (1) A complet weighted graph

The connectivity of a graph is a fundamental property, and a graph is connected if there exists at least one path between every pair of vertices. A walk is an alternating sequence of vertices and edges in which repetitions are permitted. A closed trail or circuit is a walk that begins and ends at the same vertex and does not repeat any edge. And, a closed path or cycle is a walk that begins and ends at the same vertex and does not repeat any vertex or edge, except for the initial and terminal vertex. A spanning cycle is a cycle that visits every vertex of the graph exactly once. A graph is Hamiltonian if it contains a spanning cycle, known as a Hamiltonian cycle, and Eulerian if it contains an Eulerian circuit that traverses every edge exactly once.

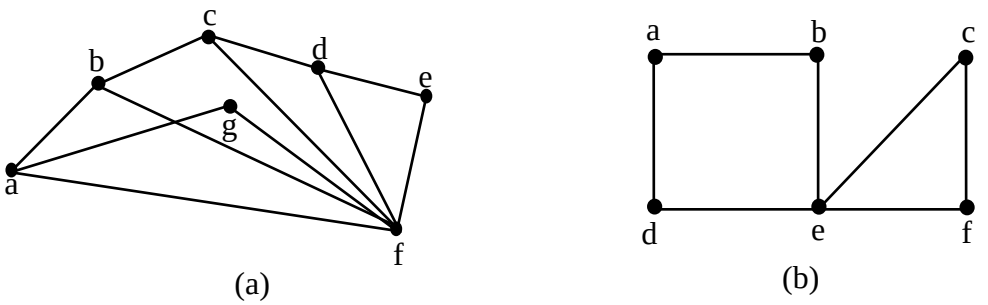

Figure (2): (a) Hamiltonian graph and (b) Eulerian graph

A tree is a connected, acyclic graph, and a spanning tree of G is a spanning subgraph of G that is a tree. And, a minimum spanning tree is a spanning tree of a weighted graph with the minimum possible total edge weight.

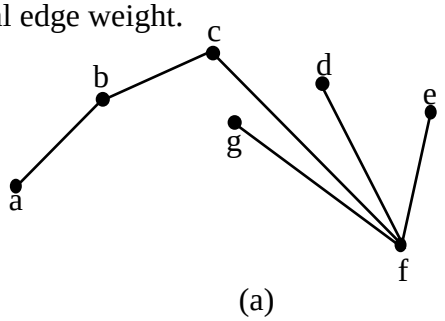

Figure (3): Tree

A matching M in a simple graph G = (V, E) is a subset of the set E of edges of the graph such that no two edges are incident with the same vertex. A perfect matching in a graph is a subset of edges where every vertex is incident to exactly one edge, matching all vertices.

The Travelling Salesman Problem (TSP)

The Travelling Salesman Problem (TSP) is a fundamental combinatorial optimization problem that seeks a tour visiting all locations exactly once while minimizing the total travel distance. In the context of tourism route planning, each location represents a tourist destination, and the travel distance between locations corresponds to the cost of moving from one destination to another. By modeling tourism routes as a complete weighted graph, where vertices represent locations and edges represent feasible travel routes, the problem can be formulated as finding a Hamiltonian cycle that efficiently connects all destinations. This representation provides a structured framework for applying algorithmic approaches, such as the Christofides algorithm, to generate near-optimal solutions that are practical for real-world applications.

Christofides Algorithm

The Christofides algorithm is an approximation algorithm for the Travelling Salesman Problem, where the edge weights satisfy the triangle inequality. It guarantees a solution that is the weight of the optimal tour. To solve the Travelling Salesman Problem using the Christofides algorithm we can use the following steps:

Step 1: Find a minimum spanning tree (T) using Kruskal's algorithm.

(Build the minimum spanning tree that connects all vertices (tourism locations) with the minimum weight edge without forming cycle.)

Step 2: Find a minimum weight perfect matching (M) among vertices with odd degree in (T).

Step 3: Combine the minimum spanning tree (T) and the edges of the minimum weight perfect matching (M) to make a multigraph.

Step 4: Find an Eulerian circuit.

Step 5: Convert the Eulerian circuit into a Hamiltonian cycle.

Finding Near-optimal tourism route with Christofides Algorithm

This section describes the application of Christofides algorithm to determine a near-optimal tourism route in Southern Shan State. The selected cities are Taunggyi (T), Pindaya (P), Ywangan (Y), Mt. Osi (O), Kalaw (K), and Inle Lake (I). The tour starts and ends at Taunggyi, with the remaining cities included in the route planning.

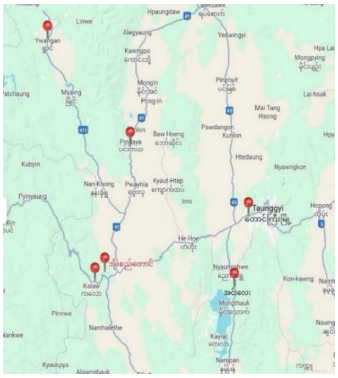

Figure (4) Tourism Network in Southern Shan State

A route network in Southern Shan State can be represented as a complete weighted graph, where each vertex corresponds to a town, each edge corresponds to a highway connecting two cities, and the weight of each edge represents the distance (in miles) between the towns.

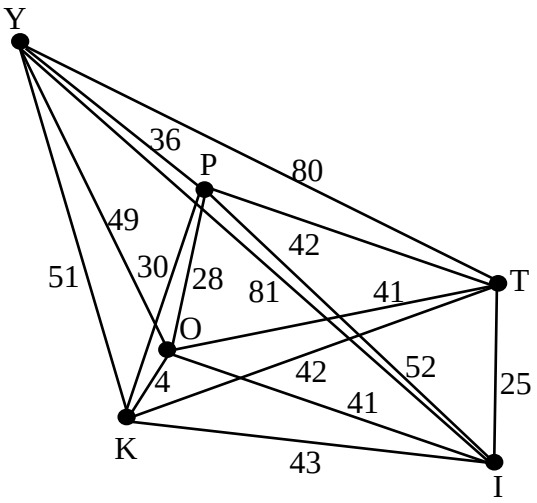

Figure (5) Transforming Real Routes into Complete weighted graph of Graph Theory

After transforming the route network into a complete weighted graph, a tour is planned starting from Taunggyi in Southern Shan State to minimize distance and costs, using the Christofides algorithm to obtain a near-optimal solution. Subsequently, fuel consumption is computed based on this route.

Step 1: Construct the Minimum Spanning Tree (MST) using Kruskal's algorithm for the given graph.

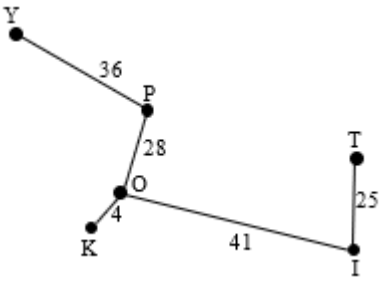

Figure (6) Minimum Spanning Tree (T)

Step 2: By step (2), we construct the minimum weight perfect matching (M) among vertices with odd degree in (T)

In Figure (6), the vertices with odd degrees are (Y, O, T, K).

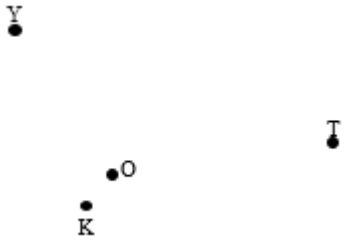

Figure (7) The vertices having odd degree in (T)

Let M be the minimum weight perfect matching among these vertices.

The possible matchings and their weights are (YK, OT) = 92, (YT, OK) = 84 and (YO, TK) = 91. The minimum weight perfect matching (M) is (YT, OK) = 84.

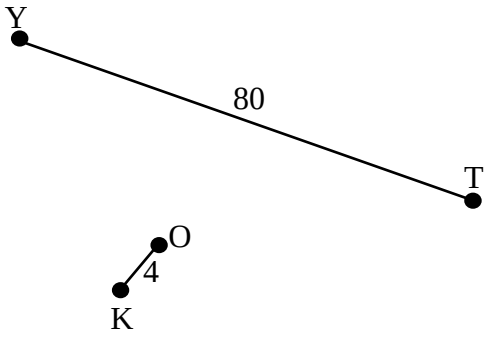

Figure (8) Minimum weight perfect matching (M)

Step 3: Combine the minimum spanning tree (T) and the minimum weight perfect matching (M).

Then, we obtain an Eulerian multigraph (all vertices have even degree).

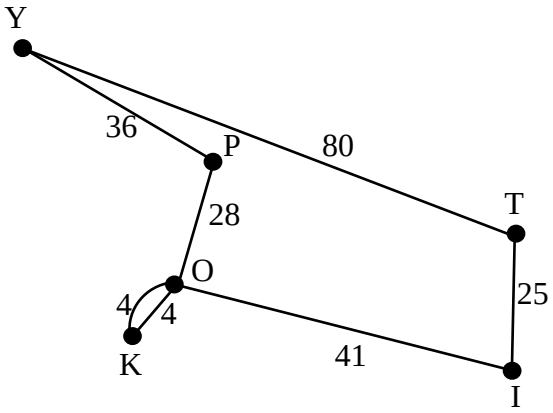

Figure (9) Eulerian multigraph

Step 4: In figure (9), Eulerian circuit in (T) is (T-I-O-K-O-P-Y-T).

Step 5: The first vertex to be repeated is O and the first vertex after O that is not repeated is P, so we replace the trail (K-O-P) by (K-P). There are no more repeated vertices and the resulting spanning cycle is (T-I-O-K-P-Y-T).
Finally, we obtain the Eulerian circuit into a Hamiltonian cycle.

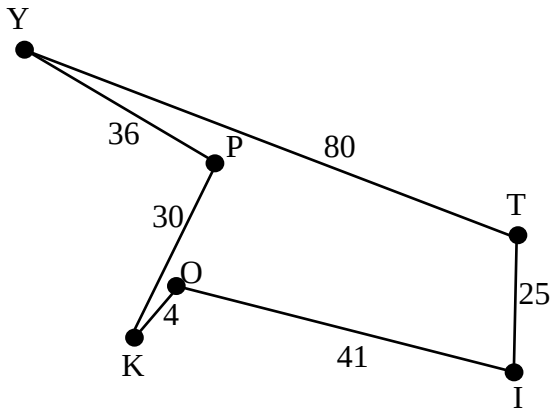

Figure (10) Hamiltonian cycle

The Hamiltonian cycle (T-I-O-K-P-Y-T) has the total weight 25+41+4+30+36+80 = 216.

Thus, the Christofides algorithm is an approximation algorithm that guarantees the total tour length is a near-optimal solution TSP distance. The tourism planning is forming a Hamiltonian cycle (T-I-O-K-P-Y-T) has a total distance is 216 miles. This solution can be computed quickly, making it suitable for practical tour planning.

Fuel Consumption and Cost Analysis for Mountain Route

Fuel consumption and costs are important factors in planning transportation on mountainous roads due to challenging terrain and variable speeds. This section evaluates fuel consumption and costs for different hybrid vehicles, providing insights for logistical and budget planning.

For this analysis, a Honda Insight (1.3 CC, Hybrid mode) was used, with a fuel efficiency of 0.085277 liters per mile. Fuel cost was calculated using the local price of 1 liter = 3000 MMK, and assuming an average speed of 50-60 mph. Subsequently, the fuel consumption (liters) and cost of two fuel-efficient vehicles commonly used in Southern Shan State, including the Honda Insight, were calculated and compared.

For a route of 216 miles, fuel consumption for three types of vehicle is calculated as following table:

Table 1 Comparison of Fuel Consumption and Cost for three types of vehicle

No	Type of Vehicle	Fuel Efficiency (L/mile)	Fuel (liters)	Fuel Cost (MMK)
1	Honda Insight (Hybrid)	0.0853	18.42	55,260
2	Honda Fit	0.0952	20.6	61,800
3	Hyundai Accent	0.104	22.5	67,500

Results and Discussion

This study shows that the route Taunggyi –Inle Lake–Mt.Osi–Kalaw–Pindaya–Ywangan–Taunggyi forms a Hamiltonian cycle, covering all selected cities. The total distance of the route is 216 miles, making it near-optimal tourism route for the region. To assess travel efficiency, three popular hybrid vehicles were compared based on fuel consumption and travel cost. The Honda Insight 1.3 CC Hybrid required approximately 18.42 liters of fuel for the route, with a total cost of 55,260 MMK. In comparison, the Honda Fit and Hyundai Accent consumed slightly more fuel and incurred higher costs. These results confirm that the Honda Insight is the most economical choice for this tourism route.

Conclusion

This study demonstrates that applying graph theory with the Christofides algorithm can effectively determine a near-optimal and cost-efficient tourism route in Southern Shan State, with a total distance of 216 miles. Among the vehicles analyzed, the Honda Insight 1.3 L Hybrid proved the most economical, consuming the least fuel and minimizing travel costs.

These findings highlight that graph theory-based tourism route planning provides a practical approach to reduce expenses and enhance the overall travel experience.

Acknowledgements

The author would like to sincerely thank Professor Dr. Ohnmar Nwe, Head of the Department of Mathematics at Meiktila University, and my supervisor, Professor Dr. Yuzana Min Hlaing, Department of Mathematics, Taunggyi University, for granting me permission and providing support throughout this research. I am also very grateful to Capt. Zwe Hein Htet, Assistance lecturer from the Faculty of Mathematics at Defence Service Academy for providing detailed assistance with my paper and continuous guidance throughout this research. Finally, I would like to thank all the University of East Yangon officials for allowing me to review the necessary documents and information.

References

Bondy, J.A., and Musty, U.S.R., “Graph Theory with Applications,”Macmillan Press Ltd, London, 1976.

PRIYADARSHAN G., “Christofides Algorithm: The Secret Weapon for Route Optimization”, Feb14, 2025. https://priyadarshanghosh26.medium.com/christofides-algorithm-the-secret-weapon-for-route-optimization d2b9ec68d66e

Periplus Editors “Myanmar Travel Map” (Fourth Edition), Periplus Publishing, 2015.

An Investigation of The Crucial Role of Blood Flow in The Human Body

Sai Saw Khant Maung[1]

Abstract

This paper presents an overview of fundamental fluid dynamics phenomena, with a specific focus on the principle governing laminar flow in cylindrical tube. The "Hagen-Poiseuille Flow" equation is introduced and applied to a relevant example to demonstrate its practical utility. Based on this equation, the formula for shearing stress is derived and analyzed. Furthermore, a comparative study is conducted on the shearing stress experienced by two patients, considering variations in their pressure gradients and overall vascular health conditions. Finally, this paper concludes by offering recommendations aimed at promoting and maintaining optimal vascular health.

Keywords: endothelial, fluid dynamics, laminar flow, pressure gradient, shearing stress, turbulent flow, viscous fluid

Introduction

Fluid mechanic is the branch of mathematics that deals with the behavior of fluid and the forces action on them. Hydromechanics is a sub-branch of fluid mechanics. Fluid includes both liquid and gas. The study of fluid in motion is called **hydrodynamics** and the study of fluid at rest is called **hydrostatics**. Analyze the properties of fluid and their behavior are essential function to solve the various problem of real-life engineering. This paper highlight mathematics is not only theorical studying but also the relation between mathematical theory and the problem solving for human society. In this research, we are mainly studying about **"Hagen-Poiseuille Flow"**. This flow is also known as **pipe flow concept**. This paper emphasizes analyzing the blood flow of human blood circulation with pipe flow concept. Blood flow is effectively controlled by radius of the vessel according to **"Hagen-Poiseuille Flow".** Based on the radius of vessel, it can change the shearing stress on the vessel. Depend on this shearing stress, we can predict the health situation in blood vessel.

Aim and Objectives

The primary aim of this research is to explore the interrelationship between mathematics and medicine. Specifically, it seeks to model blood flow using the **"Hagen-Poiseuille flow"** framework and to analyze the wall shearing stress in blood vessels in order to predict the behavior of blood flow within vascular systems.

The Fundamental Phenomena of Fluid Dynamics

Fluid dynamics is the branch of **fluid mechanics** that deals with the motion of fluids and the forces acting on them. **Fluid** is any substance that can **flow** and take the **shape** of its **container.** Fluid can divide into two types such as **liquid** and **gas**. In mathematical term, liquid is called **incompressible fluid** and gas is called **compressible fluid**. When a pressure is acting on liquid, the **density** and **volume** of liquid **do not change**. That's why liquid is incompressible fluid. But gas is different with liquid. The density and volume of gas is change when a pressure is acting on it. Therefore, gas is compressible fluid.

[1] Tutor, Department of Mathematics, Taunggyi University

A **viscous fluid** is a fluid that **resists flow** due to **internal friction** between its layers. This resistance is called **viscosity**. A fluid that has **no internal friction** is called **non-viscous fluid**. There are two types of fluid flow such as **laminar flow** and **turbulent flow**. **Laminar flow** is a type of fluid flow where the fluid moves in smooth parallel layers or streamlines with minimal mixing between the layers. But turbulent flow is different. **Turbulent flow** is a type of fluid flow characterized by chaotic, irregular and unpredictable motion of fluid particles.

In the next section, we introduce the concept of **"Hagen-Poiseuille Flow"** and drive the require equation and formulae. And then, we demonstrate with some appropriate examples relevant with pipe flow concept.

Hagen-Poiseuille Flow (Pipe Flow Concept)

The Hagen-Poiseuille flow is a classical solution in fluid dynamics that describes the steady, incompressible, laminar flow of a Newtonian fluid through a long, straight, circular pipe. The Hagen-Poiseuille equation provides a fundamental model for describing laminar flow in cylindrical pipe. This equation gives the pressure drop of an incompressible and Newtonian fluid in laminar flow through a long cylindrical pipe of constant cross section. The historical development of this concept is attributed to the independent works of **"Gotthilf Heinrich Ludwig Hagen (German engineer and physicist)"** and **"Jean Leonard Marie Poiseuille (French Physician and Physiologist)"** during in 19^{th} century.

In the next section, we calculate the shearing stress on vessel wall based on the velocity distribution for circular pipe flow. Specifically, we discuss the important of **Endothelial cells** and the effect of shearing stress on **vascular health**. And then, comparing the **shearing stress** of **normal person** and **stroke patient** by using their **pressure gradient**.

An Observation of the Diseases in Blood Vessel

The principle of the pipe flow, have significant applications which is biomedical engineering particularly in modeling blood flow and other fluid dynamics in the human body. Blood flow in arteries, veins and capillaries can often be approximated as laminar flow through circular pipe. This principle is useful to estimate the flow rate in a vessel based on pressure drop and vessel dimensions. Additionally, we can analyze the shearing stress on vessel walls by observing the velocity profile of blood flow.

The Important Role of Endothelial Cells

Endothelial cells are specialized cells that form the inner lining of blood vessels and lymphatic vessels. They create a barrier between the blood or lymph in vessel lumen and the surrounding tissues. Then, it can help white blood cells migrate to infection sites and supports the formation of new blood vessels. These cells play a crucial role in maintaining vascular health and regulating blood flow.

Shearing Stress in Vessel Walls

Shearing stress in vessel walls is the tangential force per unit area exerted by blood flow on the endothelial lining of blood vessels. It arises due to the viscosity of blood and the velocity gradient between the layers of blood flow near the vessel wall.

The shearing stress of the vessel is $\tau_w = -\mu\left[\frac{du}{dr}\right]_{r=R}$.

The velocity distribution for blood flow is $u(r) = -\frac{1}{4\mu}\frac{dp}{dz}\left(R^2 - r^2\right)$.

The velocity gradient at the wall is $\frac{du}{dr} = \frac{1}{2\mu}\frac{dp}{dz}r$.

Therefore, the shearing stress of the vessel wall is $\tau_w = \frac{1}{2}\frac{dp}{dz}R$.

High Shearing Stress and Low Shearing Stress

High shearing stress is generally protective and associated with better cardiovascular health. Low shearing stress is pathological, linked to conditions like atherosclerosis, thrombosis and other cardiovascular diseases. Now, we analyze the shearing stress of normal person and stroke patient. The pressure gradients of two patients are $500 Pam^{-1}$ and $50 Pam^{-1}$ respectively. The radius of vessel (R) is $0.005m$ and the blood viscosity is 0.0035 *Pa.s*.

For Normal Person

The pressure gradient is $\frac{dp}{dz} = 500\, Pam^{-1}$.

The shearing stress is $\tau_w = \frac{1}{2}\times 500 \times 0.005 = 1.25\, Pa.$

For Stroke Patient

The pressure gradient is $\frac{dp}{dz} = 50 Pam^{-1}$.

The shearing stress is $\tau_w = \frac{1}{2}\times 50 \times 0.005 = 0.125\, Pa.$

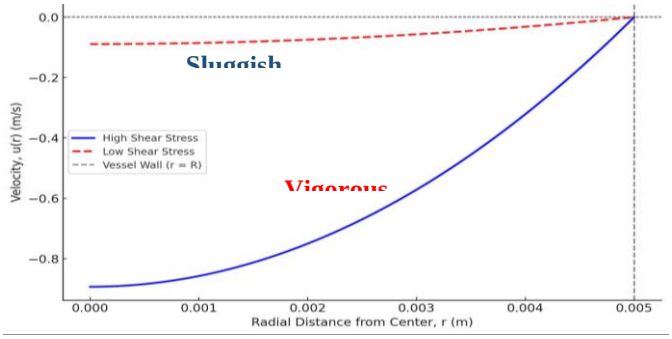

Velocity Profile of High and Low Shearing Stress

In comparison of these two results, high shearing stress observes during high blood flow. It can encourage endothelial cell alignment, which maintains healthy blood vessel function. Low shearing stress observes in low blood flow region. It can disrupt endothelial cell alignment contributing to inflammation and plaque formation.

In the above cases, the blood flow becomes **sluggish** and shearing stress is low. This type of flow can occur commonly in **stroke, after major operation** and **sedentary lifestyle**. The person, who has high blood lipids or cholesterol level, the lipids precipitate on the vessel wall or endothelial lining. This can lead the **blood clotting** process and forming a **plaque**. The plaque reduces the blood flow of the respective organ. It grows and occludes the vessels causing the organ failure. When the flowing blood encounters an obstacle, its laminar flow is disrupted and turbulent flow occurs.

Finding and Results

Based on the analyzed data, elevated shearing stress is associated with vasodilation and the prevention of **platelet aggregation** and **thrombus formation**. Furthermore, it

supports the alignment of endothelial cells, thereby contributing to reduced plaque formation and promoting vascular health. Elevated shearing stress has been shown to enhance overall cardiovascular function and human well-being. Conversely, regions of low shearing stress are linked to disturbed flow patterns, which can result in increased oxidative stress and lipid accumulation both of which are risk factors for atherosclerosis.

Suggestion

In light of these findings, it is recommended that individuals adopt strategies to maintain optimal blood circulation and vascular function. Regular physical activity should be prioritized, as it plays a crucial role in enhancing shearing stress and preventing arterial narrowing and obstruction. Additionally, reducing the intake of high-fat foods and adhering to a balanced, nutritious diet are essential components of a healthy lifestyle aimed at supporting long-term cardiovascular health.

Conclusion

In conclusion, the application of the "Hagen-Poiseuille Flow" equation provides valuable insights that can be effectively utilized in medical practice. This mathematical principle can also be adapted for use in biomedical engineering, particularly in the design of devices and interventions aimed at improving vascular function. By understanding the relationship between shearing stress and vascular health, we can target strategies such as promoting physical activity to enhance shearing stress or implementing medical treatments to mitigate the adverse effects of low shearing stress can be developed to support cardiovascular well-being. Furthermore, this research paper constitutes a socially impactful scientific study that aims to contribute meaningfully to the improvement of public health and the well-being of all individuals within human society.

Acknowledgements

I would like to express our deepest gratitude to Dr Kay Thi Thin, Rector, Taunggyi University, for her suggestion and encouragement on my research. Then, I would like to express Dr Ko Ko Naing and Dr Aung Nay Myo, Pro-rector, Taunggyi University, for their interest on my research paper. Additionally, I would like to express my gratitude to Dr Ngwe Kyar Su Khaing, Professor, Head of Department of Mathematics, Taunggyi University, for her kind permission to present this paper. I am also thankful to Professor Dr Yuzana Min Hlaing, Professor Dr Win Win Khin Lin, Department of Mathematics, Taunggyi University, for their kind advices to conduct this research. Specifically, I would like to appreciate my Ph.D co-supervisor Dr Zin Thwet Khine Phay , Professor, Head of Department of Mathematics, Panglong University, for her giving suggestion and interest on my research. Then, I am also appreciating to Dr Aung Kyaw Thu, Professor, Head of Department of Medicine, University of Medicine Taunggyi, Dr Nang Kaythi Myint Aung, Lecture, Department of Physiology, Dr Htunzayar Wai, Junior Consultant Microbiologists, Department of Laboratory, Soa San Tun General Hospital, for their encouraging in data collection of stroke patient.

References

Ba Kyi. Dr., *"Lecture Notes on Fluid Mechanics Part I and Part II",* Mathematics Department, University of Mandalay, 1976.

Barrett, K.E., Barman S.M, Brooks H.L, *"Review of Medical Physiology" 26th Edition,* McGraw-Hill Education, United States, 2019.

Batchelor, G. K., *"An Introduction to Fluid Dynamics"*, Cambridge University Press, Cambridge, 1993.

Frank M, White., *"Fluid Mechanics" 4th Edition,* McGraw-Hill Education, United States, 2019.

Raisinghania, Dr. M.D., *"Fluid Dynamics with Complete Hydrodynamics and Boundary Layer Theory", 11th Edition,* S. Chan & Company PVT. LTD, New Delhi, 2013.

Wilson, D. H., *"Hydrodynamics",* Edward Arnold (Publisher) Ltd., London, 1959.

Transitive Tournaments and Their Applications in Directed Graph

Tin Laie Laie Khaing[1]

Abstract

A tournament is a complete directed graph in which each pair of distinct vertices is connected by exactly one directed edge. Transitive tournaments form an important subclass of tournaments, characterized by the absence of directed cycles and the existence of a total ordering of vertices consistent with edge orientations. Associated with every tournament is a score sequence, defined as the sequence of vertex out-degrees, which provides a compact representation of the tournament's structural properties. This paper investigates transitive tournaments and their score sequences within the framework of directed graph theory. Relevant classical theorems from tournament theory are reviewed and applied to characterize these sequences completely. Furthermore, the paper explores applications of transitive tournaments and score sequences in ranking theory and decision-making models, where acyclic dominance relations are essential. The results provide a theoretical foundation for understanding ordered dominance structures in directed graphs and their practical implications.

Keywords: score sequence, tournament, transitive tournament.

Introduction

Graph theory is a fundamental area of discrete mathematics concerned with the study of relationships between objects. A graph consists of a set of vertices together with a set of edges that represent connections between pairs of vertices. A tournament is a special type of directed graph obtained by orienting every edge of a complete graph. Among all tournaments, transitive tournaments form a distinguished subclass. A tournament is transitive if it contains no directed cycles. This paper builds upon the basic concepts of graph theory and tournament theory to study transitive tournaments and their score sequences in directed graphs. By analyzing the connection between acyclicity, vertex ordering, and score distribution, the study aims to clarify the structural role of transitivity and provide insight into the characterization and applications of score sequences in tournaments.

Some Results on Graph Theory Terms and Notations

We first recall some definitions, notations and theoretical terms which are used in this paper.

Definition. A ***graph*** (or undirected graph) $G = (V, E)$ consists of a finite set V of ***vertices*** (or nodes) and a set E of ***edges*** (or arcs) such that each edge $e \in E$ is associated with ***an unordered pair*** of vertices. If there is a unique edge e associated with vertices u and v, we write $e = (u, v)\ or\ e = (v, u)$.

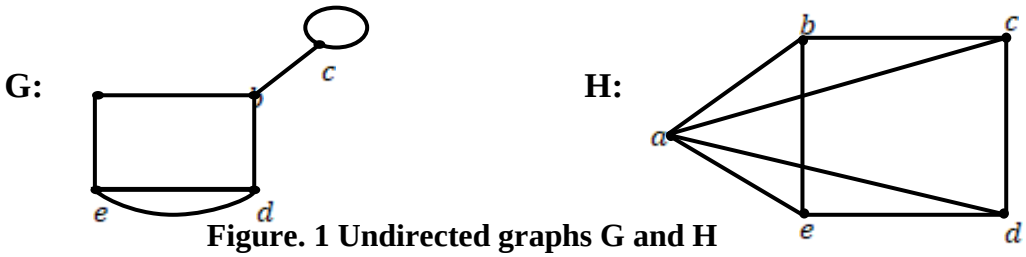

Figure. 1 Undirected graphs G and H

[1] [1]Lecturer, Department of Mathematics, East Yangon University

Definition. A ***directed graph*** (or digraph) G consists of a finite set V of ***vertices*** (or nodes) and a set E of ***edges*** (or arcs) such that each edge $e \in$ E is associated with ***an ordered pair*** of vertices. If there is a unique edge e associated with the ordered pair (u , v) of vertices, we write e = (u , v).

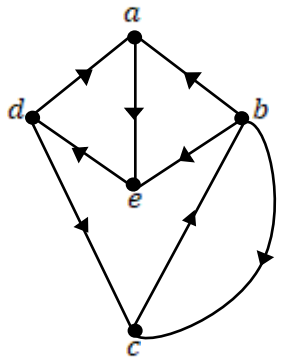

Figure. 2 A directed graph G

Definition. An edge e consists of two (possibly equal) vertices called its ***endpoints.***

Definition. Two vertices which are incident with a common edge are ***adjacent***.

Definition. An edge of a graph with identical ends or an edge that joins a vertex to itself is called a ***loop***.

Definition. An edge with distinct ends is a ***link***.

Definition. Two edges are said to be ***parallel*** if they have same ends.

Definition. ***Parallel edges*** or ***multiple edges*** are edges that have the same pair of endpoints.

Definition. A vertex that is not incident on any edge is called an ***isolated vertex.***

Definition. A graph with just one vertex is called a ***trivial graph*** and all other graphs are ***nontrivial graph.***

Definition. A graph with no loops or multiple edges is called a ***simple graph.***

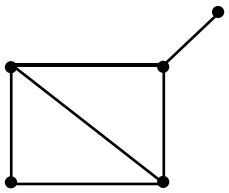

Figure. 3 Simple graph

Definition. Two or more edges of a graph G joining the same pair of vertices are called ***multiple edges*** (parallel edges), the corresponding graph is known as ***multigraph***.

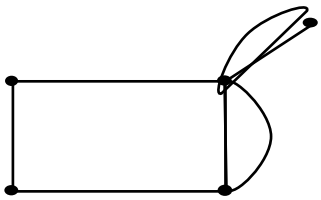

Figure. 4 Multigraph

Definition. The ***degree of a vertex*** v ∈ V in a graph G = (V, E) denoted by d(v), is the number of edges incident to v. We denoted by δ(G) the minimum degree of vertices of G.

Definition. The ***degree sequence*** of a graph is a list in non- increasing order of the degrees of all vertices.

Definition. A graph H = (U, F) is a subgraph of a graph G = (V, E) if U ⊆ V and F ⊆ E.

G: H:

Figure. 5 Subgraph

Definition. A simple graph in which each pair of distinct vertices is joined by an edge is called a ***complete graph***. The graph Kn called the complete graph on n vertices, has n vertices and every vertex is joined to every other vertex by an edge.

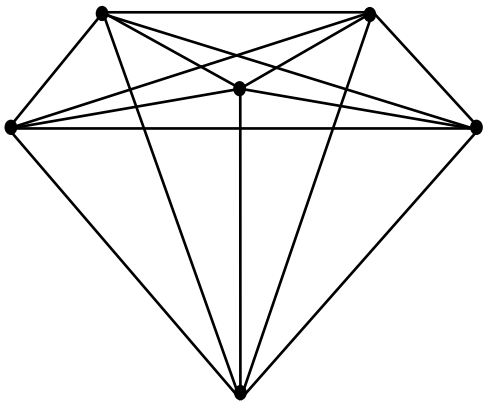

Figure. 6 A complete graph

Example. Fig 7 shows complete graph with five vertices, K_5 and complete bipartite graph $K_{3,3}$.

K_5: $K_{3,3}$:

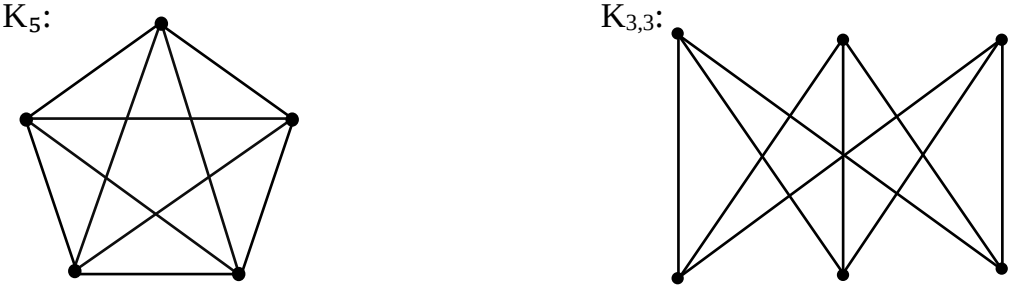

Figure. 7

Tournament (Directed graph) and Their Score Sequences

In this section, we present some concept of tournament (directed graph) definitions and their successive examples.

Definitions. ***A tournament*** is a directed graph in which every pair of vertices is jointed by exactly one arc. If the arc joining vertices v and w is directed from v to w, then v is said to ***dominate*** w, as well as to be adjacent to w. The score (out-valency) $s(v)$ of the vertex v is the number of vertices dominated by v and $s'(v)$ is the co-score (in-valency) of v, and equals the number of vertices dominating v. A tournament is called ***transitive***, if whenever u dominates v, and v dominates w , then u dominates w. The ***score sequence*** of a tournament is a listing of the out-degrees of the vertices.

Theorem. Let $[s_1, s_2, \ldots, s_n]$ be the score sequence of a tournament. Then the lowest score of the tournament is zero if $\sum_{i=1}^{n} s_i^2$ is maximum.

Proof. Let v_1 be the vertex of the tournament with lowest score s_1.We prove that $s_1 = 0$. Suppose a contradict $s_1 > 0$.Then there exist a vertex v_p with score s_p such that $v_1(1-0)v_p$. Since $s_p \geq s_1$, therefore there exist another vertex v_q with score s_q such that $v_p(1-0)v_q$. By changing the arcs $v_p(1-0)v_q$ and $v_p(1-0)v_q$ to $v_1(0-1)v_p$ and $v_p(0-1)v_q$ respectively. We get a new score sequence $[t_1, t_2, \ldots, t_n]$

where $t_1 = s_1 - 1, t_q = s_q + 1,\ t_r = s_r$ for all $r, 2 \leq r \leq n$ with $r \neq q$. Then

$$\begin{aligned}
\sum_{i=1}^{n} t_i^2 &= \sum_{i=2, i\neq q}^{n} t_i^2 + t_1^2 + t_q^2 \\
&= \sum_{i=2, i\neq q}^{n} s_i^2 + (s_1 - 1)^2 + (s_q + 1)^2 \\
&= \sum_{i=2, i\neq q}^{n} s_i^2 + s_1^2 + 1 - 2s_1 + s_q^2 + 1 + 2s_q \\
&= \sum_{i=1}^{n} s_i^2 + 2(s_q - s_1 + 1) \\
&> \sum_{i=1}^{n} s_i^2, \text{ since } s_q \geq s_1.
\end{aligned}$$

This is a contradiction $\sum_{i=1}^{n} s_i^2$ is maximum.

Thus, the lowest score of the tournament is zero if the sum of the score sequences is maximum.

Definitions. The out-degree of a vertex v represents the number of ***wins*** for that team and the in-degree of a vertex v represent the number of ***losses*** for that specific team.

A vertex's out-degree is represented by d^+ of wins and a vertex's in-degree is represented by d^- of losses.

Since d^+ represents the number of wins, a source of a tournament graph would be the tournament's winner and d^- represents the number of losses, a sink of a tournament graph is the overall loser.

Definitions. A vertex with zero in-degree is called a ***source*** and a vertex with zero out-degree is called a ***sink***.

For example:

Win Sequence	Lose Sequence
(3,2,1,0)	(0,1,2,3)
(3,1,1,1)	(0,2,2,2)
(2,2,1,1)	(1,1,2,2)
(2,2,2,0)	(1,1,1,3)

Lemma Let $S = (s_1, s_2, \dots, s_n)$ be a non decreasing sequence of satisfying

$\sum_{i=1}^{k} s_i \geq \binom{k}{2}, 1 \leq k \leq n$. For no $k, 1 \leq k < n$ is $\sum_{i=1}^{k} s_i = \binom{k}{2}$ and $s_k = s_{k+1}$.

Proof. Suppose the contradiction that such an integer exists, and let the smallest such be denoted k.

If $k = 1$, then $s_1 = \binom{1}{2} = 0$ and $s_2 = s_1 = 0$.

Clearly, $s_1 + s_2 = 0 < \binom{2}{2} = 1$, contradict the fact that S satisfies the given.

Now suppose $1 < k < n$. Since k is the smallest integer where $\sum_{i=1}^{k} s_i = \binom{k}{2}$, we must have $\sum_{i=1}^{k-1} s_i > \binom{k-1}{2}$.

So, $\binom{k-1}{2} + (k-1) = \binom{k}{2}$

$= \sum_{i=1}^{k} s_i = (\sum_{i=1}^{k-1} s_i) + s_k > \binom{k-1}{2} + s_k$.

This implies $s_k < k - 1$, and, as $s_{k+1} = s_k, s_{k+1} < k - 1$.

So, $\sum_{i=1}^{k+1} s_i = \left(\sum_{i=1}^{k} s_i\right) + s_k = \binom{k}{2} + s_k$

$< \binom{k}{2} + k - 1 < \binom{k+1}{2}$, again a contradiction to given. In any case, we arrive at a contradiction.

Thus, no such k, exist.

Theorem A non-decreasing list $[s_1, s_2, \dots, s_n]$ of non-negative integers is the score list of tournament if and only if for $k = 1,2, \dots, n$

$$\sum_{i=1}^{k} s_i \geq \frac{k(k-1)}{2} \qquad (2.1)$$

with equality for $k = n$.

Proof. Any k vertices of a tournament are joined by $\binom{k}{2}$ edges, by definition. Consequently, the sum of the scores of any k vertices of a tournament must be at least $\binom{k}{2}$. To prove for eq (2.1), sufficient of eq (2.1) when $n = 1$ is obvious. The proof for the general case will be by induction. Let j and k be the smallest and largest indices less than n such that $s_j = s_{s_n} = s_k$. Consider the set of integers $(s'_1, s'_2, \dots, s'_{n-1})$ defined as follows:

$s_i' = s_i$ if $i = 1,2,\dots,j-1$ or

$$i = k-(s_n - j),\dots,k-1,k;$$

$s_i' = s_i - 1$ if $i = j, j+1,\dots,k-(s_n-j)-1$ or

$$i = k+1, k+2,\dots,n-1.$$

From this definition, it follows that $s_1' \le s_2' \le \cdots \le s_{n-1}'$, that $s_1' = s_i$ for s_n values of i, and that $s_i' = s_i - 1$ for $(n-1) - s_n$ values of i. Consequently,

$$\sum_{i=1}^{n-1} s_i' = \sum_{i=1}^{n} s_i - (n-1) = \binom{n-1}{2}.$$

If there exists a tournament T_{n-1} with score list $(s_1', s_2', \dots, s_{n-1}')$, then there exists a tournament T_n with score list $(s_1, s_2, \dots, s_n)$; namely, the tournament consisting of T_{n-1} plus the vertex p_n, where p_n dominates the s_n vertices p_i such that $s_i' = s_i$ and is dominated by the remaining vertices. Therefore, we need only show that the inequality

$$\sum_{i=1}^{h} s_i' < \binom{h}{2} \qquad (2.2)$$

is impossible for every integer h such that $1 < h < n-1$ in order to complete the proof by induction. Consider the smallest value of h for which inequality (2.2) holds, if it ever holds. Since

$$\sum_{i=1}^{h-1} s_i' \ge \binom{h-1}{2},$$

It follow that $s_h \le h$. Furthermore, $j \le h$, since the first $j-1$ scores were unchanged. Hence,

$s_h = s_{h+1} = \cdots = s_f$ if we let $f = \max(h,k)$.

Let t denotes the number of values of i not exceeding h such that $s_i' = s_i - 1$. Then it must be that

$$s_n \le f - t. \qquad (2.3)$$

Therefore,

$$\begin{aligned}\binom{n}{2} &= \sum_{i=1}^{h} s_i' + \sum_{i=h+1}^{f} s_i + \sum_{i=f+1}^{n-1} s_i + s_n + t \\ &< \binom{h}{2} + (f-h)s_h + (n-1-f)s_n + f \\ &\le \binom{h}{2} + h(f-h) + f(n-1-f) + f \\ &\le \binom{f}{2} + f(n-f) \le \binom{n}{2}\end{aligned}$$

Consequently, inequality (2.2) cannot hold and the theorem is proved.

Example We consider the sequence 1,2,2,3,3,4 is the score sequence of a tournament.

k	$s_1 + \cdots + s_k$	$\frac{k(k-1)}{2}$
1	1	0
2	$1+2=3$	1
3	$1+2+2=5$	3
4	$1+2+2+3=8$	6
5	$1+2+2+3+3=11$	10
6	$1+2+2+3+3+4=15$	15

This sequence has length 6, so we will check the inequality above for $k = 1,2,\ldots,5$, with equality for $k = 6$. Since the inequality $s_1 + \cdots + s_k \geq \frac{k(k-1)}{2}$ holds for each row in the table above 1,2,2,3,3,4 is a score sequence for T_6.

Theorem. Let $[s_1, s_2, \ldots, s_n]$ be the score sequence of a tournament. Then the lowest score of the tournament is zero if $\sum_{i=1}^{n} s_i^2$ is maximum.

Proof. Let v_1 be the vertex of the tournament with lowest score s_1.We prove that $s_1 = 0$. Suppose a contradict $s_1 > 0$.Then there exist a vertex v_p with score s_p such that $v_1(1-0)v_p$. Since $s_p \geq s_1$, therefore there exist another vertex v_q with score s_q such that $v_p(1-0)v_q$. By changing the arcs $v_p(1-0)v_q$ and $v_p(1-0)v_q$ to $v_1(0-1)v_p$ and $v_p(0-1)v_q$ respectively. We get a new score sequence $[t_1, t_2, \ldots, t_n]$

where $t_1 = s_1 - 1, t_q = s_q + 1,\ t_r = s_r$ for all $r, 2 \leq r \leq n$ with $r \neq q$. Then

$$\begin{aligned}
\sum_{i=1}^{n} t_i^2 &= \sum_{i=2, i\neq q}^{n} t_i^2 + t_1^2 + t_q^2 \\
&= \sum_{i=2, i\neq q}^{n} s_i^2 + (s_1 - 1)^2 + (s_q + 1)^2 \\
&= \sum_{i=2, i\neq q}^{n} s_i^2 + s_1^2 + 1 - 2s_1 + s_q^2 + 1 + 2s_q \\
&= \sum_{i=1}^{n} s_i^2 + 2(s_q - s_1 + 1) \\
&> \sum_{i=1}^{n} s_i^2, \text{ since } s_q \geq s_1.
\end{aligned}$$

This is a contradiction $\sum_{i=1}^{n} s_i^2$ is maximum.

Thus, the lowest score of the tournament is zero if the sum of the score sequences is maximum.

Example: Ranking Tournament for 5 Players

Consider **5 players/teams**: P_1, P_2, P_3, P_4, P_5

Assume the true ranking is: $P_1 > P_2 > P_3 > P_4 > P_5$

Match Results

P_1 beats everyone

P_2 beats P_3, P_4, P_5

P_3 beats P_4, P_5

P_4 beats P_5

Directed Graph Representation

Edges are drawn **from winner to loser**

$P_1 \to P_2 \to P_3 \to P_4 \to P_5$

and all edges from higher-ranked to lower-ranked players.

So, this problem is no directed cycles, acyclic tournament and hence transitive (ranking) tournament.

Score Sequence (Out-Degrees)

Player	Wins
P_1	4
P_2	3
P_3	2
P_4	1
P_5	0

Score sequence is (0,1,2,3,4)

This is a transitive tournament on 5 vertices.

Conclusion

In this study, I examined transitive tournaments as a special class of directed graphs in which the direction of every edge is consistent with a total ordering of vertices. Such tournaments are characterized by the absence of directed cycles and provide a natural mathematical model for ranking systems. This ordering leads to a unique score sequence, namely (0,1,2, …, n−1) which completely characterizes transitive tournaments among all tournaments. The relationship between score sequences and tournament structure highlights how numerical data (scores or wins) can reflect underlying order and consistency in directed graphs. Transitive tournaments therefore play an important role in applications such as decision-making processes, and ranking problems, where clear and contradiction-free outcomes are required. Overall, the study of transitive tournaments and their score sequences shows how graph-theoretic concepts can be effectively applied to real-world ranking systems, providing both theoretical insight and practical relevance.

Acknowledgements

I would like to express my deepest gratitude to Dr. Myo Min Tun, Acting Rector of East Yangon University and Dr. Aye Aye Ko, Dr. Thida Aung, Pro-Rectors of East Yangon University, for their kind permission to do my research. I am also grateful to Professor Dr. Sandar Maw, Head of Mathematics Department, East Yangon University, for her valuable suggestions, constructive criticisms of the manuscript and supervision. I am deeply express my thanks to Dr. Aye Aye Maw and Dr. Wai Wai Tun, Professors of Mathematics Department, East Yangon University, for providing their advice for my research paper.

References

Douglas B. West, (2001) *Introduction to Graph Theory*, Second Edition, Pearson Prentice Hall, U.S.A.

J.A Bondy and U.S.R. Murty, (1982) *Graph Theory with Applications*, Fifth Printing, American Elsevier, New York.

K.B. Reid and M. Santana, *Landau's Theorem Revisited Again,* Department of Mathematics, 14, September, 2015.

T. A. Naikaoo, On scores in tournaments, Department of Mathematics, Islamia College of Science and Commerce, Srinagar, Kashmir, India, 2(2018) 257-267

Haematological Analysis of Blood Clam, *Tegillarca Rhombea* (Born, 1778) In Myeik Township, Tanintharyi Region

Khin Sabae Htut[1]

Abstract

Totally 240 blood clams, *Tegillarca rhombea* were recorded from Myeik Township, and were classified into three size groups: Group I (20–30 mm), Group II (31–40 mm), and Group III (41–50 mm). Blood samples were collected to examine red blood cells (RBCs), white blood cells (WBCs), haemoglobin (Hb), thrombocyte; differential leucocyte counts (DLC) and blood parasites. According to the results, the values of RBCs, WBCs, thrombocyte and haemoglobin, values increased in large blood clams (Group III). Lymphocytes, monocytes, and neutrophils slightly increased with size. Shell length and height were positively correlated, and RBCs counts were closely related with haemoglobin values, reflecting healthy growth. There was a moderate negative correlation between RBCs and WBCs. There was a weak positive correlation between WBCs and Hb values. There was no significant correlation found between WBCs and Hb values ($p > 0.05$). The haematological analysis increased in large blood clam sizes which were healthier and more resilient in coastal ecosystem. These findings provide important baseline information about the health of blood clams, *Tegillarca rhombea* in coastal area and safety for the human consumption.

Key words: Haematology, blood clam and *Tegillarca rhombea*

Introduction

Haematological analysis is a useful method to assess the health condition of aquatic organisms. Blood clams are filter feeding and live in intertidal estuarine areas where they are exposed to environmental changes and potential parasites. Blood clams obtain food by filtering water exposed to polluted water, parasites, and environmental changes. The blood clams suffer from infections and changes in their blood characteristics, which can be detected by haematological analysis (Venugopal *et al*., 2012). The blood clam, *Tegillarca rhombea* is important for both nature and people in Southeast Asia, including the coastal areas of Myanmar. It feeds by filtering water and lives in muddy coastal environments such as estuaries, mudflats, and mangrove areas (Sapkota *et al*., 2018). Haematological analyses indicate the blood clam's health condition, stress, and immune system (Jahan *et al*., 2015).

Haematological analysis involves the size and counts of red blood cells (RBCs), white blood cells (WBCs), thrombocyte, haemoglobin (Hb) values and haemocyte types. Haemocytes of *T. rhombea* are broadly classified into granulocytes and agranulocytes based on their morphological and functional characteristics. Granulocytes are larger and they contain cytoplasmic granules. Agranulocytes are smaller and do not contain cytoplasmic granules. Granulocytes show higher phagocytic activity, produce more lysosomal enzymes, and respond to immune challenges (Chen *et al*., 2021).

Trypanosomes and filarial-like organisms are haemoparasites. Trypanosomes and filarial-like organisms have been detected in various bivalve species worldwide. These parasites live on the blood of shellfish and may affect their health, growth, and survival. Basic background information on parasite infections and blood characteristics in wild bivalves is still lacking (Rahman *et al*., 2019).

Therefore, the haematological analysis of blood clams provides the information about both individual health and environmental quality (Rahman et al., 2019). The main aim of this study is to analyse the haematological parameters of the blood clam, *T. rhombea* in the study area.

[1] Professor, Zoology Department, East Yangon University

The objectives of present study are as follows;

- to analyse the blood values of blood clams, *T. rhombea* in different size groups
- to determine the size of blood cells in blood clams, *T. rhombea*
- to investigate the correlation of shell size, red blood cells, white blood cells, and haemoglobin value in in blood clams, *T. rhombea*
- to examine the haemoparasites detection in blood smears of the individual blood clams, *T. rhombea*.

Materials and Methods

Study area

Blood samples from live specimens of the blood clam, ***T. rhombea*** were collected from Jetty No. 2 to **shopping malls. *The study species* occur in** the intertidal zone of estuarine areas in Myeik Township. The study site is located at 12˚27´N latitude and 98˚35´E longitude (Figure 1, Plate 1).

Study period

The study period lasted from October 2024 to October 2025.

Sample collection and identification

Field survey and interview of local fishermen from the chosen study area was conducted two times per month. The blood clams, *T. **rhombea were collected from local fishermen in this study area during the period from 8 am to 9 am.*** The morphology of blood cells was identified according to Ellis (1977). The study species was taxonomically identified according to Narasimham (1988).

Morphometric measurement

The morphometric characters were measured and the scaled photographs were taken with digital camera immediately after the collection. A total of 20 individuals of *T. **rhombea was monthly collected to take the*** morphometric measurements data. Examinations on morphological and taxonomic characters were recorded for each fresh specimen. The samples were transferred into an ice box and brought back to the laboratory and preserved in 10% formalin for detailed study.

Blood sample collection

Blood samples were randomly collected from 20 individuals, ranging in size from 21 mm to 50 mm, per month. The blood samples were used for the haematological analysis. Blood was drawn from the heart region, which is located near the adductor muscle, using a sterile syringe fitted with a 25-gauge needle after the clams had naturally opened their shells.

Materials

Haemocytometer, coverslip, microscope slides (25.4×76.2mm), micropipette, haemoglobinometer and microscope were utilized in this study.

Method

Blood films preparation and staining

The blood smears by wedge method. Smeared blood samples were Leishman's stain solution and studied under the light microscope (Kumar and Sharma, 2009) (Plate 2).

Staining of blood films

The blood was allowed to dry on the glass in the open air. Fixation was brought about in two minutes with the undiluted stains which contain alcohol. Then diluted stain was applied to the smear for 10 minutes (Kumar and Sharma, 2009).

Red blood cells (RBCs) counts

RBCs count was determined by visual method. The blood was drawn by a thoma red cell pipette up to 0.5 mark. The blood sticking to the outer surface of the pipette was wiped off. In case the blood has slightly passed the 0.5 mark, it should be adjusted by touching the pipette tip against a piece of cloth or cotton. The diluent is then drawn up to 101 mark. While drawing the diluent, the pipette is then rotated between the finger and thumb to mix the blood thoroughly with the diluent. Calculations: Total red blood cell count = N x 10,000 mm^3, N $x10^4$ x 10^6/L, N $x10^{10}$/L (Kumar and Sharma , 2009).

White blood cells (WBCs) counts

WBCs count was determined by visual method. The blood was drawn by sucking in a thoma white cell pipette containing blood cells to the mark 0.5. The blood sample was drawn into a WBC diluting pipette up to the 0.5 mark. Excess blood on the outer surface of the pipette was wiped off. Blood exceeding the calibration mark was removed using cotton. Turk's fluid was drawn into the pipette up to the 11 mark. The pipette was held horizontally and mixed thoroughly by gentle rotation. Haemolysis of red blood cells and staining of white blood cells occurred due to the action of acetic acid and gentian violet respectively. After one minute of mixing, the initial drops were discarded, and a small drop of the diluted blood was placed on the ruled chamber and covered with a cover slip for microscopic observation. Calculation: Total Leucocyte counts (T.L.C) = N x 50 mm^3, N x 5x10x 10^6/L, N x $5x10^7$/L (Kumar and Sharma, 2009).

The differential blood cell counts (DLC)

The differential blood cell counts were determined by visual method. The differential leucocyte count was determined under the 100 white blood corpuscles in thin Leishman's stained blood smears (Kumar and Sharma, 2009).

Thrombocyte counts

Thrombocyte counts were determined by the indirect method. The first 100 RBCs seen on each slide were counted at random and then the number of thrombocyte (Kumar and Sharma, 2009).

Haemoglobin concentration (Hb)

Haemoglobin (Hb) was measured by using the Sahli method. The principle of this method was to convert the hemoglobin in the form of haematic acid by hydrochloric acid. Blood was taken with a pipette (20 µL) and placed into a haemoglobin tube that contain 0.1 N HCL, in it. After 3 minutes, haemoglobin was reacted with dilute HCl to form haematin acid. The resulting mixture was stirred with a glass rod, and water added gradually until matching the standard. The reading of the column scale was gram/100 mL, which means the amount of haemoglobin in grams per 100 mL of blood (Kumar and Sharma, 2009).

Statistical analysis

Statistical analysis was performed using IBM SPSS Statistics version 27, with significance levels set at $\boldsymbol{P} < 0.01$ and $\boldsymbol{P} < 0.05$.

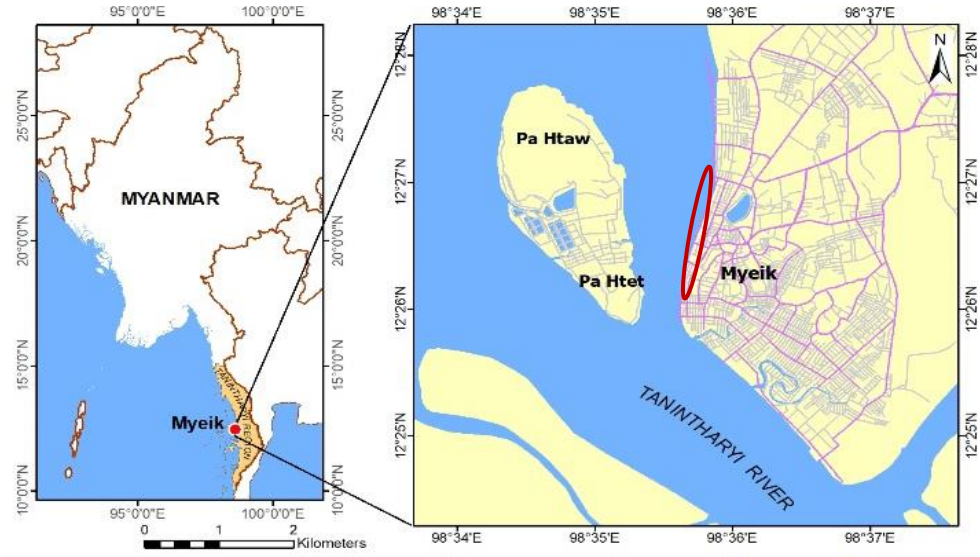

Figure 1 Map of study area (Source; Google map 2024

Plate 1 Study sites

A. Length of *T. rhombea*

B. Height of *T. rhombea*

C. Dorsal viewl

D. Ventral view

E. Flesh of *T. rhombea*

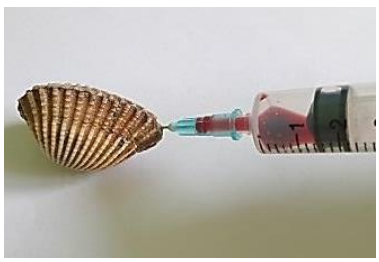

F. Taken the blood


G. Blood films

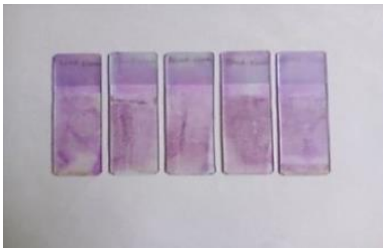
H. Stained the blood films

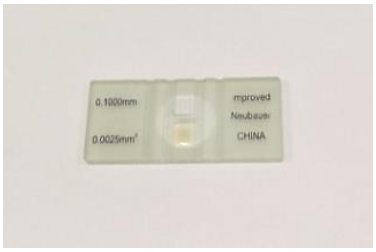

J.Haemoglobinometer


I. Haemocytometer


K.Leishman's Stain


L.Electronic Microscope

Plate 2 Collection of blood clam and preparation of blood films

Results

The 80 blood clams, ***T. rhombea*** were randomly collected in each group. Haematological analysis of the studied species were presented in Tables 1 to 5, Figures 2 to 6, and Plates 3 and 4.

Tegillarca rhombea was identified follow after by Narasimham (1988).

Systematic position of studied species

Phylum- Mollusca

Class - Bivalvia

Order - Arcida

Family - Arcidae

Genus - *Tegillarca*

Species- *Tegillarca rhombea* (Born, 1778)

Morphometric measurement of blood cells in *Tegillarca rhombea*

RBC was found in various shapes, including oval, round, teardrop, and elongated forms. Mature RBC was round shaped with nucleus but there was no visible cytoplasmic granule. Lymphocyte, monocyte, and neutrophil were found in blood clam, *T. rhombea* and eosinophils and basophils were not observed. The lymphocytes, monocytes, and neutrophils were nearly rounded. Lymphocyte and neutrophil were round nuclei, and monocyte was kidney-shaped nucleus. Thrombocytes were rounded with nucleus.

Haematological analysis of *Tegillarca rhombea*

Table 1 Haematological analysis in Group I (20mm -30mm)

Parameters	N	Minimum	Maximum	Mean	SD
Length (mm)	80	22.00	30.00	25.5307	1.52304
Height (mm)	80	12.50	24.00	15.7000	2.01401
RBCs ($x10^{12}$/L)	80	0.71	1.30	0.8967	0.29385
WBCs ($x10^{9}$/L)	80	1.79	3.80	2.8906	0.51386
Hb (g/dL)	80	1.30	3.40	2.3620	0.60813
Thrombocyte (%)	80	38.50	66.00	52.4831	6.57573
Lymphocyte (%)	80	33.00	57.00	44.9040	5.78735
Monocyte (%)	80	4.00	6.00	3.8320	0.75079
Neutrophil (%)	80	40.00	62.00	50.7000	4.81318
Lymphocyte (µm)	80	8.00	10.60	9.8667	0.49319
Monocyte (µm)	80	8.50	11.50	10.5617	0.59812
Neutrophil (µm)	80	8.40	10.80	9.8301	0.57996
Thrombocyte (µm)	80	2.00	4.00	3.5333	0.42104
RBC (µm)	80	8.10	9.40	8.4081	0.57106

Table 2 Haematological analysis in Group II (31mm - 40mm)

Parameters	N	Minimum	Maximum	Mean	SD
Length (mm)	80	31.00	40.00	38.2933	2.79034
Height (mm)	80	25.00	35.00	28.9000	2.19116
RBCs ($x10^{12}$/L)	80	1.50	2.70	2.0350	0.59816
WBCs ($x10^{9}$/L)	80	1.80	3.78	3.0357	0.36411
Hb (g/dL)	80	2.20	3.91	3.1987	0.73512
Thrombocyte (%)	80	45.00	69.00	55.6701	4.79746
Lymphocyte (%)	80	38.00	60.00	48.5133	4.91256
Monocyte (%)	80	5.00	7.00	4.5936	0.67535
Neutrophil (%)	80	40.00	65.00	50.8321	6.75218
Lymphocyte (µm)	80	8.40	11.10	10.1310	0.63118
Monocyte (µm)	80	8.50	11.60	10.8138	0.59081
Neutrophil (µm)	80	8.50	10.90	10.7657	0.61049
Thrombocyte (µm)	80	2.00	4.00	3.6010	0.41893
RBC (µm)	80	8.30	9.70	8.7394	0.53661

Table 3 Haematological analysis in Group III (41mm - 50mm)

Parameters	N	Minimum	Maximum	Mean	SD
Length (mm)	80	41.00	50.00	46.7100	2.52310
Height (mm)	80	38.00	47.00	39.2100	2.04550
RBCs ($x10^{12}$/L)	80	1.80	3.60	2.8233	0.41159
WBCs ($x10^{9}$/L)	80	1.94	4.10	3.5093	0.36754
Hb (g/dL)	80	2.27	4.70	3.6821	0.59163
Thrombocyte (%)	80	38.00	69.00	60.9000	4.36010
Lymphocyte (%)	80	38.00	61.00	48.9000	3.71934
Monocyte (%)	80	4.00	6.00	4.6667	0.60648
Neutrophil (%)	80	47.00	65.00	53.6341	4.55982
Lymphocyte (µm)	80	8.50	11.10	10.7040	0.36828
Monocyte (µm)	80	8.50	11.60	10.9627	0.43948
Neutrophil (µm)	80	8.50	10.90	10.8604	0.50841
Thrombocyte (µm)	80	3.00	4.00	3.6833	0.39913
RBC (µm)	80	8.30	9.80	9.1314	0.43461

Table 4 Correlation coefficient (r) in the all group

Parameters	Group I (n=80)		Group II (n=80)		Group III (n=80)	
	r	Sig. (2-tailed)	r	Sig. (2-tailed)	r	Sig. (2-tailed)
Length and Height	0.807**	0.000	0.863**	0.000	0.897**	0.000
Length and RBCs	0.797**	0.000	0.878*	0.035	0.895**	0.000
RBCs and WBCs	-0.592**	0.011	-0.577**	0.009	- 0.545**	0.040
RBCs and Hb	0.869*	0.007	0.891**	0.000	0.902**	0.000
WBCs and Hb	0.328	0.122	0.361	0.103	0.358	0.134

* Correlation is significant at the 0.05 level (2-tailed).

**Correlation is significant at the 0.01 level (2-tailed)

Table 5 Haemoparasites (Microfilaria parasite) in the all group

Group I (n=80)		Group II (n=80)		Group III (n=80)		Total (n=240)	
Infected	Non-infected	Infected	Non-infected	Infected	Non-infected	Infected	Non-infected
1 (1%)	79 (99%)	5 (6%)	75 (94%)	6 (7%)	74 (93%)	12 (5%)	228 (95%)

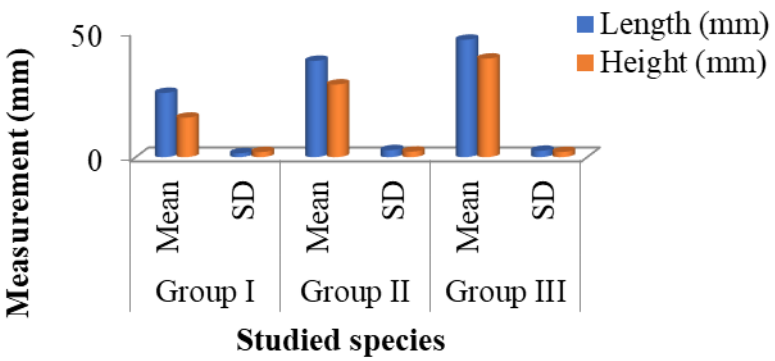

Figure 2 Comparison of length and height

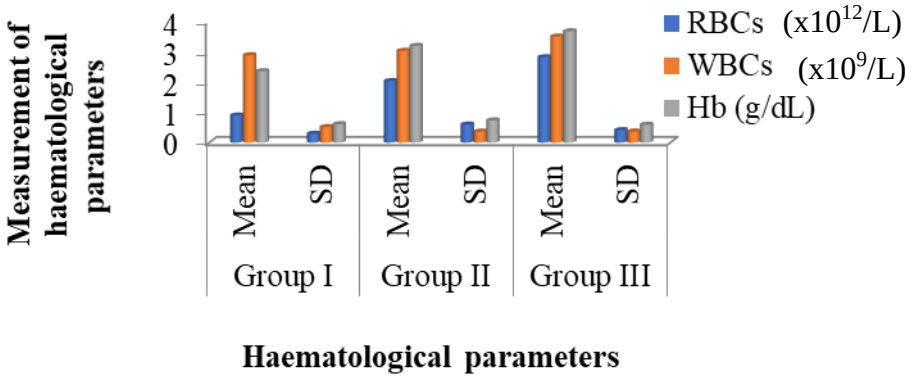

Figure 3 Comparison of haematological parameters

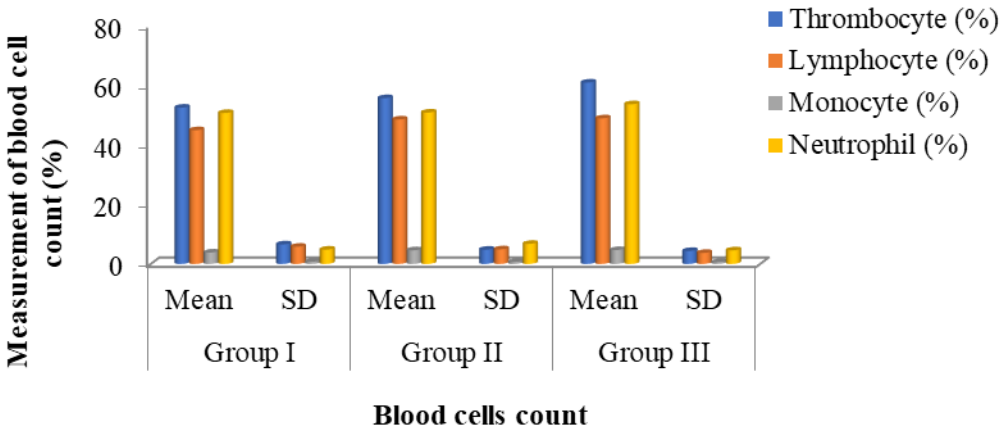

Figure 4 Comparison of blood cells count

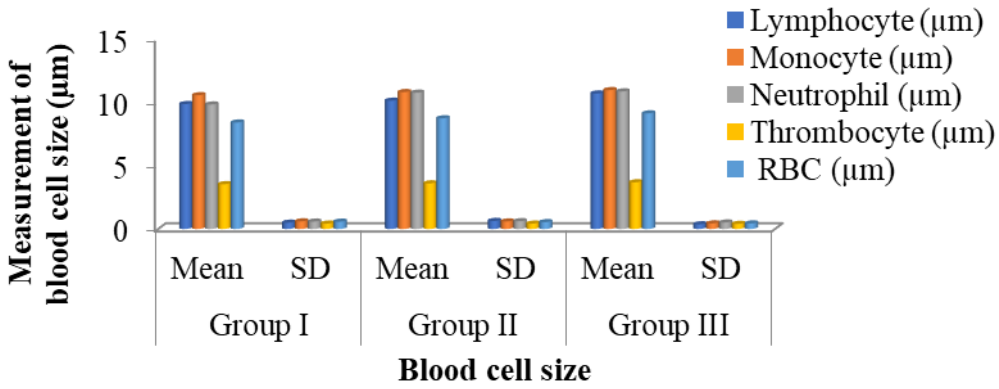

Figure 5 Composition of blood cells size

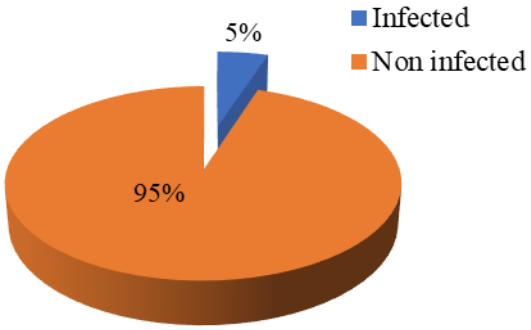

Figure 6 Composition of infected and non- infected in studied species

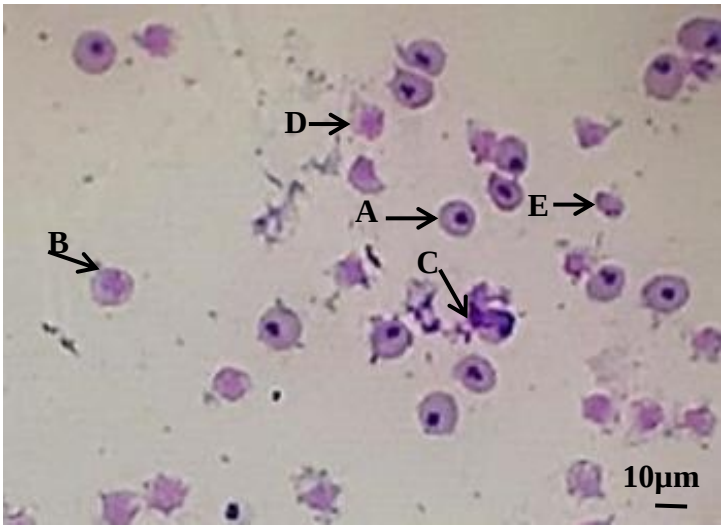

Plate 3 Blood cells of *Tegillarca rhombea*, Leishman's stain (1000X); A. Red blood cell, B. Lymphocyte, C. Monocyte, D. Neutrophil, E.Thrombocyte

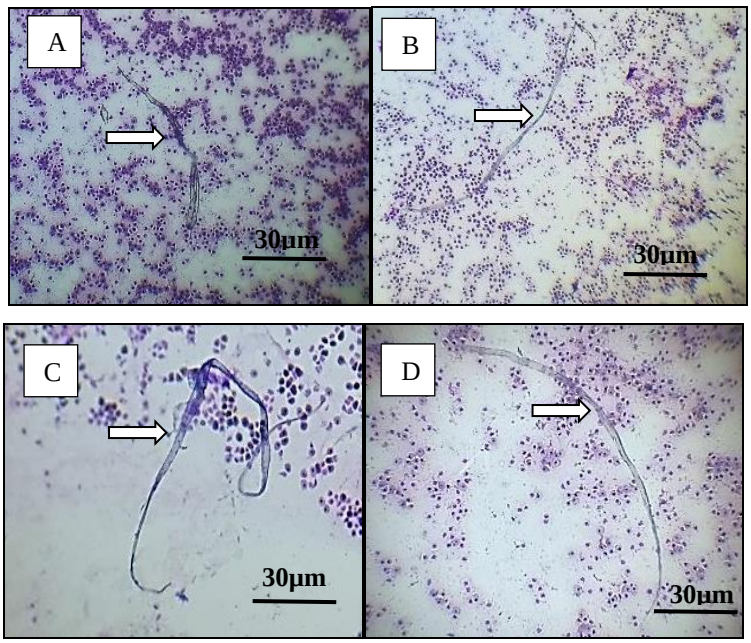

Plate 4 Microfilaria parasite (*Wuchereria bancrofti*) in the blood smears of *Tegillarc rhombea*, Leishman's stain (100X).

Discussion

The blood clams, ***T. rhombea*** were classified into grouped based on their size. There were 35-42 teeth in the small shells and 37- 49 teeth in the large shells in the study species. These results agreed with Narasimham (1988). The haematological analysis was correlated with RBCs, WBCs, Hb values, and haemoparasitic prevalence.

RBCs counts and size increased from Group I to Group III (0.897 $\times 10^{12}$/L to 2.823 $\times 10^{12}$/L; 8.4 µm to 9.1 µm). Haemoglobin (Hb) values increased in size (Group I: 2.362 g/dL, Group II: 3.199g/dL, Group III: 3.682 g/dL). Gao *et al*.(2011), Sinaei and Mashinchian (2014) and Chen *et al*.(2021) observed that the higher haemoglobin values were carried the more oxygen in large blood clam. The cells size, numbers of RBCs and haemoglobin (Hb) values increased in large blood clams, ***T. rhombea***. The large blood clams were healthier with better immunity and oxygen supply. This result indicated that the large blood clams, ***T. rhombea*** were similar to the result found in Gao *et al*. (2011), Sinaei and Mashinchian (2014) and Chen *et al*.(2021).

WBCs counts (Group I: 2.891×10^{9}/L, Group II: 3.036×10^{9}/L, Group III: 3.509×10^{9}/L) increase with size. Zhao *et al*.(2012) reported that the higher counts of WBCs had the stronger immune system to fight diseases. This result of WBCs count in studied species agreed with Zhao *et al*. (2012). **Thrombocyte** counts and size (Group I: 52.483%, 3.533 µm to Group III: 60.90%, 3.683 µm) increased. Bao *et al*. (2010) found that the thrombocyte was important in blood circulation. The higher metabolic activity the more efficient blood circulation was found in larger blood clams. These results indicated that the **thrombocyte** counts were similar to the result as observed in Bao *et al*. (2010).

The number and size of **lymphocytes**, **monocytes** and **neutrophils** slightly increased from Group I to Group III (44.904%, 9.867µm to 48.90%, 10.704µm); (3.832%, 10.561µm to 4.667%, 10.962µm) and (50.70%, 9.830µm to 53.634%, 10.860µm). Chen *et al*. (2021) observed that **larger blood clams have more immune cells** and their **immune system have more developed and stronger** than that of smaller blood clams. The functions of these cells were important for defense infections and against diseases. The immune systems increased in the large blood clams due to expose more environmental conditions. This result of studied species agreed with Chen *et al*. (2021). The haematogical analysis of this study was nearly similar as found in Mohite and Meshram (2015).

The shell length and shell height increased in all size groups of blood clams, ***T. rhombea.*** The strong positive correlation of Group I, Group II and Group III were $r = 0.807$, $r = 0.863$ and $r = 0.897$; $p < 0.01$ respectively. Meshram and Mohite (2016) found that the shell of blood clams grow longer and grow taller proportion. This result agreed with Meshram and Mohite (2016). The strong positive correlation of shell length and RBCs in Group I, Group II and Group III were $r = 0.797$ ($p< 0.01$), $r = 0.878$ ($p< 0.05$) and $r = 0.895$ ($p< 0.01$). Meshram and Mohite (2016) stated that the length of shell was increased and had more RBCs count. The larger blood clams need more RBCs to carry oxygen and support the body function. The result of studied species agreed with that found in Meshram and Mohite (2016).

There was a moderate negative correlation between red blood cells (RBCs) and white blood cells (WBCs). The significant correlation found in Group I, Group II and Group III were ($r = - 0.592$, $p<0.01$; $r = - 0.577$, $p<0.01$; $r = - 0.545$, $p< 0.01$) respectively. Cheng (2004) said that the blood clam had a balance between oxygen-carrying cells (RBCs) and immune cells (WBCs). The result of studied species agreed as observed in Cheng (2004).

There was a strong positive correlation between RBCs counts and Hb values observed

in Group I, II and III ($r = 869$, $p<0.05$; $r = 0.891$, $p< 0.01$; $r = 0.902$, $p< 0.01$) respectively. Rahman *et al*. (2019) observed that the number of RBCs increases with the Hb value. Larger blood clams carried more oxygen in their blood due to more RBCs and haemoglobin values. The blood clams survived in difficult conditions like low oxygen, changes in salinity, and muddy environments. The result of studied species agreed with that observed in Rahman *et al*. (2019).

There was a weak positive correlation between WBCs and Hb values. There was no significance was found between WBCs and Hb values in Group I, II, and III ($r = 0.328$, $p> 0.05$; $r = 0.361$, $p> 0.05$; $r = 0.385$; $p> 0.05$). Li *et al*.(2010) reported that the bivalves and other aquatic invertebrates were weak or non-significant correlation between immune cells (WBCs) and haemoglobin (Hb) maintain healthy condition for blood clam under normal environmental conditions. The result of studied species agreed with that found in Li *et al*.(2010).

Cheng (2004) reported that the microfilaria parasite in ***T. rhombea*** were transmitted mainly when blood clams **filter feed** on water containing infective larvae from intermediate hosts such as aquatic insects or small crustaceans in the estuarine environment. **The total 240 blood clams (*Tegillarca rhombea*) were examined, 12 blood clams (5%) were found to be infected** with haemoparasites. One blood clam (1%) in **Group I,** five blood clams (6%) in **Group II** and six blood clams (7%) **Group III** were infected.

Poulin (2007) and Marcogliese (2005) found that the slightly higher prevalence observed in larger clams attributed to their longer exposure to the aquatic environment and increased filtration activity, which enhances contact with parasite stages. According to Li et al. (2010), blood clams were generally healthy and resistant to filarial infections. The studied species exhibited **low haemoparasitic prevalence**, indicating that only a few individuals were infected with blood parasites. The result of studied species agreed with that observed in Poulin (2007), Marcogliese (2005) and Li *et al*. (2010). **Trypanosomes** were not found in studied species. Haematological analysis not only reflects the **health status of blood clams** but also serves as a **useful indicator of ecosystem health,** showing environmental conditions affecting bivalve populations.

Conclusion

The haematological analysis of blood clam, ***T. rhombea*** showed the higher RBCs and WBCs counts, increased haemoglobin values in larger blood clams (Group III). The slightly larger blood cell morphometric measurements were compared to smaller Group I and Group II. The oxygen-carrying capacity and immune potential were increased in large blood clam (Group III). The moderate increase of thrombocyte and leucocyte counts improved physiological and immune function in blood clam size. The microfilaria parasite prevalence was higher in larger blood clams and greater exposure in filter-feeding activity. The strong positive correlations were found between shell length and shell height, shell length and RBCs count, and RBCs count and haemoglobin (Hb) values in this study. The weak positive correlation was found between WBCs count and haemoglobin (Hb) values. The haematological analysis was not only individual health status but also serves as indicators of susceptibility to parasitic infection, providing valuable insights into clam physiology and ecosystem health.

Acknowledgements

I would like to express my thanks to acting Rector Dr Myo Min Tun, Pro-Rectors Dr Aye Aye Ko, and Dr Thida Aung, East Yangon University for their permission to write this present research paper. I would like to give special thanks to Professor Dr Ei Khine Win, Head of Zoology Department, East Yangon University for her encouragement to work on the present research.

References

Bao, Y., Wu, F., & Li, Y, (2010). Seasonal variation of haemocyte parameters in the clam *Meretrix meretrix*. *Aquaculture Research,* 41(10), 1502–1509.

Chen, Y., Zhou, X., Liu, Y., & Zhang, Y, (2021). Hemocyte immune responses of *Tegillarca rhombea* under thermal and bacterial stress. *Fish & Shellfish Immunology,* vol.109. pp 27–34.

Cheng, T. C, (2004). Immunology of molluscs. *Invertebrate Survival Journal,* vol.1. pp 1-7.

Ellis, A. E, (1977). The leucocytes of fish. *Journal of Fish Biology,* vol.11. pp 453–454.

Gao, Q., Wang, S., & Zhang, G, (2011). Haematological characteristics of mollusks and their response to environmental stress. *Aquatic Biology,* vol.13, pp 119–127.

Jahan, F., Hossain, M. A. R., & Haque, M. M, (2015). Hematological study of freshwater mussels (*Lamellidens marginalis*) under field conditions in Bangladesh. *International Journal of Fisheries and Aquatic Studies, 2*(4), 193–198.

Kumar, R., & Sharma, K. B. (2009). *Practical class manual of veterinary physiology*. Department of Veterinary Physiology, College of Veterinary & Animal Sciences, Plumper.

Li, J., Zhang, Y., Liu, X., & Wu, X, (2010). Immune responses and haemocyte function in bivalve molluscs. *Fish & Shellfish Immunology*, *28*(2), 203–210.

Marcogliese, D. J, (2005). Parasites of the superorganism: Are they indicators of ecosystem health? *International Journal for Parasitology,* vol.35. pp 705–716.

Meshram, S. R., & Mohite, S. A. (2016). Morphometric relationships in bivalve molluscs. *International Journal of Fisheries and Aquatic Studies*, 4(2), 45–49.

Mohite, S., & Meshram, A. M, (2015). Haematological characteristics of blood clam, *Tegillarca rhombea* (Born, 1778). *Journal of Aquaculture & Marine Biology, 3*(2), Article 00065. https:// doi .org/ 10.15406 /jamb.2015.03.00065

Narasimham, K. A, (1988). Taxonomy of the blood clams *Tegillarca (Tegillarca) granosa* (Linnaeus, 1758) and *T. rhombea* (Born, 1780). *Central Marine Fisheries Research Institute Bulletin,* 30(1–2), 200–205.

Poulin, R. (2007). *Evolutionary ecology of parasites*. Princeton University Press.

Rahman, M. M., Sarker, A., & Khan, M. N. (2019). Comparative haematological profiles of marine bivalves from different salinity zones. *Journal of Marine Biology and Oceanography,* 8(1), 56–63.

Sapkota, Y., Bajracharya, R., & Jha, B. R, (2018). Role of bivalves in water quality improvement and ecosystem services in tropical estuarine systems. *Ecohydrology & Hydrobiology*, 18(4), 338–346.

Sinaei, M., & Mashinchian, A,(2014). Hematological and biochemical parameters in bivalves under environmental stress. *Environmental Science and Pollution Research*, 21(6), 3805–3812.

Venugopal, V., Gopakumar, K., & Balachandran, K, (2012). Bivalves as bioindicators: Hemolymph analysis for environmental monitoring. *Environmental Research Journal,* 6(3), 173–180.

Zhao, X., Yu, H., Kong, L., & Li, Q, (2012). Transcriptomic responses to heat stress in the blood clam *Tegillarca granosa*. *PLOS ONE, 7*(11), e 46065.

Analysis on Biometric Characters of *Mystus* Spp. from Thiri Malar Market, Aung Myay Tha Zan Township

Aye Chan Pyae[1], Myo Myo[2], Win Win Mar[3]

Abstract

Mystus spp. (n=247) was collected form Thiri Malar Market to investigate their biometric characters analyzed by using SPSS during June 2024 to September 2024. The negative allometric growth patterns b < 3 observed in total length (TL) vs body weight (W) of *Mystus* spp.; the positive allometric growth pattern b > 1 observed in TL vs standard length (SL) of *M. bleekeri*, however, *M. cavasius* and *M. pulcher* was negative allometric growth pattern b < 1 and TL vs head length (HL) in *M. pulcher* and *M.bleekeri*; b > 1 in *M. cavasius*; and the value of b > 1 in TL vs body depth (BD) of *M. pulcher* and *M. bleekeri*, however the value of *M.cavasius* had b < 1. The high association of coefficient determination ($R^2 > 0.90$) was observed in TL vs SL of these fishes, however the very low association of TL vs HL was investigated in *M. pulcher* ($R^2 = 0.101$). Pearson's correlation (r) revealed the best significant relationship in *M.cavasius* followed by *M. bleekeri* and *M. pulcher* at $p < 0.01$ and $p < 0.05$. Principal component analysis (PCA) generated the highest percent of variance 72.070 % with initial Eigenvalues 10.811 in *M. cavasius* followed by 54.101 % with 8.115 in *M. bleekeri* and 39.65 % with 5.948 in *M. pulcher*. The results on sums of squared loadings revealed the similar strength of variation with initial Eigenvalues. The biometric characters revealed the variable association in these species, however the component 1 (CP1) indicated the negative association with low variability compared with other components in each species. The best condition factor (K > 1) was observed in *M. pulcher* than other species. This research will provide the foundation of biological characters of *Mystus* spp. for fishery sector.

Keywords: *Mystus* spp., biometric, PCA, Eigenvalues

Introduction

In Myanmar, the aquaculture is the second important role in socio-economic development. The variety of freshwater and marine fish species are distributed throughout the rivers, lakes, Inns, streams and ponds.

Mystus species are widely distributed in Asia. According to the FishBase, there are 49 *Mystus* species (Forese and Pauly, 2024). In which *Mystus cavasius, Mystus pulcher* and *Mystus bleekeri* and belong to the order Siluriformes and family Bagridae.

In aquaculture, the successful production of water resources is mainly depending on the management of quality control. In order to maintain the sustainable development of fish species, every species must have the standardize growth patterns that are influenced by several factors such as food, habitat, water quality and environmental conditions.

Recently, the growth performance of fishes is standardized by their universal index: allometric and isometric scales must be applied to investigate and confirm the fish's biometric characters. Thus, the healthy and good performance of fishes is needed to produce as well as these fishes must have been free from any undesirable characters. Regarding with some information about *Mystus* spp. the information on relationships between the dimensions of their biometric structure concerned with their growth performances and welfare condition are still required.

The main objectives of the present study are: to collect, identify and record the *Mystus* spp. from Thiri Malar Market, Aung Myay Tha Zan Township; to analyze the growth performance and condition factor of *Mystus* spp. and to evaluate the biometric indices and welfare of *Mystus* spp.

[1] Demonstrator, Department of Zoology, Meiktila University
[2] Lecturer, Department of Zoology, Kalay University
[3] Associate Professor, Department of Zoology, University of Mandalay

Materials and Methods

Study site

The Thiri Marlar Market is located between North Latidude 21˚50′ 10″ N and 21˚59 ′ 05″ N, and East Longitude between 96˚ 03 ′ 40 ″ E and 96 ˚ 03 ′ 45 ″ E (Plate 1).

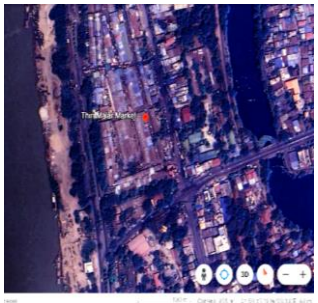

Plate 1 Map of the Thiri Malar Market. Source: Google earth, 2024.

Study period

The study period was started from June 2024 to September 2024.

Specimen collection

Mystus spp. such as *Mystus cavasius* (n=82), *M. pulcher* (n=95) and *M. bleekeri* (n=70) were collected from Thiri Malar Market weekly and transported to the Laboratory, Department of Zoology, University of Mandalay for further analysis (Plate 2).

Identification of species

The *Mystus* spp were identified by Talwar and Jhingran (1991) and Froese and Pauly (2024).

Morphometric measurements

Fishes were photographed by Oppo F19 pro smart phone. Fishes collected were grouped, marked serially on each species, and 14 morphological characters were measured by using ImageJ software (1.51 j8) in the nearest 0.01 cm. The head length (HL), total length (TL), standard length (SL), dorsal fin base (DFB), adipose fin base (AdpFB), caudal peduncle (CPD), caudal fin length (CFL), anal fin base (AnalFB), pelvic fin base (PFB), body depth (BD), pelvic fin length (PFL), anal fin length (AnalFL), adipose fin length (AdpFL), dorsal fin length (DFL).The body weight of each fish was recorded with digital kitchen scale with the nearest 0.01 g (Plate 3).

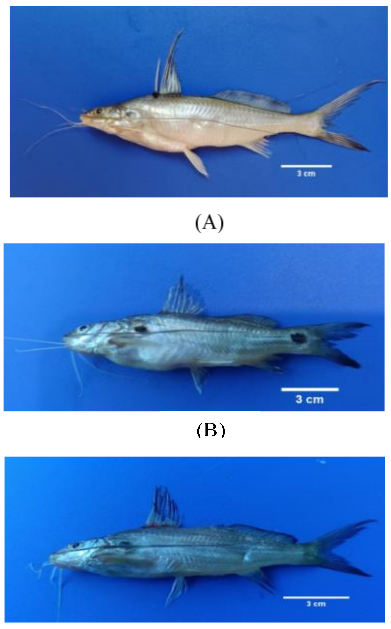

(A)

(B)

(C)

Plate 2 Lateral view of *Mystus cavasius* (A), *M. pulcher* (B) and *M. bleekeri* (C)

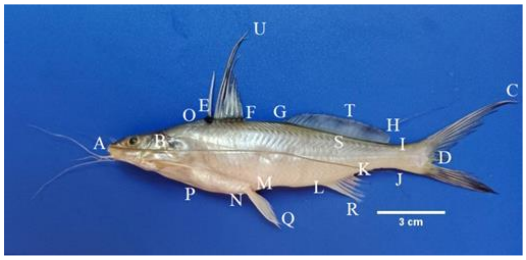

Plate 3 Landmark point of morphometric measurements in Mystus spp.

AB - Head length
AC - Total length
AD – Standard length
EF - Dorsal fin base
GH - Adipose finbase
IJ - Caudal peduncle length
DC - Caudal fin length
KL - Anal fin base
MN - Pelvic fin base
OP - Body depth
NQ - Pelvic fin length
LR - Anal fin length
ST - Adipose fin length
EU - Dorsal fin length

Growth performance

The length-weight relationships (LWR) and length-length relationships (LLRs) of *Mystus pulcher* were expressed by using Cube Law (Le Cren, 1951) as follows; $W = al^b$: Where, W is the weight in gram (g), l is the total body length in centimeters (cm), a is the intercept and b is regression slope. The value of a and b were estimated by means of linearized form of above equation, namely: $Log\ y = Log\ a + b\ Log\ x$

Condition factor

The condition factor of fish was deduced by Le Cren (1951): $K = \frac{W}{L^3}\ x100$: Where K is weight of the fish in grams, L is the total length of the fish in centimeters and b is the value obtained from the length-weight equation formula.

Data Analysis

All data for various biometric parameters of *Mystus* spp were generated by using SPSS (version. 21).

Results

Three species of *Mystus* spp were collected from Thiri Malar Market to investigate their biometric attributes. The mean values of total length (cm) of each species were presented in Table 1.

Table 1 Descriptive statistics in *Mystus* spp.

Parameters	*Mystus cavasius*	*Mystus pulcher*	*Mystus bleekeri*
Body weight (BW,g)	11.03 ± 5.40	6.67 ± 1.93	4.68 ± 2.33
Head length (HL,cm)	1.72 ± 0.38	1.25 ± 0.16	1.31 ± 0.22
Total length (TL,cm)	11.86 ± 2.23	8.33 ± 0.64	8.31 ± 0.93
Standard length (SL,cm)	9.50 ± 1.70	7.00 ± 0.53	6.90 ± 0.80
Dorsal fin base (DFB,cm)	1.16 ± 0.20	0.99 ± 0.13	0.87 ± 0.10
Adipose fin base (AdpFB,cm)	3.27 ± 0.85	1.60 ± 0.40	2.41 ± 0.40
Caudal peduncle (CPD,cm)	0.77 ± 0.15	0.76 ± 0.09	0.66 ± 0.39
Caudal fin length (CFL,cm)	2.49 ± 0.58	1.38 ± 0.18	1.56 ± 0.24
Anal fin base (AnalFB,cm)	0.93 ± 0.19	0.71 ± 0.12	0.63 ± 0.14
Pelvic fin base (PFB,cm)	0.32 ± 0.18	0.27 ± 0.10	0.23 ± 0.21
Body depth (BD,cm)	2.05 ± 0.50	1.77 ± 0.22	1.50 ± 0.31
Pelvic fin length (PFL,cm)	1.51 ± 0.29	0.92 ± 0.11	1.00 ± 0.11
Anal fin length (AnalFL,cm)	1.39 ± 0.28	1.01 ± 0.12	0.98 ± 0.13
Adipose fin length (AdpFL,cm)	0.49 ± 0.14	0.29 ± 0.07	0.40 ± 0.08
Dorsal fin length (DFL,cm)	2.67 ± 0.67	1.17 ± 0.14	1.24 ± 0.16
Condition factor (*K*)	0.66 ± 0.25	1.15 ± 0.30	0.78 ± 0.13

Total length (TL) vs body weight (BW)

The negative allometric growth patterns b < 3 were investigated in *Mystus* species. The value of b = 2.16 with coefficient of determination R^2 =0.592 in *Mystus cavasius*, b = 2.07 with R^2 =0.271 in *M. pulcher* and b = 2.83 with R^2 =0.765 in *Mystus bleekeri* were observed (Fig. 1).

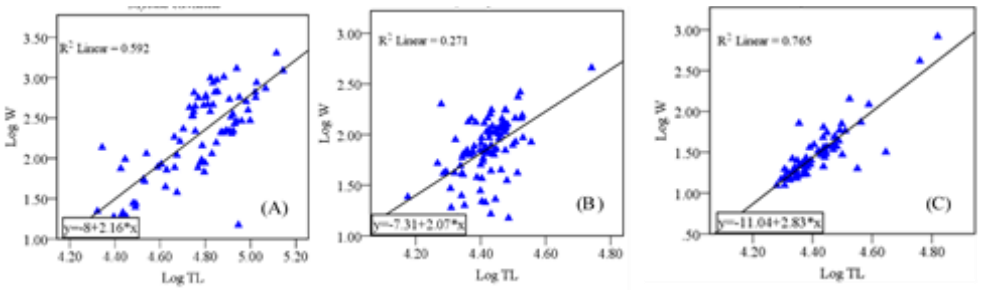

Fig.1 The relationship of total length (TL) and body weight (BW) of *Mystus cavasius* (A), *M. pulcher* (B) and *M. bleekeri* (C).

Total length (TL) vs standard length (SL)

The negative allometric growth pattern b < 1 with coefficient of determination R^2 > 0.903 whereas the positive allometric growth pattern b > 1 was observed in *M. bleekeri* with R^2 = 0.978 were observed (Fig.2.)

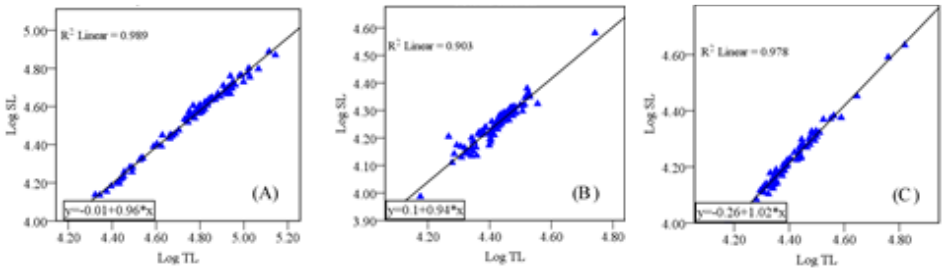

Fig.2 The relationship of total length (TL) and standard length (SL) of *Mystus cavasius* (A), *M. pulcher* (B) and *M. bleekeri* (C).

Total length (TL) vs head length (HL) in *Mystus* spp.

The positive allometric growth pattern b > 1 was observed in *M. cavasius* with coefficient of determination R^2 = 0.861, whereas the negative allometric growth patterns b < 1 revealed *M. pulcher* with R^2 = 0.101 and *M. bleekeri* R^2 = 0.444 (Fig.3).

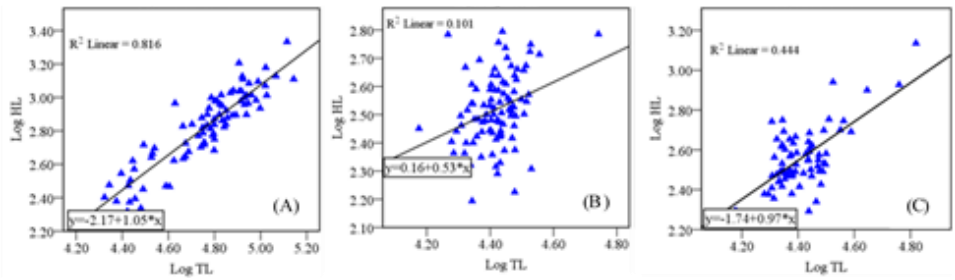

Fig.3 The relationships of total length (TL) and head length (HL) of *Mystus cavasius* (A), *M. pulcher* (B) and *M. bleekeri* (C).

Total length (TL) vs body depth (BD)

The positive allometric growth patterns b > 1 coefficient of determination R^2 = 0.583 and R^2 = 0.483 in *Mystus pulcher* and *M. bleekeri* whereas the negative allometric growth pattern b < 1 with R^2 = 0.861 was observed in *M. cavasius* (Fig.4).

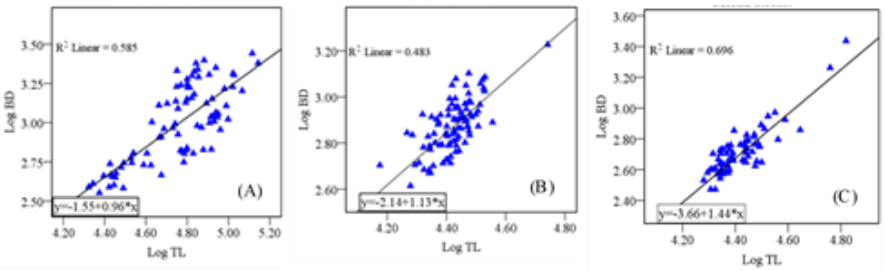

Fig.4 The relationships of total length (TL) and body depth (BD) of *Mystus cavasius* (A), *M. pulcher* (B) and *M. bleekeri* (C).

Pearson's correlation

A significant linear association was detected at significant level p < 0.01 and p < 0.05 level (2-tailed) in *Mystus cavasius* (Table 2).

In *Mystus pulcher*, most of the biometric attributes showed linear association at the significant level p < 0.01 and p < 0.05, however the very low association in head length (HL) with other characters was observed. The negative association was found in adipose fin length (AdpFL) to body depth (BD), weight (W) and caudal peduncle depth (CPD) (Table 3).

In *Mystus bleekeri*, the positive linear relationship was observed at the significant level p < 0.01 and p < 0.05. The very low association of biometric attributes was observed in pelvic fin base and negatively associated with body depth of fish r = -0.157 (Table 4).

Principle Component Analysis (PCA) in *Mystus* spp.

The principal component analysis (PCA) generated the three components in *M. cavasius*, four components in *M. pulcher* and three components in *M. bleekeri*. The results of the highest percent of variance 72.070 % with initial Eigne values 10.811 were observed in component 1 (C1) followed by *M. pulcher* with 39.654 % having Eigenvalues 5.948 and 54.101 % with Eigenvalues 8.115 in *M. bleekeri.* These initial Eigenvalues were similar to extraction sums of squared. However, the rotation sums of squared revealed the percent of cumulative was 86.520 % in *M. cavasius*, 67.689 % in *M. pulcher* and 75.364 % in *M. bleekeri* (Table 5 and Fig.5, 6 and 7).

Table 2 Correlation in biometric attributes of *Mystus cavasius*

Parameters	Log TL	Log SL	Log HL	Log BD	Log W	Log DFB	Log AdpFB	Log CPD	Log CFL	Log AnalFB	Log PelFB	Log PelFL	Log AnalFL	Log AdpFL	Log DFL
Log TL	1														
Log SL	.994**	1													
Log HL	.903**	.903**	1												
Log BD	.765**	.789**	.732**	1											
Log W	.770**	.795**	.736**	.900**	1										
Log DFB	.903**	.918**	.851**	.832**	.818**	1									
Log AdpFB	.910**	.911**	.828**	.785**	.794**	.854**	1								
Log CPD	.854**	.875**	.778**	.880**	.899**	.867**	.835**	1							
Log CFL	.941**	.920**	.838**	.715**	.703**	.850**	.842**	.788**	1						
Log AnalFB	.859**	.861**	.840**	.725**	.733**	.826**	.805**	.817**	.786**	1					
Log PelFB	.493**	.512**	.504**	.583**	.569**	.574**	.496**	.623**	.445**	.605**	1				
Log PelFL	.932**	.935**	.870**	.775**	.763**	.887**	.858**	.860**	.876**	.839**	.546**	1			
Log AnalFL	.900**	.902**	.824**	.662**	.714**	.840**	.778**	.790**	.866**	.833**	.489**	.868**	1		
Log AdpFL	.839**	.836**	.752**	.657**	.617**	.795**	.787**	.703**	.794**	.708**	.306**	.771**	.790**	1	
Log DFL	.947**	.929**	.836**	.595**	.614**	.828**	.822**	.738**	.913**	.804**	.431**	.894**	.882**	.785**	1

**. Correlation is significant at the 0.01 level (2-tailed). *. Correlation is significant at the 0.05 level (2-tailed).
a. Cannot be computed because at least one of the variables is constant.

Table 3 Correlation in biometric attributes of *Mystus pulcher*

Parameters	Log TL	Log SL	Log HL	Log BD	Log W	Log DFB	Log AdpFB	Log CPD	Log CFL	Log AnalFB	Log PelFB	Log PelFL	Log AnalFL	Log AdpFL	Log DFL
Log TL	1														
Log SL	.950**	1													
Log HL	.318**	.313**	1												
Log BD	.695**	.750**	0.173	1											
Log W	.521**	.567**	0.146	.570**	1										
Log DFB	.520**	.571**	0.146	.634**	.380**	1									
Log AdpFB	.398**	.370**	0.168	0.155	0.015	0.02	1								
Log CPD	.581**	.640**	.240*	.786**	.623**	.608**	0.041	1							
Log CFL	.652**	.513**	.216*	.384**	.313**	.348**	0.166	.353**	1						
Log AnalFB	.383**	.387**	0.187	.459**	.290**	.390**	-0.06	.537**	.325**	1					
Log PelFB	.395**	.416**	0.043	.419**	.408**	.467**	-0.13	.483**	.262*	.487**	1				
Log PelFL	.407**	.393**	0.028	.223*	0.08	0.19	.365**	0.147	.275**	0.139	0.03	1			
Log AnalFL	.293**	.369**	.233*	.292**	0.126	.360**	0.061	.277**	0.1	.392**	0.19	.296**	1		
Log AdpFL	.226*	0.177	0.115	-0.019	-0.03	0.13	.388**	-0.02	0.13	0.07	0.19	.342**	0.114	1	
Log DFL	.643**	.591**	0.169	.409**	.238*	.311**	.412**	.340**	.508**	.209*	.280**	.475**	.266**	.263*	1

**. Correlation is significant at the 0.01 level (2-tailed). *. Correlation is significant at the 0.05 level (2-tailed).
a. Cannot be computed because at least one of the variables is constant.

Table 4 Correlation in biometric attributes of *Mystus bleekeri*

Parameters	Log TL	Log SL	Log HL	Log BD	Log W	Log DFB	Log AdpFB	Log CPD	Log CFL	Log AnalFB	Log PelFB	Log PelFL	Log AnalFL	Log AdpFL	Log DFL
Log TL	1														
Log SL	.989**	1													
Log HL	.667**	.629**	1												
Log BD	.834**	.832**	.658**	1											
Log W	.874**	.866**	.604**	.769**	1										
Log DFB	.770**	.772**	.542**	.591**	.611**	1									
Log AdpFB	.365**	.365**	.238*	.361**	.287*	.404**	1								
Log CPD	.719**	.727**	.503**	.625**	.704**	.490**	-0.12	1							
Log CFL	.381**	.327**	.362**	.524**	.291*	.290*	0.12	0.18	1						
Log AnalFB	.423**	.391**	.303*	.567**	.289*	.364**	0.084	.310**	.872**	1					
Log PelFB	0.155	0.183	0.068	-0.157	0.18	0.21	0.14	0.12	-.562**	-.510**	1				
Log PelFL	.753**	.778**	.473**	.635**	.637**	.599**	.255*	.573**	.274*	.345**	0.05	1			
Log AnalFL	.707**	.712**	.454**	.621**	.593**	.530**	.252*	.629**	.316**	.426**	0.01	.701**	1		
Log AdpFL	.461**	.450**	.352**	.407**	.433**	.484**	.353**	.355**	0.22	.250*	0.04	.407**	.470**	1	
Log DFL	.704**	.681**	.455**	.624**	.591**	.541**	.268*	.442**	.412**	.435**	0.06	.539**	.561**	.383**	1

**. Correlation is significant at the 0.01 level (2-tailed). *. Correlation is significant at the 0.05 level (2-tailed).
a. Cannot be computed because at least one of the variables is constant.

Scree plot

Three principal components analysis (PCA) were observed in *Mystus cavasius* in which the eigenvalue 10.811 appeared in y-axis of component 1 (CP1), and then a line was steep down in CP 2 and CP 3 lie on the x-axis, after that the line show slowly down at the last component. The very steep y-axis line plot appeared in the same pattern of *M. pulcher* with five CPs and *M. bleekeri* had three CPs, however the line pattern revealed the similar pattern with various Eigenvalues (Fig.5, 6 and 7).

Table 5 Principal component analysis (PCA) in *Mystus* spp.

Species	Component	Total Variance Explained[a]								
		Initial Eigenvalues			Extraction Sums of Squared			Rotation Sums of Squared		
		Total	% of Variance	Cumulative %	Total	% of Variance	Cumulative %	Total	% of Variance	Cumulative %
Mystus cavasius	1	10.811	72.070	72.070	10.811	72.070	72.070	7.262	48.416	48.416
	2	1.094	7.296	79.367	1.094	7.296	79.367	3.869	25.794	74.210
	3	1.073	7.153	86.520	1.073	7.153	86.520	1.846	12.310	86.520
Mystus pulcher	1	5.948	39.654	39.654	5.948	39.654	39.654	4.371	29.137	29.137
	2	1.949	12.996	52.649	1.949	12.996	52.649	2.544	16.963	46.100
	3	1.219	8.124	60.773	1.219	8.124	60.773	1.783	11.889	57.990
	4	1.037	6.916	67.689	1.037	6.916	67.689	1.455	9.699	67.689
Mystus bleekeri	1	8.115	54.101	54.101	8.115	54.101	54.101	6.758	45.053	45.053
	2	1.794	11.959	66.060	1.794	11.959	66.060	2.353	15.686	60.739
	3	1.396	9.304	75.364	1.396	9.304	75.364	2.194	14.625	75.364

Extraction method: Principal Component Analysis, a= species

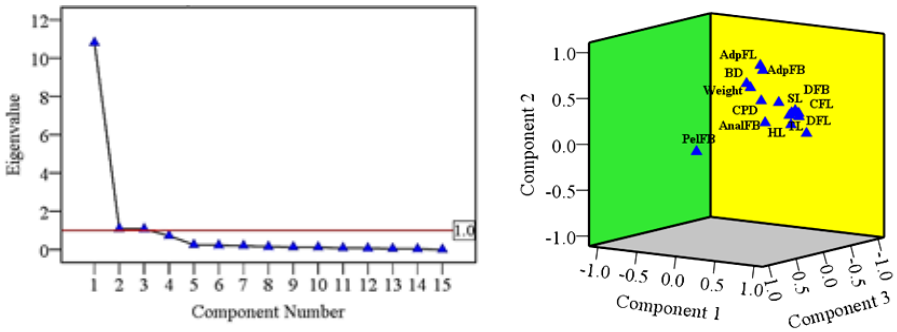

Fig.5. Principal component analysis (PCA) in *Mystus cavasius*
(Screeplot, left) and (Component plot in Rotated Space , right)

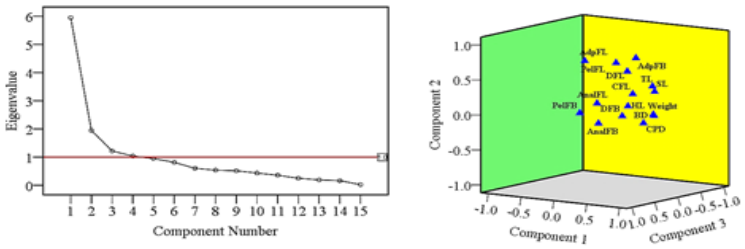

Fig.6 Principal component analysis (PCA) in *Mystus pulcher*

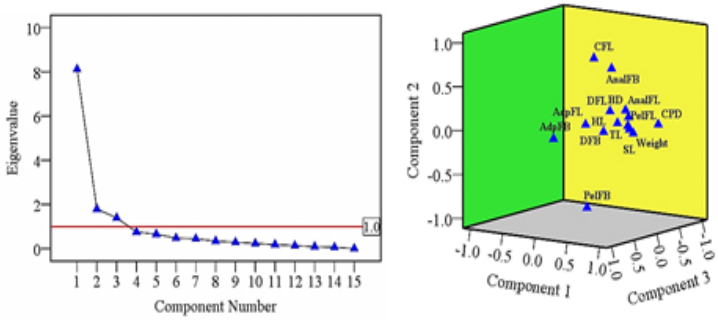

Fig.7 Principal component analysis (PCA) in *Mystus bleekeri* (Scree plot, left) and (Component plot in Rotated

Rotated component matrix in *Mystus* spp.

The rotated component matrix generated the multiple variations of biometric attributes in *Mystus* spp. with different components by analyzing with Varimax with Kaiser Normalization. The highest variation in dorsal fin length (0.951) of *M. cavasius* was observed in component 1 (C1) and the pectoral fin base (0.913) in C3. The lowest variable in pectoral fin base (0.126) in C1, (0.017) in C2 and adipose dorsal fin base (0.052) in C3.In *M. pulcher*, the highest variability of body depth (0.851) in C1, pectoral fin base (0.852) in C3 and anal fin length (0.839) in C4 were investigated, and the negative variability of biometric attributes were more observed in C2 and C3.In *M. bleekeri*, the component 1 (C1) revealed the high variability of biometric attributes were observed than C2 and C3. In addition, the negative association of attributes were investigated in the caudal peduncle depth (- 0.436) in C3 and pectoral fin base (- 0.896) in C2 (Table 6).

Table 6 Rotated component matrix in *Mystus* spp.

Parameters	*M. cavasius*			*M. pulcher*				*M. bleekeri*		
	Component			Component				Component		
	1	2	3	1	2	3	4	1	2	3
Body weight (BW)	0.454	0.675	0.397	0.770	0.043	0.047	-0.005	0.867	0.036	0.175
Head length (HL)	0.810	0.400	0.152	0.257	0.084	-0.134	0.570	0.693	0.147	0.273
Total length (TL)	0.893	0.402	0.141	0.799	0.458	0.106	0.158	0.899	0.148	0.336
Standard length (SL)	0.870	0.434	0.170	0.818	0.381	0.087	0.244	0.910	0.105	0.322
Dorsal fin base (DFB)	0.727	0.520	0.268	0.551	0.052	0.411	0.268	0.650	0.080	0.520
Adipose dorsal fin base(AdpFB)	0.372	0.804	0.052	0.209	0.734	-0.375	0.044	0.151	0.006	0.911
Caudal peduncle depth (CPD)	0.611	0.549	0.424	0.782	-0.045	0.278	0.253	0.827	0.044	-0.436
Caudal fin length (CFL)	0.864	0.354	0.094	0.548	0.334	0.176	-0.079	0.305	0.843	0.239
Anal fin base (AnalFB)	0.707	0.330	0.488	0.362	-0.036	0.658	0.315	0.503	0.730	0.132
Pectoral fin base (PFB)	0.126	0.017	0.913	0.214	0.125	0.852	-0.111	0.118	-0.896	0.125
Body depth (BD)	0.414	0.716	0.410	0.851	0.046	0.144	0.213	0.816	0.306	0.269
Pelvic fin base (PeFL)	0.836	0.386	0.230	0.162	0.712	-0.011	0.184	0.810	0.116	0.211
Anal fin length (AnalFL)	0.845	0.281	0.213	0.046	0.157	0.235	0.839	0.767	0.204	0.136
Adipose fin length (AdpFL)	0.233	0.823	-0.100	-0.123	0.751	0.263	0.026	0.371	0.133	0.518
Dorsal fin length (DFL)	0.951	0.180	0.081	0.448	0.642	0.153	0.081	0.593	0.277	0.296

Extraction Method: Principal Component Analysis. Rotation Method: Varimax with Kaiser Normalization.a,b
a. Species, b. Rotation converged in 4 iterations (*M. cavasius*) 6 iterations (*M. pulcher*) and 4 iterations (*M. bleekeri*)

Discussion

In aquaculture, the body conformation of fishes can be determined by their growth development patterns that are directly concerned with the physical environment especially the condition of their habitat (Froese, 2006). Recently, Fulton's condition factor used to compare the weight of a specimen or a group of fishes in a length class with that of "an ideal fish" which is growing without change in form according to the Cube Law. He also designated that the '*b*' value in length-weight relationship (LWR) was within the limits 2.5 - 3.5 for most fishes. Bervian *et al.* (2006) reported that when b > 1 (positive allometry), b < 1(negative allometry) b = 1 (isometry). Williams (2015) who stated that if the correlation between two variables is perfect, the correlation coefficient should be ± 1. However, the regression line should then explain all of the variance in the data, and R^2 should also be 1.

The mean range of total length (TL) in *Mystus* spp. was 8.31 - 11.36 cm with body weight 4.68 – 11.03 g. The LWRs of *Mystus cavasius*, *M. pulcher* and *M. bleekeri* showed the negative allometric growth patterns b < 3 indicating that the growth increment of body length is inversely proportional to the increment of body weight. This result is consisted with Froese (2006) stated that the growth of *Mystus pulcher* was negatively allometric, *i.e*., faster in weight than in length. In addition, Latif *et al.* (2018) reported that the negative pattern of growth development was found in *M. cavasius* from river Chenab, Punjab, Pakistan.

In fishery management, the LWRs are primary parameters as well as the length-length relationship (LLRs) are essential role in determination of body configuration. In this study, the development of growth patterns varies among the *Mystus* species. The best ideal growth performance was investigated in the relationship of total length (TL) to standard length (SL) in *M. bleekeri* and to head length (HL) in *M. cavasius*, whereas *M. pulcher* and *M. bleekeri* showed the positive allometric growth patterns in relation of TL to body depth (BD). Thus, these results are recommended to Al Nahdi *et al*. (2016) stated that temperature variation, different habit types, potential inherent differences in fish behavior and physiology across the sampling locations of different studies could change these values.

The relationship on growth pattern of fishes can be determined by using Pearson's correlation (correlation between variables) is used with the different indices (coefficients) and is not measured quantitatively. In this study, the various strength of growth development in coefficient of determination (R^2) was observed in *Mystus* spp. at $p < 0.01$ and $p < 0.05$.

On the other hand, the condition factor (*K*) used as an indicator of health in fishing biology (Le Cren, 1951)and he also recommended that if the $K < 1$, it indicates that fish growth is poor and $K > 1$ indicates that the general well-being of fish as good and condition factor (K) ≥ 1 was within the normal ranges. But he pointed out that the interpretation of the condition factor is difficult and prone to error. In this study, the best value of *K* revealed in *M.pulcher* and *M. cavasius* and *M. bleekeri* possessed $K < 1$.

Recently, the principal component analysis (PCA) is used in various fields to assess the biometric characters of various species in different levels. PCA is a statistical technique used for dimensionality reduction while preserving as much of the original data's variance as possible and this method is solved the Eigen problem in correlation matrix. The several of the largest eigenvalues can explain the large variation of analyzed random variables (Gniazdowski, 2017). Therefore, PCA method is used to analyze the biometric characters of *Mystus* spp. in this study.

Among the three species, the PCA generated highest variables with three components in *Mystus cavasius* with the initial Eigenvalues 10.811 and percent of variance 72.070 % in component 1 (PC1) tend to be reduced the total value 7.262 with 48.416 % by operating the rotation sums of squared. The lowest initial Eigenvalues with percent variability observed in

M. pulcher was 5.948 with 39.654 % in PC1 having four components and the results of rotating sums of squared loading showed the total Eigenvalues 4.371 with 29.137 %. The moderate variability of biometric characters was investigated in *M. bleekeri* having three components with the initial Eigenvalues 8.115 (54.101 %) in PC1 tend to be reduced the Eigenvalue 6.758 with 45.053 %. These variable biometric characters in each component of respective species are corresponded with the results of component transformation matrix. The association of biometric characters in each component of *Mystus* spp. revealed the highest association in PC2 of *M. cavasius* and the lowest association in PC1 of *M. pulcher.* The negative association of biometric associations was investigated in these species. Therefore, these primary findings could be utilized for estimation of biometric indices of *Mystus* population growth.

Conclusion

The negative allometric growth patterns revealed in *Mystus* species used as biometric indicators of relationship in total length (TL) vs body weight (W); the positive allometric pattern was assigned in TL vs standard length (SL) of *M. bleekeri*; TL vs HL in *M. cavasius*. The healthy body conformation was investigated in TL vs body depth (BD) of *M. pulcher* and *M. bleekeri.* Pearson's correction revealed the significant relationship between the biometric characters in each species at $p < 0.01$ and $p < 0.05$. The highest variability of biometric attributes with their components appeared by principal component analysis (PCA). The present study could prove the basis strategies of *Mystus* spp. for various purposes in fishery areas.

Acknowledgements

Special thanks to Rector Dr Ba Han and Pro-rectors, Meiktila University for their accepting this paper. I am gratefully to Dr Ni Ni Yin, Professor and Head of Department of Zoology, for her various valuable suggestions. I am thankful to Dr Aye Aye Than, Professor, Department of Zoology, for her comments and greatful to members of ERC committee of Meiktila Uniersity, for their advice and suggestions.

References

Al Nahdi, A., Garcia de Leaniz, C., and A.J. King, (2016) "Spatio-temporal variation in length-weight relationships and condition of the ribbonfish *Trichiurus lepturus* (Linnaeus, 1758): implications for fisheries management." PloS One 11(8).

Bervian, G., Fontoura, N. F. and M. Haimovici, (2006) "Statistical model of variable allometric growth: otolith growth in *Micropogonias furnieri* (Actinopterygii, Sciaenidae)." *Journal of Fish Biology*, vol.68. pp196-208.

Froese, R., (2006) "Cube law, condition factor and weight-length relationships: history, meta- analysis and recommendations." *Journal of -Applied Ichthyology*. Berlin, vol.22. pp241-253.

Froese, R., and D. Pauly, (2024) *FishBase*. World Wide Web electronic publication. www. fishbase.org, version (06/2024).

Gnizzdowski, Z., (2017) " New Interpretation of principal Components Analysis." *Zeszyty Naukowe WWSI*, vol. 16(11). pp43-65.

Latif, M. Ullah., M. Z, Minhas, I. B. and S. Latif, (2018) "The length – weight relationships of *Mystus cavasius* with special reference to body morphometric characters from river Chenab, Punjab, Pakistan" *Journal of Entomology and Zoology Studies*, vol.6(2). pp2418-2421.

Le Cren, E.D., (1951) "The length-weight relationship and seasonal cycle in gonadal weight and condition in the perch *Perca fluviatilis." Journal of Animal Ecology*, vol.62. pp113-124.

Talwar, P.K., & A.G. Jhingran, (1991) *Inland fishes of India and Adjacent Countries*. Oxford and IBH Publishing Co.Pvt, Ltd. vol.2. pp569.

Williams, B., (2015) *Biostatistics: Concepts and applications for biologists*. Chapman and Hall, 2-6 Boundary Row, London, UK. pp168-169.

Relative abundance and habitat preference of some Spider species on Phayargone village in Thanlyin Township, Yangon Region

Moh Moh Hlaing[1], Nu Sein[2]

Abstract

The aim of this research is to determine relative abundance and habitat preference of spider species with related to environmental variables. The research area of three sampled sites that sampling were carried out from November, 2024 to October, 2025 in Phayargone village, Thanlyin township. Monthly data collection was carried out in each study site. Field observation was made collected from 7:00 am to 10:00 am. Collection was conducted by three different ways such as hand collecting, beating and sweeping. Some species were collected through hand collecting. Inactive spiders were caught with gloved hands. The spider species were collected by using liquid-preserved materials, chloroform. The recorded species were identified by the external morphological characters according to Ubick (2000) and Koh (2001). During the study period, a total of 394 individuals representing 48 individuals in Site I, 257 individuals in Site II and 89 individuals in Site III were recorded. The abundance of species were found in site II > site III > site I respectively. Seasonal variation of population abundance of species and individuals are most commonly found in the winter (55%), followed by the summer (27%), and are least commonly found during the rainy season (18%) due to effect of temperature and humidity.

Keywords: Spider species, relative abundance, Phayargone village in Thanlyin Township

Introduction

Spiders are important parts of the ecological balance of this world. Spiders have a very significant role to play in the ecology by being exclusively predatory (Wise, 1993) and there by regulated insect population. Spiders may also serve as bio-control agent (Raghavendra, 2001). Spiders are members of the Phylum Arthropoda, Class Arachnida, Order Araneae and is also the largest group with the highest diversity. The large group of animals with joined legs and a hard external body shell, the exoskeleton. There are 111 families, 3642 genera, 39490 species of spiders in the world (Platnick, 2008). In Myanmar, there are 47 families 160 genera and 532 species of spider species as recorded by (Ubick, 2000).

All spiders are carnivorous. Their prey consists chiefly of insects; but they also feed on other spider, if the situation permits and even on weaker members of their species. Their social behaviour is seen by a number of individuals taking part in one hunt or sucking the same prey. Insects are the usual prey of spiders. The body remains of the dark prey are not thrown out of the nest (Tikader, 1987).

Spiders are abundant and found everywhere; occurring inside and outside of human habitats. They could be found everywhere in different habitats like in the houses, in gardens, on way side trees, in the sand, on the water surface, under the stones, vegetation in mangrove swamps, grassy areas, among the foliage, man-made structure, walls of buildings, tree trunks, etc. Spiders are found in tall and low plants, little on forest floors, curled leaves, dried leaves on tree, under bark, under stones, under fallen logs. Most spiders prefer dark and shaded location and found in caves. Some species also prefer water courses, found in shrubs and bushes near the streams and found on the shrubbery which overhangs the streams (Kaston, 1972).

[1] Daw, Demonstrator, Department of Zoology, University of Yangon
[2] Dr, Associate Professor, Department of Zoology, East Yangon University

The objectives of the present study are: 1) to observe the seasonal variations of collected spiders; 2) to explore the habitat preference of recorded spider species; 3) to determine the relative abundance of the spider species in the study area

Materials and Methods

Study area

Phayargone village in Thanlyin Township is located at the east part of Yangon Region, Myanmar. It is situated between latitudes 16°42.706´N and longitudes 96°16.846´E.

Study period

The study period lasted from November 2024 to October 2025.

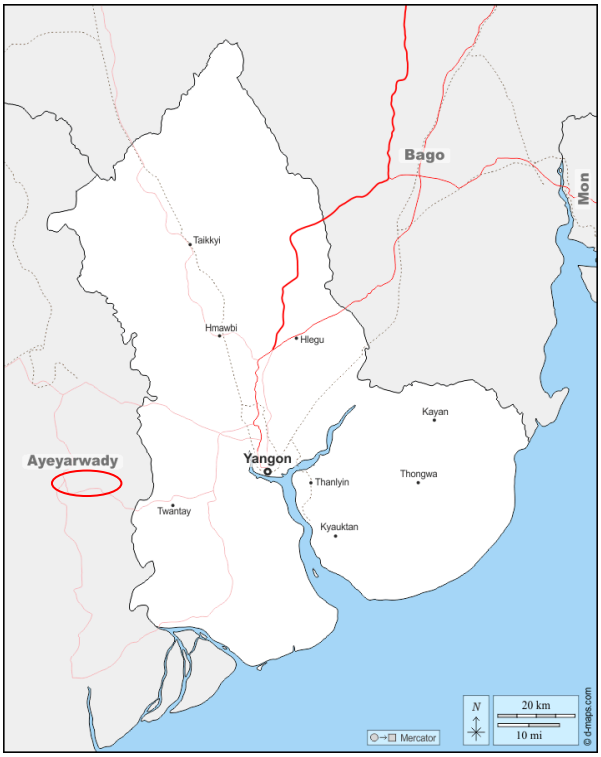

Fig. 1 Map of Thanlyin Township (Source: Google Earth)

Site I (Scattered trees) Site II (Garden) Site III (Vegetation)

Plate 1. Habitat utilization of Spider species

Collection of specimens

Collection of specimens was made fortnightly. Collection was conducted by three different ways such as hand collecting, beating and sweeping. Some species were collected through hand collecting. Inactive spiders were caught with gloved hands. Beating method was used for catching the spider hidden among the bushes and branches from the tree. Their hidden places were beaten with the stick to make the spiders come out from the hidden areas. Sweeping method was conducted for extracting spiders from vegetation that is too low or too soft for beating. The sweep net is a heavy bag attached to a stout wooden pole.

Identification of the specimens

The collected specimens were identified followed after Levi and Levi (1990), Ubick (2000) and Koh (2001).

Data analysis

Calculation of relative abundance index was according to Kumar and Sivaperu man (2005).

$$\text{Relative abundance index (or) Dominant index} = \frac{\text{Total individual no. of particular spices}}{\text{Total individual numbers of all species}} \times 100$$

Five categories were determined based on index values as follows:

Abundant	= (8.1 & above)
Common	= (6.1- 8.0)
Frequent	= (4.1- 6.0)
Uncommon	= (2.1- 4.0)
Rare species	= (0.1- 2.0)

Results

A total of 20 spider species of 20 genera, nine families under one order were recorded from the study areas.

Classification

The classification of the collected species was done according to Levi and Levi (1990), Ubick (2000) and Koh (2001).

Table 1. Species occurrence of spiders in study areas

Family	No	Scientific name	Common name
Araneidae	1	*Argiope pulchella*	Garden cross spider
	2	*Bijoaraneus mitificus*	Kidney garden spider
	3	*Cyclosa bifida*	Long-Bellid Cyclosa Spider
	4	*Cyrtophora cicatrosa*	Garden-tent web spider
	5	*Gasteracantha kuhli*	Black and white spiny spider
	6	*Neoscona orucifera*	Spotted Orbweaver
	7	*Parawixia dehami*	Common-garden spider
Family	**No**	**Scientific name**	**Common name**
	8	*Poltys illepidus*	Tree-stump spider
	9	*Thelacantha brevispina*	Asian-sided sector spider
Lycosidae	10	*Lycosa erythrognatha*	Wolf spider
Nephilidae	11	*Nephila antipodiana*	Batik golden web spider
Nesticidae	12	*Nesticus cellulanus*	Comb-footed cellar spider
Oxyopidae	13	*Oxyopes javanus*	Burmese Lynx spider
Salticidae	14	*Menemerus semilimbatus*	Half-edged Wall jumping spider
	15	*Myrmaplata melanocephala*	Ant-mimicking spider
	16	*Phintella versicolor*	Multi-coloured phintella
Scytodidae	17	*Scytodes pallida*	Pale Spitting Spider
Sparassidae	18	*Heteropoda venatoria*	Huntsman spider
	19	*Latrodectus geometricus*	Brown widow
Zodariidae	20	*Storena cinctipes*	Spotted Ground spider

Table 2 Monthly occurrence of spider species from Phayargone Village

No	Species	Nov	Dec	Jan	Feb	Mar	Apr	May	Jun	Jul	Aug	Sep	Oct	Total
1	Argiope pulchella	**2**	**2**	4	1	2	4	3	1	1	0	1	2	23
2	*Bijoaraneus mitificus*	0	1	2	1	1	0	1	1	0	0	0	0	7
3	*Cyclosa bifida*	1	0	1	0	1	0	1	0	1	1	0	0	6
4	*Cyrtophora cicatrosa*	1	6	8	2	4	1	3	1	1	1	1	2	31
5	*Gasteracantha kuhli*	0	1	1	0	0	1	1	1	0	0	0	0	5
6	*Neoscona crucifera*	0	3	6	2	1	3	2	0	1	1	1	1	21
7	*Parawixia dehami*	2	4	1	5	0	1	0	1	0	0	0	0	14
8	*Poltys illepidus*	3	5	9	1	2	4	1	0	1	1	0	1	28
9	*Thelacantha brevispina*	0	1	1	0	1	0	0	0	0	0	0	1	4
10	*Lycosa erythrognatha*	8	10	9	16	10	2	3	1	1	0	2	2	64
11	*Nephila antipodiana*	4	3	3	1	2	3	2	0	0	0	1	3	22
12	*Nesticus cellulanus*	1	2	2	1	3	2	0	0	1	0	1	2	15
13	*Oxyopes javanus*	5	7	2	4	2	5	7	2	1	1	1	3	40
14	*Menemerus semilimbatus*	1	1	1	4	2	3	1	0	0	0	0	2	15
15	*Myrmaplata melanocephala*	1	2	2	0	1	0	0	0	0	0	0	0	6
16	*Phintella versicolor*	3	2	10	2	2	3	2	1	2	0	1	2	30
17	*Scytodes pallida*	5	3	4	1	3	2	2	1	1	2	1	2	27
18	*Heteropoda venatoria*	0	1	1	0	0	0	0	0	0	0	0	0	2
19	*Latrodectus geometricus*	0	1	2	0	0	0	0	0	0	0	0	0	3
20	*Storena cinctipes*	3	5	7	1	2	2	3	1	3	1	0	3	31
	Total	40	60	76	42	39	36	32	11	14	8	10	26	394

Table 3 Seasonal variation of population abundance

Study site	Summer	Rainy	Winter	Total
Site I	15	10	23	48
Site II	64	48	145	257
Site III	28	11	50	89
Total	107	69	218	394
Percentage	27%	18%	55%	100%

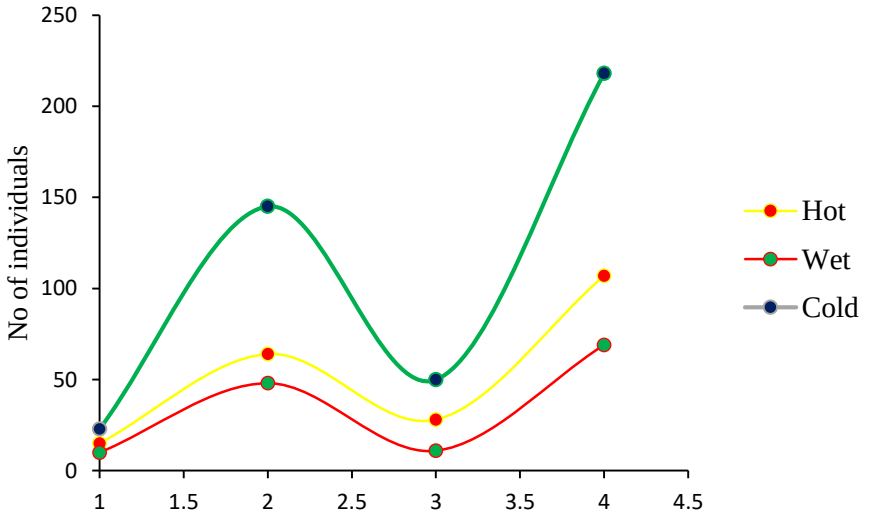

Fig. 2 Seasonal variation of population abundance

Plate 1 (A) *Argiope pulchella* **(**B) *Bijoaraneus mitificus* (C) *Cyclosa bifida* (D)*Cyrtophora cicatrosa* (E) *Gasteracantha kuhli* (F) *Neoscona crucifera* (G) *Parawixia dehami* (H) *Poltys illepidus* (I) *Thelacantha brevispina* (J) *Lycosa erythrognatha* (K) *Nephila antipodiana* (L) *Nesticus cellulanus* (M) *Oxyopes javanus* (N) *Menemerus semilimbatus* (O) *Myrmaplata melanocephala* (P) *Phintella versicolor* (Q) *Scytodes pallida* (R) *Heteropoda venatoria* (S) *Latrodectus geometricus* (T) *Storena cinctipes*

Table 4 Seasonal occurrence of temperature (C°) and humidity (%) in Phayargone Village

Season (2024 – 2025)	Temperature (C°)	Humidity (%)
Winter (Nov – Feb)	Avg. (18°C- 26°C)	Avg. (60% - 70%)
Summer (Mar – May)	Avg. (32°C - 36°C)	Avg. (74% - 86%)
Rainy (Jun – Oct)	Avg. (26°C - 30°C)	Avg. (84% _ 90%)

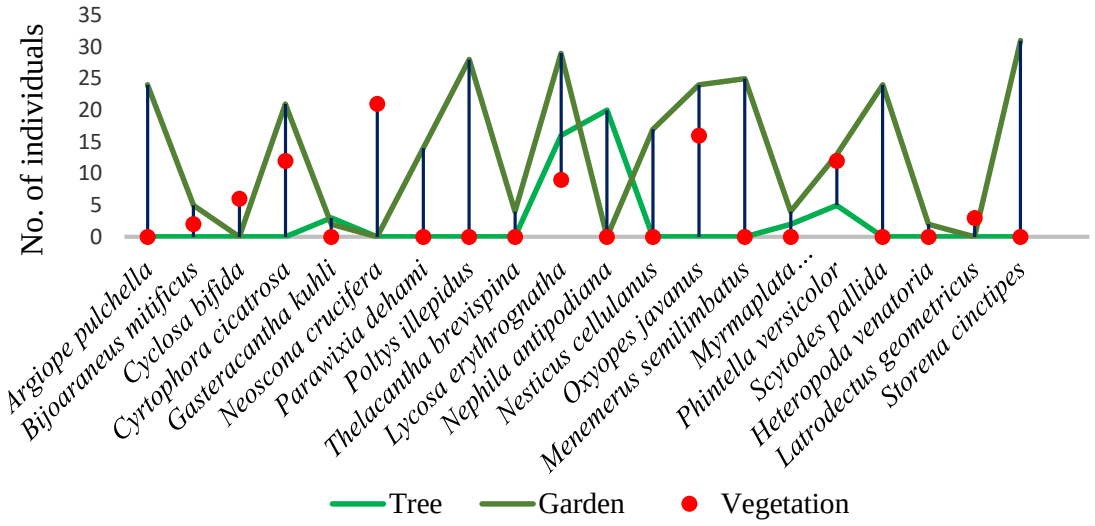

Fig. 3 Abundance of three study sites

Table 5 Individual numbers of recorded spider species in different habitats

No	Scientific name	Site I Tree	Site II Garden	Site III Vegetation	Total	Dominant Index	Abundance
1	*Argiope pulchella*	0	23	0	23	5.84	Frequent
2	*Bijoaraneus mitificus*	0	5	2	7	1.78	Rare
3	*Cyclosa bifida*	0	0	6	6	1.52	Rare
4	*Cyrtophora cicatrosa*	0	21	10	31	7.88	Common
5	*Gasteracantha kuhli*	3	2	0	5	1.27	Rare
6	*Neoscona crucifera*	0	0	21	21	5.33	Frequent
7	*Parawixia dehami*	0	14	0	14	3.55	Uncommon
8	*Poltys illepidus*	0	28	0	28	7.11	Common
9	*Thelacantha brevispina*	0	4	0	4	1.02	Rare
10	*Lycosa erythrognatha*	16	29	19	64	16.24	Abundant
11	*Nephila antipodiana*	22	0	0	22	5.58	Frequent
12	*Nesticus cellulanus*	0	15	0	15	3.81	Uncommon
13	*Oxyopes javanus*	0	24	16	40	10.15	Abundant
14	*Menemerus semilimbatus*	0	15	0	15	3.81	Uncommon
15	*Myrmaplata melanocephala*	2	4	0	6	1.52	Rare

16	*Phintella versicolor*	5	13	12	30	7.61	Common
17	*Scytodes pallida*	0	27	0	27	6.85	Common
18	*Heteropoda venatoria*	0	2	0	2	0.51	Rare
19	*Latrodectus geometricus*	0	0	3	3	0.76	Rare
20	*Storena cinctipes*	0	31	0	31	7.88	Common
	Total species	**5**	**16**	**8**	**20**		
	Total individuals	**48**	**257**	**89**	**394**		

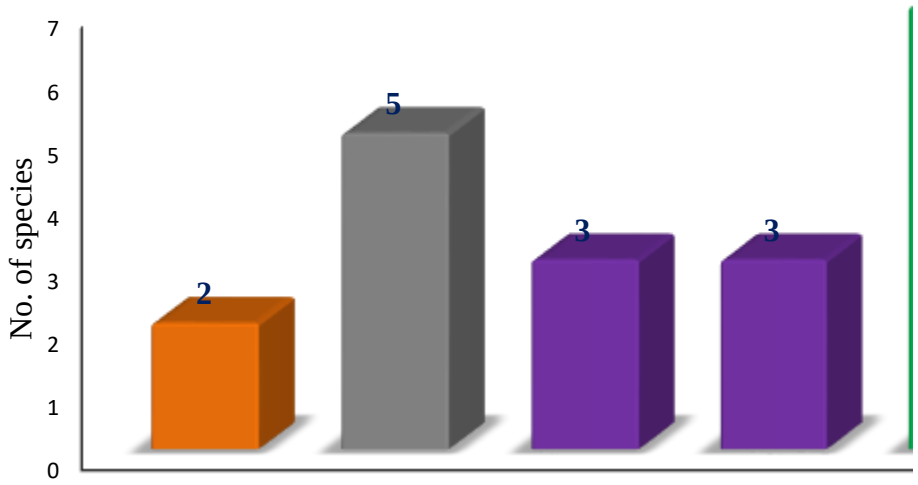

Fig. 4 Five categories of spider species from three habitat

Discussion

. A total of 20 species including 20 genera belonging to nine families under order Araneae were recorded during the study period. The present study was conducted for abundance of spiders between these three habitats types. During study period, a total of 394 individuals representing 20 species were caught. As the results, the family Araneidae was the most represented, with nine species. This was followed by Salticidae with three species, Sparassidae with two species, Lycosidae, Nephilidae, Nesticidae, Oxyopidae, Scytodidae, and Zodariidae, each represented by a single species. Levi (2002) reported that family Araneidae was the most numerically dominant taxa of the study area and spiders of this family. Moreover, Puja (2014) stated that Araneidae was the predominant family of total spider abundance in Sarangyuri Lake in India.

According to the species composition, *Lycosa erythrognatha* were the highest number of individuals. The second highest number of individual were *Oxyopes javanus.* The lowest number of individual were *Heteropoda venatoria.* Seasonal variation was examined, 218 individual numbers in winter, 107 individual numbers in summer and 69 individual numbers in rainy season due to spider's favorite temperature (Avg. 18°C - 26ºC) and humidity (Avg. 60% - 70%). Hence, seasonal variation of spider's population size was higher

in the present study. In the present work, the highest number of spider species was recorded in cold season. Jay Sat Aung (2018) reported that the highest number of species was found in cold season. So, it is agreed with the present study.

In the present study, sixteen species were observed in site II, eight species were found in Site III and five species were found site I respectively. According to the habitat utilization of the highest numbers of spiders were recorded from garden (257 individuals) followed by vegetation (89 individuals), while the lowest number (48 individuals) was found scattered tree.

The population size was highest in winter while the lowest in rainy season. It might be depending on the population density of the spider in the climatic changes of Phayargone village in Thanlyin Township. In any sustainable ecosystem, rare species are the most common and the abundance species are found in very few numbers in species (Krebs, 2001). In the Phayargone village, two abundance species, five common species, three frequent species, three uncommon species and seven rare species were assessed. In the present study, rare species were the most species numbers. Hence. These findings was good agreement with that of Kerbs and indicate that there is a high diversity of spider species in Phayargonr village, Thanlyin Township. According to the species abundance, five species of 48 individuals were recorded in site I, 16 species of 257 individuals in site II and eight species of 89 individuals in site III were found to differ in three study sites. *Lycosa erythrognatha* is important in agriculture, as this is efficient controlling agent insect pests. All types of spiders are important that control the pest population in vegetable garden.

Thanlyin Township is situated at the east part of Yangon Region, Myanmar. Phayargone village is located in the plain area. Moreover Trees, gardens and vegetation's are found in this area and have many various flora and fauna. The ecological situation is very favorable for the breeding and propagation of spiders. Therefore, it is necessary to have knowledge on the status of the spiders present in the area.

Conclusion

A total of 394 individuals of 20 species of spider falling into 20 genera under nine families were recorded. Study site contains three habitats such as scattered tree, garden and vegetation. Species numbers was highest in winter 55%, lowest in rainy season 18% were recorded in the different studies. According to the habitat preference of spider species numbers was highest in site II (garden), lowest in site I (vegetation). In the present study, two abundance species, five common species, three frequent species, three uncommon species and seven rare species were assessed. Based on these findings, the diversity of spider species was still rich in the Phayargone village in Thanlyin Township.

Acknowledgements

We wish to express our sincere gratitude to Dr Myo Min Tun, Acting Rector, Dr Aye Aye Ko and Dr Thida Aung Pro-Rector, East Yangon University, for their kind permission to participate in University Commemoratives Research Paper Reading Ceremony. Our special thanks go to Dr Kay Lwin Tun, Professor and Head of the Department of Zoology, University of Yangon and Dr Ei Khine Win, Professor and Head of the Department of Zoology, East Yangon University, for their valuable suggestions.

References

Aye Thida, 2007. Taxonomy and Ecology Study of some Spider in Hlawga Wildlife Park. MRes, Deparment of Zoology, Yangon University.

Bennett, S. M. 2000. http:// www. The piedpiper. Co. vk / th 11.htm.

Jay Sat Aung, 2018. Eecology study on some spider species in Pyay Environs, Pyay Township. MSc Thesis, Department of Zoology, Pyay University.

Kaston, B.J., Kaston, E., 1972. *How to know the Spiders:* Wm. C Brown Company.

Koh, K. H., 2001. A Guide to Common Singapore Spiders. BP Guides, Singapore

Kumar, S. and Sivaperuman, C. (2005) Bird Community Structure in Ranthambore National Park. Tiger Paper, 32, 16-17.

Levi, H.W., Levi, L.R., 1990. *Spiders and their kin*. 160pp. Golden Press, New York.Science Center.

Platick, N.I., 2008. The world spider catalogue, Version 9.5. American Museum of Natural History.

Puja, K. 2014. Diversity of spider fauna from sarang puri Lake, Arvi, Vidarbha Region. Journal of Life Science, 2(2): 165-167.

Raghavendra, N., 2001. Diversity of arboreal spiders in Cashwe orchards. *M.Sc, Dissertation*, Department of Alied Zoology, Mangalore University.

Tikader, B.K. 1987. Handbook of Indian Spiders. Calcutta. Zoological survey of India. 251pp.

Ubick, D. 2000. Arachnid identification manual. Malaysian Nature Society, KualaLumpur.

Wise, D.H. 1993. Spiders in Ecological Webs.Combridge University. Press, London. 342pp.

Investigation on Growth Performance and Nutritional Values of Black Soldier Fly, *Hermetia illucens* (Linnaeus,1758) at Different Substrates

Aung Thu Zar Tun[1], Su Hlaing Myint[2], Pa Pa Win[3]

Abstract

An investigation of the growth performance and substrate utilization of the black soldier fly, *Hermetia illucens* (Linnaeus, 1758), was conducted from April 2025 to March 2026 under laboratory conditions. A laboratory colony was maintained at 28 ± 2°C and 70 ± 10% relative humidity. First-instar larvae were reared in plastic trays (2 × 1 × 0.6 ft), each stocked with 8 g of larvae and assigned to one of three substrate treatments: rice bran, banana and watermelon peel. An initial 320 g of substrate was provided, followed by an additional 240 g after ten days. Larval growth performance was assessed every five days by randomly sampling 150 larvae per tray to measure body length, body weight, and total biomass. Feed reduction rate was calculated based on the remaining substrate weight. *H. illucens* successfully completed its entire life cycle under controlled conditions. Significant differences in initial body weight among larval, pupal, and adult stages were observed, confirmed by Welch's robust test ($p < 0.001$), indicating normal developmental progression. A strong positive relationship between body length and weight was recorded across larval instars and trial days, reflecting continuous growth and efficient nutrient assimilation. Adult morphometric analysis using the Kruskal–Wallis test revealed significant sexual dimorphism, with females exhibiting greater body length and weight than males ($p < 0.001$). Substrate type significantly influenced larval performance, with banana and watermelon peel supporting higher biomass accumulation and waste reduction rates compared to rice bran. Overall, the results demonstrated the strong bioconversion potential of *H. illucens* and highlight the importance of substrate selection for optimizing larval growth and organic waste reduction.

Keyword: Black soldier fly, *Hermetia illucens*, larval development, growth performance

Introduction

Black soldier fly ***Hermetia illucens*** larvae (BSFL) have emerged as a promising biological tool for organic waste valorization and sustainable protein production due to their rapid growth and high nutrient content (e.g., protein and lipids). Substrate type plays a central role in BSFL growth performance, waste reduction efficiency, and nutritional composition, ultimately influencing their viability as livestock feed or aquaculture ingredients (Surendra *et al*., 2022). Growth performance indicators such as larval weight gain, development time, and biomass yield differ significantly when BSFL are reared on substrates with varying nutrient profiles particularly in protein and energy content highlighting substrate quality as a critical determinant in larval productivity and nutrient accumulation (*Khasanah, et al*., 2025). Organic substrates influence not only larval growth but also the biochemical properties of BSFL. For instance, higher protein and lipid contents have been observed in BSFL when reared on nutrient-rich substrates like tofu by-products compared to general food waste, underscoring the link between substrate composition and larval nutrient profile (Lee *et al*., 2025). The ability to manipulate larval nutrient composition by substrate choice is crucial for tailoring BSF biomass for specific feed applications, such as poultry or fish nutrition (Bosch *et al*., 2022)

The present study was conducted with the following aim and objectives;

- to study the developmental stages of black soldier fly, *Hermetia illucens*
- to investigate the life parameters of BSF in laboratory condition
- to assess the nutritional values of BSFL at different substrates

Materials and methods

Study area and study site

The study site was at the University of Research Centre, EYU. It is located at North latitude 16 º44ˈ14″ N and East longitude 96 º17ˈ04″ E (Fig. 1).

Study period

The study period lasted from April 2025 to February 2026.

Preparation of specimen and data collection

A laboratory colony of *Hermetia illucens* was maintained under controlled environmental conditions (28 ± 2°C, 70 ± 10% RH). For the experiment, empty plastic trays (2 × 1 × 0.6 ft) were weighed and each stocked with 8 g of mixed-instar larvae. Each tray was assigned one of three substrate treatments: rice bran, banana, and watermelon peel, with an initial provision of 320 g of substrate. After ten days, an additional 240 g of fresh substrate was added to each tray. Every five days, 150 larvae were randomly sampled from each tray for biometric measurements, including body length (cm), body weight (g), and total biomass (g). Remaining substrate weight was recorded to calculate feed reduction rates. After 20 days, larvae were harvested, rinsed, and oven-dried at 60°C until constant weight. Dried samples were ground and analyzed at the Analytical Laboratory Unit, Department of Fisheries, Thakayta Township, for assessment of nutritional values. (Plate 1)

Data analysis

Survival Rate (%) (Percentage of Individuals that Survive to a Given Stage) Southwood & Henderson (2000).

$$\text{Survival rate (\%)} = \frac{\text{Number of surviving individuals at a specific stage}}{\text{Total number of individuals at the initial stage}} \times 100$$

Waste reduction rate (D) (Lalander *et al.*, 2018)

$$D = \frac{W - R}{R} \times 100$$

Where, D = waste reduction rate

W = weight of the waste used at time t

R = residue leftover after time t

Data were analyzed using SPSS v28. One-way ANOVA with Welch correction and Tukey's post-hoc test was applied for group comparisons. Homogeneity of variance was assessed via Levene's test, and non-parametric Kruskal–Wallis tests were used where assumptions were violated. Scatter plots and correlation analyses were conducted to examine relationships among growth and performance metrics.

Identification of species

Identification was made follow after Borror *et al.*, 1976 and Triplehorn and Johnson, 2004.

Fig. 1 Map of University of research center
(East yangon University)
Source Google earth, 2025

(A) Tray

(B) Digital Balance

(C) Weight of larvae

(D) Weight of rice bran

(E) Weight of banana

(F) Weight of watermelon peel

Plate 1 Materials used and start trial weight of larva and substrates

(A) Weight of larvae

(B) Weight of rice bran

(C) Weight of banana

Plate 2 Materials used end weight of larva and substrates

(A) Dark cage for pupation

(B) Mating cage for adult

Plate 3 Materials used for adult

(A) Preparation for nutritional assessment

Plate 4 Materials used for nutritional assessment

Results

Comparison of weight and length in instar under three substrates in growth conditions

Larval growth of ***Hermetia illucens*** showed a progressive and orderly increase in body length with advancing instar stages across all three substrates (rice bran, banana, and watermelon). Mean larval length increased consistently from the 1st instar through the 5th instar, followed by a reduction at the prepupal stage, which is typical of BSF development.

Across all instars, larvae reared on banana substrate recorded slightly higher mean lengths**,** followed by watermelon and rice bran. At the 5th instar, banana-fed larvae attained the greatest mean length (16.60 ± 2.00 mm), while rice bran-fed larvae showed the lowest (15.80 ± 1.80 mm). However, one-way ANOVA revealed no statistically significant differences ($p > 0.05$) among substrates for any instar stage.

Although length differences were not statistically significant**,** the consistent numerical advantage of banana substrate suggests improved nutrient availability, which is later reflected in significantly higher larval weight and growth performance Thus, instar-wise length development was comparable among substrates**,** while weight gain differed substantially, indicating that substrate quality influenced biomass accumulation more strongly than linear growth. (Table 1. and Fig. 2)

C**omparison of Weight and Length in Prepupa and Pupa**

At the prepupal stage, larvae exhibited a reduction in body length compared to the 5th instar**,** reflecting physiological contraction prior to pupation. Prepupal length was highest in banana-fed larvae (13.10 ± 1.65 mm), followed by watermelon (12.80 ± 1.60 mm) and rice bran (12.40 ± 1.50 mm); however, these differences were not statistically significant ($p > 0.05$)**.**

Although pupal morphometric values were not quantified by substrate, adult emergence data revealed highly significant differences ($p < 0.001$) in adult length and weight between males and females, irrespective of substrate. This indicates that sexual dimorphism strongly influenced adult size**,** while substrate effects were more pronounced during larval biomass accumulation rather than during pupal morphogenesis. (Table 1. and Fig. 2, B)

Comparison of adult morphometric measurements

Adult morphometric analysis using the Kruskal–Wallis test revealed highly significant sexual dimorphism in ***H. illucens***. Adult body length differed significantly between sexes ($\chi^2 = 694.996$, $p < 0.001$). Females recorded a greater mean body length (1.57 ± 0.14 cm) compared with males (1.34 ± 0.12 cm). Similarly, adult weight showed a highly significant difference ($\chi^2 = 1450.409$, $p < 0.001$), with females (0.1535 ± 0.1930 g) being substantially heavier than males (0.0943 ± 0.1054 g). These results clearly demonstrate that female flies attain larger body size and mass than males. (Table 2. and Fig. 3)

Comparison of total weight with waste reduction rate in three substrates

Waste reduction rate showed considerable numerical variation among substrates**,** with banana (42.9 ± 40.9%) and watermelon (37.9 ± 38.9%) exhibiting higher values than rice bran (17.9 ± 20.5%) (Table 1). However**,** Welch ANOVA indicated no significant difference ($p > 0.05$) among substrates.

Despite similar larval lengths across treatments, substrates with higher feed reduction rates were associated with greater biomass gain and superior growth efficiency**.** This indicates that feed reduction was more closely related to larval weight gain than to larval

length**,** suggesting that larvae on banana and watermelon substrates converted consumed feed more effectively into tissue mass rather than linear body extension. (Table 1. and Fig. 2. C)

Comparison of survival rate(%) in three Substrates

The survival rate of ***Hermetia illucens*** larvae remained high across all three substrates, indicating that rice bran, banana peel, and watermelon peel were all suitable for sustaining larval development under laboratory conditions. The highest survival rate is banana substrate and followed watermelon peel and rice bran. (Table 1. and Fig. 2.D)

Nutritional values of black soldier fly in different substrates

Moisture content varied markedly among substrates, with rice bran larvae exhibiting the highest moisture (27.87%), followed by banana larvae (8.00%) and watermelon peel larvae (4.95%). Crude protein content was highest in watermelon peel larvae (46.81%), followed by rice bran larvae (43.60%), while banana larvae showed lower protein content (28.87%). Crude fat content was highest in banana larvae (13.63%), indicating that lipid accumulation is strongly influenced by carbohydrate-rich substrates**.** Total ash content was highest in banana larvae (22.22%), reflecting higher mineral uptake from the substrate. Carbohydrate content was highest in watermelon peel larvae (29.49%) and banana larvae (27.28%), while rice bran larvae contained markedly lower carbohydrate levels (7.00%). Energy content ranged from 283.13 kcal/100 g (rice bran larvae) to 361.45 kcal/100 g (watermelon peel larvae). (Table 3. and Fig. 5)

Table 1 Growth performance, feed reduction rate and statistical comparison of *Hermetia illucens* reared on different substrates

Stage / Parameter	Rice bran (Mean ± SD)	Banana (Mean ± SD)	Watermelon (Mean ± SD)	Statistical test	Test value	p-value	Significance
1st instar length	1.10 ± 0.20	1.15 ± 0.22	1.13 ± 0.21	ANOVA	F = 0.18	0.84	NS
2nd instar length	2.30 ± 0.35	2.45 ± 0.38	2.40 ± 0.36	ANOVA	F = 0.41	0.67	NS
3rd instar length	5.80 ± 0.70	6.10 ± 0.75	6.00 ± 0.72	ANOVA	F = 0.56	0.58	NS
4th instar length	10.90 ± 1.20	11.50 ± 1.35	11.20 ± 1.30	ANOVA	F = 0.73	0.49	NS
5th instar length	15.80 ± 1.80	16.60 ± 2.00	16.20 ± 1.95	ANOVA	F = 0.82	0.45	NS
Prepupal length	12.40 ± 1.50	13.10 ± 1.65	12.80 ± 1.60	ANOVA	F = 0.64	0.53	NS
Pupa length	11.80 ± 1.40	12.30 ± 1.55	12.00 ± 1.48	ANOVA	F = 0.58	0.56	NS
1st instar weight	0.0020 ± 0.0004	0.0021 ± 0.0005	0.0020 ± 0.0004	ANOVA	F = 0.72	0.49	NS
2nd instar	0.0068 ±	0.0072	0.0069 ±	ANOVA	F =	0.26	NS

weight	0.0011	± 0.0012	0.0010		1.35		
3rd instar weight	0.0185 ±0.0035	0.0198 ± 0.0039	0.0189 ± 0.0036	ANOVA	F = 1.88	0.16	NS
4th instar weight	0.0452 ± 0.0078	0.0496 ± 0.0084	0.0468 ± 0.0081	ANOVA	F = 3.24	0.04	*
5th instar weight	0.0925 ± 0.0156	0.1038 ± 0.0172	0.0964 ± 0.0168	ANOVA	F = 6.87	0.001	**
Pre-pupa weight	0.1925 ± 0.0288	0.2117 ± 0.0315	0.1984 ± 0.0301	ANOVA	F = 7.91	0.001	**
Pupa weight	0.1384 ± 0.0216	0.1509 ± 0.0242	0.1417 ± 0.0228	ANOVA	F = 5.76	0.003	**
Waste reduction rate (%)	17.9 ± 20.5	42.9 ± 40.9	37.9 ± 38.9	Welch ANOVA	F = 1.32	0.31	NS
Survival Rate (%)	89.06 ± 0.85	94.61 ± 0.42	91.94 ± 0.59	One-way ANOVA	F = 28.4	<0.01	*

NS = not significant ($p > 0.05$); ** = highly significant ($p < 0.001$). Values are presented as mean ± standard deviation.

Table 2 Adult morphometric comparison of *Hermetia illucens*

Parameter	Sex	Mean ± SD	Median	Min	Max	Test	Test value	p-value	Significance
Adult length(cm)	Male	1.34 ± 0.12	1.33	1.08	1.61	Kruskal–Wallis	χ^2 = 694.996	<0.001	**
	Female	1.57 ± 0.14	1.57	1.29	1.89				
Adult weight (g)	Male	0.0943 ± 0.1054	0.073	0.010	0.310	Kruskal–Wallis	χ^2 = 1450.409	<0.001	**
	Female	0.1535 ± 0.1930	0.129	0.020	0.520				

NS = not significant ($p > 0.05$); ** = highly significant ($p < 0.001$). Values are presented as mean ± standard deviation.

Table 3 Nutritional values of black soldier fly larvae in different substrates

Sample larvae	Moisture (%)	Crude Protein (%)	Crude Fat (%)	Total Ash (%)	Carbohydrate (%)	Energy (kcal/100g)
Rice Bran	27.87	43.6	8.97	12.56	7	283.13
Banana	8	28.87	13.63	22.22	27.28	347.27
watermelon peel	4.95	46.81	6.25	12.5	29.49	361.45

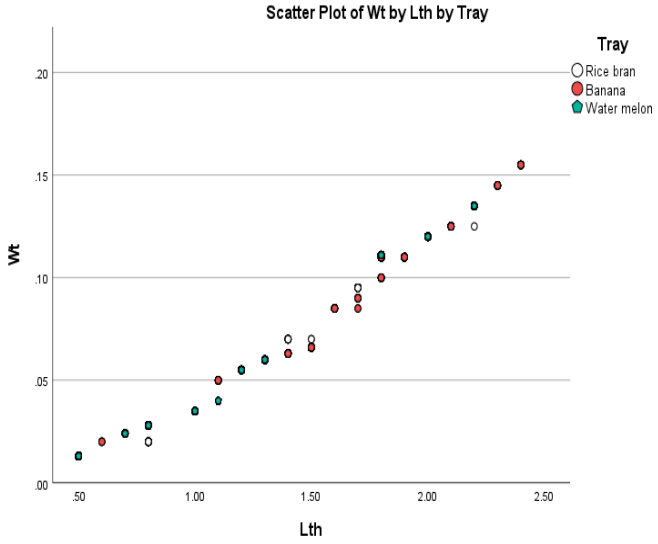

(A) Comparison of length and weight by instar in three substrates

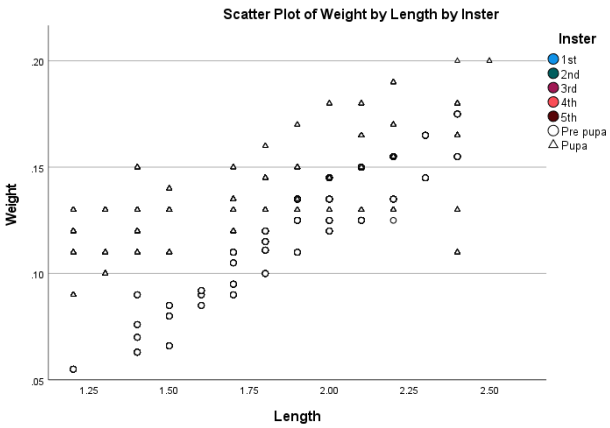

(B) Comparison of length and weight of black soldier fly prepupa and pupa

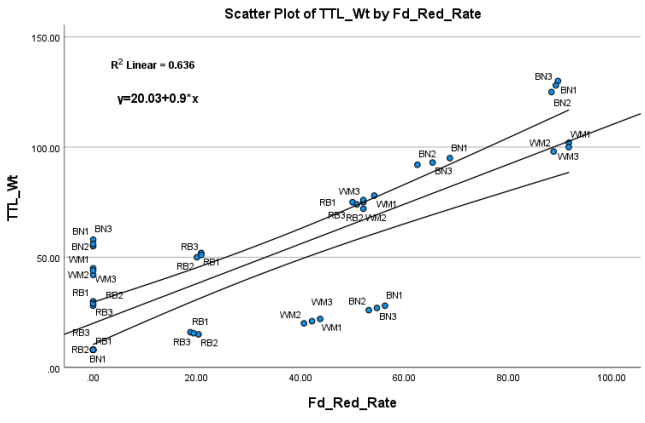

(C) Comparison of total length with waste reduction rate on three Substrates

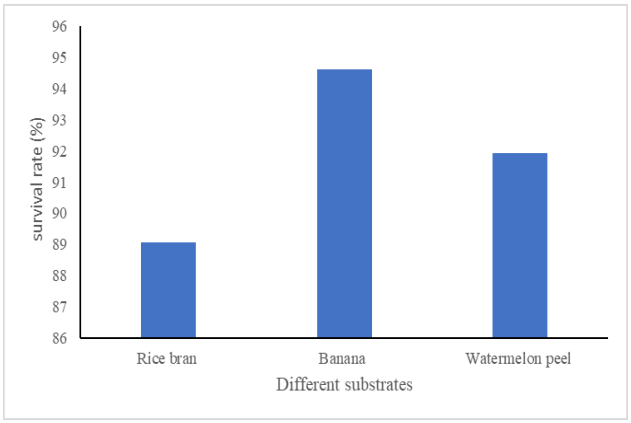

(D) Comparison of survival rate in different substrates

Fig. 3 Comparison of the developmental stages and life parameter of black soldier fly, *Hermetia illucens* in different substrates

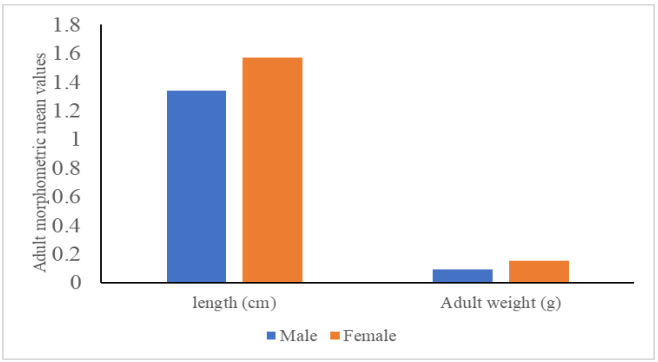

Fig. 4 Comparison of length and weight in male and female black soldier fly

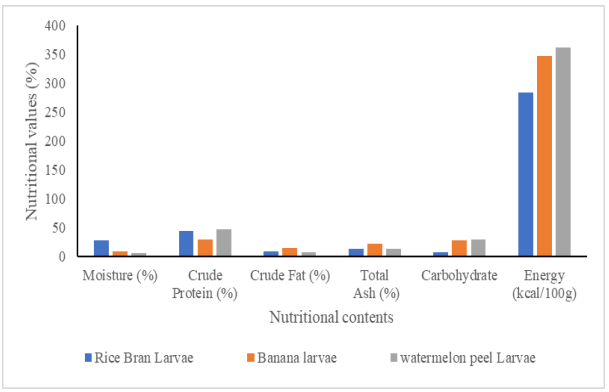

Fig. 5 Nutritional values of black soldier fly in different substrates

Discussion

The present study clearly demonstrates that substrate type influences growth performance, feed reduction efficiency, and biomass accumulation of ***Hermetia illucens***, while linear body growth (length) remains comparatively stable across substrates. Similar patterns have been widely reported in BSF research, where substrate quality affects larval weight and nutrient conversion more strongly than body length (Diener *et al*., 2009). Larval length increased progressively from the 1st to the 5th instar across all substrates, followed by a reduction at the prepupal stage. This growth trajectory is characteristic of ***H. illucens*** development and reflects normal molting and physiological preparation for pupation (Tomberlin*etal*.,2002). The absence of statistically significant differences among substrates (ANOVA, $p > 0.05$ for all instars) indicates that substrate type did not affect linear body extension, supporting findings by Diener et al. (2009), who reported that BSFL length is relatively conserved under different organic diets when environmental conditions are stable.

However, banana-fed larvae consistently exhibited numerically higher mean lengths at advanced instars. Although not statistically significant, this trend suggests improved

nutrient availability and digestibility, consistent with observations by (Surendra *et al*., 2016), who emphasized that carbohydrate-rich substrates enhance larval metabolic activity without necessarily altering body length significantly. Prepupal and pupal morphometric interpretation.

The observed reduction in prepupal length compared to the 5^{th} instar reflects internal tissue reorganization and dehydration prior to pupation, a well-documented phenomenon in holometabolous insects (Chapman,2013). The lack of substrate-related differences at the prepupal stage suggests that substrate effects diminish once larvae cease feeding**,** aligning with findings by (Lalander *et al*., 2019).

Adult morphometric analysis revealed highly significant sexual dimorphism ($p < 0.001$), with females larger and heavier than males. This agrees with (Tomberlin *et al*., 2002) who reported that female BSF require larger body reserves to support egg production, independent of larval substrate type.

Banana and watermelon substrates showed substantially higher mean feed reduction rates than rice bran, although Welch ANOVA indicated no statistical significance ($p > 0.05$). The high variability (large SD values) likely reduced statistical power, a common issue in waste-based feeding trials (Lalander *et al*., 2018).

Despite non-significant p-values, the biological relevance of higher feed reduction in banana and watermelon substrates is important. Several studies emphasize that BSFL fed moist, easily degradable substrates exhibit improved waste reduction efficiency due to enhanced microbial activity and larval digestion (Surendra *et al*., 2022).

The strong positive relationship between larval length and weight across instars indicates efficient nutrient assimilation and normal growth progression. However, the lack of length differences alongside improved feed reduction suggests that substrate quality primarily affects tissue density and biomass accumulation rather than external morphology**.** Similar conclusions were reported by (Spranghers *et al*., 2017), who found that BSFL protein and lipid deposition varied substantially with diet while body length remained relatively unchanged.

The present study demonstrates that substrate type strongly influences the growth performance and biomass accumulation of ***Hermetia illucens***, while linear body length across larval instars remains relatively stable among substrates. Although no significant differences were observed in instar length, banana and watermelon substrates consistently produced numerically larger larvae, suggesting improved nutrient availability. Similar findings were reported by (Diener *et al*., 2009), who noted that larval length is less sensitive to diet quality than larval weight and biomass accumulation.

Survival rate was also significantly influenced by substrate, with banana peel producing the highest survival (94.61%). This agrees with (Barragan-Fonseca *et al*., 2017), who reported that moisture-rich substrates improve larval survival and reduce metabolic stress. In contrast, rice bran resulted in lower growth and biomass conversion, likely due to lower moisture content and reduced digestibility.

Conclusion

This study confirms that ***Hermetia illucens*** can successfully complete its life cycle under controlled laboratory conditions and efficiently utilize diverse organic substrates. Although larval body length did not differ significantly among substrates, banana peel and watermelon peel promoted higher biomass accumulation and feed reduction efficiency, indicating superior substrate suitability.

Statistical analyses demonstrated that instar-wise larval length was not significantly influenced by substrate type. Pre-pupal size reduction followed normal developmental patterns. Adult size differences were driven by sexual dimorphism rather than diet. Feed reduction efficiency was biologically higher in fruit-based substrates despite high variability.

Substrate type strongly influences the nutritional composition and energy value of ***Hermetia illucens*** larvae. Rice bran resulted in higher larval moisture, whereas fruit-based substrates produced drier biomass. Watermelon peel supported the highest protein content and energy value, indicating its suitability for producing protein- and energy-rich larvae. In contrast, banana peel promoted higher lipid and mineral accumulation, reflecting its potential for producing fat-rich biomass.

Acknowledgements

I would like to express my profound gratitude to Dr Myo Min Tun, Acting Rector of East Yangon University for his keen interest and also for his permission. I am indebted to Dr Aye Aye Ko (Pro-rector) and Dr Thida Aung (Pro-rector), East Yangon University for their supports, permitting to conduct this work and confidence in the implementation of this research. I am also grateful thanks to Professor Dr Ei Khine Win, Head of Zoology Department, East Yangon University, for her valuable suggestions, constructive criticisms of the manuscripts and supervision. I am deeply thanks to Dr Khin Sabae Htut, Professor of Zoology Department, East Yangon University, for providing advices and support of this research paper.

References

Barragan-Fonseca, K. B., Dicke, M., & van Loon, J. J. A. (2017). Nutritional value of the black soldier fly (***Hermetia illucens***) and its suitability as animal feed – A review. Journal of Insects as Food and Feed, **3**, 105–120.

Bosch, G., et al. (2022). ***Effects of various organic substrates on growth performance and nutrient composition of black soldier fly larvae: A meta-analysis***. ***Bioresource Technology Reports***, 18, 101061. https://doi.org/10.1016/j.biteb.2022.101061

Chapman, R. F. (2013). ***The insects: Structure and function*** (5th ed.). Cambridge University Press.

Diener, S., Zurbrügg, C., & Tockner, K. (2009). Conversion of organic material by black soldier fly larvae: Establishing optimal feeding rates. ***Waste Management & Research***, 27(6), 603–610. https://doi.org/10.1177/0734242X09103838

Gold, M., Cassar, C. M., Zurbrügg, C., Kreuzer, M., Boulos, S., Diener, S., & Mathys, A. (2018). Biowaste treatment with black soldier fly larvae: Increasing performance through the formulation of biowastes. ***Waste Management***, 80, 319–330. https://doi.org/10.1016/j.wasman.2018.09.005

Khasanah, H., Tyas, I., Kusbianto, D. E., Jadmiko, W., & Muhlison, W. (2025). ***Comparative evaluation of Hermetia illucens larvae reared on different substrates: Effect on growth and nutritional properties***. ***Buletin Peternakan***, 48(3), 1–10.

Lee, J. H., et al. (2025). ***Impact of substrate type and growth stage on nutrient composition and conversion efficiency in Hermetia illucens larvae***. ***Journal of Animal Science and Technology***.

Lalander, C., Diener, S., Magri, M. E., Zurbrügg, C., Lindström, A., & Vinnerås, B. (2018). Faecal sludge management with the black soldier fly (***Hermetia illucens***)—From a hygiene aspect. ***Science of the Total Environment***, 458–460, 312–318. https://doi.org/10.1016/j.scitotenv.2013.04.033

Lalander, C., Nordberg, Å., & Vinnerås, B. (2019). A comparison in product-value potential in four treatment strategies for food waste and faeces—Assessing composting, fly larvae composting and anaerobic digestion. ***GCB Bioenergy***, 10(6), 402–414.

Southwood, T. R. E., & Henderson, P. A. (2000). Ecological Methods–Blackwell Science. 462-502

Spranghers, T., Ottoboni, M., Klootwijk, C., Ovyn, A., Deboosere, S., De Meulenaer, B., … De Smet, S. (2017). Nutritional composition of black soldier fly (***Hermetia illucens***) prepupae reared on different organic waste substrates. ***Journal of the Science of Food and Agriculture***, 97(8), 2594–2600. https://doi.org/10.1002/jsfa.8081

Surendra, K. C., Olivier, R., Tomberlin, J. K., Jha, R., & Khanal, S. K. (2016). Bioconversion of organic wastes into biodiesel and animal feed via insect farming. ***Renewable Energy***, 98, 197–202.

Surendra, K. C., Tomberlin, J. K., van Huis, A., Cammack, J. A., Heckmann, L. H., & Khanal, S. K. (2022). Rethinking organic wastes bioconversion: Evaluating the potential of the black soldier fly (***Hermetia illucens***). ***Waste Management***, 117, 58–80.

Tomberlin, J. K., Sheppard, D. C., & Joyce, J. A. (2002). Selected life-history traits of black soldier flies reared on three artificial diets. Annals of the Entomological Society of America, 95, 379–386.

Taxonomic Study On Eight Ferns Species From The East Yangon University Campus, Thanlyin Township

Hnin Yu*

Abstract

The taxonomic study on eight ferns species from the East Yangon University Campus, Thanlyin Township have been undertaken. The study area is situated between North Latitude 16º44′08″ and East Longitude 96°17′11″. The specimens were collected from June 2024 to October 2024. The eight species belonging to eight genera and six families were examined. Most of the ferns are found as terrestrial and epiphytes on the trunk of tree. *Adiantum philippense* L., *Pteris vittata* L., *Thelypteris arida* (D.Don) C.V. Morton, and *Nephrolepis cordifoila* (L.) C. Pres are terrestrial species. *Drynaria* quercifolia (L.) J. Sm., *Davallia* denticulate (Burmu.f) Mett., and *Pyrrosia* are epiphytes species. Of these, the aquatic fern is a *Marsilea quadrifolia* L. The collected specimens are described with figures of photographs. An identification has been provided their distribution, habitat, morphological and GPS. Each specimens was identified, with the help of standard literature and documented by herbarium sheets. An artificial key to the collected plants, comparable characteristics of the species were studied.

Keywords: Taxonomy study, Ferns, East Yangon University, artificial key

Introduction

Ferns and fern allies are an natural group of plants in a major division of the plant kingdom called Pteridophyta. The term “Pteridophyte” is derived from two Greek words: “Pteron” meaning “feather” and “Phyton” meaning “Plant”. They do not have any flowers or seeds like flowering plants. Their method of reproduction is spores. Hence, pteridophytes also known as the first vascular cryptogram.

Ferns first appeared at the beginning of the Carboniferous, about 340 million years ago. Ferns and fern allies are an ancient group of plants on the earth with a fossil record dating back to the middle Devonian period from 350 million years ago (Moran, 2011).

There are about 12,000 species worldwide, the majority of these plants are commonly grown in tropical rainforests. They also grow in other warm, moist places where there is plenty of shade. Very few species of ferns are found in dry, cold places. In wet tropical forest they abound on the forest floor, lower portions of tree truck, and as high canopy epiphytes. (Jone, 1987).

Today, pteridophytes occurs worldwide, from icy tundras above the arctive Circle to sweltering tropical forests at the equator. The majority of ferns, especially in the temperate areas, have a fairly standard growth form and life cycle. Ferns and fern allies are woody plants, which grow on the ground (terrestrial), on rocks (lithophytes), or on trees (epiphytes). A few ferns are climbers and aquatic species.

The ferns leaves, called fronds, from below ground and push up as a coiled structure called a crozier, or fiddlehead. It unfurls above ground in a pattern called circinate vernation.

Sporangia are usually clustered on the lower side of fertile fronds, and each cluster is called a sorus; it may be covered with a thin flap called an indusium. Some species sporangia, sometimes specialized panicles or spikes (Ophioglossaceae) and sporocarps (Marsileaceae).

The two kinds of sporangia within ferns and fern allies: eusporangiate and leptosporangiate. Eusporangiate ferns, in which the sporangium wall has two or more cell layers, and leptosporangiate, in which the sporangium wall is composed of just one cell layer.

* Lecturer, Department of Botany, Hinthada University

Pteridophytes have been a prominent part of the Earth's vegetation for millions of years. Ferns provide a variety of contribution to the ecosystems in which they exist. For example, they provide shelter, shade, erosion protection, chemical sequestration, and microhabitats that serve other species. Ferns and fern allies are of minor economic significance to mankind today.

When eaten raw the croziers are crisp but with a mucilaginous texture. Preparation for cooking simply consists of washing and removal of all scales or hairs. The croziers may be cooked whole or sliced up like beans. Cooking consists of boiling in salty water for 30-60 minutes, until they are soft enough for eating, steaming until soft. The flavor is similar to that asparagus (Jone, 1987).

Ferns have been used by herbalists and purveyors of folk medicine for centuries. A few ferns are poisonous to livestock and cause stock losses when animals feed on them.

The aim and objectives of the study are to classify and identify the ferns species, to record their distribution and morphological characteristics, and to provide the knowledge on the natural resources in the study area.

Materials and Methods

Ferns were collected from East Yangon University Campus, in Thanlyin Township in the southeastern suburbs of Yangon. The study area is situated between East longitude 96°17′11″ and North latitude 16º44′08″, having 6 m above the sea level in elevation, Phayar Gon village. The specimens were collected from June 2024 to October 2024. Member of terrestrial and epiphytes were included. Herbarium sheets were prepared referring to method of Forman (1989).

The plants were pressed directly in the plant press and plant habit, especially the sori bearing surfaces were recorded by coloured photographs.

The collected specimens were examined their internal and external morphological characters. Fern specimens were identified by using keys and descriptions from taxonomic literatures, such as floras, manuals, monographs as well as research papers. They are: Beddom (1892), Copeland (1947), Holttum (1949), Tagawa and Iwatsuki (1979- 1989), Winter & Amoroso (2003), Moran (2011) and Wu *et al*., (2013). The classification systems of ferns follows that of PPG I (Pteridophyte Phylogeny Group) (2006).

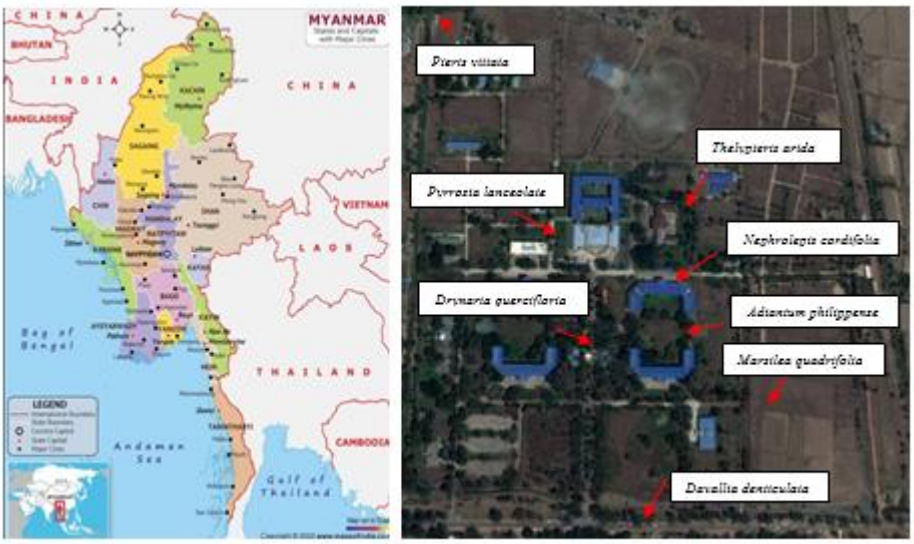

Figure.1. A-Myanmar map, B-Location map of East Yangon University Campus

Results

In this study, a total of **8** species of ferns were collected from different location as shown in Table-1 and have been classified into **1** classes; **2** order, **6** families, **8** genera and **8** species based on the system of PPGI (Pteridophyte Phylogeny Group, 2016).

Table 1. the list of the collocted species

Class	Order	Families	Genus & Species
	1. Salviniales	1. Marsileaceae	1. *Marsilea quadrifolia*
1.Polypodiopsida	2. Polypodiales	2. Pteridaceae	2. *Pteris vittata*
			3. *Adiantum philippense*
		3. Thelypteridaceae	4. *Thelypteris arida*
		4. Nephrolepidaceae	5. *Nephrolepis cordifolia*
		5. Davalliaceae	6. *Davallia denticulata*
		6. Polypodiaceae	7. *Drynaria quercifloria*
			8. *Pyrrosia lanceolate*

Scientific Name : *Marsilea quadrifolia* L., Sp. Pl: 1099. 1753.

Family : Marsileaceae

Common Name : Water clover fern

Outstanding characters

Plants small, herbaceous-ferns, 5-16 cm long. Rhizome long creeping, 2.0-3.0 mm in diameter, glabrous pale green, irregularly branched, rooting at the nodes of floating or emergent, bearing simple hairs. Fronds erect, solitary to clustered; stipe terete, 4-15 cm long in exposed place, green, glabrous; lamina quadrifoliate, pinna 4, obovate to fan-shaped, 5-16 mm long, base cuneate, margin entire, apex round, veins anastomosing with narrow aeroles. Sporocarp oblong, 3-4 mm long, convex on lateral sides, 1-2 each frond, attached at base of stipe, stalk 2-4 mm long, covered densely soft hairs, 2 kinds of spores, megaspores and microspores.

Collect date : 1.9.2024

Medicinal uses : Diuretic, anti-inflammatory, depurative, febrifuge and refrigerant

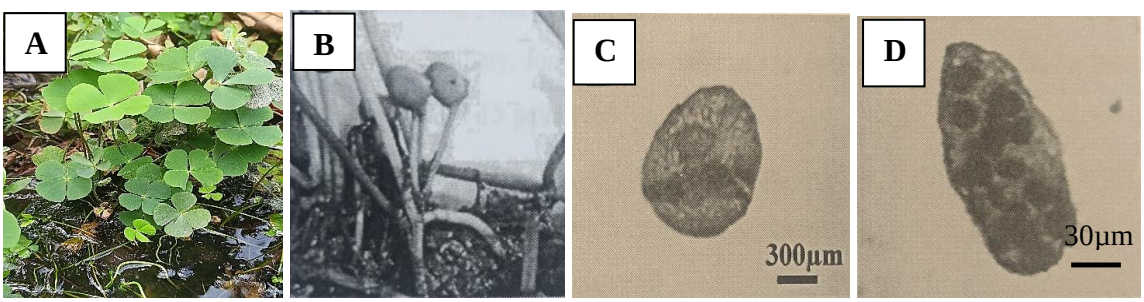

Figure.2. A-Habit, B-Sporocarps, C-Megaspore, D-Microspore of ***Marsilea quadrifolia*** L.

Scientific Name : *Adiantum philippense* L., Pl.:1094.1753.

Family : Pteridaceae

Common Name : Walking maidenhair fern

Outstanding characters

Terrestrials, 20-50 cm high. Rhizome erect, 1-1.5 cm in diameter, scaly; scale basifixed, lanceolate, 3-5 mm long, bicolour, along center dark brown. Fronds monomorphic, tufted; stipe terete, 10-25 cm long, scaly at the base, shinny, dark brown; lamina unipinnate, lanceolate, 10-25 cm long and 4-8 cm wide, pinnae 8-10 pairs, 2.5-4.5 cm long and 1-2.5 cm wide, crescent shaped, stalk long 10-20 mm long, costa and costule dark browned, base cuneate, margin undulate lobed; veins free and forked, multicostate venation. Sori borne on the margin of pinnae, 2-6 per pinnae, false indusia, membranous reflexed; sporangia ovoid, 200-250 µm in diameter, stalk long; spores smooth, trilete, 30-40 µm in diameter, pale brown.

Collect date : 15.4.2024

Medicinal uses : Dysentery, ulcers, fevers, cooling, and elephantiasis

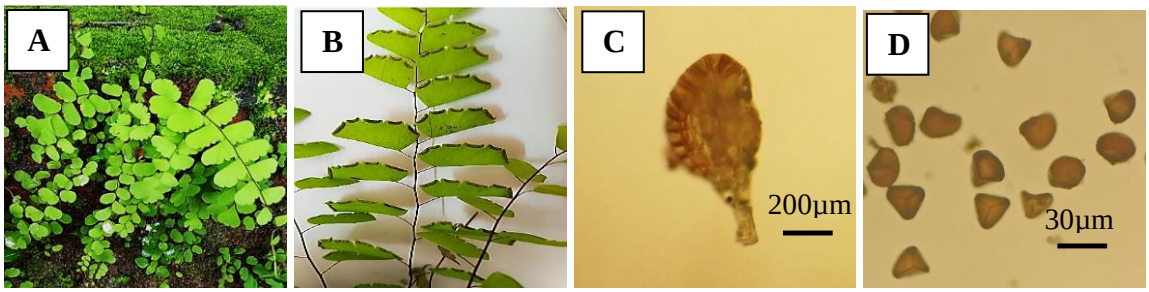

Figure.3. A-Habit, B-Sori with pinnae, C-Sporangium, D-Spores of ***Adiantum philippense*** L**.**

Scientific Name : *Pteris vittata* L., Sp. Pl. 2: 1074. 1753.

Family : Pteridaceae

Common Name : Brake fern

Outstanding characters

Terrestrials, 0.5-1 m high. Rhizome short creeping, 1-1.5 cm in diameter, densely scales; scale basifixed, lanceolate, 2-5 mm long. Fronds tufted, monomorphic; stipe terete, 10-25 cm long, grooved, reddish brown, scales at base; lamina unipinnate, elliptic-lanceolate, 40-75 cm long and 15-25 cm wide, pinnae 20-40 pairs, linear-lanceolate, 8-15 cm long and 0.5-1 cm wide, sessile, apex acuminate, margin minutely toothed, base cordate, a terminal leaflet (pinnae) at the tip, costae hairy; veins free and forked. Sori along of marginal pinnae, false indusial formed by reflexed margin of lobes; sporangia oblong, 200-250 µm in diameter, stalk long; spores trilete, 25-35 µm in diameter, triangular faces, pale green.

Collect date : 14.7.2024

Medicinal uses : Wound healing

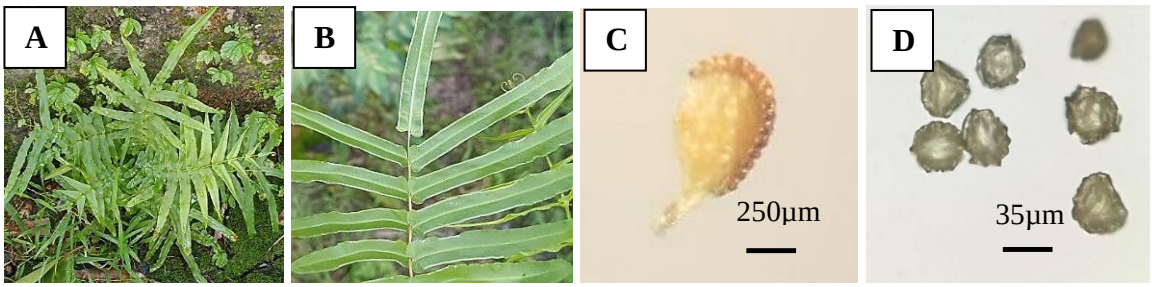

Figure.4. A-Habit, B-Sori with pinnae, C-Sporangium, D-Spores of ***Pteris vittata*** L.

Scientific Name : *Thelypteris arida* (D.Don) C.V. Morton, Amer. Ferns J.49: 113.1959.

Family : Thelypteriaceae

Common Name : Not Known

Outstanding characters

Plant terrestrial, 70-100 cm high. Rhizome long creeping; scale densely, basifixed, lanceolate, 4-10 mm long, stramineous. Fronds monomorphic, 70-100 cm long and cm wide, stipe terete, 15-25 cm long, scaly at the base, dark brown; lamina pinnately compound, bipinnate, oblong, 50-70 cm long and 15-30 cm wide, base truncate, pinna 15-20 pairs, 8-14 cm long and 1.5-2 cm wide, pinnatifid, apex acuminate, pinnules oblong, 0.5-1cm long and 0.2-4 cm wide, apex obtuse, base sessile, margin serrate, veins free and forked, lateral veins 4-5 pairs. Sori borne on middle of veinlets, orbicular, indusia reniform; sporangia ovate, 150-200 µm in diameter, stalk short, spores monolete, oblong, 30-40 µm in diameter, perispore, brown.

Collect date : 9.1.2024

Medicinal uses : Malaria, tuberculosis, and cancer

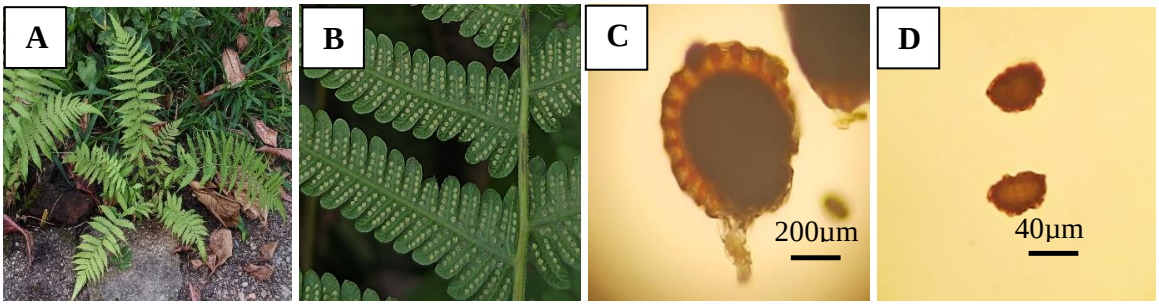

Figure.5. A-Habit, B-Sori with pinnae, C-Sporangium, D-Spores of ***Thelypteris arida*** (D.Don)

Scientific Name : *Nephrolepis cordifolia* (L.) C. Presl., in Tent. Pterid.: 79.1836.

Family : Nephrolepidaceae

Common Name : Fishbone fern

Outstanding characters

Terrestrials, 35-70 cm high. Rhizome, short creeping, 1-2 cm in diameter, scaly; scale linear, gradually top to needle like, 4-12 mm long, center dark coloured, stramineous. Fronds, monomorphic, lanceolate, 35-70 cm long and 3-4.5 cm wide; stipe 7-10 cm long, scaly at the along stipe and base, brown; lamina uni-pinnate, 30-45 cm long and 3-4.5 cm wide, pinnules triangular, base hastate, margin serrate, apex lobed; veins free. Sori abaxial surface of frond, nearly margin, indusium reniform; sporangia ovoid, 200-300 µm in diameter, stalk long, spores monolete, oblong, 30-40 µm in diameter, orange.

Collect date : 5.3.2024

Medicinal uses : Skin disease, anti-ulcer, snakebite

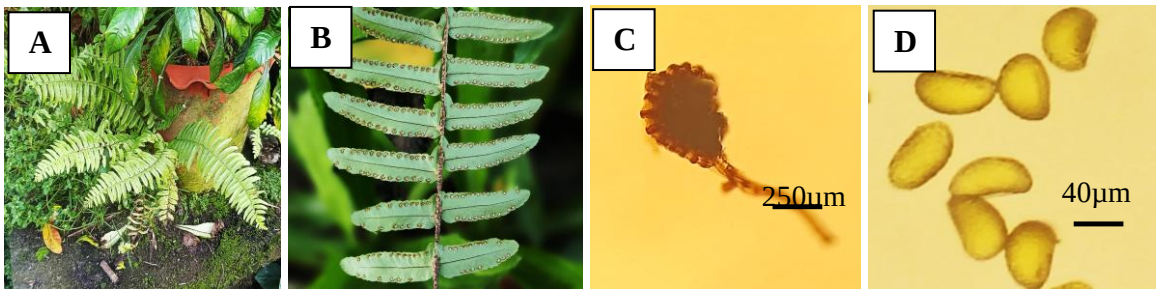

Figure.6. A-Habit, B-Sori with pinnae, C-Sporangium, D-Spores of ***Nephrolepis cordifolia*** (L.)

Scientific Name : *Davallia denticulata* (Burm.f.) Mett., F.A.M.Kuhn, Filic.Afr.: 27(1867)

Family : Daviliaaceae

Common Name : Rabbit's Foot Fern

Outstanding characters

Epiphytes, 60-80 cm high. Rhizome long creeping, 0.5-0.7 cm in diameter, scaly; scale basifixed, 4-5 mm long, stramineous, margin entire. Fronds monomorphic; stipe terete, 15-30 cm long, scaly at the base; lamina tri-pinnately compound, deltoid, 40-50 cm long and 15-35 cm wide, primary pinnae 15-20 pairs, 13-20 cm long and 3-8 cm wide, secondary pinna 7-12 pairs, 3-6 cm long and 1-2 cm wide, pinnules ovate, shallowly lobed, 0.6-0.8 cm long and 0.3-0.5 cm wide, apex 2-4 lobed, sessile, margin entire; veins free. Sori terminal on veins, small oblique lobes, indusia cup shaped; sporangia obovate, 150-250 µm in diameter, stalk long; spores monolete, smooth, oblong, 25-35 µm in diameter, orange.

Collect date : 5.3.2024

Medicinal uses : Antiflammations, cancers

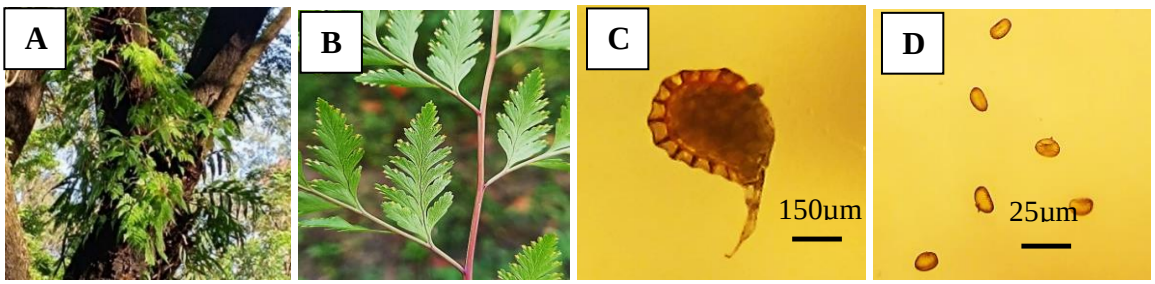

Figure.7. A-Habit, B-Sori with pinnae, C-Sporangium, D-Spores of ***Davallia denticulata*** (Burm.f) Mett.

Scientific Name : *Drynaria quercifloria* (L.) J. Smith, J. Bot. (Hooker). 3:398. 1841.

Family : Polypodiaceae

Common Name : Oak-leaf fern

Outstanding characters

Plant epiphyte, 60-100 cm high. Rhizome creeping, 3-4 cm in diameter, densely scaly throughout; scale peltate, cm long. Fronds dimorphic; nest leaves sessile, ovate-oblong, 23-35 cm long and 12-17 cm wide, middle lobed, 10-12 pairs margin lobes, the apex obtuse, veins pinnate; foliage leaves paripinnate; stipes 10-12 cm long, narrowed winged almost to the base; lamina unipinnate, deeply pinnatified, 45-60 cm long and 25-30 cm wide, pinna 12-18 pairs, oblong-lanceolate, 15-20 cm long and 4-5 cm wide, margin entire, apex acute, leathery, veins anastomosing, 6-8 rows of aeroles between the main veins. Sori round, two rows between main veins, sporangia ovoid, 200-250 µm in diameter, stalk long; spores oblong, monolete, slightly curved, spines, 30-35 µm in diameter, brown.

Collect date : 11.7.2024

Medicinal uses : Traumatic injury, ligament injury

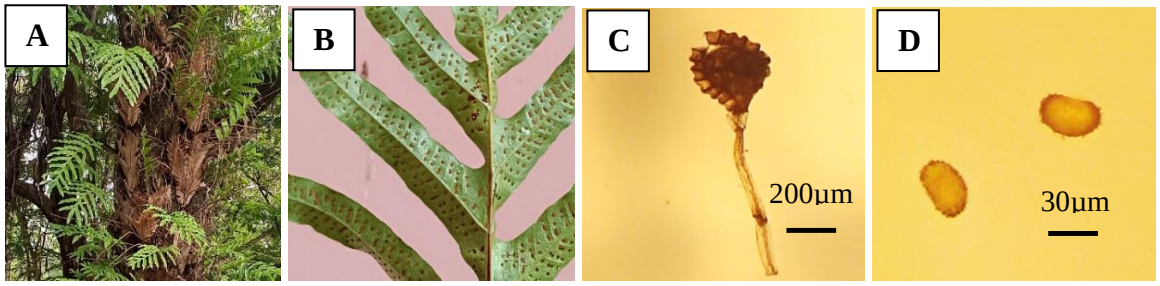

Figure.8. A-Habit, B-Sori with pinnae, C-Sporangium, D-Spores of ***Drynaria quercifloria*** (L.) J. Sm.

Scientific Name : *Pyrrosia lanceolata* (L.) Farw., Amer. Midl. Naturalist 12: 245.1930

Family : Polypodiaceae

Common Name : Lanceleaf toungue fern

Outstanding characters

Plant epiphyte, 10-18 cm long. Rhizome long creeping, 4-6 mm in diameter, densely scales throughout; scales peltate, 5-10 mm long, center dark brown, stramineous, margin hairy. Fronds monomorphic, stipe terete, 5-9 cm long, scaly at the base; lamina simple, elliptic-lanceolate, 5-10 cm long and 1.5-2 cm wide, veins free. Sori borne at ends of included veinletes, in one to several rows on each side of main veins, the lower one densely stellate-hairy throughout, sporangia ovoid, stalk long, µm in diameter, spore oblong, µm in diameter, cristae.

Collect date : 10.9.2024

Medicinal uses : Skin disease and sore throat

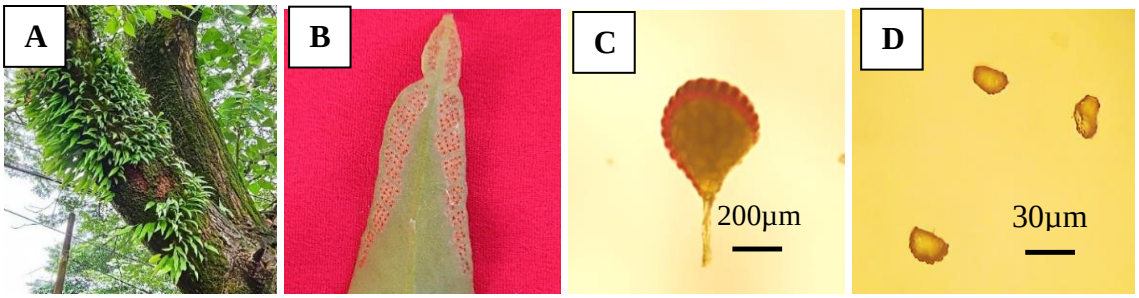

Figure.9. A-Habit, B-Sori with pinnae, C-Sporangium, D-Spores of ***Pyrrosia lanceolate*** (L.) Farw.

Artificial key to the studied Species of ferns

1. Dimorphic ferns ……. 3
1. Monomorphic ferns ……..…….. 2
    2. Aquatic ferns ……..……..……...……..…. *Mersilea quadrifolia*
    2. Epiphytic ferns ……... *Drynania quercifolia*
3. Fronds simple ……..…..… *Pyrrosia lanceolate*
3. Fronds compound ...…….……..……. 4
    4. Lamina crescent shaped …… *Adiantum philippense*
    4. Lamina elliptic lanceolate ……. 5
5. Spores triletes …….. *Pteris vittata*
5. Spores monoletes ……..…….……. 6
    6. Sori indusial cup-shaped ……..…… *Davallia denticulate*
    6. Sori false indusial …… 7
8. Lamina uipinnate ……. *Nephrolepis cordifolia*
8. Lamina bipinnate ……...…….. *Thelypteris arida*

Discussion and Conclusion

A total of 8 species of ferns belonging to 8 genera and 6 families haves been recorded in the present study. According to habitat types, terrestrial plants are the most dominant among the groups were found in this study area. *Adiantum philippense* L., and *Thelypteris aridus* (D.Don) Ching, are abundantly distributed in this study area. *Nephrolepis cordifolia* (L.) C. Presl., and *Pteris vittat*a L., are also found in that study area.

Epiphytic plants usually occur on shady branches or tree truck. *Drynaria quercifolia* (L) J.Sm., *Pyrossia lanceolate* (L.) Farw., and *Davallia denticulate* (Burm.f) Mett., are epiphytic plants. Among them, *Drynaria quercifolia* was found abundantly in the study area. Aquatic fern species of *Marsilea quadrifolia* L., was found in the study area.

Among these species, monomorphic fronds are recorded in 6 species and two species are dimorphic fronds. Trilete spores were found in *Adiantum philippense* and *Pteris vittata*; monolete spores were observed in *Thelypteris aridus, Drynaria quercifolia, Pyrosia lanceolate, Davallia denticulate*, and *Nephrolepis cordiofolia*.

Among these, *Adiantum philippense* L. are found as growing on the main road beside of the campus. The distinguished characters of this species are pinna crescent shaped, sori at margin of leaflets and false indusium, reflexed, its agreed with those mentioned by Winter & Amoroso (2003).

Marsilea quadrifolia L., the sporophyte plants are heterosporous and the rest 7 species are homosporous plants. *Marsilea quadrifolia* plants are distinctive in being rhizomatous, aquatic ferns, the leaves lacking blade tissue or palmate with two or four, sessile leaflets, sori developing within seed-like, dessication-resistant sporocarps, which upon imbibing water, each release an elongate, gelatinous sporophore bearing the sori and sporangia, the spores heterosporous, are agreed with those mentioned by Moran (2011).

Pteris vittata L., is found in sori on the margin of fronds. *Thelypteris aridus* (D.Don) Ching is characterized by indusial reniformed, are agreed with those mentioned by Jone (1987).

The two species of exindusiate ferns are *Pyrossia costata* and *Drynaria quercifolia* and the rests are indusium. *Davallia denticulate* plants sori small, at margin of lobes, indusia cup-shaped. It agrees with the report of Winter & Amoroso (2003).

Ferns are generally not poisonous to humans and many species are edible. Ferns croziers may be collected and eaten raw in a salad but are more frequently cooked.

Ferns are rich in antioxidants and essential fatty acids, particularly vitamin C and beta-carotene that may reduce cancer and heart disease. They have potassium, which helps regulate fluid in the body, may also reduce blood pressure.

In conclusion, ferns may be controlled by the environmental factors such as temperature, rainfall and humidity. Ferns have be found to be useful in the removal of heavy metals, especially arsenic, from contaminated soils. Ferns are generally not poisonous to humans and many species are edible.

Therefore, East Yangon University Campus is very suitable for the growing of ferns rich resources of more species are found in this area. This research can be effective and beneficial for further Pteridophyte research.

Acknowledgements

We would like express my deepest gratitude to Dr Khaing Khaing San, Rector, Hinthada University, Dr Cho Kyi Than and Dr Moe Min Soe, Pro-Rectors, Hinthada University, for permission me to study and for giving invaluable advice. My special thanks to Dr Khin Thu Zar Myint, Professor and Head, Department of Botany and Dr Aye Aye Mar, Professor, Department of Botany, Hinthada University for their advice and suggestions.

References

Boonkered, T. & R. Pollawatn (2000). **Pteridophytes in Thailand.** Thailand, Bangkok: Office of Environmental Policy and Planning.

Copeland, E.G., (19460. **The Ferns of Burma.** The Ohio Journal of Science, 46:109 141.

Dickason, F. G., (1937). **The Pteridophytes of Burma.** MA thesis, University of the Ohio State, U.S.A.

Jones, D.L. 1987. **Encyclopedia of Ferns**. An Introduction, Structure and Botany of Ferns, pp1-76. Portlands, Oregon: Timber press

Moran, R. C., (2011). **Generos Neotropicales de Helechos y Licofitas.** The New York Botanical Garden, Quito, 23-28 de mayo 2011. PPG 1. 2006. **A community-derived classification for extant lycophytes and ferns**. Journal of Systematics and Evolution 54(6):563-603. htts://doi.org/

Singh, G. (2010). **Plant Systematics**: An Integrated Approach, Third Edition,

Smith, A. R., K. M.. Pryer, E Schuettpelz, P. Korall, H. Schneider & P. G. Wolf, (2006). "A Classification for Extant ferns". Taxon 55 (5): 705-731.

Tagawa, M. & K. Iwatsuki. (1985-89). **Flora of Thailand.** Volume I, II, II, IV**.** The Tistpress, Bangkok. Tagawa. Thailand.

Taylor, T.N., Taylor, E.L. & Krings, M., (2009). **Paleobotany the Biology and Evolution of Fossil Plants**, Second Edition, 2009.

Thet Yu New (2009). **Diversity of Ferns and Its Identification in Kyaikhtiyoe Wild Life Sanctuary.** PhD Dissertation, February, Department of Botany, University of Yangon.

Thin Yu Khaing (2007). **Ferns flora and communicates in the Yangon Division**. PhD Dissertation, July, Department of Botany, University of Yangon, Yangon, Myanmar.

Thuzar Myint (2023). **Floristic study of ferns and fern allies in Dawei Distric, Tanintharyi Region.** PhD dissertation, Department of botany University of Yangon Myanmar.

Winter, W. P. & V. B. Amoroso (2003). **Plant resources of South-East Asia.** No 15 Cryptogams : Ferns and fern allies: Prosea Foundation, Bogor, Indonesia.

Wu, Z. Y., P. H. Raven & D.Y. Hong, eds. (2013). **Flora of China**. Vol. 2-3 (Pteridophytes). Science Press, Beijing, and Missouri, Botanical Garden Press, St. Louis.

Study on Morphological Characters and Larvicidal Activity of Leaves of *Pluchea Indica* (L.) Less.

Nyo Nyo Khine[1], Ni Ni Htun[2]

Abstract

Pluchea indica (L.) Less. Belong to the family Asteraceae. It is known as khayu in Myanmar. Based on the morphological characters of collected plant, the plant was identified by using literatures and recorded by photographs. *Pluchea indica* (L.) Less. is shrubs, margins of leaves is dentate. Inflorescence is capitulum and consists of central florets and marginal florets. Calyx is modified into pappus. The insecticidal property from ethanol extract of leaves was also investigated on *Aedes aegypti* mosquito. In this experiment, *Aedes aegypti* larvae were found 91.2% knockdown at 0.8g in 100 mL dilution of *P. indica* leaves ethanol extract. Highest mortality of 3rd of 4th instar of *Aedes aegypti* larvae was found 98.4 % at 0.8 g dilution. Lowest mortality was found10.0 % of larvae at 0.05 g dilution of leaves ethanol extract.

Keywords*:* morphological characters, larvicidal activity, *Aedes aegypti*, *Pluchea indica*

Introduction

The plant of *Pluchea indica* (L.) Less. is commonly known as Khayu in Myanmar and belonging to the family Asteraceae (Kress, 2003). It is known as Indian camphorweed in India, vernacular names are beluntas in Malaysia, Khlu in Thailand, kuo bao ju in China and kalapini in Philippines. *Pluchea indica* (L.) Less is mainly found in the subtropical and tropical zones of Asia, Africa, Australia, America and in warm temperature regions of countries (Cronquist, 1981).

Pluchea indica (L.) Less. is an evergreen shrub found abundantly in salt marshes and mangrove swamps (Backer, 1965). This Family consist of more than 1100 genera and about 25,000 species (Nyo Maung 2002). It has been widely distributed in Hainan, Fujian, Taiwan, Myanmar, Thailand, Indonesia and Malaysia (Heywood, 2007). The traditional community uses *Pluchea indica* (L.) Less. leaves as a diaphoretic, an appetite enhances and an antipyretic.

Pluchea indica (L.) Less. plants are used in medicine to ward against illness. Dengue fever is one them. The *Aedes aegypti* mosquito is the sources of dengue illness. Mosquito bite prevention is essential since, in addition to dengue fever, mosquitoes can transmit disease. Like malaria, elephantiasis and acute inflammation of the neurological system. Extracts from the leaves of Indian camphorweed possess significant larvicidal activity against various insect larvae, including those of mosquitoes and agricultural pests. This effect is attributed to the plants rich content of secondary metabolites (Priya *et al.*, 2023). The aim and objectives of this research were to verify the specific morphological characters of *Pluchea indica* (L.) Less., to observe the powered samples of leaves for larvicidal activity.

Materials and Methods

Morphological Studies of *Pluchea indica* (L.) Less.

The fresh specimens of *Pluchea indica* (L.) Less. were collected from Mawlamyine Township, Mon State. The morphological characteristics of the vegetative and reproductive parts of plant specimens are observed and the plant is identified with the help of available literatures (Hooker, 1885; Backer, 1965; Cronquist, 1981; Dassanayake, 1997; Kress, 2003).

Larvicidal activity of *Pluchea indica* (L.) Less.

Aedes mosquito larvae were collected from water storage containers in 31st Ward Dagon North Township Yangon Region. All collected Aedes larvae were carried by labeled plastic bags, oxygen was supplied using battery oxygen pumps to Medical Entomology Research Division, Department of Medical Research (DMR).

[1] Lecturer, Department of Botany, Maubin University
[2] Professor, Dr, Department of Botany, University of Yangon

Species identification of mosquitoes

For species identification, larvae and adult mosquitoes emerged from larva survey were morphologically identified according to the key of Rampa and Prachong [1].

***Pluchea indica* (L.) Less. leaves collection and preparation of ethanol extraction**

Pluchea indica (L.) Less. leaves were collected from Panga village, Thanphyuzayet Township, Mon State was used for the extraction by Ethanol. A total of 400 gram of *Pluchea indica* (L.) Less. green leave was cleaned and dried in room temperature in shade. Dried leaves were grinned by grander to make powder and extracted with 95% ethanol 500ml at 70°C for 4 hours and 300 ml at 60°C for 2 hours (2 times) on the water bath and filtrated by filter-paper. The total combined filtrate was evaporated under reduced pressure by means of a rotary evaporator to get 95% ethanol extract 3gram of Ethanol extract was obtained from 400 gm of fresh *Pluchea indica* (L.) Less. leaves powder. The extract was kept at 4°C in refrigerator until use. The extraction was done in Department of Botany, University of Yangon.

Results

Morphological Characters of *Pluchea indica* (L.) Less.

Scientific Name - ***Pluchea indica* (L.) Less.**

Family - Asteraceae

Myanmar Name - Khayu

English Name - Indian camphorweed

Perennial shrubs with aromatic smell, 2-3 m high; stem slender, erect and much branched. Leaves simple, alternate; leaf blade obovate, 3.5-5.5 x 1.5-2.0 cm, base attenuate, margin dentate, thick, smooth and shining on both sides; petioles sessile; exstipulate. Capitula narrowly cylindric, 0.5-0.8 x 0.2-0.3 cm, arranged in terminal and axillary corymbs. Involucre bracts ovate; phyllaries 6 or 7-seriate, margins ciliolate, apex obtuse, margins entire, apex obtuse. Receptacle densely hirsutulous. Marginal florets numerous, 0.2-0.5 mm, several rows, fusiform, purple, regular, actinomorphic, incomplete, unisexual, epigynous; corolla 5-lobed, tubular and filiform, 0.6-0.7 mm long, 0.1-0.2 mm wide; pappus white colour, 0.5-0.7 mm long, basally connate. Central florets tubular, 0.5-0.8 mm, sessile, purple, regular, actinomorphic, complete, bisexual, epigynous; corolla 5-lobed, tubular and filiform, 0.6-0.7 x 0.1-0.2 mm; stamens 5, syngenesious, inserted on the corolla tube, anthers radiate and obtuse at apex, introrse, basifixed, dithecous, longitudinal dehiscence; ovary inferior, unilocular, bicarpellary, syncarpous, axile placentation; style simple; stigma bifid; achenes indehiscent; pappus as along as corolla, white colour (Figures 1 and 2).

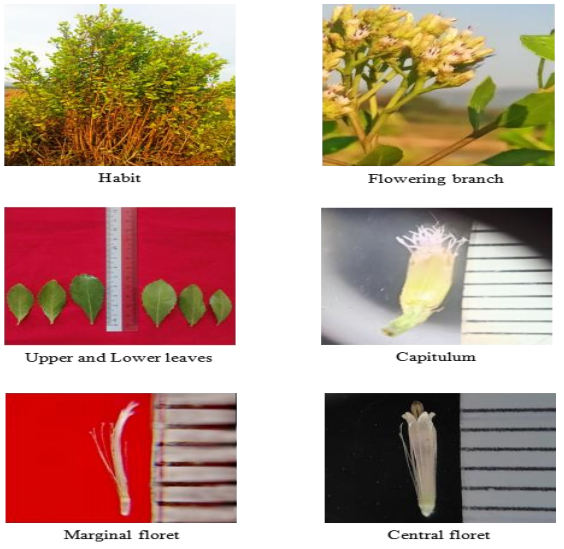

Figure 1. Morphological characters of *Pluchea indica* (L.) Less.

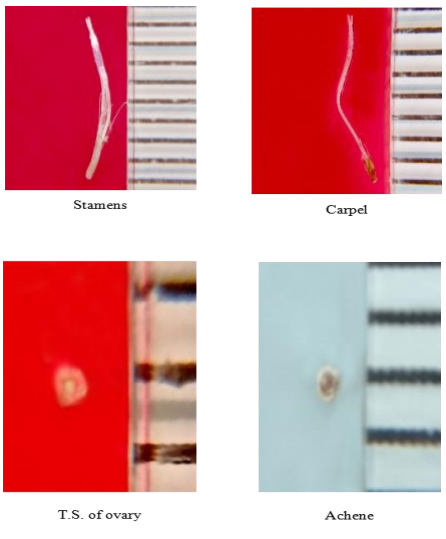

Figure 2. Morphological characters of *Pluchea indica* (L.) Less.

Larvicidal activity of leaves of *Pluchea indica* (L.) Less.

Aedes aegypti larvae were found 91.2% knockdown at 0.8g in 100 ml dilution of *Pluchea indica* (L) Less of the leaves Ethanol extract. Lowest knockdown effect was found 7.2% at 0.05g dilution of leaves Ethanol extract. Highest mortality of 3rd & 4th instar *Aedes aegypti* larvae was found 98.4% at 0.8g dilution and followed by 82.4% at 0.4g dilution of *Pluchea indica* (L) Less leaves Ethanol extract. Lowest mortality was found 10.0% of larvae at 0.05g dilution of green leaves Ethanol extract. This results show in Table (1 and 2) and Figure (3).

Table 1. Knockdown and mortality effect of different concentrations of *Pluchea indica* (L.) Less leaves Ethanol extract against 3rd and 4th instar *Aedes aegypti* larvae

Concentration (gm)	Total larvae	Knockdown	% Knockdown	Mortality	% Mortality
0.8g	250	228	91.2	246	98.4
0.4g	250	186	74.4	206	82.4
0.2g	250	113	45.2	123	49.2
0.1g	250	69	27.6	72	28.8
0.05g	250	18	7.2	25	10.0
Control	250	0	0	0	0

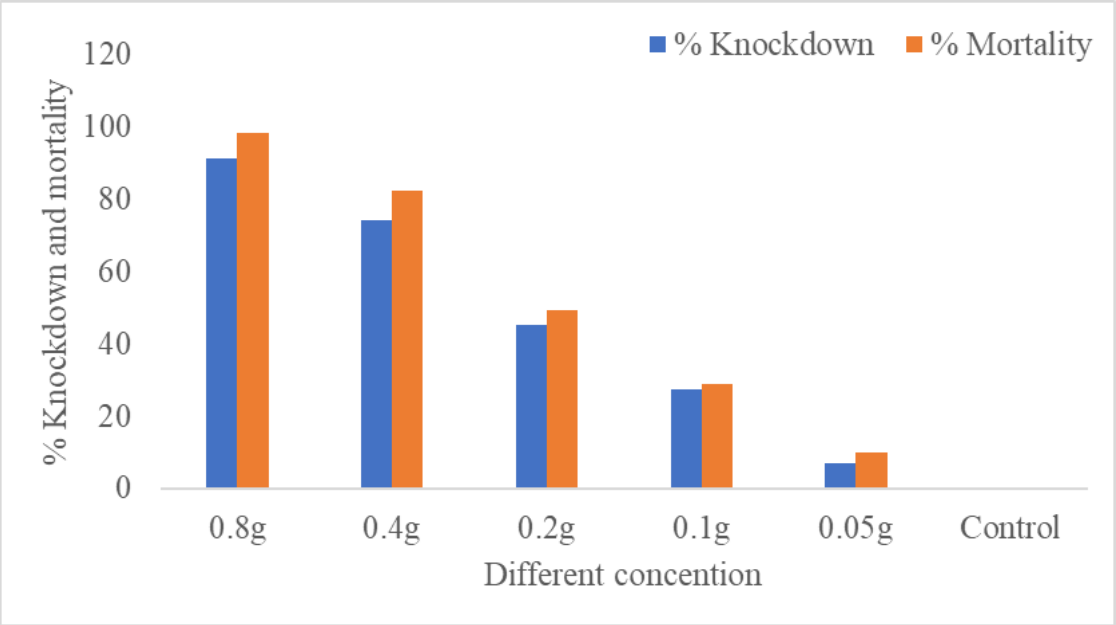

Figure 3. Percentage of Knockdown and mortality of 3rd and 4th instar Aedes aegypti larvae at different concentrations of *Pluchea indica* (L) Less leaves Ethanol extract

Table 2. LC50 and LC90 values of *Pluchea indica* (L.) Less leaves Ethanol extract on 3rd and 4th instar *Aedes aegypti* larvae

Treatment	Hours	Extract	X2, P<0.05	df	LC_{50} corrected limits (95% confidence interval) dose	LC_{90} corrected limits (95% confidence interval) dose
Pluchea indica (L) Less leaves Ethanol extract	24	*Pluchea indica* (L) Less leaves Ethanol extract	X2 = 0.0624 p<0.05	4	0.2427g	0.7317g

Discussion and Conclusion

In this present research, *Pluchea indica* (L.) Less. was selected because local people used this plant both in medicinal plant and nutritious vegetable. In morphological study, *Pluchea indica* (L.) Less. is shrub with aromatic smell. Leaves are simple, alternate, obovate, irregularly dentate, margins, sessile or shortly petiolate and exstipulate. These characters are in agreement with observation of Hooker (1885) and Backer (1965).

Inflorescence is capitulum in terminal or axillary corymbs. The central floret is sessile, regular, actinomorphic, complete, bisexual, tubular and functionally in staminate. The marginal floret is numerous, in several rows and fusiform. Calyx is modified into pappus and corolla, is 5-Lobed and tubular which are in agreement with those given by Nyo Maung (2001) and Cronquist (1981). Stamens are free and inserted on the corolla tube. Gynoecium, bicarpellary; syncarpous, unilocular axile placentation, ovary inferior, stigma bifid and style simple. Fruits are achene and very small and exalbuminous. These characters are in agreement with Dassanayake (1997) and Hooker (1885).

The leaves of *Pluchea indica* (L.) less. were used as larvicidal activities with colony Ades larva. As a result, Mortality of Ades larva was occurred in ethanol extract of leaves of *Pluchea indica* (L.) less. Highest mortality of *Aedes aegypti* larvae was found 98.4% and 82.4% in 0.8 gm and 0.4 gm concentration respectively of *Pluchea indica* (L) Less leaves ethanol extract. It is evident that the 0.8 gm concentration is the most effective concentration and the percentage of mosquito kills increases with the amount of leaf extract applied. LC_{50} corrected limits does is 0.2427 g and LC_{90} does is 0.7317 g. This results statement agrees with WHO, (2005) and Bahri *et al.*, (2022). In conclusion, *Pluchea indica* (L.) Less. leaves can be utilized as a natural insecticide to kill mosquitoes according to the research findings.

Acknowledgement

I would like to thank Dr. Thet Thet Mar Win, professor and Head, Dr. Ni Ni Htun, professor Department of Botany, University of Yangon for their kind permission to work for this research paper.

References

Backer, C.A and Van Den Brink. (1965). Flora of Java. Vol. II. N.V.P. Noordhoof Groningen. The Netherlands.

Bahri, S., Lestari, A., Devi, V. M., Rahmayanti, B. F., & Rosyidi, M. A. (2022). Effect of beluntas leaf (Pluchea indica) ethanol extract on mortality of instar II larvas (Spodoptera litura F.) on long bean plant (Vigna sinensis L.). Jurnal Pijar Mipa 17(4),538-543.

Cronquist. (1981). "An Integrated System of Classification of Flowering Plants". Vol. I. Columbia University Press, New York.

Dassanayake, M.D. (1997). Flora of Ceylon. Vol XI. University of Peradeniya Department of Agriculture, Peradeniya, Sri Lanka.

Hooker, J.D. (1885). Flora of British India, Vol. IV. L Reeve and Co., 5, Henrietta Street, Convent Garden, England.

Kress, J.W., Robert A. Ellen Fare & Yin Yin Kyi. (2003). A check list of the Trees, Shrubs, Hers & Climber of Myanmar. Department of Systematic Biology-Botany, National Museum of Natural History, Washington, DC.

Nyo Maung. (2002). Taxonomy of Angiosperms. Department of botany, University of Mandalay.

Priya, S. S., Vasantha-Srinivasan, P., Altemimi, A. B., Keerthana, R., Radhakrishnan, N.,Senthil-Nathan, S., Kalaivani, K., Chandrasekar, N., Karthi, S., Ganesan, R., Alkanan, Z. T., Pal, T., Verma, O. P., & Proćków, J. (2023). Bioactive Molecules Derived from Plants in Managing Dengue Vector Aedes aegypti (Linn.). Molecules, 28(5), https://doi.org/10.3390/molecules28052386 2386.

World Health Organization (2005). Guidelines for laboratory and field testing of mosquito larvicides. WHO Geneva 2005, WHO/CDS/WHOPES/GCDPP/1.3

Effect of Edible Coatings on the Postharvest Quality of Eggplant

Mya Mya Than[1]

Abstract

The postharvest studies were carried out on *Solanum melongena* L. (Eggplant) using the different postharvest techniques to minize their deteorioration quality and storage life under room temperature. The studies showed that storing the eggplant inside the aloe rera gel and cellophane wrap treatments for Factor A T1 (control), T2 (aloe vera gel 5%), T3 (aloe vera gel 10%), T4 (aloe vera gel 15%), for factor B t1cellophane 1- layered), t2 (cellophane 2-layered), t3(cellophane 3- layered), on two factors were beneficial to minize weight loss on fresh fruits retention in peel color development of eggplant during storage at ambient for 18 days compare to control. Among these treatments factor A has the lowest fruit weight loss T4 (aloe vera get 15%) (86.55 g), the highest fruit weight loss T3 (aloe vera get 10%) (103.33 g), the maximum fruit length and diameter T1 (control), 24.53 cm and T4 (aloe vera get 15%) (7.06 cm). The factor B data the lowest fruit weight loss t1 (cellophane 1 layered) (100.77 g), the maximum fruit weight loss t3 (cellophane 3 layered) (115.6 g), the maximum fruit length and diameter t2 (cellophane 2 layered) 24.53 cm and t2 (cellophane 2 layered) (21.86 cm). The maximum total soluble solid (TSS) were also found in factor B t2 (cellophane 2 layered) (6.75 Brix) and the highest pH (liquid) level were found in factor B t2 (cellophane 2 layered) 6.73%. The greatest value of hardness in factor A T2 (aloe vera get 5%) (0.11 Kg) in this study.

Introduction

Postharvest handling of vegetables and fruits should be extracted very consciously after having observed the required degree of maturity and consistency. Since, fruit decrease the shelf-life and raise of the spoilage. Postharvest management is a series of postharvest producer that include; sweeping, washing, collection, marking, drying, disinfection, packaging and storage. After harvesting, the importance of fruits and vegetables is applied at successive stages to the point that they are consumed. The goal of postharvest management is too optimized this value added. This could potentially favor the local population either by growing export eating or by increasing the supply of fresh produce during the year. Postharvest control will have an effect on all of them and will temperature regulation and packing being the most significant fields. (Canteuell, 1998). Postharvest storage of eggplant at room temperature decreases the quality of the fruit rapidly, primarily due to loss in water content, skin discoloration and shrinkage, so that could storage is commonly used to preserve postharvest fruit quality (Dhatt , 2007)

Low temperature conditioning (LTC) means short-term storage of could-sensitive plants above low temperature to stimulate tolerance to sequence storage at lower temperature. As it provides ensures a minimal degree of quality assurance for consumer. Another reason for establishing these standards in almost all horticulture product is that they are harvested by hand (Mota 2003). Maturity is the crucial factor that determines final quality such as texture, appearance, nutritive value and favor off the harvested crap and their postharvest life.

The aim of the research is to protect the mature quality food safety and to reduce losses between harvest and consumptions. To optimize the Aloe vera gel coating and cellophane warp the MA (modified atmosphere) storage of eggplants. Objectives are to evaluate the changes of postharvest characteristics and deterioration of eggplant and to trend their shelf-life.

[1] **Lecturer, Department of Botany, Sittway University**

Materials and methods

The experiments were conducted at VFRDC (vegetables and fruit research and development center, yemon, Hlegu Township, Yangon Division Myanmar during October 2025.

Preparation of materials

Different sizes and shapes of physiological matured fresh eggplant fruit were harvested from the Thuwuana Township, Yangon. Eggplants were harvested when they are full-size and before the seeds mature. The physiological mature stage of the harvested eggplants is characterized by full-size, fleshy, fresh softness, firmness, freshness of calyx and pedicel, bright color and glossy appearance on peel as maturity indice. Eggplants were gently picked up by hand and put into the baskets and then covered with the fresh banana leaves during transport from to field to VFRDC laboratory. Freshy harvested eggplants were immediately stored based on the size, weight and peel color development within 24 hours upon arrival at VFRDC. Fresh fruits selected for the study of eggplant which were free from diseases, injuries, bruises, defects and damage were used for the study.

Experimental Design

Each treatments of four eggplants were used in factor A T1 (control), T2 (5% of the Aloe vera gel), T3 (10% of Aloe vera gel), T4 (15% of Aloe vera gel), in factor B t1(1.layered of cellophane warp), t2(2-layered of cellophane warp), t3(3-layered of cellophane no warp) for postharvest. Each treatment consisted of 3 replications. Experimental design was laid out in CRD (Completely Randomized Design).

Table (1). Lay out design of eggplant on postharvest

	R1	R2	R3		R1	R2	R3
T1				t1			
T2		Factor A		t2	Factor B		
T3				t3			
T4							

Fig. (1) 3 days of eggplant shelf-life

Fig. (2) 9 days of eggplant shelf-life

Fig. (3) 15 days of eggplant shelf-life

Data collection

All results were recorded at three-days intervals of data to determine the cumulative weight loss and peel color development of fresh eggplant fruits during storage, total the internal pulp temperature, fruit length diameter, firmness, soluble solids (TSS), terrible, acidity (TA) and pH level, hardness, shrinkage and defects-

Methods

The methods used for the determination of cumulative weight, percent weight loss, length and diameter of fruits, peel color development, terrible acidity (TA), total soluble solid (TSS), firmness and pH level, hardness, shrinkage and defects were the same as in the experiment.

Preparation and Dilution method of Aloe vera Gel

Healthy and fresh leaves of aloe vera were collected from the plants using a sharp knife and washed with clean water their sterile distilled water. The top and bottom were removed and then the aloe vera gel obtained. After separating aloe vera gel from the outer cortex, this colourless hydro parenchyma was blended to remove fiber and put in clean and sterilized glass bottles. The traping point of the leaf top and the sharp spines located along the leaf margin were removed by sharp spines and then the knife was introduced into the mucilage layer below the green rind avoiding the buscular bundles. These bottles were stored in the fridge at 4-6℃ unit ready for use. The liquid obtained constituded fresh aloe vera gel.

Serial dilution of the aloe vera gel were prepared to give 5%, 10%, 15% resceptively. To obtain gel concentration of 5%, 5 milliter of aloe vera gel was measured in a measuring cylinder and 95 milliters of sterile distilled water was added. To obtain 10% gel concentration, 10 milliters of gel was measured in a measuring cylinder and 90 millititers of sterile distilled waster added. To obtain 15% gel concentration, 15 millititers of gel was measured in a measuring cylinder and 85 millititers of sterile distilled water added.

Results

The statistical results showed that the weight loss, fruit length, diameter, total acidity (TA), totals soluble solid (TSs), pH (liquid), pH (solid), shrinkage, hardness, defects, shelf-life of eggplants were highly statistically significant differences at 7 days, 14 days, 18 days.

Weight loss

In factor A, the lowest mean weight loss was found in T4 (86.55)g and the highest mean weight loss was found in T3 (103.38)g. In factor B, the lowest mean weight loss was found in t1 (100.79)g and the highest mean weight loss was found in t3 (115.6)g . The interaction between 5 aloe vera gel and cellophane warp treatments were little significant differences during the whole period of storage.(as show in Table 2)

Treatment	0 Day	3 Day	6 Day	9 Day	12 Day	15 Day	18 Day
Factor A T4 (15% aloe gel	164.79	134.67	113.36	105.63	101.01	92.07	88.55
Factor B T1 (cellphane Layer)	154.54	146.73	127.84	118.26	112.01	105.23	100.79

Table (2). Weight loss of Eggplant on Postharvest

Fruit length

In factor A, the maximum fruit length was observed in T1 (24.53 cm) and the shortest fruit length was observed in T3 20.75 cm. In factor B, the maximum fruit length was observed in t2 21.86cm and the shortest fruit length was observed in t1 21.86 cm. According to the factor A and B, the fruit length had no significant differences at 6 days and 18 days. (as show in Table 3)

Treatment	0 Day	3 Day	6 Day	9 Day	12 Day	15 Day	18 Day
Factor A T1 (control)	25.43	24.97	24.27	25.1	24.6	24.4	24.53
Factor t2 (2-layered cellophane)	24.12	13.63	23.29	22.69	22.03	21.95	21.86

Table (3). Fruit length of Eggplant on Postharvest

Fruit Diameter

In factor A, the mean of maximum fruit diameter was observed in T4 7.06cm and the shortest diameter was observed in T1 6.9cm. In factor B, the maximum fruit diameter was observed in t2 7.14cm , and the shortest diameter was observed in t1 6.77cm. According A and B the fruit diameter had no significant differences. (as show in Table 4)

Treatment	0 Day	3 Day	6 Day	9 Day	12 Day	15 Day	18 Day
Factor A T1(15% Aloe gel	8.8	8.37	7.58	7.31	7.18	7.18	7.06
Factor B (t2 layered Cellophane)	8.74	8.34	7.72	7.69	7.6	7.54	7.41

Table (4). Fruit diameter of Eggplant on Postharvest

Total acidity (TA)

In factor A, the highest mean of TA contents was obtained in T3 1.59% while the lowest in T2 1.22%. In factor showed that the value of total acidity were no significant from each other at 12

and 18 days. The highest mean of TA contents among all treatments was obtained in factor B t3 2.33% . In the interaction of factor A and B, highest significant differences was observed. (as show in Table 5)

Treatment	0 Day	3 Day	6 Day	9 Day	12 Day	15 Day	18 Day
Factor A T3 (10% Aloe gel	1.09	1.09	1.11	1.17	1.51	1.57	1.59
Factor B T4 (2 layered Cellophane)	2.27	2.47	2.43	2.53	2.54	2.46	2.33

Table (5). Total acidity of Eggplant on Postharvest

Total soluble solids (TSS)

In factor A, the sweetness of eggplant among the treatments showed that T1 had highest TSS of 6.21 Brix, while the least in T3 was 4.59 Brix. In factor B, the sweetness of eggplant among the treatments showed that in t2 had the highest TSS of 6.75 Brix while the least in t3 was 6.21 Brix. In the interaction of factor A and B, less significant differences was observed. (as show in Table 6)

Treatment	0 Day	3 Day	6 Day	9 Day	12 Day	15 Day	18 Day
Factor A T1 (control)	7.08	7.17	6.98	6.99	6.84	6.77	6.21
Factor B T4 (2 layered Cellophane)	7.22	7.51	7.47	7.3	7.22	7.06	6.75

Table (6). Total soluble solids of Eggplant on Postharvest

pH (Liquid)

In factor A, the maximum value of pH (Liquid) was obtained in T1 4.94 and the minimum pH (Liquid) was obtained in T3 4.12. In factor B, the maximum value of pH (Liquid) was obtained in t3 6.73 and the minimum pH (Liquid) was obtained in t1 4.59. In the interaction o factor A and B, highly significant differences was observed. (as show in Table 7)

Treatment	0 Day	3 Day	6 Day	9 Day	12 Day	15 Day	18 Day
Factor A T1 (control)	5.55	5.09	4.91	5.56	5.47	4.89	4.94
Factor B T4 (3 layered Cellophane)	5.62	5.7	5.95	6.4	6.63	6.74	6.75

Table (7). pH (liquid)of Eggplant on Postharvest

pH (Solid)

In factor A, the maximum value of pH (Solid) was obtained in T4 6.99 and the minimum pH (Solid) was obtained in t3 3.56. In factor B, the maximum value of pH (Solid) was obtained in t2 6.75 and the minimum pH (Solid) was obtained in t3 6.21. In the interaction o factor A and B, less significant differences was observed. (as show in Table 8)

Treatment	0 Day	3 Day	6 Day	9 Day	12 Day	15 Day	18 Day
Factor A T4 (15% Aloe vera gel)	5.37	5.45	5.7	5.72	6.45	6.55	6.99
Factor B T2 (2 layered Cellophane)	7.22	7.51	7.47	7.3	7.22	7.06	6.75

Table (8). pH (solid) of Eggplant on Postharvest

Shrinkage

In factor A, the maximum shrinkage of postharvest fruit was observed in T_1 4.53% and the minimum shrinkage was observed in T_4 3.87%. In factor B, the maximum shrinkage of postharvest fruit was observed in t_1 3.13% and the minimum shrinkage was observed in t_3 2.66%. The interaction results of the aloe vera gel and cellophane warp treatments have the highly significant differences. (as show in Table 9)

Treatment	0 Day	3 Day	6 Day	9 Day	12 Day	15 Day	18 Day
Factor A T1 (control)	3.13	3.18	3.47	3.84	4.27	4.25	4.53
Factor B t1 (1 layered Cellophane)	1.7	1.77	1.87	2.35	2.71	2.99	3.13

Table (9). Shrinkage of Eggplant on Postharvest

Hardness

In factor A, the maximum reduction in hardness of fruit was obtained in T2 0.11% and the minimum reduction was obtained in T3 0.04%. In factor B, the maximum reduction in hardness of fruit was obtained in t2 0.09% and the minimum reduction was observed in t1 0.04%. In the interaction of factor A and B, no significant differences was observed. (as show in Table 10)

Treatment	0 Day	3 Day	6 Day	9 Day	12 Day	15 Day	18 Day
Factor A T2 (50% Ale gel))	0.23	0.11	0.07	0.1	0.09	0.1	0.11
Factor B t2 (2 layered Cellophane)	0.06	0.07	0.08	0.09	0.7	0.08	0.09

Table (10). Hardness of Eggplant on Postharvest

Defects

In factor A, the maximum defects was obtained in T1 4.7% and the minimum defects was obtained in T2 2.25%. In factor B, the maximum defects of eggplant was obtained in t2, t3 2.67% and the minimum the defects was obtained in t2 2.08%. In the interaction of factor A and B, less significant differences was observeded. (as show in Table 11)

Treatment	0 Day	3 Day	6 Day	9 Day	12 Day	15 Day	18 Day
Factor A T1(control)	3.06	3.18	3.78	4.07	4.18	4.43	4.7
Factor B t3 (3 layered Cellophane)	1.03	1.12	1.71	2.1	2.26	2.35	2.67

Table (11). Defects of Eggplant on Postharvest

Shelf-life

In factor A, the maximum shelf-life of eggplant fruits was obtained in T2 10.5 and the minimum shelf-life was obtained in T3 7.7. In factor B, the maximum shelf-life of eggplant was obtained in t2 15.5 and the minimum shelf-life was obtained in t3 11.2. In the interaction of factor A and B, highly significant differences was observed. (as show in Table 12)

Treatment	Shelf-life (day)
Factor A T2 (5% Aloe gel)	10.5
Factor BT2 (2 layered Cellophane)	15.5

Table (12). pH Shelf-life of Eggplant on Postharvest

Discussion and Conclusion

In this study, the effect of aloe vera gel and cellophane warp treatment in fruit weight loss, fruit diameter, fruit pH (Solid Liquid), TSS, TA, hardness, shrinkage, defect, shelf-life of eggplant *(Solanum melongena* L.) were investigated at VFRDC (vegetable and fruit research and development conter, Yeman, Hlegu township, Yangon division, Myanmar during 2025. The result of the study showed that the cellophane warp and aloe vera gel treatment indicated that the maximum reduction of fruits weight loss during storage compare to control. In fact, fruit weight of eggplant were obviously decreased over time in control and aloe vera gel treatments throughout of the storage period at ambient temperature for 15 days 18 days respectively . According to the factor A data the lowest fruit weight loss T4 (86.55g), the highest fruit weight loss T3 (103.33g), the maximum fruit length and diameter T1 24.53cm and T4 7.06cm. According to the factor B data the lowest fruit weight loss T1 (100.77g), the highest fruit weight loss t3(115.6g), the maximum fruit length and diameter in 24.53cm and t2 21.86cm. This research agreed Willer, (2019) , who reported that cellophane wrapping will reduce the weight loss and maintain the firmness of the eggplant fruit. Weight loss was caused by water less from the fruit through the process of transpiration. Among the

treatments, the maximum total soluble solid (TSS) were also found in factor B t2 (6.75 Brix). D' Aqunio, (1998) reported that the increase of the total soluble solid level contributes to increase of the sugar level of the fruit. Dhatt (2007) reported that the effects of cellophane warp treatments gives highest TSS in eggplant. Moreover, the lowest was found in T3 4.59% as compare with control. These findings were in agreement with the Statements of Leif Marvin (2019). They mentioned the decrease in total soluble solids and terrible acidity were also observed in green eggplants. These decreases to the participation of these compounds as respiratory metabolites during the maturation process. In addition, Cantwell and Suslow (1998) stated that the TSS, TA and sugar content of eggplant have strong retain and affect the flavor of eggplant fruit. According to the pH (Liquid) levels, the results showed that the highest pH (Liquid) levels were found in t2 6.73% compared to other treatments during storage. Willer, (2019) stated that the pH level increased happens due to a decrease in the amount of hydrogen ions supplied by organic acids during the ripening process. Moreover, T2 also gave the greatest value of hardness (0.11 kg) compared to other treatments. These findings were agreed with L.Suria, (2020) who reported that the quality of eggplant fruit found the highest values of hardness in the postharvest treatments. In order to factor B, the result showed that the cellophane wrapping treatments indicated the less reduction of fruit weight and qualities during storage period while compare to control. Among to the data the postharvest treatments with cellophane wrapping makes eggplants treatments last after 18 days storage life. D' Aqunio (1998)also stated that cellophane wrap was the most efficient in reducing the fresh matter loss percentage and the shrinkage. These finding were agreements with Mota (2003). They reported that the wrapping of Nagpur mandarin fruit after 21 days of storage under refrigerated condition. Mohajan. 2007. Stated that cellophane wrap acts as a semipermeable barrier, which effectively reduces water loss and helps the eggplant fruit maintain their weight loss and firmness for a longer period compared to unwrapped. From above research findings, it was concluded the fruit quality of eggplant fruits showed 1-layered and 2-layered of cellophane wrap treatment was the best quality along the storage period. Cellophane wrap treatments is an important key to post harvest of eggplant fruit because it maintained prolong shelf-life for eggplants. Moreover, cellophane wrap on fruit found to be beneficial on majority of physical, physiological and most fruit quality related traits up to 18 days of storage. Therefore, wrapping on eggplant fruit with cellophane found to be recommended.

References

Canteuell, M, and T.y. Suslow 1998. Eggplant and winter squashes. **Recommendation for Maintaining Post harvest quality.** Perishables Handling Quality 84: 5-16

D' Aqunio, S, A.Piga, M. Agabbo, T.G. Mc collum, 1998. Film Wrapping Delays Ageing of **" Mimmeola" tangelos under shelf-life Condition**. Postharvest Biology and Technology, 14(1), PP.107-116, doi: 10.1016150925-5214(98)00019-2.

Dhatt A.S and B. Mohajan. 2007. Harvesting, **Handling and Storage of Harticultural Crops.**

Javed Ali Sugash Pandey. Vaishali Singh. Prena Joshi April 2016**; Effects of Coating of Aloe vera Gel on shelf-life of graps.**

L.Suria, March 2020; **Characteristic fillet of aloe vera gel as edible coating.**

Leif Marvin R. Gonzales. Marilou M. Benitez: December 2019, **Polysaccharide – Based Edible Coatings Improve Eggplant Quality of postharvest storage.**

Mota, W.F.2003. **Waxes and plastic film in Relation to the Shelf-life of Eggplant Fruits.** Scientia Agricola, 60(1),pp. 51-57 doi: 103-90162003000100008.

Willer, H. and J. Leround, 2019. **The World of Organic Agriculture Statistics and emerging trends**. Research institute of organic agriculture (FiBL) international federation of organic agricultural movements (IFOAM). Friclk (CH), bonn (DE)

Websites

https://en .Wikipedia.org/ wiki/ parafilm (cellophane)

https://en . Liebertpub.com/ postharvest/ shelf-life/

https://en . Hasanuzzman.weekly.com/ Aloe vera gel/ postharvest/ treatments/

Palynological Study on Ten Species from Hlawga National Park in Mingalardon Township, Yangon Region

Aye Myat San[1], Kyi Kyi Lwin[2]

Abstract

The pollen morphological characteristics of 10 species belonging to 10 genera of 7 families were studied. The specimens were collected from Hlawga National Park in Mingalardon Township, during the flowering period. The collected specimens represent only one species in family of Urticaceae, Balsaminaceae, Verbenaceae, Lamiaceae and two species in family are Fabaceae, Polygonaceae and Acanthaceae. The morphological characters on pollen grains of each species were polyads and the rest of the nine species were monads. In this paper, the type of pollen grains, the shape of pollens and the type of exine ornamentation were studied. The pollen photomicrographs of each species were presented by polar and equatorial view. Pollen morphology is conducted as an aid to the morphological study and a significant tool for modern taxonomist for the delimitation of species.

Keywords: polyads, monads, exine ornamentation.

Introduction

Palynology is the study of pollen and spore of plants. The term palynology was first of all introduced by Hyde & Williams in 1944. Pollen grains have a number of morphological and ultrastructural features. These palynological features have provided a wealth of characters that have been important in inferring phylogenetic relationship of plants (Simpson, 2006).

The palynological research can be either basic or applied. To the basic aspects belong the pollen morphology in relation to taxonomy and to the applied aspects belong geopalynology, aeropalynology, iatropalynology, melitopalynology (Bhojwani & Bhatnagar, 2005).

The most important diagnostic features of a pollen grains depend on its size, shape, surface, aperture (shape, number and position) and exine sculpture (Schivanna *et al*, 2009).

The study of pollen morphology helps in the confirmation of relationship and affinities between the related taxa. Pollen of related families and genera are usually of more or less the same type. The sculpture and pattern of the outer wall, exine, the number of apertures on the wall, size and shape of the pollen grains, etc. play an important role in identification and relationship of plants at various taxonomic levels (Nair *et al*., 1964).

The aim and objectives of this research work are to study the collected species systematically from morphological and palynology point of view and to provide the valuable pollen characters that can be used in plant classification and identification.

Materials and Methods

Materials

Plant Collection

The specimens were collected from Hlawga National Park. The study areas located in Mingalardon Township, Yangon Region. The collected plants were photographed to record their habitats, inflorescences, flowers, and stamens. Identification of specimens were carried out by referring the floristics and monographic of by using floristics literatures of Hooker (1885), Backer (1963-1968), Ali and Nasir (1979-1990), Gilbert (1994), Dassanayake (1983-

[1] Daw, Assistant Lecturer, Department of Botany, East Yangon University
[2] Dr, Associate Professor, Department of Botany, East Yangon University

2000) and HU-Qi-ming & WU Delin (SCBG), (2007-2009). Myanmar names were referred to Hundley and Chit Ko Ko (1987) and Kress *et al* (2003).

Pollen Collection

Pollen samples of the specimens were freshly collected from the anthers in blooming flowers. Pollens of each species were stored in glass vials with 1 cc of glacial acetic acid and the specimen was labeled with its scientific name.

Methods

Acetolysis of pollen grains (Erdtman, 1952)

The anther specimens in a glass vial was crushed with a glass rod and 1 cc of acetic acid was added to it. The above mixture was transferred into a test tube and 5-9 drops (depending on the quantity of the specimen) of concentrated sulphuric acid was added. The test tube was put in a water-bath (in a water of beaker, heated to 70º C- 80º C) for 15-30 minutes (depending on the size, sculpturing and structure of the pollen grains).

Preparation of glass slide

The glass slide mounted with pollen sample was examined under electric light microscope with (X 400) and photomicrograph taken (camera of Vivo V 40). The size of the pollen was measured at polar axis and equatorial diameter when observed form the equatorial view and 10 specimens from each species were measured and recorded. The terminology used in the identification of pollen was according to Erdtman, (1952-1969), Moore *et al*., (1991), Hoen (1999), Paldet (2005), Punt (2007) and Hesse *et al*., (2009).

The shape of a pollen grains or spores in which the ratio between the polar axis (P) and equatorial diameter (E) is designated (Erdtman, 1946) as follows:

Peroblate	<	0.50 µm	Prolate spheroidal	1.00-1.14 µm
Oblate		0.50-0.75 µm	Subprolate	1.14-1.33 µm
Subspheroidal		0.75-1.33 µm	Prolate	1.33-2.00 µm
Suboblate		0.75-0.88 µm	Perprolate	2.00 µm
Oblate spheroidal		0.88-1.00 µm		

The following size classes based on the length of the longest spore axis have been suggested (Erdtman, 1945).

Very small spores	<	10 µm	Large spores	51-100 µm
Small spores		11-25 µm	Very large spores	101-200 µm
Medium size spores		26-50 µm	Gigantic spores	201 µm >

Results

In pollen morphology, 10 species belonging to 10 genera of 7 families have been studied. They are eudicotyledonous plants. The families were listed according to APG IV (2016) systems as follows and the species according to alphabetical order.

Table. List of collected species in Hlawga National Park

No	Family	Scientific Name	Myanmar Name
1.	Fabaceae	1. *Calliandra haematocephala* Hassk 2. *Clitoria ternatea* L.	Not Known Aung-me-nyo
2.	Urticaceae	3. *Urtica dioica* L.	Phat-yar
3.	Polygonaceae	4. *Antigonon leptopus Hook & Arn* 5. *Persicaria chinensis L.H.Gross*	Tike-pam Maha-gar-kyar-sit
4.	Balsaminaceae	6. *Impatiens balsamina L.*	Dam-pam
5.	Acanthaceae	7. *Asystasia gangetica (L.)* 8. *Hygrophila ringens (L.) R.Br.ex steud*	Kyauk-kwe-pin Mi-kyaung-kwan-phat
6.	Verbenaceae	9. *Duranta repens L.*	Not known
7.	Lamiaceae	10. *Hyptis capitata jacq.*	Not known

1. *Calliandra haematocephala* Hassk., Retzia 1:216 (1855).

Family : Fabaceae

Myanmar name : Not known

English name : Red powder puff

Flowering period : Novermber-May

Pollen Morphology

Polyads (8 cells), isopolar, oblate, large, 62.5-75.0 x 90.0-102.5 μm in length and breadth; amb drop-shaped; each grain triporate, oblate, medium, 22.5-25.0 x 30.0-35.0 μm in length and breadth;

amb sub-quadrangular; pori circular, 2.0 μm in diameter; exine about 0.9 μm thick, sexine thinner than nexine; sculpturing granulate.

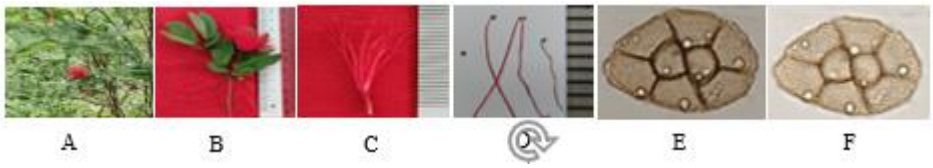

Fig 1. *Calliandra haematocephala* Hassk
A. Habit B. Inflorescence C. Flower D. Stamens E&F. Surface view

2. *Clitoria ternatea* L., Sp. Pl. 2:753 (1753).

Family : Fabaceae

Myanmar name : Aung-me-nyo

English name : Blue-pea

Flowering period : October-March

Pollen Morphology

Tri-tetracolporate, zonocolporate, oblate, large, 32.5-35.0 x 52.5-55.0 µm in length and breadth; amb tri-tetra angular; colpi parasyncolpate, the apocolpia triangular with slightly concave side, about 25.0 µm in diameter; pori lolongate, 12.5-17.5 x 7.5-12.5 µm in length and breadth; exine 0.75-1.0 µm thick, sexine as thick as nexine; sculpturing faintly reticulate.

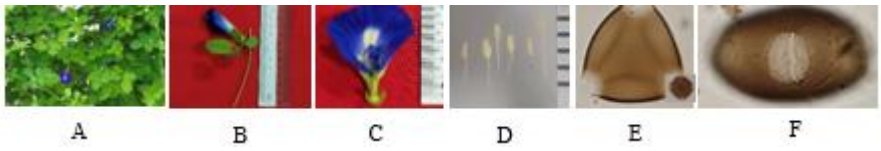

Fig 2. *Clitoria ternatea* L.

A. Habit B. Inflorescence C. Flower D. Stamens E. Polar view F. Equatorial view

3. *Urtica dioica* L., Sp. Pl. [Linnaeus] 2:984 (1753)

Family : Urticaceae

Myanmar name : Phat-yar-pin

English name : Burn nettle

Flowering period : Throughout the year

Pollen Morphology

Hexaporate, pantaporate, spheroidal, very small, 7.5-10.0 µm in diameter; amb circular; pori circular, 1.0-1.5 µm in diameter; exine 1.75-2.25 µm thick, sexine as thick as nexine; sculpturing faintly reticulate.

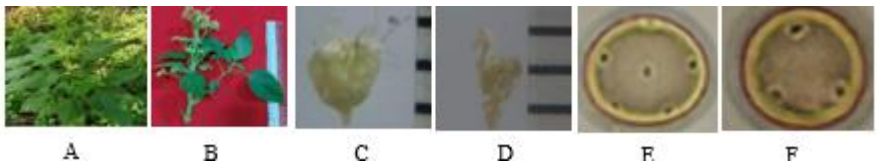

Fig 3. *Urtica dioica* L.

A. Habit B. Inflorescence C. Flower D. Stamens E. Polar view F. Equatorial view

4. *Antigonon leptopus* Hook&Arn., Bot. Beechey Voy. 308 (1838).

Family : Polygonaceae

Myanmar Name : Tike-pam

English Name : Coral vine

Flowering Period: February-April

Pollen Morphology

Tricolporate, zonocolporate, prolate spheroidal, medium, 35.0-41.2x 32.5-36.2 µm in length and breadth; amb rounded; colpi parasyncolpate, the apocolpia triangular with slightly concave side, about 12.5 µm in diameter; pori lalongate, 2.8-2.9 x 3.2-3.5 µm in length and

breadth; exine about 1.3 µm thick, sexine thicker than nexine; sculpturing reticulum-cristatum, the lumina heterobrochate, 1.2-3.0 µm in width,the muri simplibaculate, about 0.7 µm in width.

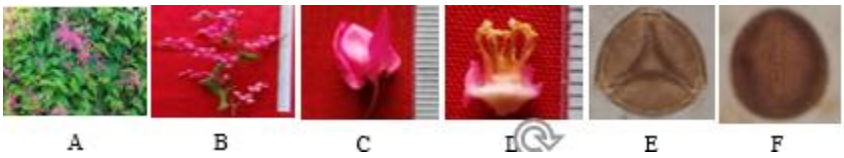

Fig 4. Antigonon leptopus Hook&Arn.

A. Habit B. Flower C. Stamens D. Stamens E. Polar view F. Equatorial view

5. *Persicaria chinensis* L.H. Gross

Family : Polygonaceae

Myanmar name : Maha-gar-kyan-sit

English name : Smartweed

Flowering period: July-October

Pollen Morphology

Tricolpate, zonocolpate, spheroidal, medium, 26.25-30.0 µm in diameter; amb rounded; colpi brevicolpate, 10.0-12.5 x 1.0-2.0 µm in length and breadth; exine 2.5-3.75 µm thick, sexine thicker than nexine; sculpturing distinctly reticulate, the lumina heterobrochate, 2.5-5.0 µm in width, the muri simplibaculate, about 2.0 µm in width.

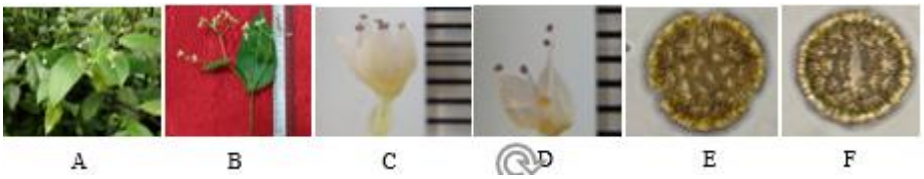

Fig 5. *Persicaria chinensis* L.H. Gross

A. Habit B. Inflorescence C. Flower D. Stamens E. Polar view F. Equatorial view

6. *Impatiens balsamina* L., Sp. Pl. 2:938 (1753).

Family : Balsaminaceae

Myanmar name : Dam-pan

English name : Rose balsam

Flowering period : October-March

Pollen Morphology

Tetracolpate, stephanocolpate, peroblate, medium, 10.0-12.5 x 26.0-27.5 µm in length and breadth; amb quadranngular;colpi brevicolpate, 2.5-3.75 x 1.25-1.87 µm in length and breadth; exine about 1.25 µm thick, sexine thinner than nexine;sculpturing distinctly

reticulate, the lumina heterobrochate, 1.25-2.5 µm in width, the muri simplibaculate, about 0.75 µm in width.

Fig 6. *Impatiens balsamina* L.

A. Habit B. Inflorescence C.Flower D. Stamens E. Polar view F. Equatorial view

7. *Asystasia gangetica* (L.)T. Anderson, Enum. Pl. zeyl. [Thwaites] 235 (1860).

Family : Acanthaceae
Myanmar name : Kyauk-kwe-pin
English name : Creeping fox glove
Flowering period : Throughout the year

Pollen Morphology

Tricolporate, zonocolporate, planaperturate, prolate, medium, 47.5-50.0 x 35.0-37.5 µm in length and breadth; amb rounded triangular; colpi syncolpate, faintly pseudocolpi present, the number of pseudocolpi 6, the colpi alternate with 2 faintly pseudocolpi; pori lalongate, 2.5 x 3.0-3.75 µm in length and breadth; exine 1.25-2.5 µm in thick, sexine thicker than nexine; Sculpturing distinctly reticulate, the lumina heterobrochate, 1.25-2.5 µm in width; the muri simplibaculate, about 0.5 µm in width.

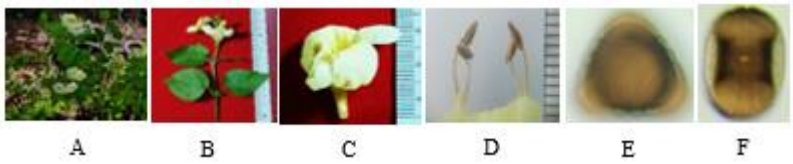

Fig 7. *Asystasia gangetica* (L.)

A. Habit B. Inflorescence C.Flower D. Stamens E. Polar view F. Equatorial view

8. *Hygrophila ringens* (L.) R.Br.ex Steud.

Family : Acanthaceae
Myanmar name : Mi-kyaung-kwan-phat
English name : Miramar weed
Flowering period : May-December

Pollen Morphology

Tetracolporate, zonocolporate, suboblate, medium, 25.0-30.0 x 30.0-35.0 µm in length and breadth;amb elliptic;colpi longicolpate, 20.0-25.0 x 1.0-1.75 µm in length and breadth, the pseudocolpi present, the number of pseudocolpi 20;pori circular, 3.0-3.75 µm in diameter;exine about 2.5 µm thick, sexine as thick as nexine;sculpturing distinctly reticulate, the lumina heterobrochate, 1.25-2.5 µm in width, the muri simplibaculate about 0.5 µm in width.

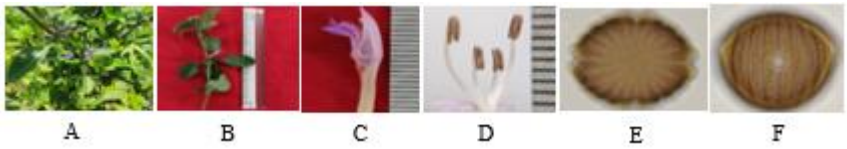

Fig 8. *Hygrophila ringens* (L.)

A. Habit B. Inflorescence C. Flower D. Stamens E. Polar view F. Equatorial view

9. *Duranta repens* L., Sp. Pl. 2:637 (1753).

Family	:	Verbenaceae
Myanmar name	:	Not Known
English name	:	Golden dewdrop
Flowering period	:	Throughout the year

Pollen Morphology

Tetracolporate, zonocolporate, spheroidal, small, 12.5-15.0 µm in diameter;amb rounded tetrangular;colpi longicolpate, 7.5-10.0 x 0.25-0.75 µm in length and breadth;pori circular, 1.25-2.5 µm in diameter;exine about 2.5 µm thick, sexine thicker than nexine;sculpturing distinctly reticulate, the lumina heterobrochate, 2.5-3.75 µm in width, the muri simplibaculate, about 1.25 µm in width.

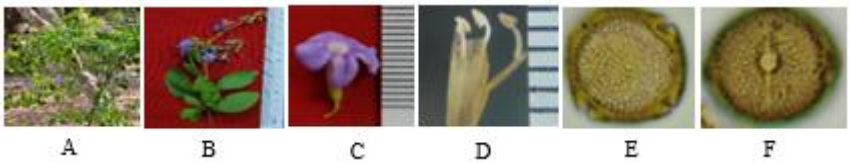

Fig 9. *Duranta erecta* L.

A. Habit B. Inflorescence C. Flower D. Stamens E. Polar view F. Equatorial view

10. *Hyptis capitata* Jacq., Icon. Pl.Rar.[Jacquin] 1:t.114 (1787).

Family	:	Lamiaceae
Myanmar Name	:	Not Known
English Name	:	Not Known
Flowering Period	:	January-March

Pollen Morphology

Hexacolpate, stephanocolpate, oblate, small, 12.5 x 16.2- 17.5 µm in length and breadth; amb rounded;colpi longicolpate, 8.0-8.7 x 1.2-2.5 µm in length and breadth;exine 1.2-2.5 µm thick, sexine thicker than nexine;sculpturing distinctly reticulate, the lumina heterobrochate, 1.2-3.7 µm in width, the muri simplibaculate, about 1.2 µm in width.

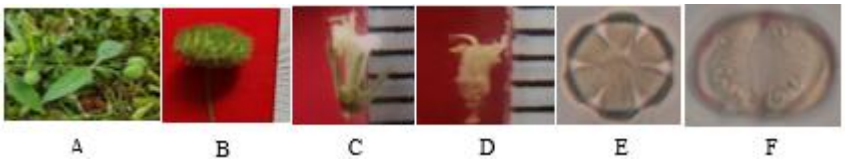

Fig 10. *Hyptis capitata* Jacq.

A. Habit B. Inflorescence C. Flower D. Stamens E. Polar view F. Equatorial view

Discussion

In pollen morphology, 10 species belonging to 10 genera of 7 families have been studied. All the species of these families were collected from Hlawga National Park. The collected species were classified according to the habit of the plants, shape of stems, leaves, stipules, types of inflorescences, characters of flowers and type of fruits. They are eudicotyledonous plants.

Almost all palynological discussion of plant relationships are based on the aperture form, their number, position and character (NPC). According to phylogeny point of view, Erdtman (1969) proposed the NPC system for the classification of pollen grains based on the number, position and character of the aperture. In the study, the type of pollen grains were one species of polyads and the rest of the nine species are monads. With respect to the number of aperture, pollen may be classified as inaperturate and aperturate.

In aperturate, the investigated pollens were colpate, colporate and porate. In present study, one species (*Urtica dioica* L.) was porate and the rest of the five species (Clitoria ternatea L, *Antigonon leptopus* Hook & Arn, *Asystasis gangetica* (L.), *Hygrophila ringens* (L.) R.Br.ex steud and *Duranta repens* L. were colporate and the rest of the three species were colpate.

In colpate grains, *Persicaria chinensis* L.H.Gross was tricolpate, *Impatiens balsamina* L. was tetracolpate and *Hyptis capitata* jacq was hexacolpate. Therefore, the resulting characters were agreed with the previous investigation.

In colporate conditions, tri, tri-tetra, tetra grains were included. Among them *Antigonon leptopus* Hook & Arn, *Asystasia gangetica* (L.) were tricolporate, *Clitoria ternatea* L. was tri-tetracolporate, while the rest of the species were tetracolporate. Therefore, the present result was agreed with the previous findings.

In porate type, hexaporate grains were included. *Urtica dioica* L. was hexaporate type. Therefore, this character were agreed with the previous investigation.

Based on the nature of colpi, pike (1956) recognized three pollen types (1) longicolpate, (2) Syn or parasyncolpate, (3) brevicolpate. In the study, parasyncolpate grains were found in Clitoria ternatea L., and *Antigonon leptopus* Hook & Arn, syncolpate grains were *Asystasia gangetica* (L.), brevicolpate grains were found in *Persicaria chinensis* L.H.Gross and *Impatiens balsamina* L., the rest of the three species were longicolpate. Therefore, the present results were agreed with the previous findings.

Based on the nature of pori, Walker and Doyle (1975) described three pori shaped (1) circular, (2) lalongate and (3) lolongate. In this study, the pori lalongate shaped of grains were found in *Antigonon leptopus* Hook & Arn, *Asystasia gangetica* (L.), the pori lolongate shaped of grains were found in *Clitoria ternatea* L., and the rest of the four species were circular. So, the resulting characters were agreed with previous examination.

Based on the shape of equatorial view, angiosperms pollen can be grouped nine classes such as peroblate, oblate, suboblate, oblate spheroidal, subspheroidal, prolate spheroidal, subprolate, prolate and perprolate grains (Erdtman 1946; Walker and Doyle, 1975). In this research, *Antigonon leptopus* Hook & Arn was prolate spheroidal, *Asystasia gangetica* (L.) was prolate, *Impatiens balsamina* L. was peroblate, *Hygrophila ringens* (L.) R.Br.ex steud was suboblate and the rest of the species were oblate and spheroidal.

Conclusion

In conclusion, the present palynological study demonstrates that pollen morphological characters such as size, aperture type, and exine ornamentation provide significant taxonomic value for the studied taxa.

Many scientists around the world involved in studying pollen from different point of view and from different point of interest and practical uses. This research work not only for the taxonomic verification based on morphological and palynological point of view but also providing the classification and identification of plants by valuable pollen characters.

The importance of pollen in environmental studies, ancient geography of the continents, climates in certain places were also enlightened in this paper. It is sincerely hoped that the present study will support as a useful information for further studies and identification of families distributed in Myanmar.

Acknowledgements

I would like to express my most sincere appreciation and deeply gratitude to Dr Myo Min Tun (Rector), Dr Thida Aung and Dr Aye Aye Ko (Pro-rector), University of East Yangon, for their permission and encouragement for this research paper. I wish to express my deepest gratitude to Dr Thaw Maw Moe, Professor and Head, Dr Khin Cho Cho Oo and Dr Kyawt Kyawt Khine, Professor, Department of Botany, University of East Yangon, for their encouragement and suggestions.

References

Ali, S. I. and Y.J.Nasir. 1979-1990. **Flora of West Parkistan**. Department of Botany, University of Karachi, Karachi.

APG IV. (2016) An update of the Angiosperm Phylogeny Group Classification For Ordered Families of the flowering plant APG IV by the Angiosperm.

Backer, C.A. (1963-1968). **Flora of java Vol.1-3**. Noordhoof & Groningen. The Netherlands.

Dassanayake, M.D.1980-2000. **A Revised Handbook to the flora of Ceylon**, Vol 1-14. Washington.D.C., U.S.A.

Gilbert, G.M (1994). **Flora of China**. 17:1-49.

Hesse, M,R.Zette., H.Hakbritter and M.Weber. (2009). **Pollen Terminology**. University of Vienna, Austria.

Hooker, J.D.1993. **Flora of British India**, Vol-L Reeve and Co., Ltd. London.

Hundley, H.G. and Chit Ko Ko. (1987). List of Trees, Shrubs, Herbs and Principle Climbers of Myanmar. Government Printing Press, Yangon.

HU.Qi-ming and WU Delin (SCBG), Hong Kong Herbarium. 2007-2009. **Flora of Hong Kong. (Vol 1-3)**, Agriculture, Fisheries and Conversation Department, Hong Kong.

Kress et al.2003. **A checklist of the Trees, Shrubs, Herbs and Climber of Myanmar**. Department of Systematic and Biology-Botany, National Museum of Natural History Washington, D.C.

Pike (1956) as Cited in John, L. (2014). Dicussion – shodhganga. Infllbnet.ac.in>16-Chapter 5.

Schivanna, K.R., & N.S. Rangaswany, 1992. **Pollen Biology**. A laboratory Manual Springer. Verlas Berlim Heidelberg.

Simpson., M.G. (2006). **Plant Systematic**. Elsever Academic Press. Theobaid's Road, London WC IX & UK.

Walker, I. W. and J.A.Doyle (1975). **The based of angiosperm phylogeny. Palynology**. Ann. Missouri Bot.Gard., 62:664-723.

Species Diversity of Menetaung Hopong Township in Southern Shan State

Nyo Lei Yi[1]

Abstract

Vegetation analysis was carried out in October 2023 at Menetaung, Hopong township in Southern Shan State. A total of 20 sample plots (30 m x 30 m)² were established in three different study sites San Phun Village area, Kyauk Ka Charr Village area (East) and Kyauk Ka Charr Village area (North).Species diversity and evenness were calculated by Shannon-Wiener's index (H), Simpson's index (D), Sorenson's index for Coefficient of similarity and species richness per study area was used by Jackknife estimate. According to the result of three study areas Kyauk Ka Charr Village area (North) possess the high diversity value (H = 2.8), (D = 0.9), Kyauk Ka Charr Village area (East) possess diversity value (H = 2.4), (D = 0.86) and San Phun Village area with the low diversity value (H = 0.36), (D = 0.72).As a result of evenness and richness, the plant species in Kyauk Ka Charr Village area (North) (E = 0.84), (S^=30.39) are more evenly distributed among the species than that in Kyauk Ka Charr Village area (East) and San Phun Village area.

Keyword: Menetaung Hopong Township, Species diversity

Introduction

Biodiversity is defined as the kinds and number of organism and their patterns of distribution (Barnes *et al*., 1998 as cited in Eshaghi *et al*., 2009). Biological diversity can be considered on different hierarchial levels of life; gene, population, species, genus, family, order, phylum, and ecosystem (Groombridge 1992 as cited in Baumgartner 2005). Moreover, diversity has become an increasingly popular topic within the discussion of sustainability in the last decade, though the maintenance of diversity of forest ecosystems is required since many years (Schuler, 1998; Swindel *et at*., 1984 as cited in Eshaghi *et al*., 2009).

Today's plant communities are the result of long-term interactions between vegetation and site factors including man-made impacts. The survival, growth and development of plants depend upon suitable environmental conditions, which are themselves dynamic and susceptible to impacts from human activities. Current species diversity reflects historical as well as environmental factors since environmental change and human activities lead to changes in species composition and competition through biological invasions. It means that biodiversity as an indicator for the well-being of ecosystems must consider the effects of invaders on an ecosystem (Li and Krauchi , 2003). Forest types and their distribution are dominated by geological factors (soil and slope), rainfall regimes, and species associations (Kyaw, 2003).

This study was aimed to describe the species diversity, species richness, species evenness and investigation of Menetaung Hopong township, Southern Shan State.

Materials and Methods

Data Collection

The plots were established through quadrat sampling technique and laid depending on vegetation characteristics and landscapes to determine the species diversity in the study areas. There were 20 quadrats (30 x 30) m² established in study area. Inside each plot, all trees with at least 10 cm girth at breast height (GBH) were identified and measured the trunk diameters (cm) and total height (m). The location (latitude and longitude) of each were recorded by using a Global Positioning System (GPS).

[1] Daw, Assistant Lecturer, Department of Botany, Monywa University

Study area

Hopong Township is located at a distance of 12 miles from Taunggyi City. Hopong Township is located between 20º 31′- 21º 27′ N latitude and between 97º 13′ E longitude. It is 21 miles from east to west and 57 miles from South to North.

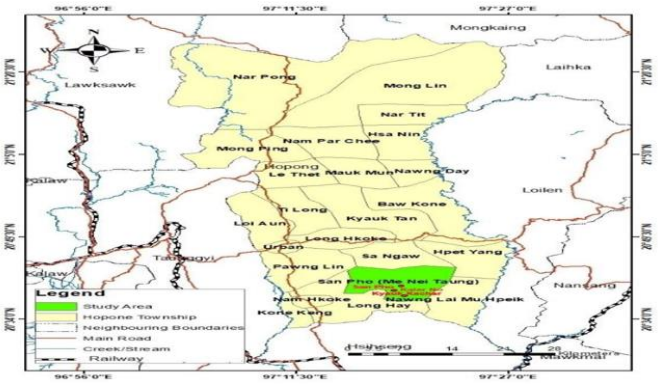

Data Analysis

Jackknife Estimate of Species Richness

Jackknife estimate of species richness was used in order to estimate the species richness per study area. According to the Heltshe and Forrester (1983), the equation of Jackknife estimate of species richness is

$$\hat{S} = S + \left(\frac{n-1}{n}\right)^{k}$$

Where,

$\hat{S}$ = Jackknife estimate of species richness

S = Observed total number of species in “n” sample plots

n = Total number of plot sampled

k = Number of unique species

Plants Species Diversity

Plant species diversity is a combination of both species richness and evenness of a community. Species diversity varies greatly from one community to another. Species diversity is often expressed by the Shannon-Wiener Index (H), Simpson’s Index (D) and Evenness (E) (Magurran, 1988).

Shannon-Wiener Index (H)

$$H = -\sum_{i=1}^{S} (P_i)(\log_2 P_i)$$

Where,

H = Index of species diversity

S = Number of species

P_i = Proportion of total sample belonging to the i^{th} species

Simpson's Index (D)

$$D = 1 - \sum_{i=1}^{S} (P_i)^2$$

Where,

D = Simpson's index of species richness

S = Number of species

P_i = Proportion of species i^{th} in the community

Evenness (E)

Species evenness is a measure of the relative abundance of individuals within a species in an area. E is between 0 and 1. The value 1 represents that all species are equally abundant. The value E gradually goes down to zero (0) when the number of species decreases. Evenness is calculated by Shannon-Wiener function (1963), as follows:

$$E = \frac{H}{H_{max}} \qquad H_{max} = \log_2 S$$

Where,

E = Shannon's evenness (Evenness measurement range, 0-1)

H = Shannon diversity index

H_{max} = Species diversity under conditions of maximal equitability

S = Number of total species found in the sample plot

Coefficient of similarity

To calculate coefficient of similarity, the floristic and structural point of views have to be taken into account for the comparison of both investigated stands (Lamprecht, 1989). The study sites were composed by means of coefficient similarity calculated using Sorenson's, (1948) index of similarity between two forests. The formula is as follows;

$$Ks = \frac{2c}{a+b} \; x \; 100$$

Where,

Ks = Coefficient of similarity

a = number of species in the one stand

b = number of species in the other stand

c = number of species common to both stand

Result

Plant species diversity

In the study area of San Phun village area, a total of 550 individuals, representing 33 species, 30 genera and 22 families were recorded. The dominant families of tree species were Rosaceae (4 species), Lauraceae (3 species).

In the study area of Kyauk Ka Charr Village area (North), a total of 549 individuals, representing 30 species, 28 genera and 20 families were recorded. The dominant families of tree species were Fagaceae (4 species) and Fabaceae (3 species).

In the study area of Kyauk Ka Charr Village area (East), a total of 342 individuals, representing 21 species, 20 genera and 16 families were recorded. The dominant families of tree species were Fabaceae (3 species) and Fagaceae (2 species).

Jackknife Estimate of Species Richness

The species richness is commonly expressed as the number of species per unit area, which is also mentioned as species density. The Jackknife estimator for species richness of trees showed that San Phun village area occupied the highest number of species richness (33.20) , Kyauk Ka Charr Village area (North) has the second highest number of species richness (30.39) and Kyauk Ka Charr Village area (East) with the lowest of species richness (21.42).

Coefficient of similarity

Lamprecht's modified the Sorensen's index (based on common species) revealed that structural similarity between San Phun Village area and Kyauk Ka Charr Village area (North) was 50.79 %, between San Phun Village area and Kyauk Ka Charr Village area (East) was 30.18 % ,between Kyauk Ka Charr Village area (North) and Kyauk Ka Charr (East) Village area was 66.66 % .

Evenness

A higher value (E) indicates the presence of many species in approximately equal quantities. As a result of Shannon Wiener evenness (E), the three study areas had 0.84, 0.82 and 0.70. According to this result, the study area was evenly distributed species.

Species diversity indices

Among the different measurement of species diversity indices, Shannon Wiener index (H), Simpson's index (D), Shannon Wiener Evenness (E) because these indices do not only taxa richness into account but also depend on the relative distribution of individuals. Shannon Wiener index more weight on the rare species while Simpson's index emphasized on the common species.

It was observed that Shannon Wiener index of San Phun Village area (H = 2.45) (D = 0.85), Kyauk Ka Charr Village area (North) (H= 2.87) and Simpson's index (D = 0.92) respectively and (H = 2.47), (D = 0.86) of Kyauk Ka Charr Village area(East).

Table (1) Ranking of dominant family by number of species composition in San Phun Village area

No.	Family	No. of genera	No. of species	No. of Individuals
1	Rosaceae	3	4	50
2	Lauraceae	2	3	120
3	Rutaceae	2	2	18
4	Ebenaceae	1	2	16
5	Myrtaceae	2	2	23
6	Anacardiaceae	2	2	14
7	Euphorbiaceae	2	2	8
8	Fabaceae	2	2	8
9	Fagaceae	1	1	138
10	Theaceae	1	1	103
11	Salicaceae	1	1	2
12	Sapindaceae	1	1	4
13	Lamiaceae	1	1	4
14	Bignoniaceae	1	1	2
15	Pentaphylacaceae	1	1	2
16	Thymelaeaceae	1	1	6
17	Capparaceae	1	1	2
18	Proteaceae	1	1	14
19	Meliaceae	1	1	8
20	Ebenaceae	1	1	2
21	Aquifoliaceae	1	1	4
22	Boraginaceae	1	1	2
	Total	30	33	550

Table (2) Ranking of dominant family by number of species composition in Kyauk Ka Charr Village area (North)

No.	Family	No. of genera	No. of species	No. of Individuals
1	Fagaceae	3	4	82
2	Fabaceae	3	3	52
3	Rutaceae	2	2	70
4	Lauraceae	1	2	76
5	Euphorbiaceae	2	2	16
6	Rosaceae	2	2	8
7	Rubiaceae	2	2	6
8	Meliaceae	1	1	62
9	Malvaceae	1	1	41
10	Thymelaceae	1	1	38
11	Aquifoliaceae	1	1	32

12	Theaceae	1	1	20
13	Proteaceae	1	1	16
14	Anacardiaceae	1	1	12
15	Capparaceae	1	1	4
16	Pentaphylacaceae	1	1	4
17	Bignoniaceae	1	1	4
18	Dipterocarpaceae	1	1	2
19	Moraceae	1	1	2
20	Sapindaceae	1	1	2
	Total	28	30	549

Table (3) Ranking of dominant family by number of species composition in Kyauk Ka Charr Village area (East)

No.	Family	No. of genera	No. of species	No. of Individuals
1	Fabaceae	3	3	60
2	Fagaceae	2	2	38
3	Lauraceae	1	2	26
4	Rubiaceae	2	2	8
5	Euphorbiaceae	1	1	104
6	Meliaceae	1	1	23
7	Myrtaceae	1	1	15
8	Dipterocarpaceae	1	1	14
9	Proteaceae	1	1	12
10	Thymelaeaceae	1	1	12
11	Rutaceae	1	1	12
12	Aquifoliaceae	1	1	6
13	Capparaceae	1	1	4
14	Anacardiaceae	1	1	4
15	Pentaphylacaceae	1	1	2
16	Malvaceae	1	1	2
	Total	20	21	342

Table (4) Consolidated Detail of Tree Species Inventory in San Phun Village area

Description	San Phun Village area
No. of sample plots	8
No. of species	33
Individual species	550
Unique species	12
Species richness	33.201
Shannon - Wiener Diversity Index (H)	2.458
Simpson's Diversity Index (D)	0.854
Simpson's Evenness (E)	0.703

Table (5) Consolidated Detail of Tree Species Inventory Kyauk Ka Charr Village area (North)

Description	Kyauk Ka Charr Village area (North)
No. of sample plots	8
No. of species	30
Individual species	549
Unique species	7
Species richness	30.393
Shannon - Wiener Diversity Index (H)	2.878
Simpson's Diversity Index (D)	0.928
Simpson's Evenness (E)	0.846

Table (6) Consolidated Detail of Tree Species Inventory Kyauk Ka Charr Village area (East)

Description	Kyauk Ka Charr Village area(East)
No. of sample plots	4
No. of species	21
Individual species	342
Unique species	3
Species richness	21.422
Shannon - Wiener Diversity Index (H)	2.478
Simpson's Diversity Index (D)	0.864
Simpson's Evenness (E)	0.812

Table (7) Sorensen's index on coefficient of similarity in the study area

Study area	Species Level (%)
San Phun Village area and Kyauk Ka Charr Village area (North)	50.79
San Phun Village area and Kyauk Ka Charr Village area (East)	30.18
Kyauk Ka Charr Village area (North) and Kyauk Ka Charr Village area (East)	66.66

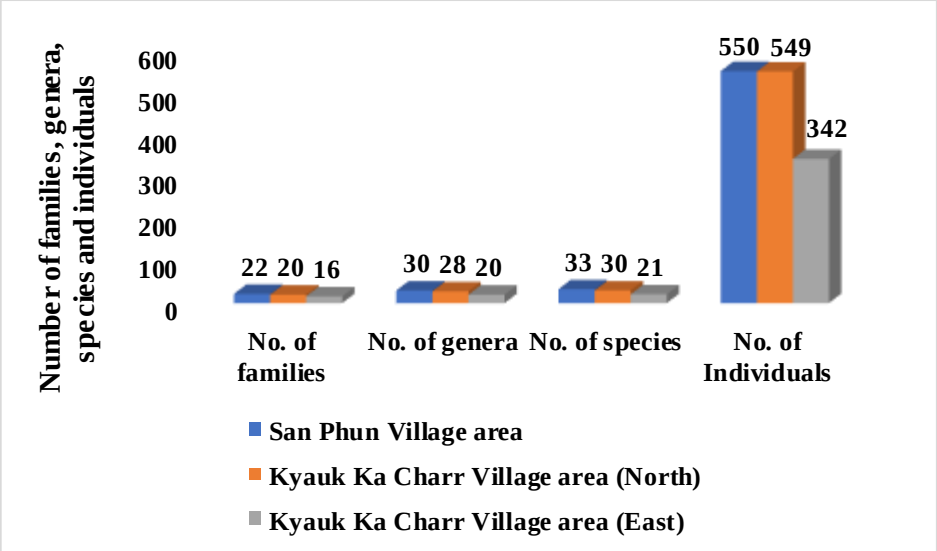

Figure 1 Number of families, genera, species and individual of tree species in study area

Discussion and Conclusion

In this part of study, species composition and diversity of San Phun Village area, Kyauk Ka Charr Village area (North) and Kyauk Ka Charr Village area (East). In San Phun Village area, 22 families comprising 30 genera, 33 species and 550 individuals were recorded, 20 families, 28 genera and 30 species with 549 individuals were found in Kyauk Ka Charr Village area (North) and 16 families, 20 genera and 21 species with 342 individuals were found in Kyauk Ka Charr Village area (East).

The result of Shannon Wiener (H) and Simpson's index (D) diversity of the San Phun Village area (2.45, 0.85), Kyauk Ka Charr Village area (North) (2.87, 0.92) and Kyauk Ka Charr Village area (East) (2.47, 0.86) .

According to the results, the diversity value of Kyauk Ka Charr village area (North) was relatively higher than the diversity of San Phun village area and Kyauk Ka Charr village area (East) although these results showed, three the study area had maximum diversity index.

Evenness for tree species was high at 0.84 in Kyauk Ka Charr Village area (North) and low at 0.70 in San Phun Village area. The Species evenness or Species Abundance Distribution (SAD) is important in characterizing ecosystems (Paul *et al*., 2005). According to quantitative analysis results of evenness, both study areas were suggested to be evenly distributed species.

The species richness of 33.20 was recorded for the San Phun Village area, 30.39 was recorded for Kyauk Ka Charr Village area (North) and 21.42 in Kyauk Ka Charr Village area (East). According to the results, San Phun Village area was more higher than Kyauk Ka Charr Village area (North) and Kyauk Ka Charr Village area (East). Species richness is widely used in ecology as a measure of species diversity (Baumgärtner, 2005).

The coefficient of similarity is generally used as a means of comparing stands from floristic point of view (Lamprecht, 1989). According to the result, San Phun Village area and Kyauk Ka Charr Village area (North) had similarity (50.79%), San Phun Village area and Kyauk Ka Charr Village area (East) (30.18%) and Kyauk Ka Charr Village area (North) and Kyaut Ka Charr Village area (East) (66.66%).The least similarity was observed in San Phun village area and Kyauk Ka Charr village area (East) (coefficient of similarity value 30.18) .The result of coefficient of similarity among study sites are heterogenous stand.

It can be concluded that, the purpose of this research is to be a source of information for the management of forest vegetation to ensure the conditions and sustainability of the ecosystem. Moreover, the forest vegetation analysis such as species diversity, species richness, evenness, coefficient of similarity and abundance must be applied to the monitoring of habitat and conservation management of Menetaung Hopong township, Southern Shan State.

Acknowledgement

I would like to express my gratitude to Dr. Than Than Win, Rector of the Monywa University and I also wish to express our gratitude to Dr. Thet Thet Mar Win, professor and Head, Department of Botany, Yangon University for giving us the opportunity to do this research and providing invaluable guidance throughout this research.

References

Baumgärtner, S, (2005a) Measuring the diversity of what? And for what purpose?A conceptual comparison of ecological and economic biodiversity indices. Working Paper, University of Heidelberg.

Eshaghi, J. R., M. Manthey, and A. Mataji, (2009) Comparison of plant species diversity with different plant communities in deciduous forest. Int.j. Environ. Sci. tech., 6(3), pp.389-394.

Heltshe, J. F. and N. E. Forrester, (1983) Estimating species richness using Jackknife procedure. Biometric 39, 1;1-11 International Society of Mangrove Ecosystem.

Kyaw, N. N, (2003). Site Influence on Growth and Phenotype of Teak (Tectona grandis Linn. f.) in Natural Forests of Myanmar (163 p.). PhD Disserta Göttingen: Der Georg -August-Universität Göttingen Cuvillier Verlag.

Lamprecht, H, (1989) Silviculture in the Tropics: Tropical Ecosystem and their Tree Species-Possibilities and Methods for their Long-term utilization (GTZ)GMBH.

Li, M. and N. Krauchi, (2003) A Method for Estimating Vegetation Change Over Time and space. Journal of Geographical Sciences pp.447 – 454.

Magurran, A. E, (1988) Ecological diversity and its measurement. Chapman and Hall,

London. 179 pp.

Paul, E. H., Anderson and J. Jeldtoft, (2005) Journal of Theoretical Biology pp.551-558.

Shannon, C. E and W. Wiener, (1963) The Mathematical Theory of Communication,

University of Illinois Press, Urbana, USA.

Sorenson , T. A, (1948) Method of establishing groups of equal amplitude in a plant society based on similarity of species content. K. Dan Vidensk. Selsk., 5: 1-34.

Some Chlorophyta Found In Yan Aung Mingalar Lake, Thaketa Township

Yoon Noe Noe Kay[1]

Abstract

In this study, algae specimens were collected from upper surface of five sampling stations, from November 2025 to January 2026 Yan Aung Mingalar Lake, Thaketa Township. All the collected specimens had been listed by the classification system of Prescott (1962). A total of 20 species belonging to 10 genera and 8 families, which were distributed under 5 orders in the class Chlorophyceae, were identified. In November 2025, *Tetraedron, Coelastrum, Scenedesmus, Closterium* were abundantly occurred in Station 1 and *Ankistrodesmus* in Station 2, while *Tetraedron, Closterium* and *Scenedesmus* were commonly occurred in station 3 and *Volvox, Crucigenia* in station 4 and *Spirogyra* in station 5. In December 2025, *Pediastrum* commonly found in station 1 and *Tetraedron, Coelastrum, Pediastrum* in station 2 and *Crucigenia, Staurastrum* were found in station 3 and *Pediastrum, Staurastrum* were abundantly occurred in station 4 and *Scenedesmus, Closterium* were occurred in station 5. In January 2026, *Pediastrum, Scenedesmus, Tetraedron* were commonly occurred in all stations. It was concluded that, according to the result, *Pediastrum* species were abundantly occurred in all stations. As well, temperature range were within 26 – 30 ºC and the range of pH values were within 5.0 – 8.9 in all stations. Therefore, it was designated that mesotrophic lake.

Keywords: Algae specimens, identified, morphological characters

Introduction

The green algae are one of the most diverse groups of eukaryotes, showing morphological forms ranging from flagellated unicells, coccoids, branched or unbranched filaments to multinucleated macrophytes and taxa with parenchymatic tissues. They are characterized by the presence of chloroplasts with two envelope membranes, stacked thylakoids and chlorophyll a and b (Proschold & Leiliaert, 2007).

Algae have been used to assess environmental conditions in aquatic habitats throughout the world. During the early part of the twentieth century, algae were explored as indicators of organic pollution in European streams and rivers (Kolkwitz and Marsson, 1908). Nutrient stimulation of algal growth made algae part of the problem in the eutrophication of lakes such that trophic status of lakes was also characterized by the amount of algae (Carlson, 1977).

The aim of this research study were to record some species of Chlorophyta growing in Yan Aung Mingalar Lake. The objective of this research provide the information for those interest in managing and monitoring the aquatic ecosystem.

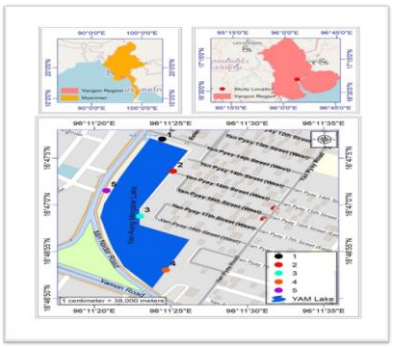

Figure 1. Location map of Yan Aung Mingalar Lake, Thaketa Township

[1] Demonstrator, Department of Botany, East Yangon University

Materials and Methods

The water samples containing algae were collected from the upper surface of the Yan Aung Mingalar Lake, Zayar Thirir Ward, Thaketa Township. The collected algal specimen were observed by using a microscope (Eliza) and photomicrographs of the specimens recorded in this study have been taken by s digital camera (sony). Many filamentous green algae are attached to a substratum during the early stages of their development but later become free floating, forming mats or balls composed of many interwined filaments (Hoek *et al.* 1995). According to Smith (1955), the Chlorophyceae show an extraordinary variety of forms and shapes unmotile forms, palmellate forms, coccoids forms, filamentous forms, heterotrichous forms and siphoneous forms. The Chlorophyta or green algae, have their photosynthetic pigments localized in chromatophores which are grass – green because of the predominance of chlorophylls a and b over the carotenes and xanthophylls (Smith, 1950). The first step in identifying an unknown sample is to determine to which family it belongs. The second step in identifying the unknown sample is to decide to which genus it belongs and lastly to identify species, the morphological characteristics of such unknown sample was compared with the descriptions and illustration of Prescott (1962), Graham & Wilcox (2000) and John *et al.* (2002). Temperature of the water body in each station were measured by thermometer.

Results

The 20 species confined to the division Chlorophyta were reported in five sampling stations of the Yan Aung Mingalar Lake, Zayar Thiri Ward, Thaketa Township.

Table 1. Classification of some species of Chlorophyta found in Yan Aung Mingalar Lake

No.	Class	Order	Family	Genus	Species
1.	1.Chlorophyceae	1.Volvocales	1.Volvocaceae	*1.Volvox*	.*1.V. aureus* Ehrenberg
		2.Chlorococcales	2.Hydrodictyaceae	*2.Pediastrum*	*2.P. sculptatum* G.M Smith
					3.P. simplex (Meyen) Lemmermann
					4.P. simplex var. duodenarium (Bailey)
					5.P. duplex Meyen
			3.Scenedesmaceae	*3.Coleastrum*	*6.P. duplex* var. reticulum Lagerheim
					7.*C. astroideum* De Notaris
				4.Scenedesmus	8.*C. microporum* Nageli
				5.Crucigenia	*9.S. quadricauda* var. parous G.M.Smith
			4.Oocystaceae	*6.Ankistrodesmus*	*10.C.lauterbornii* Schmidle
			5.Botryococcaceae	*7.Tetraedron*	11.*A. falcatus* (Corda.) Ralf
					12.*T. trigonum* Naeg. Hansgirg
					13. *T. enorme* (Ralfs) Hansgirg

	3.Zygnematales	6.Zygnemataceae	*8.Spirogyra*	14.*T. pusillum* (Wallich) West and West
			9.Closterium	15.*S. scrobiculata* (Stock.) Czurda
		7.Desmidiaceae		16.*C. dianae* Ehrenberg
				17.*C. setaceum* Ehrenberg
			9.Staurastrum	18.*C. praelongum* Brebisson
				19.S. excavatum var. minimum Bernard
				20.S.johnsonii West

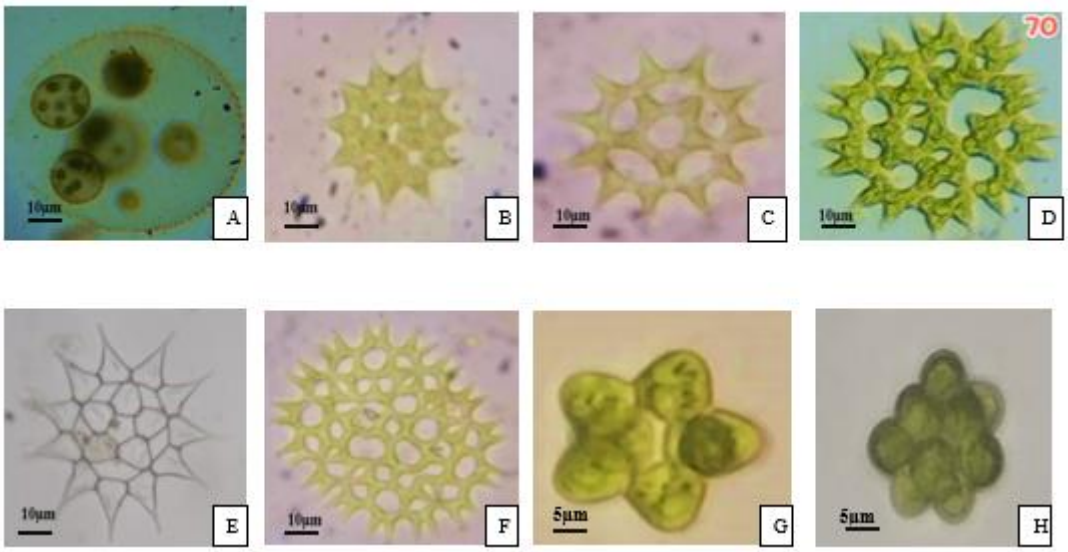

Figure 2. **A.** *Volvox aureus* Ehrenberg

B. *Pediastrum sculptatum* G.M Smith

C. *Pediastrum simplex* (Meyen) Lemmermann

D. *Pediastrum simplex* var. duodenarium (Bailey)

E. *Pediastrum duplex* Meyen

F. *Pediastrum duplex* var. reticulum Lagerheim

G. *Coelastrum astroideum* De Notaris

H. *Coelastrum microporum* Nageli

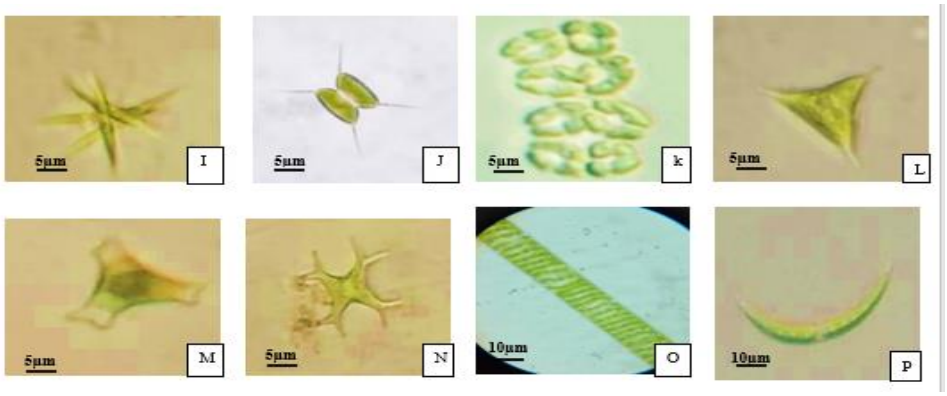

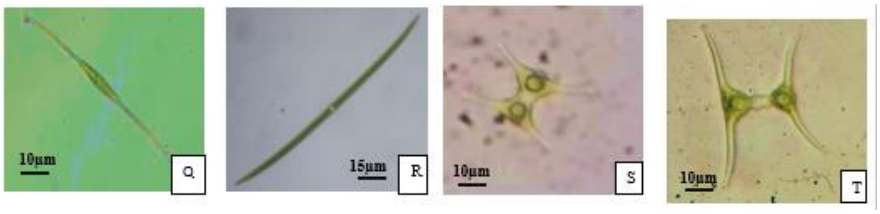

Figure 3.

I. *Ankistrodesmus falcatus* (Corda.) Ralf

J. *Scenedesmus quadricauda* var. parous G.M.Smith

K. *Crucigenia lauterbornii* Schmidle

L. *Tetraedron trigonum* Naeg. Hansgirg

M. *Tetraedron enorme* (Ralfs) Hansgirg

N. *Tetraedron pusillum* (Wallich) West and West

O. *Spirogyra scrobiculata* (Stock.) Czurda

P. *Closterium dianae* Ehrenberg

Q. *Closterium setaceum* Ehrenberg

R. *Closterium praelongum* Brebisson

S. *Staurastrum excavatum* var. minimum Bernard

T. *Staurastrum johnsonii* West

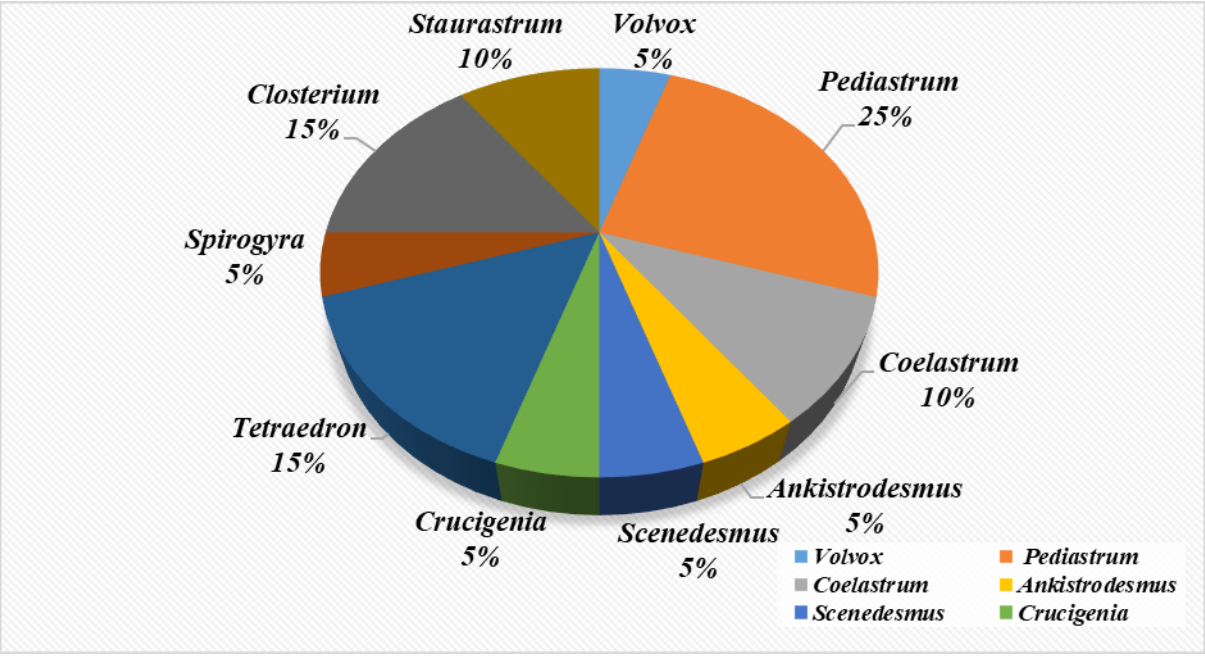

Figure 4. Density of microalgae

Discussion

Algae are important as primary producers of organic matter at the base of the food chain. They also provide oxygen for other aquatic life. They may contributed to economic well-being in the form of food, medicine and other products. Algae specimens Were collected from Thaketa Township of Yan Aung Mingalar Lake during April 2025 to December 2025.

Algal taxonomists believed that there were from 36,000 to 50,000 and more than 10 millions species of algae (Hoek *et al*. 1995).

In the present study, the totals of 20 species, 9 genera, 7 families, 3 orders, 1 class in the division Chlorophyta were found in this study area. The morphological characteristics of the species documented here are highly with the description of Prescott (1962), Philipose (1967), Graham & Wilcox (2000) and John *et al.* (2002). When the number of algal species assigned to respective orders was taken into consideration, it was displayed that Chlorococcales followed by Zygnematales and Volvocales each.

Among them, 9 genera recorded 4 genera, *Tetraedron, Coelastrum, Scenedesmus, Closterium* were abundantly occurred in Station 1 and 1 genus, *Ankistrodesmus* in Station 2, while 3 genera, *Tetraedron, Monoraphidium* and *Chlorococcum* were commonly occurred in station 3 and 2 genera, *Volvox, .Excentrosphaera* in station 4 and 1 genus, *Spirogyra* in station 5. 1 genus, *Pediastrum* commonly found in station 1 and 3 genera, *Tetraedron, Coelastrum, Pediastrum* in station 2 and 2 genera, *Crucigenia, , Staurastrum* were found in station 3 and 2 genera, *Pediastrum, Chlorococcum* were abundantly occurred in station 4 and 2 genera, *Scenedesmus, Closterium* were occurred in station 5. 3 genera, *Pediastrum, Scenedesmus, Tetraedron* were commonly occurred in all stations.

In this study, *Pediastrum, Tetraedron, Closterium* were abundantly occurred in Yan Aung Mingalar Lake under temperature range from 26 º - 30 ºC in December 2025; this finding is highly agreeable with the report of Philipose (1967) and Bellinger (2010), who stated that those genera can grow well under the temperature usually ranged from 26.5 º - 29.5º C. It has been stated that some members of green algae can be used as a food supply in many parts of the world.

Temperature range was within 26 º - 30 ºC in all stations in December 2025, during which the taxa abundantly observed were *Pediastrum, Tetraedron, Closterium* were abundantly occurred in all stations. When the temperature was dropped into 26. 3 ºC in station 1 and 2 and 28. 4 º C in station 3 and 4 and 27 ºC in station 5 in August 2025, which no taxa were observed abundantly.

In April 2025, temperature in station 1, 2 and 3 respectively, were 27.6º C. 28. 4ºC in station 4 and 5, at the time the taxa abundantly observed were *Pediastrum, Coleastrum* and *Tetraedron* 1, 2 and 3, whereas no taxa observed abundantly in station 4 and 5. Therefore, temperature appears to have had a moderate influence on the abundance of algae collected in each month. Furthermore, a large amount of green algae *Pediastrum* in lake water is primarily linked to specific environmental conditions, particularly warmer water temperatures and high nutrient levels (eutrophication), often exacerbated by climate change and human activities.

And then, *Pediastrum* species such as *Pediastrum* simplex are often associated with nutrients rich (eutrophic to mesotrophic) freshwater environment. Therefore, a high concentration of *Pediastrum* in a lake often indicates a productive, well-lit and warm environment with ample nutrient availability. (John *et al*, 2002). According to the John *et al*, 2002 and study results, this lake was designated that mesotrophic lake.

Conclusion

According to the result of the present study, it can be concluded that Chlorophyta algae was found in Yan Aung Mingalar Lake. Through studying, some green algae are polluted in lake and other beneficial for irrigation and domestication. Therefore, it is hoped that those nine genera recorded in this work have potential utilization as a food. Some members of algae (e.g. diatoms and euglenoids) and cyanobacteria were also detected in the

course of microscopic observations; indicating that further studies are required to describe the remaining taxa in Yan Aung Mingalar Lake, Thaketa Township. Furthermore, this presentation is made in order to provide knowledge and understanding about microalgae, which are one of the microscopic organisms living in the lake water that cannot be seen with the naked eye.

Acknowledgements

I am greatly thanks to Dr. Myo Min Htun Rector and Dr. Aye Aye Ko. and Dr. Thida Aung Pro-rectors of East Yangon University for their permission to submit this research paper. I would like to express thanks my lovely Dr. Thaw Maw Moe, Professor and Head her kindness, examine and permission and I would like to express thanks my kindly Dr. Khin Cho Cho Oo and Dr. Kyawt Kyawt Khaing, Professors, Department of Botany, East Yangon University, for their suggestion and encouragement.

References

Bellinger (2010), E. G. and Sigee, D.C. (2010). **Freshwater Algae: Identification and use as Bioindicators.** John Wiley & Sons, Ltd. pp. 271.

Carlson, R. E. (1977). **A tropic state index for lakes limnology and Oceanography**. 22:361:69.

Graham, L. E. and Wilcox, L.W. (2000). **Algae.** Wisconsin University Prentice – Hall, Inc. Upper Saddle River, NJ 07458, printed in United States of America.

Hoek, van den. C., Mann, D. G and John, H.M. (1955). **Algae: An Introduction to Phycology**. Cambridge University Press, Cambridge, U.K.

John, D. M., Whitton. B.A and Brook, A.J. (2002). **The Freshwater Algae Flora of the British Isles.** Cambridge University Press.

Kolkwitz, R. and M. Marsson. (1908). **Okologie der pflanzlich saprobien berichte der deutschen botanischen gessellsedaft**. 26: 505 -519.

Philipose, M. T. (1967). **Chrococcales.** Indian Council of Agricultural Research, New Delhi.

(Proschold, T. & Leliaert, F. (2007). **Systematics of the green algae: conflict of classic and modern approaches,** Inc: Unravelling the algae the past, present and future of algal systematics (Ed. by Brodie, J. and Lewis, J.) CRC Press. pp. 123-153.

Prescott, G. W. (1962). **Algae of the Western Great Lake area with an illustrated key to the general of desmids and freshwater diatoms.** M. C. Brown Co. Inc., Dubuque. Iowa Printed in the United States of America.

Smith, G. M. (1950). **Cryptogamic botany algae and fungi**. Vol. I. Mc Graw – Hill Book Company, Inc., New York.

Smith, G. M. (1955**). Cryptogamic botany**. Vol. I. Mc Graw – Hill Book Company, Inc., New York.

Mineralogical and Geochemical Characteristics of Gold Mineralization in Nankwe Area, Yemathin Township

Lal Lawm Sanga[1], Aung Zaw Myint[2]

Abstract

Nankwe is one of the gold deposits located in the northern part of the low-grade metasediments of the Mergui-Mawchi Belt, Central Myanmar. The deposit is characterized by an array of quartz veins hosted in slaty mudstone of the Kogwe Formation, which is slightly weathered and intensively oxidized in places. Primary gold-bearing sulfide quartz veins have a generally segmented structure with brecciated and banded textures. Mineralogically, quartz dominates all mineralized veins, and a variety of textures, including massive, comb, mosaic, sheared, and brecciated quartz, are present. The mineralization is associated with a stockwork vein system. Gold occurs as specks within sulfide-bearing quartz veins. Hydrothermal alteration associated with the mineralization includes chloritization, silicification, sericitization, and pyritization. Sulfide minerals in the ore zone are mainly pyrite, with minor chalcopyrite, sphalerite, and galena. Pyrite is the dominant sulfide mineral, occurring in various morphologies, including porous core with compact rim, euhedral, homogeneous, and compact forms. Sphalerite and chalcopyrite generally occur together, and both show multiple crystal textures, which may indicate emplacement during multiple mineralizing events. XRF trace-element analyses indicate enrichment in base metals, likely Cu, Pb, and Zn, in the ore system, with locally heavy concentrations of Sn and As. These assemblages indicate mineralization under moderate-temperature, sulfur-rich conditions, consistent with a mesozonal to epizonal orogenic gold system.

Keywords: Nankwe, mineralogy, geochemistry, vein texture, hydrothermal alteration.

Introduction

Myanmar is rich in various kinds of natural resources such as tin-tungsten, lead-zinc-silver, nickel-chromite, gold, oil, and gas. Many ore deposits have been developed as world-class in the last decade (Zaw, 2017; Mitchell, 2018). The study area is located in the northern part of the Modi Taung - Nankwe gold district, in Mandalay Region, which is one of the most important gold districts in Myanmar. Geologically, the study area is formed as a segment of the Mergui-Mawchi Belt (MMB) at the western margin of Shan Highland, and to the west is the central lowland. The Mergui Belt was intruded by several granitic rocks of the Central Belt of Myanmar, which extends into peninsular Thailand, and these granites form part of the Western Granite Province of Southeast Asia Tin Belts (Cobbing et al., 1986). The occurrence of the orogenic gold deposits in Myanmar has been recorded in the form of gold-quartz veins at the Tatlet, Phayaung Taung, Nankwe, Modi Taung, Shwegyin, Kyaiktho, and Russell Island (Shwekyun) areas with the Mergui Belt. The main purpose of this study is to present the petrology and geochemical characteristics of the Nankwe gold district.

Regional Tectonic Setting

The tectonic setting of Myanmar has been affected by at least two major Tethyan plate collisions related to the closure of the Palaeo-Tethys and the Neo-Tethys oceans, represented by the Triassic-Early Jurassic Indonesian and Cenozoic Himalayan orogenies, respectively. Geologically, Myanmar can be divided into seven north-south tectonic units. From west to east, these are: (1) Indo-Myanmar Ranges, (2) West Myanmar Block, (3) Mogok Metamorphic Belt, (4) Mergui-Mawchi Belt, (5) Paunglaung Mawchi Zone, (6) Shan Scarps Area, and (7) Shan Plateau (Barber et al, 2017). The Mergui-Mawchi belt hosts high-grade metamorphic rocks and collision-related granitic rocks with late-stage crustal melt-

[1] Lecturer, Department of Geology, West Yangon University
[2] Dr, Professor & Head, Department of Geology, East Yangon University

derived granitic rocks (Searle et al., 2007), and the southern part of the belt is composed of the Carboniferous Mergui Group.

Gold mineralization is recognized at numerous localities throughout the Mogok-Mandalay-Mergui Belt in Myanmar (Bender, 1983; Zaw, 2017). The study area is geotectonically situated in the Mergui-Mawchi Belt (Fig. 1). It is chiefly composed of sedimentary rocks (Mergui Group), late Paleozoic, including quartzite, slate, pebbly graywackes, massive to laminated, locally calcareous mudstones and siltstones interbedded with quartzose sandstones. In the Mogok Metamorphic Belt (MMB), the granites are found in the east of the Sagaing Fault and at the west of the Panlaung-Mawchi Zone, located west of the Shan scarps, which is bordered on the west by schists, gneisses, marbles, and granites intruded by alkaline dykes and granites (Chibber, 1934; Mitchell et al., 2004).

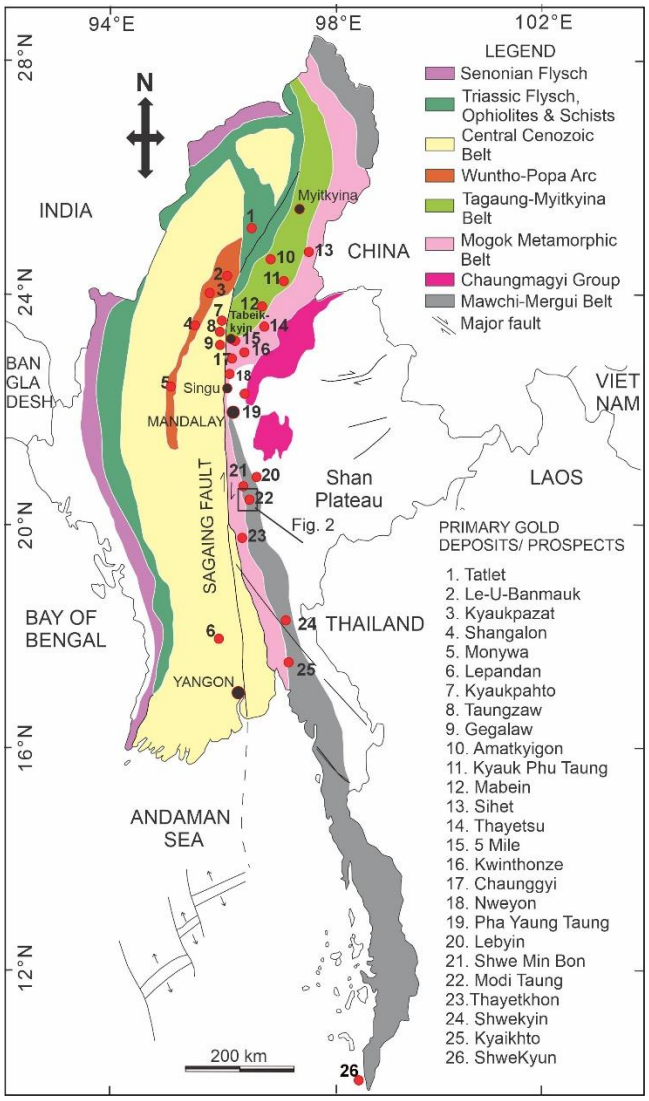

Figure 1. Simplified geological map of Myanmar showing the major gold deposits (Swe et al., 2017)

Deposit Geology of the Study Area

The Nankwe area is the northernmost extension of the Mergui Belt, which is mainly composed of metasedimentary rocks such as slate, slaty mudstone, and sandstone, which is situated in the eastern part of the Mogok Metamorphic Belt. The Mergui-Mawchi Belt is composed of two sedimentary facies associations, massive to bedded shale, sandstone, and

pebbly wackes (Mitchel et al., 2004). In this area, there are two formations, Kogwe mudstone and Poklokkale Pebble Wackestone (Fig. 2). The Kogwe Mudstone mainly consists of massive to laminated and locally calcareous mudstone and siltstone interbedded with quartzose sandstone, which generally dips to the northeast beneath Poklokkale Pebble Wacke. In the lower part, the Kogwe Mudstone includes channel-fill disorganized conglomerates with rafts of mudstones. It passes up transitionally into the Poklokkale Pebbly Wacke. These pebbly quartz wackes and pebbly mudstones or diamictites are interbedded with massive and laminated mudstones and siltstones, and phyllite.

Slate crops out in the east-west part of the study area and along the Nankwe to Natinn car road. Low-grade metamorphism of mudstone, shale, or volcanic ash, and moderately compact, foliated, dark gray on the weathered surface, light gray on fresh color, fairly foliated with cut calcite & quartz veinlets. It is a fine-grained, slaty-textured rock, compacted and metamorphosed mudstone or shale. The constituent minerals are clay, quartz, muscovite, biotite, chlorite, and pyrite, and can also be observed as foliation. Mudstone crops out throughout the whole region of the lease area; the thickness of this unit is unknown in some places. In some cases, the mudstone is well-bedded in nature and ranges from thin to medium and medium to thick bedded nature. Mudstone can also be bleached and occasionally cut by carbonate veins, which broadly occur in the cleavage plane. The mudstone is very fine-grained, predominantly clay minerals 70%, brown to cloudy in PPL, silt-size quartz, calcite 25%, and others 5%. Sometimes tiny flakes of glittering mica and larger grains of feldspar and quartz can be identifed small iron oxide and disseminated grains of pyrite as accessories.

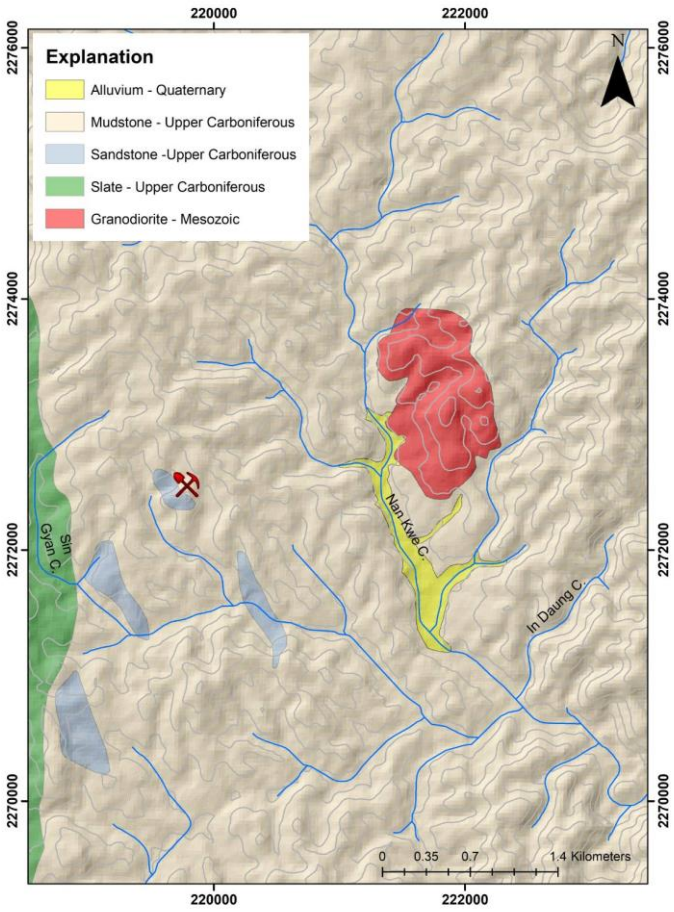

Figure 2. Geological map of Nankwe area (modified after Mitchell et, al. 2004)

Sandstone is also exposed in several regions of the study area, especially in Shwelone Chaung, west and northwest of Nankwe. The sandstone is fine to medium-grained, reddish to yellowish in weathered color, gray in fresh color, thin to medium-bedded and massive, highly silicified, and jointed in some outcrops. The rock is mainly composed of quartz, rock fragments, and feldspar, with a clastic texture. Grains are poorly sorted and very angular, set in a clayey matrix. Quartz is the most common detrital grain, comprising 60 to 75% of total detrital grains. The quartz grains are subangular to subhedral in form, and some grains possess mineral inclusions. Feldspar constitutes 5% to 15% of detrital grains. Plagioclase feldspar displays lamellae twinning in minor amounts; some feldspars show a dusty to cloudy appearance. Mica comprises 1% to 2% of total detrital grains. Muscovite mica displays a variable color range. Rock fragments comprise 4% to 10% as subrounded grains. The iron oxide cement ranges from 10% to 20% of the whole rock volume and is observed as grain coatings on detrital grains, as pore-filling material, and in the alteration of mica grains.

To the west of the gold prospect, there is a pluton, likely granitic, intruded into the mudstone. It occurs not only as a large, massive boulder body but also as highly weathered outcrops along the Nankwe Chaung. Two distinct compositions are recognized: granite has a coarse-grained, porphyritic texture, comprising quartz, plagioclase, alkali feldspar, and biotite; granodiorite consists of quartz, alkali feldspar, plagioclase, and hornblende. The relationship between the mineralization and intrusive rocks is unclear.

Mineralization

The vein-type deposit in the mineralization style of the study area deposit is hosted by deformed, jointed, and brecciated quartz veins interbedded with slate, mudstone, and sandstone. The gold mineralization is associated with quartz veins occurring along the fractures of the host rock. The deposit suggests that mineralization is most likely related to orogeny because a strong compressional and transpressional (shear) environment (Groves et al., 1998) was clearly developed, indicating the strong structural control. Regionally, the study of gold mineralization lies within the shear zone between the Sagaing Fault and the Shan Scarp Fault. The main controlling factor is the regional structure that has a nearly north-south trend and possibly formed by the activity of the Skhanya Taung Fault, causing deformation, shearing, and brecciation in favourable for mineralization. In the field, gold-bearing mineralized veins were observed mostly brecciated and crushed.

Figure 3. Photo showing (a)Veinlets and stringers system of sulfide quartz vein in mudstone, (b) individual vein system of sulfide quartz vein in sandstone

Occurrences of gold-bearing quartz vein systems are primary gold-bearing sulfide quartz veins and secondary auriferous deformed or remobilized quartz veins. Veins occur mostly as veinlets and stringers, and stockwork veins (Fig. 3a). The vein thickness ranges from 0.5 to 11 cm. Veins are hosted in sandstone. Mostly, veins are steep dipping 60°-75° and vein direction range NNE-SSW within host rocks (Fig. 3b). Secondary auriferous deformed/ remobilized quartz veins are commonly developed near the E-W post-mineralization

structures, and they are much brecciated, deformed in the oxidized zone. The thickness of veins is from 0.5cm to 4cm. Visible gold associated with secondarily formed hematite, Fe-hydroxides are rich in deformed quartz veins filling in micro fractures and at the crest of the vein and brecciated quartzite zone.

Quartz Vein Textures

The texture has been grouped as primary, recrystallization, and replacement to aid in the interpretation of their origin and environment of formation. Primary growth textures represent initial open-space vein fill. Recrystallization textures reflect the transformation of amorphous silica or chalcedony to quartz. Replacement textures represent partial or complete pseudomorphs of other minerals by silica minerals within veins. The primary gold-bearing sulfide quartz veins in the study area are commonly massive, brecciated and laminated/banded textures (Fig.4a-e). They are composed predominantly of reddish-brown to milky whitish quartz. Auriferous deformed quartz veins developed in a brecciated and oxidized zone. Vein internal texture of crystals is irregular in form, containing many micro-fractures/crack in, which are filled with secondary oxidized minerals. Quartz textures are excellent indicators of the nature and intensity of deformation prevailing during vein formation (Jébrak,1992; Vearncombe,1993; Bouchot et al.,1994). Mineralogically, quartz dominates in all the mineralized veins and commonly displays multiple growth stages and a variety of textures, such as comb quartz, recrystallized quartz (mosaic texture quartz), crushed and fractured characteristics of quartz (sheared quartz), and mechanical breakdown

of quartz (Fig. 5f-h).

Figure 4. Photo showing (a) Massive quartz vein, (b) oxidized quartz vein, (c) a sample of quartz vein, (d) photomicrograph of mineralized quartz vein consisting of quartz and pyrite under XPL.

Hydrothermal Alteration

In the field, the mineralized vein system is bordered by the zones of alteration with variable intensity and thickness. The variation in alteration styles has been interpreted as a direct reflection of the depth of deposit formation (Groves, 1998). At the deposit scale, distribution and intensity of wall-rock alteration are largely controlled by composition and competence of

the host rocks and their associated structures. Alterations are commonly associated with the mineralized zone, which may range from simple recrystallization to addition, removal, or rearrangement of chemical compounds. It may take place in advance of the emplacement of the ore minerals.

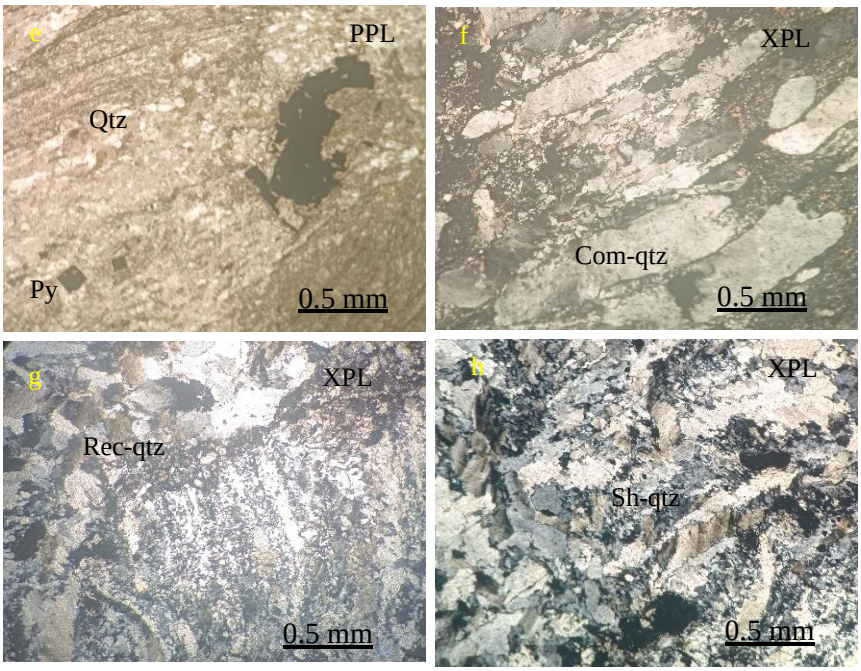

Figure 5. Photomicrograph of mineralized quartz vein consisting of quartz and pyrite under PPL. Photomicrograph showing (f) Comb quartz texture, (g) recrystallized quartz texture, (h) sheared quartz texture in quartz vein between XN.

Silicification represents one of the dominant hydrothermal alteration styles observed within the study area and plays a critical role in the development of gold mineralization zones. This alteration process involves the replacement of primary silicate minerals by silica, principally in the form of microcrystalline quartz, chalcedony, and finely intergrown silica phases. It mainly occurs as the open space-filling in vugs, veinlets and replacing along the fractures (Figure 6a, b). Under the microscope, quartz grains are found as aggregates with interlocking crystalline mosaic in various shapes, strongly deformed rock, and observed as granulated grains with suture contact. Quartz in veinlets is fine-grained and a chalcedonic variety; pyrite and chalcopyrite are associated with the silicified quartz vein and quartz. This alteration style is commonly associated with gold precipitation and, therefore, serves as a key exploration and genetic indicator. In the field, Silicified rocks typically exhibit quartz vein stockworks, breccia textures, and vuggy silica zones formed by dissolution of unstable minerals and subsequent silica deposition. Silicification zone is characterized by an increase of quartz, silica, and the abundance of quartz, calcite, and illite. The groundmass is strongly silicified. Silica may be introduced from the hydrothermal solutions, and it's often a good guide to ore (Evans, 1993). Gold commonly occurs within or adjacent to these silicified domains, either disseminated in fine sulfide minerals or associated with quartz-sulfide veinlets.

Chlorite is interpreted to be a product of hydrothermal alteration. It may alter from the mafic minerals (biotite). The most common alteration product of sturdy area and can be found in the margin of quartz vein (Fig. 6c). Chloritization is widespread not only on the fracture but also in stringers, veinlets, quartz veins, and surrounding wall rocks. Chlorite may be present alone or with quartz as a very simple assemblage. The development of secondary chlorite may

result from the alteration of mafic minerals present in country rocks or from the introduction of Mg and Fe; of course, both processes can occur together (Evans, 1993). Under microscopic study, chlorite can be observed as intergranular fibrous green minerals among the quartz grains in a silicified quartz vein, recognized by its optical properties of pale green in color, low relief, parallel extension, and low to moderate birefringence. Opaque minerals (mostly pyrite) and chlorites, silicification and chloritization occur along the fracture of quartz in silicified quartz veins.

In this sericitization is interpreted to be a product of hydrothermal alteration. It represents a visual indication of invisible mineralization. Microscopic studies suggest that it is also a common alteration occurred in the mineralized zone and is often associated with silicification. The quartz-sericite assemblages are very common near the fluid source. Under the microscope, sericite can be identified by its fibrous form, colorless, high relief, second-order interference bright colors, and parallel extension between X.N. Intense sericitization process occurs together with the late phase of silicification. Which formed intergranular space and fracture of crushed quartz grains (Fig. 6d).

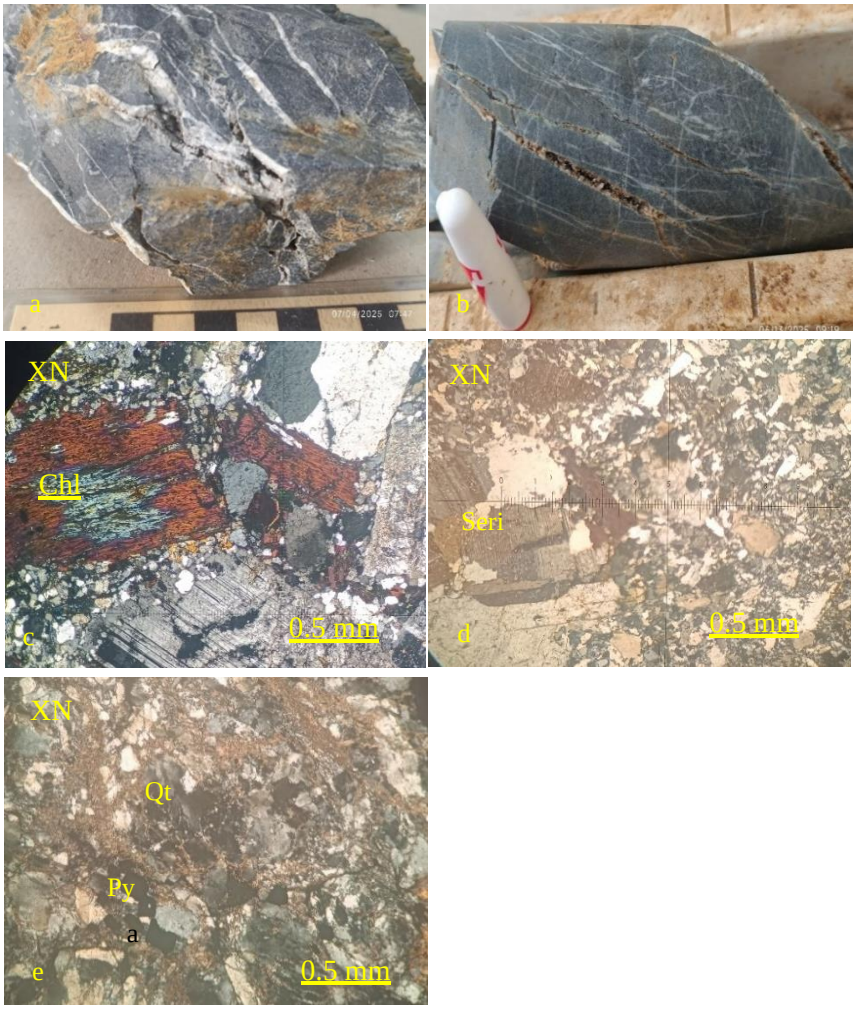

Figure 6. (a) Vuggy quartz represents one of the silicification (b) Drusy and com textures of slaty mudstone. Drill hole ZDH 38, 116-meter depth, (c) Biotite partially altered by chlorite with berlin blue interference colors in granodiorite, (d) Partial sericitization (Seri) of crushed plagioclase in sandstone, (e) Pyritization associated with silicification (Chl- Chlorite, Qtz-Quartz, Py-Pyrite, XN- cross-polarized light)

Pyritization is a widespread hydrothermal alteration process characterized by the replacement of primary poor sulfide minerals by the introduction of sulfur-rich fluids. This process affects such minerals as biotite, hornblende, feldspar, and carbonate, where host minerals react with dissolved sulfur in the fluids. In gold mineralization systems, pyritization plays a main role as pyrite acts as a principles host of invisible or refractory gold. The abundance and distribution of pyrite are closely related to zones of high gold grade in many hydrothermal deposits (Pirajno, 2009). Pyritization may also be formed at the same time as silicification. It is represented by the deposition of pyrite. The ore mineralization is followed by a crushed margin of deformed grains. Pyrite is a common alteration product around the sulfide ore bodies. Pyrite formed where sulfur is added to a host rock containing iron or ferro-magnesian minerals (Fig. 6e). Oxidation of pyrite produces a reddish-brown color in weather-zoned pyrite, which breaks down to form iron oxides such as goethite and hematite, producing gossan zones that are important indicators for subsurface gold mineralization (Myo Kyaw Hlaing et al., 2021). It is well developed in the host rocks, and it is especially associated with chloritization in some places.

Ore Mineralogy

The ore minerals are examined by a transmitted polarizing microscope. Form of the ore minerals observed as irregular patches, disseminated grains, small veinlets, and pods in the veins. The main sulfides in the ores comprise pyrite, sphalerite, chalcopyrite, galena, and quartz-dominated gangue minerals. Gold occurs in fractures of quartz veins within pyrite and between the crystal boundaries of pyrite (Fig. 7c). Pyrite is the dominant sulfide mineral, having a yellowish color, a metallic luster, and showing different morphologies. These grains are also observed in the mineralized veins. The texture of pyrite in this deposit is a porous core, compact rim, euhedral, homogeneous, and compact pyrite. These grains are fine to coarse in grain size, and these coarse grains are again connected to form bands of pyrite (Fig. 7b). Sphalerite is not as abundant as pyrite. It is fractured and replaced by the later sulfides. Sphalerite and chalcopyrite generally occur together, and both show multiple crystal textures, which may indicate that they were emplaced in multiple mineralizing events. Quartz and calcite are the dominant gangue minerals, as would be expected in a vein-type deposit. Chalcopyrite mainly occurs in the brecciated and silicified rocks. Chalcopyrite has brass yellow and is closely associated with sphalerite and pyrite (Fig.7a). It appears somewhat earlier than or synchronously with sphalerite. Based on their textures, which may rarely fill a pore of pyrite, including anhedral to subhedral zoned pyrite, which consists of a porous core and a compact rim. The grain size of this is approximately 3–20 μm thick. Chalcopyrite has brass yellow and is closely associated with sphalerite and pyrite (Fig.7a). It appears somewhat earlier than or synchronously with sphalerite. Based on their textures, which may rarely fill a pore of pyrite, including anhedral to subhedral zoned pyrite, which consists of a porous core and a compact rim. The grain size of this is approximately 3–20 μm thick.

Vein Geochemistry

XRF trace-element analyses indicate that the studied samples are characterized by significant enrichment in base metals, likely Cu (121-792 ppm), Pb (4-769), and Zn (19-820), with locally heavy concentrations of Sn and As. The homogenous elemental associations are typical of hydrothermal systems, concentration of Cu–Pb–Zn is interpreted to reflect the presence of sulfide mineral assemblages, which are dominated by chalcopyrite, galena, and sphalerite, these are commonly associated with hydrothermal quartz veins and these metals are transported and precipitated from mineralizing fluids within quartz vein networks and their adjacent alteration halos (Mitchell 2018). These assemblages of base metals indicate mineralization under moderate temperature and sulfur-rich conditions, consistent with

mesothermal to epithermal hydrothermal environments. The observed variation in base-metal concentrations localized structural controls on fluid flow, resulting in heterogeneous sulfide deposition within fractures and shear-related vein systems. The presence of base metals together with arsenic is considered a significant indicator of gold-bearing hydrothermal systems, as a pathfinder element for gold in orogenic and structurally controlled gold deposits.

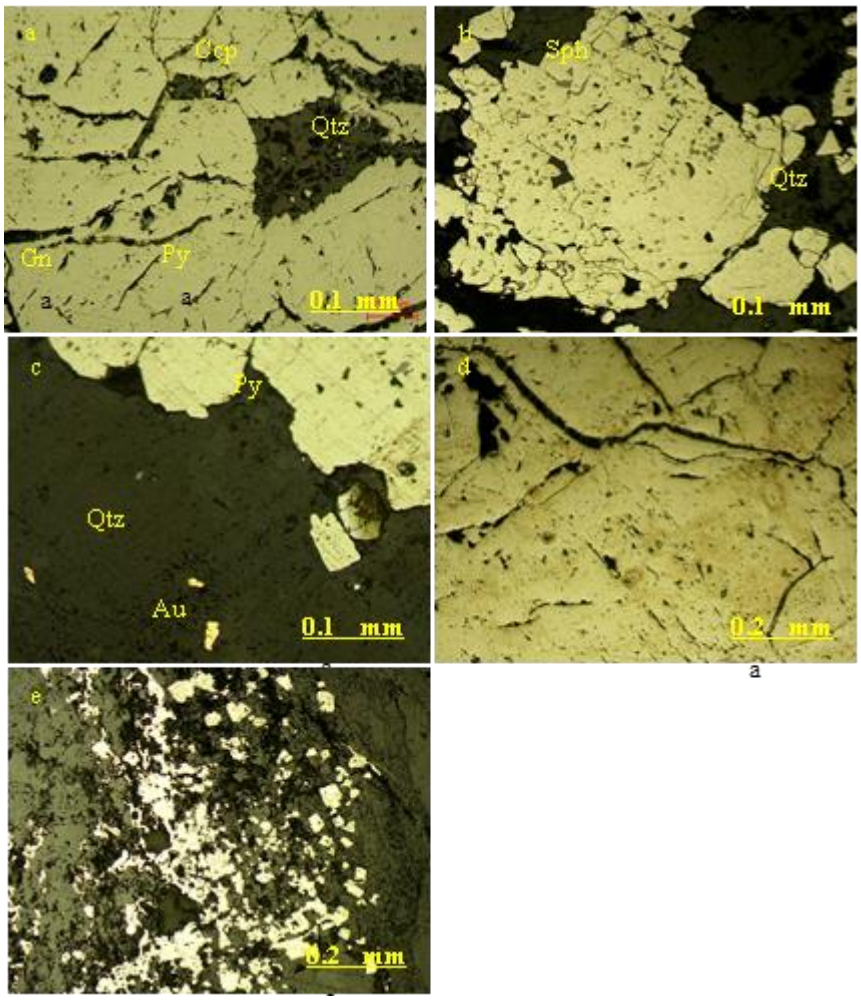

Figure 7. Photomicrograph showing the ore mineral assemblages: (a) chalcopyrite and galena in pyrite and within the fracture of pyrite, (b) chalcopyrite and sphalerite are filled in voids of pyrite, (c) photomicrograph of native gold in quartz, (d) triangular-pitted galena replaces pyrite, (e) Coalescent and banded framboidal pyrite in slate.

Although golds were not directly determined by XRF analysis, the observed base-metal with arsenic association suggests that the mineralizing fluids were capable of transporting gold. This signature supports the interpretation that the studied mineralization formed within a structurally focused hydrothermal system related to regional tectonic activity. Frequency histogram analysis of Cu, Pb, Zn, and Ag reveals strongly positively altered distributions characterized by low background concentrations and a limited number of high-value outliers (Fig. 8). This pattern is typical of hydrothermal mineralization, where metals are concentrated within structurally controlled quartz–sulfide veins rather than being uniformly distributed in the host rocks. Copper, lead, and zinc enrichment is interpreted to reflect localized precipitation of chalcopyrite, galena, and sphalerite, respectively, whereas silver occurs as a minor constituent associated with base-metal sulfides. Gold concentrations determined by XRF are predominantly below detection limits and do not display a meaningful statistical

distribution; the analytical limitations of XRF for Au analysis, rather than the absence of gold mineralization. XRF trace-element data from the study area reveal systematic enrichment in base metals, where metals are concentrated within discrete structural features distributed throughout the host rocks. The presence of high-value tails in the Cu, Pb, and Zn distributions indicates localized zones of sulfide mineralization within quartz vein systems.

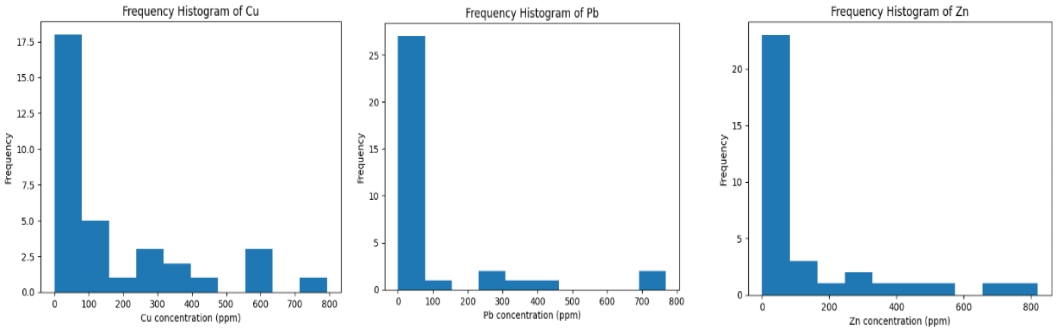

Figure 8. Frequency histogram of copper, lead, and zinc

Granite Geochemistry

Whole rock XRF data of the igneous rocks indicate that they are siliceous (SiO_2 = 64.2 to 74.9 wt.%), confirming their felsic nature. The CaO contents in the granodiorite (4.29 to 4.74 wt.%) are higher than those of granite (0.17 to 0.25 wt.%). The total alkali contents (Na_2O + K_2O) vary between 6.7 and 10.6 wt.%, and they fall in granite and granodiorite fields on the Total Alkali–Silica (TAS) diagram (Fig.9a). Based on the geochemical data, (Fig.9b), the plutonic rocks of the study area belong to the peraluminous and metaluminous characters.

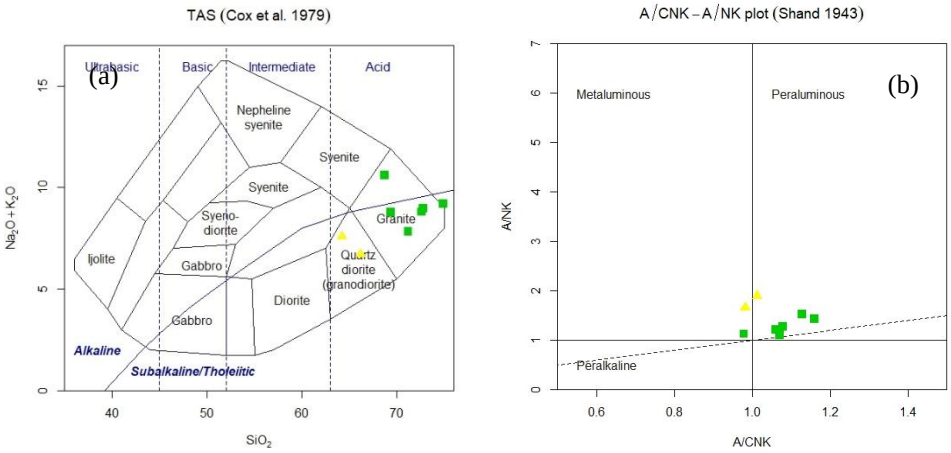

Figure 10. (a) TAS diagram (Cox et al., 1979) showing the granitoid composition, (b) A/CNK Vs. A/NK diagram (Shand, 1943) showing the metaluminous and peraluminous nature of granites

Discussion

The mineralization style of the study area is hosted by deformed, jointed, and brecciated quartz veins interbedded with slate, mudstone, and sandstone. Gold mineralization is all over hosted within quartz veins developed along shear zones and fracture networks, reflecting strong structural control on fluid resettlement and ore deposition. The quartz veins commonly display massive, laminated, brittle-ductile, comb texture and locally brecciated textures, indicating multiple stages of fracturing and vein associated with episodic fluid flow during progressive deformation. These textures indicate vein formation within a transitional deformation regime typical of mesozonal orogenic gold systems. These vein textures are

typical of orogenic gold deposits formed at mid-crustal depths under greenschist to lower amphibolite facies conditions (Groves et al., 1998; Goldfarb et al., 2005). Brecciation is an excellent precursor to mineralization, as circulating hydrothermal fluids will readily interact with the fractured rocks. Thus, breccias are associated with numerous types of ore deposits both in surface and subsurface environments (Jebrak, 1997).

Hydrothermal alteration associated with the quartz veins is dominated and forming well-developed alteration halos within the wall rocks. Silicification represents silica addition from hydrothermal fluids and provides vein development and sulfide precipitation. Sericitization is the replacement of feldspar and mafic minerals by fine-grained white mica, indicates fluid conditions within shear zones. Pyritization is widespread and commonly occurs within quartz veins and in adjacent altered wall rocks, reflecting sulfur-bearing fluids and iron-bearing host minerals. These alteration assemblages are characteristic of orogenic gold systems and are closely linked to gold precipitation through changes in fluid chemistry and redox conditions (Groves et al., 1998; Goldfarb et al., 2005).

Major-element oxides indicate strong hydrothermal alteration associated with gold mineralization in the Nankwe area. Locally very high SiO_2 contents (up to ~88 wt.%), and quartz vein development within structurally controlled shear zones. Although orogenic gold deposits are typically gold-dominant, many systems—particularly those formed at mesozonal levels—exhibit significant base-metal enrichment due to prolonged or multi-stage hydrothermal activity and evolving fluid compositions (Zaw et al., 2014). Structural controls act the part of fundamental role in the localization of mineralization at Nankwe. Quartz veins and alteration zones are spatially associated with shear zones, faults, and fracture networks that acted as high-permeability pathways for hydrothermal fluids. But rather reflects fluid evolution and multi-stage mineralization within a brittle–ductile deformation regime. Repeated reactivation of these structures promoted cyclic fracturing, mineral precipitation and leading to the development of localized high-grade zones. Such structurally controlled mineralization is a defining feature of orogenic gold systems worldwide and is well documented in gold deposits throughout Myanmar and Southeast Asia (Mitchell, 2018; Zaw et al., 2017). The addition of structural analysis, alteration mineralogy, vein textures, and base-metal geochemistry therefore strongly supports that the study deposit area represents an orogenic (mesothermal) gold system formed during regional tectonic evolution.

The geochemical characteristics of granitic rocks display high K calc-alkaline and calc-alkaline magma series, as evidenced by moderate to high SiO_2 contents, enrichment in total alkalis, and relatively low MgO and TiO_2 concentrations. Such features are diagnostic of magmas generated in subduction-related tectonic environments. Since these granitic rocks are spatially associated with the gold occurrences, they are likely related to the gold mineralization. However, more detailed evidence is still required to prove the genetic relationship between granitic rocks and gold mineralization in this area.

Conclusion

The mineralization style of the study area is vein-type, hosted by jointed and brecciated slaty mudstone of the Mergui Group. These mineralized rocks are distributed along NS-trending faults, which were related to the introduction of hydrothermal fluids that caused alteration and mineralization at Nankwe. Gold-bearing quartz veins and veinlets fill NW-SE-trending dilational fault zones. Gold-bearing mineralized veins are mostly brecciated and crushed. Quartz and calcite are the dominant gangue minerals, as expected in a vein-type deposit. Carbonate accounts for less than 15% of vein minerals, consistent with the orogenic gold deposit model. The observed Cu–Pb–Zn geochemical association is interpreted as reflecting the presence of hydrothermal sulfide assemblages. These signatures, defined by base-metal

enrichment and associated Ag, are characteristic of orogenic gold systems within the Mergui-Mawchi Belt.

Acknowledgement

The authors would like to express our sincere thanks to Dr. Myo Min Tun, Rector of East Yangon University, for his permission to do the present research.

References

Bender, F. 1983. *Geology of Burma*, Borntraeger, Berlin, 293 pp.

Baber, A.J., Zaw, K. and Crow, M.J. 2017. The pre-Cenozoic tectonic evolution of Myanmar. *Geological Society (London) Memoirs*., 48, 687-712.

Chhibber, H. L. 1934. *The mineral Resources of Burma*. London: Macmillan.

Cobbing et al. 1992. The granites of the South-East Asian tin belt. Overseas Memoir 10, *British Geological Survey*, London, pp. 369

Groves, D.I, Goldfarb, R. J., and Robert, F. 1998. Orogenic Gold Deposits: a Proposed Classification in the Context of Their Crustal Distribution and Relationship to Other Gold Deposit Types. *Ore Geology. Rev* 13, 7-27.

Kyaw Lin Zaw, 2017. *Geology, Geochemistry and Ore Genesis of Modi-Momi Gold Deposit, Yemethin Township, Mandalay Region.* P.hD Thesis. Department of Geology, University of Yangon. (Unpublished)

Mitchell, A.H.G., 1977. Tectonic settings for emplacement of Southeast Asian tin granites. *Geological Society of Malaysia* Bulletin 9, 123–140.

Mitchell, A.H.G., Ausa, C.A., Deiparine, L., Tin Hlaing, Nyunt Htay and Aung Khine. (2004). The Modi Taung-Nankwe gold district, Slate Belt, Central Myanmar, mesothermal veins in the Mesozoic orogen. *Journal of Asian Earth Science*, 23, 321-341.

Mitchell, A.H.G., 2018. Geological Belts, Plate Boundaries and Mineral Deposits in Myanmar. *Amsterdam: p. 509.*

Pettijohn, F. J., 1975. *Sedimentary rocks*, 3rd edition. New York: Harper and Row.

Thein, M., 1973. A preliminary synthesis of the geological evolution of Burma with reference to the tectonic development of Southern Asia. *Geological Society of Malaysia* Bulletin 6, 87–1166.

Rollinson, H. R., 1993. *Using Geochemical Data: Evaluation, Presentation, Interpretation, Geochemistry Series, Longman.*

Searle et al., 2007. Tectonic evolution of the Mogok Metamorphic Belt, Myanmar, constrained by U-Th-Pb dating of Mogok Metamorphic and Magmatic Rocks.

Sone, S, P., Yonezu, K., Imai, A., Watanabe, K., Tindell, T & Sanematsu, K. 2022. Geological, mineralogical and ore fluid characteristics of the Tagun-Khin-dan gold mineralization in Mogok-Mandalay-Mergui Belt, Central Myanmar. *Resource Geology, 72(1), e12298*.

United Nations, 1978c. Geology and exploration geochemistry of the Shan Scarps area, east of Kyaukse, Thazi and Tatkon, central Burma. Technical Report UN/BUR/72/002, No. 3. United Nations Development Programme, New York.

Zaw, K. 2019. "Tectonic and Metallogenic Significance of Orogenic Gold Deposits in mainland SE Asia" in *The Society of Resource Geology Annual Meeting*, Tokyo, Japan, June 26-28.

Determining rock sequences and petrogenesis of the Volcanic Rocks of Mt. Popa, central Myanmar, using elemental contour maps

Yin Yin Oo[1], Aung Zaw Myint[2], Nyi Nyi Aung[3], Day Wa Aung[4]

Abstract

In the Mount Popa area, two distinct sequences of volcanic rocks occur overlying the Irrawaddy Formation. Mt. Popa is situated on a line of widely-spaced, calc-alkaline volcanic centers in the central lowlands of Myanmar. Older volcanic rocks consist of white tuff, Myage Taung andesite, rhyolite, and rhyodacite whereas younger volcanic sequence comprises andesite bombs, augite andesite, and olivine basalt. Geochemical data indicates these areas have high SiO_2 values (75-90 wt%). This is characteristic of felsic rocks such as rhyodacite and rhyolite, which are typically more viscous and associated with explosive eruptions. The outer, wider regions have lower SiO_2 content (45-60 wt%). These are characteristic of mafic to intermediate rocks like basalt and andesite, which are typically more fluid and linked to lava flows. High MgO (4-6 wt%) is characteristic of mafic (basaltic) rocks, which originate from relatively primitive, mantle-derived magmas. The outer regions have lower MgO content (0-3 wt%). These areas generally correlate with more evolved, felsic to intermediate rocks like andesites and rhyolites, which are formed by the fractional crystallization of magma at shallower crustal levels.The spatial distribution of major oxides (SiO_2, MgO) and trace element ratios (Ba/Yb, Sr/Y ,Th/Nd, Nb/Yb, and Zr/Hf) confirms a high-K calc-alkaline magmatic evolution typical of an active continental volcanic arc. The highlight an adakitic affinity in the central Quaternary volcanics (Sr/Y≥40;) suggesting deep-seated melting under high-pressure conditions with residual garnet. This signature indicates significant potential for porphyry Cu-Au mineralization. Spatial variations in Th/Nd and Nb/Yb ratios differentiate a highly crustally-contaminated Miocene basement from more primitive, mantle-derived Quaternary lavas. Furthermore, the enrichment in Ba/Yb and underscores the dominant role of slab-derived fluids from the subducting Indian Plate in metasomatizing the mantle wedge. The presence of anomalous Nb/Y suggests complex mantle dynamics, likely involving asthenospheric upwelling through a potential slab window or tear.

Keywords: Mount Popa, Volcanic rocks, Sequence, Primitive mantle, Adakitic affinity

Introduction

The Mount Popa area under the present investigation is situated in the Central Myanmar Basin and is underlain by various orderly succession of Cenozoic sedimentary strata and some igneous and metamorphic rocks which is possibly the older basement of Central Myanmar Basin. It is noteworthy that the volcanics of the Mount Popa area are located on the central volcanic line which is tectonically known as the volcanic arc, passing through the Wuntho massif, Monywa volcanic, and Mount Popa areas from north to south. Throughout the Pliocene time, the fluvial sedimentation of the Irrawaddy Formation took place in the Central Myanmar Basin with intermittent volcanism occurring in the Mount Popa area and most of the pyroclastic rocks are interbedded with a fluvial deposit of the upper Irrawaddy Formation.

The volcanic area of Mount Popa was first studied by Chhibber, who described old volcanic rocks, as basement rocks that interbedded with the sediments of the Irrawaddy Formation and young volcanic rocks composed of andesitic, and pyroclastic flows forming a composite cone of the Mount Popa (1518 m above sea-level). The old volcanic rocks are placed in the Upper Pliocene and young volcanic rocks are occupied during the Pleistocene to Holocene. Young volcanic rocks mainly covered an area of 153 square km in the studied

[1]Lecturer, Department of Geology, East Yangon University
[2] Professor and Head, Department of Geology, East Yangon University
[3] Part-time Demonstrator, Department of Geology, East Yangon University
[4] Part-time Professor, Department of Geology, University of Yangon

area, comprising a steep-sided, slope angle of about 25°-30°, forming composite cone-shape topography rising 1150 m above the surrounding plain. The composite cone, covering approximately 90 square km of moderately rugged terrain, consists of basaltic andesite and basalt flows, that form coarse porphyritic rocks and scoria.

Geological Background

Regional Geology

Myanmar is divided tectonically and topographically in to three major areas, the Indoburma Hill Ranges, the Central Lowlands, and the Eastern Highlands (Fig. 1).

Igneous rocks ranging in age from Lower Jurassic to Pleistocene or early Recent occur sporadically in a 1500 km long 'volcanic arc' throughout the Central Lowlands (Chhibber 1934). A southern extension includes the recently- active volcanoes of Narcondam and Barren Islands in the Andaman Sea. Most volcanic rocks are of post- Oligocene age. The arc concides with an axis within the Central Lowlands sedimentary basin, dividing it into Western and Eastern Troughs. Both troughs contain sequences of deformed shallow- marine and fluviatile sediments, up to 8000 m thick, which reflect a gradual infilling of the basin and southward migration of the Irrawaddy delta during the Tertiary Era (Aung Kin & Kyaw Win. 1968,1969).

The Indoburma Ranges consist of intensely- deformed Upper Cretaceous to Eocene flysch, with associated ophiolitic rocks and cherts. The area is divided into blocks by a series of eastward- dipping thrusts. Within each block the succession youngers to the E, although overall the rocks become younger to the W in a manner characteristic of plate- margin accretion (Mitchell & Mckerrow 1975).

The Eastern Highlands craton, which extends east- wards into Thailand and southwards into Tenasserim and the Malay peninsula, is separated from the Eastern Trough by the major strike-slip Sagaing- Namyin Fault System. Tin and tungsten-bearing granitic batholiths of Upper Cretaceous to Eocene age occur in a 50 km-wide belt along the W of the craton.

The generation of these tectonic units is related to several episodes of plate convergence since the mid- Jurassic, culminating during the Tertiary with westward movement of thecontinental China Plate relative to oceanic crust of the Indian plate. The present northward movement of the India plate relative to the china plate is reflected by dextral strike- slip displacement of up to 450 km on the Sagaing- Namyin Fault since the early Miocene (Mitchell & Mckerrow 1975; Mitchell 1981; Curray et al (1979, 1980).

Geology of Mt. Popa

Mt. Popa segment of the Wuntho-Popa Arc has two distinct volcanic sequences. The younger Quaternary volcanic sequence is characterized by andesite bombs, augite andesite, olivine basalt, and the older volcanic sequence of the Miocene age (tuff, andesite, rhyolite, rhyodacite). A petrographic study indicates that the older volcanic sequence comprises rhyodacite, rhyolite, Myage Taung andesite, and tuff and the younger volcanic sequence consists of olivine basalt, augite andesite, andesite bombs.

Older Volcanic Sequence

Rhyodacite

It is well exposed in the north eastern of Wetkyikan Village. The rock is light grey in color and contains phenocryst minerals (Fig. 4a).

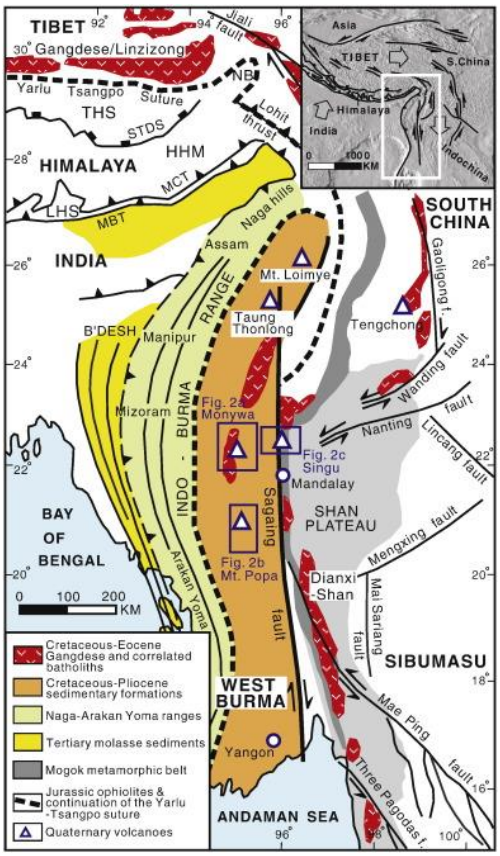

Figure (1) Regional geological map of Popa area and environs
(Mitchell and McKerrow, 1975)

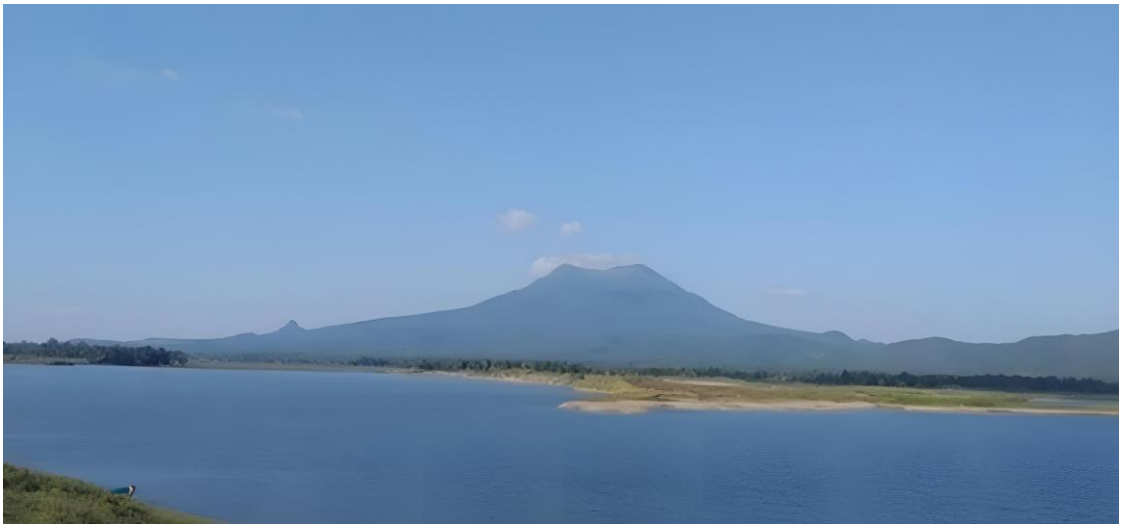

Figure (2) The composite cone of the Mount Popa volcano rises majestically above the surrounding ground (Looking North).

Silicified lavas

This unit is mainly characterized by the rhyolite that occupies the isolated Taungnauk hill, situated in northeast of Kyaukpadaung. Rhyolite is white, grey, glassy texture with small

vesicles (Fig. 4b).

Latite flows

It is locally termed as Myage Taung andesite, exposed at or close to the southern flank of Mount Popa cone and extends to the south of the Shawdaw village in the vicinity of Myage Taung (Fig. 4c).

Ignimbrite sheet (Sebauk white tuff)

This unit mainly consists of tuff that is well exposed near the Sebauk village. To the north and northeast of the Sebauk, the tuff is white, friable, and presents a chalky appearance with course texture (Fig. 4d).

Younger Volcanic Sequence

Basalt flows (olivine basalt)

It is located on the northwestern slope of Mt. Popa. The rock is dark grey but oxidized parts shows purplish colour. This unit contains numerous phenocrysts of dull brown hornblende, greenish augite and olivine grains (Fig. 4e).

Basalt, Basaltic andesite & Pyroclastic cone

It is exposed on the southern and eastern flanks of the Mount Popa cone. These exposures are in-situ flow layers overlying the pyroclastic beds and are well exposed at the stream section (Fig. 4f, 4g).

Lahar deposits

This rock unit is highly distributed around the Kyauktaga- Legyi car road. This pyroclastic flow deposit is generally grey and unconsolidated consists of bombs, blocks, lapilli, ash, and aggregation of pumices, and scorias are also observed in the unit (Fig. 4h, 4i).

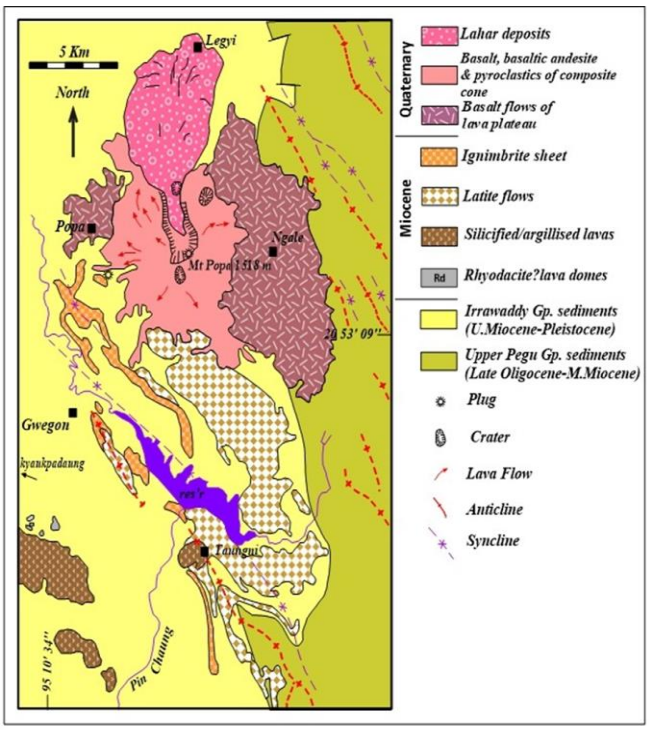

Figure (3) Geological map of the Mt. Popa area

(Modified after Stephenson and Marshall, 1984)

Materials and Methods

A total of forty-five representative samples from the study area were collected for the major elements, and nineteen samples for the trace elements in geochemical studies. Major and trace elements of volcanic rocks were determined by an XRF (X-ray Fluorescence). A total of nineteen representative samples from the study area were collected, and trace elements of volcanic rocks were determined by an XRF (X-ray Fluorescence) and ICPMS. To interpret the determining of volcanic sequences and petrogenesis of the study area, elemental contour maps were illustrated by using Arcgis Pro software.

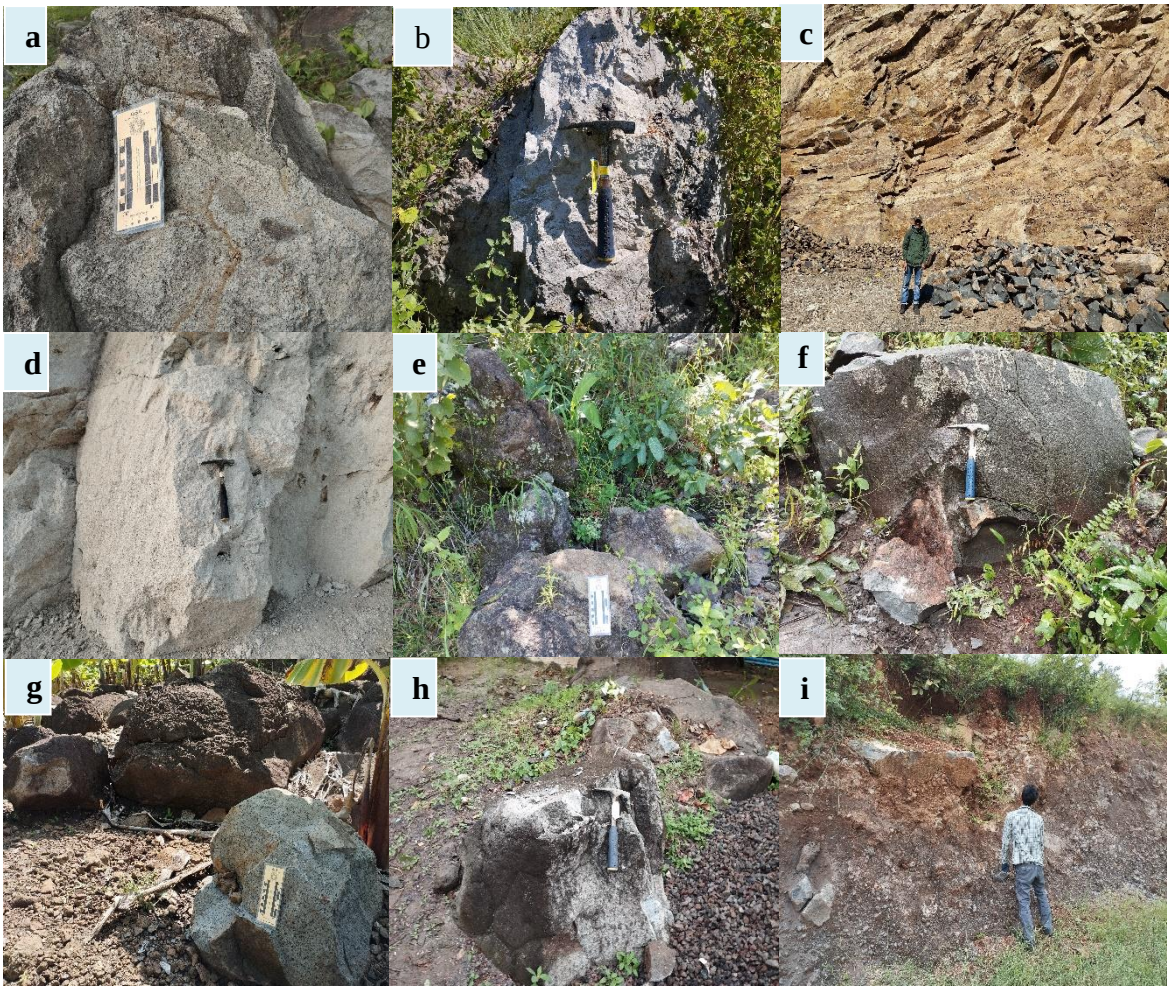

Figure (4) Field photographs showing the (a) flow structure of rhyodacite found in the north of the Wetgyigan village, (b) rhyolite found at the Taungnauk Taung (c) highly jointed andesite found in the quarry at the eastern part of the Kyaukpadaung – Letpanbya car road, (d) layers of tuff deposit near the Sebauk Stream, (e) blocky and fragment of the olivine basalts are also found near the Taungbaw village, (f-g) blocky nature of basaltic andesite at the top of Mt. Popa, (h-i) andesite blocks occurred on the Kyaukpadaung- Myingyan car road.

Results

Major Element and Trace Element Contour Maps

Found closer to the central and southern parts, these areas have high SiO_2 values (75-90 wt%), indicating the characteristics of felsic rocks (Fig. 5a). The outer, wider regions have

lower SiO_2 content (45-60 wt%), revealing the existence of mafic to intermediate rocks (Fig.5a). Near the center of the area, around the volcanic cone, these areas show high MgO values (4-6 wt%), showing the occurrence of mafic (ferromagnesium) rocks such as basalt. The outer regions have lower MgO contents (0-3 wt%). These areas generally correlate with more evolved, felsic to intermediate rocks (Fig. 5b) such as rhyodacite, rhyolite and andesite.

The variation in Yb values in volcanic rocks suggests different degrees of partial melting or crustal contamination in the magma source over time (Fig. 5c). The colored contours show that the concentration of Yb (in parts per million, ppm) generally increases towards the south-central part of the mapped area, reaching values of 2.4–2.6 ppm. Lower values (1–1.2 ppm) are found in the northern and western regions. The contours of strontium (Sr) values range from a lowest of 100–200 ppm to a highest of 900–1000 ppm. The Sr concentrations are elevated in the northern and central regions, near and around Mount Popa, where it is depleted significantly towards the southern boundary of the map area (Fig.5d).

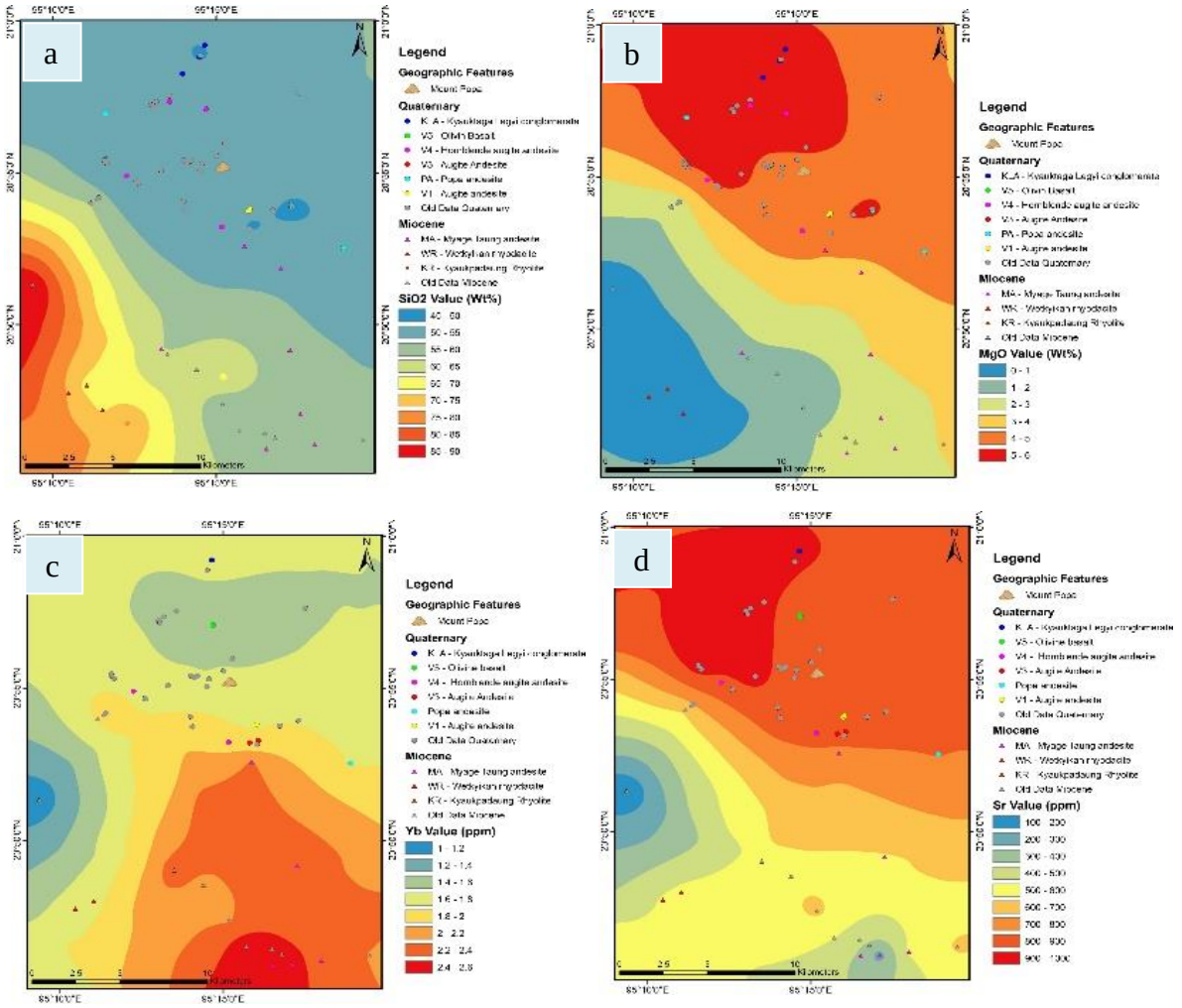

Figure (5) Elemental contour maps of major elements and trace elements (a) SiO_2, (b) MgO, (c) Yb, (d) Sr in the volcanic rocks.

Element Ratio Contour Map of Volcanic Rocks

The highest Th/Nd ratios (0.8–0.9 ppm) are concentrated in the southwestern portion of the map. High ratios typically indicate significant contamination or interaction with the continental crust, as the continental crust is generally enriched in Th relative to the mantle source. These areas correlate strongly with the older, Miocene-age units like the Kyaukpadaung rhyolite (KR) and Wetkyikan rhyodacite (WR). The lowest Th/Nd ratios (0.2–0.4 ppm) are located in the northern portion of the mapped area, specifically around the main Mount Popa edifice and associated with Quaternary units such as olivine basalt and andesites (Fig. 6a).

The Ba/Yb ratios can also differentiate the younger volcanic sequence from the older ones. Red and orange areas indicate high concentrations of Barium (Ba) relative to Yttrium (Yb) (Fig. 6b). Indicate high concentrations of Barium (Ba) relative to Yttrium (Yb). In arc volcanism, a high Ba/Yb ratio is a key indicator of enrichment by slab-derived fluids and/or sediments that have chemically modified the mantle source from the subducting Indian Plate beneath the Eurasian Plate.

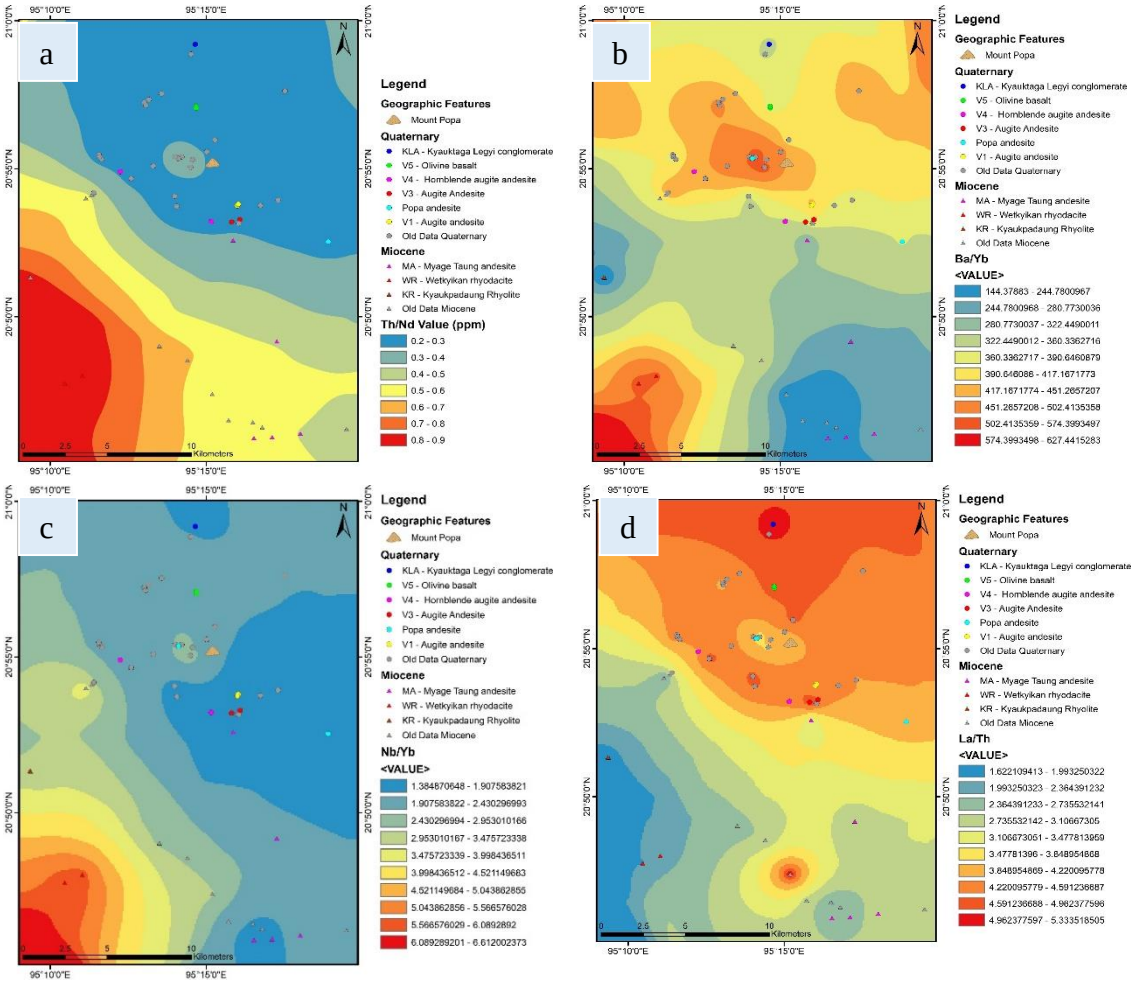

Figure (6) The geochemical contour map of the Mount Popa region in central Myanmar, illustrating the spatial distribution of the trace element ratio (a) Th/Nd, (b) Ba/Yb, (c) Nb/Yb, and (d) La/Th in local volcanic rocks.

A high field strength element (HFSE) that is highly incompatible in most mantle minerals. High Nb concentrations often indicate magmas derived from enriched mantle

sources, such as oceanic island basalts (OIB) or within-plate environments. A heavy rare earth element (HREE) that is more compatible than Nb and readily integrates into minerals like garnet and pyroxene. Yb is used to characterize the depth and source region of the magma. The ratio helps differentiate between subduction-related magmas, which typically have low Nb/Yb values and negative Nb anomalies, and non-subduction magmas (MORB/OIB), which plot along a mantle array with higher values (Fig. 6c). At Mount Popa, the relatively lower La/Th ratios are compared to other parts of the area. The map shows significant variation in La/Th values across the region, ranging from 1.6 to over 5.3. This La/Th map refers to an increase in the concentration of the Light Rare Earth Element (LREE) Lanthanum (La) relative to the Heavy Rare Earth Element (HREE) Yttrium (Yb) within the volcanic rocks. We are discussing about the ratios La/Th observed near the central volcanic edifice is linked to the incorporation of slab-derived fluids or sediments into the mantle wedge. Thorium (Th) is highly incompatible and tends to be enriched in magmas during differentiation processes and can be transported by fluorine-rich fluids. Lanthanum (La) is also an LREE (Fig. 6d).

The Zr/Hf ratios map displays significant spatial variation in the Popa area, ranging from 33.1 to 49.2 across the region (Fig. 7a). The Sr/Y ratio is valuable because the behaviour of Sr and Y is opposite under high-pressure conditions: Sr becomes more incompatible and enters the melt phase, while Y becomes compatible and stays in residual minerals like garnet and amphibole. The map shows a range of Sr/Y values from a low of 0 ppm up to over 60 ppm. The colour scale clearly categorizes the data into eight distinct ranges. The highest ratios (50–60+ ppm, red areas) are concentrated in the central portion of the map, coinciding with the main Mount Popa edifice and the young, Quaternary units (e.g., V5 - Olivine Basalt and various Andesites). High Sr/Y ratios are often indicative of magmas evolving at deeper crustal levels or under higher pressure conditions where plagioclase (Sr host) is unstable and garnet/amphibole (Y host) is stable. The lowest ratios (0–30 ppm, blue/green areas) dominate the southwestern and southeastern corners of the map. These areas correlate strongly with the older, Miocene-aged volcanic units, such as the Kyaukpadaung Rhyolite (KR) and Wetkyikan Rhyodacite (WR). Low ratios suggest magma differentiation occurred at shallower depths (Fig. 7b).

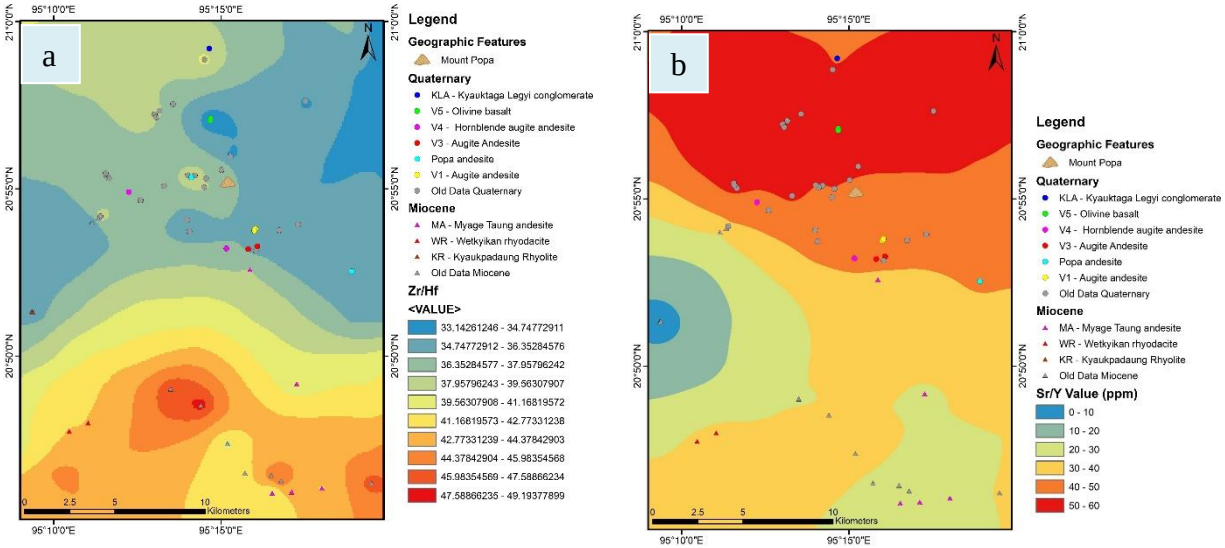

Figure (7) The elemental contour maps of (a) Zr/Hf and (b) Sr/Y

Disscussion

Determining Rock Sequences

The geochemical classification of volcanic rocks defines the particular rock types of older and younger sequences. Found closer to the central and southern parts, these areas have high SiO_2 values (75-90 wt%). The outer, wider regions have lower SiO_2 content (45-60 wt%). Concentrated near the center of the map around the volcanic cone, these areas show high MgO values (4-6 wt%). The outer regions have lower MgO content (0-3 wt%). The main volcanic cone of Mount Popa is composed of basalts, basaltic andesites, and associated pyroclastic deposits in the Quaternary sequence. Older Miocene sequence like rhyodacites and rhyolites are also present.

Petrogenesis

The spatial distribution of Ytterbium (Yb), a rare earth element, around the Mount Popa volcano in Central Myanmar. Yb values are crucial for determining the tectonic setting where volcanic rocks originated. High concentrations of heavy rare earth elements (HREE) like Yb in some felsic rocks can reflect specific melting conditions or sources. The variation in Yb values suggests different degrees of partial melting or crustal contamination in the magma source over time (Wang et al., 2022). Variations in Sr concentrations are critical for geologists to infer petrogenetic processes like magma mixing, crustal assimilation, and fractional crystallization. The range of values across different rock types suggests complex magma chamber dynamics and potential interactions with the surrounding crust, typical of a volcanic arc setting.

The spatial variation in the Th/Nd ratio is a strong indicator of an arc setting, where magmas derived from the subducting plate and mantle wedge (low Th/Nd) ascend and interact variably with the overlying continental lithosphere (high Th/Nd) (Wang et al., 2022). The map illustrates the degree of crustal involvement in the formation of these different volcanic rock types. The spatial distribution suggests that the older Miocene magmas in the south experienced significantly more interaction with the continental crust or were derived from a source highly enriched by sediment components, while the younger Quaternary lavas near Mount Popa are more primitive.

In arc volcanism, a high Ba/Yb ratio is a key indicator of enrichment by slab-derived fluids and/or sediments (Wang et al., 2014) that have chemically modified the mantle source from the subducting Indian Plate beneath the Eurasian Plate. These areas, mostly concentrated around the main volcanic edifice, highlight zones of significant magmatic processing related to the active subduction system. Blue and green zones (Fig. 6b) are suggested lower influence of these slab-derived components and more basic, mantle-derived compositions modified only slightly by fractional crystallization.

High Nb/Yb values, particularly concentrated around the main volcanic edifice in the center of the map, represent a significant finding. Ratios exceeding 4 are often associated with the interaction between different mantle sources or potentially alkaline arc magmatism. Low Nb/Yb values away from the central edifice align more typically with expected arc-like signatures, confirming the general interpretation of the region as an active continental margin volcanic arc (Wang et al., 2022). High ratios suggest more primitive, mantle-derived compositions, while low ratios indicate significant differentiation within the crust (Wang et al., 2022). The map effectively contrasts the geochemical signatures of the older Miocene units and the younger Quaternary units, illustrating the complex evolution of the magmatic system related to the active subduction of the Indian Plate beneath the Eurasian Plate.

Adakitic Affinity: Potential of Cu-Au mineral resources

Adakites are characterized by $SiO_2 \geq 56$ wt %, $Al_2O_3 \geq 15$ wt %, MgO < 3 wt %, $Na_2O \geq 3.5$ wt %, Sr > 400 ppm, Y < 18 ppm, Yb < 1.8 ppm, Cr 30–50 ppm, Ni 20–40 ppm, Mg# (100 x [Mg/(Mg + Fe)] in mole) ~ 51, $Sr/Y \geq 40$, $La/Yb \geq 20$, $K_2O/Na_2O \sim 0.5$, FeO + MgO + MnO + TiO_2 ~ 7 wt % and $^{87}Sr/^{86}Sr < 0.7040$. Such rocks were initially found in convergent margins associated with subduction of young (< 25 Ma) oceanic lithosphere. Adakites have typically been interpreted as products of slab melting in young subduction settings, but several studies have challenged the viability of the slab melting hypothesis for adakitic or adakite-like rocks.

The high Sr/Y ratios along with **high La/Yb ratios** observed in andesite and basalt rock units of the younger volcanic sequence from Mount Popa are a key indicator of an adakitic affinity, a specific geochemical signature with significant implications for the potential formation of porphyry copper-gold (Cu-Au) mineral deposits. Adakitic compositions derived from the deep, water-rich, oxidized magmas to potentially host significant porphyry copper or gold deposits. The geochemical mapping of Mount Popa reveals a classic calc-alkaline magma sequence typical of a continental subduction zone, where primitive mantle-derived magmas have evolved into diverse compositions through fractional crystallization and crustal interaction.

Conclusion

Two distinct volcanic sequences of Mt Popa area were identified by the elemental contour maps. The younger Quaternary volcanic sequence is characterized by higher SiO_2 (60 wt%) and values and lower SiO_2 (45 wt%) values while the older volcanic sequence of the Miocene age possesses higher SiO_2 (90 wt%) and lower SiO_2 (75 wt%) values. According to geochemical trace elements ratio contour map data indicates the older volcanic sequence characterizes from the melting of a mantle wedge that was intensively modified by subducted continental sediments, and the younger volcanic sequence represents the primitive magmas derived from the partial melting of a mantle wedge metasomatized by subduction fluids. Adakitic compositions were determinable in the younger volcanic sequence, revealing the potential of Cu-Au mineralization in the area.

Acknowledgements

We would like to express our thanks to Dr. Myo Min Tun (Acting Rector of East Yangon University), Dr. Aye Aye Ko and Dr. Thidar Aung (Pro-rectors of East Yangon University) for their encouragement to carry out this research.

References

Aung Kin & Kyaw Win. 1968. Preliminary studies of the palaeogeography of Burma during the Cenozoic. Union of Burma J. Sci. & Tech. 1, 241-51.

Aung Kin & Kyaw Win. 1969. Geology and hydrocarbon prospects of the Burma Tertiary grosyncline. Union of Burma J. Sci. & Tech. 2, 53-81.

Bender, F., 1983. Geology of Burma, Stuttgart, Borntraeger, 293 p.

Curray, J.R., Moore, D.G., Lawver, L.A., Emmel, F.G., Raitt, R.W., Henry, M. and Kieckhefer, R., 1979. Tectonics of the Andaman Sea and Burma. In: Geological and geophysical investigation of continental slopes and rises, American Association of Petroleum Geologists Memoris 29 (ed, J. S Watkins, L. Montadert, and P. W Dickerson), Mem, Am, Assoc. Pet. Geol. Vol. 39, pp 189-198.

Chhibber, H.L., 1934. The Geology of Burma. Macmillan, London, 538 p.

Mitchell, A.H.G., McKerrow, W.S., 1975. Analogous evolution of the Burma orogen and the Scottish Caledonides. Geological Society of America Bulletin, 86(3), 305-315.

Sano, T., Tani, K., Yoneda. *et al.* (2022). Petrogenesis of isotopically enriched Quaternary magma with adakitic affinity associated with subduction of old lithosphere beneath central.

Stephenson, D., Marshall, T.R., 1984. The petrology and mineralogy of Mt Popa Volcano and the nature of the Late Cenozoic Burma Volcanic Arc. Journal of the Geological Society of London 141, 747-762.

Streckeisen, A., 1976. To each plutonic rock its proper name. Earth-science reviews, 12(1), 1-33.

Wang, J.G., Wu, F.Y., Tan, X.C., Liu, C.Z., 2014. Magmatic evolution of the Western Myanmar Arc documented by U–Pb and Hf isotopes in detrital zircon. Tectonophysics, 612, 97-105.

Wang, J., Gleeson, M., Smith, W., , L., Lei, Z., Shi, G., & Chen, L. (2022). The factors controlling along-arc and across-arc variations of primitive arc magma compositions: A global perspective. , 10.

Zhang, L. Y. *et al.* (2020). Quaternary volcanism in Myanmar: A record of Indian slab tearing in a transition zone from oceanic to continental subduction. *Geochem. Geophys.*

Optimization of Soxhlet Extraction Parameters and Physicochemical Characterization of Lemongrass Essential Oil

Taw Yan Yan Chant[1], Ei Myat Mon[2], Hsu Wint Htet[3], Soe Myint[4]

Abstract

The lemongrass (*Cymbopogom Citratsus)* is a native plant in Myanmar locally named "Sa-ba-lin". Preliminary phytochemical screening was performed to determine the chemical constituents of the lemongrass sample. After that lemongrass essential oil was extracted with ethanol by using Soxhlet extraction at the different ratios of lemongrass to ethanol, extraction times and extraction temperatures and then the yield percentages were determined. Physico-chemical properties of extracted oils such as pH, acid value, specific gravity, solubility in water, color, odor and peroxide value were then analyzed. The composition of extracted lemongrass essential oil was also analyzed by Fourier-Transform Infrared Spectroscopy (FT-IR) and Gas Chromatography-Mass Spectrometry (GC-MS). The extracted lemongrass essential oil was successfully utilized as an active ingredient in the formulation of chemical-free mosquito repellent sticks. The prepared mosquito repellent stick was evaluated for its baseline odor, burning time, mosquito repellent effectiveness is infested areas, and overall acceptability.

Keywords: Soxhlet Extraction, Phytochemical Screening, Essential Oil, FT-IR, GC-MS

Introduction

Myanmar is a rich country in resources and natural products. Lemongrass (*Cymbopoagon citratus)* is a perennial tall grass which includes rhizomes. Lemongrass is a sub-tropical and tropical herb that is developed in Southeast Asia and Africa. (Sharma,S., et al., 2020). Essential oil is a volatile oil obtained from plants, having the odor and good fragrance. The essential oils have high commercial value and are applicable in various fields like food, pharmaceutical, and cosmetic industries. (Gashaw, 2021). Lemongrass essential oil may be extracted by many different methods like steam distillation, solvent extraction, Soxhlet extraction, hydro-distillation (HD) and microwave-assisted hydro-distillation (MAHD). (Majewska, E., et al. ,2019)

An essential oil is described as a concentrated hydrophobic liquid containing chemical constituent from plants. Essential oils are volatile oils or just the oil of the plant because of it contains the "essence of the plant's fragrance, volatile oil is not actually an oil because it doesn't contain fatty substance. It is essence rich in natural flavors and active ingredients that it secretes the cells of certain parts of plants. A herbal extraction from a botanical material is introduced with a solvent within which number of the raw material components dissolve. Ultimately, the solvent becomes infused with botanical materials that is pulled from the source plant, and this is often called as "extract". The tip product of the extraction is liquid, or the liquid is removed to show the remnants of the botanical into a solid. The solvents can used as preservatives or as agents that help plant cells to interrupt down and release their contents. (Gashaw, 2021).

The aims of this study is to optimize the Soxhlet extraction parameters to obtain the maximum yield of lemongrass essential oil. Specifically, the objectives are to investigate the effect of lemongrass to ethanol ratios, extraction times, and temperatures on the yield percent of essential oil, to characterize the physicochemical properties and chemical constituents of

[1] M.Sc., student, Department of Industrial Chemistry, University of Mandalay.
[2] B.Sc (IC), Department of Industrial Chemistry, University of Mandalay.
[3] M.Sc.,student, Department of Industrial Chemistry, University of Mandalay.
[4] Dr, Professor,Rted., Department of Industrial Chemistry, University of Mandalay.

the oil using FT-IR and GC-MS, and to apply the extracted oil in the production of chemical-free mosquito repellent stick.

Materials and Methods

Selection of Raw Material

Lemongrass was collected from Myit Nge Township, Amarapura District, Mandalay Region. Ethanol was purchased from Mercury Store, 22nd street, between 83rd & 84th street, Aung Myae Thar Zan Township, Mandalay Region.

Types of Lemongrass Sample Preparation

Fresh Sample

The collected lemongrass was cut into 9 inches from the top of the root and washed with tap water for three times to remove dust and soil. The cleaned lemongrass was sliced approximately 2 mm thick.

Sun-dried Sample

The sliced lemongrass was sun-dried for three days. Then the dried lemongrass was ground with a grinder, screened with 100-mesh sieve and the powder was then ready for the Soxhlet extraction.

Air-dried Sample

The sliced lemongrass was air-dried for three days at room temperature and then the dried lemongrass was ground with a grinder, screened with 100-mesh sieve and the powder was then ready for the Soxhlet extraction.

Extraction of Lemongrass Essential Oil

50 g of fresh lemongrass was placed in the extraction thimple. 150 mL of ethanol was added into 500 mL of round-bottomed flask and set in a heating mantle at the temperature of 80°C for 4 hr as shown in Figure 1. Ethanol vapor was condensed in a condenser and dropped down into the extraction thimple as a liquid. Then the ethanol-essential oil mixture was collected to the round-bottomed flask through a siphon arrangement. After that the ethanol-essential oil mixture was separated by simple distillation. The resulting oil was weighed and yield percent was calculated.
The same procedure was carried out for air-dried and sun-dried lemongrass.

Figure 1 Extraction of Essential Oil by Soxhlet Extractor

This procedure was carried out for different ratio of solid to solvent (1:3,1:4, 1:5, 1:6 and 1:7), extraction time (4hr, 5hr, 6hr, 7hr and 8hr) and extraction temperature (60°C, 70°C, 80°C, 90°C and 100°C) .

Analysis of Lemongrass Essential Oil

Determination of pH

The pH of extracted lemongrass essential oil was determined using a HANNA Digital pH Meter (Model: pHep ® 5(HI98128), HANNA Instruments, China).

Determination of Acid Value

The acid value of extracted lemongrass essential oil was determined by the titration method according to the AOAC official method (AOAC 940.28).

Determination of Specific Gravity

The specific gravity of extracted lemongrass essential oil was determined using a specific gravity bottle at room temperature, following the standard procedure of AOAC official method (AOAC 920.212).

Determination of Solubility in Water

The solubility test was performed by adding approximately 6 drops of distilled water to 3 drops of lemongrass essential oil and stirring thoroughly. The phase separation was observed and supplemented by pH measurement to confirm its water-insoluble nature.

Determination of Peroxide Value

The peroxide value of the extracted lemongrass essential oil was determined by the iodometric titration method according to the AOAC official method (AOAC 965.33).

Composition Analysis of Lemongrass Essential Oil

Composition Analysis by FT-IR

The various functional groups in extracted lemongrass essential oil were determined by Fourier-Transform Infrared Spectroscopy (|FT-IR) (IRPrestige-21, Shimadzu, made in Japan).

Composition Analysis by GC-MS

The chemical compositions in extracted lemongrass essential oil were determined by Gas Chromatography-Mass Spectroscopy (GC-MS) (GC-MS_QP2010_Ultra Shimadzu, made in Japan).

Application of Extracted Lemongrass Essential Oil

Preparation of Chemical-Free Mosquito Repellent Stick

200 g of collected neem leaves were dried and ground into a fine powder with a grinder. The obtained neem leaf powder was then screened with 100-mesh sieve and mixed with 50 g of saw dust, 30 g of corn starch and a few drops of lemongrass oil. After that, the mixture was well stirred with a stirrer while water was gradually added to the mixture until a moldable paste was obtained. The paste was then molded into stick shapes by hand. The chemical-free mosquito repellent sticks were allowed to dry completely in the range of temperature between 30°C to 32°C. After drying, the chemical-free mosquito repellent sticks were packed with plastic bag.

Tests for Chemical Free Mosquito Repellent Stick

Determination of Baseline Observation

The odor of the chemical-free mosquito repellent stick was observed from user feedback.

Determination of Effectiveness

The prepared chemical-free mosquito repellent stick was placed in a mosquito-infected area and mosquito activity was measured with and without the stick by the user feedback.

Determination of Burning Time

The burning time of the chemical-free mosquito repellent stick was determined by the user feedback.

Likert Scale Test of Chemical-free Mosquito Repellent Stick

The likert scale test was carried out with 20 well-trained panelists (Age: 20-25) for overall acceptability. For likert scale test, the baseline observation such as odor was determined according to good, satisfactory and smoky. Similarly, the effectiveness and irritability were determined according to Yes or No question type and duration was conducted according to burning time (min) noted from user feedback.

Results and Discussion

The preliminary phytochemical screening of lemongrass is shown in Table 1 and it was found that the presence of flavonoids, glycosides, phenolic compounds, polyphenol, terpenoids and Tannins in lemongrass. Steroids and Saponins are absent in lemongrass. The comparison of three types of lemongrass sample such as fresh, air-dried and sun-dried of lemongrass on the yield percent of lemongrass essential oil. It was found that yield percent of air drying is the highest, 1.58% due to air drying is mostly preferred instead of sun drying. Because sun drying can cause loss of some volatile components and also the fresh lemongrass did not give the effective yield. The results are shown in Table 2. The effect of lemongrass to ethanol ratio on the yield of lemongrass essential oil was observed. Different lemongrass to ethanol ratio such as (1:3), (1:4), (1:5), (1:6) and (1:7) were tested from this observation. It was obvious that the ratio of lemongrass to ethanol (1:4) gives the highest yield percent (2.1%) because this ratio allows for a sufficient volume of solvent to be continuously cycled through the extraction process. While higher ratios offer more solvent for extraction, they can also lead to limitations such as prolonged extraction times, excessive solvent usage, and difficulties in handling large volumes of solvent. The results are shown in Table 3. The effect of extraction time on the yield of lemongrass essential oil was observed. Different extraction times such as 4 hr, 5 hr, 6 hr, 7 hr, and 8 hr were measured to obtain the highest yield percent of lemongrass oil. It was seen that the most suitable condition of the extraction time was 5 hr and the yield percent was 2.56% as shown in Table 4. Longer extraction time do not give higher yield, and diminishing extraction efficiency also shorter extraction time is not effective for continuously extracting. The effect of extraction temperature on the yield of lemongrass essential oil was observed. It was found that the suitable temperature was 80˚C and the yield percent was 2.53% due to it optimizes the solubility of target compounds, enhances extraction kinetics, and minizes the risk of thermal degradation. Higher temperatures might increase extraction rates, as well as can also risk thermal degradation of sensitive compounds in the lemongrass. The results are shown in Table 5. The pH value of lemongrass essential oil was 4.28. The acid value of the lemongrass oil was 4.49 mg KOH/g. The specific gravity of the lemongrass essential oil was 0.89. It was agreed with the acceptable region. A specific gravity of 0.89 provides that lemongrass oil is less dense than water, which is typical for many essential oils. The lemongrass essential oil was insoluble in water. The peroxide value of lemongrass oil was 13.52 meq O_2/ kg. These obtained values shown in Table 6 are in good agreement with reported literature values, ensuring the quality of the extracted lemongrass essential oil.

The functional groups present in the extracted Lemongrass oil are shown in the figure 2. It was observed that the sharp, prominent peak at 1712.79 cm^{-1} is the most significant indicator of quality, as it represents the carbonyl (C=O) stretching vibration of aldehydes. Citral (geranial and neral) is the major constituent of lemongrass oil, and this peak confirms its successful extraction. The strong absorption bands at 2924.09 cm^{-1} corresponds to the C-H stretching of aliphatic chains. This is consistent with the hydrocarbon structure of terpenes like myrcene and limonene, which typically accompany citral in Cymbopogon citratus. The broad peak at 3394.72 cm^{-1} indicates O-H stretching. While this can represent alcohol components like geraniol, it may also suggest a slight moisture content in the extract or the beginning of oxidative processes. The peak at 1651.07 cm^{-1} indicates C=C unsaturation. The presence of both C=O and C=C peaks suggests that the citral remains in its unsaturated aldehyde form, which is essential for its characteristic aroma and antimicrobial properties. The identification of the extracted lemongrass essential oil components was achieved by comparing of their mass spectra and retention times to reference standards. The 20 components identified within the extracted lemongrass essential oil are presented in Figure 3. The primary constituents include Cyclopentane, Methyl- (39.87%), Selina-6-en-4-ol (13.60%), Methyl Isobutyl Ketone (12.17%), Toluene (5.52%), Naphthalene, 1,2,4a,5,8,8a-hexahydro-4,7-di (4.83%). Among the identified constituents, Citral is the most significant bioactive compound in Cymbopogon oil. It is widely recognized for its antimicrobial, antioxidant, and anti-inflammatory properties. Its significant presence enhances the oil's efficacy as a natural insect repellent, making it an ideal active ingredient for chemical-free mosquito repellent stick.

Table 1 Phytochemical Screening of Lemongrass

No	Constituents	Reagent used	Observation	Inference	Results
1	Flavonoids	Small pieces of Mg ribbon,Conc: HCl	Pink color solution	Flavonoids was presence.	+
2	Glycosides	10% lead acetate solution	White precipitate	Glycosides was presence.	+
3	Phenolic compounds	10% ferric chloride solution	Blue-black color solution	Phenolic compounds were presence.	+
4	Polyphenol	1% $FeCl_3$, 1%K_3 [$Fe(CN_6)$]	Dark green precipitate	Polyphenol was presence	+
5	Saponins	Distilled water, shake	No foam	Saponins was absence	_

6	Steroids	Chloroform and concentrated H_2SO_4	No blue or green color solution was appeared	Steroids was absence	_
7	Terpenoids	Chloroform and concentrated H_2SO_4	Red color solution	Terpenoids were presence	+
8	Tannins	10% $FeCl_3$, dilute H_2SO_4	Yellowish brown precipitate	Tannins was presence	+

(+) = presence of constituents, (-) = absence of constituents

Table 2 Comparison of three types of lemongrass sample on the Yield Percent of Lemongrass Essential Oil

Extraction Temperature = 80˚C

Extraction Time = 4 hr

Lemongrass to Ethanol Ratio = 1:3

Weight of Lemongrass Powder = 50 g

Sr No.	Types of Sample	Yield Percent (%)
1	Fresh	0.71%
2	Air drying*	1.58%
3	Sun drying	1.42%

*The most suitable condition

Table 3 Effect of Lemongrass to Ethanol Ratio on the Yield Percent of Lemongrass Essential Oil

Extrtaction Temperature = 80˚C

Extraction Time = 4 hr

Weight of Lemongrass Powder = 50 g

Sr No.	Lemongrass to Ethanol Ratio	Yield Percent (%)
1	1:3	2.06
2	1:4*	2.10
3	1:5	1.58
4	1:6	0.87
5	1:7	0.63

*The most suitable condition

Table 4 Effect of Extraction Time on the Yield Percent of Lemongrass Essential Oil

Extraction Temperature = 80˚C
Lemongrass to Ethanol Ratio = 1:4
Weight of Lemongrass Powder = 50 g

Sr No.	Time (hour)	Yield Percent (%)
1	4	1.86
2	5*	2.66
3	6	2.42
4	7	1.73
5	8	1.52

*The most suitable condition

Table 5 Effect of Extraction Temperature on the Yield Percent of Lemongrass Essential Oil

Extraction Time = 5 hr
Lemongrass to Ethanol Ratio = 1:4
Weight of Lemongrass Powder = 50 g

Sr No.	Temperature (˚C)	Yield Percent (%)
1	60	1.66
2	70	2.48
3	80*	2.53
4	90	2.34
5	100	1.89

*The most suitable condition

Table 6 Physical and Chemical Properties of Lemongrass Essential Oil

No	Parameters	Values	Literature value*
1	pH	4.28	4-6
2	Acid value (mg KOH/g)	4.49	3-10
3	Specific gravity	0.89	0.80-0.903
4	Solubility	Insoluble in water	Insoluble in water
5	Peroxide value (meq O_2/ kg)	13.52	5-15
6	Color	Brown	Dark yellow

* (Source: Edeh, I ., & Okpo, S., O., 2023)

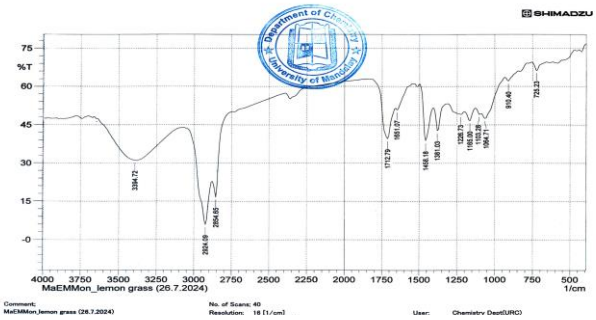

Figure 2 FT-IR Analysis of Extracted Lemongrass Oil

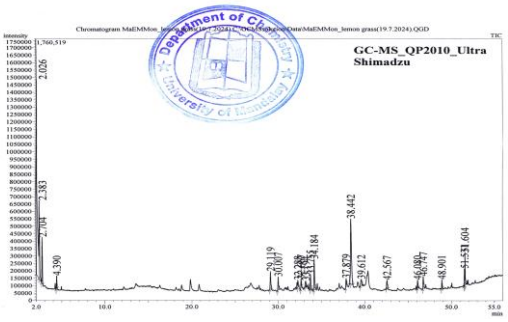

Figure 3 GC-MS Analysis of Extracted Lemongrass Oil

Conclusion

In this study, the extraction conditions were adjusted to achieve the highest efficiency for lemongrass essential oil production. The experimental results indicated that air-drying is the most effective pretreatment, yielding 1.58% of lemongrass essential oil while preserving its volatile potency. The optimal extraction conditions were found to be 80°C for 4 hours with a 1:4 lemongrass to ethanol ratio. While higher solvent ratios are possible, they are not recommended due to increased solvent consumption and extended processing times. Furthermore, the extracted oil was effectively utilized as an active ingredient in the production of mosquito repellent stick. These findings provide a standardized framework for producing chemical-free mosquito repellents using optimized extraction parameters to maximize both yield and quality.

Acknowledgements

We would like to thank Dr Khin Mar Hlaing, Professor and Head of Department of Industrial Chemistry, University of Mandalay, for her kind permission to carry out this work. And then we thank to Dr Mon Mon Maung Professor, Department of Industrial Chemistry, University of Mandalay and Daw Ei Thu Zar Naing, Lecturer, Department of Industrial Chemistry, University of Mandalay, for their comments and suggestions on this work.

References

Edeh, I., & Okpo, S. O. (2023). Determining the physicochemical properties of lemongrass oil extract for suitability in various applications. Journal of Nutrition and Food Processing, 6(2), 1-6.

Gashaw, S., (2021). Extraction, Characterization and Optimization of Sweet Basil (*Ocimom Basilicum*) Essential Oil, Degree of Master, School of Chemical and Bioengineering, ADDIS ABABA University, Ethiopia (Published),1-32.

Majewska. E.,Kozlowska, M.,Sekowska, E.G., Kowalska.D., Tarnowska ,K.,(2019). Lemongrass (Cymbopogon Citratus) Essential Oil: Extraction, Composition, Bioactivity and Uses for Food Preservation A Review: Polish Journal of Food and Nutrition Sciences, 69(4), 327-341.

Sharma, S., Sharma, S., & Soni, K., (2020). Lemongrass: it's uses, medicinal and industrial properties, *JUST AGRICULTURE*, 1,1.